



# Solid-Liquid Two Phase Flow

Sümer M. Peker and Şerife Ş. Helvacı



# **Solid–Liquid Two Phase Flow**

This page intentionally left blank

# Solid–Liquid Two Phase Flow

Sümer M. Peker  
Şerife Ş. Helvacı

*Department of Chemical Engineering,  
Ege University, İzmir, Turkey*

with contributions by

H. Banu Yener  
Berrin İkizler  
Alp Alparslan



ELSEVIER

Amsterdam • Boston • Heidelberg • London • New York • Oxford  
Paris • San Diego • San Francisco • Singapore • Sydney • Tokyo

Elsevier  
Radarweg 29, PO Box 211, 1000 AE Amsterdam, The Netherlands  
Linacre House, Jordan Hill, Oxford OX2 8DP, UK

First edition 2008

Copyright © 2008 Elsevier B.V. All rights reserved

No part of this publication may be reproduced, stored in a retrieval system or transmitted in any form or by any means electronic, mechanical, photocopying, recording or otherwise without the prior written permission of the publisher

Permissions may be sought directly from Elsevier's Science & Technology Rights Department in Oxford, UK: phone (+44) (0) 1865 843830; fax (+44) (0) 1865 853333; email: [permissions@elsevier.com](mailto:permissions@elsevier.com). Alternatively you can submit your request online by visiting the Elsevier web site at <http://www.elsevier.com/locate/permissions>, and selecting *Obtaining permission to use Elsevier material*

#### Notice

No responsibility is assumed by the publisher for any injury and/or damage to persons or property as a matter of products liability, negligence or otherwise, or from any use or operation of any methods, products, instructions or ideas contained in the material herein. Because of rapid advances in the medical sciences, in particular, independent verification of diagnoses and drug dosages should be made

#### Library of Congress Cataloging-in-Publication Data

A catalog record for this book is available from the Library of Congress

#### British Library Cataloguing in Publication Data

A catalogue record for this book is available from the British Library

ISBN: 978-0-444-52237-5

For information on all Elsevier publications  
visit our website at [books.elsevier.com](http://books.elsevier.com)

Printed and bound in The Netherlands

08 09 10 11 12 10 9 8 7 6 5 4 3 2 1

Working together to grow  
libraries in developing countries

[www.elsevier.com](http://www.elsevier.com) | [www.bookaid.org](http://www.bookaid.org) | [www.sabre.org](http://www.sabre.org)

ELSEVIER

BOOK AID  
International

Sabre Foundation

*This book is dedicated to the remembrance of  
İffet and Hayri Peker*

*and*

*to the dear parents  
of all who contributed to the writing of this book.*

This page intentionally left blank

# Preface

Being an ‘underpinning technology’, fluid flow closely reflects and sometimes precedes the developments of the ‘core technologies’ of the time. Only in the second half of 19th century that the term ‘two-phase flow’ was pronounced and added as a chapter to fluid mechanics and unit operations books. At that time, two-phase flow term was used predominantly to denote gas–liquid flow, which is not coincidental, as the leading technologies were nuclear and thermal, addressing mainly vapor–liquid systems. Development of secondary and tertiary oil recovery technologies in 1980s focused the attention of the scientific world on surfactants and liquid–liquid systems incorporating surfactants. The new millennium brought with it a vision toward a change in the scale of processes and dimensions from macroscale to microscale. Along with it came the need for a fundamental understanding of processes in the molecular scale, in place of empirical models.

The subject of solid–liquid two-phase flow is something we live with. Man is acquainted with solid–liquid mixtures since he first made his brick house, and she, her bread. Solid–liquid systems are within us, as our blood, around us in our everyday living and in fundamental technologies such as ceramics, cement, plastics, and grain-based food industries. However, the outlook on solid–liquid systems has changed in the meantime, in parallel with the advancement in the global interests and technologies. The excellent books written on solid–liquid two-phase flow about two decades ago addressed particulate technologies of noncolloidal materials. Reduction in the scale of the particulate materials brought with it inevitable involvement in surface sciences. Inspection of the foresight and research framework contents gives an insight into the powerful role of liquid–solid interactions and two phase flow in the technologies of the future. Some new concepts are expected to be introduced in the future; for example, the ‘solid wall’ was generally meant to be the metal pipe wall, or a particle of a mineral. In the future, it may mean a surfactant bilayer, the cell membrane, or a tissue. Until that time there is a great gap to be covered.

Solid–liquid two-phase flow in its present state of development is a multidisciplinary subject: The size of the particles being processed in the developing technologies has reduced from the order of micrometers to nanometers. Solid–particle interactions in this scale are investigated in the field of colloid and surface science. Interfacial phenomenon is an indispensable counterpart of the rheology of colloidal suspensions. The nonlinear rheological behavior, in turn, affects the fluid dynamics of solid–liquid mixtures. On the other hand particles of noncolloidal dimensions settle under the action of gravity. Transport phenomena together with the averaging techniques are required to analyze the flow problems of settling suspensions. The analysis of the flow of settling slurries is still not free of empiricism brought by the use of drag coefficients and friction factors.

Thirty years of experience of one of the authors in teaching fluid mechanics showed us that a thorough understanding of fluid mechanics is possible only when the mechanism underlying empirical results can be explained on a molecular scale. Models can then be used for the prediction of the phenomena. The present book is written with this understanding. The Solid–Liquid Two Phase Flow book consists mainly of three parts.



The first three chapters handle the flow behavior of micron and submicron particles. The next three chapters are related with particle sizes where Brownian motions are negligible. The final two chapters are related with mixing and separation processes that are an inseparable part of solid–liquid flow. Within this context, a coherent and consistent approach is adopted in interrelating the individual chapters.

Chapter 1 deals with the formation of the particulate phase of colloidal suspensions starting with the molecular interactions. The role of surface forces in the aggregation of primary particles is then taken up. This chapter is fundamental in the understanding of the behavior of solid–liquid suspensions on all concentration levels and frequently referred to in the subsequent chapters.

Chapter 2 gives the fundamentals of non-Newtonian flow together with examples for the visualization of flow in channels of various geometries.

Chapter 3 is founded on the concepts given in Chapters 1 and 2 and extends these concepts to concentrated suspensions where the interactions between particles predominate the flow behavior. The chapter also deals with the effect of viscoelasticity of the suspending medium and the particulate phase and recapitulates these effects in the most complicated of all the flow systems, that of blood flow.

Chapter 4 takes up the motion of primary and aggregated particles. In parallel with the contents of Chapter 1, the motion of porous, fractal aggregates and the particles with a nonuniform density distribution and shape are also taken into consideration. This chapter is closely interrelated with Chapters 6–8.

Chapter 5 reviews mathematical tools such as Eulerian and Lagrangian approaches and averaging techniques that can be used in transport equations in analyzing dispersed systems on microscale and macroscale.

Chapter 6 deals with the flow behavior of settling solids based on the concepts given in Chapters 4 and 5. The flow patterns, concentration distribution of particles in each flow pattern and the pressure losses are taken up in this chapter.

Chapter 7 takes up the introduction of solids into the liquid phase. The interfacial phenomena associated with the dispersion of solids is taken up first followed by the introduction of the solid phase into the liquid phase. Principles of macroscale mixing in agitated vessels, static mixers and micromixers are then given.

Chapter 8 deals with the classification of particles according to their sizes and its extension, separation of solids from the liquid phase. Principles of continuous classification processes in sedimentation, fluidization, and hydrocyclones are given as frequently used macroscale processes. Examples of novel separation processes in the microscale are also introduced in this chapter.

With this content, the book gives an overview of the recent developments in solid–liquid two-phase flow. In writing the book, we tried to reach all the available literature on subjects within the scope of this book, to the best of our knowledge. We looked for experimental work supported by theoretical development or modeling work supported with experiments in the selection of material to be included within the text, whenever possible. We hope that it will be a useful guide to graduate students, researchers and professionals working in the industry who are interested in solid–liquid systems.

We are grateful for the enthusiasm and support given by our graduate students, Alp Alparslan, H. Banu Yener, and Berrin İközler who contributed so much in shaping up

this book. The help of our graduate students Volkan Çakır and Selin Şarkaya are gratefully acknowledged. We deeply appreciate the peaceful working environment provided by Prof. Dr. Süheyda Atalay, the Head of the Chemical Engineering Department during the writing of this book. We are grateful to Prof. Dr. Mustafa Demircioğlu for critical reading of some of the chapters Prof. Dr. Deniz Üner for her helpful suggestions and to Pakize Peker for her help extended in the drawing of the Figures. Suggestions by the academic members of Clinical Biochemistry and Hematology Divisions of Faculty of Medicine of Ege University are highly appreciated.

This book would have never been written if it were not for the positive energy of Sybrand Boer-Iwema, Publishing Editor of Chemistry and Chemical Engineering of Elsevier Science Ltd. to whom we are deeply indebted. We also thank our Editors Joan Anuels and Kristi Green for their helpful suggestions, guidance and support throughout the writing of this book and Dr. M.S. Rajkumar for the careful typesetting. Finally we are thankful to our families and friends who waited patiently for us to finish the writing of this book symbolized as “Chapter 4”.

Sümer M. Peker  
Şerife Ş. Helvacı

This page intentionally left blank

# Contents

<i>Preface</i> .....	vii
<i>List of Contributors</i> .....	xvii

<b>1</b>	<b>The Particulate Phase: A Voyage from the Molecule to the Granule</b> .....	<b>1</b>
1.1	Molecular Interactions .....	1
1.1.1	Attractive forces among molecules .....	4
1.1.2	Repulsive forces among molecules .....	5
1.2	Interactions of Electrical Origin Between Particles .....	6
1.2.1	Attractions between particles .....	6
1.2.2	Ionic interactions between charged surfaces .....	9
1.2.3	The DLVO theory .....	14
1.3	Interaction of Particles due to Non-DLVO Forces .....	17
1.3.1	Forces of entropic origin .....	18
1.3.2	Forces of energetic origin .....	24
1.4	Aggregation of Particles .....	24
1.4.1	Kinetics of aggregation .....	26
1.4.2	Structure of aggregates .....	27
1.4.3	Role of polymers and polyelectrolytes on the coagulation of suspensions ..	32
1.5	Aggregation of Ferromagnetic Particles .....	36
1.5.1	Effect of the direction of the magnetic field on the aggregate structure ...	38
1.5.2	Reversibility of aggregation .....	38
1.5.3	Light-induced aggregation of ferrofluids .....	39
1.6	Formation of Glasses and Gels .....	39
1.6.1	The glassy state .....	40
1.6.2	Formation of gels .....	41
1.7	Self-Assemblies of Surfactants .....	42
1.7.1	Thermodynamics of self-assembly of surfactants .....	45
1.7.2	Self-assemblies in solution .....	46
1.7.3	Self-assemblies on solid surfaces .....	49
1.8	Stabilization of Suspensions .....	50
1.8.1	Stabilization by surfactants .....	50
1.8.2	Stabilization by polymers and polyelectrolytes .....	55
1.8.3	Stabilization by nanoparticles .....	58
1.9	Aggregation in Biological Systems .....	59
1.9.1	Aggregation behavior of blood cells .....	59
1.9.2	Aggregation of microorganisms .....	65
<b>2</b>	<b>Non-Newtonian Behavior of Solid–Liquid Suspensions</b> .....	<b>71</b>
2.1	Viscoelasticity .....	71
2.1.1	Effect of viscoelasticity on flow behavior .....	72
2.1.2	Assessment of viscoelasticity .....	75
2.1.3	Dynamic methods in the assessment of viscoelasticity .....	76

2.2	Rheological Models of Time-Independent Non-Newtonian Fluids . . . . .	86
2.2.1	Models which describe the rheological behavior with a viscosity function . . . . .	87
2.2.2	Models for fluids with a yield stress . . . . .	90
2.2.3	Models for specific end-use . . . . .	92
2.2.4	Significance of the terms used in the constitutive equations . . . . .	94
2.3	Flow of Non-Newtonian Fluids through Cylindrical Pipes . . . . .	95
2.3.1	Laminar flow of non-Newtonian fluids . . . . .	97
2.3.2	Turbulent flow of non-Newtonian fluids . . . . .	121
2.3.3	Flow through sudden expansions and fittings . . . . .	135
2.4	Flow through Noncylindrical Channels. . . . .	141
2.4.1	Flow through annular channels . . . . .	141
2.4.2	Flow through rectangular channels . . . . .	153
2.4.3	Flow in microchannels . . . . .	157
2.4.4	Flow in open channels . . . . .	160
<b>3</b>	<b>Concentrated Suspensions . . . . .</b>	<b>167</b>
3.1	Ordering in Concentrated Suspensions . . . . .	167
3.1.1	Characterization of the particle size . . . . .	169
3.1.2	Phases and states in concentrated suspensions. . . . .	170
3.2	Rheology of Concentrated Hard-Sphere Suspensions . . . . .	174
3.2.1	Colloidal glasses and jamming . . . . .	174
3.2.2	Relative viscosity of colloidal suspensions . . . . .	177
3.2.3	Theoretical models of concentrated suspension viscosity . . . . .	178
3.2.4	Shear behavior of concentrated hard-sphere suspensions. . . . .	188
3.2.5	Viscoelastic behavior of hard-sphere gels . . . . .	193
3.3	Rheology of Soft-Particle Suspensions . . . . .	200
3.3.1	Control of rheology through manipulation of surface forces . . . . .	201
3.3.2	Flow behavior of soft-particle suspensions under steady shear . . . . .	206
3.4	Migration, Slip, and Drag Reduction . . . . .	212
3.4.1	Migration . . . . .	212
3.4.2	Slip flow. . . . .	213
3.4.3	Drag reduction by surfactants and polymers . . . . .	215
3.5	Shear Flow of Viscoelastic Suspensions . . . . .	217
3.5.1	Effect of the viscoelasticity of suspending medium. . . . .	217
3.5.2	Effect of the viscoelasticity of the particles. . . . .	218
3.5.3	Elastic behavior of soft particles with a microstructure . . . . .	221
3.6	Flow of Biological Fluids: Blood Flow in the Circulatory System . . . . .	225
3.6.1	Flow conditions of blood . . . . .	225
3.6.2	The vascular system . . . . .	227
3.6.3	Rheology of blood . . . . .	228
<b>4</b>	<b>Motion of Particles in Fluids . . . . .</b>	<b>245</b>
4.1	Motion of the Fluid Phase . . . . .	245
4.1.1	Creeping flow. . . . .	246
4.1.2	Velocity distribution around a sphere in creeping flow . . . . .	246
4.1.3	Pressure and shear stress distribution on the surface of a sphere . . . . .	251

4.2	Forces Acting on Particles . . . . .	252
4.2.1	Gravitational force . . . . .	253
4.2.2	Buoyancy force . . . . .	253
4.2.3	Magnetic force . . . . .	254
4.2.4	Electrostatic force . . . . .	254
4.2.5	Acoustic force . . . . .	255
4.2.6	Shear force . . . . .	255
4.2.7	Drag force . . . . .	255
4.3	Motion of Spherical Particles . . . . .	257
4.3.1	Correlations for drag coefficient . . . . .	258
4.3.2	Correlations for terminal velocity . . . . .	259
4.4	Motion of Nonuniform Particles . . . . .	263
4.4.1	Motion of nonspherical particles . . . . .	263
4.4.2	Motion of porous aggregates . . . . .	268
4.4.3	Motion of particles with nonuniform density distribution . . . . .	276
4.5	Hindered Settling . . . . .	278
4.5.1	Sedimentation of monodisperse suspensions . . . . .	279
4.5.2	Sedimentation of polydisperse suspensions . . . . .	282
<b>5</b>	<b>Modeling the Flow of Settling Suspensions . . . . .</b>	<b>291</b>
5.1	Basic Concepts in Modeling of Two-Phase Flow . . . . .	291
5.1.1	Eulerian and Lagrangian approaches for single-phase flow . . . . .	291
5.1.2	Eulerian and Lagrangian approaches in solid–liquid suspension flow . . . . .	292
5.2	Averaging Techniques for Model Equations . . . . .	297
5.2.1	Time averaging techniques . . . . .	297
5.2.2	Volume and area averaging techniques . . . . .	298
5.2.3	The ensemble averaging techniques . . . . .	299
5.3	Mathematical Requirements for Averaging Transport Equations . . . . .	300
5.4	Basic Equations for Solid–Liquid Suspension Flows . . . . .	303
5.5	Ensemble Averaged Equations for Two-Fluid Model . . . . .	305
5.5.1	Ensemble averaging of the generalized equation . . . . .	305
5.5.2	Ensemble averaged continuity equations . . . . .	307
5.5.3	Ensemble averaged momentum equations . . . . .	308
5.6	Eulerian Single Fluid Model: Mixture Model . . . . .	312
5.6.1	Mixture model in laminar flow . . . . .	312
5.6.2	Mixture model in turbulent flow . . . . .	314
5.7	Mixture Model on Macroscale: General Balance Equations . . . . .	315
5.7.1	Total mass balance . . . . .	316
5.7.2	Linear momentum balance . . . . .	320
5.7.3	Total mechanical energy balance . . . . .	322
5.8	Drift Flux Model . . . . .	324
<b>6</b>	<b>Flow of Settling Slurries . . . . .</b>	<b>329</b>
6.1	Flow Patterns and Flow Regimes . . . . .	329
6.1.1	Flow patterns . . . . .	330
6.1.2	Particle support mechanisms in the flow of settling slurries . . . . .	332
6.1.3	Parameters describing the flow of slurries . . . . .	332

6.2	General Balance Equations for Flow of Slurries through Pipes . . . . .	334
6.2.1	Fully suspended flow . . . . .	335
6.2.2	Two-layer flow . . . . .	336
6.2.3	Three-layer flow . . . . .	342
6.3	Dispersion Mechanisms of Solid Particles . . . . .	346
6.3.1	Shear-induced particle migration. . . . .	347
6.3.2	Flow-induced particle dispersion: turbulent diffusion . . . . .	348
6.3.3	Particle-dispersion mechanisms in settling suspensions . . . . .	349
6.4	Mechanism of Frictional Losses . . . . .	353
6.4.1	Frictional losses due to viscous flow . . . . .	353
6.4.2	Frictional losses due to particle–pipe wall interactions . . . . .	354
6.5	Pressure Losses in Pipe Flow . . . . .	358
6.5.1	Pressure losses in horizontal flow of suspensions . . . . .	360
6.5.2	Pressure losses in vertical flow of suspensions . . . . .	364
6.5.3	Pressure losses in flow through inclined pipes . . . . .	365
6.6	Particle Concentration Distributions in Different Flow Patterns . . . . .	366
6.6.1	Effect of particle size on flow pattern . . . . .	366
6.6.2	Effect of flow velocity on flow pattern . . . . .	369
6.6.3	Effect of fine particles on flow pattern . . . . .	369
6.7	Deposition Velocity . . . . .	371
6.8	Settling Flow of Solid–Liquid Suspensions with Stationary Bed . . . . .	372
6.8.1	Pressure drop correlations . . . . .	373
6.8.2	Limit deposition velocity correlations . . . . .	373
6.9	Flow Pattern Maps in Pipe Flow . . . . .	376
<b>7</b>	<b>Mixing in Solid–Liquid Systems . . . . .</b>	<b>385</b>
7.1	The Role of Surface Tension in Wetting of Solids . . . . .	385
7.1.1	Phenomena involving surface and interfacial tensions . . . . .	385
7.1.2	Surface tension related phenomena in particulate systems . . . . .	390
7.2	Discharge of Solids into Liquids . . . . .	394
7.2.1	Discharge of solid–liquid suspensions from hoppers . . . . .	394
7.2.2	Dispersion of solids upon introduction into the liquid . . . . .	397
7.3	Mechanisms of Mixing . . . . .	400
7.3.1	Mixing through turbulent convection . . . . .	401
7.3.2	Mixing through lamination . . . . .	401
7.3.3	Mixing by chaotic advection . . . . .	402
7.3.4	Quantification of mixing efficiency . . . . .	402
7.4	Mechanically Agitated Mixers . . . . .	403
7.4.1	General concepts in the design of mixers . . . . .	403
7.4.2	Dispersion of solids in mixers . . . . .	407
7.4.3	Power consumption in mixers . . . . .	412
7.4.4	Scale-up in agitated mixers . . . . .	420
7.5	Static Mixers . . . . .	424
7.6	Mixing of Concentrated Suspensions . . . . .	426
7.6.1	Kneading . . . . .	426
7.6.2	Extrusion . . . . .	428
7.7	Mixing in the Microscale . . . . .	431
7.7.1	Passive mixing . . . . .	432
7.7.2	Active mixing . . . . .	433

<b>8</b>	<b>Classification and Separation of Solid–Liquid Systems</b>	<b>439</b>
8.1	Classification and Separation in a Gravitational Field	439
8.1.1	Sedimentation as a separation process	440
8.1.2	Fluidization as a separation process	443
8.1.3	Classification in hydrocyclones	448
8.2	Separation in a Magnetic Field	457
8.2.1	Separation of magnetic particle	459
8.2.2	Separation of nonmagnetic particles in a magnetic medium	459
8.3	Separations in the Microscale	459
8.3.1	Field flow fractionation techniques	460
8.3.2	Separations in flow through microfluidic bifurcations	460
8.3.3	Ultrasonic separations	461
8.3.4	Separations based on magnetic properties	465
8.3.5	Separations based on electrical properties	466
<i>Appendix A Mathematical Operations</i>		471
<i>Appendix B Population Balances</i>		493
<i>Appendix C Tables for Use in Plug Flow in an Annulus</i>		503
<i>Index</i>		509



This page intentionally left blank

## List of Contributors

*Sümer M. Peker*

Ege University, Faculty of Engineering,  
Chemical Engineering Department, 35 100 Bornova,  
Izmir, Turkey. E-mail: [sumer.peker@ege.edu.tr](mailto:sumer.peker@ege.edu.tr)

*Serife Ş. Helvacı*

Ege University, Faculty of Engineering,  
Chemical Engineering Department, 35 100 Bornova,  
Izmir, Turkey. E-mail: [serife.helvaci@ege.edu.tr](mailto:serife.helvaci@ege.edu.tr)

This page intentionally left blank

# – 1 –

## The Particulate Phase: A Voyage from the Molecule to the Granule

---

Flow behavior of solid–liquid two-phase flow systems depends on the properties of the dispersed solid phase, the continuous liquid phase that suspends the solids and the interactions between the two phases. This chapter is an overview of molecular interactions leading up to the formation of solid particle aggregates and surface forces responsible for the stability of suspensions.

### 1.1 MOLECULAR INTERACTIONS

Molecules of all matter at a temperature above absolute zero possess internal energy expressed as motion in the form of rotation, vibration, and translation, provided there is enough space to permit these motions. Because of the random translatory motion, the molecules frequently collide with each other. The statistical average distance traveled between two collisions is called the mean free path. When the energies of the colliding molecules are not “high enough” to end-up in a coalition, the original molecules keep colliding with other molecules on their paths, their energies being redistributed after each collision. This random motion, called Brownian motion, is expressed as thermal energy in the terms of  $k_B T$ , where  $k_B$  is the Boltzmann constant [ $1.381 \times 10^{-23} \text{ JK}^{-1}$ ] and  $T$ , the absolute temperature in [K]. All the molecules would be free and would move randomly within the medium, if thermal energy or internal energy were the only sources of energy the molecules possess. If there is any aggregation or some kind of an order between the molecules, it is due to the attractive forces existing between the molecules. For the attractive forces to be effective, the potential energy they generate should be equal or greater in magnitude than the thermal energy. The thermal energy at 25°C amounts to  $1.381 \times 10^{-23} \times 298 = 4.12 \times 10^{-21} \text{ J}$ , so bonds with energies less than this are bound to break up at 25°C.

All the interactions between atoms and simple molecules are essentially electrostatic in origin. This stems up from the structure of the atom: A positively charged nucleus surrounded by a negatively charged electron cloud. The electron density in between atoms of equal electronegativity, making up a molecule is symmetrical. If there is a deficiency of electrons in this cloud in comparison with a neutral atom or a molecule, the molecule

attains a positive charge, called a cation. If, on the other hand, there is a surplus of electrons, the molecule becomes negatively charged and is called an anion. Two similarly charged ions repel and dissimilar ions attract each other. The ionic charge  $Q$  of the ionic molecule is the product of the number of missing/surplus electrons, the valence  $z_i$ , and the charge of a single electron  $e$  in Coulombs,  $e = 1.602 \times 10^{-19} \text{ C}$ ,  $Q = z_i e$ . Due to the symmetry of the electron cloud, the electric field,  $E$ , around an ion is considered to have spherical symmetry and to decrease with the square of the radial distance  $r$ :

$$E = \frac{Q / \epsilon_0 \epsilon_r}{4\pi r^2} = \frac{z_i e / \epsilon_0 \epsilon_r}{4\pi r^2} \quad (1.1)$$

Charge alone does not determine the electric field; the electrical permittivity of vacuum,  $\epsilon_0$  [ $\epsilon_0 = 8.854 \times 10^{-12} \text{ C}^2 \text{ J}^{-1} \text{ m}^{-1}$ ], and the relative permittivity with respect to vacuum of the medium in which the charged ions exist,  $\epsilon_r$ , determine the effective charge around which the field is set up. If an ion of charge  $Q_2$  is brought into the electrical field of another ion,  $E$ , it acquires potential energy given by

$$U_{\text{ion-ion}} = \frac{Q_1 Q_2}{4\pi \epsilon_0 \epsilon_r r} = \frac{z_1 z_2 e^2}{4\pi \epsilon_0 \epsilon_r r} \quad (1.2)$$

The potential energy  $U$  is positive if the charges are similar, and negative if they are not. The interaction force,  $F$ , is the negative of the derivative of the potential energy with respect to  $r$ , the distance between the central  $Q_1$  and the incoming  $Q_2$  charges

$$F = -\nabla U_{\text{ion-ion}} = \frac{Q_1 Q_2}{4\pi \epsilon_0 \epsilon_r r^2} = \frac{z_1 z_2 e^2}{4\pi \epsilon_0 \epsilon_r r^2} \quad (1.3)$$

If the charges  $Q_1$  and  $Q_2$  are similar, the ions repel each other, both the potential and the force being positive. Unlike charges attract each other and are denoted by a negative force and potential. Since this force of attraction or repulsion is much larger than  $k_B T$ , the interaction is not affected by random molecular motions in the temperature range of solutions or suspensions under ordinary conditions.

The basic assumption of these equations is that the ions act like point sources and do not disturb the electron density distribution of each other. When the molecules are composed of atoms with different electronegativity, the electron distribution departs from symmetrical in favor of the more electronegative component. The electronegative atom acquires a slightly negative charge, while the other atom or group of atoms, a slightly positive charge: The molecule acts like a rod with different charges at either end. When such a dipole enters into the electric field of an ion, the ion attracts the end carrying the opposite charge and repels the other end. This dual interaction causes the dipole to rotate within the electric field of the ion to orient itself with respect to the other ion and monoatom-diatom transition takes place. The charge on a dipole is denoted by the dipole moment,  $m$ , the product of the charge on one of the poles and the length  $l$  of the molecule in between the two charged ends.

$$m = Q^+ l = Q^- l \quad (1.4)$$

Even though the origin of the charge is not due to deficiency or excess of electrons, dipoles also interact like ions with the charge  $Q_i$  replaced by the dipole moment,  $m$  (Stokes and Evans, 1997). In this way, the potential energy between a dipole and an ion, a distance  $r$  apart is given by

$$U_{\text{ion-dip}} = -\frac{Q_i m \cos \theta}{4\pi\epsilon_0\epsilon_r r^2} \quad (1.5)$$

$\theta$  is the angle between the axis of the dipole and the line joining the centers of the ion and the dipole.  $\cos \theta$  term takes into account the interaction of both the positive and the negative ends of the dipole with the ion. For a cation,  $z_i$  is positive and the maximum interactions (attraction and repulsion in sequence) occur when the angle is a multiple of  $\pi$  radians and the axis of the dipole is congruent with the line joining the centers. For this same reason, a sphere of dipoles oriented radially toward the ion surrounds an ion in solution in a polar compound, such as water.

Dipoles also interact with each other. Since the potential created by the dipoles is not as strong as that of the ions, the dipoles are free to rotate. Hence, the potential energy between the dipoles is a function of distance  $r$  between their centers, as well as the angles in  $\theta$  and  $\phi$  directions between their axes in spherical coordinates. Through trigonometric calculations, the potential between the two dipoles is obtained with an equation similar to eq. (1.5)

$$U(r, \theta_1, \theta_2, \phi) = -\frac{m_1 m_2}{4\pi\epsilon_0\epsilon_r r^3} (2 \cos \theta_1 \cos \theta_2 - \sin \theta_1 \sin \theta_2 \cos \phi) \quad (1.6)$$

To take into account all possible orientations of the dipoles, the angle average of the potential energy is taken through the use of Boltzmann distribution

$$x_i = e^{-(U_i/k_B T)} \quad (1.7)$$

which gives the fraction of the ions  $x_i$  that possess a given potential energy,  $U_i$ , to the disturbing thermal energy,  $k_B T$ , ratio. The free rotation of the dipoles signifies that their thermal energy is greater than their interaction potential,  $U(r, \theta, \phi) < k_B T$ . The exponential term can then be expanded and integrated

$$U(r) = \frac{\int U(r, \theta, \phi) \exp(-U(r, \theta, \phi)/k_B T) \sin \theta d\theta d\phi}{\int_0^{2\pi} \int_0^{2\pi} \sin \theta d\theta d\phi} \quad (1.8)$$

to give the angle-averaged potential between two dipoles, known as the *Keesom* interaction

$$U_{\text{dip-dip}} = -\frac{2m_1^2 m_2^2}{3(4\pi\epsilon_0\epsilon_r)^2 k_B T r^6} \text{ for } k_B T > \frac{m_1 m_2}{4\pi\epsilon_0\epsilon_r r^3} \quad (1.9)$$

This angle-averaged interaction potential between two dipoles is always attractive (due to the negative sign) and is the only interaction dependent on temperature, decreasing as the temperature increases.

Dipoles, when close enough to another molecule, perturb their electronic cloud and cause a redistribution of electrons opposite to their own. This redistribution shifts the charge center of the molecule from the positively charged nucleus, generating a restoring force, analogous to Hooke's law, which counteracts the attractive force of the electric field of the dipole. The total potential created between the permanent and induced dipoles is the sum of the attractive and restoring forces, given in terms of polarization coefficient,  $\alpha$

$$U = -\frac{1}{2}\alpha E^2 = -\frac{1}{2}(\alpha E)(E) \quad (1.10)$$

as one half the potential between a dipole and an ion of electric fields  $\alpha E$  and  $E$ , respectively. The full potential energy cannot be used in the case of induced dipoles because half the potential energy is expended during the inducement, in the displacement of the electron cloud from its original distribution. The electric field to which the polarized molecule is subjected to is dependent on the angle between the permanent and induced dipole,  $\theta$ , and the distance between their centers,  $r$

$$E(r, \theta) = \frac{m(1 + 3\cos^2 \theta)^{1/2}}{4\pi\epsilon_0\epsilon_r r^3} \quad (1.11)$$

where  $m$  is the dipole moment of the polar molecule. Replacing this expression for  $E$  in eq. (1.10) and angle averaging the resultant equation gives

$$U_{\text{dip-ind dip}} = -\frac{m_1^2\alpha_2 + m_2^2\alpha_1}{(4\pi\epsilon_0\epsilon_r)^2 r^6} \quad (1.12)$$

where the subscripts 1 and 2 refer to permanent and induced dipoles. This equation is known as the *Debye* interaction potential which is always attractive.

The induced dipole in turn, induces a dipole in an adjacent molecule. The interaction potential derived theoretically from the Schrödinger equation is known as the *London* potential

$$U_{\text{ind dip-ind dip}} = -\frac{3}{2} \frac{\alpha_1\alpha_2}{(4\pi\epsilon_0\epsilon_r)^2 r^6} \left( \frac{\hbar v_1 v_2}{v_1 + v_2} \right) \quad (1.13)$$

In this equation,  $\hbar$  is the Planck constant [ $\hbar = 6.626 \times 10^{-34}$  Jsec],  $v$  the characteristic vibrational frequency of electrons [ $\text{sec}^{-1}$ ], and their product  $\hbar v$  the ionization energy of the atoms.

### 1.1.1 Attractive forces among molecules

Attractive forces among molecules are classically grouped as electrostatic or electrodynamic in origin. Ions with opposing electrostatic charges create a potential given by eq. (1.2) and

attract each other with a force given by eq. (1.3). The attractions between ions and permanent dipoles also belong to this group, the potential or the free energy of interaction given by eq. (1.5). It should be noted that the free energy of interaction of ion–ion interactions vary inversely with the distance in between the ions while that of ion–dipole interactions vary with the square of the distance. This means that these forces are effective over long distances of separation of the molecules.

### *van der Waals attractions*

The interaction potential between permanent dipoles, the *Keesom* equation (eq. (1.9)), between permanent and induced dipoles, the *Debye* equation (eq. (1.12)), and between induced dipoles, *London* equation (eq. (1.13)) are collectively known as *van der Waals attractions*. These forces originate from the asymmetry in the distribution of electrons within the molecules and are created by induction of a polar or an induced-polar molecule in close proximity in the process of constant rotational and translational motion. So, these forces are dynamic in origin and are short-range attractive forces as shown by the  $r^{-6}$  dependence in each case. Keesom interactions are effective in the alignment of polar molecules; on the other hand, the London interactions are effective among all types of molecules and mainly responsible for the attraction of particles as will be shown in the next section.

## 1.1.2 Repulsive forces among molecules

Like attractive forces, repulsive forces also arise between ions carrying similar charges and dipoles the magnitudes of which are calculated with the same equations. Due to the similarity of the charges, both the force and the potential energy are always positive.

Apart from these forces of electrostatic origin, repulsion can also arise due to overlapping of electron clouds, at extremely short distances. The potential energy that arises due to repulsive interaction of electron clouds are given by the general expression

$$U(r) = \left( \frac{\sigma}{r} \right)^n \quad (1.14)$$

$\sigma$  is related to the size of the molecule defined by the very short-range steric repulsive forces that determine the identity of the molecule by setting the limits of closest approach.  $r$  is the distance between the “closest-approach boundaries” of the atoms. In the hard-sphere concept of the molecule, the exponent  $n$  is taken as  $n = \infty$ . In such a case, the potential energy is either zero, when  $r \gg 0$ , or goes to infinity when  $r \ll 0$ . Generally, the electron clouds show a limited flexibility, so the Lennard–Jones potential is the most widely used potential energy expression

$$U(r) = -\frac{A_{LJ}}{r^6} + \frac{B_{LJ}}{r^{12}} \quad (1.15)$$

The first term on the right hand side (RHS) that shows a 6th power variation with distance separating the molecules signifies the three van der Waals attractions and the second term,



with the 12th power variation signifies the repulsion due to the close approach of the electron clouds.  $A_{LJ}$  and  $B_{LJ}$  are adjustable constants related with the size of the molecules.

## 1.2 INTERACTIONS OF ELECTRICAL ORIGIN BETWEEN PARTICLES

The same forces that exist between a pair of molecules also exist between a great number of molecules aggregated in the form of a particle. The interactions may be attractive based on electronic distributions (van der Waals) or repulsive due to ionic distributions (double layer repulsions).

### 1.2.1 Attractions between particles

If the particles are not ionic, and have a uniform distribution of molecules, one of the components of the van der Waals forces will be effective in forming attractive forces between the particles. Assuming each molecule in one particle to interact with a molecule on another particle and that, these interactions can be added pair wise, attractive forces between two bodies can be calculated. In the original derivation of Hamaker (1937), the number distribution of molecules in a differential volume element is taken and the potential energy between the molecules of the control element and a single molecule is calculated (Stokes and Evans, 1997). The general form of the van der Waals interaction potential can be written as

$$U(r) = -\frac{A_{LJ}}{r^6} \quad (1.16)$$

All the molecules in the differential volume  $dv$ ,  $(\rho N_A/M)dv$ , will interact with this single molecule, that is situated at a normal distance along the axis in cylindrical coordinates, causing the evolution of a potential

$$U(h) = -\int_v A_{LJ} \left( \frac{\rho N_A}{M} \right) dv = -A_{LJ} \left( \frac{\rho N_A}{M} \right) \left( \frac{\pi}{6h^3} \right) \quad (1.17)$$

where  $\rho$  is the density of the particle,  $N_A$  the Avogadro number [ $6.023 \times 10^{23}$  molecules per mol], and  $M$  the molecular weight. If this single molecule is one of the many in another particle, then the potential due to all the molecules per unit area [ $J m^{-2}$ ] facing the first particle  $((\rho N_A/M)dh)$  would be

$$U(h) = -\int_h^\infty A_{LJ} \left( \frac{\rho N_A}{M} \right)^2 \frac{\pi}{6} \frac{dh}{h^3} = -A_{LJ} \left( \frac{\rho N_A}{M} \right)^2 \frac{\pi}{12h^2} \quad (1.18)$$

The integration limits in eq. (1.18) is the distance between the parallel plates,  $h$ , and the other end of the planar particle that is at a very large distance approaching infinity, in terms of the attraction range. The result turns out to be inversely proportional to the square of the distance separating the particles, which can be classified as long-range interaction. The coefficient of the interaction potential  $A_{LJ}$  and the term related with the number of

molecules are collected in a single parameter, which is a material constant called the *Hamaker constant*,  $H$ .

$$H_{11} = A_{LJ} \left( \frac{\rho N_A \pi}{M} \right)^2 \quad (1.19)$$

The attractive interaction potential between two flat plates in vacuum is given as

$$U(h) = -\frac{H_{11}}{12\pi h^2} \quad (1.20)$$

As only the particle–particle interactions are considered in the derivation, it is denoted by the symbol,  $H_{11}$ , where the subscript 1 indicates that the two particles are made of the same material. The most general attractive force effective between all types of molecules is the dispersion or the London forces between two induced dipoles. For particles composed of identical particles, eq. (1.13) is reduced to

$$U(r) = -\frac{3}{4} \frac{\alpha^2 \hbar \nu}{(4\pi\epsilon_0)^2 r^6} \quad (1.21)$$

and the Hamaker constant for the two particles interacting in vacuum becomes

$$H_{11} = \frac{3}{4} \left( \frac{\rho N_A \pi}{M} \right)^2 \frac{\alpha^2 \hbar \nu}{(4\pi\epsilon_0)^2} \quad (1.22)$$

If the particles are suspended in a liquid medium, the attractive potential is greatly reduced due to the intervening medium. Denoting the intervening liquid with the subscript 2, the Hamaker constant would be denoted by  $H_{121}$ , approximated as

$$H_{121} = (H_{11}^{1/2} - H_{22}^{1/2})^2 \quad (1.23)$$

Water as the most frequently suspending agent has a Hamaker constant of  $H_{22} = 3.7 \times 10^{-20}$  J. If the two particles are not identical in properties, the interactions between the first particle 1 and the medium 2, as well as the second particle 3 and the medium 2 should be taken into account, approximated by the expression

$$H_{123} = (H_{11}^{1/2} - H_{22}^{1/2})(H_{33}^{1/2} - H_{22}^{1/2}) \quad (1.24)$$

Eq. (1.23) is always positive due to the squared term, so unless the Hamaker constant in vacuum of the suspending medium is equal to that of the particles, the two particles will always attract each other. Naturally when  $H_{121}$  equals zero, the particles will be inert toward each other. When two dissimilar particles are under consideration, the value of the Hamaker constant of the medium becomes important: If  $H_{22}$  is in between  $H_{11}$  and  $H_{33}$  in value then  $H_{123}$  in eq. (1.24) will be negative and the particles will repel each other leading onto a stable suspension.

An expression similar to eq. (1.20) for planar particles is derived for spherical particles by using the Derjaguin approximation (Stokes and Evans, 1997), assuming the surface of the sphere is made up of an infinite number of planar steps. Applying the equation for planar surfaces to each vertical surface of the step and integrating over the surface of the particle, gives the interaction potential between two spheres of equal radii  $R$  as

$$U(h)_{\text{sphere}} = -\frac{H_{11}R}{12h}, \quad R \gg h \quad (1.25)$$

and for spheres of unequal radii  $R_1$  and  $R_3$  at a distance  $h$  much smaller than the radius of either particle

$$U(h) = -\frac{H_{13}R_1R_3}{6h(R_1 + R_3)} \quad (1.26)$$

In both cases, the potential changes inversely with the distance separating the spherical particles and the attractive force, equal to the derivative of the potential, changes with the square of the distance.

If the particles were suspended in a liquid medium, eq. (1.20) for flat plates, eqs. (1.25) and (1.26) for spheres would be

$$U(h)_{\text{plate}} = -\frac{H_{121}}{12\pi h^2} \quad (1.20a)$$

$$U(h)_{\text{sphere}} = -\frac{H_{121}R}{12h}, \quad R \gg h \quad (1.25a)$$

$$U(h)_{\text{sphere}} = -\frac{H_{123}R_1R_3}{6h(R_1 + R_3)} \quad (1.26a)$$

In the above derivation originally made by Hamaker in 1937, the sum of all the pair-wise interactions among the molecules or atoms in a particle were taken into account. Hamaker constant is a material constant of the interacting particles and the medium within which they are suspended in terms of polarizabilities and number densities of the molecules making up the particles, as given in eq. (1.22). In the more rigorous treatment of Lifshitz (1956), instead of being considered in terms of their component molecules, the particles are taken as a continuum with given dielectric properties. van der Waals interaction is the result of fluctuations in the electromagnetic field between the two particles, modified by the intervening suspension medium. Hamaker constant can be estimated from knowledge of frequency-dependent dielectric properties of the interacting materials together with the intervening medium and the geometry of the particles. Accuracy of the Hamaker constant is related to the precision and accuracy of dielectric spectra and mathematical representation of the data. Bergstrom (1997) has critically evaluated the available optical data in the

**Table 1.1**

Hamaker constants

Material	Crystal structure	Hamaker constant $\times 10^{20}$ J	
		In vacuum	In water
$\alpha$ -Al <sub>2</sub> O <sub>3</sub>	Hexagonal	15.2	3.67
PbS	Cubic	8.17	4.98
SiO <sub>2</sub> (quartz)	Trigonal	8.86	1.02
SiO <sub>2</sub> (silica)	Amorphous	6.50	0.46
TiO <sub>2</sub>	Tetragonal	15.3	5.35
ZnO	Hexagonal	9.21	1.89
ZnS	Cubic	15.2	4.80
ZnS	Hexagonal	17.2	5.74

*Source:* With permission of Elsevier Science Ltd.

literature and calculated the Hamaker constant by the full Lifshitz method. Table 1.1 is abridged from the results of Bergstrom.

### 1.2.2 Ionic interactions between charged surfaces

Particle surfaces in a liquid medium acquire surface charge either through dissolution and diffusion of ions of the particle from the surface into the solution leaving the particle surfaces in an ionized state, or through adsorption of ions from solution onto the particle surface. If in addition, the suspension medium is an electrolyte solution, then ions of the solution will interact with the ions on the surface of the particle. If the ionization or adsorption sites are uniformly distributed over the surface, the charge concentration on the particle surface can be quantified in terms of surface charge density,  $\sigma_0$  [Cm<sup>-2</sup>]. In the solution side of the solid/liquid interface, ions of opposite charge will accumulate nearby the surface to maintain electrical neutrality. The charge density in solution ( $z_i e C_{iN}$ ), will increase as the particle surface is approached. A potential,  $\Phi$ , will then be created between the surface of the particles and the ions in solution that have accumulated near the particle. The charge density in solution is proportional to the potential gradient, in accordance with the Poisson equation

$$\nabla^2 \Phi = - \frac{1}{\epsilon_r \epsilon_0} \sum_i z_i e C_{iN} \quad (1.27)$$

where  $C_{iN}$  is the number concentration. The proportionality constant, the inverse of the permittivity or the dielectric constant of the solution,  $\epsilon_r \epsilon_0$ , takes into account the van der Waals interactions among the molecules of the solution, so that only the ions are taken into consideration. The concentration term  $C_{iN}$  in the expression giving the charge density of the solution is the number of ions per unit volume [m<sup>-3</sup>] of the solution. These ions have sufficient potential energy to overcome the dispersive thermal or internal energy ( $k_B T$ ) to

gather around the particle, instead of being uniformly distributed in random in the solution. So the Boltzmann distribution, analogous to eq. (1.7) can be used to relate the fraction of ions in solution with the potential created by the particle  $\Phi$

$$x_i = \frac{C_{iN}}{C_{iN}^0} = \exp\left(-\frac{z_i e \Phi}{k_B T}\right) \quad (1.28)$$

where  $C_{iN}^0$  is the concentration when there is no potential ( $\Phi = 0$ ). Replacing eq. (1.28) into eq. (1.27), Poisson–Boltzmann equation is obtained which relates the potential gradient with the concentration of ions in solution.

$$\nabla^2 \Phi = -\frac{1}{\epsilon_r \epsilon_0} \sum_i z_i e C_{iN}^0 \exp\left(-\frac{z_i e \Phi}{k_B T}\right) \quad (1.29)$$

Assuming the particles as flat flakes with surfaces exposed to the solution in one direction only, eq. (1.29) is solved to give the Gouy–Chapman relation, valid for symmetrical electrolytes containing equal numbers of cations and anions in a molecule (Stokes and Evans, 1997)

$$\Phi(h) = \frac{2k_B T}{ze} \ln\left(\frac{1 + \Gamma_0 \exp(-\kappa h)}{1 - \Gamma_0 \exp(-\kappa h)}\right) \quad (1.30)$$

The potential  $\Phi$  is given implicitly in terms of the Boltzmann distribution in the  $\Gamma_0$  term as

$$\Gamma_0 = \frac{\exp(ze\Phi_0 / 2k_B T) - 1}{\exp(ze\Phi_0 / 2k_B T) + 1} \quad (1.31)$$

In eq. (1.30),  $h$  is the distance from the particle surface and  $\kappa$  the gradient of the potential near the surface. From dimensional analysis,  $\kappa$  must have the dimension of inverse length [ $L^{-1}$ ].  $\kappa^{-1}$  is called the *Debye screening length*.

It should be noted that eqs. (1.30) and (1.31) relate the potential  $\Phi$  created by the charged particle to the charge distribution in the solution. On the ground that electrical neutrality should be maintained within the particulate suspension, the total charge on the particle surfaces should be neutralized by the opposite charged ions in the solution. Stokes and Evans (1997) related the potential  $\Phi$  to the charge density on the surface of the particle,  $\sigma_0$ , using the Poisson–Boltzmann relation

$$\sigma_0 = (2\epsilon_r \epsilon_0 k_B T C_{iN}^0)^{1/2} \left[ \exp\left(\frac{z_i e \Phi_0}{2k_B T}\right) - \exp\left(-\frac{z_i e \Phi_0}{2k_B T}\right) \right] \quad (1.32)$$

The concepts and the effect of different parameters introduced so far are illustrated schematically in Figure 1.1. The potential decreases steeply with distance from the solid surface as the ionic concentration increases as shown in the left hand side (LHS) of the plate corresponding to Figure 1.1(a), in accordance with eq. (1.29). The effect of the

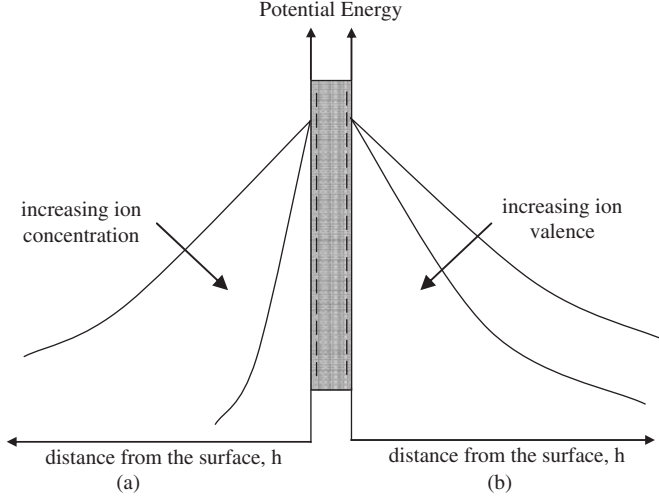


**Figure 1.1** Effect of (a) ion concentration (b) ion valence (1:1 (NaCl), 2:2 ( $\text{ZnSO}_4$ )) on the potential as a function of distance from the surface.

valence number in symmetrical electrolytes containing equal numbers of cations and anions in a molecule are shown on the RHS of the plate corresponding to Figure 1.1(b). Higher valence (2:2) causes a steeper decline of the potential with distance from the surface according to eq. (1.30).

The distribution of ions around a particle is given in Figure 1.2(a), in an exaggerated scale to show the different layers. The ions of the particle are shown as being homogeneously distributed over the surface area. A layer of ions of opposite charge adjacent to the particle is called the *Stern layer*. As the Debye length, designated as  $\kappa^{-1}$ , is an imaginary layer without a physical existence, it is arbitrarily shown to be several atomic diameters in thickness. The Debye length is defined by the simplified solution (Stokes and Evans, 1997) of the Poisson–Boltzmann equation valid for  $ze\Phi \ll k_B T$  as

$$\Phi(h) = \Phi_0 \exp(-\kappa h) \quad (1.33)$$

Debye length is defined as the distance from the surface ( $h = 1/\kappa$ ), where the electrical potential decreases to 37% of its value at the particle surface:

$$\frac{\Phi}{\Phi_0} = e^{-1} = 0.37 \quad (1.33a)$$

and changes parametrically with the electrolyte concentration and charge, permittivity of the medium and temperature according to eq. (1.34)

$$\frac{1}{\kappa} = \left[ \frac{\epsilon_r \epsilon_0 k_B T}{\sum (z_i e)^2 C_{iN}^0} \right]^{1/2} \quad (1.34)$$

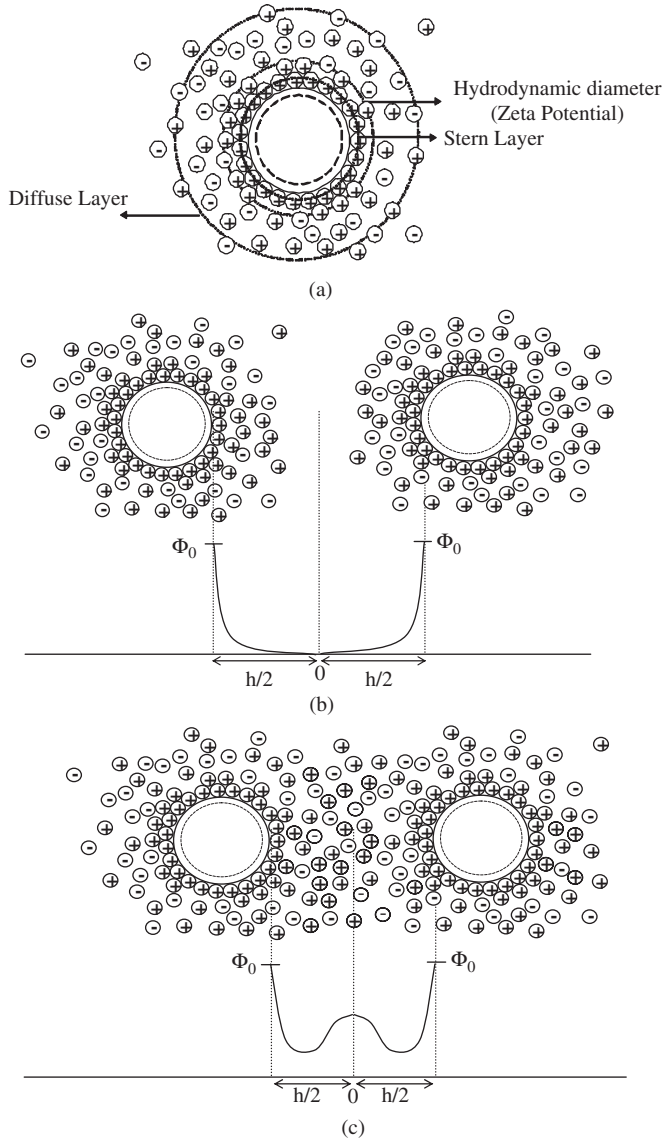


**Figure 1.2** Distribution of counterions around charged particles. (a) Various layers defined within the diffuse ions. (b) Variation of electrical potential between two approaching ions. (c) Potential increase due to overlap of diffuse ions on close approach of the particles.

A decrease in Debye length,  $\kappa^{-1}$ , signifies closer approach of the particles, and in the limit, one of the particles being entrapped in the secondary or primary energy minimum of the other, leading on to coagulation, as will be explained in the following sections. Concentration of electrolytes in solution,  $C_{in}^0$ , should be increased if coagulation is desired to take place among the particles. Debye length varies inversely with the square of the

valence of the ions. For this reason, multivalent ions with  $z_i > 1$  are able to approach very closely to charged surfaces. This effect has a bearing in many important cases such as in the aggregation of red blood cells (RBCs), and the production of metal oxides in microemulsions, where the metal ion is situated very close to the hydrophilic heads of the anionic surfactants, making up the inner surface of the micelles that serve as nanoreactors.

Zeta potential is the only experimentally measurable length scale in the ionic diffuse layer that can be measured with electrophoresis. The method is based on the calculation of the particle diameter based on the diffusion rate of the particle in an electric field. The hydrodynamic diameter,  $d_h$ , includes not only the particle diameter itself but also the Stern layer and a portion of the diffuse layer; i.e., the ions on which the effect of attractive forces of electrostatic origin are greater than the hydrodynamic shear forces acting on the particle during its travel.

Hitherto, the charged molecules were simply referred to as “ions” without regard to their interactions with the particles. The ions can be classified into three groups in terms of their effect on the particle: Indifferent ions, potential determining ions, and charge reversing ions.

Indifferent ions do not affect the potential or the charge distribution on the particle surface; they affect the Gouy–Chapman diffuse layer of ions surrounding the particle. An increase in the concentration of indifferent ions in the suspension medium causes a decrease in the Debye length, permitting closer approach of the charged particles, eventually leading up to coagulation. Generally, sodium chloride (NaCl) is used to bring about the indifferent electrolyte effect.

Potential determining ions change the surface potential  $\Phi_0$  of the particle when adsorbed on the surface. If the particles are ionic, such as metal salts or metal hydroxides, then the potential of the ions in solution and those adsorbed on the surface are equal according to the Gibbs adsorption isotherm ( $\mu_{EC}^{sol} = \mu_{EC}^{surf}$ ).  $\mu_{EC}$  includes both the electrical and chemical effects (Reid, 1990)

$$(z_i F \Phi_i + \mu_0 + k_B T \ln a_i)^{surf} = (z_i F \Phi_i + \mu_0 + k_B T \ln a_i)^{sol} \quad (1.35)$$

Rearrangement of eq. (1.35) gives

$$\Phi_i^{surf} - \Phi_i^{sol} = \left( \frac{k_B T \ln(a_i^{sol} / a_i^{surf})}{z_i F} \right) = \left( \frac{k_B T}{z_i F} \ln a_i^{sol} - \frac{k_B T}{z_i F} \ln a_i^{surf} \right) \quad (1.36)$$

where  $a_i$  is the activity,  $F$  the Faraday constant [ $9.648 \times 10^4 \text{ C mol}^{-1}$ ],  $z_i$  the valence of the ion, and  $\Phi_i^{surf} - \Phi_i^{sol}$  the electrical surface potential  $\Phi_0$  on the particle. For dilute solutions, the activity of the solution approaches 1 and eq. (1.36) is reduced to the Nernst equation

$$\Phi_0 = -\frac{k_B T}{z_i F} \ln a_i^{surf} = -\frac{k_B T}{z_i F} \ln a \quad (1.36a)$$

In addition, activity can be replaced by concentration for dilute solutions.

When the ions are adsorbed from the solution in amounts equivalent to the surface charge, the electrical potential of the particle surface is zero. These zero surface potential concentrations can be calculated from the Nernst equation by setting  $\Phi_0 = 0$ . The particle



grows in size under the condition of zero surface potential. At other concentrations, the particle acquires a positive or a negative potential according to the ion that is preferentially adsorbed on the particle surface. For colloidal particles that have weak acidic or basic groups,  $H^+$  and  $OH^-$  ions are potential determining. In such a case, pH of the suspension medium is taken into consideration, instead of the ion concentration as in the case of ionic particles. At the pH corresponding to zero surface charge (isoelectric point), repulsive forces no longer exist and attractive forces dominate the interactions between the particles.

Charge reversing ions are selectively adsorbed from the suspension medium which changes the composition of the surface as well as the potential and the charge. Examples are the cationic surfactants adsorbed on clay (montmorillonite) particles and polyelectrolytes adsorbed on nanosized particles to maintain stabilization.

### 1.2.3 The DLVO theory

Charged particles are so abundant in nature and in industrial operations that their interactions were the first to be investigated historically. As initially formulated by the authors (Derjaguin and Landau, 1941; Verwey and Overbeek, 1948), the theory accepts the total interaction energy between two charged particles to be the sum of the repulsive and attractive forces:

$$U_T(h) = U_{att}(h) + U_{rep}(h) \quad (1.37)$$

The assumptions behind this statement are:

1. Particles have smooth surfaces with a uniform charge distribution.
2. Electrical double layer does not affect the van der Waals forces and these two forces are additive.
3. The charge density and the electrical potential of the surface are constant.
4. Uniform charge distribution is assumed to prevail at the surface.
5. The solid particles do not affect the molecular structure of the liquid suspension medium even at very close distances to the interface.

The attractive interaction potential is given by eq. (1.20a) for plate-like, flaky particles and by eqs. (1.25a) and (1.26a) for spherical particles. The repulsion term in eq. (1.37) inherently includes the molecular repulsion term of the Lennard–Jones potential given as the second term in the RHS of eq. (1.15). But this repulsion varies inversely with the 12th power of the distance between molecules and the range of effectiveness is too short to be significant in particle–particle interactions. As the particles approach each other under attractive forces in the suspension medium, another force of entropic origin evolves that keeps off the particles from approaching each other. The ionic distribution in the solution as two negatively charged particles approach each other is shown in Figure 1.2(b). As the particles approach each other, the diffuse double layer ions are confined in the space between the particles and the ionic concentration increases (Figure 1.2(c)). This confinement ends up with the evolution of a repulsion force due to the decrease in entropy in the interparticle space

that opposes further approach of the particles. If an electrolyte is present in the medium, the compressed diffuse layer will be in equilibrium with the bulk solution. In this case, the net pressure pushing the particles apart can be taken as the osmotic pressure between the compressed double layers and the suspension medium. Gouy–Chapmann solution permits linearization of the Poisson–Boltzmann equation, yielding the interaction energy *between flat plates* due to osmotic pressure as (Stokes and Evans, 1997)

$$U_{\text{rep}}(h) = 64C_{\text{IN}}^0 k_B T \Gamma_0^2 \frac{\exp(-\kappa h)}{\kappa} \quad (1.38)$$

A similar expression can be obtained for *two spherical particles* of radius  $R$ , with the Derjaguin approximation

$$U_{\text{rep}}(h) = 64\pi R C_{\text{IN}}^0 k_B T \Gamma_0^2 \frac{\exp(-\kappa h)}{\kappa^2} \quad (1.39)$$

With this expression, DLVO interaction energy given by eq. (1.37) for *two spherical particles* becomes

$$U_{\text{T}}(h) = -\frac{H_{121}R}{12h} + 64\pi R C_{\text{IN}}^0 k_B T \Gamma_0^2 \frac{\exp(-\kappa h)}{\kappa^2} \quad (1.40)$$

This equation states that as the distance  $h$  between the particles increases, both the attractive and the repulsive terms tend to zero. If attractive forces dominate in the system, the total potential becomes negative, and if this domination is for a limited  $h$  range only, it results in a minimum in the total energy curve. If the repulsive forces dominate, the total potential becomes positive, resulting in a peak (repulsive energy barrier) if this domination is for a limited range in  $h$ , only. The shape of the attractive  $U_{\text{att}}$  and repulsive  $U_{\text{rep}}$  potentials are given in Figure 1.3(a), and the general shape of the total interaction potential in Figure 1.3(b). Core repulsion energy  $U_{\text{CR}}$  evolving from the overlap of the electron clouds is too short ranged to affect the total energy  $U_{\text{T}}$ , which determines the interactions between the particles. Figure 1.3(c) represents a case with an easily surmountable energy barrier  $U_{\text{max}}$  coupled by a deep potential energy minimum, the primary energy minimum (PM). Under such a case, the reaction or aggregation rate is controlled by the resistance of the suspension medium toward the motion of the particles only. Figure 1.3(d) represents a case of selectivity, where only the molecules with energies high enough to surmount the potential energy barrier (PEB) can aggregate. In Figure 1.3(e), a secondary minimum (SM) in the total energy profile is observed at distances of approach greater than the energy barrier. This means that there is no resistance to bonds formed in the range of the secondary minimum; but the reverse is also true: There is no resistance to the breakage of the bonds also. Reversible attachments as in the case of flocculation are formed in the range of the secondary minimum. Figure 1.3(f) is a case where there is no secondary minimum, but neither the energy minimum PM is very deep, nor the energy barrier  $U_{\text{max}}$ , very high. This allows the molecules with high enough energies to wander around for a better place to bond on the particle, called *restructuring*, as will be discussed in the next section.

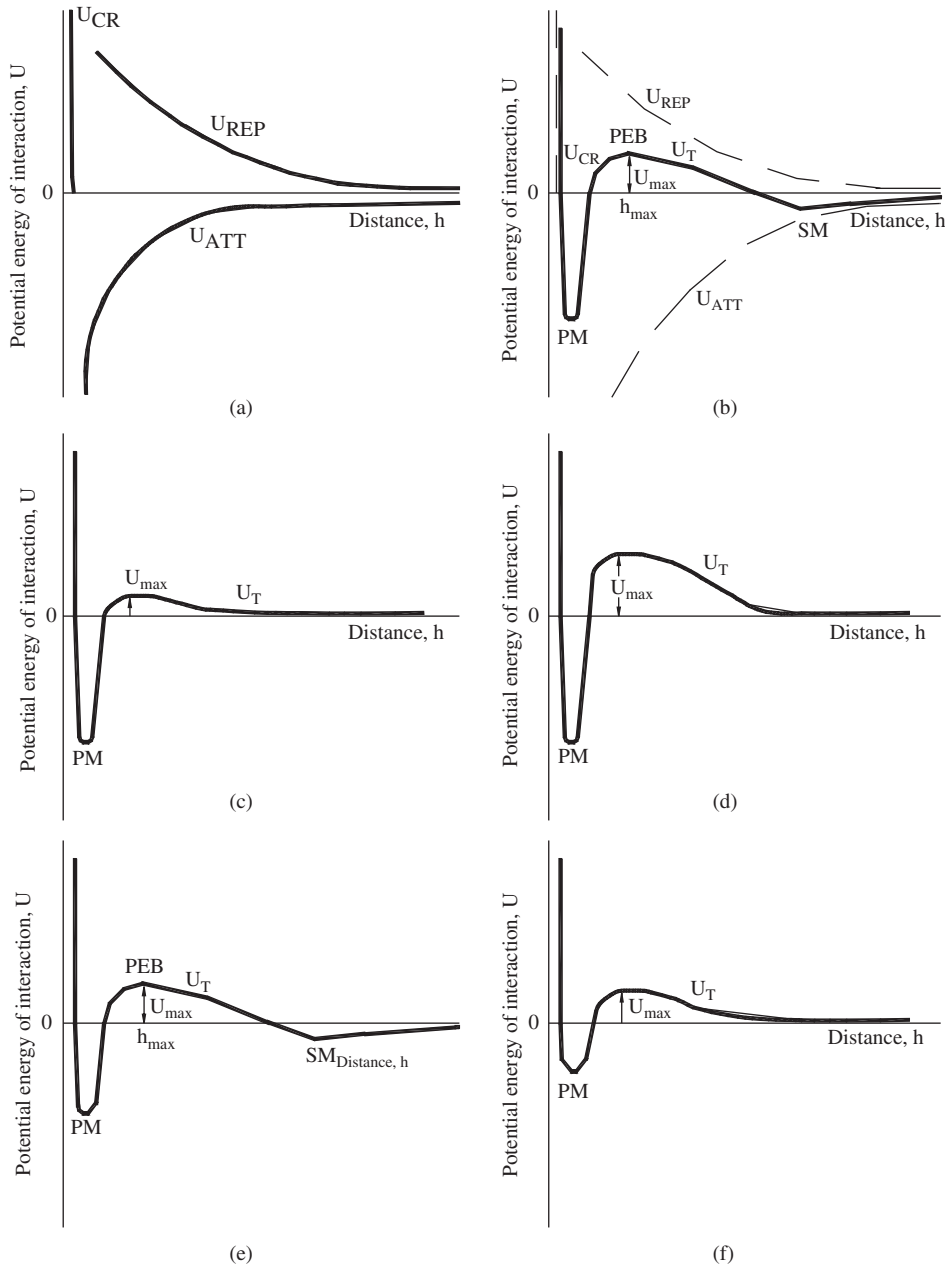


**Figure 1.3** Variations in the potential energy of interaction with distance  $h$  from the surface of the particle. (a) Variation of potential energy under attractive and repulsive forces, (b) total potential energy of interaction, (c) total potential energy under low repulsive, high attractive forces, (d) case of a high repulsive energy barrier, (e) appearance of a secondary energy minimum and (f) low attractive and repulsive potential energies.

In any system of particles suspended in an electrolytic solution, the attractive and repulsive forces can be manipulated to maintain stabilization of the suspension, or to aid coagulation to bring about settling of the solid particles. The shape of the total interaction energy function determines which process will take place according to the average distance  $h$  between the particles. This distance is determined by electrostatic and hydrodynamic forces, as well as by the shape of the particles. The last two factors will be discussed in the following sections in connection with cluster formation. Electrostatically, the distance between the particles can be controlled by the Debye length, which in turn is a function of temperature, dielectric constant of the suspension medium, valence of the ions of the electrolyte, and the ionic concentration through eq. (1.34). The attraction and repulsion potentials are related to the properties of the suspension medium, through the parameters of the Hamaker constant and Debye length, respectively. For a given system of particles and suspension medium, the total interaction potential can be adjusted toward a given aim through the manipulation of repulsion forces by the addition of salt, an electrolyte, or by changing the temperature. Solution properties also affect the charge density on the surface of the particle,  $\sigma_0$ , in accordance with eq. (1.32). This effect on the charge density of the particle is not taken into account, according to the third assumption of the DLVO theory.

The validity of the DLVO theory at low to moderate ionic strengths of electrolyte solutions, where the distances between surfaces are large in comparison with molecular dimensions, is established through extensive experimental work. Electrostatic forces are present in a wide range of colloidal systems under moderate conditions and DLVO theory can be successfully used to evaluate the interactions between the particles. The DLVO theory fails to explain the interactions under (1) high ionic strengths, (2) heteroaggregation, (3) discrete surface charges, (4) strong electrostatic interactions as in the case of multivalent counterions or low dielectric constant of the solvent, and (5) specific ion effects. As the theory is based on bulk phase physical properties such as density and permittivity, it cannot be used to predict interaction potentials at very close distances of approach of the particles where the intervening suspension medium can no longer be taken as a continuum. Under such cases, solvation forces determine the interactions between particles.

When other colloids such as polymers, nanoparticles, and surfactants are present in the suspension medium, different forces, collectively called the non-DLVO forces, control the particle interactions.

### 1.3 INTERACTION OF PARTICLES DUE TO NON-DLVO FORCES

As the particles approach each other within a few molecular diameters, the intervening fluid behaves as discrete particles that have different properties from the bulk. Under these conditions, non-DLVO forces mainly of *entropic* origin dominate at very small separations and may overcome the effect of the DLVO forces. Depending on the interactions between the solid surface and the components of the suspending medium, these forces can be *oscillatory*, attractive (*hydrophobic*), or repulsive (*hydration*). In all cases, they decay exponentially within a few nanometers, corresponding to several molecular diameters, from the surface and coincide with the effective long-range DLVO forces between the particles.

Other non-DLVO forces of entropic origin arise due to the effect of osmotic pressures in the presence of adsorbed short-chain molecules (*steric forces*) or nonadsorbing polymers (*depletion forces*). Another non-DLVO force that is effective over long ranges and of energetic origin is called the *bridging force*. Bridging forces cause aggregation through simultaneous adsorption of high molecular weight polymers to more than one particle. Another type of bridging force arises when polymers grafted (chemically bonded) on different particles attract each other.

### 1.3.1 Forces of entropic origin

The fifth assumption of the DLVO theory, that the liquid in which the particles are suspended is not affected by the particle surfaces is believed not to be valid based on measurements with surface force apparatus (SFA) and atomic force microscope (AFM). The potential between a pair of particles can be affected by the interactions among the molecules of the suspending liquid medium; and between the liquid molecules and the molecules at the surfaces of the particles, called the *many-body interactions*. Especially if the solid surfaces are smooth and orderly structured, the liquid molecules in the immediate vicinity of the particles are affected also and form an ordered solvation layer, with properties significantly different from the bulk physical properties due to increased level of compaction. *Solvation (structural)* forces arise in between two particles when the free energy associated with the configuration of the surrounding solvent molecules changes as the particles approach each other (Israelachvili, 1991).

From the first and second laws of thermodynamics, the change in the free energy of interaction  $dw$  can be related to the internal energy and entropy through the relation

$$dw = dU - T dS \quad (1.41)$$

The change in the free energy of interaction is brought about by the decrease in the volume of the intervening liquid between the two particles. The increase in the concentration of this intervening layer causes the evolution of osmotic pressure between this layer and the bulk liquid phase

$$dw = -P^{\text{osm}} dv \quad (1.42)$$

Equating these two expressions for the free energy of interaction, the osmotic pressure can be related to the variation of internal energy and entropy with the decreasing volume in between the two particles through

$$P^{\text{osm}} = -\frac{dU}{dv} + T \frac{dS}{dv} \quad (1.43)$$

If there are no interactions between the molecules or colloids suspended in the medium, the internal energy does not change as the particles approach each other, the first term on the RHS of eq. (1.43) becomes zero and the osmotic pressure is controlled solely by variations in entropy. Entropy is related to the number of configurations  $\Omega$ , which is a

function of the quantum states of the intervening molecules through the relation (Kuhn and Försterling, 2000)

$$dS = k_B \ln \frac{\Omega + d\Omega}{\Omega} \cong Nk_B \ln \left( 1 + \frac{dv}{v} \right) \quad (1.44)$$

where  $N$  is the number of solute molecules (or colloidal entities other than the particles) in the suspension medium. Since  $\ln(1 + dv/v) \approx dv/v$ , the equation simplifies to

$$dS = Nk_B \frac{dv}{v} \quad (1.45)$$

and the osmotic pressure can be related to the concentration  $C_i$  of colloidal entities through

$$P^{\text{osm}} = k_B T \frac{N}{v} = R_G T C_i \quad (1.46)$$

where  $R_G$  is the universal gas constant. The difference between the osmotic pressures in the intervening layer and the bulk liquid gives the repulsive (or attractive) pressures operating between the particles: Regular arrays of molecules lead to a crystal-like structure with a packing density greater than that in the bulk. The osmotic pressure in the confined volume in between the particles then becomes greater than the bulk osmotic pressure, resulting in a net repulsive force. When the packing density of the distorted layers are approximately equal to the bulk packing density, the osmotic pressures become equal and the interaction between the particles are controlled by other forces operative at those distances. On the other extreme, when the intervening layer between the particles is so short as not to allow in the molecules or colloids, the osmotic pressure in between the particles become zero and less than the bulk osmotic pressure leading to strong attractive forces.

If there are only solvent molecules in between the particles, eq. (1.46) reduces to the *contact value theorem*

$$P(h) = k_B T [\rho_s(h) - \rho_s(\infty)] \quad (1.47)$$

where  $\rho_s$  is the molar density [ $\text{mol m}^{-3}$ ] of the liquid at the surface of the particles, which is a function of the distance between the particles,  $h$ , with  $0 < h < \infty$ . Contact value theorem gives the pressure that arises due to a density increase in between two approaching particles, provided there is no interaction between the components of the intervening liquid and the particle surfaces (Israelachvili, 1991). This theorem can be used to find the pressure between two charged particles when  $\rho_s$  is used for the ion concentration at the surfaces; to give solvation interactions when  $\rho_s$  is the surface concentration of solvent molecules or to give the steric and depletion interactions when  $\rho_s$  is the surface concentration of polymers. The significance of this general application is that as long as a variation in the configurations of molecules or colloids in the intervening liquid are involved in the interaction of particles, the underlying mechanism is basically entropic in origin, even though energetic variations may also be present.

### 1.3.1.1 Oscillatory forces

In the case of simple molecules separating hard-sphere particles, a solvation force was found to arise when the liquid density changes as the surfaces approach each other. If the surfaces of the particles are smooth and unyielding, and the molecules in the confined space spherical with free access to the bulk liquid phase, the solvation force is a decaying oscillatory function of distance (Israelachvili, 1991)

$$P(h) \approx -k_B T \rho_s(\infty) \cos\left(\frac{2\pi h}{\sigma}\right) \exp\left(\frac{-h}{\sigma}\right) \quad (1.48)$$

where  $\sigma$  is the diameter of a liquid molecule. With simple molecules without any electrostatic repulsion, oscillations are superimposed on the attractive van der Waals force curve; i.e., the attractive force curve oscillates with a decaying amplitude until it converges with the long range van der Waals forces. The intercept of the oscillating curve with the force axis at contact ( $h=0$ ) gives the *adhesion force*. Depending on the relative dominance of other attractive and repulsive forces, oscillations were found to coincide with the attractive, repulsive, or total energy curves. If the liquid molecules are not symmetric, or the particle surfaces are not smooth, then no oscillations were observed. Instead, the energy curves varied monotonically with distance of separation (Israelachvili, 1991).

Similar oscillating phenomena are observed when colloids with regular shapes such as nanoparticles (Wasan *et al.*, 2005), and spherical micelles (Adler *et al.*, 2000) are suspended in a liquid used as a suspension medium for larger microparticles. The total potential energy curve oscillates in this case, due to unavoidable alignment of the nanoparticles at distances that are multiples of the nanoparticle diameters as the microscale particles approach each other. The oscillations in the interaction forces are given schematically in Figure 1.4 to illustrate the role of entropy. The unyielding hard walls of the microparticle surfaces force the smaller particles into alignment, which becomes more regular as the possible number of columns that can be formed decrease. The decrease in entropy due to ordering of the particles creates a repulsive force proportional to the order in the alignment. Thus, the amplitude of oscillations increase as the number of columns that can be fitted into the confined space decreases. Oscillations always end-up with a negative value, a strong attraction, at  $h=0$  due to depletion forces.

The oscillations die out after a separation distance of about five diameters of depletant molecules or colloids. Thus, the oscillatory forces are short ranged in comparison with the van der Waals forces with a range of 5 nm, when only simple molecules with a diameter of few Angstroms are present in the suspending medium. When the depletant molecules are colloids with diameters of several nanometers, the oscillating forces are considered to be long ranged in comparison with van der Waals forces.

There are two other forces whose existence are proven by experimental measurements (Israelachvili, 1991), even though the origins are not clearly understood but thought to be of entropic origin: Repulsive *hydration* forces and attractive *hydrophobic* forces in an aqueous suspending medium.

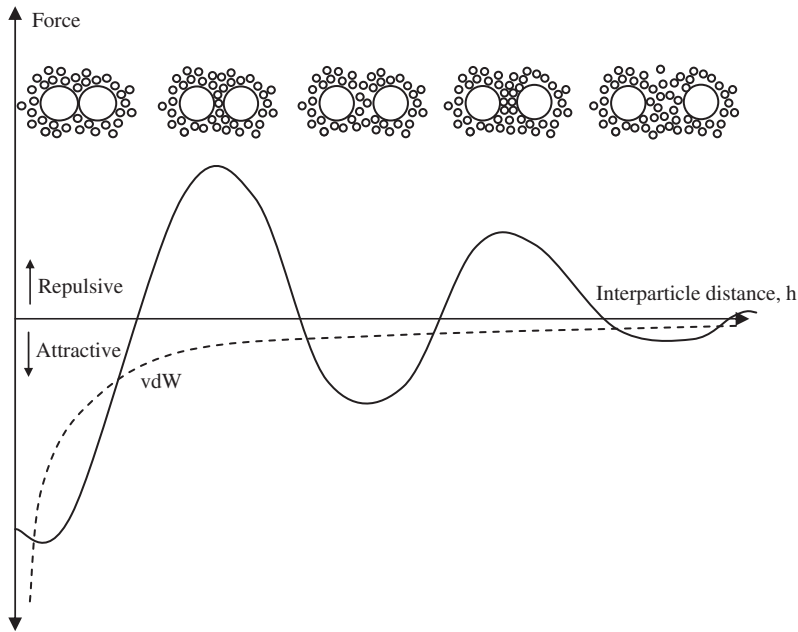


**Figure 1.4** Oscillating forces.

#### 1.3.1.2 Hydration forces

It is believed that, affected by the regular arrays of solid phase molecules, water molecules exist in a crystal structure adjacent to solid surfaces. The network extends a long distance away from the particle surface due to hydrogen bonds (type of van der Waals forces between H and O atoms in a molecule). If the hydrophilic surface of a particle forms stronger bonds with water, a strong repulsive force develops that decays exponentially within about 3–5 nm. Hydration forces can be controlled if the hydrophilicity of the surface can be regulated by ion exchange. If the hydrophilic groups are in-built within the surface structure of a particle, hydration forces exist under all conditions and stabilize the suspension.

#### 1.3.1.3 Hydrophobic forces

Contrary to hydration forces, hydrophobic forces arise when the surface molecules of the particles have no attraction to water molecules, such as hydrocarbons and fluorocarbons and are responsible for the enclosure of the hydrocarbon groups within self-assemblies of surfactants. Hydrophobic forces are strongly attractive with a range and magnitude greater than the van der Waals forces. Recently, the attraction between two mica surfaces made hydrophobic with physisorbed double-chained cationic surfactant (dimethyl dioctadecyl ammonium bromide) was measured with the dynamic method in a SFA (Lin *et al.*, 2005). With this method, the distance–time variations of the surfaces could be detected down to separations of 10 Å. As the surfaces approached each other, the distance versus time paths first deviated from the trajectory based on viscous forces only and then converged to a single path



at the same points for all velocities of approach ( $10, 75, 115 \text{ \AA sec}^{-1}$ ). The slope of this single path decreased at very short distances of approach ( $50 \text{ \AA}$  in the experiments) until the clarity was lost at the end ( $10 \text{ \AA}$ ). The deceleration at very close distances was taken to be an indication of frictional losses within the liquid medium that persists even at such short separation distances. The convergence of the different paths was taken as an indication of a very strong short-range attraction that affects the stability. The authors concluded that what appears to be a hydrophobic force might be a combination of short-range and long-range forces as was suggested previously by other researchers. Reduced force curves as a function of distance are obtained by integration of experimental data taken as the variation of distance–time and are strongly dependent on the assumed boundary conditions which cannot be verified at the present. The reduced force curves calculated with the no slip assumption confirm the strong increase in force very near the surface ( $h < 50 \text{ \AA}$ ), the origins of which are still unknown.

Polymers, short-chain hydrocarbon groups and nanoparticles also cause forces of entropic origin, repulsive *steric forces* and attractive *depletion forces*, as shown in Figure 1.5. They are analogous to attractive and repulsive counterparts of oscillating forces encountered at various distances of separation from the surface. The conditions in the colloidal system can be designed or engineered to enable these forces to be effective in stabilization or destabilization of suspensions.

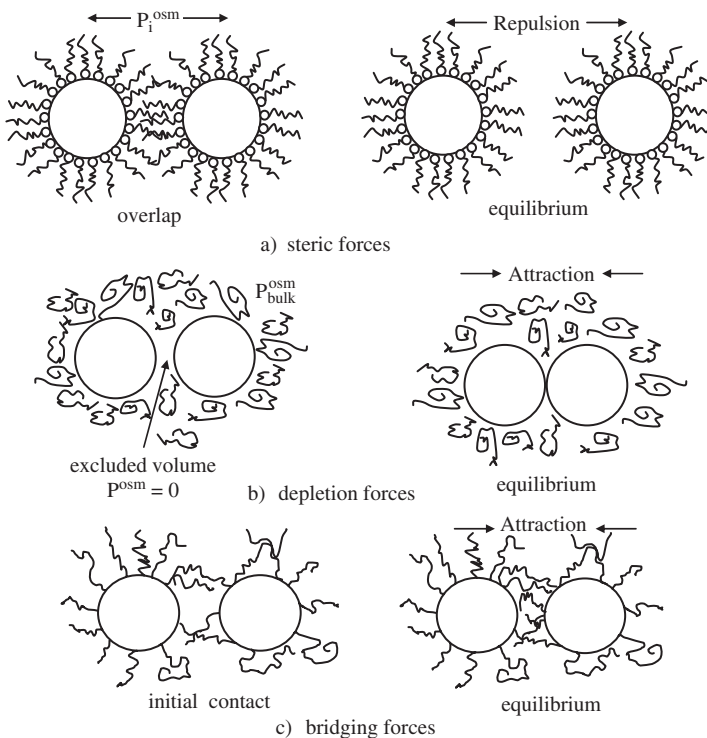


**Figure 1.5** (a) Steric, (b) depletion, and (c) bridging forces at the initiation of the interaction and at equilibrium.

#### 1.3.1.4 Depletion forces

Depletion forces arise when nonadsorbing polymers are present in the suspension medium. At a ratio of polymer to particle concentration depending on the properties and conditions of the system under consideration, the particles can approach each other up to such short distances that polymer molecules cannot enter the intervening layer. The osmotic pressure of the bulk liquid will then force the particles toward each other, as the  $P^{\text{osm}}$  will be zero in the confined intervening (excluded) volume (Figure 1.5(b)). The same effect can also be produced by nanoparticles, which do not adsorb on the surfaces of the micro- or macro-scale particles but create an osmotic pressure outside of the confined layer sufficient to cause depletion forces to arise (Tohver *et al.*, 2001; Wasan *et al.*, 2005).

Basing on AFM measurements, Burns *et al.* (2002) found the depletion layer in polyacrylic acid (PAA) on polystyrene latex dispersion to decrease as the concentration of the polymer increased. The decrease was found to be very sharp at very low concentrations of the polymer, leveling off to a constant value of about 2 nm as the concentration increased. In very dilute polymer solutions, the thickness of the depletion layer increases as the molecular weight increases.

Fleer *et al.* (1984) relate the depletion force,  $F_{\text{dep}}$ , between a sphere and a flat plate to the depletion layer thickness  $\Delta$ , through the area on which the osmotic pressure acts with the equation

$$F_{\text{dep}} = \pi P^{\text{osm}} (h + 2R_0)(h - 2\Delta) \quad (1.49)$$

where  $R_0$  is the radius of the particles,  $h$  the interparticle separation, and  $\Delta$  the depletion layer thickness. Accepting the depletion force to be additive to the attractive and repulsive forces of the DLVO theory, it is possible to observe a secondary minimum in the total energy curve, even when no such minimum exists in the presence of DLVO forces only.

#### 1.3.1.5 Steric forces

Contrary to depletion forces, steric forces arise due to adsorbed molecules. These molecules could be surfactants, physically adsorbed polymers, grafted polymers that are chemisorbed at specific sites on the particle surface, freely dangling sections of polymers that are a part of the integral structure of the particle surface, or nanoparticles adsorbed on the particle surfaces. Repulsive forces arise when the adsorbed layers of the particles overlap on close approach, as sketched in Figure 1.5(a). Then, the increase in  $P_i^{\text{osm}}$  due to increased concentration in the overlap layer will cause the particles to repel each other. The closest distance of approach of the particles are determined by the chain length of surfactants, diameter of nanoparticles or radius of gyration  $R_g$  of the polymers given by

$$R_g = \frac{l(M/M_0)^{1/2}}{\sqrt{6}} \quad (1.50)$$

where  $M_0$  is the molecular weight of the unit monomers with length  $l$ ,  $M$  the molecular weight of the polymer made up of these monomers. Radius of gyration depends on the

compatibility of the polymer with the solvent. The polymer volume based on  $R_g$  includes the void spaces in between the coils and excluded volume within the polymer coils where solid segments cannot enter.

### 1.3.2 Forces of energetic origin

If the molecules or colloidal entities interact, then the internal energy term in eq. (1.43) should also be taken into account, where the internal energy,  $U$

$$U = U_{\text{el}} + U_{\text{trans}} + U_{\text{rot}} + U_{\text{vib}} \quad (1.51)$$

is the sum of electronic, translational, rotational, and vibrational internal energies of the molecules, respectively. If the molecules attract each other, one or more of these internal energy components will change, causing the interaction to be *energetic* in origin, even though entropic considerations still play a role in the extension of the polymer chains. “*Bridging force*” is a term used to denote binding of particles within a network formed by simultaneous adsorption of polymers to more than one particle: If the solvent serving as the suspending medium for the particles is compatible with the polymer, the polymer stretches fully into the suspension medium. This is observed above a critical temperature called the *theta temperature*,  $T_\theta$ , above which the liquid becomes an ideal solvent for the polymer. Polymers adsorbed on different particles may attract each other if there are segments available on the polymer chain that can react with each other. These segments can also adsorb on neighboring particles if there are available sites for adsorption on the particles. If the polymer length is long enough as in Figure 1.5(c), then the particles can be attracted to each other even though the net interactive DLVO force between the particles is repulsive.

Steric forces stabilize the particles in suspension. The microstructure of the aggregates formed by depletion forces is closely spaced particles. Bridging forces create highly porous clusters. The consequences of the microstructure of the aggregates on their rheological properties will be examined in Chapter 3, and on their sedimentation rate in Chapter 4. The surface forces responsible for interactions between particles and cases where such interactions are observed are summarized in Table 1.2.

## 1.4 AGGREGATION OF PARTICLES

Unless the particles are neutrally buoyant, that is they have the same density as the suspending medium, all particles will settle under the action of gravity. The smaller the particle diameter, the slower will be the settling rate as will be explicated in Chapter 4. In the case of colloidal particles, the settling rate may be extremely slow for the suspension to be kinetically stable, even though it is thermodynamically unstable. Kinetic stability is maintained if aggregation is prevented through repulsive forces. Destabilization begins when repulsive forces cannot counterbalance attractive forces.

**Table 1.2**

Summary of surface forces

Force	Effect <sup>a</sup>	Cause	Observed in
van der Waals	A	Asymmetric distribution of electrons	van der Waals forces are present in every case from the molecule to the particles and will tend to aggregate particles if not resisted by a repulsive force.
Double layer	R	Decrease in entropy due to overlap of diffuse ionic layers	Charged particles, microorganisms, uncharged particles that adsorb charged ions from the medium, ionic surfactant micelles, red blood cells
Oscillatory	A/R	Decrease in entropy due to alignment in the confined volume between approaching particles	Smooth, hard surfaced particles suspended in symmetric molecules or in nanofluids
Hydration	R	Entropic due to attractions between water and surface being greater than that among water molecules	Colloids with hydrophilic surfaces such as those bearing silicate, phosphate groups or polyalcohols: clays, silicates in ceramics, particles on which sugar based surfactants are adsorbed
Hydrophobic	A	Entropic due to incompatibility of surface molecules with water molecules	Folding of protein chains, self-assemblies of surfactants, nonwetting characteristics, separation of minerals by froth flotation
Depletion	A	Entropic due to excluded volume between particles	Red blood cell aggregation to form rouleaux, destabilization of colloidal particle suspensions at low polymer or nanoparticle concentration
Steric	R	Entropic due to increase in $P^{\text{osm}}$ in regions of overlap	Stabilization of particle suspensions in all scales, pattern formation in nanoparticles, prevention of collapse in micelles and bilayers
Bridging	A	Energetic due to simultaneous adsorption of a polymer chain to more than one colloidal particle	Coagulation for separation of colloids in wastewater treatment plants. Aggregation of microorganisms

<sup>a</sup>R, repulsive; A, attractive.

### 1.4.1 Kinetics of aggregation

The crucial step in the destabilization of colloids is the formation of a dimer, as implicated within the context of surface forces given above. Once formed, these dimers aggregate through further collisions. After a nucleus is formed, the initial growth process proceeds by the addition of individual particles to the cluster. If the shear rate prevalent in the aggregation medium is not high enough to break apart the attachments formed, cluster–cluster unions may also take place.

The aggregation process involves two basic steps: The first step is the transportation of the particles to the aggregation site. Transportation can be brought about by random thermal Brownian motion (*perikinetic aggregation*), by the effect of a shear field inducing different velocities to the particles (*orthokinetic aggregation*), or through a difference in the terminal velocities in differential sedimentation. Transportation step ends with an inevitable collision between the particles. The frequency with which the particles collide with each other per unit time and unit volume is called the *collision frequency*. Collision frequency depends on the hydrodynamics of the medium, the volume occupied by the clusters (Birdi, 1993; Vicsek, 1999), and the average number concentration of particles within a cluster, which in turn depends on the level of shear stress the bonds within the clusters can withstand.

The second step is the formation of a bond between the two particles. The success of the collision in causing such a bond is rated as the *collision efficiency*, which depends on the shape of the interaction potential between the particles. A deep minimum in the potential with a negligible repulsive barrier, as in Figure 1.3(c) leads to *diffusion-limited aggregation* (DLA), whereas, an increase in the repulsive energy barrier (Figure 1.3(d)) causes reaction limited aggregation (RLA). In the limiting case of an insurmountable energy barrier, colloidal stability is maintained under the prevalent conditions.

The presence of a high repulsive barrier is not enough to prevent destabilization if there is a second minimum observed in the potential energy profile, as given in Figure 1.3(e). An energetically low second attractive minimum at distances larger than the repulsive barrier in the potential energy curve leads to reversibility in cluster formation: Aggregation and fragmentation processes occur simultaneously during growth, since the escape of a captured particle cannot be prevented if the depth of the minimum is not deep enough. If the captured particle is in the primary minimum that is not deep enough with a relatively surmountable energy barrier, as in Figure 1.3(f), then external forces applied can only bring about restructuring, ending up with the formation of more compact clusters.

The rate processes involved in aggregation can be given compactly by the expression

$$r = \alpha(i, j) \beta(i, j) n_i n_j \quad (1.52)$$

where  $r$  is the rate of aggregation in terms of number of particles [ $\text{m}^{-3}\text{t}^{-1}$ ],  $\alpha$  the dimensionless collision efficiency factor, and  $\beta$  the collision frequency factor [ $\text{m}^3\text{t}^{-1}$ ],  $n_i$  and  $n_j$  the number concentrations of components  $i$  and  $j$ , respectively.

Aggregation rate based on a particle population balance was formulated for the first time by Smoluchowski (1917), and still used with some modifications and revisions today:

$$\frac{dn_k}{dt} = \frac{1}{2} \sum_{i+j=k} \beta(i, j) n_i n_j - \sum_{i=1}^{\infty} \beta(i, k) n_i n_k \quad (1.53)$$

The theory underlying population balances is given in Appendix B. This balance equation written for the conservation of particles of size  $k$  states that the rate of accumulation of particles of size  $k$  is equal to that formed by the collision of particles of size  $i$  and  $j$  (the first term on the RHS) minus the loss of particles of size  $k$ , due to enlargement through collision and aggregation with another particle of size  $i$ . This equation should be written for all sizes of particles within the range of high probability of occurrence. Smoluchowski made a number of assumptions to simplify the solutions of the resulting equations given in Appendix B. Collision efficiency  $\alpha$  was taken as equal to one to eliminate the resistances due to adsorption and bond formation. This assumption presumes that all collisions end-up with bond formation. In later developments regarding the rate equations, the collision efficiency factor,  $\alpha$ , is taken into account by the stability ratio  $W$  (Fuchs, 1934), defined as the inverse of collision efficiency factor  $\alpha$ , or as the ratio of the rate constant of the fast diffusion limited aggregation (DLA) to the rate constant of the slow reaction limited aggregation (RLA)

$$W = \frac{k_{\text{fast}}}{k_{\text{slow}}} = \frac{1}{\alpha} \quad (1.54)$$

Stability ratio can also be defined in terms of potential energy of interaction, taking into account the effect of surface forces through the total energy potential,  $U_T$

$$W = (R_i + R_j) \int_{r_i+r_j}^{\infty} \frac{\exp(-U_T / k_B T)}{s^2} ds \quad (1.55)$$

In this equation,  $R_i$  and  $R_j$  are the radii of the colliding particles,  $U_T$  the total energy including the repulsive and attractive forces,  $k_B$  the Boltzman constant,  $T$  the temperature, and  $s$  the distance between the centers of the particles.

$U_T$  is generally calculated with the DLVO theory. If other forces are also effective, the necessary terms are added to the  $U_T$  expression if they can be identified. In actual practice, it is a hard task to integrate the effective forces, theoretical basis of which are not well developed yet.

### 1.4.2 Structure of aggregates

*Aggregates* range from highly porous structures with weak bonds in between the primary particles, called *flocculates*, to gel-like structures, called *coagulates*. *Cluster* is a more general term denoting aggregates of any size range, heterogeneity, and strength of interactive forces. Structure of clusters can range from extreme order as in a crystal to a completely amorphous mass. Clusters are formed by random collisions of particles in suspension.

Crystal structures can not form unless all the particles are homogeneous and strong attractive forces exist among them. On the other hand, completely amorphous clusters are formed by heterogeneous particles and polymers. The most frequently encountered structure in the aggregation of particles is a self-repeating pattern, called a *fractal*, which reflects the sequential stepwise formation mechanism of the cluster.

#### 1.4.2.1 Fractal theory

Steric effects orient the collision of particles to such an extent that aggregation proceeds through preferable sites, resulting in a pattern formation. Sterically inhibited sites result in an increase in the porosity and in the variation in the distribution of porosity within the volume of the aggregate, so that its shape cannot be described by any of the geometrical forms. Fractal theory developed by Mandelbrot (1983) defines the volume,  $v$ , of the particles with a noninteger power of the characteristic dimension,  $L$

$$v \approx L^{d_f} \quad (1.56)$$

where  $d_f$ , the *fractal dimension*, is a nondigit number, a fraction, whence the name fractal originates. The fractal dimension  $d_f$  of a particle is always less than three, the dimension of the geometrical form enveloping the fractal object

$$v \propto L^3 \quad (1.57)$$

The relation between the mass,  $M$ , and the characteristic length, such as the average radius  $R_{\text{agg}}$  of a fractal aggregate, arises from the repeating forms of fractal aggregates. For a fractal object made up of  $N$  particles of mass  $m$  and radius  $R_0$

$$N = \frac{M(R_{\text{agg}}, R_0)}{m(R_0)} = \frac{\rho_{\text{agg}} R_{\text{agg}}^3}{\rho_p R_0^3} \quad (1.58)$$

Clearly, the density of the aggregate is less than the density of the particle ( $\rho_{\text{agg}} < \rho_p$ ) proportional to the porosity of the aggregate. To take into account the porous structure of the aggregates, the mass  $M$  can be expressed with the  $d_f$  power of  $R_{\text{agg}}$ , where  $d_f < 3$

$$N = \frac{M(R_{\text{agg}}, R_0)}{m(R_0)} \propto \frac{R_{\text{agg}}^{d_f}}{R_0^3} \quad (1.59)$$

If the same repeating structure prevails throughout the aggregate, then  $d_f$  becomes independent of the size of the cluster. This equation also describes the scale invariance or self-similarity of the fractal aggregates: The geometrical shape remains the same under isotropic rescaling of lengths (Meakin, 1998), such as that between two aggregates of mass  $M_2$  and  $M_1$  and radius  $R_2$  and  $R_1$

$$d_f = \frac{\log(M_2 / M_1)}{\log(R_2 / R_1)} \quad (1.60)$$

Clusters can grow by two types of mechanisms (Vicsek, 1999): In the first type of cluster formation, the structure of the whole cluster can affect the probability of addition to a site at a given position. Clusters formed under *diffusion-limited* (DLA) or *reaction-limited* (RLA) conditions, and clusters undergoing simultaneous aggregation–fragmentation processes (*restructuring*) during the growth process belong to this group. In these cases, fractal clusters are characterized by the radius of the cluster, fractal dimension and related with it, the density of the aggregates, as given by eqs. (1.56–1.58). In homogeneous fractal aggregates, an increase in the characteristic radius  $R$  at a ratio of  $\lambda$ , is reflected onto the mass of the aggregate as the  $d_f$  power of  $\lambda$ ,  $\lambda^{d_f}$

$$M(\lambda R) \approx C_1 \lambda^{d_f} (R)^{d_f} \quad (1.61)$$

Since the mass of the aggregate varies with a power of  $R$  that is less than the variation of its volume ( $d_f < 3$ ), density of the aggregates decreases with an increase in their size. This decrease in density toward the edges of fractal clusters is exemplified in the case of  $\text{ZnCO}_3$  nanoparticles forming a fractal aggregate (Ikizler, 2005) in Figure 1.6.

In the second type of cluster formation, the growth is local and depends only on the immediate environment of the position to which a new particle or cluster is to be added. *Percolation clusters* and *gels* belong to this group and may have a much greater porosity than the first type of clusters if growth proceeds along preferential sites. Self-similarity of the structure with an increase in the size is not valid in the case of gels described by percolation theory (Meakin, 1998; Berthon *et al.*, 2001; Takenaka *et al.*, 2004). These types of clusters are called *statistically self-similar fractals*, as the statistical quantities used in characterization remain invariant to a change in length scales, provided the length scale remains in the range between the characteristic length of the particles,  $r$ , and the cluster,  $R$ .

The composition of the medium between the particles affects the mechanism of cluster formation through its effect on the surface forces bringing about the interactions. In the previous sections, attractive forces were observed to have different ranges causing bonds of different strengths among particles. Fractal dimension represents the mechanisms effective in the aggregation process; namely, the effect of surface forces binding

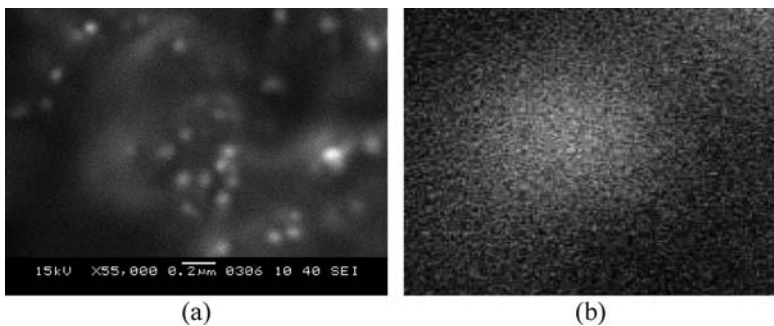


**Figure 1.6** Fractal structure of  $\text{ZnCO}_3$  nanoparticles (a) clusters and (b) detail of a cluster.



the components of the cluster and the hydrodynamics of the system, which may be effective in bringing together or tearing apart the components of the cluster. Under stagnant conditions where particles form the cluster through collisions resulting from random Brownian motion, the fractal dimension,  $d_f$ , represents the role of surface forces on the structure of resulting aggregates. When only DLVO forces are effective in the process, the magnitude of  $d_f$  gives an indication of the kinetics of aggregation during the formation, and the extent of fragmentation and restructuring in later stages. Non-DLVO forces operative in the aggregation process change the variation of the magnitude of  $d_f$  with the rate of aggregation from that expected under the action of DLVO forces alone.

#### 1.4.2.2 Factors that affect the fractal dimension

Fractal dimension is affected by (a) the size and shape of component or primary particles, (b) the hydrodynamic forces that bring them to close approach, and (c) the surface forces that bind these particles. Only a brief review on these three basic factors will be given here. Actually all the factors that affect the surface forces also affect the aggregate structure and the fractal dimension. A more extensive review of these issues on the structure of fractal aggregates is given in Peker (2006).

##### 1.4.2.2.1 Effect of the shape factor of primary particles on the fractal dimension

The primary particles making up the aggregates are generally assumed spherical for mathematical simplicity. Advent of nanotechnologies necessitates the stability of suspensions of hexagonal micelles, rod shaped nanoparticles and nanotubes, which cannot be handled with the assumption of spherical geometry. These dimensionally anisotropic particles are characterized by their length-to-diameter ratio, called the *aspect ratio*. Recently, Mohraz *et al.* (2004) studied the aggregation behavior of rod type boehmite colloids with aspect ratios,  $\zeta = 3.9, 8.6$ , and  $30.1$ , and compared the results with the aspect ratio of spheres,  $\zeta = 1$ . Fractal dimension of the clusters formed under DLA conditions was found to be an increasing function of the monomer aspect ratio, with values of  $d_f = 1.81, 1.94, 2.14$ , and  $2.21$  for  $\zeta = 1, 3.9, 8.6$ , and  $30.1$ , respectively. The simulated fractal dimensions varied in the range,  $1.80 < d_f < 2.16$  for the aspect ratios  $1 < \zeta < 11$ , in good agreement with experimental results. In the aggregation of rod shaped particles, DLA and RLA regimes cannot be distinguished. As  $\zeta$  increases, a more branched and compact structure is formed in comparison with the structure of the aggregates formed by spherical primary particles. Above an aspect ratio  $\sim 8.6$ ,  $d_f$  values of the aggregate structures were found to be approximately the same for both the DLA and RLA regimes. This was explained by the excluded volume effect of the rods that prevented them from penetrating into the pores of the aggregate structure, which were already compact due to the orientation of the rods.

Another work by Chen *et al.* (2004) on the aggregation behavior of nanotubes support the results obtained by Mohraz and coworkers (2004). Due to the flexibility and large aspect ratios of the nanotubes, entanglement becomes inevitable under the action of strong attractive dispersion forces. Determination of the fractal dimension by light scattering gave  $d_f = 2.27$  for sterically stabilized and  $d_f = 2.5$  for acid treated nanotubes.

#### 1.4.2.2.2 Effect of fragmentation and restructuring on the fractal dimension

Shear stresses deform the aggregates, convective motion of the suspending medium causes the aggregates to extend, and stretch the bonds, collisions with other aggregates cause compression of the aggregates. These external forces cannot exert their full effect on the component particles, due to the fractal structure of the aggregates, i.e., the porosity and limited number of contacts per particle within the structure. The aggregate responds to the acting external forces by undergoing structural revision: If there is a weak bond in the structure, it may fracture and break apart, known as *fragmentation*. It may then recombine with the same or another aggregate under conditions that are more favorable. If the weak points can withstand the stress, then parts of the aggregate can rotate and form more bonds within it, called *restructuring*. In both cases, the aggregate becomes more compact reflected as an increase in the fractal dimension. Particles in the range of a few hundred nanometers undergo restructuring rather than fragmentation under low to moderate shear rates. In the process of restructuring, the diameter of the aggregate increases, passes through a maximum and then decreases, and levels off to an equilibrium size range. An increase in the diameter of the primary particles causes the equilibrium diameter of the aggregate to decrease.

The light scattering index (scattering exponent) SE in light scattering methods of particle size characterization is equivalent to fractal dimension  $d_f$  in compact structures and is used to characterize the degree of restructuring. In aggregates formed by small diameter particles in the order of a few hundred nanometers, SE is found by Selomulya *et al.* (2002) to approach the 2.6–3.0 range with time, much above the RLA limit of 2.1 for electrolyte induced aggregation. On the other hand, when the diameter of the primary particles approach the micrometer range, fragmentation–reaggregation process predominates over restructuring. The scattering index SE asymptotically approaches an equilibrium constant value in the range of 2.6–2.8 with time. The rate of approach to the equilibrium scattering index (SE) is directly proportional with the shear rate for all primary particle sizes.

#### 1.4.2.2.3 Effect of DLVO forces on the fractal dimension

If the suspending medium of the colloids is a solution of indifferent electrolytes only, the colloids aggregate under the action of DLVO forces. The value of  $d_f$  is then determined only by the *mechanism* controlling the rate of aggregation. When *transport to the aggregation site is the only rate limiting factor* (DLA), the value of  $d_f$  was shown to vary in the range 1.7–1.8 by theoretical considerations (Jullien and Botet, 1987), and confirmed by experimental results of the aggregation of various colloids in solutions of different electrolytes (Lin *et al.*, 1990). When *adhesion to the cluster is the rate limiting step* (RLA),  $d_f$  was found to be in the range of 2.1–2.2 through simulations and experiments with electrolytes indifferent to the surfaces of the particles. These values are taken as criteria for testing the effect of a variable on the structure of the aggregates formed.

The rate of aggregation proceeding slowly due to PEBs (Figure 1.3) or steric hindrance is related to the rate of diffusion controlled aggregation through the stability ratio  $W$ . Aggregation may also proceed at an intermediate rate in between the two limiting cases of DLA and RLA,

representing zero and maximum PEBs for dimer formation, the initial step in aggregation. Berka and Rice (2005) obtained the relation

$$d_f = 0.17(\log W) + 1.67 \quad (1.62)$$

in the range,  $5 < W < 100$ , with dilute suspensions of natural kaolinite of particle size  $R_h \approx 100 \pm 5$  nm through light scattering experiments. The limiting values of  $d_f$  estimated with this equation (eq. (1.62)) are 1.78 and 2.1, in agreement with the universally accepted values for the DLA and RLA regimes, respectively. Similar results were found for salt-induced aggregation of polystyrene particles (Tirado-Miranda, 2003). Fractal dimension varied linearly from 1.75 to 2.1 with an increase in the electrolyte concentration. In the more concentrated suspensions employed in industrial applications the compaction of the clusters and hence, the fractal dimension, may change during aggregation.

### 1.4.3 Role of polymers and polyelectrolytes on the coagulation of suspensions

Polymers and polyelectrolytes present in a suspension of solid particles, as in the case of paints, surface coatings, ceramics, wastewater suspensions, slow-release vehicles, bioreactors, blood, etc., have such a wide range of application that they deserve special attention. The effect of polymers on colloidal stability depends on the bonds formed with the particles, as well as on the chemical or electrolytic nature of the polymer. So a classification in terms of nonadsorbed and adsorbed polymers, and in the case of the latter, neutral or polyelectrolyte type of polymers would be more appropriate in terms of their effect on colloid stability. This classification should be preferred over grouping in terms of surface forces, since several forces can be simultaneously effective in particle–polymer interactions. Forces induced by the interactions of polymers present in the suspension such as *depletion*, *steric*, and *bridging* forces come to be effective in the aggregation of particles, *in addition to the DLVO forces* with a change in the pH, and ionic strength of the medium.

#### 1.4.3.1 Particle–polyelectrolyte interactions

As most solid particles have charged surfaces, the interactions become more complicated when the polymer is a polyelectrolyte. In fact, polymer–particle interactions can be considered as a subgroup of polyelectrolyte–particle interactions at the *isoelectric point* of the polyelectrolyte when it is completely neutral. Recently, Claesson *et al.* (2005) reviewed polyelectrolyte–solid particle interactions under four categories.

##### 1.4.3.1.1 Category 1: Polyelectrolytes adsorbed on oppositely charged particle

In this group of interactions, the charge density of both the polyelectrolyte and the particles affect the interaction as well as the pH and ionic strength of the medium. When polyelectrolytes and particles carry opposite charges, simple electrolytes such as  $\text{Na}^+\text{Cl}^-$  become competitive in adsorbing to vacant sites on the particle reducing the polyelectrolyte adsorption on the particles (*screening-reduced adsorption*). Repulsions between segments

of polyelectrolyte chains are affected by the screening also, ending up with large loops and extended polymer chains, increasing the thickness of the steric layer on the particles. On the other hand, if electrostatic forces are not negligible, screening reduces the repulsions between polyelectrolyte chain segments increasing the number of contact points with the particle surface, resulting in a thinner steric layer (*screening-enhanced adsorption*). Repulsion forces existing in the absence of polyelectrolyte can be converted into attractions at low concentrations of polyelectrolyte and ionic strengths sufficient to extend the polymer chains. If the particle/polymer ratio is sufficient to bring different particles within the reach of adsorbed polyelectrolytes, particles may be bridged together within a flocculate. Higher polyelectrolyte concentrations decrease the repulsive forces between particles through neutralization of their surface charge and may even cause charge reversal if adsorption is increased by nonelectrostatic attractions. Increase in the polymer charge density produces a thinner coating due to increased attachment sites along the chain; whereas, a decrease in the charge density of the polymer produces a thicker steric layer due to the size of loops in between the adsorption sites. On the other side, decrease in the charge density of the particle surface leads to adsorption of polyelectrolytes around the *discrete charges* increasing the *heterogeneity* of the particle surfaces.

#### 1.4.3.1.2 Category 2: Polyelectrolytes adsorbed on uncharged particles

As adsorption decreases the entropy of the polyelectrolytes through restriction of random motion of polymer segments, adsorption is possible only if the enthalpy (energetic) variations are very favorable for adsorption to take place. Due to repulsion between chain segments, the polymers lie flat on the particle surfaces where the energetic effect is maximized. Presence of electrolytes in the medium screens the repulsive forces between polyelectrolyte segments, favoring the attractive forces between the particle and the polymer.

#### 1.4.3.1.3 Category 3: Polyelectrolytes adsorbed on similarly charged particles

Polyelectrolytes adsorb on particles bearing the same charge only if the charge density is low and screened by the presence of simple electrolytes. If the charge densities of both the polyelectrolyte and the particle are high, then adsorption can be brought about by linkages with the cations of the second group in the periodic table. This linkage is strongly dependent on the hydration level of the cation: With the heavier cations in the group having low hydration levels, adsorption of charged polymer on the charged surface becomes quantitative leading to strong long-range repulsive forces and suspension stability. On the other hand, highly hydrated ions form limited number of bonds with the surface; but, as they also form bonds between polymer segments, bridging forces may lead to destabilization. These effects are optimized in the case of  $\text{Ca}^{2+}$  that can form bridges between similarly charged entities. The role of  $\text{Ca}^{2+}$  concentration is extremely important in such divergent cases as in coagulation and viscosity increase of blood and in determining the green (wet) and dry strengths of sand-clay mixtures in molds used for casting metals in the foundries. If the polyelectrolyte is not adsorbed on the particles and is linear, oscillatory forces can be observed that are of longer range and smaller amplitude in comparison with the oscillatory forces observed in pure liquids described above.

#### 1.4.3.1.4 Category 4: Grafted polymers

Grafted polyelectrolytes are attached by chemisorption onto the particle surface; the type of interaction, steric or bridging, depends on the length of the polymer segments. This in turn is a function of the theta temperature,  $T_\theta$ , in the case of neutral polymers and electrolyte concentrations in the case of charged polymer segments. In biological cells, segments of proteins extending out of the membrane as sensors also act as grafted polymers. Elasticity of the membrane of biological cells and microorganisms also has an effect on the interactions as explained in the next section.

#### 1.4.3.2 *Effect of polyelectrolyte interactions on the fractal dimension of clusters*

There is only a limited number of experimental work done to determine the effect of parameters on the fractal dimension of the aggregate formed. Some of the results given in the literature are discussed here in terms of (1) nonadsorbing and (2) adsorbing polyelectrolytes to show their effect through depletion, bridging and steric forces.

##### 1.4.3.2.1 Effect of nonadsorbing polyelectrolytes

AFM studies show that a secondary minimum in the potential energy profile of the particles may result because of the presence of nonadsorbing polymers (Milling, 1996, 1997; Burns *et al.*, 1999, 2002; Biggs *et al.*, 2000). The variation of the reduced force (force measured in an atomic force microscope (AFM) divided by the cantilever tip radius) with the distance of separation between the silicon-nitride cantilever tip and a flat silica surface is given by Burns *et al.* (2002) as a function of polyelectrolyte poly acrylic acid (PAA) concentration and molecular weight in Figure 1.7(a) and (b), respectively. The sections given in Figure 1.7(a) and (b) correspond to the secondary minimum after the PEB in Figure 1.3(e). The secondary minimum is caused by the summation of attractive depletion force and electrostatic repulsion force. In addition to the depletion forces, the increase in attractive forces is attributed to the reduction of electrical double layer repulsion in the presence of the charged polymers. At extremely low polyelectrolyte concentrations, depletion forces are negligible and the net force is repulsive without a secondary minimum. As the concentration of polymer increases, depletion forces also increase. The depth of the minimum increases and its position changes to lower separation distances. Increase in polyelectrolyte concentration produces a combined effect of reduction in double layer and depletion layer thicknesses. This effect is partially offset by a decrease in the depletion forces depending on the size and concentration of the polymer resulting in a leveling off of the total force at high concentrations as shown in Figure 1.8(a).

The depth of the secondary energy minimum given in Figure 1.7(a) in terms of force units is expressed as potential energy per unit surface area as a function of concentration of PAA in Figure 1.8(a), for the three molecular weights investigated by Burns *et al.* (2002). The negative sign of the ordinate indicates attractive energy. The secondary minimum approaches zero at extremely low concentrations of the polyelectrolyte. The energy of attraction decreases to lower negative values (the depth of the minimum increases in force units) as the concentration of polyelectrolyte increases, leveling off to a constant value at concentrations greater than  $20 \text{ g L}^{-1}$ . Clearly, the depth of the attractive minimum

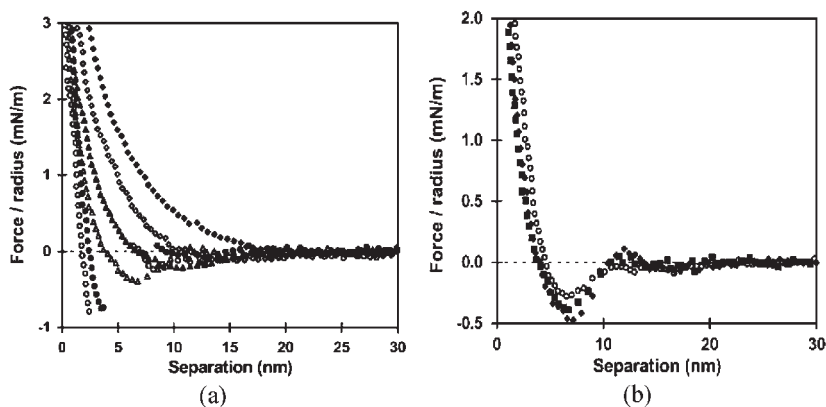


**Figure 1.7** Reduced force ( $F/r_0$ ) versus surface separation curves for a silicon nitride cantilever tip interacting with a flat silica surface: (a) in the presence of various concentrations of PAA (50,000 g mol<sup>-1</sup>): (◆) 1 g L<sup>-1</sup>, (◇) 3 g L<sup>-1</sup>, (▲) 5 g L<sup>-1</sup>, (△) 10 g L<sup>-1</sup>, (●) 20 g L<sup>-1</sup>, and (○) 40 g L<sup>-1</sup>; (b) in the presence of various PAA molecular weights: (◆) 250,000 g/mol, (■) 50,000 g mol<sup>-1</sup>, and (○) 5000 g mol<sup>-1</sup>, all at a fixed PAA concentration of 10 g L<sup>-1</sup>. (Reproduced from Burns *et al.*, 2002, with permission of Elsevier, Figures 6 and 7 in the original.)

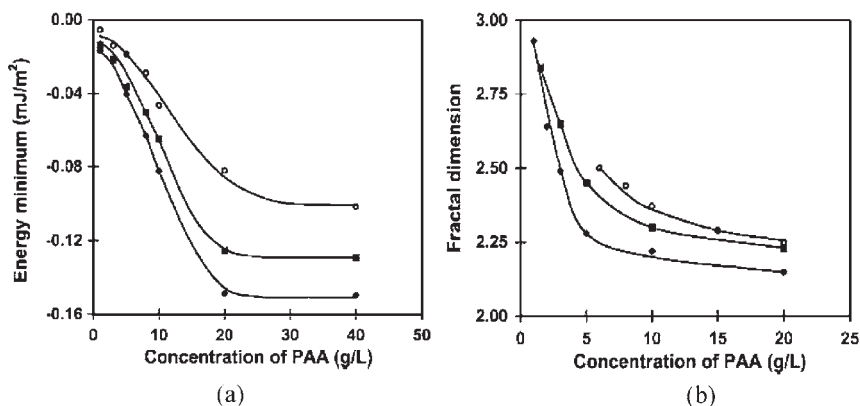


**Figure 1.8** Dependence of the: (a) secondary energy minimum, (b) mass fractal dimension of aggregates of polystyrene latex particles, on changes in the PAA molecular weight and concentration (notation given in Figure 1.7(b)). (Reproduced from Burns *et al.*, 2002, with permission of Elsevier, Figures 5 and 8 in the original.)

decreases as the molecular weight decreases. This shows that the bonds formed become reversible as molecular weight decreases. The shift of the minimum to smaller separation distances shows that more compact structures are to be expected as the concentration of polyelectrolyte increases.

The fractal dimensions of polystyrene latex particle aggregates in the presence of PAA in the same range of concentrations and molecular weights as in Figures 1.7(a) and 1.8(a) are given in Figure 1.8(b). The similarity in the shapes of the curves in Figures 1.8(a) and

(b) shows the effect of the depth of the secondary energy minimum on the structure of the aggregates. The low-energy of the secondary minimum allows the flocs to escape from their initial location and move around until they find an energetically more favorable place. The wandering of the detached flocs was physically observed by the authors under the microscope (Burns *et al.*, 1999). A high-energy minimum located at a short distance from the surface of the particle, observed at high polymer concentrations causes the aggregation to proceed in the RLA regime. The scattering exponent (SE) equivalent to the fractal dimension  $d_f$ , determined by static light scattering method, confirmed this physical model: At very high concentrations of the polymer, SE was found in the range of 2.0–2.2, inversely proportional with the particle concentration. At polymer concentrations less than  $5 \text{ g L}^{-1}$ , SE sharply increased with decreasing polymer concentration reaching a limit of 2.99 at  $1 \text{ g L}^{-1}$  confirming the extensive restructuring that had taken place.

#### 1.4.3.2.2 Effect of adsorbed polyelectrolytes

Effect of the presence of polymers on the structure formed by DLVO forces alone were observed by partially coating polystyrene particles with bovine serum albumin (BSA) molecules (Tirado-Miranda, *et al.*, 2003). An overall increase in  $d_f$  of 0.3 units was observed irrespective of the pH, even though the configuration of the BSA molecules changed in the range investigated. At pH 4.8, the isoelectric point, the polyelectrolyte is at its most compact configuration. At pH 9, both the polystyrene particles and the polyelectrolyte are negatively charged. Polyelectrolyte coated particles were stable at pH 9 but aggregated with a close-packed structure of  $d_f \sim 2.2$  at pH 4.8. The observed instability at the isoelectric point was attributed to the partial shielding of the particle charges by the neutral polyelectrolyte at its isoelectric point, causing the particles to come as close as 3 nm, a distance comparable with the length of polymer segments which “bridge” them within a compact aggregate.

Effect of the *steric* forces was investigated by varying the configuration of grafted polystyrene chains on silica particles in cyclohexane by varying the temperature above and below the theta ( $\theta$ ) point (Huang and Berg, 2004). The fractal dimension  $d_f$  was found to be a function of both time and temperature: It increased from a value of 1.75 at the transition temperature, to its equilibrium value of 2.13 with time while this equilibrium value increased to 2.84 as the temperature was decreased toward the end of the transition interval. Transformation to a more compact structure with time was attributed to spontaneous restructuring due to reduced rate of aggregation as the cluster size increased.

## 1.5 AGGREGATION OF FERROMAGNETIC PARTICLES

Interest in the aggregation of particles with magnetic properties increased recently due to the possibility of controlling their rheological and physical properties by an external magnetic field. A suspension of ferromagnetic particles of about 10 nm in diameter sterically stabilized by long-chain surfactants, or through electrostatic repulsion of adsorbed ions, is called a *ferrofluid*. As in other colloidal systems, the ferromagnetic particles interact through surface forces, such as van der Waals, electrostatic repulsion and steric forces.



In addition, the particles of a ferrofluid interact through long-range anisotropic dipole–dipole potentials. At low particle concentrations where there are no interactions between the suspended particles, a ferrofluid system behaves like an ideal paramagnetic gas. In this case, the equilibrium magnetization of the ferrofluid system  $M_L$  is given by the equation (Wang *et al.*, 2002)

$$M_L = n \frac{m}{\mu_0} \left( \coth \left( \frac{mH}{k_B T} \right) - \frac{k_B T}{mH} \right) \quad (1.63)$$

where  $n$  is the number concentration of particles,  $m$  the magnetic moment of the particles,  $\mu_0$  the magnetic permeability of vacuum,  $H$  the magnetic field, and the term in parenthesis is the Langevin function, connoting the relative effects of thermal energy ( $k_B T$ ) and magnetic energy ( $mH$ ). The initial susceptibility of the medium toward the effect of a magnetic field,  $\chi_i$  is given by

$$\chi_i = \left( \frac{\mu_0 \mu^2}{3} n \right) \frac{1}{k_B T} \quad (1.64)$$

Dipole moment of a ferromagnetic particle,  $\mu$ , is given as the product of its volume  $v_M$  based on its magnetic radius,  $r_M$ , and its magnetization at saturation,  $m_s$ :

$$\mu = \left( \left( \frac{4}{3} \right) \pi r_M^3 \right) m_s = v_M m_s \quad (1.65)$$

The initial magnetic susceptibility is seen to be a function of the volume fraction of particles,  $nv_M$ , from eqs. (1.64) and (1.65)

$$\chi_i = \frac{\mu_0 \mu m_s}{3} (nv_M) \frac{1}{k_B T} \quad (1.66)$$

Eq. (1.66) predicts a linear increase of the initial susceptibility with the particle concentration. Deviation from linearity signifies interaction between the particles, depicted by the dipolar coupling constant  $\lambda$

$$\lambda = \frac{m^2}{4\pi\mu_0 d_p^3 k_B T} \quad (1.67)$$

where  $d_p$  is the particle diameter. Interaction between the particles increases as  $\lambda$  increases, or equivalently formation of aggregates enhances the magnetization of ferrofluids at weak magnetic fields. The thermal energy term in eq. (1.67) signifies that the aggregates formed are subjected to thermal fluctuations and are flexible. Under an applied external magnetic field, the dipole moments tend to align in the direction of the applied field in proportion to the field strength. This causes a lengthening of the needle-like strings into flexible chains together with unavoidable entanglement that causes the viscosity to increase.



### 1.5.1 Effect of the direction of the magnetic field on the aggregate structure

The structures formed on application of an external magnetic field depend on the relative directions of the magnetic field and the plane of the film of ferrofluids. Formation of chains of needle-like aggregate structures is observed when the magnetic field acts parallel to the film of magnetic particles. An increase in the field strength or in the concentration of particles causes more particles to aggregate, increasing the number and length of the chains. The spacing between the chains and the chain width decreases as the field strength  $H$  increases. When the magnetic field acts perpendicular to the ferrofluid film cylindrical magnetic columns are formed. The distance between the columns decreases as the field strength increases. The characteristic spacing in the ordered structures could be manipulated (Horng *et al.*, 2001) within a range from submicrometers to many micrometers by adjusting controlled parameters such as the magnetic field, the sweep rate, the film thickness, the concentration of the fluid and the temperature. Significant optical properties could be generated with these ordered structures.

### 1.5.2 Reversibility of aggregation

Reversibility of aggregate formation is an important issue if the end use of the ferrofluids is in the field of electronics. Ferromagnetic particles aggregate to reduce their enthalpy; but alignment in the form of strings decreases their entropy, so that aggregation and disintegration should be in balance dictated by the equilibrium conditions of the system. Klokkenburg and Ern  (2006) tested the reversibility of zero-field aggregation of magnetic nanoparticles in a ferrofluid by two methods: By decreasing the dipole moments of the particles and by decreasing their concentration. Unoxidized iron–carbon particles ( $\text{Fe}_{0.75}\text{C}_{0.25}$ ) in decalin stabilized sterically by polyisobutene were used in the first case. The particles were subjected to gradual oxidation to decrease their magnetic moments. Oxidation turned out to cause chemical interactions between the particles making the aggregation irreversible. Effect of a concentration decrease was tested on colloidal magnetite dispersions stabilized by surfactants. The results showed that zero-field dipolar structures disintegrated upon dilution indicating the reversibility of aggregation process through dipolar attractions.

Small-angle neutron scattering and light scattering measurements were used by Shen *et al.* (2001) to elucidate the structure of magnetite aggregates in aqueous and organic solvents stabilized by surfactants *in situ*. The magnetite particles were stabilized by a monolayer of adsorbed decanoic acid in organic (hexane) solvents. A second adsorptive coating by dodecanoic acid that would form a bilayer with the already adsorbed decanoic acid was necessary to reduce the attractive forces among hydrophobic surfaces in aqueous solutions and maintain stability through repulsion of the charged head groups. The results of the measurements indicated the formation of fractal structures with  $d_f = 2.52$  and a characteristic dimension of  $350 \text{ \AA}$  in aqueous media. As long as the second (outer) surfactant layer of the bilayer stabilizing the clusters could be kept intact, the cluster size remained stable. This was attributed to the increasing height of the PEB formed by the charged hydrophilic groups of the surfactants as the size of the cluster increased, approaching the  $15k_B T$  limit for

electrostatic stability (Vold and Vold, 1983). The stability of these clusters in aqueous media was strongly dependent on the ionic strength of the medium, as stability is maintained by electrostatic forces only. In organic solvents where there is no electrostatic repulsion, small chain-like clusters with  $d_f = 1.22$  and a characteristic dimension of  $400 \text{ \AA}$  were formed, which were sensitive to volume fraction of the clusters in solution. Because of the orientation of the surfactant molecules of the coating in organic media, the surfactant layer does not make any contributions to the Hamaker constants because of the similarity of surfactant chains and the solvent molecules. In the absence of repulsive forces and weak van der Waals forces, the magnetite particles are expected to form chain-like structures by coupling end-to-end through the action of magnetic dipole moments. This is only a weak bond, however, because the magnetic dipole–dipole interactions are counteracted by the steric effect of the surfactant layer as well as the thermal energy,  $k_B T$ , resulting in the small size of the clusters, low  $d_f$  values and fragile chain-like structures that are sensitive to dilution.

### 1.5.3 Light-induced aggregation of ferrofluids

Recently, reversible light-induced aggregation in the absence of a magnetic field of ferro-magnetic particles were reported (Hoffmann and Köhler, 2003; Kellner and Köhler, 2005). Magnetite particles of about  $10 \text{ nm}$  in size suspended in kerosene and initially stabilized by the steric action of an adsorbed layer of surfactants were found to aggregate when exposed to light. Light absorbance of the particles was maximum around  $400 \text{ nm}$  that decayed rapidly to a negligible constant value at wavelengths greater than  $650 \text{ nm}$ . The particles were found to aggregate to sizes reaching a few micrometers and moving randomly with Brownian motion when exposed to white tungsten light at an intensity of  $100 \text{ W m}^{-2}$ . The aggregates were found to disintegrate upon the use of a filter that permitted radiation greater than  $645 \text{ nm}$ . Two different rates of growth under reduced light intensities were attributed to fast initial aggregation of particles and a sequent slower growth of the clusters. The process was found to be completely reversible with no aging effects. When the same ferrofluid was subjected to a weak magnetic field, no aggregation was observed; but if light-induced aggregation was conducted under a weak magnetic field, isotropic clusters were formed as in the absence of a magnetic field, which then aligned along the magnetic field lines to form highly anisotropic linear superstructures. As a possible mechanism underlying the observed phenomenon of light-induced aggregation, an increase in the average population of the electronic states with higher electric polarizability than in the absence of light was proposed. The enhanced van der Waals forces could then overcome the steric barrier and cause the reversible aggregation.

## 1.6 FORMATION OF GLASSES AND GELS

Equilibrium states of solid particles are the crystal, liquid and gas states. Crystal states require close packed conditions satisfied through strong attractive forces between the particles at solid volume fractions of approximately,  $\phi = 0.74$ . When this close-packed structure is expanded in volume by about one-third,  $\phi \approx 0.545$ , rigidity of the hard sphere

crystal is lost (Poon, 2002 and the cited references). If the particles are still within the attractive potential field of each other, a dense liquid phase is observed. If the distance covered by the attractive potential field is less than the interparticle distance, a gas state is reached where the particles act independent of each other. A configuration different from the one expected at equilibrium for the same volume fraction of particles leads to non-equilibrium states of the suspension.

### 1.6.1 The glassy state

There are cases when crystallization is not observed even at  $\phi \geq 0.58$ . This is attributed to the local caging of particles, each particle being entrapped itself, besides being a member of a cage for surrounding particles (see Figure 3.1(e)). This nonequilibrium solid state is called, *glass*.

Pham *et al.* (2002) showed that two types of glass states could exist in a mixture of polymers and hard spheres at two different polymer to solid sphere ratios, corresponding to different modes of repulsive and attractive interactions. With a model system of sterically stabilized polymethylmethacrylate (PMMA) spheres ( $R = 202$  nm) suspended in decalin, which also contains nonadsorbing polystyrene ( $R_g = 17$  nm) they obtained the phase diagram given in Figure 1.9. When there is no polymer in the suspension fluid, fluid–crystal coexistence and crystal regions are observed as the volume fraction of PMMA particles

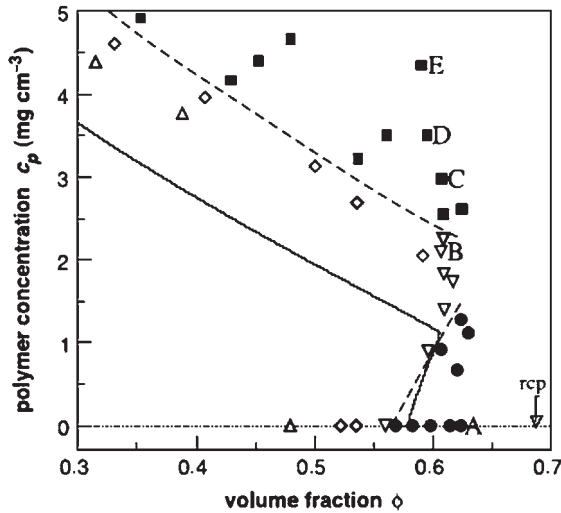


**Figure 1.9** Equilibrium and nonequilibrium behavior of a colloid–polymer mixture at  $R_g/R=0.08$ . Samples that reached thermal equilibrium (open symbols) are as follows: fluid (triangles), fluid–crystal coexistence (diamonds), and fully crystalline (inverted triangles). Samples that did not reach thermal equilibrium (solid symbols) are as follows: repulsion-driven glass (circles) and attraction-driven glasses (squares). Dashed curves are guides for the observed glass transition lines. Solid curves are Mode Coupling Theory predictions of glass transition lines. (Reproduced with the caption of Pham *et al.*, 2002, Figure 1 in the original with permission of Science AAAS.)

increased. Steric repulsion between the particles prevented crystal formation and glass state was observed above  $\phi \geq 0.58$ . As the polymer concentration was increased at constant solid particle fraction of  $\phi \approx 0.6$ , crystalline particles were observed again due to the action of depletion forces. Above the dashed line, denoting the glass transition lines, glassy states reentered the phase diagram, this time brought about by attractive forces. Glassy states are observed at high volume fractions of solid particles. This topic will be taken up again in relation to concentrated suspensions in Chapter 3.

### 1.6.2 Formation of gels

Another type of aggregation that confers non-Newtonian behavior to solid–liquid suspensions is gelation. A gel is a nonequilibrium state where the diffusive motions of the particles are prevented through long-range attractions. Recent studies show that even short-range forces in the order of a fraction of a particle radius can bring about gelation out of a homogeneous liquid phase if the attractive forces are strong, and concentrations high enough (Shah *et al.*, 2003 and the cited references). The requirement for gel formation is the existence of attractive forces between the particles sufficient to form a network spanning the available volume. The attractive forces can be anything such as bridging or electrostatic as in the case of clay (electrostatic), microemulsions (bridging of inverse micelles) and polymer suspensions (bridging) as given in Figure 1.10(a)–(c), respectively. In the case of particle–polymer mixtures where the polymers do not adsorb on the particles, depletion forces supply the required attraction. The stability of the suspensions depends on the strength of these attractive forces acting against thermal energy ( $k_B T$ ) and hydrodynamic forces, as well as on the volume fraction of solids that maintain the stability of the network toward the action of gravity on the solid particles. The rheological properties are an indication of the stability of the gels, as will be explained in Chapter 2 for polymer gels and Chapter 3 for clay gels.

Gels are also formed by fractal aggregates. When the number and the size of the clusters are sufficient to fill the available space through edge-contact. Clusters formed by diffusion limited aggregation (DLA) are greatly ramified at the edges. Restructuring increases the compaction of the cluster indicated as an increase in  $d_f$  above that for reaction limited aggregation (RLA), simultaneously enlarging the void space between clusters opening up space for percolation of the suspending medium. If the cluster structure is very dense and particle concentration not sufficient to form a compact gel structure, clusters

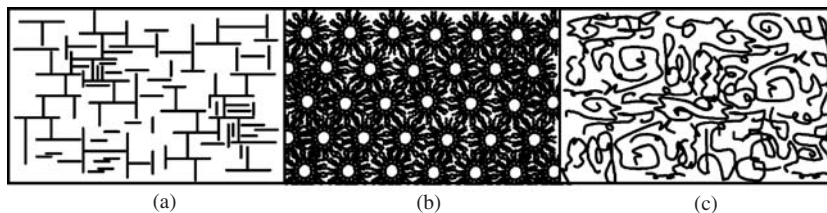


**Figure 1.10** Various types of gels: (a) clay suspensions, (b) microemulsions, and (c) polymers in solution.

may settle under the action of gravity, as will be explained in Chapter 4. Very compact structures can also form in gels with a high volumetric fraction of particles (Shah *et al.*, 2003). The heterogeneity in the particle distribution necessitates the formation of voids, though they are very small as the attraction is controlled by depletion forces with the range of attraction proportional to the radius of gyration of the polymer,  $R_g$ , which is much less than the particle radius,  $R$ .

Fractal aggregates are also observed in gels of polymeric (Huang and Berg, 2004; Takenaka *et al.*, 2004) or microemulsion origin (Bordi *et al.*, 1996; Antalek *et al.*, 1997; Letamendia *et al.*, 1998), in fat-crystal networks (Narine and Marangoni, 1999) or in the sol–gel processes (Berthon *et al.*, 2001; Chiavacci *et al.*, 2004). Fractal dimension not only determines the compactness of the aggregate structure, but also affects the rheological behavior of concentrated suspensions (Lapasin *et al.*, 1998), and migration of charges resulting in an increase of the conductivity (Bordi *et al.*, 1996; Antalek *et al.*, 1997). Relaxation phenomena in critical microemulsion systems is attributed to the formation of transient polydispersed fractal aggregates of  $d_f \sim 2.5$ . Fractal dimension of  $\sim 2.5$  was also obtained in different gel systems in experimental observations (Narine and Marangoni, 1999; Berthon *et al.*, 2001; Chiavacci *et al.*, 2004; Takenaka *et al.*, 2004).

Another type of gel of current interest is that formed by wormlike micelles, used as nanoreactors containing nanoclusters for the production of nanowires. Cylindrical micelles are made of surfactant molecules that pack-up in a liquid crystal structure. These cylindrical micelles align in a hexagonal order and continue growing length-wise until they span the available volume. Bouchama *et al.* (2004) investigated the thermal gel–fluid transitions of the hexagonal phase and showed that hexagonal phase can melt and recrystallize repeatedly, allowing trapping of various metal clusters in pre-prepared hexagonal phases.

## 1.7 SELF-ASSEMBLIES OF SURFACTANTS

In the previous sections, the polyelectrolyte molecules with electrophilic groups attached to a hydrocarbon chain were discussed in terms of the forces created by their local concentration and interactions with the particle surfaces. Surface active agents, or shortly surfactants, are similar to polyelectrolytes in that they are also amphiphilic molecules that have both a hydrophilic and a hydrophobic moiety in their structure. The main differences are that the hydrocarbon chains of the surfactants are much shorter than the backbone chain of the polyelectrolytes and they usually have only one or two hydrophilic groups gathered at one end of the molecule instead of being dispersed along the chain length. Surfactants have an immense area of applicability in processes related with emulsions, foams, as dispersion agents in suspensions, and in emerging technologies based on vesicles and microemulsions. The significance of surfactants in solid–liquid two phase flow resides on their use as stabilizing agents for microparticles, as flotation agents in mineral processing, as reactors for nanoparticles, as carriers in targeted delivery and slow release of drugs in the blood stream, as building blocks of the membranes of “soft” particles such as microorganisms and red blood cells (RBCs), and in drag reduction. Surfactants can be synthesized by conventional chemical synthesis or produced by living cells and microorganisms. Biologically produced surfactants generally have a much more complicated structure than the synthetically produced surfactants. Examples for the types of surfactants and their structures are given in Table 1.3.

**Table 1.3**

Types of surfactants and their structures

Type of surfactant	Example	Molecular structure
Anionic	Sodium dodecylbenzenesulphate	$\text{Na}^+ \text{O}_3\text{S}-\text{C}_6\text{H}_4-\text{C}_{12}\text{H}_{25}$
Cationic	Cetyltrimethylammonium bromide	$\text{C}_{16}\text{H}_{33}\text{N}^+(\text{CH}_3)_3 \text{Br}^-$
Nonionic	Polyoxyethylenesorbitan monooleate (Tween 80)	$\begin{array}{c} \text{O} \begin{array}{c} \diagup \text{---} (\text{OCH}_2\text{CH}_2)_w \text{OH} \\ \diagdown \text{---} (\text{OCH}_2\text{CH}_2)_x \text{OH} \end{array} \\   \\ \text{CH} \text{---} (\text{OCH}_2\text{CH}_2)_y \text{OH} \\   \\ \text{CH}_2 \text{---} (\text{OCH}_2\text{CH}_2)\text{O} \text{---} \text{C}(=\text{O}) \text{---} \text{C}_{17}\text{H}_{33} \end{array}$ $w+x+y \approx 20$
	Sorbitan monostearate (Span 60)	$\text{C}_{18}\text{H}_{35}\text{O}_6$
Zwitter ionic	Phosphatidyl ethanolamine	$\text{OCH}_2\text{CH}_2\text{N}^+\text{H}_2 \text{---} \text{C}(\text{CH}_2\text{OC}(=\text{O})\text{C}_{17}\text{H}_{33})_2 \text{---} \text{OCH}_2\text{P}(=\text{O})(\text{O}^-)\text{OCH}_2$
Double-chained	Sodium-bis(2-ethylhexyl)-sulfosuccinate (AOT)	$\text{Na}^+ \text{O}_3\text{S} \text{---} \text{C}(=\text{O}) \text{---} \text{C}(=\text{O}) \text{---} \text{O} \text{---} \text{C}_8\text{H}_{17} \text{---} \text{O} \text{---} \text{C}_8\text{H}_{17}$
	Gemini surfactant	$\text{CH}_3 \text{---} \text{N}^+(\text{CH}_3) \text{---} (\text{CH}_2)_n \text{---} \text{N}^+(\text{CH}_3) \text{---} \text{CH}_3$

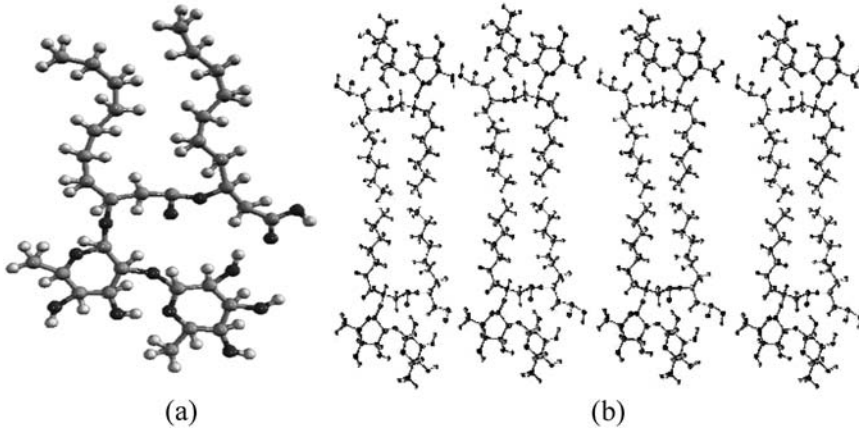


**Figure 1.11** Rhamnolipid R2 surfactant, (a) in its minimum energy configuration and (b) in the form of bilayers.

To help in the visualization of the amphiphilic nature of a surfactant molecule and understanding of its orientation at interfaces, a render model of a biosurfactant, rhamnolipid R2, produced by *Pseudomonas aeruginosa* is given in Figure 1.11(a). The dark spheres denote oxygen, the small spheres, hydrogen, and large spheres, carbon atoms in the structure. The surfactant modeled at its minimum energy position with ChemSite Pro software has two decanoic acid groups coupled with an ester bond. A free carboxylic acid group is attached to one of the hydrocarbon chains and two rhamnose groups attached to the other chain. The two hydrocarbon chains are separated by the ester group. The lower part of the molecule including the carboxylic acid, rhamnose, and interconnecting ester group is rich in oxygen atoms and constitute the hydrophilic part of the molecule. The rest of hydrocarbon chains are rather short, with effectively eight methylene groups each, so the molecule preferentially dissolves in water. As the hydrophylic functional groups are connected by single bonds to the hydrocarbon chains they can reorientate depending on the interactions between the hydrophilic groups and the constituents of the aqueous medium (Peker *et al.*, 2003; Helvacı *et al.*, 2004; Özdemir *et al.*, 2004).

The presence of the hydrophobic groups within the structure of the surfactant molecule, makes its existence energetically unfavorable within the bulk medium, so the surfactant molecules are distributed in the form of *monomers* in solution, as *monolayers* at gas/liquid, liquid/liquid, or solid/liquid interfaces, whichever exists, or in the form of *micelles*. The total concentration of surfactants  $C_s^o$  in a system is the sum of all the concentration of surfactants in different states:

$$C_s^o = C_{\text{mon}} + C_{\text{mly}} + C_{\text{mic}} + C_{\text{ads}} \quad (1.68)$$

where  $C_{\text{mon}}$  is the monomer concentration,  $C_{\text{mly}}$  the concentration of surfactants that are associated as monolayers at gas/liquid interfaces,  $C_{\text{ads}}$  the concentration of surfactants adsorbed on solid surfaces and  $C_{\text{mic}}$  is the concentration in micellar aggregates. The solubility of the



monomers in aqueous solutions is determined by the relative volumes of the hydrophobic and hydrophilic groups in its structure, increasing with an increase in the latter. Surfactant molecules decrease their free energy by residing at interfaces, with the hydrophobic group oriented toward the nonpolar liquid in the case of two-liquid systems, toward air in the case of liquid–gas systems, toward the solid in the case of uncharged solid particles in an aqueous medium.  $C_{\text{mly}}$  is limited by the extent of gas/liquid interfacial area available in the macrosystem and the minimum area occupied by a surfactant molecule at the interface,  $a_{\text{int}}$ .  $C_{\text{ads}}$  is limited by the total surface area of the solids and the fraction of this area available for adsorption (*distribution of adsorption sites* or *fractional coverage*) depending on the heterogeneity of the solid surface. Finally, the remaining surfactants in solution will aggregate in the form of micelles.

### 1.7.1 Thermodynamics of self-assembly of surfactants

All forms of existence of surfactant molecules will be in equilibrium with each other including surfactants adsorbed on solid surfaces if adsorption is through reversible physical bonds only. Equilibrium condition, in the case of reversible aggregation, dictates that the free energy of a molecule (equivalent to its chemical potential) should be the same under all conditions. It is possible to find the concentration of each form of existence using the free energy relations. The number of surfactant molecules making up a micelle can be calculated starting with this principle. Adopting the notation of Israelachvili (1991), the chemical potential can be written as

$$\mu = \mu_N = \mu_N^0 + \frac{k_B T}{N} \ln \frac{X_N}{N} = \text{constant} \quad (1.69)$$

In this equation  $\mu$  denotes the chemical potential,  $\mu_N^0$  is the mean interaction free energy per molecule or the standard free energy,  $N$  the number of surfactant molecules making up the aggregate and  $X$  is the concentration of the molecules in the aggregate in terms of mol fraction. As this relation is general it can be used to relate the free energy of the monomer with that of a molecule in the fully aggregated state:

$$\mu = \mu_N^0 + \frac{k_B T}{N} \ln \frac{X_N}{N} = \mu_1^0 + k_B T \ln X_1 \quad (1.70)$$

$$(\mu_1^0 - \mu_N^0) + k_B T \ln X_1 = \frac{k_B T}{N} \ln \frac{X_N}{N} \quad (1.71)$$

where the subscripts  $N$  and  $1$  indicate the aggregate and monomer, respectively.

The ratio of the concentrations in the associated and unassociated states is

$$\frac{(X_N / N)}{X_1^N} = \exp \left( - \frac{N(\mu_N^0 - \mu_1^0)}{k_B T} \right) \quad (1.72)$$



The term on the LHS of the equation is by definition, the equilibrium reaction constant  $K$  for the reversible formation and dissociation rates of the micelles

$$K = \frac{(X_N / N)}{X_1^N} = \frac{k_{\text{formation}}}{k_{\text{dissociation}}} \quad (1.73)$$

Micelles are dynamic aggregates with surfactant molecules going in and out of the micelle. The residence time of a surfactant molecule in the micelle,  $t_R$ , depends on the interactions of the molecule with the surrounding molecules in solution and in the aggregate, or equivalently the difference in the mean interaction free energies,  $\mu_N^0 - \mu_1^0$ . Characteristic collision time,  $t_0$ , of a molecule is then equal to the product of the mean residence time the molecule spends in the micelle and the probability that the energy of the collision will be sufficient for escape from the surrounding interacting molecules:

$$t_0 = t_R \exp\left(\frac{-\Delta E}{k_B T}\right) = t_R \exp\left(\frac{-(\mu_N^0 - \mu_1^0)}{k_B T}\right) \quad (1.74)$$

Characteristic collision time of surfactants is in the order of  $10^{-9}$  sec for micelles and  $10^{-7}$  sec for bilayers (Israelachvili, 1991). Therefore, the residence time of a surfactant in the micelle is a function of its interactions with the neighboring molecules. These interactions depend on the charge of the hydrophilic group, the van der Waals interactions between the hydrocarbon chains and between the O and H atoms in the hydrophilic group (H-bonds). As these interactions will be much stronger in double-chained surfactants with compact structures, their mean interaction free energies,  $\mu_N^0$  will be much lower than that of surfactants aggregated as spherical micelles, where the distance between hydrocarbon groups are increased due to curvature. Based on the characteristic collision time of surfactants, the membrane forming bilayers are expected to be much more stable than the spherical micelles.

### 1.7.2 Self-assemblies in solution

The concentration at which aggregation starts is called *critical micelle concentration* (CMC). This term is used exclusively for self-assembly of surfactants in solution. A more general term *critical aggregation concentration* (CAC), is also used for surfactant aggregation on solid surfaces, and aggregations in polymer–surfactant mixtures. The CMC depends on the *temperature, through the solubility*; and *structure* of surfactant molecules, *through steric effects*: Solubility of surfactants increase slightly with temperature up to a point called the *Krafft point*, after which it increases drastically. At concentrations below the solubility limit, the surfactant molecules exist in the form of monomers. The temperature should be above the Krafft point to prevent solubility becoming a parameter in the aggregation of surfactants. Micelles are formed at concentrations above the solubility and temperatures above the Krafft point of the surfactant. Various shapes of micelles are given in Figure 1.12. A model of bilayer formation by rhamnolipid R2 molecules is given in Figure 1.11(b). The shape that

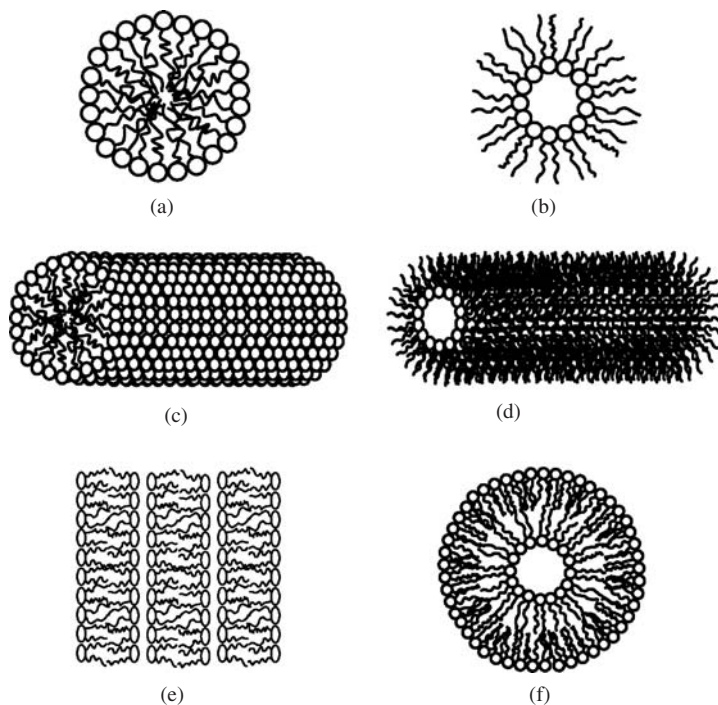


**Figure 1.12** Types of micelles: (a) normal spherical, (b) reverse spherical, (c) normal hexagonal, (d) reverse hexagonal, (e) lamellar (bilayer) and (f) vesicle.

will be favored by a surfactant system depends on the type and structure of the surfactant, and the ionic strength of the solution, which will be discussed next.

The model of a rhamnolipid molecule, a double-chained surfactant at its minimum energy position given in Figure 1.11(a) could be circumscribed by a cylinder in three-dimensional space. Had there been only one hydrocarbon chain, the geometrical shape that would circumscribe the molecule would be a cone. The bulky hydrophilic head group would constitute the base and the hydrocarbon tail would determine the height of the cone. When a number of molecules would assemble, the preferred shape of the aggregate of single-chained surfactants would be a sphere and that of the double-chained, a flat layout, such as a bilayer, due to the inflexibility of the cylindrical form. In a bilayer, either the head groups, or the tails could be encompassed within the bilayer, depending on the continuous phase in between the double-layers. In the case of spherical micelles, the group that occupies the larger volume fraction constitutes the external surface. The compatibility of the external surface structure with that of the continuous medium determines in which phase the micelles exist: In the aqueous phase, the hydrophilic group constitutes the external phase, whereas in the oil phase, the hydrocarbon tails protrude out from the surface (inverse micelles). The in-between case would be a truncated cone, where cylindrical micelles would be favored, and orientation of the molecules being dependent on the external continuous phase. In geometrical terms, these conditions are expressed in terms of the

base area and height of the circumscribed volume of the molecule, known as the *critical packing parameter* (CPP):

$$\text{CPP} = \frac{v}{a_s l_c} \quad (1.75)$$

where  $v$  is the volume of the molecule,  $a_s$  the area occupied by a molecule at an interface, and  $l_c$  the length of the hydrocarbon chain given in [Å] units by the equation

$$l_c = 1.54 + 1.265 n_c \quad (1.76)$$

where  $n_c$  is the number of carbon atoms in the hydrocarbon chain. A CPP value less than 1/3 signifies spherical micelles,  $1/3 < \text{CPP} < 1/2$ , cylindrical micelles,  $1/2 < \text{CPP} < 1$ , vesicles, and  $\text{CPP} \approx 1$ , bilayers.

The bilayer structure is of particular interest as it constitutes the cell membranes. Two properties of the bilayer are of particular importance, *elasticity*, and *bending modulus*. Balance between attractive and repulsive forces (in the case of ionic surfactants) determines the optimum interfacial area  $a_0$  for a surfactant molecule, where the total interactive energy will be minimum. Just as in the case of spring forces, if the interfacial area is stretched, attractive forces will act to draw the molecules to the minimum area. In other words, the molecules at the interface behave elastically toward an extension or compression in the same plane. The elastic energy  $E_{\text{el}}$  [J], is given by

$$E_{\text{el}} = \frac{1}{2} K_{\text{el}} \left( \frac{(a - a_0)^2}{a} \right) \quad (1.77)$$

where  $a_0$  is the optimum interfacial area,  $a$  the area under stretched conditions, and  $K_{\text{el}}$  the modulus of elasticity [ $\text{Jm}^{-2}$ ]. Through energy considerations, modulus of elasticity is found to be  $K_{\text{el}} \approx 2\gamma$  for monolayers and  $K_{\text{el}} \approx 4\gamma$  for bilayers where  $\gamma$  is the surface tension (Israelachvili, 1991). Experimental values of the modulus of elasticity of fluid lipid bilayers and free biological cell membranes are found to be in the range of  $0.10$ – $0.23 \text{ Jm}^{-2}$  (Kwok and Evans, 1981; Evans and Rawicz, 1990; Marsh, 1990).

Interaction between the hydrophilic and hydrophobic groups also leads to a resistance to bending or variation of radius of curvature of the bilayer (Israelachvili, 1991):

$$E_b = -2\gamma\delta \frac{d}{R^2} = \frac{1}{2} \frac{K_b}{R^2} \quad (1.78)$$

where  $E_b$  is the energy of bending [ $\text{Jm}^{-2}$ ],  $\delta$  the bilayer thickness,  $d$  the distance from the hydrocarbon–water interface where the repulsive forces are centered,  $R$  the radius of curvature,  $\gamma$  the surface tension [ $\text{Jm}^{-2}$ ], and  $K_b$  the bending modulus [J]. When head-group repulsion dominates,  $d$  is positive and  $K_b$  is negative; and when chain repulsion dominates,  $d$  is negative and  $K_b$  is positive. Experimental values of  $K_b$  (positive) of fluid bilayers are in the range of  $(2 - 20) \times 10^{-20} \text{ J}$ . When  $K_b$  is negative, stable vesicles cannot form, which occurs in the case of large repulsive head groups and short hydrocarbon chains.

Bilayers, biological membranes and other surfactant aggregates such as vesicles and micelles in microemulsions are not rigid but fluid-like, moving constantly under thermal fluctuations. In the case of bilayers and membranes, the component surfactant layers can move in wave-like motion (undulation), bringing about forces of entropic origin during these random motions (Israelachvili, 1991). The first of these, the *protrusion force* arises if a side chain dangling into the space between the component layers becomes “squeezed” during the random motion of the layers. The response is repulsion due to entropy decrease on confinement within a limited space. An *undulation force* arises during the wave-like motion of the membrane and is associated with the bending modulus  $K_b$ , as given above. The component surfactant layers of a membrane can also undergo peristaltic motion: The component layers may approach and retract from each other without bending. In this case, a *peristaltic force* arises related with the modulus of elasticity (or resistance to expansion)  $K_{el}$ . Resistance to close approach of the component layers also contributes to this force.

### 1.7.3 Self-assemblies on solid surfaces

Surfactants aggregate on the surfaces of solids on which they are adsorbed with the same motivation of reducing their free energy by secluding their hydrophobic groups from the aqueous phase. Surfactants may adsorb on surfaces either with their hydrophobic or with their hydrophilic groups. The first case occurs when the solid is hydrophobic. The hydrocarbon chain of the surfactant molecule is adsorbed on the solid surface, leaving the hydrophilic ends suspended in the aqueous solution. The net effect of this adsorption is similar to formation of micelles, with the particle enclosed by a layer of surfactants.

Since most solid surfaces are negatively charged, cationic surfactants are preferably adsorbed on the surfaces of the particle rendering it hydrophobic. This may be a desirable situation if the aim is suspension of the particles. Stabilization of the suspension occurs over a limited range of concentrations only, for the surfactants form a second layer (bilayer) on the free hydrocarbon chains with the hydrophilic groups facing the aqueous solution when present in concentrations in excess of that required for full coverage of the particle surfaces. Spherical or disc shaped micelle formation is also possible if the attractive forces between the hydrophobic chains are greater than the attractive forces between the solid surfaces and the hydrophilic groups. The CPP is an indication of the strength of adsorption of surfactants whether the solid surface is hydrophobic or hydrophilic: Adsorption increases as CPP increases (Jönsson *et al.*, 1998). Therefore, double-chained surfactants with CPP value  $\approx 1$  are preferably adsorbed on solid surfaces and are excellent suspension reagents. In the case of Gemini surfactants with double hydrocarbon chains and two cationic groups, both the increased adsorption energy of the two hydrophilic groups and density of the hydrocarbon chains contribute to the compactness of the adsorbed monolayer (Rabinovich *et al.*, 2005). A high repulsive barrier toward aggregation is formed even at the low CMC values of these surfactants. Addition of an electrolyte also increases the CPP leading to increased adsorption of ionic surfactants on solid surfaces. Maximum repulsive force was found to increase linearly with the chain length of the cationic surfactants (Adler *et al.*, 2000) at surfactant concentrations twice the CMC value. This maximum repulsion force that is an order of magnitude greater than expected from

electrostatic repulsion forces was attributed to elastic deformation of adsorbed surfactant layers and specifically to the resistance to compression of surfactant self-assemblies in the adsorbed layer, as will be explained below.

## 1.8 STABILIZATION OF SUSPENSIONS

In some processes, particularly technologies related with nanoparticles, stability of the suspension and control of the size distribution of the particles is a prerequisite for the expected performance of the particles. The only long-range repulsive forces that can be employed to overcome the attractions caused by ubiquitous van der Waals forces are double layer repulsions and steric forces. Double layer repulsions handled by the DLVO theory is relevant under mild strengths of electrolytes and pH. Stabilization by repulsive forces is used with success in operations involving particles in the micrometer scale. As the particle size is reduced to nanoranges, the charges carried by these small volume bodies decrease. The repulsive ionic cloud around these particles is not sufficient to overcome the attractive van der Waals forces, necessitating the employment of steric forces to maintain stabilization. Steric repulsion can be brought about by the adsorption of three different entities: (1) surfactants, (2) polymers and polyelectrolytes, (3) nanoparticles. As each of these methods is an issue of current interest and intensive research, some of the recent developments are summarized below.

### 1.8.1 Stabilization by surfactants

Stabilization by surfactants is a complicated phenomenon involving surfactant–surface, surfactant–surfactant, surfactant–solvent, and solvent–surface interactions. By manipulating these interactions, surface morphology, hydrophobicity, surface layer strength, and rheological properties can be changed according to the process requirements. In the flow of concentrated suspensions, in high shear processes such as mixing, and in extrusion of pastes, the adsorbed surfactant layers are forced to interact under high shear and close distances. To reduce the deformative and destructive effect of close approach under stress, the surfactant layer should have adequate yield strength and modulus of elasticity (Rabinovich *et al.*, 2004). In this section, structure of surfactant layers will be related to resistance toward deformation.

It is possible to change the surface morphology of solid particles by adsorption of surfactants. The surface concentration of surfactants  $\Gamma$  [mol m<sup>-2</sup> or molecules Å<sup>-2</sup> units] on solid or liquid surfaces is in equilibrium with the bulk phase concentration or more correctly with the activity of surfactants in solution, determined by the Gibbs adsorption isotherm. Increase in the bulk concentration above that required for compact film formation at solid surfaces ( $\Gamma_{\text{max}}$ ) changes the structure of the surfactant film on the solid surfaces. This concentration is closely related with the CMC or CAC of the surfactant. The structure of the film depends not only on the concentration but also on the structure of the surfactant and the hydrophobicity of the solid surface: Surfactants adsorb with their hydrocarbon chain on hydrophobic solid surfaces. As the bulk concentration increases, surface

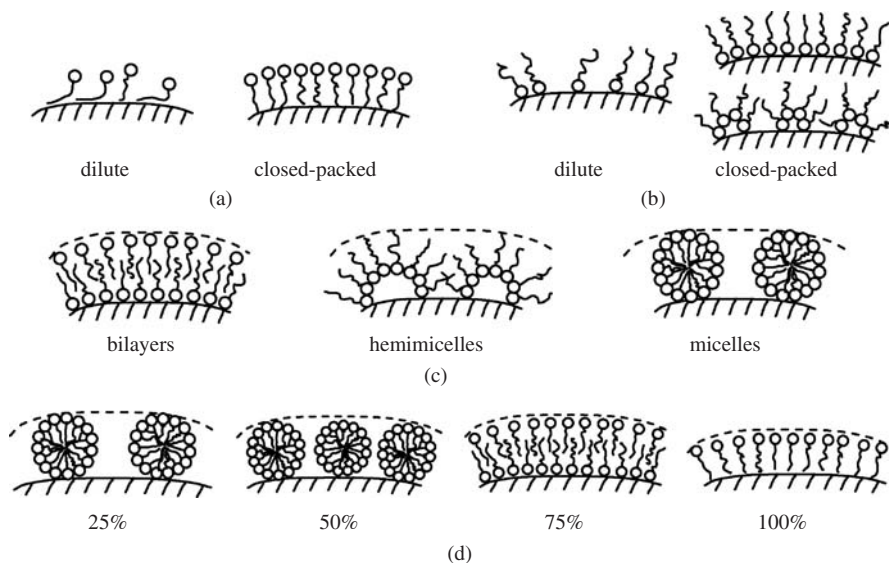


**Figure 1.13** Structure of surfactant layers on solid surfaces. (a) Hydrophobic surfaces, (b) hydrophilic surfaces, (c) possible configurations at high surfactant concentrations and (d) variation of the layer structure with the hydrophobicity of the surface related with Figure 1.14.

concentration also increases, bringing the surfactant molecules into an upright position as depicted in Figure 1.13(a). At maximum concentration, only the hydrophilic groups are accessible from the exterior, rendering the particle hydrophilic. Surfactants adsorb with their hydrophilic groups on solids bearing an opposite charge, such as in the case of preferential adsorption of cationic surfactants on negatively charged clay surfaces. The structure of the surfactant film depends on the surface charge density of the solids. If uniform charge density prevails, as in the highly charged solids, then a similar compact monolayer forms rendering the solid surfaces hydrophobic, as in Figure 1.13(b). The surface morphology depends on the surfactant structure at higher concentrations. Possible configurations are shown in Figure 1.13(c).

#### 1.8.1.1 Variation of surface forces with the structure of the surfactant layer

The structures in Figure 1.13(c) are for surfactants with head groups made up of electrophilic atoms only. Ethoxylate type of surfactants with hydrophilic end groups of the form  $[-O(-CH_2-CH_2-O)-H]$  are widely used in many processes and are of special interest. This group can attach to the surface by hydrogen bonds via  $-O-$  atoms, or through hydrophobic forces via the ethylene groups. Grant *et al.* (2000) prepared engineered surfaces by chemisorbing thiohexadecane ( $CH_3(CH_2)_{15}-SH$ ) and thiohexadecanol ( $CH_2OH(CH_2)_{15}-SH$ ) via  $-S-$  bridges on gold surfaces, so that the external surface of the particle would have known percentages of  $-CH_3$  and  $-OH$  groups, thus, known percentage of hydrophobicity. They adsorbed an ethoxylate type of surfactant octa(oxyethylene) *n*-dodecyl ether ( $C_{12}E_8$ ) on the engineered surface and measured the surface forces as a function of configuration of the

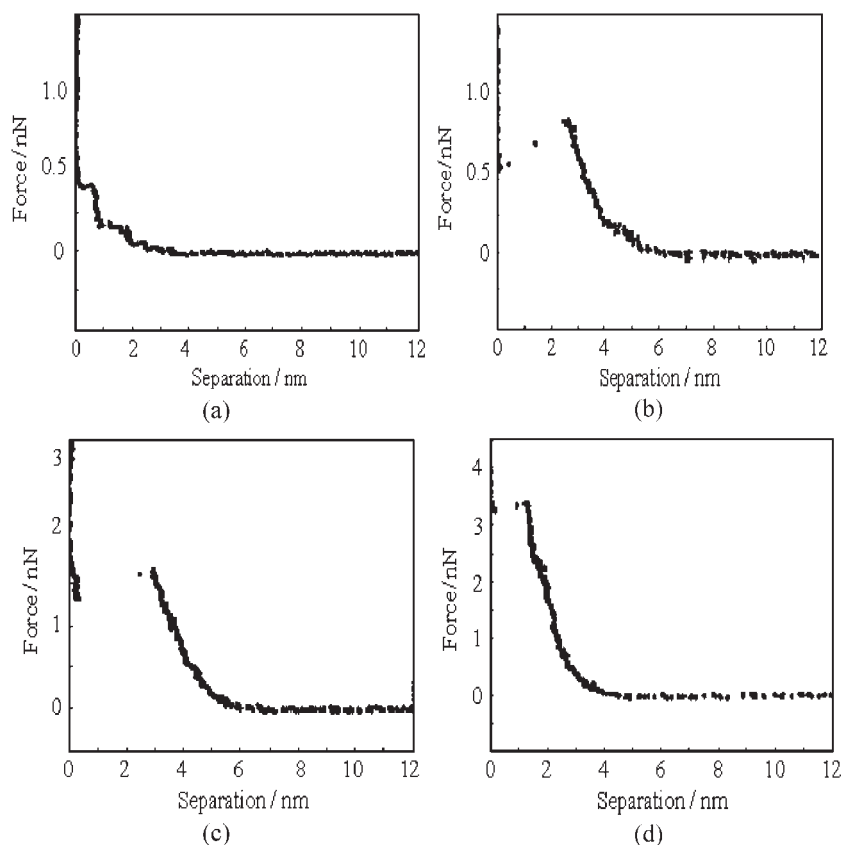


**Figure 1.14** Forces between the AFM tip and the surface. (a) 25%  $\text{CH}_3$  surface, (b) 50%  $\text{CH}_3$  surface, (c) 75%  $\text{CH}_3$  surface and (d) 100%  $\text{CH}_3$  surface (Redrawn from Grant *et al.*, 2000. Figure 5 in the original, with permission of American Chemical Society).

surfactant layer. Possible surfactant layer structures in conformation with AFM images and force measurements are redrawn in Figure 1.13(d) and the variation of interactive forces with distance of approach are shown in Figure 1.14(a)–(d).

Figure 1.14(a) shows that there are no interactive forces between the AFM tip and the particle with a surface of 25% hydrophobicity up until a separation distance of  $\sim 2$  nm. Resistive barrier is observed on further approach. The stepwise character of resistance implies that layers or groups with different adsorption strengths are being removed on approach of the tip, before the tip adheres with the surface, indicated by the steep rise in force at  $\sim 0$  nm. The surface of adherence is the external surface of the thiohexane/hexadecanol layer that behaves as a solid surface because of the high strength of chemisorption. The continuity of the force curve indicates that the adsorbed ethoxylate layer is labile and escapes from the site of compression without being disrupted. The sharp rise of the repulsion barrier on approach of the tip and the break in the force curve indicates that the adsorbed ethoxylate layer structure is disrupted before the tip “jumps” into contact with the solid surface. As the hydrophobicity of



the surface increases, the height of the repulsion barrier before the disruption increases to higher values (Figure 1.14(b)). This shows the strength of adsorption, confirming that adsorption takes place through hydrophobic forces far outreaching the effect of van der Waals forces (hydrogen bonds) under the competition of water molecules of the suspension medium, which also try to adsorb to those hydrophilic  $-\text{OH}$  groups. The onset of the repulsive barrier indicates the layer thickness. The layer thicknesses at 50 and 75% hydrophobicity (Figure 1.14(b)–(c)) are similar ( $\sim 6\text{nm}$ ) almost twice the length of ethoxylate molecules. Either close-packed micelle formation or bilayer formation could have a layer thickness of this magnitude. Bilayer formation at 75% (Figure 1.14(c)) was inferred from the smooth appearance of the adsorbed layer (Grant *et al.*, 2000). The decrease in the onset value of resistance, together with an increase in the barrier height (force) indicates that a monolayer has formed with a concomitant reversal in the configuration of surfactant molecules, adsorbing much more strongly through the hydrocarbon chains than through the ethylene groups of the ethoxylate groups.

### 1.8.1.2 Deformability of surfactant coated particles

Work conducted on the resistance of adsorbed layers toward compression inferred from the force–distance profiles in AFM (Grant *et al.*, 2000; Adler *et al.*, 2000) show that surfactant chain length and configuration of the surfactants in the adsorbed layer has a strong bearing on the steric repulsion of the particles, sustaining the suspension stability. Steric repulsion acts through the yield stress and modulus of elasticity in terms of rheological properties (see Chapter 2). Rabinovich *et al.* (2004) analyzed the mechanical strength of the adsorbed layers through the Hertz (1986) theory taking the effect of the underlying hard-sphere core into account by the Shull *et al.* (1998) correction. The authors assumed the surface of the coated particle as a plane, in comparison with the dimensions of the penetrating sphere, to simplify the mathematical treatment. The adsorption layer is accepted as a homogeneous elastomer with an average thickness of  $h_0$ . Hertz theory relates the contact area of a penetrating sphere of radius  $R$  with the force through the bulk modulus of elasticity,  $K_{\text{elb}}$  [ $\text{Nm}^{-2}$ ] related to the young's modulus of elasticity  $E$  through the poisson

ratio  $\nu$   $\left[ K_{\text{elb}} = \frac{3E}{2(1-\nu^2)} \right]$ :

$$F = \frac{K_{\text{elb}} a^3}{R} \quad (1.79)$$

where  $a$  is the radius of the contact area. The force applied by the colliding (penetrating) sphere, is shown in Figure 1.15(a). The penetrating body causes an indentation  $\delta$  in the adsorbed layer proportional with the contact area:

$$\delta = \frac{a^2}{R} \quad (1.80)$$

The indentation can be related to the applied force through these equations by

$$F = K_{\text{elb}} R^{1/2} \delta^{3/2} \quad (1.81)$$



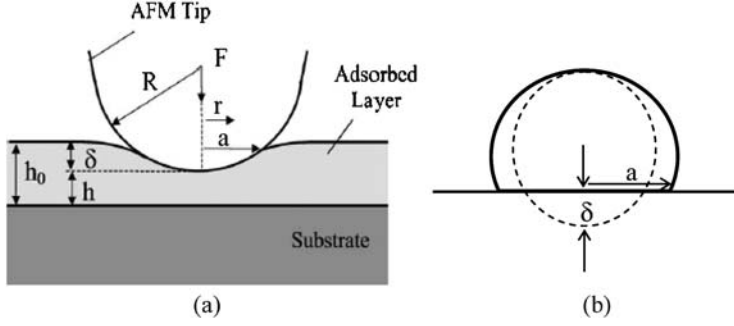


**Figure 1.15** Dimensions related with deformabilities (a) of surfactant coating (Reproduced from Rabinovich *et al.*, 2004. Figure 2 in the original, with permission of Elsevier.); (b) of an elastic particle on interaction with a hard surface.

The indenting sphere causes the evolution of normal stresses within the elastomer film. The distribution of normal stresses  $p(r)$  along the indenting sphere is given by Hertz theory as

$$p(r) = \frac{3K_{\text{elb}}a}{2\pi R} \left( 1 - \left( \frac{r}{a} \right)^2 \right)^{1/2} \quad (1.82)$$

The pressure just when the sphere begins to indent into the adsorbed layer is the yield stress in the normal direction,  $Y$ :

$$Y = \frac{3F_Y}{2\pi a_Y^2} \quad (1.83)$$

where the subscript  $Y$  indicates the values of the variables at the yield point. The yield stress is associated with the “jump-in” value of the force as shown in Figure 1.14(b)–(c), where the force curve is interrupted at its maximum value and the distance suddenly drops to zero as the two surfaces adhere. Hertz theory is valid for low values of indentation, expressed as,  $a/h_0 \ll 1$ , after which the hard core beneath the elastomer film affects the stress distribution. This effect is taken into consideration by the Shull correction factors for the indentation

$$\delta = \delta_H \left( 0.4 + 0.6 \exp \left( \frac{-1.8a}{h_0} \right) \right) \quad (1.84)$$

and for the force assumed to act in a frictionless medium

$$F = F_H \left( 1 + 0.15 \left( \frac{a}{h_0} \right)^3 \right) \quad (1.85)$$

where the subscripts H denote the values found by the Hertz equation. At low values of  $al/h_0$  the indentation and force approach the Hertz values. Increasing values of  $al/h_0$  cause an increase in the force created.

The yield stress  $Y$  bears significance as an indication of suspension stability. Rabinovich *et al.* (2004) showed that a linear relation exists between the yield stress and the number of carbon atoms in the alkyl chain of the adsorbed surfactants, the yield stress increasing linearly with the length of the chain. They also showed that the yield stress of adsorbed layers on hydrophobic surfaces and of layers with compact worm-like micelles to be greater than that of hydrophilic surfaces and spherical micelles, respectively, confirming the results of Grant *et al.* (2000).

#### 1.8.1.2.1 Effect of particle deformability

In addition to the deformability of the adsorbed layers, the particle itself may also be deformable as in the case of polymer colloids, elastomers, and biological cells such as the red blood cells (RBCs). In such a case the contact area between the two particles becomes flattened by the repulsive force causing an increase in the contact area and hence the force, as shown in Figure 1.15(b). Vakarelski *et al.* (2003) analyzed the forces created in deformable bodies theoretically, backed up by experiments with AFM. They found that the critical force  $F_c$  necessary to destroy the adsorbed layers on deformable particles and to bring the surfaces into adhesive contact was  $\sim 10$  times higher than that for the case of solid particles. If the force is below the critical force, the particles rebound and do not adhere. This result is significant in explaining the stability of deformable particles under variable forces, such as in the case of RBCs flowing in blood vessels of different diameters.

### 1.8.2 Stabilization by polymers and polyelectrolytes

Interactions of polymers and polyelectrolytes with particles were presented in Section 1.4.3 in connection with aggregation of particles. Steric forces brought about by adsorbed polymers can be used in stabilizing the suspensions. An advantage of steric stabilization is the possibility of complete coverage of the surface in maintaining the stability of particles. The disadvantage of this method is the difficulty in determining critical concentration of polymers at which the particle surfaces will be completely covered but the chains will be prevented from extending into the solution to avoid bridging between particles. Polyelectrolytes could also be used for steric stabilization. At pH values other than the isoelectric point of the polyelectrolytes, the stability will be maintained essentially by the steric repulsion between the functional groups of the polyelectrolytes. In this case, a thick adsorbed layer of polyelectrolytes will decrease the effect of van der Waals forces as well as the charge density on the particle, both helping the stabilization of the particles. The disadvantage of this method is that the repulsions between the charged layers will decrease at high ionic strengths making this procedure usable only under moderate strengths where DLVO theory is relevant.

An issue that is more challenging than the stability of individual particles is the stability of clusters within a narrow size range. This becomes a problem in the use of ferromagnetic nanoparticles in the high-gradient magnetic separation of proteins under high

ionic strengths. Particle clusters together with their adsorbed proteins should be above a definite size range to overcome the drag forces to be captured within the retention time in the separator. The difficulty of the situation lies in the control of the “start” and “stop” procedures for aggregation: It is easy to start the aggregation but very hard to stop it when a certain size range is reached and then ensuring that stability is maintained under all conditions prevalent in the environment of application. A comprehensive approach to the problem is reported recently by Ditsch *et al.* (2005) where magnetic particles of nanometer size range were subjected to partial coating by random copolymers of acrylic acid/styrene sulfonic acid/vinyl sulfonic acid (AA/SSA/VSA). By applying the polymers in amounts below that required for full coating, and adjusting the hydrophobicity by SSA and attachment density by AA, the cluster size could be kept under control. The authors found that the size and stability of the clusters could not be maintained by a single coating of polymer, no matter what the composition of the polymer or the ratio of polymer to particle is. Clusters of any desired charge or hydrophobicity could be made by applying the coating in two steps: First to proceed the clustering to the desired size range and the second to stabilize the already formed clusters. The critical parameters in the first coating were found to be the molecular weight of the polymer (denoted as the extent of polymerization, or number of repeating units,  $X_w$ ) and the amount of polymer used. At low molecular weights of the polymer, coverage of the particles is not complete and large-sized clusters were formed under the action of van der Waals forces. As the molecular weight increased, better coating of the particles could be achieved and steric stabilization decreased the cluster size down to single primary particles. Bridging forces became dominant with further increase in the number of repeating units of polymer and caused the formation of clusters approximately two orders of magnitude larger than the size of primary particles. An example to the variation of the hydrodynamic diameter with the degree of polymerization is reproduced in Figure 1.16. The size of the clusters formed under the dominance of van der Waals forces were calculated for an energy barrier of  $15k_B T$ .

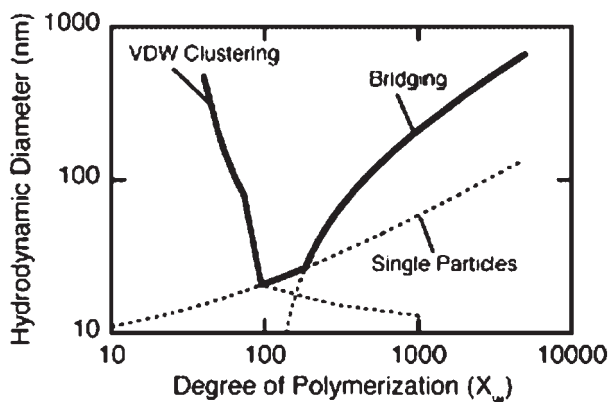


**Figure 1.16** An example to the variation of cluster sizes with the degree of polymerization of the coating polymer (Reproduced from Ditsch *et al.*, 2005. Figure 11(a) in the original, with permission of American Chemical Society).

The three dotted-lined curves depict the variation of the hydrodynamic diameter of the cluster if only the represented force (i.e., van der Waals or bridging) were operative and the size of single particles sterically stabilized with a polymer of given molecular weight. The heavy line indicates the net effect, with the largest force controlling the hydraulic diameter for any given molecular weight of polymer used in the process. Contrary to low molecular weight polymers that produce particle-rich clusters, high molecular weight polymers were found to produce stable aggregates of bridged polymer networks low in solid particle content. Regardless of the charge of the hydrophilic group (cationic or anionic), all dimensionless diameters (diameter scaled to the minimum diameter) fell on the same curve at the same value of  $X_w/X_{\min}$ , where  $X_{\min}$  is the number of repeating units in the polymer causing the formation of minimum diameter clusters. These results showed that hydrophobicity of the polymer chain is effective in determining the minimum number repeat units that should be present to minimize the diameter of the cluster and not the charge of the hydrophilic group. When limited amounts of polymer were used in the first stage of coating, the size of the clusters was found to reflect the relative rates of particle–particle aggregation and polymer–particle aggregation. Due to the insufficient amount of polymer used, the initially formed clusters are unstable. These clusters are stabilized soon after they are formed by a second polymer coating in amounts adequate to fill in the empty adsorption sites on the particle but not to cause bridging among the particles.

The authors (Ditsch *et al.*, 2005) modeled the aggregation process during the first stage of coating by the DLVO theory, using the Vold generalized van der Waals attractions applied to the polymer-coated materials:

$$-U_{\text{vdw}} = \frac{(H_m^{1/2} - H_c^{1/2})^2}{12} h\left(\frac{s - 2\delta}{d + 2\delta}; 1\right) + \frac{(H_c^{1/2} - H_p^{1/2})^2}{12} h\left(\frac{s}{d}; 1\right) \\ + \frac{2(H_m^{1/2} - H_c^{1/2})(H_c^{1/2} - H_p^{1/2})}{12} h\left(\frac{s - \delta}{d}; \frac{d + \delta}{d}\right) \quad (1.86)$$

This equation is a combination of eqs. (1.23), (1.24), and (1.25a) with  $R$  term nondimensionalized with the core diameter  $d$ ; and separation distance  $s$ , scaled with the pertinent diameter, combined as an equation of the form:

$$h(s^*; R^*) = \frac{R^*}{s^{*2} + 2s^*R^* + s^*} + \frac{R^*}{s^{*2} + 2s^*R^* + s^* + R^*} \\ + 2 \ln \frac{s^{*2} + 2s^*R^* + s^*}{s^{*2} + 2s^*R^* + s^* + R^*} \quad (1.87)$$

where  $s^*$  and  $R^*$  are nondimensional distance and nondimensional diameter, respectively, the values of which are indicated in the functions of eq. (1.86).  $H_m$ ,  $H_c$ , and  $H_p$  are the Hamaker constants for the medium, polymer coating and core particle, respectively. The other dimensions are shown in Figure 1.17.

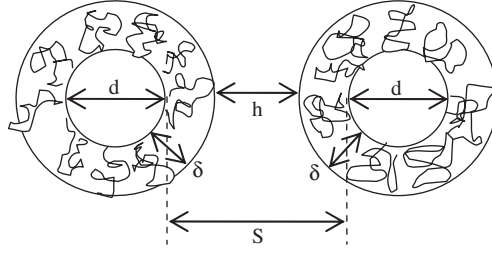


**Figure 1.17** Dimensions of coated particles as used in eqs. (1.86)–(1.87).

The energy of repulsion between two coated spheres is estimated (Reiner and Radke, 1993) by

$$U_{\text{rep}} = 2\pi\epsilon_r\epsilon_0 r \Phi_0^2 \frac{2}{2 + (s - 2\delta)/r} \exp[-\kappa(s - 2\delta)] \quad (1.88)$$

The sum of eqs. (1.86) and (1.88) will give the total interaction potential between two particles. Vold and Vold (1983) gives the required energy barrier for stabilization to be at least 15 times the thermal energy,  $15k_B T$ . The required thickness of the polymer coating  $\delta$  is estimated from the solution of eqs. (1.86) and (1.88). The height of the energy barrier in the resulting total interactive energy is a strong function of the ionic strength. Therefore, the authors suggest the employment of higher  $\delta$  values than required for stabilization if the synthesized particles are to be used under higher ionic strengths. Typical value of the thickness  $\delta$  is around twice the radius of gyration of the polymer (Aubouy and Raphael, 1998). As the radius of gyration of the polymer increases, the curvature of the particle limits the effective thickness of the layer.

The core size of the clusters are found (Ditsch *et al.*, 2005) from the rate of particle aggregation, and the cluster size  $d_{\text{clus}}$ , is related to the primary magnetic particle size  $d_c$ , by an equation similar to eq. (1.59):

$$d_{\text{clus}} = d_c \left( \frac{M_{\text{clus}}}{m} \right)^{1/d_f} + 4R_g \quad (1.89)$$

where  $M_{\text{clus}}/m$  is the number of primary magnetite particles in an average cluster, also called the *aggregation number* and  $d_f$  is the fractal dimension, for diffusion-limited colloidal aggregation. The thickness of the polymer coating around the cluster is approximated as twice the radius of gyration of the polymer,  $R_g$ , given by eq. (1.50).

### 1.8.3 Stabilization by nanoparticles

Another recent development involved the use of nanoparticles to stabilize the microparticles (Tohver *et al.*, 2001). As in the case of polyelectrolytes, surfaces of uncharged particles are energetically more favorable places for adsorption of charged nanoparticles.

Repulsions between microparticles coated with nanoparticle halos are essentially electrostatic in action. However, it also depends on the sizes of the nano- and microparticles and the ratio of their diameters, as well as on their volume fraction. Particle mixtures exhibit phase behavior much like their fluid counterparts. In a study of phase equilibrium among binary mixtures of different diameter particles (radius of nanoparticles = 3 nm and radii of microparticles either 285 or 590 nm), Tohver *et al.* (2001) found that a region of stability exists in between two gel phases, where the suspension acts like a fluid. This phenomenon was attributed to microspheres coated with charged nanoparticle halos. The phenomenon opens up many possibilities. Lee and Kramer (2004) used nanoparticle haloing to enhance self-assembly of colloidal crystals on patterned surfaces. Theoretical model studies of nanoparticle haloing (Karanikas and Louis, 2004) showed that halos are not a static layer of adsorbed particles, as in the case of steric stabilization. The nanoparticle halo is dilute and is in dynamic equilibrium with the bulk of the suspending fluid. A consequence of the dynamic nature of the halos is that stabilization cannot be maintained if the velocity of the microparticle is too fast for the nanoparticles to catch-up with. Nanoparticle haloing is a promising technology but needs further research for wide-scale application.

## 1.9 AGGREGATION IN BIOLOGICAL SYSTEMS

Aggregation takes place among living cells also: Aggregation in algae and microorganisms and subsequent sedimentation of the aggregates are responsible for the carbon cycle in the seas. Aggregation of microorganisms together with other inorganic colloids is desired in wastewater treatment. Reversible aggregation of red blood cells (RBCs) in blood regulates the retention time of these cells in various blood vessels through variations in viscosity, while irreversible aggregation of platelets help to repair injuries of the blood vessel wall even under high shear rates. The mechanisms that bring about aggregation of inorganic particles are also effective in the case of microorganisms. Two typical cases, blood cells and algae, will be taken up in this chapter as examples of cell aggregation.

### 1.9.1 Aggregation behavior of blood cells

Presence of blood cells, generally called *hematocrit*, give non-Newtonian characteristics to blood rheology through their aggregation and redispersion under the effect of shear. Hematocrit is mainly composed of RBCs, called *erythrocytes*, white blood cells (WBCs), called *leucocytes*, and platelets, called *thrombocytes*, at an approximate order of magnitude ratio of  $10^6:10^3:10^5$ , respectively, in terms of number of cells per cubic millimeter. The liquid phase, *plasma*, is a solution of proteins (albumin, globulin, and fibrinogen), coagulation factors and electrolytes, mainly  $\text{Na}^+$ ,  $\text{K}^+$ , and  $\text{Ca}^{2+}$ . Interaction and aggregation of blood cells are thus complex mechanisms involving electrostatic forces, van der Waals forces, surface forces related with polymers, and molecular recognition of receptors on another cell or colloid, all within a context of interrelated functions. As either aggregation or stabilization of the suspension is desired in various parts of the circulatory system in accordance with the function of the cells, the respective mechanisms must be in a

delicate balance. The mechanism of aggregation is determined by the requirement of these cells to perform their functions: RBCs are responsible for mass transfer of  $O_2$ ,  $CO_2$ , and various nutrients and their consecutive transportation throughout the body. The velocity of the RBCs is reduced through aggregation under low shear rates to allow the required retention time for mass transfer. To speed up the transportation in between the sites of mass transfer, for example, to and from the lungs, the aggregates have to be broken up under high shear rates in the arteries and veins. In order to pass through narrow capillaries of diameter equal to their width they have to disaggregate into individual cells to be able to pass through. Therefore, the aggregation mechanism of RBC should be reversible, and be a function of the balance between attractive forces and shear stresses acting over the external surfaces. Platelets are mainly responsible for the repair of the damaged blood vessel walls, so the aggregates they form should be able to withstand the action of high shear rates. In addition, they should not form nonspecific aggregates with all the particles but only with those with which they can form a network for repair of the injured vessel wall. Therefore, aggregation based on molecular recognition of specific receptors is suitable with their function.

A water soluble protein, fibrinogen, plays a crucial role in the aggregation of all blood cells; therefore, its structure deserves special attention: Fibrinogen is an acute phase reactant whose concentration increases in times of injury to blood vessel walls, besides due to other factors. It is a glycoprotein with two symmetric parts, called D domains, each consisting of a set of three polypeptide chains denoted as  $A\alpha$ ,  $B\beta$ , and  $\gamma$ , linked together by disulfide bridges which forms the central amino-terminal E domain of the elongated complex (MW=340,000 Da). Adsorption to other entities take place only at specific sites at a specific orientation, i.e., there are sites on the D and E domains, which specifically bind to platelets, endothelial cells, thrombin, leukocytes or other blood components (Herrick *et al.*, 1999; Mosesson, 2000). Fibrinogen does not directly adhere to erythrocytes (RBCs) and also blocks erythrocyte–platelet aggregations. (Goel and Diamond, 2002). The self-association (D:D) sites are present at the two ends of the elongated molecule making possible the end-to-end linkages among the molecules (Mosesson, 2000). Thrombin generated upon vascular injury cleaves the complex molecule into fibrin and other cleavage products. The remaining fibrin monomers polymerise spontaneously and form insoluble fibrin clots after being cross-linked by transglutaminase (factor XIIIa) (Herrick *et al.*, 1999; Mosesson, 2000).

#### 1.9.1.1 Aggregation of RBCs

Aggregation of RBCs is controlled by two factors: Their surface structure and their shape.

##### 1.9.1.1.1 Surface structure of RBCs

A typical section of a cell membrane is given in Figure 1.18(a). A purely viscous phospholipid bilayer constitutes the cell wall of RBCs. Dispersed among the lipids are the membrane proteins with sialic acid residues suspended freely outside of this membrane. No receptor sites are reported in the literature for RBCs, so there are no specific adsorption sites for proteins and other molecules on the cell surface. Due to dissociation of the sialic acid groups, the surface bears a negative charge, with a surface charge density of

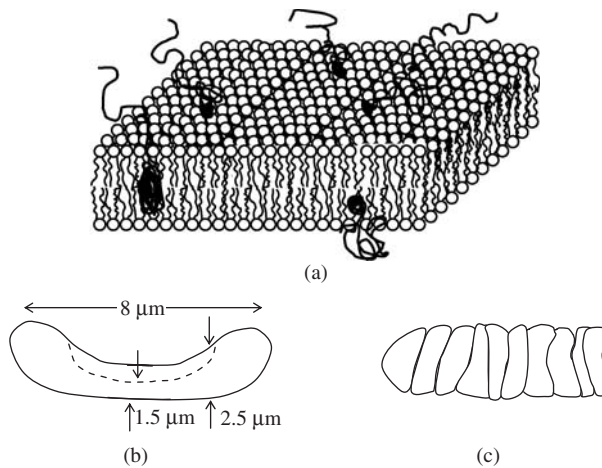


**Figure 1.18** Red blood cells. (a) Surface structure, (b) shape and dimensions and (c) rouleaux formation in different sections of the circulatory system.

$0.036 \text{ C m}^{-2}$  (Vargas *et al.*, 1989; van Damme *et al.*, 1994). These charges are not fixed in space but are free to move together with the section of the polymer to which it is attached. The mobility of the hydrocarbon segments to which the sialic acids are attached cause the RBCs to act as soft particles instead of behaving as hard solid spheres. The average length of this section is around 5 nm which can be approximated as the width of the glycocalyx of an RBC. Debye length of the counterions is  $\kappa^{-1} = 0.76 \text{ nm}$  (Neu and Meiselman, 2002). Viscoelasticity of the phospholipid membrane which resists expansion also contributes to the effect of the mobile glycocalyx on the aggregation mechanism.

#### 1.9.1.1.2 Shape of the RBCs

The attractive forces, mainly van der Waals, between the hydrophilic and hydrophobic sections of the membrane lipids resist stretching during an increase in surface area upon deformation of the shape. A cytoskeleton made up of a network of proteins, mainly spectrin, is attached to the cell wall through interactions with membrane proteins. This protein network is responsible for the shape of the RBCs and the elasticity of the cell. The RBCs are elliptical concave discs of length equal to  $8 \mu\text{m}$  and thickness  $1.5 \mu\text{m}$  at the center and  $2.5 \mu\text{m}$  around the circumference as sketched in Figure 1.18(b). The second centrally located concavity in the cell permits flexibility in cellular motion, making shape changes possible without an increase in surface area (Baskurt and Meiselman, 2003). These shape changes are required in the stacking of the aggregates, as well as orientation under shear forces to reduce drag.

Under the given conditions of surface structure and shape, interactions among RBCs are expected to be due to electrostatic charges, to van der Waals attractions and to the effect of polymers suspended in the plasma and integrated within the cell membrane.



#### 1.9.1.1.3 Experimental observations of RBC aggregation

Ellipsoid disc shaped RBCs form stacks sketched in Figure 1.18(c), called rouleaux, when the shear rate is low. This aggregation is reversible, the rouleaux being dispersed into individual cells under high shear stresses. RBCs do not form aggregates in electrolyte (isotonic salt) solutions indicating the effect of repulsive electrostatic forces in the aggregation mechanism. It also indicates the role of polymers in bringing about the aggregation.

#### 1.9.1.1.4 Effect of electrostatic charges

Erythrocytes, as other biological cells have a negative surface charge due to sialic acid end groups of glycoproteins located in the cell membrane. Sialic acid groups leave the cell wall with age or under the action of other molecules in the plasma such as trypsin and neuraminidase (Godin and Caprani, 1997). The surface charge density of normal and fresh erythrocytes is  $-0.036 \text{ Cm}^{-2}$ . The negative surface charge on RBCs reduce the aggregation effect due to van der Waals forces and the bridging or depletion forces brought about by the polymers in the suspension medium (Armstrong *et al.*, 2004). This charge density decreases with the age of RBC, the decrease becoming more significant after 6 days. Cell rigidity accompanies the decrease in surface charge probably due to the modification of the integrated protein structure of the cell membrane, reducing the effect of viscoelasticity on cell repulsion and favoring aggregation.

The attractive and repulsive forces are important not only in the self-association of RBCs but also in their adherence to other surfaces, such as artificial organs. Measurement of forces between a RBC and a hydrophilic glass surface immersed in phosphate buffered saline with AFM (Luckham, 2004) showed the existence of repulsive forces at all interparticle separations. The repulsive interactions were found to become significant around 60nm to the cell surface and increased very slowly as the cell surface was approached. A very strong repulsive force similar to the hydrophobic forces in inorganic systems was observed around 10nm.

#### 1.9.1.1.5 Effect of van der Waals forces

Attractive interactions of RBCs due to van der Waals forces were observed with hydrophobic surfaces by AFM (Luckham, 2004). When a glass surface was hydrophobized with silane, essentially replacing ( $-\text{OH}$ ) groups with ( $-\text{CH}_3$ ) groups, a minimum was observed at distances less than 100 nm, signifying the existence of attractive forces.

#### 1.9.1.1.6 Effect of polymers

Polymers are present in blood in the form of proteins in plasma, or as sections of membrane proteins in the glycocalyx. Thus, steric, bridging, and depletion forces could all be effective in the polymer-mediated interactions. Steric forces evolve because of the repulsion between short-chain hydrocarbons adsorbed on particle surfaces. In the case of RBCs, the free end groups of polymers integrated into the cell membrane can create a repulsive steric force effect. However, due to high electrostatic repulsion, cell-cell distances at which minimal interaction energy occurs are always greater than twice the thickness of the cell's glycocalyx. Thus, steric interactions between glycocalyx on adjacent RBCs can be neglected (Neu and Meiselman, 2002).

Structures of plasma proteins are much more complicated than the nonionic polymers used in medical practices, such as dextran, and can be of various sizes and shapes. The most important plasma proteins in the order of decreasing concentration are albumin, globulin, immunoglobulins (IgA, IgG, and IgM) and fibrinogen. The presence of polymers suggests two possible mechanisms of aggregation: That of bridging through adsorbed polymers and that of depletion forces due to unadsorbed polymers. As explained above, bridging involves bonding of different cells together with the same polymer chain or direct bonding to polymers. To be able to form a bridge between different cells, the polymer should be long enough on expansion to span the distance between the cells. This rules out the short-chain polymers with low molecular weights and polymers with a spherical shape, such as immunoglobulins from bridge formation. Binding by depletion forces requires only the existence of an excluded volume in between the cells, on which the osmotic pressures act. As no bonds or polymer-particle interactions are involved in aggregation through depletion forces, it is relatively more reversible than aggregation through bridging which requires the simultaneous breakage of more than one bond on different cells. Armstrong *et al.* (2004) observed the molecular weight dependence of aggregation, when brought about by synthetic polymers, dextran, PVP and POE: Polymers with hydraulic radius less than 4 nm were either found to inhibit or not to affect the aggregation, whereas, polymers with hydraulic diameters greater than 4 nm were found to be strongly pro-aggregant. The aggregation effect was maximum in the range  $6 \leq r_H \leq 12\text{nm}$ , slightly greater than the size range of the RBC glycocalyx. Polymers of size,  $r_H \geq 12\text{nm}$  were found to deteriorate the aggregation of RBCs causing the formation of rounded and compressed clumps rather than elongated rouleaux (Armstrong *et al.*, 2004). Photographs taken *in vivo* by Pearson and Lipowski (2004) of rat RBCs flowing through a precapillary bifurcation after administration of fibrinogen (a) and Dextran 500 (b) are reproduced in Figure 3.14 in Chapter 3. Whereas, the rouleaux formed by fibrinogen cannot resist the shear under turbulent conditions existing at a bifurcation and tend to break up into irregular shapes, the rounded clumps formed by the action of Dextran 500 are quite stable. As the hydraulic radius  $r_H$  of Dextran 500 is 15.90 nm while that of fibrinogen is 10.95 nm (Armstrong *et al.*, 2004), the observed deterioration may perhaps be due to the effect of bridging bonds in addition to the action of depletion forces.

#### 1.9.1.2 Aggregation of platelets

When a blood vessel is injured, the punctured endothelial cell lining of the vessel wall opens up, exposing the underlying extracellular cells. Disc shaped cells 1–4  $\mu\text{m}$  in diameter, called platelets, are responsible for the control of bleeding (*hemostasis*) from these disrupted blood vessels. So they are equipped with receptor sites which selectively adhere to specific molecules on endothelial cells, collagen of the extra cellular matrix, other platelets, or on ligand complexes which form bridges between platelets and the cells to which they adhere. This selection mechanism, called *molecular recognition*, controls the adhesion to correct entities during the process of coagulation. Coagulation proceeds through the steps of molecular recognition, adhesion, signaling, activation of binding sites and final aggregation. Molecular recognition is carried out mainly by glycolipids (GP) acting as adhesion receptors embedded within the platelet membrane (Yip, *et al.*, 2005). Examples of adhesion receptors are GPVI that binds to collagen and GPIb-IX-V that binds

collagen-bound von Willebrand Factor (vWF). The latter, vWF, is an adhesive glycoprotein secreted by the platelets or endothelial cells into plasma or subendothelial matrix. Their very large size ( $MW = 20 \times 10^6$  Da) and string-like shape facilitate the adhesion even under high shear rates observed in cases of high volumetric rates of blood flow. An arginine–glycine–aspartine (RGD) peptid sequence present in one of the subunits of vWF recognizes and strongly binds to an integrin in the platelet membrane, GPIIb/IIIa ( $\alpha_{IIb}\beta_3$ ), responsible for strong aggregations with vWF, and similarly with fibrinogen. Because of the critical role played by the platelets in stopping blood flow, there are more than one mechanism (molecular pathways) for controlling blood flow, *in vivo*. However, at high shear rates above  $\sim 650 \text{ s}^{-1}$  the pathway involving GPIb-IX-V becomes critical: A subunit of GPIb-IX-V in the platelet membrane, GPIb $\alpha$ , has a negative patch in its peptid sequence which strongly attracts a positive patch (A1) on vWF. The energy potential of this electrostatic attraction makes the adhesion resistant to shear forces.

When a plaque adherent on the interior lining of arteries is broken, a signal similar to vessel wall rupture may be transmitted to the platelets. This signal starts a similar procedure of aggregation of platelets within the internal cross section (lumen) of the blood vessel causing blockage of the vessel (*thrombosis*), observed in heart attacks and strokes, [Andrews and Berndt, 2004].

#### 1.9.1.2.1 Prevention of blood coagulation

$\text{Ca}^{2+}$  ions are closely involved in the aggregation of platelets and fibrin, through its effect on the activation of GPIIb/IIIa ( $\alpha_{IIb}\beta_3$ ) (Guyton and Hall, 2006) and in the conversion of prothrombin to thrombin that converts fibrinogen into fibrin that enmesh the blood cells in forming the clot. Inhibition of coagulation is maintained by removing  $\text{Ca}^{2+}$  ions from the blood to decrease its concentration below the threshold level. This can be accomplished by precipitating the  $\text{Ca}^{2+}$  ions with *citrate* or *oxalate* anions.

Another way to inhibit coagulation is by addition of heparin to the blood. Heparin is normally present in blood, secreted by mast cells around capillaries where the probability of coagulation is highest due to slow rates of blood flow. When its concentration is increased, it forms a complex with antithrombin III, greatly increasing the effectiveness of the latter in removing thrombin and many other coagulation factors.

Still another way of preventing coagulation is through the addition of ethylenediamine tetracetic acid (EDTA). EDTA changes the shape of the platelets from discoids into spiny (thorny) spheres. The fibrinogen receptor located in the membrane matrix of the cells, GPIIb/IIIa ( $\alpha_{IIb}\beta_3$ ) dissociates into its constituents, GPIIb and GPIIIa under the action of EDTA. The platelets exposed to EDTA lose their binding ability to fibrinogen with a decreased response to thrombin and collagen. As a result, clotting of blood is prevented. Recent studies show that this effect is reversible, and the platelets can bind to fibrins through which they can sustain clot retraction which necessitates tension development, even after being exposed to EDTA. The causes for this reversibility in the functions of EDTA are not clear as yet. Presence of GPIIb/IIIa deep in the glycocalyx matrix not reachable by EDTA molecules could be one reason (White, 2000), reassociation of GPIIb and GPIIIa be another, as well as another receptor such as an integrin assuming the functions of GPIIb/IIIa (Cohen *et al.*, 1989; Rooney *et al.*, 1998). The effect of EDTA on blood rheology will be discussed in Chapter 3.

### 1.9.2 Aggregation of microorganisms

Similar mechanisms, with some provisions, are operative in the aggregation of microorganisms including bacteria, algae, and yeasts. Aggregation processes include adhesion among microorganisms; between microorganisms and inorganic particles within a floc structure; and formation of microcolonies which develop into biofilms on solid surfaces. Aggregation of microorganisms to produce flocs involves a sequence of steps in the order:

1. weak reversible attraction, generally within the second energy minimum from the surface,
2. strengthening of the attraction through the excreted polymers to form a compact microaggregate of several cell diameters in characteristic dimension,
3. flocculation of these compact microaggregates in a loosely bound porous floc, generally described by the fractal theory.

The first step is sensitive to the ionic strength of the medium and takes place if attractive forces overcome the effect of electrostatic repulsion and shear forces when the suspension medium is in motion. DLVO theory should be used with caution in the case of microbial adhesion, taking into account the structural differences between inorganic particles and living microorganisms that have different capabilities. Pieterse and Cloot (1997) outlined these differences as:

1. The electrostatic charge distribution on a cell surface is not uniform. Overall, they are negatively charged but local positively charged sites cause specific orientations to be favored. Especially, if the microorganisms have fibrils that have positively charged areas along its length, attachment is maintained by the fibrils, even though the cell itself is negatively charged.
2. Microorganisms have irregular shapes. They have the ability to change their shapes to reduce the hydrodynamic resistance during motion.
3. Separation distance between cells is not well defined. As the length of the fibrils approaches the cell diameter in some microorganisms, the separation distance between the particles in the DLVO theory cannot be defined clearly.
4. Microorganisms with flagella can swim out of the flocs. Since the attractive forces in the second energy minimum are not strong, the living microorganisms can easily overcome these forces.
5. Gravitational forces may not be negligible. Gravitational forces,  $F_g$ , are of the same order of magnitude as the van der Waals forces for microorganisms of  $\sim 10\text{--}30\ \mu\text{m}$  in diameter

$$F_g = G \frac{m_1 m_2}{s^2} \quad (1.90)$$

where  $G$  is the universal gravitational constant ( $6.670 \times 10^{-11} \text{m}^3 \text{kg}^{-1} \text{s}^{-2}$ ),  $m_1$  and  $m_2$  are the masses of two colliding bodies and  $s$  is the center-to-center distance ( $s = h + R_1 + R_2$ ) between the bodies of radii  $R_1$ , and surface-to-surface separation  $h$ . Under the

action of gravitational forces the two microorganisms revolve around their common center of mass, facilitating aggregation.

6. *Mass transfer during photosynthesis can affect the hydrodynamics around the cell.* Algal cells assimilate  $\text{CO}_2$  and other nutrients and excrete  $\text{O}_2$  and organic molecules during photosynthesis. The net mass uptake perturbs the hydrodynamics in favor of flocculation. The photosynthetic pulling force,  $F_{ph}$ , can be approximated by

$$F_{ph} \approx \frac{3}{2} \frac{\pi \eta U r^4}{h^3} \quad (1.91)$$

where  $U$  is the mass up-take speed ( $\text{m s}^{-1}$ ) and  $\eta$ , the viscosity of the suspension medium (Pas)

7. Algal cells can react to perturbations in their environmental conditions. In case their charge is neutralized by the addition of flocculants to reduce the intercellular repulsion, the algal cells can react to re-establish their initial negative charge.

The second step in the floc formation involves the strengthening of the bonds formed by DLVO forces by the action of non-DLVO forces, generally exerted as bridging by polymers. These polymers could be provided by the cells as excretions or could be added as flocculants, as in the case of wastewater treatment (Chu and Lee, 2004).

The third stage of floc formation encountered in wastewater treatment processes involves other suspended solids and macromolecules to form irregularly shaped, fragile, highly porous and heterogeneous flocs (Chu and Lee, 2004). A minimum of two fractal dimensions,  $d_{f1}$  and  $d_{f2}$  were suggested to be used to describe the micro- and macrostructure of biological flocs: Wu *et al.* (2002) determined the fractal dimensions of sludge flocs by light scattering to elucidate the structure of the micro flocs of kaolin and activated sludge, presumably mixtures of kaolin and bacteria, captivated within macro clusters formed by a cationic polyelectrolyte. In the absence of polyelectrolytes, the fractal dimension of kaolin aggregates were  $d_f \sim 2.0$ , and those of activated sludges,  $d_f \sim 2.12$ , designating close-packed structures formed by electrostatic attractions. Addition of a cationic polyelectrolyte to the kaolin flocs caused a reduction in  $d_f$ , determined by light scattering down to DLA levels. Fractal dimensions of activated sludge clusters determined by free settling tests were much less, in the order of  $d_f \sim 1.33$ – $1.48$ , denoting a loose, porous structure which controls the settling rate. In view of the fact that much smaller amounts of polymer are required for charge neutralization, the authors propose that the flocculation mechanism of activated sludge could be through bridging by polymers rather than charge neutralization of kaolinite.

## REFERENCES

- Adler, J.J., Singh, P.K., Patist, A., Rabinovic, Y.I., Shah, D.O., Moudgil, B.M., 2000. Correlation of particulate dispersion stability with the strength of self-assembled surfactant films. *Langmuir*, 16, 7255–7262.
- Andrews, R.K., Berndt, M.C., 2004. Platelet physiology and thrombosis. *Thrombosis Research*, 114, 447–453.

- Antalek, B., Williams, A.J., Texter, J., Feldman, Y., Garti, N., 1997. Microstructure analysis at the percolation threshold in reverse microemulsions. *Colloids and Surfaces A: Physicochemical and Engineering Aspects*, 128, 1–11.
- Armstrong, J.K., Wenby, R.B., Meiselman, H.J., Fisher, T.C., 2004. The hydrodynamic radii of macromolecules and their effect on red blood cell aggregation. *Biophysical Journal*, 87, 4259–4270.
- Aubouy, M., Raphael, E., 1998. Scaling description of a colloidal particle clothed with polymers. *Macromolecules*, 31, 4357–4363.
- Baskurt, O.K., Meiselman, H.J., 2003. Blood rheology and hemodynamics. *Seminars in Thrombosis and Hemostasis*, 29, 435–450.
- Bergstrom, L., 1997. Hamaker constants of inorganic materials. *Advances in Colloid and Interface Science*, 70, 125–169.
- Berka, M., Rice, J.A., 2005. Relation between aggregation kinetics and the structure of kaolinite aggregates. *Langmuir*, 21, 1223–1229.
- Berthon, S., Barbieri, O., Ehrburger-Dolle, F., Geissler, E., Achard, P., Bley, F., Hecht, A., Livet, F., Pajonk, G.M., Pinto, N., Rigacci, A., Rochas, C., 2001. DLS and SAXS investigations of organic gels and aerogels. *Journal of Non-Crystalline Solids*, 285, 154–161.
- Biggs, S., Burns, J.L., Yan, Y., Jameson, G.J., Jenkins, P., 2000. Molecular weight dependence of the depletion interaction between silica surfaces in solutions of sodium poly(styrene sulfonate). *Langmuir*, 16, 9242–9248.
- Birdi, K.S., 1993. *Fractals in Chemistry, Geochemistry, and Biophysics*, Plenum Press, New York.
- Bordi, F., Cametti, C., Rouch, J., Sciortino, F., Tartaglia, P., 1996. Cluster formation in water-in-oil microemulsions at percolation: Evaluation of the electrical properties. *Journal of Physics: Condensed Matter*, 8, A19–A37.
- Bouchama, F., Thathagar, M.B., Rothenberg, G., Turkenburg, D.H., Eiser, E., 2004. Self-assembly of a hexagonal phase of wormlike micelles containing metal nanoclusters, *Langmuir*, 20, 477–483.
- Burns, J.L., Yan, Y., Jameson, G.J., Biggs, S., 1999. Relationship between interaction forces and the structural compactness of depletion flocculated colloids. *Colloids and Surfaces A: Physicochemical and Engineering Aspects*, 162, 265–277.
- Burns, J.L., Yan, Y., Jameson, G.J., Biggs, S., 2002. The effect of molecular weight of nonadsorbing polymer on the structure of depletion-induced flocs. *Journal of Colloid and Interface Science*, 247, 24–32.
- Chen, Q., Saltiel, C., Manickavasagam, S., Schadler, L.S., Siegel, R.W., Yang, H., 2004. Aggregation behavior of single-walled carbon nanotubes in dilute aqueous suspension. *Journal of Colloid and Interface Science*, 280, 91–97.
- Chiavacci, L.A., Santilli, C.V., Pulcinelli, S.H., Bourgaux, C., Briois, V., 2004. Role of surface state and structural feature in the thermoreversible sol–gel transition of a zirconyl aqueous precursor modified by sulfuric acid. *Chemistry of Materials*, 16, 3995–4004.
- Chu, C.P., Lee, D.J., 2004. Multiscale structures of biological flocs. *Chemical Engineering Science* 59, 1875–1883.
- Claesson, P.M., Poptoshev, E., Blomberg, E., Dedinaite, A., 2005. Polyelectrolyte-mediated surface interactions. *Advances in Colloid and Interface Science*, 114–115, 173–187.
- Cohen, I., Burk, D.L., White, J.G., 1989. The effect of peptides and monoclonal antibodies that bind to platelet glycoprotein Ib-IIIa complex on the development of clot tension. *Blood*, 73, 1880–1887.
- Derjaguin, B.V., Landau, L., 1941. *Acta Physicochimica U.S.S.R.*, 14, 633.
- Ditsch, A., Laibinis, P.E., Wang, D.I.C., Hatton, T.A., 2005. Controlled clustering and enhanced stability of polymer-coated magnetic nanoparticles. *Langmuir*, 21, 6006–6018.
- Evans, E., Rawicz, W., 1990. Entropy-driven tension and bending elasticity in condensed-fluid membranes. *Physical Review Letters*, 64, 2094–2097.

- Fleer, G.J., Scheutjens, J.M.H.M., Vincent, B., 1984. In: *Polymer Adsorption and Dispersion Stability* (eds. E.D. Goddard, B. Vincent), ACS Symposium Series 240, American Chemical Society, Washington, DC.
- Fuchs, N., 1934. Über die Stabilität und Aufladung der Aerosole. *Zeitschrift für Physik*, 89, 736–743.
- Godin, C., Caprani, A., 1997. Effect of blood storage on erythrocyte/wall interactions: Implications for surface charge and rigidity. *European Biophysics Journal*, 26, 175–182.
- Goel, M.S., Diamond, S.L., 2002. Adhesion of normal erythrocytes at depressed venous shear rates to activated neutrophils, activated platelets, and fibrin polymerized from plasma. *Blood*, 100, 3797–3803.
- Grant, L.M., Ederth, T., Tiberg, F., 2000. Influence of surface hydrophobicity on the layer properties of adsorbed non-ionic surfactants. *Langmuir*, 16, 2285–2291.
- Guyton, A.C., Hall, J.E., 2006. *Textbook of Medical Physiology*, 11th edn., Elsevier Saunders, Philadelphia (Chapters 14 and 36).
- Hamaker, H.C., 1937. The London van der Waals attraction between spherical particles. *Physica*, 4, 1058.
- Helvacı, S., Peker, S., Özdemir, G., 2004. Effect of electrolytes on the surface behavior of rhamnolipids R1 and R2. *Colloids and Surfaces B: Biointerfaces*, 35, 225–233.
- Herrick, S., Blanc-Brude, O., Gray, A., Laurent, G., 1999. Fibrinogen. *The International Journal of Biochemistry and Cell Biology*, 31, 741–746.
- Hertz, H., 1986. *Miscellaneous Papers*, MacMillan, London.
- Hoffmann, B., Köhler, W., 2003. Reversible light-induced cluster formation of magnetic colloids. *Journal of Magnetism and Magnetic Materials*, 262, 289–293.
- Hong, H.E., Hong, C.Y., Yang, S.Y., Yang, H.C., 2001. Novel properties and applications in magnetic fluids. *Journal of Physics and Chemistry of Solids*, 62, 1749–1764.
- Huang, A.Y., Berg, J.C., 2004. Aggregate restructuring by solvency effects. *Journal of Colloid Interface and Science*, 279, 440–446.
- İkizler, B., 2005. *Production of ZnO Nanoparticles Using Microemulsion Method*. Master Thesis, Ege University.
- Israelachvili, J.N., 1991. *Intermolecular and Surface Forces*, 2nd edn., Academic Press, London.
- Israelachvili, J.N., Pashley, R.M., 1984. *Journal of Colloid and Interface Science* 98, 500–514.
- Jönsson, B., Lindman, B., Holmberg, K., Kronberg, B., 1998. *Surfactants and Polymers in Aqueous Solution*, John Wiley and Sons, Chichester.
- Jullien, R., Botet, R., 1987. *Aggregation and Fractal Aggregates*, World Scientific.
- Karanikas, S., Louis, A.A., 2004. Dynamic colloidal stabilization by nanoparticle halos. *Physical Review Letters*, PRL93, 248303.
- Kellner, R.R., Köhler, W., 2005. Short-time aggregation dynamics of reversible light-induced cluster formation in ferrofluids. *Journal of Applied Physics*, 97, 034910 (1–6).
- Klockenburger, M., Ern , B.H., 2006. Comparison of reversible and irreversible dipolar assemblies in a ferrofluid. *Journal of Magnetism and Magnetic Materials*, 306, 85–91.
- Kuhn, H., Försterling, H.-D., 1999. *Principles of Physical Chemistry-Understanding Molecules, Molecular Assemblies, Supramolecular Machines*. John Wiley and Sons Ltd., Madras, India (Chapters 13 and 14).
- Kwok, R., Evans, E., 1981. Thermoelasticity of large lecithin bilayer vesicles. *Biophysical Journal*, 35, 637–652.
- Lapasin, R., Grassi, M., Priol, S., 1996. Rheological modeling of fractal and dense suspensions. *The Chemical Engineering Journal and the Biochemical Engineering Journal*, 64, 99–106.
- Lee, C., Kramer, T.A., 2004. Prediction of three-dimensional properties of fractal aggregates. *Advances in Colloid and Interface Science*, 112, 49–57.



- Letamendia, L., Louisor, E., Pru-Lestret, E., Rouch, J., Sciortino, F., Tartaglia, P., Ushiki, H., 1998. Relaxation phenomena in critical microemulsion systems. *Colloids and Surfaces A: Physicochemical and Engineering Aspects*, 140, 289–293.
- Lifshitz, E.M., 1956. *Soviet Physics JETP*, 2, 73.
- Lin, M.Y., Klein, R., Lindsay, H.M., Weitz, D.A., Ball, R.C., Meakin, P., 1990. The structure of fractal colloidal aggregates of finite extent. *Journal of Colloid and Interface Science*, 137, 263–280.
- Lin, Q., Meyer, E.E., Tadmor, M., Israelachvili, J.N., Kuhl, T.L., 2005. Measurement of the long- and short-range hydrophobic attraction between surfactant-coated surfaces. *Langmuir*, 21, 251–255.
- Luckham, P.F., 2004. Manipulating forces between surfaces: Applications in colloid science and biophysics. *Advances in Colloid and Interface Science*, 111, 29–47.
- Mandelbrot, B.B., 1983. *The Fractal Geometry of Nature*, W.H. Freeman, New York.
- Marsh, D., 1990. *CRC Handbook of Lipid Bilayers*, CRC Press, Boca Raton, FL.
- Meakin, P., 1998. *Fractals, Scaling and Growth Far From Equilibrium*, Cambridge University Press.
- Milling, A.J., 1996. Depletion and structuring of sodium poly (styrenesulfonate) at the silica-water interface. *Journal of Physical Chemistry*, 100, 8986–8993.
- Milling, A.J., Vincent, B., 1997. Depletion forces between silica surfaces in solutions of poly (acrylic acid). *Journal of the Chemical Society-Faraday Transactions*, 17, 3179–3183.
- Mohraz, A., Moler, D.B., Ziff, R.M., Solomon, M.J., 2004. Effect of monomer geometry on the fractal structure of colloidal rod aggregates. *Physical Review Letters*, 92, 155503, 1–4.
- Mosesson, M.W., 2000. Fibrinogen functions and fibrin assembly. *Fibrinolysis and Proteolysis*, 14, 182–186.
- Narine, S.S., Marangoni, A.G., 1999. Microscopic and rheological studies of fat crystal networks, *Journal of Crystal Growth*, 198/199, 1315–1319.
- Neu, B., Meiselman, H.J., 2002. Depletion mediated red blood cell aggregation in polymer solutions. *Biophysics Journal*, 23, 2103–2109.
- Özdemir, G., Peker, S., Helvacı, S., 2004. Effect of pH on the surface and interfacial behavior of rhamnolipids R1 and R2. *Colloids and Surfaces A: Physicochemical Engineering Aspects*, 234, 135–143.
- Pearson, M. J., Lipowsky, H. H., 2004. Effect of fibrinogen on leukocyte margination and adhesion in postcapillary venules. *Microcirculation*, 11, 295–306.
- Peker, S., 2006. Role of surface forces on the formation and stability of fractal structures. In: *Colloid Stability-The Role of Surface Forces*, Vol. 1 (ed. Th. Tadros), Weinheim, 73–97.
- Peker, S., Helvacı, S., Özdemir, G., 2003. Interface-subphase interactions of rhamnolipids in aqueous rhamnose solutions. *Langmuir*, 19, 5838–5845.
- Pham, K.N., Puertas, A.M., Bergenholtz, J., Egelhaaf, S.U., Moussaïd, A., Pusey, P.N., Schofield, A.B., Cates, M.E., Fuchs, M., Poon, W.C.K., 2002. Multiple glassy state in a simple model system. *Science*, 296, 104–106.
- Pieterse, A.J.H., Cloot, A., 1997. Algal cells and coagulation, flocculation and sedimentation processes. *Water Science and Technology*, 36, 111–118.
- Poon, W.C.K., 2002. The physics of a model colloid–polymer mixture. *Journal of Physics: Condensed Matter*, 14, R859–R880.
- Rabinovich, Y.I., Kanicky, J.R., Pandey, S., Oskarsson, H., Holmberg, K., Moudgil, B.M., Shah, D.O., 2005. Self-assembled Gemini surfactant film-mediated dispersion stability. *Journal of Colloid and Interface Science*, 288, 583–590.
- Rabinovich, Y.I., Vakarelski, I.U., Brown, S.C., Singh, P.K., Moudgil, B.M., 2004. Mechanical and thermodynamic properties of surfactant aggregates at the solid–liquid interface. *Journal of Colloid and Interface Science*, 270, 29–36.
- Reid, C.E., 1990. *Chemical Thermodynamics*, Mc-Graw Hill, New York (Chapter 10).



- Reiner, E.S., Radke, C.J., 1993. Double layer interactions between charge-regulated colloidal surfaces: Pair potentials for spherical particles bearing ionogenic surface groups. *Advances in Colloid and Interface Science*, 47, 59–147.
- Rooney, M.M., Farrell, D.H., Van Hemel, B.M., de Groot, P.G., Ford, S.T., 1998. The contribution of the three hypothesized integrin binding sites in fibrinogen to platelet-mediated clot retraction. *Blood*, 92, 2374–2381.
- Selomulya, C., Bushell, G., Amal, R., Waite, T.D., 2002. Aggregation mechanisms of latex of different particle sizes in a controlled shear environment. *Langmuir*, 18, 1974–1984.
- Shah, S.A., Chen, Y.-L., Ramakrishnan, S., Schweizer, K.S., Zukoski, C.F., 2003. Microstructure of dense colloid-polymer suspensions and gels. *Journal of Physics: Condensed Matter*, 15, 4751–4778.
- Shen, L., Stachowiak, A., Fateen, S.K., Laibinis, P.E., Hatton, T.A., 2001. Structure of alkanolic acid stabilized magnetic fluids. A small-angle neutron and light scattering analysis. *Langmuir*, 17, 288–299.
- Shull, K.R., Dongchan, A., Chen, W.C., Flanigan, C.M., Crosby, A.J., 1998. Axisymmetric adhesion tests of soft materials. *Macromolecular Chemistry and Physics*, 199, 489–511.
- Smoluchowski, M., 1917. Versuch Einer Mathematischen Theorie der Koagulations-Kinetik Kolloider Lösungen. *Zeitschrift für Physikalische Chemie*, 92, 129.
- Stokes, R.J., Evans, D.F., 1997. *Fundamentals of Interfacial Engineering*, Wiley-VCH, Inc., New York (Chapters 2, 4).
- Takenaka, M., Kobayashi, T., Saijo, K., Tanaka, H., Iwase, N., Hashimoto, T., Takahashi, M., 2004. Comparison in fractal dimension between those obtained from structure factor and viscoelasticity of gel networks of 1,3:2,4-bis-*O*-(*p*-methylbenzylidene)-D-sorbitol in polystyrene melt at gel point. *Journal of Chemical Physics*, 121, 3323–3328.
- Tirado-Miranda, M., Schmitt, A., Callejas-Fernandez, J., Fernandez-Barbero, A., 2003. Aggregation of protein coated colloidal particles: Interaction energy, cluster morphology, and aggregation kinetics. *Journal of Chemical Physics*, 119, 9251–9259.
- Tohver, V., Chan, A., Sakurada, O., Lewis, J.A., 2001. Nanoparticle engineering of complex fluid behavior. *Langmuir*, 17, 8414–8421.
- Vakarelski, I., Toritani, A., Nakayama, M., Higashitani, K., 2003. Effects of particle deformability on interaction between surfaces in solution. *Langmuir*, 19, 110–117.
- Van Damme, M.-P.I., Tiglias, J., Nemat, N., Preston, B.N., 1994. Determination of the charge content at the surface of cells using a colloid titration technique. *Analytical Biochemistry*, 223, 62–70.
- Vargas, F.F., Osorio, M.H., Ryan, U.S., De Jesus, M., 1989. Surface charge of endothelial cells estimated from electrophoretic mobility. *Membrane Biochemistry* 8, 221–227.
- Verwey, E.J.W., Overbeek, J.Th.G., 1948. *Theory of the Stability of Lyophobic Colloids*, Elsevier, Amsterdam.
- Vicsek, T., *Fractal Growth Phenomena*, 2nd edn., World Scientific, Singapore, 1999.
- Vold, R.D., Vold, M.J., 1983. *Colloid and Interface Chemistry*, Addison-Wesley, London, 1983.
- Wang, Z., Holm, C., Müller, H.W., 2002. Molecular dynamics study on the equilibrium magnetization properties and structure of ferrofluids. *Physical Review E*, 66, 021405, 1–13.
- Wasan, D., Nikolov, A., Moudgil, B., 2005. *Colloidal dispersions: Structure, stability and geometric confinement*. *Powder Technology*, 153, 135–141.
- White, J.G., 2000. EDTA-induced changes in platelet structure and function: Clot retraction. *Platelet*, 11, 49–55.
- Wu, R.M., Lee, D.J., Waite, T.D., Guan, J., 2002. Multilevel structure of sludge flocs. *Journal of Colloid and Interface Science*, 252, 383–392.
- Yip, J., Shen, Y., Berndt, M.C., Andrews, R.K., 2005. Primary platelet adhesion receptors. *IUBMB Life*, 57, 103–108.

## – 2 –

# Non-Newtonian Behavior of Solid–Liquid Suspensions

---

Rheological behavior of solid–liquid suspensions are dependent on the interactions between the dispersed components and the suspending medium which cause the diversion of the shear stress versus shear rate relation from the linearity observed in Newtonian fluids. The type and extent of this diversion will again depend on the strength of the attractive and repulsive forces, and the ratio of the time for reorientation of the components to their original configuration to the timescale of measurement. The relationship between the surface forces and the rheology of the suspension will be taken up in Chapter 3. In this chapter, an overview of non-Newtonian fluids will be given.

Metzner (1965) classified the non-Newtonian fluids into three categories: (1) Viscoelastic fluids where a part of the stress is recovered after the removal of deforming shear, (2) fluids with shear stress–shear rate relations independent of the time over which the shear is applied, or purely viscous fluids, (3) fluids with shear stress–shear rate relations dependent on the duration of the application of shear, or thixotropic, rheopectic fluids and fluids with “memory.” The first two categories will be taken up in this chapter with special emphasis on the second category that constitutes the majority of the non-Newtonian fluids. The third category is closely related with concentrated suspensions and will be covered in Chapter 3 together with the interfacial and physicochemical background of the time-dependent behavior.

## 2.1 VISCOELASTICITY

Elasticity originates from the potential energy associated with extensional stretching of bonds. Atoms, forced to be displaced from their equilibrium positions, store this energy in the form of potential energy. After the removal of the force, the molecules will relax and return to their minimum energy configuration. Presence of extendable bonds and adequate lattice space to allow stretching within the molecular network are two prerequisites for the manifestation of elasticity.

Under low stresses, the rate of deformation of the fluid is slow in comparison with the characteristic time for the reorientation of the molecules in the direction of the applied

stress. Then there will be no need for the stretching of the bonds and the response of the fluid will be purely viscous.

In intermediate cases, the bonds of some of the molecules will be broken down, while others will be stretched. The simultaneous existence of elastic and viscous behavior is called viscoelasticity. Another cause for viscoelasticity is the retardation in the relaxation of the stored potential energy in the stretched bonds due to the complexity of the molecular structure or the high viscosity of the medium in which the molecules are suspended and reorientation takes place. In the latter case, the rheological behavior of the fluid will be time dependent.

The stretching and relaxation of the bonds may pertain to individual molecules entangled in a network, or molecules at the surfaces of “particles.” Various cases where viscoelasticity are observed are summarized in Table 2.1. The examples given in the table will be extended and mechanisms underlying the viscoelastic behavior will be explicated in Chapter 3.

### 2.1.1 Effect of viscoelasticity on flow behavior

Stretching of the bonds, solely responsible for the elastic behavior of the fluid, can be brought about either by extension or by shearing of the fluid. Generally, these two stresses are simultaneously in action in operations such as kneading, mixing, and extrusion through

**Table 2.1**

Cases and causes of viscoelasticity

Case	Viscoelasticity due to	Reference
Suspensions: Neutrally buoyant noncolloidal glass spheres in non-Newtonian binder (poly (dimethyl siloxane)).	Viscoelasticity of the suspending medium, a polymer solution.	Aral and Kalyon (1997)
Gels: Uniform spherical silica particles with grafted octadecyl chains on their surfaces suspended in decalin or tetradecane.	Interactions between the grafted octadecyl chains on the particles and the suspending medium and overlapping among flocs of particles.	Rueb and Zukoski (1997)
Pastes: Soft deformable-particle pastes (colloidal pastes, micro-granular suspensions) with jammed amorphous microstructures.	Repulsive forces at jammed flat facets.	Seth <i>et al.</i> (2006)
Nanoparticle gels: Fractal nanoparticle—polymer mixtures.	Polymer bridging and depletion forces among particles.	Surve <i>et al.</i> (2006)
Blood	Deformability of erythrocytes and depletion forces between cells; polymers in plasma	Başkurt <i>et al.</i> (2002); Schramm (1994)

a contracting die. Elastic counterpart of the fluid will be activated on sudden expansion and contraction of the channel; on withdrawal of the fluid as a thin film or fiber (as in stretching of polymer films and spinning of fibers); in coating operations (as in paints and coating of latex layers on surfaces); in change of direction (as in flowing around a submerged body, in elbows, in packed beds); in couette flow or flow induced by impellers in mixers and centrifugal pumps. Even in the simplest case of flow through cylindrical channels, viscoelastic aspect of the fluid will become overt in the appearance of normal stresses, and becomes more so in converging channels.

As stretching of the fluid increases the potential energy of the molecules from the level of minimum energy, the molecules tend to escape from regions of higher to lower energy, or equivalently from regions of high to low extension zones. Thus, for example, the linear velocity of the fluid will increase radially outwards from the shaft for constant angular velocities of the impeller. Molecules subjected to high levels of extension in the peripheral regions try to escape inwards where the linear velocity is low. The crowding of the molecules around the impeller end up with the excess fluid climbing up the shaft that is known as the *Weissenberg* effect. This tendency to escape from regions of high extension is responsible for the emergence of forces normal to the shear plane, denoted in general as  $\tau_{ii}$ . Generally, the differences in these stresses are used in conformation with their effect on the system. The first normal stress difference,  $N_1$ ,

$$N_1 = \tau_{zz} - \tau_{rr} \quad (2.1)$$

exerts an axial pressure, while the second normal stress difference,  $N_2$ ,

$$N_2 = \tau_{rr} - \tau_{\theta\theta} \quad (2.2)$$

is related with the pressure variation in the radial direction (Schramm, 1994). Thus, three relations are needed to describe the general flow of viscoelastic fluids: the first and second normal stress coefficients  $\psi_1(\dot{\gamma})$  and  $\psi_2(\dot{\gamma})$ . For flow in cylindrical channels in the  $z$ -direction

$$\psi_1(\dot{\gamma}) = \frac{(\tau_{zz} - \tau_{rr})}{\dot{\gamma}^2} \quad (2.3)$$

$$\psi_2(\dot{\gamma}) = \frac{(\tau_{rr} - \tau_{\theta\theta})}{\dot{\gamma}^2} \quad (2.4)$$

together with any of the shear viscosity relations given in Section 2.1.3. Relative magnitude of the normal stresses to shear stresses in a viscoelastic fluid due to its dual nature is represented by the dimensionless *Weissenberg number*,  $W_s$ ,

$$W_s = \frac{(\tau_{zz} - \tau_{rr})}{\tau_{rz}} \quad (2.5)$$

Another manifestation of shear dependency of viscoelasticity is observed in the swelling (instead of contracting) of a viscoelastic fluid on sudden expansion, generally known as

die swelling. The molecules forced to extend and stretch in passing through the narrow tube relax on sudden expansion resuming their minimum energy configuration. In doing so, they occupy more space resulting in the expansion of the fluid. Another dimensionless number, the Deborah number,  $De$ , controls this expansion.

$$De = \frac{\lambda}{\theta} \quad (2.6)$$

In this equation,  $\lambda$  is the characteristic relaxation time of the fluid, and  $\theta$  the characteristic time associated with the flow situation. It can be the inverse of the typical deformation rate  $\dot{\gamma}^{-1}$ , or  $L/V_{av}$  in macro scale quantities in flow through channels, and amplitude of the oscillatory strain times its frequency,  $(\gamma_0\omega)^{-1}$  in oscillatory flows (Macosko, 1994; Papanastasiou, 1994).

Resistance of the fluid molecules toward stretching is quantified by the extensional viscosity,  $\eta_e$ , defined as

$$\eta_e = \frac{\tau_{zz} - \tau_{rr}}{dV_z/dz} \quad (2.7)$$

Extensional viscosity is measured in contracting channels where the area varies as

$$A = \frac{\pi}{4} \left( \frac{(dV/dz)L}{V_1 D_1^2} \left( \frac{z}{L} - 1 \right) + \frac{1}{D_2^2} \right)^{-1} \quad (2.8)$$

in the flow direction  $z$ , to keep the velocity gradient in the flow direction ( $dV_z/dz$ ) constant. In this equation,  $V_1$ ,  $L$ ,  $D_1$ , and  $D_2$  indicate the velocity at the inlet of the channel, the total length, diameter at the entrance, and the exit of the channel, respectively. The extensional viscosity is three times the shear viscosity in dilute polymer solutions exhibiting Newtonian behavior, known as the Trouton's rule (1906). Generally, the extensional viscosity is much higher than the shear viscosity in viscoelastic fluids, increasing with an increase in the shear rate. In polymer solutions, this increase is attributed to forced parallel orientation of the macromolecules. Addition of fibers to polymeric materials increases the extensional viscosity by several orders of magnitude with the applied strain (Ooi and Sridhar, 2004), known as *strain hardening*. The phenomenon is beneficially used in increasing the strength and toughness of lightweight composites.

With the advent of laser Doppler anemometry (LDA) technique of local velocity measurement, it became possible to elucidate the effect of viscoelasticity on flow behavior in the micro scale. The resistance of polymer molecules to reorientation and stretching was found to increase the laminar boundary layer and alter the turbulence structure, by enhancing the turbulent fluctuations in the axial direction and reducing fluctuating velocities in the normal directions (Escudier and Smith, 2001; Poole and Escudier, 2004). Viscoelasticity was also found to be responsible for the enlargement of the vortex region in sudden expansions. Effect of elasticity in increasing the size and intensity of recirculation vortices in sudden contractions was confirmed by numerical computations as a function of Deborah number and contraction ratio (Alves *et al.*, 2004).

### 2.1.2 Assessment of viscoelasticity

A wide range of materials ranging from elastic solids to viscous liquids is covered by the term “viscoelasticity.” *Creep and recovery tests* are performed to assess the elastic nature of the fluid through its response to a given stress and recovery after the release of the stress under steady conditions. A constant stress in the form of a step function is assigned for a definite period; deformation created in the fluid and its recovery afterwards is measured as a function of time in creep and recovery tests (Schramm, 1994). The deformation of the fluid may range between two limit responses: (1) Storage of all the energy given as potential energy and relaxing to the original configuration immediately after release, (2) deforming irreversibly under the applied stress and dissipating the energy as heat in the process. Materials showing the first response are called *ideal solids*. The induced strain,  $\gamma$  is related to the applied shear stress  $\tau$ , through the relation

$$\tau = G\gamma \quad (2.9)$$

where  $G$  is the *shear modulus*, a material constant that indicates how easily the material can be deformed. A similar relation holds if a tensile stress  $T_T$ , is applied on the material

$$T_T = E\gamma \quad (2.10)$$

where  $E$  is *Young's modulus of elasticity* and  $\gamma$  the *deformation* expressed as the difference in the final and initial length to the initial characteristic length. As  $\gamma (= \Delta L/L)$  is a dimensionless extension in length, the moduli have stress units.

Materials that deform irreversibly are called *ideal Newtonian liquids*. The *rate of deformation*,  $\dot{\gamma}$ , brought about by the applied stress is dependent on another material constant, the *dynamic viscosity*,  $\mu$

$$\tau = \mu\dot{\gamma} = \mu \frac{d\gamma}{dt} \quad (2.11)$$

As these materials dissipate all the given energy through the applied stress as friction during deformation, they cannot recover their original configuration after the release of the stress.

Viscoelastic materials show a combination of these two limiting responses: The applied stress and the induced deformation are related with the equation

$$\gamma(t) = J(t) \cdot \tau \quad (2.12)$$

The time related proportionality constant  $J(t)$ , is called *compliance*, and is a material constant of the fluid. The higher the compliance, the more deformable is the fluid under a given stress. Even though the responses of ideal solids and Newtonian liquids are not dependent on time, the response of viscoelastic materials is. The time dependence is introduced through the viscous resistance to elastic deformation under stress and in the rate of recovery to the original configuration after the release of the stress. If the applied stress and the resulting strain are below the rupture limits of the bonds between the molecules, the relation

between the stress and strain is linear and the test is a nondestructive method for the evaluation of the rheological behavior of the fluid. As long as these *linear viscoelasticity* conditions are retained, the compliance of the fluid will be independent of the magnitude of the applied stress. Under stresses higher than the limit of linear viscoelasticity, the structure of the fluid is broken down and its compliance becomes nonreproducible.

### 2.1.3 Dynamic methods in the assessment of viscoelasticity

Creep and recovery tests will show if a fluid is more solid- or liquid-like in its response but it will not give a quantitative measure of these aspects. For this end, dynamic tests are used under *controlled shear rate* (CR), where an *oscillatory strain*,  $\gamma$ , with an *amplitude*  $\gamma_a$  and *angular velocity*  $\omega$

$$\gamma = \gamma_a \sin(\omega t) \quad (2.13)$$

is assigned to the system and the induced stress with an *amplitude*  $\tau_a$  and *phase shift angle*  $\delta$

$$\tau = \tau_a \sin(\omega t + \delta) \quad (2.14)$$

is evaluated. In the more sensitive *controlled stress mode* of operation (CS), a sinusoidal stress with an amplitude  $\tau_a$ , and frequency  $f$ , is assigned and the response of the system in terms of induced strain and phase angle is evaluated. The angular velocity is related to the frequency of oscillation through

$$\omega = 2\pi f \quad (2.15)$$

*Complex modulus of elasticity*,  $G^*$ , is defined as

$$G^* = \frac{\tau_a}{\gamma_a} \quad (2.16)$$

and denotes the total resistance of the fluid to the imposed strain. The complex modulus of elasticity can be broken down to its real and imaginary parts as

$$G^* = G' + iG'' \quad (2.17)$$

where  $G'$  is the *elastic or the storage modulus* defined as

$$G' = G^* \cos \delta = \left( \frac{\tau_a}{\gamma_a} \right) \cos \delta \quad (2.18)$$

and  $G''$  is the *viscous or loss modulus* given by

$$G'' = G^* \sin \delta = \left( \frac{\tau_a}{\gamma_a} \right) \sin \delta \quad (2.19)$$

where  $\delta$  is the *delay* or the *phase shift angle* by which the stress response lags behind the assigned strain. For an ideal elastic solid, the stress is in phase with the strain and  $\delta = 0$ ; for an ideal Newtonian fluid, the stress is  $90^\circ$  ( $\pi/2$  radians) out of phase with the strain.

The total resistance of the fluid to dynamic shear can also be expressed in terms of *complex viscosity*,  $\eta^*$ ,

$$\eta^* = \frac{G^*}{\omega} \quad (2.20)$$

which can be broken down as *storage viscosity*,  $\eta''$ , related with the *elastic counterpart*

$$\eta'' = \frac{G'}{\omega} = \left( \frac{\tau_a}{\gamma_a \omega} \right) \cos \delta \quad (2.21a)$$

and *dynamic viscosity*, related with the *viscous counterpart*,  $\eta'$

$$\eta' = \frac{G''}{\omega} = \left( \frac{\tau_a}{\gamma_a \omega} \right) \sin \delta \quad (2.21b)$$

These concepts will now be illustrated over an experimental case.

### Example 2.1: Viscoelastic behavior of starch gels

#### The case

Starch exists in the form of granules, in which the amylose and amylopectin polymers exist in a compact wound-up state. Under the action of heat and stirring in water, these granules are swollen. The soluble amylose polymers diffuse out and are solvated to produce a gel through interaction with each other and the remaining swollen granules of amylopectin [Beşün, *et al.*, 1996]. The consistency of the gel increases as the volume fraction of starch  $\phi$ , increases. In this case, the rheological behavior of gels with 3%, 8% and 19% by volume of starch are investigated in a controlled stress rheometer with cone and plate sensors to illustrate the use of equations given in Section 2.1.

#### Rheological analysis

The behavior of ideal elastic solids and viscous Newtonian liquids in a creep and recovery test are given in Fig. 2.1(a) in terms of induced deformation under an assigned stress of 1.5 Pa for a period of 45 seconds, as an example. The response of an elastic solid is immediate: it is deformed in proportion to the applied shear stress ( $\gamma = 1$  in the example given), and then snaps back to its original configuration as soon as the stress is relaxed. Since no bonds are broken up, viscous effects do not exist and the response of the ideal solid does not change with time as long as there is no change in the applied stress. When the applied stress is greater than the chemical and physical bonds of the material can withstand, the bonds are broken reversibly in proportion to the applied stress. The breakage of the bonds



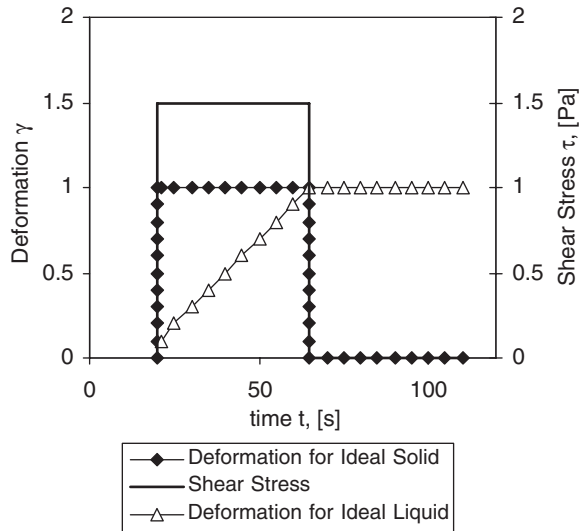


**Figure 2.1** (a) Steady response of ideal elastic solids and non-Newtonian liquids to the applied stress.

is displayed as a linear increase of strain with the shear stress. As the energy is dissipated during the break-up process, the material cannot return to its original minimum energy state at the cessation of the applied stress and remains permanently deformed. The material showing this behavior acts as an ideal or Newtonian fluid.

Depending on the magnitude of the shear stress exerted, the material can give a response that has ideal solid and liquid counterparts, or in other words, act viscoelastically. An example to a viscoelastic response in creep and recovery tests of the gels is given in Fig. 2.1(b) for 3% starch. If it were not for the curved section in the first 150 seconds (and for approximately the same time during relaxation after the termination of the stress), the gel would behave almost like a solid. The immediate hop of the strain to  $\approx 0.01\%$  is a result of the ideal solid response of the curve. If it were not for the viscous counterpart, the initial jump would be up to the equilibrium value. The rate at which the equilibrium value is reached, both on the application of the stress and on relaxation, depends on the relative magnitude of the viscous counterpart. The magnitude of the equilibrium value after relaxation gives the strain left in the gel that cannot be recovered due to irreversible dissipation of energy by the viscous counterpart.

Dynamic tests give the response of the material under periodically oscillating conditions. The conditions can be the amplitude of shear stress or strain. The response of the material toward a variation in the frequency of oscillations can also be investigated as a parameter. The immediate response of ideal elastic solids is expressed by zero lag; the strain response of the ideal solid is in phase with the oscillatory stress input. On the other hand, the strain response of Newtonian liquids is  $90^\circ$  ( $\pi/2$  radians) out of phase with the sinusoidal stress input, as shown in Fig. 2.1(c). These responses are shown by ideal elastic and plastic materials. Many of the fluids, including gels and suspensions show a response which has both plastic and elastic components activated under different modes, as shown by the filled circles

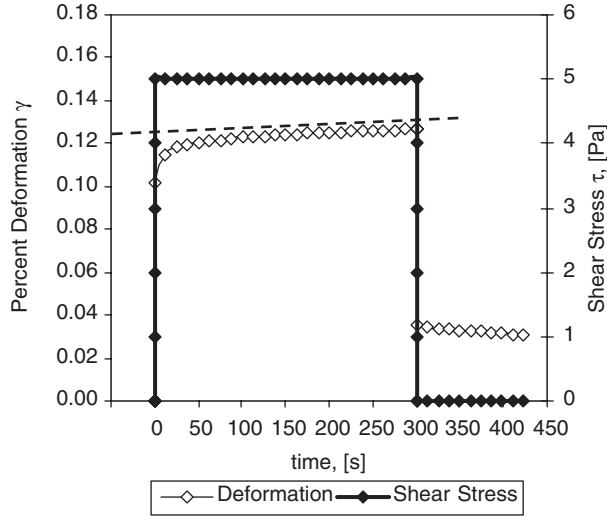


**Figure 2.1** (b) Response of 3% starch gel to an applied stress of 0.5 Pa.

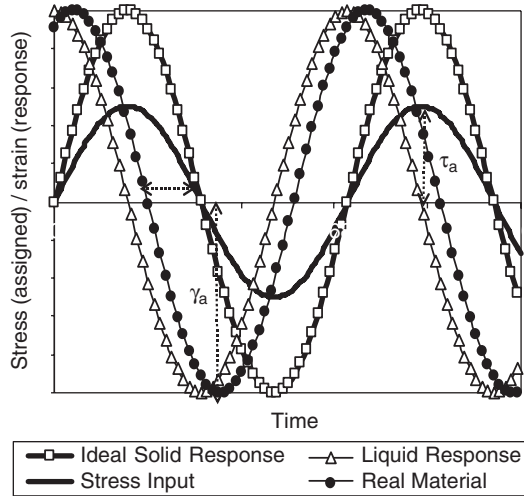


**Figure 2.1** (c) Dynamic response of ideal elastic solids and non-Newtonian liquids to the applied stress.

in Fig. 2.1(c). The lag in the response to the input stress in this example is shown in the figure as a double sided arrow and expressed as the phase shift angle  $\delta$ , a fraction of the total period of  $2\pi$  radians.  $\delta$  has a value in between the two limits of zero and  $\pi/2$  radians in the case of real materials. The maximum amplitudes of the assigned stress and the resulting strain response variations shown as  $\tau_a$  and  $\gamma_a$ , respectively, are used to calculate the complex modulus of elasticity,  $G^*$ .

It is a good idea to start characterization of the rheological behavior by determination of the linear viscoelastic range. For this end, an initial amplitude sweep test is run, where maximum strain is recorded as a function of the maximum amplitude of stress assigned, at an oscillation frequency of 1 Hertz. The *elastic range*, phase shift angle, *complex modulus of elasticity*  $G^*$  (eq. (2.16)) and its elastic counterpart, the *storage modulus*  $G'$  (eq. (2.18)), and its viscous counterpart, the *loss modulus*  $G''$  (eq. (2.19)), *complex viscosity*  $\eta^*$  (eq. (2.20)) and its elastic  $\eta'$  (eq. (2.20a)), and viscous  $\eta''$  (eq. (2.20b)) counterparts and *yield stress* of the gel can be all obtained from the results of this test. Frequency sweep tests are run at the constant value of the shear stress in the linear viscoelastic region obtained from the stress amplitude sweep tests. Maximum strain amplitude is recorded as a function of frequency, from which variations of  $G'$ ,  $G''$  and  $\eta^*$  with frequency of oscillations are calculated.

Termination of the linear viscoelastic region can further be confirmed by running a yield stress test. In this test, the shear stress is increased steadily and variation in strain is recorded. The yield stress is identified by a divergence in the strain, as illustrated in Fig. 2.1 (d). The slope of the linear region before the yield stress is the *compliance*  $J(t)$  (eq. (2.12)), the inverse of  $G$ , the *shear modulus of elasticity* (eq. (2.9)).

Normal stresses arise in polymeric solutions exhibiting viscoelastic behavior due to resistance of entangled polymer molecules to stretch. The polymers escape from the plane of maximum shear toward the normal directions, exerting a pressure in that direction. Normal stresses are expressed as stress differences  $N$ . In the case of rotational flow, the first normal stress difference  $N_1$  is the difference between the normal stress in the direction of motion and the axial direction,  $N_1 = \tau_{\theta\theta} - \tau_{zz}$ , is analogous to eq. (2.1). The second normal stress difference involves the difference in normal stresses in the radial and the axial directions, and is much smaller than the first normal stress difference. Shear stress  $\tau_{z\theta}$  and the first normal stress difference  $N_1$  that evolve under steady application of shear at a predetermined rate of increase of the shear rate  $\dot{\gamma}$  are recorded. Dynamic shear viscosity is obtained from the slope of the  $\tau_{z\theta} - \dot{\gamma}$  data. First normal stress coefficient  $\psi_1(\dot{\gamma})$  is calculated

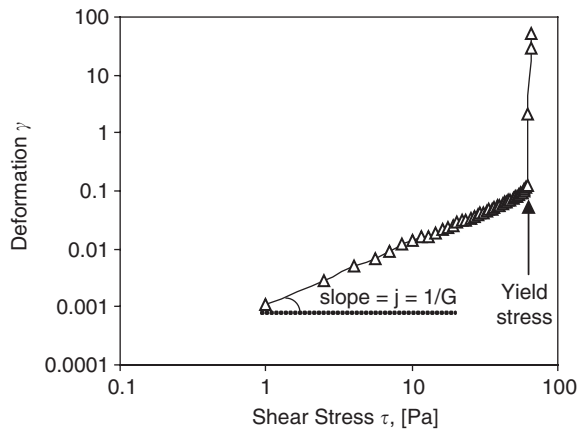


**Figure 2.1** (d) Evaluation of yield stress, compliance and shear modulus of elasticity. Data given for 8% starch gels.

from the  $N_1 - \dot{\gamma}$  data using eq. (2.4) and Weissenberg number from the ratio of first normal stress difference to the shear stress, using eq. (2.5).

### *Evaluation of results of the rheological tests*

Stress amplitude sweep; frequency sweep; creep and relaxation; steady shear and yield stress tests are run with gels of 3%, 8% and 19% by volume starch content in this case to illustrate the use of eqs. (2.1)–(2.5) and (2.9)–(2.20) in this example.

A stress amplitude sweep test is run at the start in controlled stress mode of operation of the rheometer to determine the linear elastic range for each starch gel. In these tests, the amplitude of the input stress ( $\tau = \tau_a \sin(\omega t)$ ) is increased gradually within a program, and the response of the system is given as strain ( $\gamma = \gamma_a \sin(\omega t + \delta)$ ) and phase shift angle  $\delta$ , from which all the other properties are evaluated. At each level of the assigned stress amplitude  $\tau_a$ , the ratio of  $\tau_a/\gamma_a$  is calculated to give the complex modulus of elasticity  $G^*$  given by eq. (2.16). The elastic part of the complex modulus, the storage modulus, is calculated with eq. (2.18) and the viscous counterpart, the loss modulus, is calculated with eq. (2.19) and the results plotted in Fig. 2.1 (d), for 8% starch gel.

The almost horizontal section between the two cross-over points of  $G'$  and  $G''$  signify the linear viscoelastic region. At very low values of the stress, the viscous modulus is greater than the elastic modulus, as the material has to start deformation before being counteracted by elastic forces. Shortly afterwards, the moduli cross over with the elastic modulus  $G'$  being greater than the viscous modulus  $G''$ . In the range of shear stresses where the moduli are linear and horizontal, the gel is linearly viscoelastic. At the yield point the moduli crossover once more, after which the gel flows. This transformation is marked by the value of  $\delta$ , given in the same figure. If the transition were from an ideal elastic solid to a Newtonian liquid, then the value of  $\delta$  would jump up from zero to  $90^\circ$ , the phase lag of viscous Newtonian fluids. Both the lowest ( $\delta \approx 3^\circ$ ) and the highest ( $\delta \approx 85^\circ$ ) value show that the gel is not an ideal elastic solid and the remaining inter-chain bonds after the yield point prevent it from being a viscous Newtonian fluid where there should be no interaction between the components. Nevertheless, in the linear viscoelastic region, the value of  $\delta$  is close enough to zero for elastic modulus  $G'$  to be nearly equal to complex modulus of elasticity  $G^*$ , and viscous modulus  $G''$  to be more than an order of magnitude less than  $G'$  according to eqs. (2.18) and (2.19). Both the elastic and the viscous moduli increase with the volumetric fraction of solids in the order, 58, 1125, and 15040 Pa in the case of  $G'$  and 6, 55, and 638 Pa in,  $G''$  for the same order of increase in the volumetric fraction of solids. As the compaction of the starch polymers increase, the recoil of the gel increases due to decrease in the entropy and the material resists with a greater force to elastic compression brought about by shear forces, in comparison with the resistance to viscous shear of the polymers.

The complex viscosity  $\eta^*$  and its elastic  $\eta''$ , and viscous  $\eta'$  counterparts are obtained from the same dynamic tests, by dividing the respective moduli with the angular velocity  $\omega = 2\pi \text{ rad s}^{-1}$  in this case, through eqs. (2.20), (2.20a), and (2.20b). The magnitude of the complex viscosity in the linear viscoelastic region constitutes a point value corresponding to  $f = 1$  Hertz in the complex viscosity curve in Fig. 2.1(g), calculated from the data obtained in frequency sweep tests. Complex viscosity is very sensitive to variations in the concentration of polymer and conformation of the polymer molecules. This is especially important in the case of starch where the polymers unwind and leave the swollen granules under shear.

The gel yields right after the arrow marking the yield stress at  $\approx 60$  Pa in Fig. 2.1(e). This value of the yield stress obtained under dynamic oscillatory stress, is confirmed with the yield stress value obtained by the application of steadily increasing shear stress in a yield stress test given in Fig. 2.1 (c) for the 8 % starch gel. The point marked yield stress,  $\approx 60$  Pa is nearly the same value as obtained in a dynamic test. The slope of the linear section

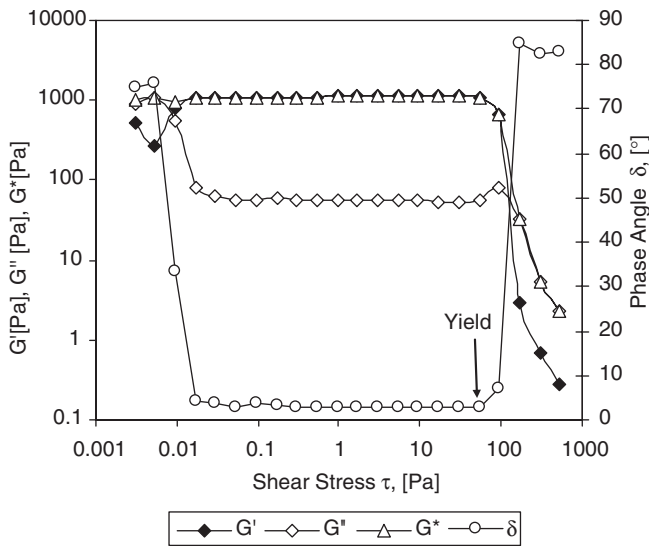


**Figure 2.1** (e) Elastic, viscous and complex moduli and phase shift angle of 8 % (v) starch gels.

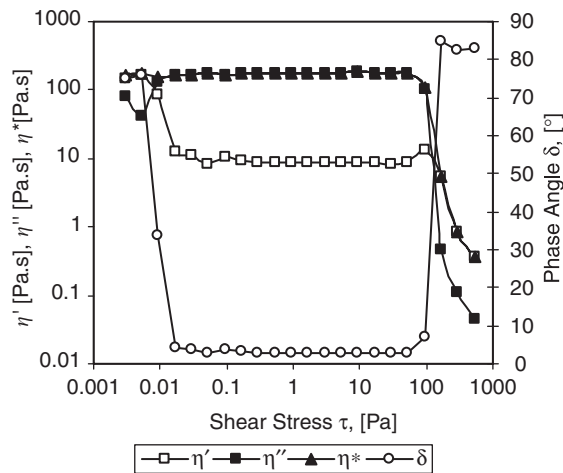


**Figure 2.1** (f) Complex viscosity and its dynamic and storage counterparts; and phase shift angle of 8 % (v) starch gels.

below the yield stress in Fig. 2.1 (c), gives the compliance,  $J(t)$  by eq. (2.12), the inverse of the shear modulus  $G$  eq. (2.9). The variation of compliance and yield stress with the polymer concentration, given as % by volume, is given in Fig. 2.1(h).

Yield stress is an important property, as it gives the firmness to the gel and determines the flow behavior as will be given in the following sections. The yield stress shows an almost order of magnitude increase,  $\approx 7, 63$  and  $1286$  Pa, while compliance shows a steeper decrease,  $4.5 \times 10^{-2}, 2 \times 10^{-2}$ , and  $8.5 \times 10^{-1} \text{ Pa}^{-1}$  as the volumetric concentration of solids increase in the order, 3, 8, and 19%, respectively. The practical significance of these values is that the gels become harder to process.

Normal stresses are evaluated together with shear stresses by increasing the shear rate at a predetermined rate under steady rotational flow. The results of such a test are given in Fig. 2.1(i). The first normal stress difference shows the same trends but is about an order of magnitude less than the shear stress. The dynamic viscosity  $\eta$ , defined as the ratio of the shear stress to shear rate, decreases non-linearly with an increase in the shear rate, as commonly observed in polymer solutions with viscoelastic properties. The shear behavior of the starch gels can be described by the Herschel-Bulkley model with a regression constant  $r^2 \geq 0.99$ , using the yield stress values given in Fig. 2.1(h). The consistency  $K$  values are 1.0, 23.0, and 31.3 and the viscosity index  $n$  values, 0.67, 0.49 and 0.58, for 3.8. and 19 % concentration, respectively. The significance of these constants and the model will be discussed in the following sections.

Dynamic viscosity  $\eta$  is the resistance of the fluid to steady shear, while the complex viscosity  $\eta^*$  is the resistance to dynamic oscillating shear. Comparison of Fig. 2.1(g), and Fig. 2.1(i) show that complex viscosity is greater than the dynamic viscosity by an order of magnitude or two and is more sensitive to variation in shear rate.

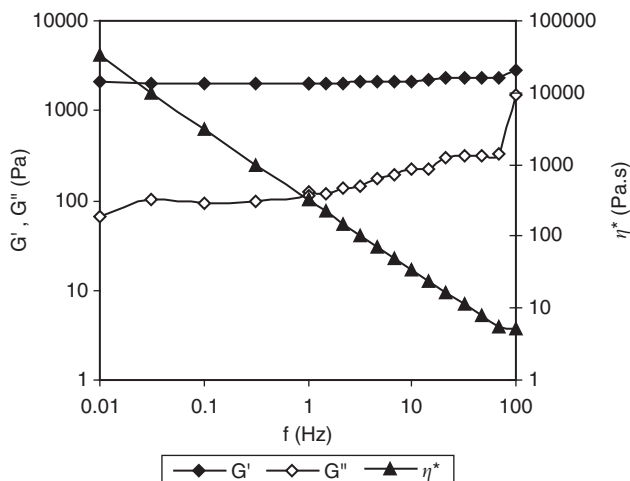


**Figure 2.1** (g) Variation of the elastic and viscous moduli and complex viscosity with frequency of oscillations in 8% starch gels.

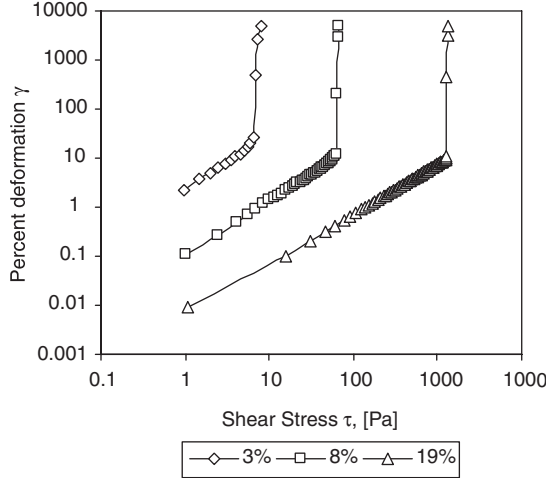


**Figure 2.1** (h). The variation of yield stress and compliance with the volumetric fraction of solids.

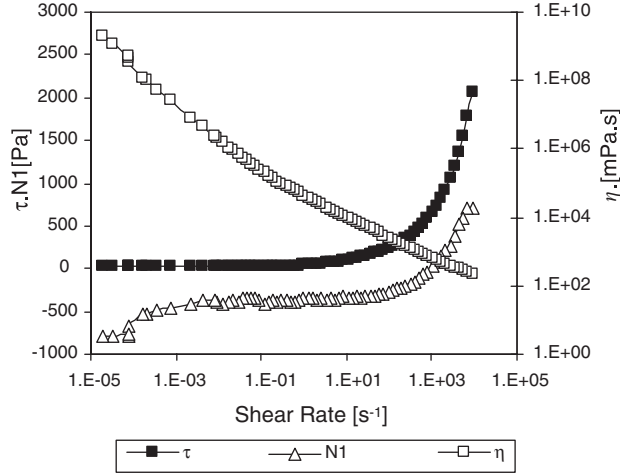


**Figure 2.1** (i) Shear and normal stresses and dynamic viscosity observed in 8% starch gels.

An analogous property to dynamic shear is the first normal stress difference coefficient  $\psi_1$  calculated by using eq. (2.3) and given in Fig. 2.1 (j). The coefficients approach to zero at high shear rates, due to very large values of  $\dot{\gamma}^2$  in the denominator. The behavior of the gels at low shear rates is more significant. The negative values of 8 and 19 % starch gels indicate that the normal stress in the axial direction  $\tau_{zz}$  that exerts a thrust on the cone of the rheometer is greater than the normal stress  $\tau_{\theta\theta}$  in the flow direction. The positive value of 3% gel shows that compaction in the gel network is required for the development of this thrust.

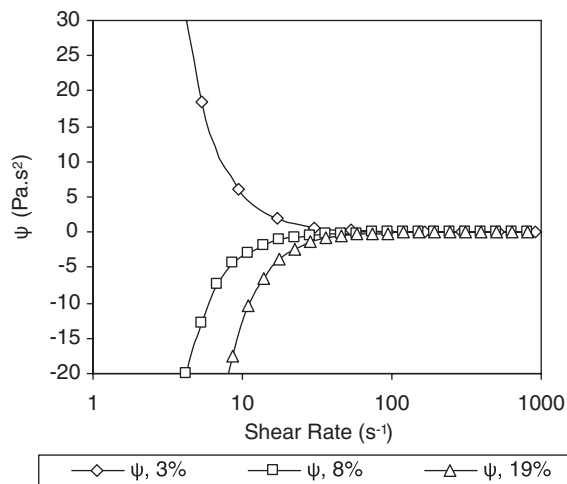


**Figure 2.1** (j) First normal stress difference coefficients of the starch gels.

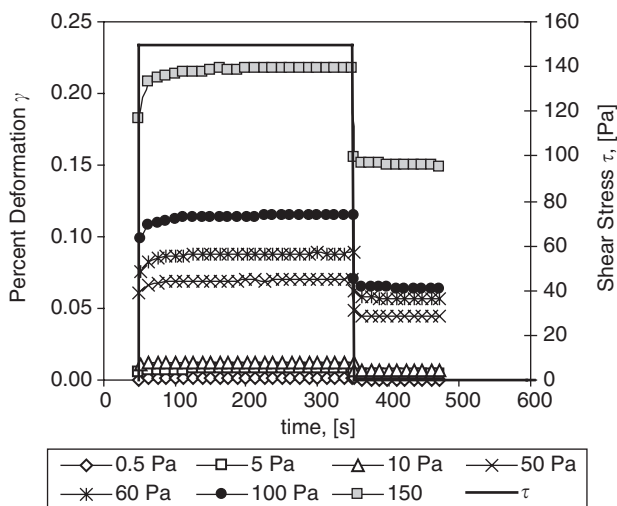


**Figure 2.1** (k) Response of 8% (v) starch gel within the linear viscoelastic region.

The viscoelastic behavior of the gels can be quantitatively characterized with the help of these rheological tests. Creep and recovery tests are qualitative but nevertheless, give significant insight into the behaviour of the gels. The effect of the magnitude of the shear stress applied is given in Fig. 2.1(k) and (l) for 8 % starch gel. As the yield stress is approached the initial immediate response increases, but the permanent strain level after relaxation increases, also. The gel yields progressively with increasing stress until it flows like a



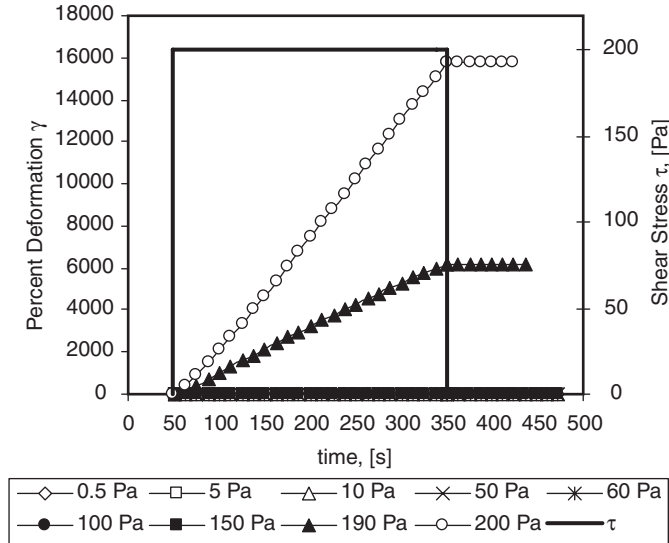


**Figure 2.1** (l). Response of 8% (v) starch gel above the linear viscoelastic region.

Newtonian liquid at stresses above 150 Pa, as given in Fig. 2.1 (l), in full confirmation with the dynamic test results.

## 2.2 RHEOLOGICAL MODELS OF TIME-INDEPENDENT NON-NEWTONIAN FLUIDS

This group of non-Newtonian fluids is characterized by viscosity relations that are a function of shear rate, but not a function of time of application of shear. The rheological behavior of these fluids, of which solid particle suspensions in liquids is a special case, are described by governing relations, called *constitutive equations*, between shear stress ( $\tau$ ) and shear rate ( $\dot{\gamma}$ )

$$\tau = f(\dot{\gamma}) \quad (2.22)$$

This form of the equation is generally used for simple, unidirectional shear flows of Newtonian and non-Newtonian fluids. However, under the action of interparticle attractions and in the presence of complex molecular structures, such a relation between shear stress and shear rate cannot encompass all the stresses associated with the deformation. Manipulation is more convenient with the use of tensors in three-dimensional space. Macosko (1994) generalized the constitutive equations for a variety of fluids with different rheological behavior as a single equation for viscous flow: Starting with the postulate that the total stress tensor,  $\mathbf{T}$  depends only on the rate of deformation tensor  $\dot{\gamma}$

$$\mathbf{T} = f(\dot{\gamma}) \quad (2.23)$$

An equation form covering all possible stresses are obtained through the expansion of the function in a power series

$$\mathbf{T} = f_0 \dot{\gamma}^0 + f_1 \dot{\gamma}^1 + f_2 \dot{\gamma}^2 + \dots \quad (2.24)$$

For an incompressible fluid, the shear rate tensor raised to the zero power, is the identity tensor with its invariant equal to the negative of the pressure. With the use of Cayley–Hamilton theorem, eq. (2.24) can be written in terms of the scalar functions  $\eta_1$  and  $\eta_2$  of the invariants of  $\dot{\gamma}$

$$\mathbf{T} = -p\mathbf{I} + \eta_1(I_{2,\dot{\gamma}}, I_{3,\dot{\gamma}})\dot{\gamma} + \eta_2(I_{2,\dot{\gamma}}, I_{3,\dot{\gamma}})\dot{\gamma}^2 \quad (2.25)$$

This general constitutive equation is known as the *Reiner–Rivlin* equation. The  $\eta_1$  term is the viscosity function that determines the shear behavior of the system. The  $\eta_2$  term gives rise to normal stresses in steady shear flow. As the normal stresses in steady shear flow cannot be related to any function of the rate of deformation tensor in this group of fluids,  $\eta_2$  term is set equal to zero. The general constitutive equation for viscous fluids then reduces to

$$\mathbf{T} = -p\mathbf{I} + \eta_1(I_{2,\dot{\gamma}}, I_{3,\dot{\gamma}})\dot{\gamma} \quad (2.26)$$

In simple shear flows, like flow through pipes  $I_{3,\dot{\gamma}} = 0$  (see Appendix A2), reducing the general constitutive equation to

$$\mathbf{T} = -p\mathbf{I} + \eta_1(I_{2,\dot{\gamma}})\dot{\gamma} \quad (2.27)$$

or, in terms of a relation between shear stress and shear rate to

$$\tau = \eta_1(I_{2,\dot{\gamma}})\dot{\gamma} \quad (2.28)$$

### 2.2.1 Models which describe the rheological behavior with a viscosity function

The viscosity function,  $\eta(I_{2,\dot{\gamma}})$  determines the rheology of the fluid in the absence of a yield stress. If the function turns out to be too complex, numerical solution of the equation is called for. Some of the functions that lend themselves to analytical solution and the models for which they form the constitutive equation are given below:

#### 2.2.1.1 Newtonian fluids

The simplest function, where  $\eta_1(I_{2,\dot{\gamma}}) = \eta$ , a material constant defines a Newtonian fluid with the equation

$$\tau = \eta \dot{\gamma} \quad (2.29)$$

or in the case of unidirectional flows

$$\tau_{ij} = \eta \dot{\gamma}_{ij} \quad (2.30)$$

The material constant  $\eta = \mu$ , the dynamic viscosity of the fluid is a physical property in the case of liquids and gases made up of simple molecules.

### 2.2.1.2 Power-law model

In dispersions with moderate concentration of dispersed phase, a widely observed phenomenon is a decrease in the apparent viscosity with an increase in the shear rate. In the case of concentrated dispersions, shear thickening is observed following a shear-thinning process, with an increase in the shear rate. This rheological behavior is described by the power-law model, also known as the Ostwald–de Waele model:

$$\eta_1(I_{2,\dot{\gamma}}) = K |I_{2,\dot{\gamma}}|^{(n-1)/2} \quad (2.31)$$

$$\tau = K |I_{2,\dot{\gamma}}|^{(n-1)/2} \dot{\gamma} \quad (2.32)$$

In steady, unidirectional shear flows  $|I_{2,\dot{\gamma}}| = \dot{\gamma}^2$ , and the constitutive equation is reduced to

$$\tau_{ij} = (K \dot{\gamma}_{ij}^{n-1}) \dot{\gamma}_{ij} = K \dot{\gamma}_{ij}^n \quad (2.33)$$

with the apparent viscosity given by the equation

$$\eta = K \dot{\gamma}^{n-1} \quad (2.34)$$

The *viscosity index*  $n$  is less than one in shear-thinning fluids, also called *pseudoplastic* fluids; whereas, it is greater than one in shear thickening or *dilatant* fluids.  $K$ , the *consistency*, is the value of the shear stress when  $\dot{\gamma} = 1$ . The model becomes identical to Newton's model when the viscosity index is equal to one. The power-law model is widely used for medium range of shear rates. In processes covering a wide range of shear rates the model is unable to converge to steady-state values at the limits. Of special importance is the case of  $n \leq 1$  at extremely low shear rates, where the apparent viscosity calculated by the power-law approaches infinity. Experimental observations of suspensions and dilute polymer solutions show that the apparent viscosity approaches a constant value at low shear rates, and that Newtonian behavior is observed at high shear rates.

### 2.2.1.3 Sisko model

A correction for the approach to a steady-state value of the apparent viscosity at high values of shear rate,  $\eta_\infty$ , is made in the model developed by Sisko (1958).

$$\tau_{ij} = (\eta_\infty + K \dot{\gamma}_{ij}^{n-1}) \dot{\gamma}_{ij} \quad (2.35)$$

This equation can be considered as the sum of Newton and power-law expressions with different viscosity functions. Since the apparent viscosity is defined as the ratio of shear stress to shear rate, the apparent viscosity  $\eta$  is given as

$$\eta = \eta_\infty + K \dot{\gamma}_{ij}^{n-1} \quad (2.36)$$

The three-dimensional form of the Sisko model is given with the equation

$$\tau = (\eta_\infty + K |I_{2,\dot{\gamma}}|^{(n-1)/2}) \dot{\gamma} \quad (2.37)$$

#### 2.2.1.4 Cross model

To overcome the shortcomings of the power-law, Cross (1965) developed an expression for the viscosity function,  $\eta(I_{2,\dot{\gamma}})$ , to describe the experimentally observed apparent viscosity variations.

$$\frac{\eta - \eta_\infty}{\eta_0 - \eta_\infty} = \frac{1}{1 + (K^2 |I_{2,\dot{\gamma}}|)^{(1-n)/2}} \quad (2.38)$$

For simple shear flows,  $\lambda = K^{1-n}$  and  $|I_{2,\dot{\gamma}}| = \dot{\gamma}^2$ , so the Cross model reduces to

$$\frac{\eta - \eta_\infty}{\eta_0 - \eta_\infty} = \frac{1}{1 + \lambda \dot{\gamma}^{1-n}} \quad (2.39)$$

For very low shear rates, the apparent viscosity approaches to its zero value,  $\eta_0$ , whereas, at high shear rates it approaches a steady-state value of  $\eta_\infty$ . In between the two extremes, the Cross model approaches the power-law model.

#### 2.2.1.5 Carreau–Yasuda models

These models developed by Carreau *et al.* (1979) and Yasuda *et al.* (1981) are very similar and can be regarded as the generalizations of the Cross model with the general fitting parameter  $a$ , replacing the exponent 2 in the Cross equation. The Yasuda equation in terms of the shear rate invariant is

$$\frac{\eta - \eta_\infty}{\eta_0 - \eta_\infty} = \frac{1}{1 + (K^a |I_{2,\dot{\gamma}}|)^{(1-n)/a}} \quad (2.40)$$

This equation reduces to eq. (2.36) for simple shear flow. Carreau equation is expressed as the difference between the apparent viscosity at the given value of shear rate and its value at zero shear, instead of at high shear rates:

$$\frac{\eta - \eta_0}{\eta_\infty} = [1 + (\lambda \dot{\gamma})^a]^{(n-1)/a} \quad (2.41)$$

### 2.2.2 Models for fluids with a yield stress

Fluids which do not deform below a threshold stress  $\tau_0$ , called the *yield stress*, and flow readily above it are called *plastic fluids*. During flow through a channel, only those regions where the shear stress is greater than the yield value will deform continuously or flow. Regions where the shear stress remains below the yield value will have a much higher apparent viscosity and will form either stagnant regions or be dragged along as a plug over the flowing annular region, depending on the geometry of the channel. The behavior of these fluids below the yield stress is an unresolved issue as regards instrument-dependency of the measured values of the yield stress: In the original models, it was assumed that there would be no flow, or deformation, below the yield stress, denoted by the equation

$$\tau < \tau_0 \quad \dot{\gamma} = 0 \quad (2.42)$$

This equation implies the acceptance of an initial rise in shear stress as an unsteady behavior before the establishment of steady-state conditions, depending largely on the sensitivity of the instrument, that should be totally disregarded in the stress measurements with the use of eq. (2.42).

On the other hand, the nearly linear initial rise in the shear stress at very low shear rates during measurement in a rheometer is accepted as viscous shear behavior by some researchers, who propose a two-viscosity model to describe the rheology of these fluids. As there is no yield stress concept in such an interpretation,  $\tau < \tau_0$  condition is replaced by a critical shear rate  $\dot{\gamma}_c$ , where a sudden change in apparent viscosity is observed:

$$\dot{\gamma} < \dot{\gamma}_c \quad \eta = \eta_I \quad (2.43a)$$

$$\dot{\gamma} > \dot{\gamma}_c \quad \eta = \eta_{II} \quad (2.43b)$$

where  $\eta_I$  and  $\eta_{II}$  are the slopes of the shear stress–shear rate plots before and after the critical shear rate, respectively. With this condition, eq. (2.42) is restated as

$$\dot{\gamma} < \dot{\gamma}_c \quad \tau = \eta_I \dot{\gamma} \quad (2.44)$$

A further refinement to eq. (2.42) is made by accepting the fluid to deform elastically below, and undergo plastic deformation above the yield stress (Macosko, 1994), which can be expressed as

$$\tau < \tau_0 \quad \tau = G\gamma \quad (2.45)$$

$\tau_0$  denotes the critical stress after which the physical bonds between the molecules, or the colloidal particles are broken and the material yields under stress. Either one or all of the conditions expressed by eqs. (2.42)–(2.45) may be valid depending on the interactive forces and microstructure of the fluids. In the case of starch gels analyzed in Example 2.1, linear elasticity implied by eq. (2.45) is shown to be valid through different measurements.

The models with a yield stress term differ from each other in the flow behavior observed at stresses above the yield value: Bingham model predicts a linear dependence of the shear stress on the shear rate, while the Herschel–Bulkley model, a power-law relation. Casson model takes into account the gradual transformations within the microstructure of the fluid that bring about yielding and flow.

### 2.2.2.1 Bingham plastics

As originally given by Bingham (1922), plastic behavior with a constant viscosity describes the rheological behavior of the fluids for stresses above the yield value.

$$\tau \geq \tau_0 \quad \tau = (\tau_0 + \eta \dot{\gamma}) \quad (2.46)$$

To convert the Bingham equation to three-dimensional form, a scalar function of the invariants of  $\tau$  should be used instead of the yield stress. The most commonly used method (Macosko, 1994) is the von Mises criterion, which uses the second invariant of  $\tau$

$$I_{2,\tau} \geq \tau_0^2 \quad \tau = \left( \eta + \frac{\tau_0}{|I_{2,\dot{\gamma}}|^{1/2}} \right) \dot{\gamma} \quad (2.47)$$

### 2.2.2.2 Herschel–Bulkley model

In effect, Herschel–Bulkley (1926a, b) model is similar to the Bingham model, in terms of discontinuity in behavior. Unlike Bingham plastics, at stresses greater than the yield stress, Herschel–Bulkley fluids exhibit shear-thinning behavior obeying power-law

$$\tau_{ij} \geq \tau_0 \quad \tau_{ij} = \tau_0 + K \dot{\gamma}_{ij}^n \quad (2.48)$$

Defining the apparent viscosity as the ratio of shear stress to shear rate, eq. (2.48) can be written in the form

$$I_{2,\tau} \geq \tau_0^2 \quad \tau = \left( \frac{\tau_0}{|I_{2,\dot{\gamma}}|^{1/2}} + K |I_{2,\dot{\gamma}}|^{(n-1)/2} \right) \dot{\gamma} \quad (2.49)$$

for deformation in three dimensions.

### 2.2.2.3 Casson model

A model similar to the Herschel–Bulkley model but with a more gradual transformation over the discontinuity in the rheological behavior is derived by Casson (1959)

$$\tau \geq \tau_0 \quad \tau^{1/2} = \tau_0^{1/2} + \eta^{1/2} \dot{\gamma}^{1/2} \quad (2.50)$$

Eq. (2.50) can be written in three-dimensional form as

$$I_{2,\tau} \geq \tau_0^2 \quad |\boldsymbol{\tau}|^{1/2} = \left[ \left( \frac{\tau_0}{|I_{2,\dot{\gamma}}|^{1/2}} \right)^{1/2} + (K |I_{2,\dot{\gamma}}|^{(n-1)/2})^{1/2} \right] \dot{\gamma}^{1/2} \quad (2.51)$$

Papanastasiou (1987) modified the Herschel–Bulkley model with a continuous exponential equation

$$\tau = \left\{ K + \frac{\tau_0[1 - \exp(-a\dot{\gamma})]}{\dot{\gamma}} \right\} \dot{\gamma} \quad (2.52)$$

where  $a$  is a fitting parameter. The approach of the equation to the original model improves with an increase in the value of  $a$ . Papanastasiou modifications of Herschel–Bulkley and Casson equations can be expressed with eqs. (2.53) and (2.54), respectively.

$$\boldsymbol{\tau} = \left( K |I_{2,\dot{\gamma}}|^{(n-1)/2} + \frac{\tau_0[1 - \exp(-a |I_{2,\dot{\gamma}}|^{1/2})]}{|I_{2,\dot{\gamma}}|^{1/2}} \right) \dot{\gamma} \quad (2.53)$$

$$|\boldsymbol{\tau}|^{1/2} = \left( (K |I_{2,\dot{\gamma}}|^{(n-1)/2})^{1/2} + \left( \frac{\tau_0[1 - \exp(-a |I_{2,\dot{\gamma}}|^{1/2})]}{|I_{2,\dot{\gamma}}|^{1/2}} \right)^{1/2} \right) \dot{\gamma}^{1/2} \quad (2.54)$$

### 2.2.3 Models for specific end-use

Models given in Sections 2.1 and 2.2 are general, widely used equations without a specified application. There are constitutive equations specifically developed to describe the rheological behavior of industrially important fluids, also. One example is the Robertson and Stiff model developed in 1976 (Robertson and Stiff, 1976) to describe the rheology of drilling fluids in petroleum wells and cement slurries, though it can be used for other fluids as diverse as maize flour pastes (Nunez-Santiago and Santoya, 2003) and gels. Another example is the Quemada model (1978) generally used for blood flow.

#### 2.2.3.1 Robertson–Stiff model

Similar to Herschel–Bulkley (1926) and Casson (1959) models, the constitutive equation of this model takes into account the yield stress and the power-law variation of the apparent viscosity. In addition, the yield stress is also taken as a power-law function of shear rate

$$\tau^{1/n} = \left[ K^{1/n} |\dot{\gamma}|^{(n-1)/n} + \left( \frac{\tau_0}{|\dot{\gamma}|} \right)^{1/n} \right] \dot{\gamma}^{1/n} \quad (2.55)$$

Eq. (2.55) can be written in an alternative form

$$\tau \leq \tau_0 \quad \dot{\gamma} = 0 \quad (2.56a)$$

$$\tau > \tau_0 \quad \tau = K(\dot{\gamma} + \dot{\gamma}_0)^n \quad (2.56b)$$

where the yield stress is defined as

$$\tau_0 = K\dot{\gamma}_0^n \quad (2.56c)$$

Robertson–Stiff model requires an initial estimate for one of the three parameters. Gücüyener and Mehmetoğlu (1992) used the following procedure for the estimation of these parameters:  $\dot{\gamma}_0$  is estimated first with the equations (Kök and Alikaya, 2005)

$$\dot{\gamma}_0 = \frac{(\dot{\gamma}_{\min} \dot{\gamma}_{\max} - \dot{\gamma}^{*2})}{(2\dot{\gamma}^* - \dot{\gamma}_{\min} - \dot{\gamma}_{\max})} \quad (2.57a)$$

where  $\dot{\gamma}^*$  is the shear rate corresponding to the geometric mean of the maximum and minimum shear stresses

$$\tau^* = (\tau_{\min} \tau_{\max})^{1/2} \quad (2.57b)$$

Taking the logarithm of eq. (2.56b),

$$\log \tau = \log K + n \log(\dot{\gamma} + \dot{\gamma}_0) \quad (2.58)$$

and plotting it on logarithmic coordinates of  $\tau$  versus  $(\dot{\gamma} + \dot{\gamma}_0)$ , one obtains, the flow behavior index,  $n$ , from the slope and  $K$ , by calculation.

### 2.2.3.2 Quemada model

The model is specifically developed to predict the viscosity of blood based on its composition and volume fraction of hematocrit (Quemada, 1978). The constitutive equation

$$\tau = \eta_{pl} \left( 1 - \frac{1}{2} \frac{k_0 + k_\infty \sqrt{\dot{\gamma}/\dot{\gamma}_c}}{1 + \sqrt{\dot{\gamma}/\dot{\gamma}_c}} \phi_H \right)^{-2} \dot{\gamma} \quad (2.59)$$

contains three parameters,  $\dot{\gamma}_c$ ,  $k_\infty$ , and  $k_0$  which are in turn a function of the hematocrit level:  $\dot{\gamma}_c$  is the critical shear rate level for the associations ( $\dot{\gamma} \ll \dot{\gamma}_c$ ) and dispersion ( $\dot{\gamma} \gg \dot{\gamma}_c$ ) of rouleaux. Hematocrit,  $\phi_H$ , is the volume fraction of the RBCs.  $k_0$  and  $k_\infty$  are the lower and the upper limit of the constants indicating the RBC aggregation at zero-shear stress, and orientation of the dispersed RBCs at significant shear stress and shear rate levels.  $\eta_{pl}$ , the



viscosity of plasma, remains more or less constant around  $1.2 \times 10^{-3}$  Pa sec. Eq. (2.59) can be written in terms of apparent viscosity of the blood  $\eta$  as

$$\eta = \eta_{\text{pl}} \left( 1 - \frac{1}{2} \left( \frac{k_0 + k_\infty \dot{\gamma}_r^{1/2}}{1 + \dot{\gamma}_r^{1/2}} \right) \phi_H \right)^{-2} = \eta_{\text{pl}} \left( 1 - \frac{1}{2} k \phi_H \right)^{-2} \quad (2.60)$$

where  $\dot{\gamma}_r = \dot{\gamma}/\dot{\gamma}_c$  is the relative shear rate under the prevalent condition and  $k$  is a constant characterizing the conditions of the solid contents, and the flow rate of the blood.

### 2.2.4 Significance of the terms used in the constitutive equations

The models given in Sections 2.1 and 2.2 are general in that they can be applied to all kinds of non-Newtonian fluids with strong interactions between their constituents, including colloidal solutions, emulsions, foams, and suspensions. It must be emphasized here that the models are only descriptive relations that represent the effect of the combined surface forces and the concentration of the dispersed phase. One or more of these models can describe a dispersion depending only on the goodness of fit to the experimental data, i.e., the regression coefficient. A closer inspection of the models shows that they can be regrouped into two “families.” In the first group given in Table 2.2, the equations are obtained by partial simplifications. Herschel–Bulkley model is obtained from the Casson model by equating all the exponents to one except that on the shear rate term. Bingham,

**Table 2.2**

Rheological models for interactive particle suspensions

Models	Constitutive equations	General application
Casson (1959)	$\tau^{1/2} = \tau_0^{1/2} + \eta^{1/2}(\dot{\gamma})^{1/2}$	Blood, paint, chocolate, xanthan gum solutions, waxy crude oil slurries, wastewater sludge, viscoplastic slurries
Herschel–Bulkley (1926a, b)	$\tau = \tau_0 + K\dot{\gamma}^n$	Synthetic clay dispersions, sludge suspensions, drilling fluids, semisolid metals, plastic propellant, dough, mineral tailings, kaolin slurries
Power-law [Ostwald–de Waele]	$\tau = K\dot{\gamma}^n$	Colloidal suspensions such as clay, milk, gelatin, blood, starch, polymer solutions
Bingham (1922)	$\tau = \tau_0 + \eta\dot{\gamma}$	Toothpaste, paint, ash–gypsum slurries
Newtonian	$\tau = \mu\dot{\gamma}$	All fluids made up of simple molecules

**Table 2.3**

Rheological models used for concentrated particle suspensions

Models	Constitutive equations	Applications
Carreau <i>et al.</i> (1979)	$\eta = \eta_0 + \eta_\infty [1 + (\lambda \dot{\gamma})^a]^{(n-1)/a}$	Aqueous solutions of flexible elongated micelles
Cross (1965)	$\eta = \eta_\infty + (\eta_0 - \eta_\infty) / (1 + \lambda \dot{\gamma}^{1-n})$	Colloidal stable suspensions of ceramic powders and whiskers
Sisko (1958)	$\eta = \eta_\infty + K \dot{\gamma}^{n-1}$	Suspensions of synthetic clay, minerals (TiO <sub>2</sub> , laterite, silica flour), coal in water

power-law and Newton model equations can be obtained from the Herschel–Bulkley equation by further simplifications, even though their proposal as constitutive equations followed the opposite trend historically. On the same table are given examples to the application areas, though by no means they are exhaustive.

The second family of equations given in Table 2.3 has as the common characteristic, a function of a power-law term, corrected for the viscosity at high shear rates,  $\eta_\infty$ . The equations do not have a yield stress term, but have an equivalent term in terms of viscosity at zero-shear rate,  $\eta_0$ . The group of equations in Table 2.3 is generally used to describe the flow behavior of concentrated suspensions, whereas the ones given in Table 2.2 are used in suspensions stabilized with surface forces, although there are no hard and fast rules as to which model to use for a given suspension, except for the goodness of fit.

The terms generally used in these equations and their significance are summarized in Table 2.4. The rheological parameters in Table 2.4 and the surface forces that affect them will be dealt with in Chapter 3 on the flow behavior of concentrated suspensions. In this chapter, moderately concentrated suspensions stabilized with interactive forces, flowing under moderate shear rates will be taken up. The flow behavior will be explicated in terms of shear and velocity distributions in pipes, design equation for pipe-flow systems in laminar, and turbulent flow regimes for four constitutive equations in Table 2.2, e.g., Herschel–Bulkley, Bingham, power-law, and Casson models.

## 2.3 FLOW OF NON-NEWTONIAN FLUIDS THROUGH CYLINDRICAL PIPES

Many industrially important solid–liquid suspensions such as cement slurries, mineral tailings, drilling fluids, and clay suspensions are generally conveyed in cylindrical pipes. Non-Newtonian fluids falling into group 2 and 3 of the Metzner classification (1965) given in the introduction to this chapter flow under an applied shear stress (or equivalently, pressure gradient in the flow direction). Viscoelastic fluids can flow only if their viscous modulus  $G''$  is greater than their elastic modulus  $G'$ . In what follows, velocity distributions and design relations for the flow of non-Newtonian fluids in cylindrical pipes will be given. The velocity distributions of non-Newtonian fluids depend on the flow regime coupled to

**Table 2.4**

Significance of the parameters used in the constitutive equations

Term	Units	Significance	Affected by	Used in <sup>a</sup>
Yield stress, $\tau_0$	[N/m <sup>2</sup> $\equiv$ Pa]	The limiting stress below which the fluid is stagnant or else gives an elastic response and above which, deforms plastically.	Type of surface forces involved; concentration, size distribution, and aspect ratio of particles.	B, HB, Cs
Consistency, $K$	[kg/ms <sup>2-n</sup> $\equiv$ Pa·s <sup><i>n</i></sup> ]	Resistance to deformation determined by the magnitude of particle interactions remaining under applied shear.	Magnitude of the attractive forces between particles.	PL, HB, Ca, Cr, S
Flow behavior (Viscosity) index, $n$	[-]	The ease with which the microstructure can be broken down or restructured: $n < 1$ signifies shear thinning, $n > 1$ signifies shear thickening suspensions.	The shape and coordination number of the particles; the strength of interparticle bonds.	PL, HB, Cs, Ca, Cr, S
Zero-shear viscosity, $\eta_0$	[Pa·s]	Asymptotic viscosity at zero-shear rate: the maximum resistance to flow shown by the suspension just before its initial structure is broken down.	The same parameters that affect the yield stress in concentrated suspensions.	Ca, Cr
Limiting viscosity, $\eta_\infty$	[Pa·s]	Asymptotic viscosity at infinite shear rate: the limiting particle interactions which cannot be broken down by further application of shear.	Structural factors in alignment of particles.	Ca, Cr, S

<sup>a</sup>B: Bingham, HB: Herschel-Bulkley, Cs: Casson, Ca: Carreau, Cr: Cross, S: Sisko, PL: power-law.

the rheological model through the viscosity term in the Reynolds number. Information on flow parameters, which can be used in the present state until a more coherent theory is established, will be given next. The section will end with the available information on flow through fittings and sudden expansions, for a complete overview of non-Newtonian flow through cylindrical pipes.

### 2.3.1 Laminar flow of non-Newtonian fluids

Laminar regime, where the fluid flows in concentric layers of infinitesimal thickness is more commonly encountered in nonsettling solid–fluid suspensions due to high viscosities of these non-Newtonian fluids. High volumetric concentration of solids employed in practical applications and/or a high level of interaction between particles cause an increase in the apparent viscosity of the suspensions, or create a yield stress within the suspension, increasing the resistance to flow, in either case. Flow in the laminar regime becomes economically feasible, in view of the much higher costs of power and equipment required for flow in the turbulent regime. Only in the case of dilute suspensions, such as fruit juices, can turbulent flow be feasible. In the intermediate cases, working just above the critical Reynolds number for transition to turbulence becomes economically the optimum choice with rather low operating costs and relatively higher throughputs. Determination of the velocity distributions in flow through pipes is important from the standpoint of local modifications of microstructure within the flowing fluid. Velocity distributions also affect the rate of heat transfer from the walls and other processes such as mass transfer or a reaction that may be taking place within the flowing fluid.

#### 2.3.1.1 Velocity distributions in the laminar regime

Velocity distributions are obtained through differential momentum balances applied over a differential control volume of thickness  $\Delta r$  within a section of pipe of length  $L$  as given in Figure 2.2.

The general momentum balance,

$$\{\text{rate of momentum flow out of the pipe}\} - \{\text{rate of momentum flow into the pipe}\} - \{\text{sum of external forces acting on the fluid}\} = \{\text{rate of accumulation of momentum}\}$$

yields

$$\tau \cdot \mathbf{A}|_{\text{out}} - \tau \cdot \mathbf{A}|_{\text{in}} \pm \sum \mathbf{F} = \frac{d(m\mathbf{V})}{dt} \quad (2.61)$$

where,  $\tau$  is the shear stress tensor,  $\mathbf{A}$  the area vector, defined as a vector equal in magnitude to the peripheral area, directed normally outwards,  $\mathbf{V}$ , the average velocity vector in the pipe,  $m$ , the mass of the fluid, and  $t$ , the time. The force vector  $\mathbf{F}$  represents the external forces acting on the system. Eq. (2.61) written in scalar form for steady-state flow in pipes under the action of combined gravity and pressure forces becomes

$$2\pi r L \tau_{rz}|_{r+\Delta r} - 2\pi r L \tau_{rz}|_r + (2\pi r \Delta r \Delta P) + (2\pi r L \Delta r \rho g) = 0 \quad (2.62)$$

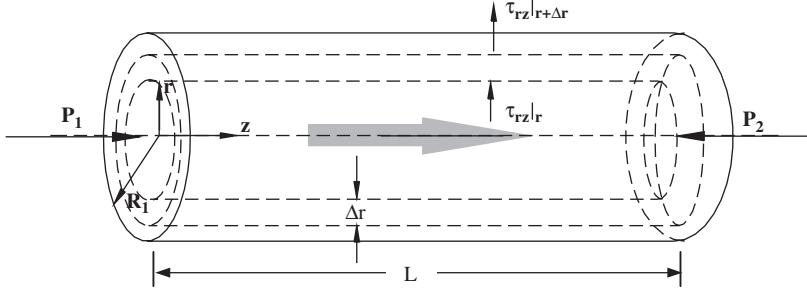


**Figure 2.2** Differential control volume for the application of a momentum balance within a pipe.

Division by the control volume and taking the limit as  $\Delta r$  approaches zero gives,

$$\frac{d(r\tau_{rz})}{rdr} = \frac{\Delta P}{L} + \rho g = \Phi \quad (2.63)$$

The same equation could have been obtained from Navier-Stokes equation in Table A3.2 in Appendix A by taking the pertinent terms.

Since the RHS of the equation is not affected by the shear stress distribution, it is denoted by a constant such as  $\Phi$ . Integration and division by  $r$  yields

$$\tau_{rz} = \frac{\Phi r}{2} + \frac{C_1}{r} \quad (2.64)$$

The value of  $C_1$  can be found and the shear stress distribution can be evaluated if a boundary condition in terms of stress exists in the system.

For cylindrical channels, maximum velocity is encountered at the center of the pipe, at  $r = 0$ , where the shear rate ( $\dot{\gamma} \equiv dV/dr$ ) is zero since the first derivative of maximum velocity is zero,

$$\tau = -\mu \frac{dV}{dr} = 0 \quad (2.65)$$

shear stress is zero at the center of the pipe. Since  $C_1$  becomes zero in eq. (2.64), a linear distribution is obtained for shear stress

$$\tau_{rz} = \frac{\Phi r}{2} = \left[ \frac{\Delta P}{L} + \rho g \right] \frac{r}{2} \quad (2.66)$$

The shear stress distribution by reference to wall conditions is obtained by taking the ratio of eq. (2.66) to the shear stress at the wall ( $r = R$ ,  $\tau = \tau_w$ )

$$\frac{r}{R} = \frac{\tau}{\tau_w} \quad (2.67)$$

This equation is valid for all types of flow, independent of the rheological model with which the fluid flow is described. The velocity distribution, however, is determined by the constitutive equation of the fluid. The velocity distribution of Herschel–Bulkley fluids will be derived below as an example.

The constitutive equation for Herschel–Bulkley fluids, eq. (2.48) is substituted in eq. (2.66) to find a relation between the velocity gradient (shear rate) and the shear stress

$$\tau = \frac{\Phi r}{2} = \tau_0 + K \left( -\frac{dV}{dr} \right)^n \quad (2.68)$$

Integrating eq. (2.68), after some rearrangement, the equation is solved for  $V$ .

$$V = -\left( \frac{1}{K} \right)^{1/n} \frac{2n}{(n+1)\Phi} \left( \frac{\Phi}{2} r - \tau_0 \right)^{(1+n)/n} + C_1 \quad (2.69)$$

Applying the boundary condition,  $V = 0$  at  $r = R$  to evaluate  $C_1$ , the velocity distribution is found as

$$V = \left( \frac{1}{K} \right)^{1/n} \frac{2n}{(n+1)\Phi} \left[ \left( \frac{\Phi}{2} R - \tau_0 \right)^{(1+n)/n} - \left( \frac{\Phi}{2} r - \tau_0 \right)^{(1+n)/n} \right] \quad (2.70)$$

If the yield stress is not exceeded at the center of the pipe, the region  $0 < r < r_p$  will flow at constant velocity,  $V = V_p$ , where  $r_p$  and  $V_p$  are the radius and the velocity of the plug zone, respectively. Velocity distribution of Herschel–Bulkley fluids in the sheared region between the radii of plug zone  $r_p$  and the wall,  $R$ ,  $r_p \leq r \leq R$  can also be written as a function of the wall shear stress,  $\tau_w$

$$V = \left( \frac{1}{K} \right)^{1/n} R \frac{n}{(n+1)} \frac{1}{\tau_w} \left[ (\tau_w - \tau_0)^{(1+n)/n} - \left( \frac{\tau_w}{R} r - \tau_0 \right)^{(1+n)/n} \right] \quad (2.71)$$

where

$$\tau_w = \frac{(\Delta P + \rho g L) R}{2L}$$

The velocity gradient within the plug zone will be zero and the boundaries of the plug zone can be defined by solving eq. (2.72) for  $r_p$

$$\left. \frac{dV}{dr} \right|_{r=r_p} = -\left( \frac{1}{K} \right)^{1/n} \left( \frac{\tau_w}{R} r_p - \tau_0 \right)^{1/n} = 0 \quad (2.72)$$

$$r_p = \frac{R \tau_0}{\tau_w} \quad (2.73)$$

Replacing  $r$  with  $r_p$  in eq. (2.71) gives the velocity of the plug region

$$V_p = \left(\frac{1}{K}\right)^{1/n} R \frac{1}{\tau_w} \frac{n}{n+1} (\tau_w - \tau_0)^{(n+1)/n} \quad (2.74)$$

Mean velocity for Herschel–Bulkley fluids is obtained by integrating the local velocities in the plug zone (eq. (2.74)) and the annular region along the walls of the pipe (eq. (2.71)) over the cross-sectional area

$$V_{av} = \frac{\int_A V dA}{\int_A dA} = \frac{\int_0^{r_p} V_p 2\pi r dr + \int_{r_p}^R V 2\pi r dr}{\int_0^R 2\pi r dr} \quad (2.75)$$

The indicated integrations in eq. (2.75) give the average velocity of Herschel–Bulkley fluids in flow through a pipe

$$V_{av} = \left(\frac{1}{K}\right)^{1/n} R \frac{1}{\tau_w^3} (\tau_w - \tau_0)^{(n+1)/n} \left[ \frac{n\tau_w^2}{(n+1)} - \frac{2n^2\tau_0(\tau_w - \tau_0)}{(n+1)(2n+1)} - \frac{2n^2(\tau_w - \tau_0)^2}{(n+1)(3n+1)} \right] \quad (2.76)$$

Similar derivations are made for non-Newtonian fluids conforming to the constitutive equations given in Table 2.2 and the results are summarized in Tables 2.5–2.8. In plastic fluids with a yield stress, the radial extent of the plug zone is solely determined by the ratio of yield stress to the applied pressure gradient,  $r_p = (\tau_0 R)/\tau_w = (2\tau_0)/(\Delta P + \rho g L/L)$ , increasing with an increase in the yield stress.

For very low values of the flow behavior index  $n$ , power-law fluids exhibit a velocity profile similar in shape to a plug: As  $n$  decreases, maximum velocity approaches the

**Table 2.5**

Velocity relations in fluids conforming to the Herschel–Bulkley model

Constitutive equation	$\tau_{ij} = \tau_0 + K \dot{\gamma}_{ij}^n$	(2.48)
-----------------------	--	--------

Velocity distribution	$V = \left(\frac{1}{K}\right)^{1/n} \frac{R}{\tau_w} \frac{n}{n+1} \left[ (\tau_w - \tau_0)^{(1+n)/n} - \left(\frac{\tau_w}{R} r - \tau_0\right)^{(1+n)/n} \right]; \quad r_p \leq r \leq R$	(2.71)
-----------------------	--	--------

	$V_p = \left(\frac{1}{K}\right)^{1/n} \frac{R}{\tau_w} \frac{n}{n+1} (\tau_w - \tau_0)^{(n+1)/n}; \quad r \leq r_p$	(2.74)
--	---	--------

Average velocity	$V_{av} = \left(\frac{1}{K}\right)^{1/n} \frac{R}{\tau_w^3} (\tau_w - \tau_0)^{(n+1)/n} \left[ \frac{n\tau_w^2}{(n+1)} - \frac{2n^2\tau_0(\tau_w - \tau_0)}{(n+1)(2n+1)} - \frac{2n^2(\tau_w - \tau_0)^2}{(n+1)(3n+1)} \right]$	(2.76)
------------------	---	--------

**Table 2.6**

Velocity relations in fluids conforming to the Casson model

Constitutive equation	$\tau_{ij}^{1/2} = \tau_0^{1/2} + \eta^{1/2} \dot{\gamma}_{ij}^{1/2}$	(2.50)
-----------------------	---	--------

	$V = \frac{R\tau_w}{4\eta} \left[ \frac{16}{3} \left( \frac{\tau_0}{\tau_w} \right)^{1/2} \left( \left( \frac{r}{R} \right)^{3/2} - 1 \right) + 4 \left( \frac{\tau_0}{\tau_w} \right) \left( 1 - \frac{r}{R} \right) + 2 \left( 1 - \left( \frac{r}{R} \right)^2 \right) \right]$	(2.77)
--	--	--------

Velocity distribution	$r_p \leq r < R$	
	$V = \frac{R\tau_w}{4\eta} \left[ 2 - \frac{2}{3} \left( \frac{\tau_0}{\tau_w} \right)^2 - \frac{16}{3} \left( \frac{\tau_0}{\tau_w} \right)^{1/2} + 4 \left( \frac{\tau_0}{\tau_w} \right) \right]$	(2.78)

	$r \leq r_p$	
Average velocity	$V_{av} = \frac{R\tau_w}{4\eta} \left[ 1 - \frac{16}{7} \left( \frac{\tau_0}{\tau_w} \right)^{1/2} + \frac{4}{3} \left( \frac{\tau_0}{\tau_w} \right) - \frac{1}{21} \left( \frac{\tau_0}{\tau_w} \right)^4 \right]$	(2.79)

**Table 2.7**

Velocity relations in fluids conforming to the Bingham model

Constitutive equation	$\tau_{ij} = (\tau_0 + \eta \dot{\gamma}_{ij})$	(2.46)
-----------------------	---	--------

Velocity distribution	$V = \frac{1}{\eta} \left[ R \left( \frac{\tau_w}{2} - \tau_0 \right) - r \left( \frac{\tau_w r}{2R} - \tau_0 \right) \right] \quad r_p \leq r \leq R$	(2.80)
-----------------------	--	--------

	$V_p = \frac{R}{\eta} \left[ \frac{\tau_0^2}{2\tau_w} + \frac{\tau_w}{2} - \tau_0 \right]; \quad r \leq r_p$	(2.81)
--	--	--------

Average velocity	$V_{av} = \frac{R\tau_0^4}{12\eta\tau_w^3} + \frac{R\tau_w}{4\eta} - \frac{R\tau_0}{3\eta}$	(2.82)
------------------	---	--------

**Table 2.8**

Velocity relations in fluids conforming to the power-law model

Constitutive equation	$\tau_{ij} = K \dot{\gamma}_{ij}^n$	(2.33)
-----------------------	-------------------------------------	--------

Velocity distribution	$V = \left( \frac{\tau_w}{KR} \right)^{1/n} \left( \frac{n}{n+1} \right) R^{(n+1)/n} - r^{(n+1)/n} \quad 0 < r < R$	(2.83)
-----------------------	---	--------

	$V_{\max} = \left( \frac{\tau_w}{KR} \right)^{1/n} \left( \frac{n}{n+1} \right) R^{(n+1)/n}$	(2.84)
--	--	--------

Average velocity	$V_{av} = \left( \frac{\tau_w}{K} \right)^{1/n} R \left( \frac{n}{3n+1} \right)$	(2.85)
------------------	--	--------



average velocity,  $V_{\max}/V_{\text{av}} = (3n + 1)/(n + 1)$ . This is the case generally observed during structure evolution in a suspension or gel. Eventually, when the structure is formed,  $n$  approaches zero, deformation is prevented by the bonds formed between the constituents, and the gel acts as a viscoelastic material.

### 2.3.1.1.1 Laminar flow of viscoelastic fluids

Presence of normal stresses identifies viscoelastic fluids from other viscous, time-independent non-Newtonian fluids. Because of the complexity of their behavior, shell balances are not adequate to set up the momentum balance equations and Navier-Stokes equations become the convenient starting point. Navier-Stokes equations in Table A3.2 in Appendix A3 are used in viscoelastic fluids to give eq. (2.63), since the normal stresses cancel out in the simple, unidirectional, fully developed flow of viscoelastic fluids in laminar regime. The relation between the normal and shear stresses are then accounted for by the constitutive equations. Two widely used physical models form the basis of the constitutive equations of viscoelastic fluids: *Finitely-Extensible-Nonlinear-Elastic dumbbell (FENE-P) model with Peterlin approximation* (Bird *et al.*, 1980) and the network model of *Phan-Thien and Tanner* (1977), the (PTT) model.

The FENE-P model is based on the random motion of single polymer molecules, without any interactions with other polymer or solvent molecules in a dilute solution. Thus, the molecules move under Brownian motion (whence the  $k_B T$  thermal energy term appears in the model) among other polymer molecules taken into account by a distribution function. The general constitutive equation for the FENE-P model is given as,

$$Z(\text{tr } \boldsymbol{\tau})\boldsymbol{\tau} + \lambda \frac{\nabla}{\text{Dt}} \boldsymbol{\tau} - \lambda \left\{ \boldsymbol{\tau} - \frac{b}{b+2} nk_B T \mathbf{I} \right\} \frac{D \ln Z}{Dt} = \frac{b}{b+2} nk_B T \mathbf{I} (\Delta \mathbf{V} + (\nabla \mathbf{V})^T) \quad (2.86)$$

with the stress coefficient function  $Z(\text{tr } \boldsymbol{\tau})$  defined as,

$$Z = 1 + \frac{3}{b} \left( \frac{b}{b+2} \right) + \frac{\text{tr } \boldsymbol{\tau}}{3nk_B T} \quad (2.86a)$$

Phan-Thien and Tanner (PTT) model considers the microstructure as a network of polymers with temporary and reversible junction points, or cross-links. The model applies to concentrated polymer solutions, and can be extended to suspensions with similar microstructures. The constitutive equation of the PTT model is

$$Y(\text{tr } \boldsymbol{\tau}, T)\boldsymbol{\tau} + \lambda \left\{ \frac{\nabla}{\text{Dt}} \boldsymbol{\tau} + (\xi + \xi \boldsymbol{\tau}) \left[ \frac{1}{2} (\Delta \mathbf{V} + (\nabla \mathbf{V})^T) \right] \right\} = 2\eta \left[ \frac{1}{2} (\Delta \mathbf{V} + (\nabla \mathbf{V})^T) \right] \quad (2.87)$$

with the stress coefficient function defined as

$$Y(\text{tr } \boldsymbol{\tau}, T) = \varphi(T) f(\text{tr } \boldsymbol{\tau}) = \varphi(T) \exp \left( \frac{\varepsilon \lambda}{\eta} \text{tr } \boldsymbol{\tau} \right) \quad (2.87a)$$

$\text{tr } \boldsymbol{\tau}$  in this equation is the trace of the stress tensor ( $\text{tr } \boldsymbol{\tau} = \tau_{ii} = \tau_{zz} + \tau_{rr}$  for simple viscometric flows). In these equations,  $\boldsymbol{\tau}$  is the extra stress tensor,  $\lambda$ , the relaxation time,  $n$ , the number density of dumbbells,  $b$ , the parameter of the FENE-P model,  $T$ , the absolute temperature,  $k_B$ , the Boltzmann constant,  $\eta$  is the constant viscosity coefficient of polymer,  $\xi$  is a parameter that accounts for the slip between the molecular network and the continuum medium,  $\overset{\vee}{\boldsymbol{\tau}}$  is the Oldroyd's upper convective derivative,  $(\overset{\vee}{\boldsymbol{\tau}} + (DV/Dt) - \boldsymbol{\tau}\nabla\nabla - \boldsymbol{\tau}(\nabla\nabla)^T)$  and  $\varepsilon$  is the parameter limiting the extensional viscosity related with the stretching of the network.

The stress coefficient function  $Y(\text{tr } \boldsymbol{\tau}, T)$  has an exponential form (Phan-Thien, 1978) to take into account the large extensions in the network as may take place in converging channels. A linearized form of eq.(2.87a) can be used in flow through pipes, channels and in couette flows where only small extensions and molecular deformations take place (Tanner and Huilgol, 1975). Hence the linearized form of stress coefficient function (Phan-Thien and Tanner, 1977) at isothermal conditions ( $\varphi(T) = 1$ ) becomes

$$Y(\text{tr } \boldsymbol{\tau}) = f(\text{tr } \boldsymbol{\tau}) = 1 + \left( \frac{\varepsilon\lambda}{\eta} \right) \text{tr } \boldsymbol{\tau} \quad (2.88)$$

Eq. (2.87) reduces to a set of three equations for the normal stresses in the direction of flow and momentum transfer and the shear stress,

$$f(\tau_{ii})\boldsymbol{\tau}_{zz} = \lambda(2 - \xi) \left( \frac{dV_z}{dr} \right) \boldsymbol{\tau}_{rz}, \quad (2.88a)$$

$$f(\tau_{ii})\boldsymbol{\tau}_{rr} = -\lambda\xi \left( \frac{dV_z}{dr} \right) \boldsymbol{\tau}_{rz} \quad (2.88b)$$

$$f(\tau_{ii})\boldsymbol{\tau}_{rz} = \eta \left( \frac{dV_z}{dr} \right) - \lambda \left( 1 - \frac{\xi}{2} \right) \left( \frac{dV_z}{dr} \right) \boldsymbol{\tau}_{rr} - \frac{\lambda\xi}{2} \boldsymbol{\tau}_{zz} \quad (2.88c)$$

A simplified version of PTT model known as *simplified Phan-Thien and Tanner (SPTT)* model neglects the slip between the solvent and solute molecules by taking  $\xi = 0$ , so the normal stress equation in the radial direction vanishes and

$$f(\tau_{zz})\boldsymbol{\tau}_{zz} = 2\lambda \left( \frac{dV_z}{dr} \right) \boldsymbol{\tau}_{rz}, \quad (2.89)$$

$$f(\tau_{zz})\boldsymbol{\tau}_{rz} = \eta \left( \frac{dV_z}{dr} \right) \quad (2.90)$$

Equations of velocity distribution and average velocity for a fluid flowing through the pipe are derived based on the PTT model, widely used for concentrated suspensions, under

no slip conditions at the wall of the pipe (Oliveira and Pinho, 1999). The derivation starts with eq.(2.63), eq. (2.88) and eq.(2.87) with the simplifications encompassed in eqs.(2.89) and (2.90), to give

$$V = \frac{\Phi R^2}{4\eta} \left( 1 - \left( \frac{r}{R} \right)^2 \right) \left[ 1 + \frac{\varepsilon \lambda^2 \Phi R^2}{4\eta^2} \left( 1 + \left( \frac{r}{R} \right)^2 \right) \right] \quad (2.91)$$

$$V_{av} = \frac{\Phi R^2}{8\eta} \left[ 1 + \frac{\varepsilon \lambda^2 \Phi R^2}{3\eta^2} \right] \quad (2.92)$$

The parameter  $\Phi$  is the general pressure driving force. If the parameter limiting the elongational viscosity  $\varepsilon$  is equal to zero as in the case of non-viscoelastic fluids, eq.( 2.91) becomes similar to eq. (2.83) with  $n = 1$ . The parameter  $\varepsilon$  serves as a scale for the resistance of the molecules (and microstructure in general) toward stretching under the effect of shear and elongation. The velocity gradients are reduced and velocity profiles flatten and with increasing  $\varepsilon$  due to high viscoelastic nature of the fluid.

The effect of the viscosity contribution of the solvent can be taken into account in both PTT and FENE-P by adding relevant shear stress terms into the general Navier-Stokes equations ( Cruz *et al.*, 2005)

$$\rho \frac{D\mathbf{V}}{Dt} = -\nabla p + \nabla \cdot \boldsymbol{\tau} + \rho \mathbf{g} + \nabla \cdot \boldsymbol{\tau}_s = -\nabla p + \nabla \cdot \boldsymbol{\tau} + \rho \mathbf{g} + \mu_0 \nabla \cdot \nabla \mathbf{V} \quad (2.93)$$

Then, the axial (z) momentum equation (eq.(2.94)) is used as the starting equation, instead of eq. (2.63), to determine the velocity distribution of viscoelastic fluids in flow through pipes:

$$\frac{1}{r} \frac{\partial}{\partial r} (r \tau_{rz}) + \frac{\mu_0}{r} \frac{\partial}{\partial r} \left( r \frac{\partial V_z}{\partial r} \right) = -\frac{\partial p}{\partial z} + \rho g_z = \Phi \quad (2.94)$$

where  $\mu_0$  is the viscosity of the solvent.

### Example 2.2: Velocity distributions during flow of non-Newtonian fluids

*The case:* The velocity distribution during the flow of synthetic hectorite clay (laponite) suspensions in 4 inch pipes is to be evaluated. To illustrate the effect of model parameters on the velocity distributions for different rheological models, the equation of the fitted curve to the data of synthetic hectorite clay (laponite) suspensions obtained in controlled stress and controlled strain rate rheometers (Escudier *et al.*, 1996) will be used as a basis

$$\tau = 4.4 + 0.24 \dot{\gamma}^{0.535} \quad (2.95)$$

*Analysis of the case:* The constitutive equations used in these illustrations (Figures 2.3–2.6) are based on this equation with the values of the parameters standardized

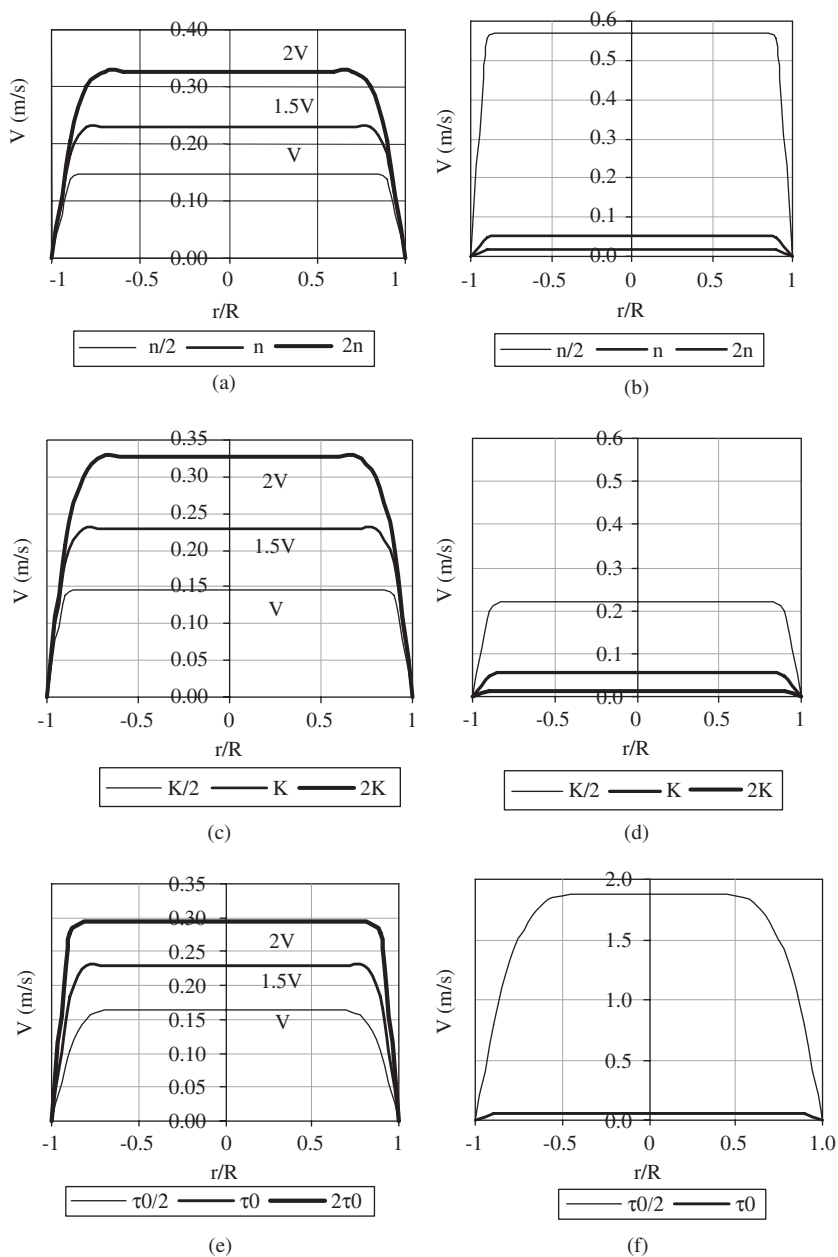


**Figure 2.3** Velocity distributions of Herschel–Bulkley Fluids: (a) effect of  $n$  at constant  $Q$ , (b) effect of  $n$  at constant  $\tau_w$ , (c) effect of  $K$  at constant  $Q$ , (d) effect of  $K$  at constant  $\tau_w$ , (e) effect of  $\tau_0$  at constant  $Q$ , (f) effect of  $\tau_0$  at constant  $\tau_w$ .

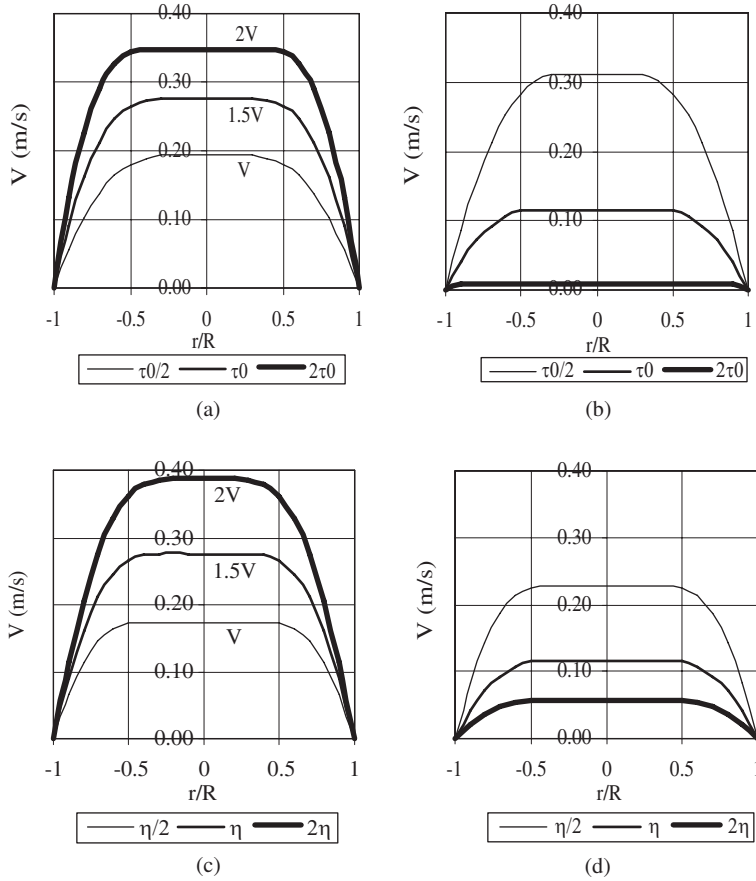


**Figure 2.4** Velocity distributions of Casson fluids: (a) effect of  $\tau_0$  at constant  $Q$ , (b) effect of  $\tau_0$  at constant  $\tau_w$ , (c) effect of  $\eta$  at constant  $Q$ , (d) effect of  $\eta$  at constant  $\tau_w$ .

as  $\tau_0 = 4.5 \text{ Pa}$ ,  $n = 0.5$  and  $K = 0.24 \text{ Pa sec}^{0.5}$ . Half and twice of these values are evaluated also, to show the effect of a change in the parameters.

The velocity distributions are evaluated both at constant  $Q$  and at constant pressure gradient  $dP/dz$ . To make the comparison on the same basis, the flow rate  $Q$  and pressure gradient (or equivalently,  $\tau_w$ ) are adjusted in these plots to maintain laminar regime. The velocity profiles nearly coincide at constant flow rate. For better visibility of the shape of the profiles, the velocity values in the overlapping distributions are multiplied by a constant factor of (1.5–2), to obtain separate curves.

For a given pressure difference ( $\Delta P$ ), equivalent to a constant wall shear stress,  $\tau_w$  and flow rate  $Q$ , the velocity distribution of Herschel–Bulkley fluids is a function of three parameters,  $K$ ,  $n$ , and  $\tau_0$ . The limits of the plug flow region at the center are only a function

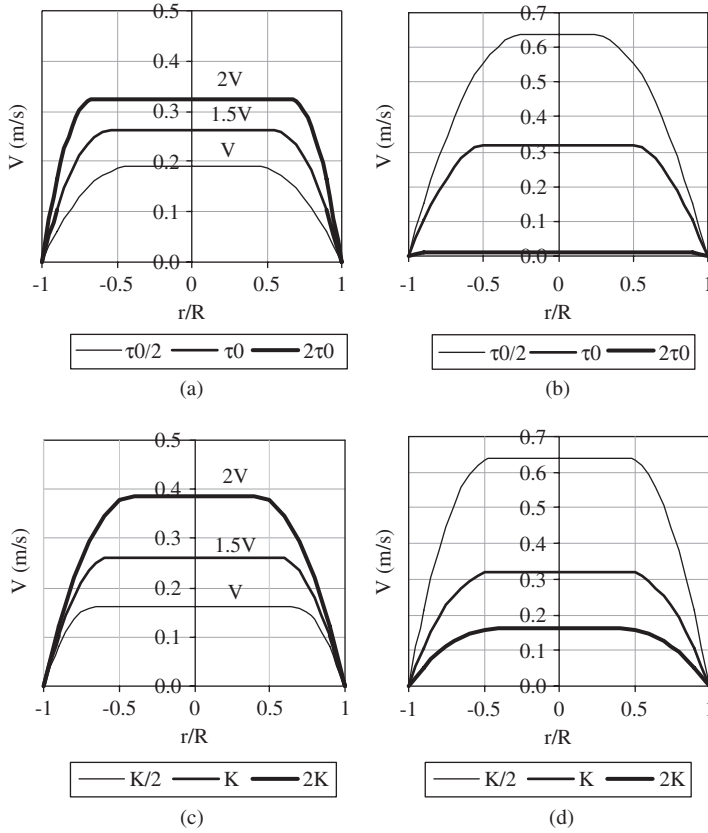


**Figure 2.5** Velocity distributions of Bingham fluids; (a) effect of  $\tau_0$  at constant  $Q$ , (b) effect of  $\tau_0$  at constant  $\tau_w$ , (c) effect of  $K$  at constant  $Q$ , (d) effect of  $K$  at constant  $\tau_w$ .

of the yield stress,  $\tau_0$  according to eq. (2.73). In other words, changing the yield stress will affect both the magnitude of the core velocity (dependent on  $n$ ) and the range of the plug flow region. Consistency  $K$ , will inversely affect the core velocity given by eq. (2.74). Viscosity index,  $n$  will affect both the core velocity and the annular velocity distribution in a complex manner, both directly and through an exponential relation with consistency and yield stress.

The effects of the parameters on the average velocity are demonstrated in Figure 2.7 for a hypothetical suspension in the ranges given in Table 2.9. Other than  $n = 1$  and  $K = \mu$  for Bingham and  $n = 0.5$  for Casson models, values of the constants are the same in each case. An increase in the values of  $K$  and  $\tau_0$  reduces the average velocity, as expected. The effect of  $n$  is negligible at these high values of  $K$  or  $\tau_0$ . However, average velocity increases synergistically when a decrease in the yield stress or consistency is coupled with a decrease in the viscosity index  $n$ .

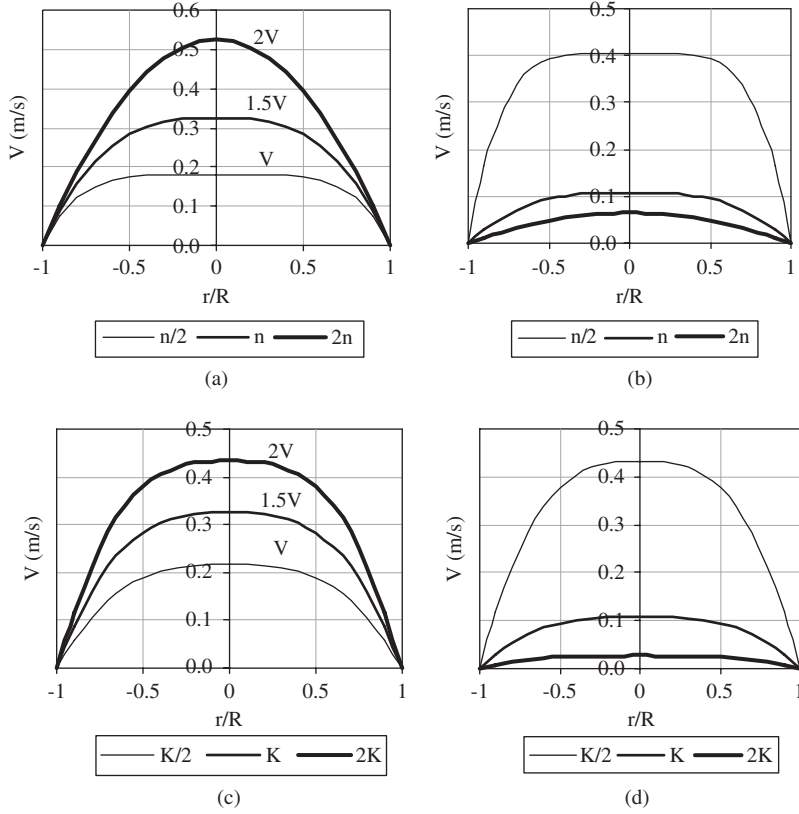


**Figure 2.6** Velocity distributions of power-law fluids: (a) effect of  $n$  at constant  $Q$ , (b) effect of  $n$  at constant  $\tau_w$ , (c) effect of  $K$  at constant  $Q$ , (d) effect of  $K$  at constant  $\tau_w$ .

A general evaluation of Figures 2.3–2.6 shows that a core region in plug flow is observed in fluids exhibiting a yield stress, and in the case of very low value of flow behavior index  $n$ , even in the absence of a yield stress. The width of this core region increases with an increase in the yield stress  $\tau_0$  and a decrease in the flow behavior index,  $n$ . Peixinho *et al.* (2005) quantified this observation by relating the radius of the plug zone to the radius of the pipe through *Herschel–Bulkley number* ( $Hb = \tau_0/K(V/R)^n$ ) and flow behavior index,  $n$ , by solving the mechanical energy and total mass balance equations for Herschel–Bulkley fluids in laminar flow. As  $Hb \rightarrow 0$ , Herschel–Bulkley fluids approach power law behavior and the relative size of the plug zone is given by

$$\frac{r_p}{R} \approx \left( \frac{n}{3+n} \right)^n Hb - \frac{1}{2n+1} \left( \frac{n}{3+n} \right)^{2n-1} Hb^2 \quad (2.96a)$$

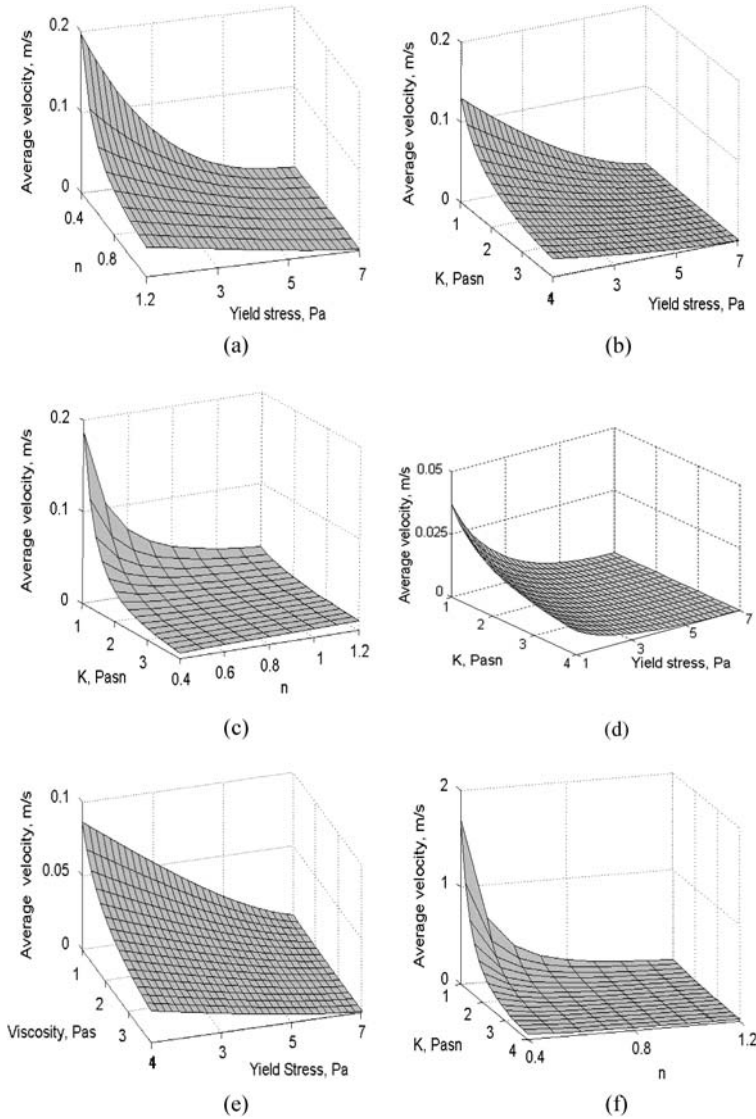


**Figure 2.7** Effect of parameters  $K$ ,  $n$ , and  $\tau_0$  on the average velocity of the (a–c) Herschel–Bulkley fluids, (d) Casson fluids, (e) Bingham fluids, (f) power-law fluids.

As  $Hb \rightarrow \infty$ , that is for very high yield stresses the relative size of the plug zone is given by

$$\frac{r_p}{R} \approx 1 - \left( \frac{n+1}{n} \right)^{n/(n+1)} \left( \frac{1}{Hb} \right)^{1/(n+1)} + \frac{2n^2}{(2n+1)(n+1)} \left( \frac{n+1}{n} \right)^{2n/(n+1)} \left( \frac{1}{Hb} \right)^{2/(n+1)} \quad (2.96b)$$



**Table 2.9**

The range of the parameters used in Figure 2.7

$\tau_0$ – $K$ relation		$n$ – $K$ relation		$n$ – $\tau_0$ relation	
Variables	Constants	Variables	Constants	Variables	Constants
$\tau_0 = 1\text{--}7\text{ Pa}$	$\tau_w = 8\text{ Pa}$	$n = 0.4\text{--}1.2$	$\tau_w = 8\text{ Pa}$	$\tau_0 = 1\text{--}7\text{ Pa}$	$\tau_w = 8\text{ Pa}$
$K = 1\text{--}4\text{ Pa}\cdot\text{s}^n$	$n = 0.8$	$K = 1\text{--}4\text{ Pa}\cdot\text{s}^n$	$\tau_0 = 4\text{ Pa}$	$n = 0.4\text{--}1.2$	$K = 2\text{ Pa}\cdot\text{s}^n$

Peixinho *et al.* (2005) experimentally verified that the maximum velocity, i.e., the core velocity, increased as the diameter of the plug region of the Herschel–Bulkley fluid decreased with an increase in the Reynolds number.

Huilgol and You (2005), applying the augmented Lagrangian method based on the concept of variational inequalities to the steady flow of Bingham, Casson, and Herschel–Bulkley fluids found that

$$\frac{r_p}{R} = 2Od \quad (2.97)$$

applies, regardless of the constitutive equation of the yield-viscoplastic fluid.  $Od$ , the *Oldroyd number* is defined as the ratio of the yield stress to the effective shear rate expressed in terms of the pressure gradient

$$Od = \frac{\tau_0}{|\Delta P/L| R} \quad (2.98)$$

Increase in the yield stress, causes a decrease in the average velocity. The value of the critical Oldroyd number,  $Od_c$ , where the fluid ceases to flow is calculated analytically by Mosolov and Miasnikov (1965) for Bingham fluids as,  $Od_c = 0.5$ .

This analytical result is confirmed by model studies as  $Od_c = 0.498$  for Bingham fluids by Moyers-Gonzales and Frigaard (2004). Basing on their model calculations, Huilgol and You (2005) give the estimates for the  $Od_c$  as 0.499 for Bingham fluids, 0.478 for Casson fluids, 0.495 and 0.483 for Herschel–Bulkley fluids with flow behavior index of 0.75 and 0.5, respectively. In general, the greater the nonlinearity, the lower is the  $Od_c$ .

The effect of flow parameters on the system curves in the design of piping systems in laminar flow is given in Section 2.3.1.2.

### 2.3.1.2 Design equations for flow of non-Newtonian fluids through pipes

Design of piping systems is based on knowledge of head (pressure) requirement, including frictional losses and potential energy, for a given transfer duty. The *system curve* is a plot of the mechanical energy balance on the piping system, drawn as the pressure requirement per unit length,  $\Delta P/L$ , as a function of flow rate,  $Q$ . This information is necessary for the selection of the pump that maintains the flow. Such a relation depends only on the flow

regime in Newtonian fluids where it is given by Hagen–Poiseuille equation in the laminar regime

$$\Delta P = \frac{8L\eta V_{av}}{R^2} = \frac{128\eta L}{\pi D^4} Q \quad (2.99)$$

In non-Newtonian fluids, the system curve depends not only on the flow regime, but also on the constitutive equation of the rheological model of the fluid. Since the constitutive equations are given as a relation between the shear stress and shear rate,  $\Delta P$ – $Q$  data should be converted into  $\tau$  –  $\dot{\gamma}$  form. Variation of shear stress with radius in flow through pipes is given with eq. (2.67). Since the maximum shear stress is exerted at the walls, it is also the region where the maximum effect of non-Newtonian behavior is observed. Consequently, the shear rate, or the velocity gradient should be evaluated at the wall region and related with the flow rate,  $Q$ .

Pressure is related to the shear stress at the wall,  $\tau_w$ , through a force balance and is independent of the flow regime and the rheological model (constitutive equation) of the fluid

$$\Delta P \left( \frac{\pi D^2}{4} \right) = \tau_w (\pi D L) \quad (2.100)$$

$$\tau_w = \frac{\Delta P D}{4L} \quad (2.101)$$

On the contrary, shear rate, or velocity gradient, at the wall depends both on the flow regime and on the rheological model through the relevant velocity distribution, which is to be derived next (Holland and Bragg, 1995).

#### 2.3.1.2.1 Relation between flow and rheological parameters

The velocity gradient at the wall is found by taking the derivative of the velocity distribution in laminar flow for Newtonian fluids. The velocity distribution for the general case of pressure and gravity acting simultaneously in the  $z$ -direction is given with the equation

$$V_z = \frac{\Delta P + \rho g L}{4\eta L} (R^2 - r^2) \quad (2.102)$$

and the maximum velocity at the center of the pipe at  $r = 0$ , with

$$V_{\max} = \frac{\Delta P + \rho g L}{4\eta L} R^2 \quad (2.103)$$

The local velocity  $V_z$  in terms of the maximum velocity at the center can be written as

$$V_z = V_{\max} \left( \frac{1 - r^2}{R^2} \right) \quad (2.104)$$

Since the average velocity is equal to one-half of the maximum velocity in the laminar regime of Newtonian fluids

$$V = \frac{\Delta P + \rho g L}{8\eta L} R^2 \quad (2.105)$$

the local velocity in terms of the average velocity is

$$V_z = 2V \left( \frac{1-r^2}{R^2} \right) \quad (2.106)$$

This equation is the starting point for the relation between the flow rate and the shear rate at the wall. *In these equations and for the rest of this section,  $V$  stands for  $V_{av}$ , the subscript showing the direction of flow, only.* The velocity gradient at  $r = R$

$$\left. \frac{dV_z}{dr} \right|_{r=R} = -\frac{4V}{R} \quad (2.107)$$

gives the flow characteristic for Newtonian fluids

$$\dot{\gamma}_{wN} = \frac{-8V}{D} \quad (2.108)$$

or, in terms of volumetric flow rate,  $Q$ , through the pipe

$$\dot{\gamma}_{wN} = \frac{-32Q}{\pi D^3} = \frac{-4Q}{\pi R^3} \quad (2.109)$$

*Flow characteristic* gives the relation between the shear rate (or velocity gradient) at the wall and the volumetric flow rate (or the average velocity). Flow characteristic for non-Newtonian fluids is obtained by multiplying the flow characteristic for Newtonian fluids with a correction factor. The relation used to obtain the correction factor is known as the Rabinowitsch–Mooney (Rabinowitsch, 1929; Mooney, 1931) equation.

The flow characteristic for Newtonian fluids does not contain any term that can be related to the rheology of non-Newtonian fluids. Therefore, an expression is required which contains a term that can be related with the constitutive equations. This could be the continuity equation written in differential form

$$\delta Q = 2V_z \pi r \delta r \quad (2.110)$$

from which, the volumetric flow rate can be found by integration.

$$Q = 2\pi \int_0^R V_z r dr \quad (2.111)$$

In Newtonian fluids the relation between  $r$  and  $V$  depends on the flow regime, whereas, that of non-Newtonian fluids depends in addition on the rheological model that best describes the physical behavior of the system. To obtain a general equation that covers all the models, eq. (2.111) is solved through integration by parts, taking  $u = V_z$  and  $v = r^2/2$ . Under the no-slip boundary conditions of  $r = 0$ ,  $V = V_{\max}$ , and  $r = R$ ,  $V = 0$ , the first term of the integral vanishes and the second term becomes

$$Q = 2\pi \int_0^R V_z r dr = 2\pi \int_0^R \frac{r^2}{2} \left( -\frac{dV_z}{dr} \right) dr \quad (2.112)$$

In flow through pipes, velocity decreases to zero as the radius increases from zero to  $R$ , at the wall. The negative sign before the velocity gradient accounts for the inherent negative value of the gradient.

The velocity gradient at the wall depends on the velocity distribution, and the applied shear stress for a given model of non-Newtonian behavior. Therefore, the relation between the velocity gradient and the radius cannot be predicted *a priori*. Since the constitutive equations of the rheological models (as in Table 2.2) are given as a relation between shear stress and shear rate, eq. (2.112) should now be written in terms of shear stress,  $\tau$ , using eq. (2.67).

$$Q = \frac{\pi R^3}{\tau_w^3} \int_0^{\tau_w} \tau^2 (-\dot{\gamma}) d\tau \quad (2.113)$$

An expression for the flow characteristic of non-Newtonian fluids can now be found by replacing eq. (2.113) into eq. (2.109)

$$\frac{4Q}{\pi R^3} = \frac{8V}{D} = \frac{4}{\tau_w^3} \int_{\tau_0}^{\tau_w} \tau^2 (-\dot{\gamma}) d\tau \quad (2.114)$$

using the equivalent expression in eq. (2.108). This equation is general and can be used for any model when the appropriate relation for  $\dot{\gamma}$  is used in the equation. In case of slip flow along the walls where the boundary condition  $V = 0$  and  $r = R$  does not hold (see Chapter 3), eq. (2.114) should be revised to include the increase in flow due to slip,

$$\frac{8V}{D} = \frac{4}{\tau_w^3} \int_{\tau_0}^{\tau_w} \tau^2 (-\dot{\gamma}) d\tau + \frac{8V_s}{D} \quad (2.115)$$

where  $V_s$  is the velocity of the fluid at the wall. Before going on to the next section, an expression for converting Newtonian shear rate at the wall,  $\dot{\gamma}_{wN}$  into its non-Newtonian equivalent  $\dot{\gamma}_w$  should be derived. Eq. (2.114) can also be expressed as the shear rate,  $\dot{\gamma}_{wN}$ , as given by eq. (2.108) for Newtonian fluids. Multiplying each term of this equation with  $\tau_w^3$ , taking the derivative with respect to  $\tau_w$  and rearranging the equation to give the shear rate at the wall, Rabinowitsch–Mooney equation is obtained which gives the shear rate at the wall for non-Newtonian fluids  $\dot{\gamma}_w$  in terms of its Newtonian equivalent  $\dot{\gamma}_{wN}$

$$3\tau_w^2 \left( \frac{8V}{D} \right) + \tau_w^3 \frac{d(8V/D)}{d\tau_w} = 4\tau_w^2 (-\dot{\gamma}_w) \quad (2.116)$$

$$-\dot{\gamma}_w = \dot{\gamma}_{wN} \left[ \frac{3}{4} + \frac{1}{4} \frac{d \ln \dot{\gamma}_{wN}}{d \ln \tau_w} \right] \quad (2.117)$$

The slope of a plot of  $\tau_w$  versus  $\dot{\gamma}_{wN}$  on logarithmic coordinates is denoted by  $n'$  (instead of  $n$ ) to signify that it is obtained from pipe flow data instead of rheometric measurements. Eq. (2.117) can be written in terms of this slope  $n'$  as

$$-\dot{\gamma}_w = \dot{\gamma}_{wN} \left[ \frac{3}{4} + \frac{1}{4n'} \right] \quad (2.118)$$

The difference between Newtonian and non-Newtonian behavior becomes most prominent at the pipe wall where the shear stress is maximum. Eq. (2.33) under the conditions at the pipe wall becomes

$$\tau_w = K \dot{\gamma}_w^n = K \left[ \dot{\gamma}_{wN} \left( \frac{3}{4} + \frac{1}{4n'} \right) \right]^n \quad (2.119)$$

Comparison of eq. (2.119) with the constitutive equation for power-law fluids give the relation between data obtained with a rheometer ( $K, n$ ) and data obtained by measurements of pipe flow ( $K', n'$ )

$$K' = K \left[ \frac{3}{4} + \frac{1}{4n'} \right]^n \quad (2.120)$$

and

$$n = n' \quad (2.121)$$

Eq. (2.114) is applied to fluids conforming to the models given in Table 2.2, and the results summarized in Table 2.10. Calculations are shown as an example for the Herschel–Bulkley model, with the constitutive equation

$$\tau = \tau_0 + K \dot{\gamma}^n \quad (2.48)$$

The equation is rearranged to give the shear rate as a function of shear stress

$$\dot{\gamma} = \left( \frac{\tau - \tau_0}{K} \right)^{1/n} \quad (2.122)$$

**Table 2.10**

Flow rate-wall shear stress relations for different models

Model	Shear rate	Design equations
Herschel–Bulkley	$\dot{\gamma} = ((\tau - \tau_0)/K)^{1/n}$	$Q = \frac{\pi D^3}{8\tau_w^3} \left( \frac{1}{K} \right)^{1/n} \left[ \frac{n(\tau_w - \tau_0)^{(1+3n)/n}}{1+3n} + \frac{2n\tau_0(\tau_w - \tau_0)^{(1+2n)/n}}{1+2n} + \frac{n\tau_0^2(\tau_w - \tau_0)^{(1+n)/n}}{1+n} \right]$
Casson	$\dot{\gamma} = (\tau^{1/2} - \tau_0^{1/2})^2/\eta$	$Q = \frac{\pi D^3}{32} \frac{\tau_w}{\eta} \left[ 1 - \frac{16}{7} \left( \frac{\tau_0}{\tau_w} \right)^{1/2} + \frac{4}{3} \left( \frac{\tau_0}{\tau_w} \right) - \frac{1}{21} \left( \frac{\tau_0}{\tau_w} \right)^4 \right]$
Bingham	$\dot{\gamma} = (\tau - \tau_0)/\eta$	$Q = \frac{\pi D^3}{32} \frac{\tau_w}{\eta} \left( 1 - \frac{4}{3} \left( \frac{\tau_0}{\tau_w} \right) + \frac{1}{3} \left( \frac{\tau_0}{\tau_w} \right)^4 \right)$
Power-law	$\dot{\gamma} = (\tau/K)^{1/n}$	$Q = \frac{\pi D^3}{8\tau_w^3} \frac{1}{K^{1/n}} \frac{n}{3n+1} (\tau_w^{(3n+1)/n})$

Substituting eq. (2.122) into eq. (2.114)

$$\frac{4Q}{\pi R^3} = \frac{4}{\tau_w^3} \int_{\tau_0}^{\tau_w} \tau^2 \left( \frac{\tau - \tau_0}{K} \right)^{1/n} d\tau \quad (2.123)$$

and integrating the resultant equation gives the relation between the flow rate and shear stress at the wall, equivalent to the pressure difference over the length of the pipe through eq. (2.101).

$$Q = \frac{\pi D^3}{8\tau_w^3} \left( \frac{1}{K} \right)^{1/n} \left[ \frac{n(\tau_w - \tau_0)^{(1+3n)/n}}{1+3n} + \frac{2n\tau_0(\tau_w - \tau_0)^{(1+2n)/n}}{1+2n} + \frac{n\tau_0^2(\tau_w - \tau_0)^{(1+n)/n}}{1+n} \right] \quad (2.124)$$

**Example 2.3: Flow curves of non-Newtonian fluids in the laminar regime**

*The case:* The system curves for the flow of synthetic hectorite clay (laponite) suspensions in 4 inch pipes, the velocity distributions of which are found in Example 2.2, will be drawn for use in the design of piping systems.

*Analysis of the case:* The relations given in Table 2.10 are converted into pressure gradient  $\Delta P/L$  versus volumetric flow rate  $Q$  from through eq. (2.101) and plotted in Figures 2.8–2.11 as a function of the flow parameters  $\tau_0$ ,  $K$ , and  $n$ . Figures 2.8–2.11 are based on fluid flow with characteristic values of  $\tau_0 = 4.5 \text{ Pa}$ ,  $n = 0.5$ , and  $K = 0.24 \text{ Pa s}^{0.5}$  as also used in Figures 2.3–2.6. The range of the flow rate,  $Q$ , values was selected so that laminar conditions would prevail in a 4 inch diameter pipe. These relations can be used as system curves in designing piping systems for non-Newtonian fluids flowing in the laminar regime. The Reynolds number ranges are given in terms of Metzner-Reed Reynolds number  $Re_{MR}$ , and  $Re \psi$  ( $Re_{HB}$  or  $Re_B$ ) for each model as explained in the following section.

### 2.3.1.3 Inverse design equations for non-Newtonian fluids

Eqs. (2.124)–(2.127) in Table 2.10 are implicit in  $\tau_w$ , and therefore, in the pressure gradient. Using these equations the design can be made as a function of pressure gradient

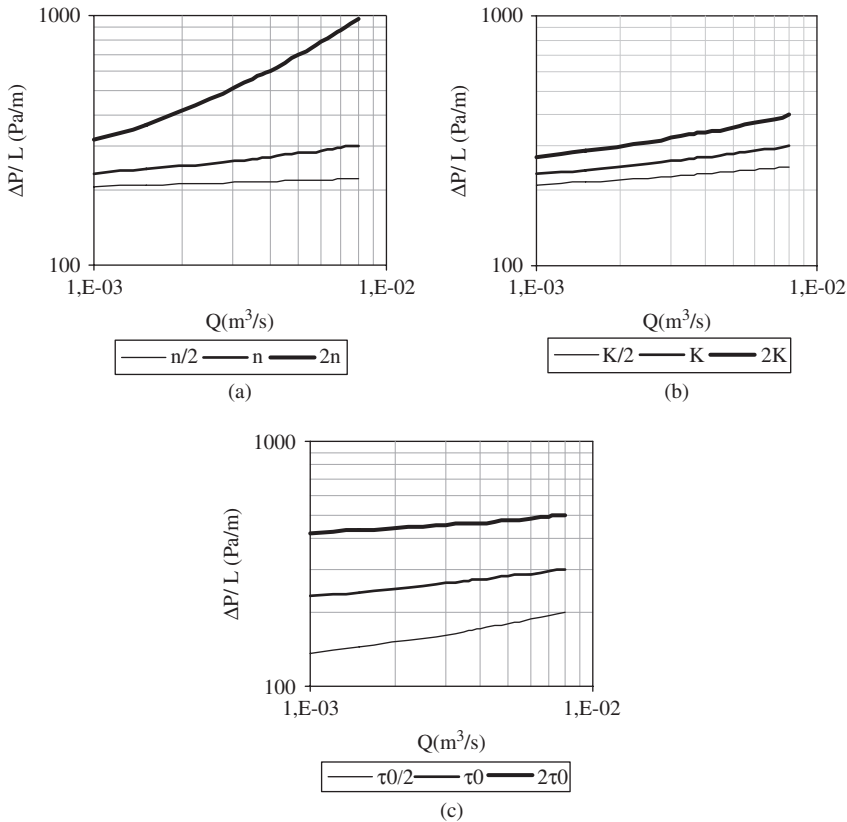


**Figure 2.8** Volumetric flow rate versus pressure difference relations of Herschel–Bulkley fluids: (a) effect of  $n$  ( $53 < Re_{MR} < 9590$  and  $15 < Re_{HB} < 1393$ ), (b) effect of  $K$  ( $73 < Re_{MR} < 6646$  and  $18 < Re_{HB} < 1241$ ), (c) effect of  $\tau_0$  ( $147 < Re_{MR} < 3323$  and  $11 < Re_{HB} < 1547$ ).

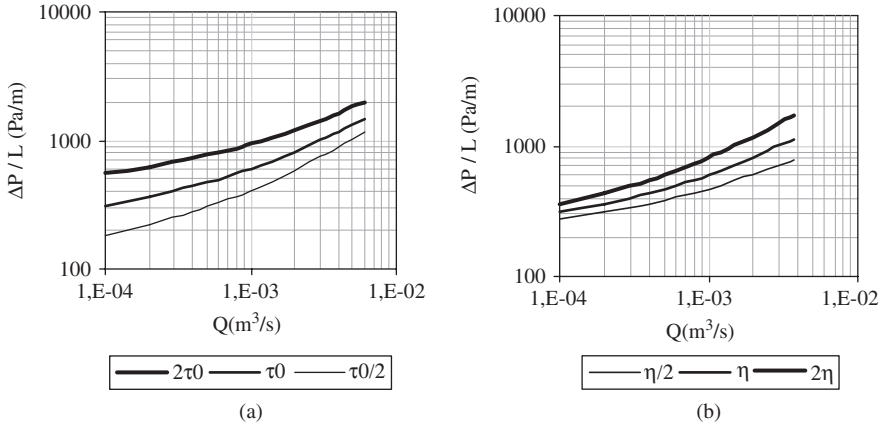


**Figure 2.9** Volumetric flow rate versus pressure difference relations of Casson fluids: (a) effect of  $\tau_0$  ( $5 < Re_{MR} < 2158$ ), (b) effect of  $\eta$  ( $5 < Re_{MR} < 1045$ ).

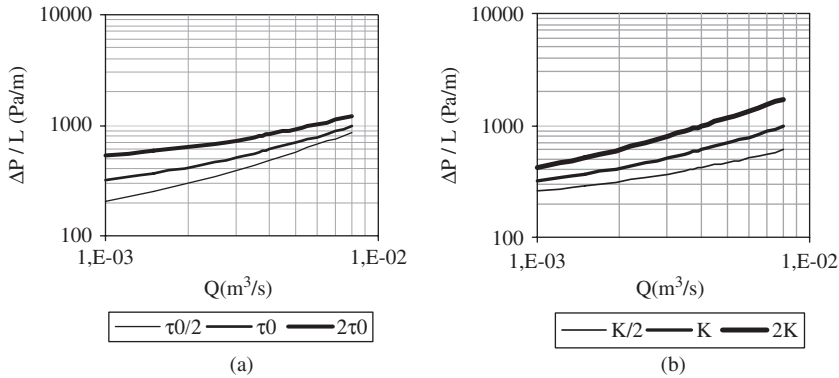


**Figure 2.10** Volumetric flow rate versus pressure difference relations of Bingham fluids; (a) effect of  $\tau_0$  ( $53 < Re_{MR} < 421$  and  $15 < Re_B < 425$ ), (b) effect of  $K$  ( $12 < Re_{MR} < 843$  and  $12 < Re_B < 514$ ).

acting on the system. This type of solution is called “direct.” It would be desirable to use an equation giving the pressure gradient as an explicit function of the flow rate using a friction factor,  $f$ , similar to Newtonian fluids. This method is called “inverse” design of non-Newtonian fluid flow. *Fanning friction factor*  $f$  is defined as the ratio of shear stresses at the wall, to the kinetic energy of the fluid

$$f = \frac{\tau_w}{(1/2)\rho V^2} \quad (2.128)$$



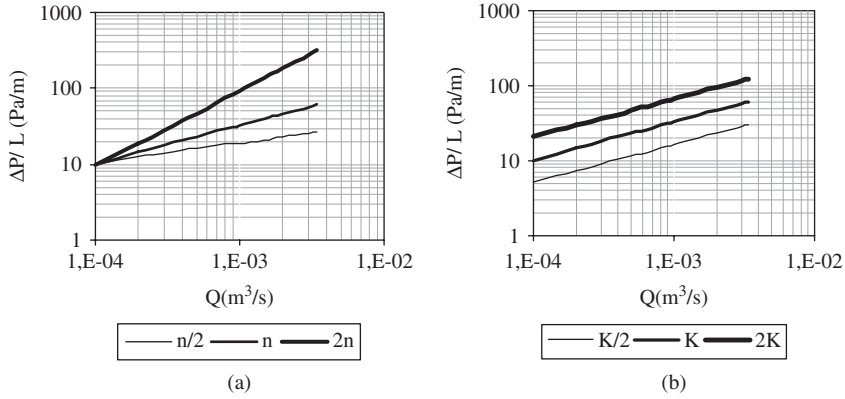


**Figure 2.11** Volumetric flow rate versus pressure difference relations of power-law fluids: (a) effect of  $n$  ( $4 < Re_{MR} < 2145$ ), (b) effect of  $K$  ( $2 < Re_{MR} < 1841$ ).

Replacing the value of the wall shear stress from eq. (2.101), one obtains the well-known *Darcy–Weisbach* equation for the pressure gradient

$$\frac{\Delta P}{L} = 4f \frac{\rho V^2}{2D} \quad (2.129)$$

For flow of Newtonian fluids in the laminar regime, pressure-driving force is given by the Hagen–Poiseuille equation, eq. (2.99)

$$\frac{\Delta P}{L} = \frac{8\eta V}{R^2} = \frac{128\eta}{\pi D^4} Q \quad (2.99)$$

Equating eqs. (2.99) and (2.129) the well-known relation for the Fanning friction factor of Newtonian fluids in laminar regime is obtained as

$$f = \frac{16}{Re} \quad (2.130)$$

Friction factor relations of non-Newtonian fluids can be derived from the  $Q - \tau_w$  relations given in Table 2.10 to obtain a relation similar to Fanning friction factor using the Reynolds number for Newtonian fluids,  $DV\rho/\eta$  with the incorporation of a correction factor for the nonlinearity,  $\psi$ .

$$f = \frac{16}{Re\psi} \quad (2.131)$$

## 2.3.1.3.1 Friction factor for power-law fluids

Eq. (2.127) can be rearranged to

$$Q = \frac{\pi D^2}{4} V = \frac{\pi D^3}{8} \frac{1}{K^{1/n}} \left( \frac{n}{3n+1} \right) \tau_w^{1/n} \quad (2.132)$$

Multiplying both the numerator and the denominator of eq. (2.85) by 4, and taking the  $n$  th power yields

$$V^n = \frac{D^n}{8^n} \frac{1}{K} \left( \frac{4n}{3n+1} \right)^n \tau_w^n \quad (2.133)$$

Replacing in the value of  $\tau_w$  from eq. (2.128) yields after rearrangement

$$f = 16 \left[ \frac{8^{n-1} V^{n-2} K}{D^n \rho (4n/(3n+1))^n} \right] \quad (2.134)$$

comparing eq. (2.134) with eq. (2.131) the Reynolds number for power-law fluids is obtained as

$$Re_{MR} = \frac{D^n V^{2-n} \rho}{8^{n-1} K ((3n+1)/4n)^n} \quad (2.135)$$

which is also known as the generalized Reynolds number of Metzner and Reed (1955). Eq. (2.134) can be rearranged to yield the general form of the friction factor relation

$$f = \frac{16}{Re\psi} \quad (2.131)$$

where

$$\psi = \left[ \frac{D^{n-1} (4n/(3n+1))^n}{8^{n-1} V^{n-1}} \right] \quad (2.136)$$

The design of the piping systems as a function of flow rate,  $Q$  can now be made using eqs. (2.129), (2.131), (2.132) and (2.136) for power-law fluids. This method is called “inverse” design.

## 2.3.1.3.2 Friction factor for Bingham fluids

Eq. (2.126) can similarly be rearranged to obtain the friction factor for Bingham fluids.

$$Q = \frac{V\pi D^2}{4} = \frac{\pi D^3}{32} \frac{\tau_w}{\eta} \left[ 1 - \frac{4}{3} \left( \frac{\tau_0}{\tau_w} \right) + \frac{1}{3} \left( \frac{\tau_0}{\tau_w} \right)^4 \right] \quad (2.126)$$

Replacing the value of  $\tau_w$  from eq. (2.128) yields after simplification

$$V = \frac{Df\rho V^2}{16\eta} \left[ 1 - \frac{4}{3} \left( \frac{\tau_0}{\tau_w} \right) + \frac{1}{3} \left( \frac{\tau_0}{\tau_w} \right)^4 \right] \quad (2.137)$$

giving the friction factor for Bingham fluids as

$$f = \frac{16}{Re\psi} = \frac{16}{Re \left[ 1 - \frac{4}{3} \left( \frac{\tau_0}{\tau_w} \right) + \frac{1}{3} \left( \frac{\tau_0}{\tau_w} \right)^4 \right]} \quad (2.138)$$

where  $Re\psi = Re_B$ .

The nonlinearity correction factor  $\psi$  in eq. (2.138) can also be written in terms of relevant dimensionless numbers, *Hedström number*,  $He = \rho D^2 \tau_0 / \eta^2$ , and *Reynolds number*,  $Re = DV\rho/\eta$ , and the definition of the friction factor, eq. (2.128)

$$\psi = \left[ 1 - \frac{8}{3} \frac{He}{fRe^2} + \frac{16}{3} \frac{He^4}{f^4 Re^8} \right] \quad (2.139)$$

Eqs. (2.138) and (2.130) can be rearranged to an equivalent friction factor expression as

$$f = \frac{16}{Re} + \frac{16}{6} \frac{He}{Re^2} - \frac{16}{3} \frac{1}{f^3} \frac{He^4}{Re^8} \quad (2.140)$$

### 2.3.1.3.3 Friction factor for Herschel–Bulkley fluids

The expression for the nonlinearity correction factor  $\psi$  in the general friction factor expression, eq. (2.141) is obtained by Hanks (1978) as

$$\psi = (1 + 3n)^n \left( 1 - \frac{\tau_0}{\tau_w} \right)^{n+1} \left[ \frac{(1 - \tau_0/\tau_w)^2}{(1 + 3n)} + \frac{2(\tau_0/\tau_w)(1 - \tau_0/\tau_w)}{(1 + 2n)} + \frac{(\tau_0/\tau_w)^2}{(1 + n)} \right]^n \quad (2.141)$$

giving the Reynolds number for Herschel–Bulkley fluids as  $Re_{HB} = Re\psi$ .  $\psi$  can also be expressed in terms of the dimensionless numbers,  $He$ , and  $Re$  as an implicit function

$$Re = 2He \left[ \frac{n}{3n + 1} \right]^n \left[ \frac{\psi}{\tau_0/\tau_w} \right]^{(2-n)/n} \quad (2.142)$$

### 2.3.2 Turbulent flow of non-Newtonian fluids

If either the yield stress or the initial viscosity of the fluids is high, then flow in the laminar regime is the economically optimum choice. Since many non-Newtonian fluids meet these conditions, flow in the laminar regime is better understood, at least for the fluids conforming to the more commonly observed rheological models. On the other hand, complications inherent in the rheology and flow behavior of non-Newtonian fluids pose difficulties in the development of a coherent theory for turbulence. Variation in the viscosity with the shear rate is mainly responsible for these complications. Even in the case of Newtonian fluids with constant viscosity, a single equation is not sufficient to characterize turbulent flow: velocity distribution in the laminar sublayer, transition (buffer) layer and turbulent core, observed under different shear stress levels existing between the pipe wall and center, demand different equations. Due to fluctuations in velocity and resulting local shear stresses, regularity in the change of viscosity across the flow cross-sectional area cannot be maintained. In addition, the presence of high yield stresses and zero-shear viscosities cause the appearance of a high viscosity core in the central region that dampens the velocity fluctuations. As a result, maximum turbulence intensity is observed in an annular region near the wall, instead of being located in the center.

Experimental work on non-Newtonian flow also involves problems that have to be resolved to obtain reliable data (Escudier and Presti, 1996; Chilton and Stainsby, 1998): Average velocity measurements bear no significance in analyzing turbulent flow. Local velocities should be measured by nonintrusive techniques such as Laser-Doppler anemometry LDA, not to interfere with velocity fluctuations. Laser techniques require transparent suspensions, transparent gels, and polymer solutions, which, albeit conforming to a rheological model, may not represent the concentrated solid suspensions and sludge met in practical applications. Use of polymers brings with it inevitable viscoelastic behavior with an increase in the concentration of solids. Viscoelastic behavior results in drag reduction and slip at the walls with a sequential increase in the velocity, extended thickness of the laminar sublayer, reduced level of tangential and radial turbulence intensity, and in general, delayed transition from laminar to turbulent regime. Rheological models, obtained over a limited range of shear rates, may not be sufficient to describe turbulent flow where a wide range of shear rates is involved. High flow rates encountered in turbulent flow do not permit equilibrium shear rates and viscosities to be established, making it difficult to use rheological data obtained under equilibrium conditions.

In spite of all these technical difficulties encountered, significant advances are being made toward the elucidation of the mechanism of the development of turbulence. In the absence of a coherent theory, advanced experimental and numerical techniques are being developed for a comprehensive understanding of turbulent flow of non-Newtonian fluids. Modeling and direct numerical simulation techniques are being developed to bypass the experimental complications, (Malin, 1997, 1998; Rudman *et al.*, 2004). Local velocities and velocity fluctuations measured with LDA with a high resolution give valuable information on the mechanism of transition to the turbulent regime, and the effect of the model parameters on this mechanism (Escudier *et al.*, 1996, 2005; Peixinho *et al.*, 2005).

Special emphasis is paid on the conditions at the onset of turbulence. Operation at the transition from laminar to turbulent regime requires the minimum energy for the transport of the

suspension. To avoid the flow instabilities during the transition, employment of flow rates just above the transition point is generally advised in the design of the transport system (Escudier and Presti, 1996; Rudman *et al.*, 2004; Vlasak and Chara, 2004; Peixinho *et al.*, 2005). Economic considerations form a strong motivation for the understanding of the flow conditions during transition to turbulence, placing the issue beyond academic interest.

### 2.3.2.1 Definitions of the Reynolds number in turbulent flow

Reynolds number is a ratio of momentum flux by convective mechanism,  $\tau_t$ , to the flux by molecular mechanism,  $\tau_l$

$$Re = \frac{\tau_t}{\tau_l} = \frac{\rho \overline{V_i V_j}}{\eta dV/dr} \quad (2.143)$$

where  $\overline{V_i}$  and  $\overline{V_j}$  denote the average fluctuating Reynolds stresses. Since the turbulent shear stresses are proportional to the kinetic energy of the fluid, Reynolds number is usually written as a dimensionless ratio in the form

$$Re \propto \frac{\rho V^2}{\eta(V/D)} \propto \frac{DV\rho}{\eta} \quad (2.144)$$

where,  $\eta$  is the *viscosity evaluated under the conditions of the wall* where momentum flux by molecular mechanism dominates over the convective mechanism. Reynolds number can also be written in the form

$$Re = \frac{8\rho V^2}{\tau_w} \quad (2.145)$$

by equating eqs. (2.128) and (2.130). In the use of the latter equation an equivalent expression for  $\tau_w$  is taken according to the rheological model to which the fluid conforms.

The Reynolds numbers and the correction factor  $\psi$ , given in Section 2.3.1.3 for laminar flow of fluids conforming to the power-law, Bingham, and Herschel–Bulkley models cannot be used in the turbulent flow of these fluids because molecular mechanism for momentum transfer does not persist throughout the cross-sectional area of flow. For this reason, an equivalent expression for the viscosity at the wall is used in Reynolds numbers as the conditions at the wall reflect best the nonideality of the fluid behavior. In the case of yield-plastic fluids, with or without shear-thinning behavior, a correction factor for the effect of yield stress is also incorporated into the Reynolds number. The generally used definition employs the expression of the viscosity of Herschel–Bulkley fluids evaluated at the wall

$$\dot{\gamma} = \frac{\tau_w}{\eta_w} = \frac{(\tau_w - \tau_0)^{1/n}}{K^{1/n}} \quad (2.146)$$

$$\eta_w = K^{1/n} \frac{\tau_w}{(\tau_w - \tau_0)^{1/n}} \quad (2.147)$$

The general Reynolds number  $Re_g$  is obtained by substituting eq. (2.147) into eq. (2.144)

$$Re_g = \frac{\rho V D}{K^{1/n} \tau_w / (\tau_w - \tau_0)^{1/n}} \quad (2.148)$$

Further modifications are also made in this equation to take into account the nonlinearity introduced by the presence of a yield stress. One such example is (Chilton and Stainsby, 1998)

$$Re_{CS} = \frac{\rho V D}{K((3/4) + (1/4n'))^n (8V/D)^{n-1} (1 - (\tau_0/\tau_w))^{-1} (1 - A(\tau_0/\tau_w) - B(\tau_0/\tau_w)^2 - C(\tau_0/\tau_w)^3)^{-n}} \quad (2.149)$$

where

$$A = \frac{1}{(2n+1)}, \quad B = \frac{2n}{(n+1)(2n+1)} \quad \text{and} \quad C = \frac{2n^2}{(n+1)(2n+1)} \quad (2.149a-c)$$

Reynolds number as defined by Metzner and Reed (1955) is used most often together with the velocity distribution (Bogue and Metzner, 1963) and friction factor (Dodge and Metzner, 1959) equations. The equation is based on eq. (2.145) with the wall shear stress  $\tau_w$ , replaced by its equivalent expression for power-law fluids, using eqs. (2.108) and (2.119)

$$Re_{MR} = \frac{8^{1-n'} \rho V^{2-n'} D^{n'}}{K'} \quad (2.135)$$

The denominator of eq. (2.135),  $K'$ , is obtained from the regression of wall shear stress versus shear rate plots of data obtained in pipe flow experiments

$$n' = \frac{d(\ln \tau_w)}{d(\ln(8V_m/D_h))} \quad (2.150)$$

and

$$\tau_w = K' \left( \frac{8V_m}{D_h} \right) \quad (2.151)$$

where  $V_m$  is the mean velocity and  $D_h$  is the hydraulic diameter. In general, for any geometrical shape of pipe with geometrical characteristics  $a$  and  $b$ , eq. (2.135) can be written as (Kozicki *et al.*, 1966, 1971)

$$Re_{MR} = \frac{8^{1-n} \rho V^{2-n} D^n}{K(b + (a/n'))^n} = \frac{8^{1-n} \rho V^{2-n} D^n}{k'} \quad (2.152)$$

and  $n'$  and  $k'$  are given by the equations

$$n' = \frac{\int_0^{\tau_w} \tau^{(b/a)-1} f(\tau) d\tau}{\tau_w^{b/a} f(\tau_w) - (b/a) \int_0^{\tau_w} \tau^{(b/a)-1} f(\tau) d\tau} \quad (2.153)$$

$$k' = a^{n'} \tau_w^{(bn'/a)+1} \left[ \int_0^{\tau_w} \tau^{(b/a)-1} f(\tau) d\tau \right]^{-n'} \quad (2.154)$$

Although originally derived for power-law fluids, the equation is used for Herschel–Bulkley fluids also, with  $K'$  and  $n'$  redefined to include yield stress, such as eqs. (2.155) and (2.156) (Peixinho *et al.*, 2005).

$$n' = \frac{(1 - r_p/R) + 2(r_p/R)(1 - r_p/R)(1 + 1/n)/(2 + 1/n) + (1 - r_p/R)^2(1 + 1/n)/(3 + 1/n)}{1/n + 1 - 3(1 - r_p/R)[(r_p/R)^2 + 2(r_p/R)(1 - r_p/R)(1 + 1/n)/(2 + 1/n) + (1 - r_p/R)^2(1 + 1/n)/(3 + 1/n)]} \quad (2.155)$$

$$k' = \left( \frac{K^{1/n}}{4} \right)^{n'} \left( \frac{\tau_0}{r_p/R} \right)^{1-n'(1/n)} \left\{ (1 - (r_p/R))^{1+1/n} \left[ 1 + \frac{2(1 - r_p/R)(1 + 1/n)}{r_p/R(2 + 1/n)} + \frac{(1 - r_p/R)^2(1 + 1/n)}{(r_p/R)^2(3 + 1/n)} \right] \right\}^{-n'} \quad (2.156)$$

where  $r_p$  is the plug radius given by

$$\frac{r_p}{R} = \frac{\tau_0}{\tau_w} \quad (2.73)$$

Use of the wall properties is advised (Pinho and Whitelaw, 1990; Rudman *et al.*, 2004; Peixinho *et al.*, 2005) to be used in the Reynolds number or any function of the Reynolds number, as it is in this region that the effect of shear stress is the maximum, which brings forth the characteristic properties of non-Newtonian fluids.

At present there is no conformity among the various definitions of Reynolds numbers in the literature, especially where the yield stresses are involved. In view of the very complex behavior of non-Newtonian fluids and furthermore, solid–liquid suspensions, a universal critical value, or a range of values, for the transition from laminar to turbulent regime cannot be assigned to the Reynolds number. Experimental verification covering a wide range of shear rates and rheological properties are needed to arrive at such a universal definition of Reynolds number for non-Newtonian fluids. A practical criterion in the absence of a

universal critical Reynolds number  $Re_c$ , is to take the intersection of theoretical pressure gradient,  $\Delta P/L$  (or equivalently  $\tau_w$ ) versus average velocity plots drawn for laminar and turbulent regimes, as the critical value of the Reynolds number (Shook and Roco, 1991). Chilton and Stainsby (1998) claim that when the Reynolds number corrected for the yield stress and flow behavior index is used (eq. (2.149)), transition from laminar to turbulent regime falls in the region  $2500 < Re_{CS} < 5000$ , increasing with an increase in  $\tau_0$ , and decrease in  $n$ . An example of criteria developed for specific models is the criterion proposed by Hanks (1963) for Bingham fluids

$$Re_{Bc} = \frac{1 - (4/3)(\tau_0/\tau_{wc}) + (1/3)(\tau_0/\tau_{wc})^4}{8(\tau_0/\tau_{wc})} He \quad (2.157)$$

The critical wall shear stress at the transition,  $\tau_{wc}$ , is related to the Hedström number through the equation

$$\frac{\tau_0/\tau_{wc}}{(1 - (\tau_0/\tau_{wc}))^3} = \frac{He}{16,800} \quad (2.158)$$

where the Hedström number relates the physical properties of the fluid and the pipe diameter  $D$  through the equation

$$He = \frac{\rho D^2 \tau_0}{\eta_B^2} \quad (2.159)$$

Results obtained by Peixinho *et al.* (2005) and Malin (1997) support the use of Hanks criterion with moderate Hedström numbers, less than about  $10^4$ .

### 2.3.2.2 Transition from laminar to turbulent regime

The mechanism of transition from laminar to turbulent regime could only be clarified recently (Peixinho *et al.*, 2005) with the advent of LDA techniques to experimental fluid flow studies. Three parameters, friction factor, centerline velocities, and average fluctuations in velocity, were used to assess transition from laminar to turbulent flow.

1. *Friction factor*: In Section 2.3.1.3, it was shown that the friction factor of all fluids show a linear variation with the Reynolds number, provided a necessary correction  $\psi$  is made for the nonlinearity in the rheology of the fluid. Termination of the linear relation between the friction factor  $f$  and the generalized Reynolds number followed by a slight increase in  $f$  signifies transition to turbulent flow.
2. *Centerline velocity* corresponds to maximum velocity in Newtonian fluids and remains at a value of two times the average velocity throughout the laminar regime. In shear-thinning fluids, the ratio of centerline to the average velocity decreases slightly as the viscosity of the fluid around the wall region decreases and velocity increases due to increasing shear. Fluids exhibiting a yield stress develop a stagnant core region at the center where the shear stress is below the yield stress of the fluid. As the flow rate and the extent of deformation increases, and the radius of the plug



flow decreases with a concomitant increase in its relative velocity. A sudden drop in the value of the ratio of centerline velocity to the average velocity,  $V_c/V_{av}$ , is an indication of the dominant role played by the velocity fluctuations in increasing the rate of momentum transfer, signifying the beginning of the transitional regime.

3. *Velocity fluctuations*: A sudden increase in the relative average velocity fluctuations at the center,  $\sqrt{u_c'^2}/V_c$ , takes place at the onset of turbulence during transition, which then decreases rapidly exhibiting a peak value at the transition. The value of the Reynolds number at which the fluctuations are first observed to increase is accepted as the critical Reynolds number signifying the start of the transition (Peixinho *et al.*, 2005). The relative increase in the velocity fluctuations is the maximum in Newtonian fluids, which decreases in shear-thinning and yield-pseudoplastic fluids, in the respective order.

In the work of Peixinho *et al.* (2005), eq. (2.135) was used, by redefining the generalized  $n'$  and  $k'$  for the Herschel–Bulkley model with eqs. (2.155) and (2.156). The critical Reynolds number for the laminar to turbulent transition was found as 2100, 2050, and 1800 for the Newtonian fluid, according to the friction factor, relative centerline velocity, and relative average fluctuation velocity at the center criteria, respectively. The authors have experimentally shown that the fluctuation measurements are the most sensitive to the onset of turbulence, in the case of Newtonian and shear-thinning fluids, and not sensitive at all for yield stress fluids due to damping by the high-viscosity region at the core. These measurements, in agreement with other experimental (Park *et al.*, 1989; Pinho and Whitelaw, 1990; Escudier and Presti, 1996), and simulation (Rudman *et al.*, 2004) work confirm that shear-thinning (low  $n$  values) and high values of yield stress delay the transition to turbulence to larger Reynolds numbers. How large these Reynolds numbers will be, depends on the rheological properties.

Maximum velocity fluctuation intensity is observed at around  $r = (0.8–0.9) R$  as a peak that rapidly declines radially toward either side, reaching a minimum level at the core region, where plug flow is observed (Escudier and Presti, 1996; Peixinho *et al.*, 2005). In this annular region, the fluctuations in the axial direction are greater by about 2–3 times in magnitude than the fluctuations in the radial or tangential directions. These experimental results are supported by direct simulation techniques (Rudman *et al.*, 2004), which show in addition that the radial and tangential fluctuations are less in shear-thinning fluids and decrease further with decreasing  $n$ . After the onset of turbulent fluctuations in the transitional regime, individual turbulence spots are observed in the core, intervened by laminar flow regions. As the Reynolds number increases, more and more of these spots are observed, gradually changing the velocity distribution with a plug zone at the center to the hyperbolic profile, typical of turbulent regime (Peixinho *et al.*, 2005). Intermittency in turbulent intensity in shear-thinning fluids in the form of slugs is also supported by simulation studies and drawn as a mechanism for the transition to turbulence (Rudman *et al.*, 2004).

An interesting observation first made by Escudier and Presti (1996) and later confirmed by other independent experimental work (Escudier *et al.*, 2005; Peixinho *et al.*, 2005) is the asymmetry in the velocity profiles during transition, which is not observed previously in the laminar regime, or the subsequent turbulent regime. The cause of the asymmetry has

not been identified yet. Several possibilities are proposed, one of them being the random high-activity puffs or slugs of turbulence sustained in a certain azimuthal location by the existence of a preferential triggering mechanism (Rudman *et al.*, 2004).

### 2.3.2.2.1 Effect of particles on the transition Reynolds numbers

Experimental (Matas *et al.*, 2003) and direct numerical simulation studies (Li *et al.*, 1999; Rudman *et al.*, 2004) have shown that the presence of particles within a given fluid increase the intensity of the turbulent fluctuations of the continuous phase, notably if the particles are large and very near the wall. Experimental results obtained through visual observations and pressure fluctuations showed that the critical Reynolds number  $Re_c$  for the onset of turbulence initially decreases with an increase in the volume fraction of solids,  $\phi$  and then increases with a further increase of  $\phi$  (Matas *et al.*, 2003) passing through a minimum point. The extent of this minimum below the critical Reynolds number of the continuous phase (2100 in the case under consideration) and the value of  $\phi$  at which the minimum is observed increases with an increase in the particle size. When the Reynolds number based on pipe diameter and average fluid velocity is converted into particle Reynolds number, through,  $Re_p = (d_p^2/D^2)Re_{\text{pipe}}$ , it was found that particles with  $Re_p \geq 1$  were effective on the transition. On the other hand, there could be a lower limit, presumably the Kolmogoroff length scale  $\ell_k$ ,  $\ell_k \propto (\mu/\rho\varepsilon^{1/3})^{3/4}$ , below which the transitional Reynolds number could not be affected by the presence of particles. Here  $\varepsilon$  denotes the energy dissipated per unit mass of fluid per unit time ( $\text{J kg}^{-1} \text{s}^{-1}$ ). The authors concluded that a steep increase in the value of the critical Reynolds number for  $\phi > 0.25$  with all particle sizes can be taken as an indication that an additional mechanism for dissipation of kinetic energy beyond that through viscous dissipation is operative in Stokes flow of concentrated suspensions.

### 2.3.2.3 Velocity distributions and average velocity in turbulent flow

Velocity distribution in the turbulent flow of Newtonian fluids is given by the boundary layer theory (Schlichting, 1955) for the laminar sublayer, transition region, and turbulent core regions by three separate equations

$$V^+ = y^+ \quad \text{for } y^+ < 5 \quad (2.160)$$

$$V^+ = 5 \ln y^+ - 3.05 \quad \text{for } 5 < y^+ < 30 \quad (2.161)$$

$$V^+ = 2.5 \ln y^+ + 5.5 \quad \text{for } y^+ > 30 \quad (2.162)$$

where the dimensionless velocity,  $V^+$ , is defined as the ratio of average velocity,  $V$ , to friction velocity  $V_*$

$$V^+ = \frac{V}{V_*} \quad (2.163a)$$

dimensionless distance, in terms of the distance from the wall  $y$ ,  $y = R - r$ , and frictional velocity  $V_*$

$$y^+ = \frac{yV_*\rho}{\eta} \quad (2.163b)$$

and frictional velocity is defined in terms of wall shear stress as

$$V_* = \sqrt{\tau_w/\rho} \quad (2.163c)$$

Similar equations can be derived for power-law fluids (Chhabra and Richardson, 1999): Shear stress at any point in the fluid in terms of wall shear stress  $\tau_w$  is

$$\tau_w \left(1 - \frac{y}{R}\right) = K \left(\frac{dV}{dy}\right)^n \quad (2.164)$$

within the laminar sublayer close to the wall,  $y \approx 0$ , and

$$\tau_w \approx K \left(\frac{dV}{dy}\right)^n \quad (2.165)$$

integration with no-slip condition and placing in the value of  $\tau_w$  from eq. (2.163c), the velocity distribution for turbulent flow of power-law fluids is obtained

$$V = \left(\frac{\tau_w}{K}\right)^{1/n} y = \left(\frac{\rho V_*^2}{K}\right)^{1/n} y \quad (2.166)$$

Eq. (2.166) can be written in standard form after dividing through by  $V_*$

$$\frac{V}{V_*} = \frac{\rho^{1/n} V_*^{(2-n)/n} y^{n/n}}{K^{1/n}} \quad (2.167)$$

$$V^+ = (y^+)^{1/n} \quad (2.168)$$

where the dimensionless distance for power-law fluids is defined as

$$y^+ = \frac{\rho V_*^{2-n} y^n}{K} \quad (2.169)$$

Velocity distribution of power-law fluids in the turbulent core, including the transition region in between the laminar sublayer and turbulent zone is given by Bogue and Metzner (1963) equation

$$V^+ = \frac{5.57}{n} \log y^+ + 0.05 \frac{\sqrt{2}}{f} \exp\left(\frac{-(y^+ - 0.8)^2}{0.15}\right) + I(n, Re_{MR}) \quad (2.170)$$

in the interval,  $10^4 < Re_{MR} < 10^5$ ,  $0.6 < n < 1.0$ .  $I(n, Re_{MR})$  can be approximated as  $I \approx 5.6$ . Increased viscosity in the plug at the core region causes a synergistic increase above the value of 5.6 when  $n < 0.6$ , and  $Re_{MR} < 10^4$ .

Based on experimental measurements where  $n$  varied in the narrow range of  $0.7 < n < 0.8$ , Clapp (1961) proposed the following equations for the transition region and the turbulent core

$$V^+ = \frac{5}{n} \ln y^+ - 3.05 \quad \text{for } 5^n \leq y^+ \leq y_T^+ \quad (2.171)$$

$$V^+ = \frac{2.78}{n} \ln y^+ + \frac{3.8}{n} \quad \text{for } y^+ \geq y_T^+ \quad (2.172)$$

where  $y_T^+$  is the  $y^+$  value at the intersection of the two equations. Simulation studies of the turbulent pipe flow of shear-thinning fluids (Rudman *et al.*, 2004) support Clapp's scaling of the velocity distribution with  $n$ , though the value of the constants 2.78 and 3.8 cause a slight under-prediction of velocity distributions.

Experimental measurements (Peixinho *et al.*, 2005) and simulation studies (Rudman *et al.*, 2004) show that the flow behavior of the non-Newtonian fluid can be successfully described when the Reynolds numbers and the friction factor relations are based on viscosities evaluated under the conditions prevalent at the wall.

The general problem with the boundary layer theory is that neither the centerline velocity nor the plug flow in the core region can be predicted with the velocity distribution equations, though a good prediction is obtained outside the core region.

Chilton and Stainsby (1998) evaluated the models for turbulent flow with the conclusion that the models which assume a negligible thickness of the laminar sublayer and in which the turbulent eddy viscosity dominates the molecular viscosity over the majority of the cross-sectional area of the pipe cannot be valid for the flow of non-Newtonian flows. This is especially true for fluids with a yield stress  $\tau_0$ , or with a very low flow behavior index  $n$ , where an undeformed core at plug flow exists in the center region. The high viscosities at the center suppress turbulent convection until very high Reynolds numbers are reached, which are not feasible in practice. They recommend the model by Thomas and Wilson (1987) as the best available analytical model for Herschel–Bulkley fluids for highly turbulent flows, because (a) it takes into account cross-sectional area occupied by the plug zone, (b) corrections for change in the thickness of the viscous sublayer according to

rheology, (c) the empirical constants take the same values for Newtonian flow, (d) has theoretical justification, and (e) is in good agreement with experimental data. Wilson's equation for the average velocity of yield-power-law fluids is

$$V = V_N + V_*[11.6(\alpha - 1) - 2.5\ln \alpha - \Omega] \quad (2.173)$$

where  $V_N$  is the average velocity of the equivalent Newtonian flow at the same  $\tau_w$  and with the same viscosity as that of non-Newtonian fluid at  $\tau = \tau_w$ .  $\Omega$  gives the effect of the plug flow region at the core

$$\Omega = -2.5\ln\left(1 - \frac{\tau_0}{\tau_w}\right) - 2.5\frac{\tau_0}{\tau_w}\left(1 + 0.5\frac{\tau_0}{\tau_w}\right) \quad (2.174)$$

with the  $\alpha$  term which takes into account the extent of the core region in plug flow given as

$$\alpha = \frac{2(1 + (\tau_0/\tau_w)n)}{1 + n} \quad (2.175)$$

Another model that takes the roughness effect of solid particles in fine-grained slurries on turbulence is the Slatter model (1995). In eq. (2.163b), the dimensionless distance is defined in terms of the fluid properties of  $\eta$ ,  $\rho$ , and wall shear stress  $\tau_w$ . Slatter (1996) assumed that the roughness effect is caused by the solid particles in the slurry, and scaled the distance with the particle dimension  $d_x$  responsible for the turbulence. For the slurries investigated,  $d_{85}$  was found to be a good representation of the turbulent roughness size effect of the solid particles;  $d_x = d_{85}$ . Subscript 85 refers to the 85th percentile of the particles passing.

$$\frac{V_{av}}{V_*} = 2.5\left(\ln \frac{R}{d_{85}}\right) + B - 3.75 \quad (2.176)$$

In case of smooth wall turbulent flow,  $B = 2.5\ln Re_r + 5.5$ , thus, the average velocity

$$V_{av} = V_* \left[ 2.5\ln \frac{R}{d_{85}} + 2.5\ln Re_r + 1.75 \right] \quad \text{for } Re_r < 3.32 \quad (2.177)$$

and in case of fully developed rough wall turbulent flow,  $B = 8.5$ , thus, the average velocity

$$V_{av} = V_* \left[ 2.5\ln \frac{R}{d_{85}} + 4.75 \right] \quad \text{for } Re_r > 3.32 \quad (2.178)$$

where the Reynolds number,  $Re_r$  a modification of eq. (2.145) for Herschel–Bulkley fluids is defined as

$$Re_r = \frac{8\rho V_*^2}{[\tau_0 + K(8V_*/d_p)^n]} \quad (2.179)$$

### 2.3.2.4 Friction factors in turbulent flow

The accuracy in the calculation of frictional losses, or the pressure gradient by the Darcy–Weisbach equation

$$\frac{\Delta P}{L} = 4f \frac{\rho V^2}{2D} \quad (2.129)$$

relies on how closely the friction factor  $f$  describes the wall conditions where the deviation from Newtonian behavior is maximum. The most extensively used equation is Dodge and Metzner's correlation (1959) originally derived for power-law fluids

$$\frac{1}{f} = A(n') \log[Re_{MR} f^{(2-n')/2}] + C(n') \quad (2.180)$$

For the flow of polymer solutions and particulate suspensions exhibiting shear-thinning power-law behavior with  $0.36 \leq n' \leq 1.0$  in the range of  $2900 \leq Re_{MR} \leq 36,000$ , the constants  $A(n')$  and  $C(n')$  are given with the relations,  $A(n') = 4(n')^{-0.75}$  and  $C(n') = -0.4(n')^{-1.2}$ . With these values of the constants Dodge and Metzner's correlation becomes

$$\frac{1}{f} = 4(n')^{-0.75} \log[Re_{MR} f^{(2-n')/2}] - \frac{0.4}{(n')^{1.2}} \quad (2.181)$$

This equation is the basis for the Fanning friction factor  $f$  versus  $Re_{MR}$  charts of Dodge and Metzner (1959). When  $n' = 1$ , the equation reduces to Nikuradse equation for Newtonian fluids. The equation can be used with fluids conforming to other models when the slope of  $\log \tau_w$  versus  $\log(8V/D)$  plot is evaluated at the relevant value of the wall shear stress. Metzner's correlation is the most widely used correlation presently, with the use of correction factors to fit into models other than the power-law, as detailed in Sections 2.3.1.3 and 2.3.2.1.

More recent work by Malin (1997, 1998) is the most comprehensive treatment of Herschel–Bulkley fluids at the present, including power-law and Bingham fluids as special cases. The parameters in the computation are the flow behavior index,  $n$ , Reynolds, and Hedström numbers. Metzner–Reed definition of the Reynolds number

$$Re_{MR} = \frac{8^{1-n} \rho V^{2-n} D^n}{K((3/4) + (1/4n'))^n} \quad (2.135a)$$

and the general Hedström number

$$He = \frac{D^2 \rho \tau^{2/n-1}}{K^{2/n}} \quad (2.182)$$

are used as parameters.

The friction factors in Figures 2.12–2.14 are found by solving the general momentum balance equation

$$\nabla \cdot \rho \mathbf{V} \mathbf{V} = -\nabla p + \nabla (\eta_l + \eta_t) \nabla \mathbf{V} + \nabla \cdot (\eta_l + \eta_t) (\nabla \mathbf{V})^T \quad (2.183)$$

taking into account the turbulence effect. The apparent viscosity,  $\eta_l$ , is based on the Herschel–Bulkley model and the turbulent viscosity,  $\eta_t$ , on Lam–Brenhorst  $k$ – $\varepsilon$  model for turbulent kinetic energy and dissipation rate of turbulent energy (Lam and Brenhorst, 1981). The equations developed are numerically solved by the finite volume solution technique.

The results of the computation are checked against the Hanks correlation, eq. (2.141) given in Section 2.3.1.3.3 for laminar flow, and against the Dodge–Metzner correlation eq. (2.181) for well-developed turbulent flow. The squares and circles give the results of these correlations, respectively, and “predictions” gives the computational results of Malin. Figures 2.12 and 2.13 give the friction factor plots of the special cases of Herschel–Bulkley fluids, power-law fluids with  $He = 0$ , and Bingham fluids with  $\underline{n} = 1$ . In the absence of a yield stress,  $n$ , does not appear to be a factor in the laminar regime. For Newtonian and shear thickening fluids  $n = 1$  and 1.2, respectively, Malin’s results over-predict, and for low values of  $n$ , such as 0.4, under-predict the friction factors in Figure 2.12, for power-law fluids.

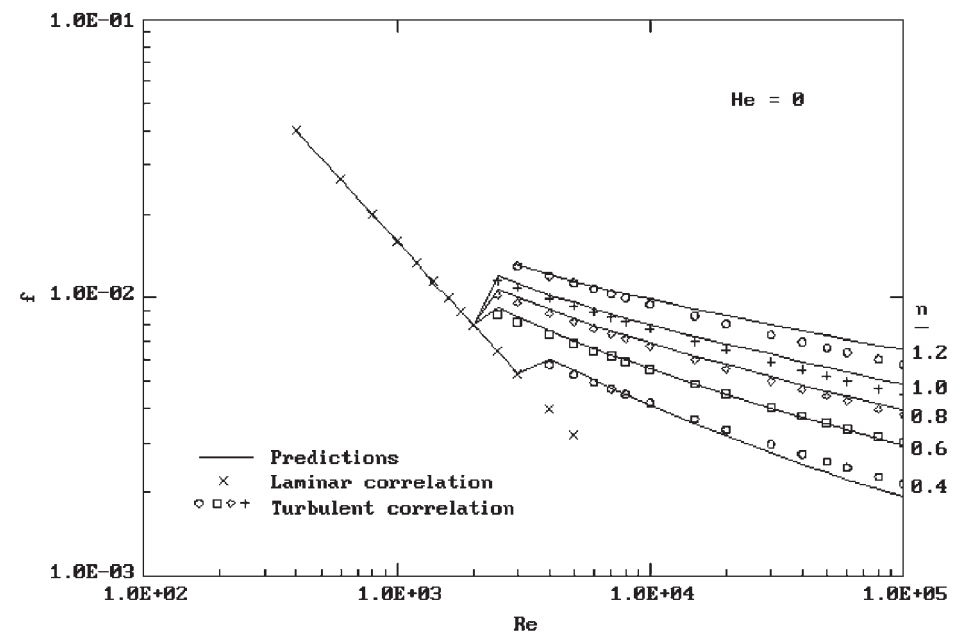


**Figure 2.12** Frictional resistance of power-law fluids. (Malin, 1998. Figure 1 in the original, reproduced with permission of Elsevier.)

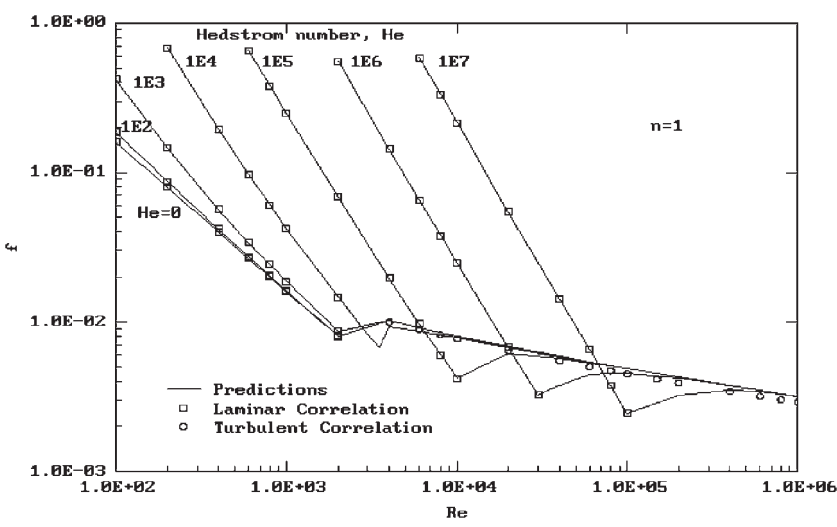
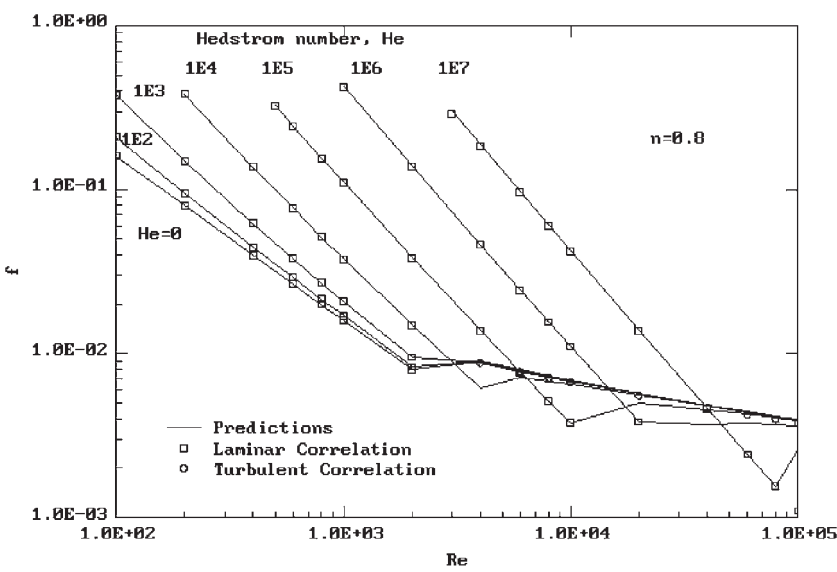


**Figure 2.13** Frictional resistance of Bingham fluids (Malin, 1998. Figure 2 in the original, reproduced with permission of Elsevier Science Ltd.)



(a)

**Figure 2.14** Frictional resistance of Herschel-Bulkley fluids with (a)  $n = 0.8$ ; (b)  $n = 0.6$ ; (c)  $n = 0.4$ . (Malin, 1998. Figure 5 in the original, reproduced with permission of Elsevier.)



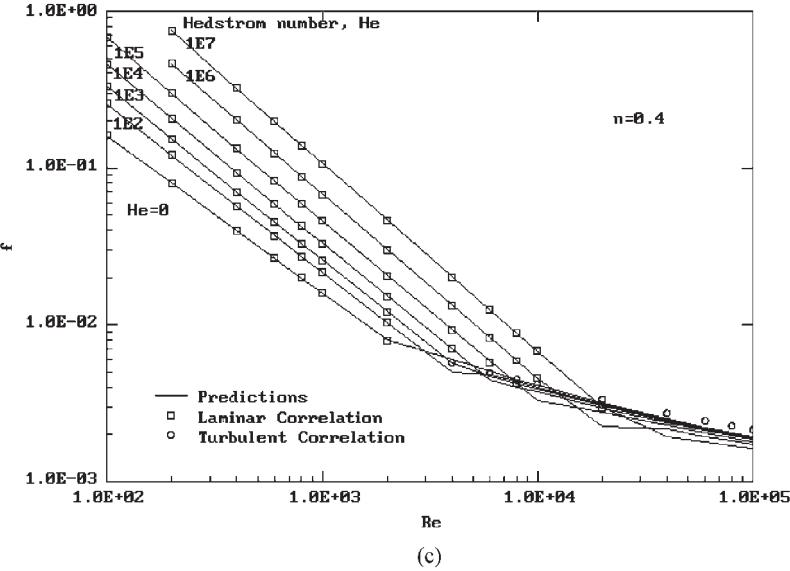
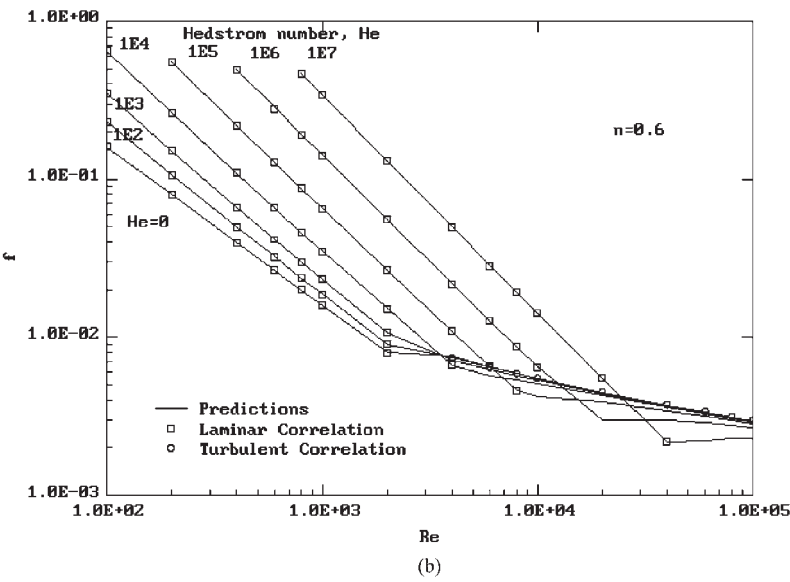


Figure 2.14 (Continued.)

In the presence of a yield stress there is a separate laminar regime curve for each value of the Hedström number. Laminar regime end point on the straight line denotes the critical Reynolds number for the transition from laminar to turbulent regime. Due to the thickening of the laminar sublayer, wall-roughness effects are negligible and the turbulent regime is represented by a single line, that of Dodge–Metzner correlation in the figures.

### 2.3.3 Flow through sudden expansions and fittings

Sudden expansions in different diameter pipes connected in series, as in heat exchangers, and entrance to process equipment are frequently used in process plants. Sudden expansions are also observed in biological systems such as in veins carrying blood. Understanding of flow behavior in sudden expansions is important from the standpoint of distortion of velocity profiles before and immediately after the expansion, as well as for the calculation of pressure losses in the design of flow systems. The distortions in the velocity profile lead to emanation of high-viscosity regions around the corners after the expansion and inside the plug flow cores leading to local variations in viscosity. Flow patterns in a sudden expansion are schematically shown in Figure 2.15.

The jet flow issuing from the upstream pipe is generally assumed to be fully developed. Recirculation motion arises at the corners of the downstream pipe. Laminar boundary layer reattaches to the wall shortly after the vortex motion. Fluid remaining in the center of the vortex and in the core region of the pipes has a high viscosity due to low shear rates. The center of the vortex is denoted by  $l_{\max}$  in the figure. Dimensions significant in the analysis of flow are the ratio of the diameter of the downstream to the upstream pipe,  $D_2/D_1$ , length to width ratio of the turbulent vortex region,  $l_c/R_a$ , the distance from the expansion plane to the point of onset of the plug flow region,  $l_p$  ( $l_{p1}$  and  $l_{p2}$  for the upstream and downstream pipes, respectively).

#### 2.3.3.1 Size of the recirculation region

The extent of the recirculation (or stagnation) zones around the periphery of the issuing jet is denoted by a dimensionless ratio,  $l_c/R_a$ , where  $l_c$  is the distance from the expansion plane to the reattachment point of the boundary layer and  $R_a = (D_2 - D_1)/2$  is the width of the recirculation zone. Pinho *et al.* (2003) numerically studied the laminar flow of shear-thinning power-law fluids through a sudden expansion with a diameter ratio of 1:2.6 as a function of the Reynolds number and flow behavior index,  $n$ . The size of the recirculation zones expressed as  $l_c/R_a$  was found to decrease linearly with the Reynolds number to a constant asymptotic value under creeping flow conditions. The value of this constant was found to be  $l_c/R_a = 0.47$  for Newtonian fluids that are supported by previous numerical

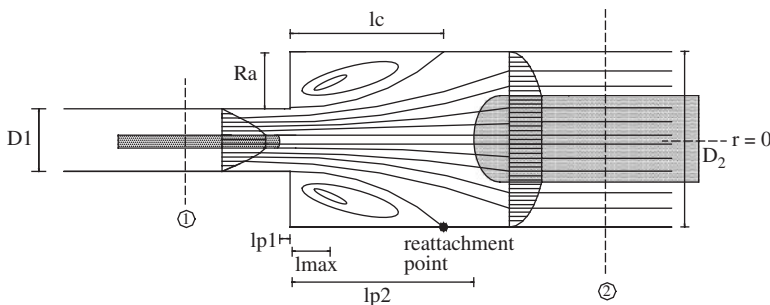


**Figure 2.15** Schematic representation of flow through a sudden expansion.

studies in the literature. The size of the recirculation zone was found to decrease with flow behavior index  $n$  to a value of approximately 0.1 when  $n = 0.2$ . The authors also found that the vortex intensity in the recirculation zone increased steeply for  $Re_{MR} \geq 1$ , leveling off at high Reynolds numbers,  $Re \approx 300$ . Calculations showed that the final intensity of recirculation at high Reynolds numbers and the value of the Reynolds number at which a steep increase was initiated, decreased with decreasing  $n$ . These results are tantamount to saying that the size and intensity of recirculation in vortices decrease and they form at greater Reynolds numbers with a decrease in the flow behavior index,  $n$ .

The effect of the yield stress on the recirculation zones in the laminar flow of Herschel–Bulkley fluids was studied numerically by Vradis and Ötügen (1997) and Hammad *et al.* (2001). The reattachment length  $l_c$  is a linear function of the Reynolds number for a fixed yield stress, and decreases rapidly with increasing yield stresses.

These results are in agreement with the synergistic effect of an increase in the yield stress with a decrease in the flow behavior index given in Section 2.3.1.1 and are confirmed by the viscosity variations in the same zones.

### 2.3.3.2 Viscosity variations on sudden expansion

Viscosity contours after a sudden expansion obtained by numerical solution of continuity and momentum equations are plotted as a function of nondimensional apparent (or effective) viscosities for shear-thinning power-law fluids (Pinho *et al.*, 2003) (Figure 2.16) and Herschel–Bulkley fluids (Hammad *et al.*, 2001) (Figures 2.17–2.18) in laminar flow. Even though the conditions are not the same, the results of the two studies are in conformation in a broad sense.

Contours given in Figure 2.16, were obtained (Pinho *et al.*, 2003) by solving the continuity and momentum equations together with the constitutive equation for power-law fluids with a general purpose CFD code developed by Oliveira (1992), which is based on the finite volume method applied to nonstaggered meshes. The dimensionless viscosity is based on the apparent viscosity, defined as the ratio of shear stress to shear rate, at the wall of the upstream pipe. Up to 10-fold increase in the viscosity is observed in the center of the recirculation zone and the core region in the downstream pipe. The increased viscosity within the recirculation zone causes a reduction in its size ( $l_c$ ).

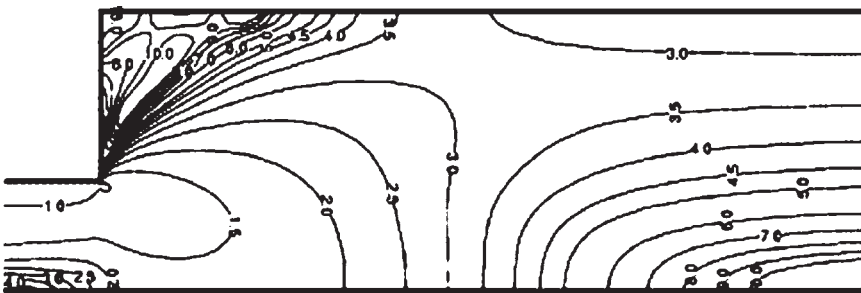


**Figure 2.16** Contours of dimensionless viscosity,  $\mu/\mu_a$  after a 1:2.6 expansion of cylindrical pipes for a power-law shear-thinning fluid ( $n = 0.6$ ) for  $Re_{MR} = 19.69$ . (Pinho *et al.*, 2003. Figure 7 in the original, reproduced with permission of Elsevier.)

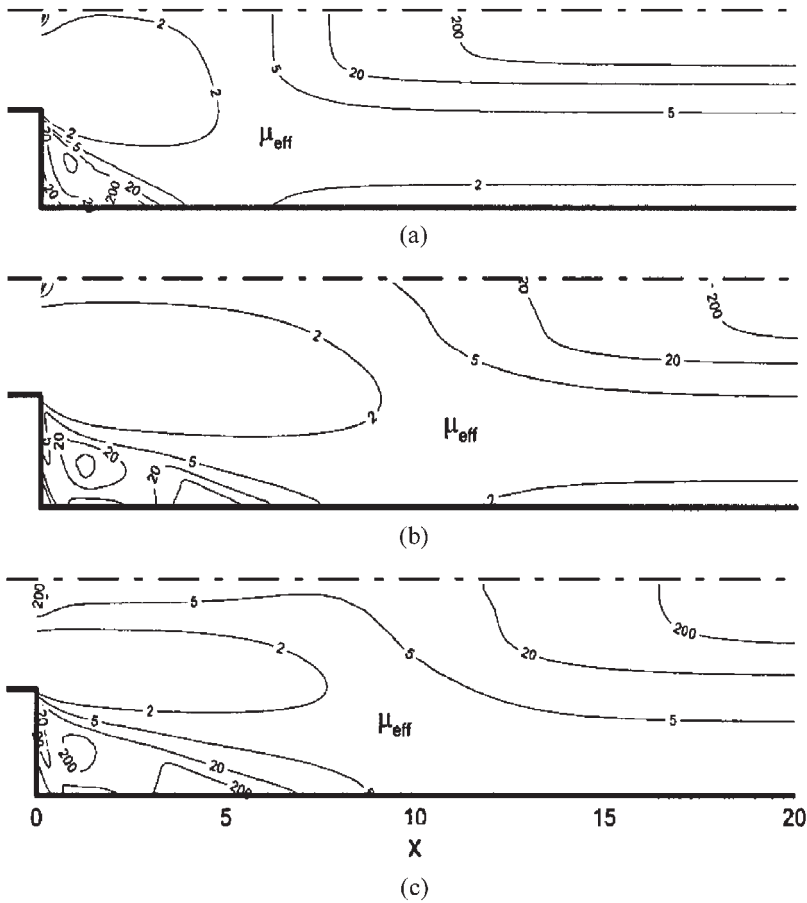


**Figure 2.17** Effective viscosity contours on sudden expansion as a function of Reynolds number (a)  $Y = 1$ ,  $Re = 50$ , and  $n = 1$ ; (b)  $Y = 1$ ,  $Re = 100$ , and  $n = 1$ ; (c)  $Y = 1$ ,  $Re = 100$ , and  $n = 0.6$ . (Hammad *et al.*, 2001. Figure 5 in the original, reproduced with permission of ASME.)

Hammad *et al.* (2001) obtained the viscosity variations of Herschel–Bulkley fluids on flow over a sudden expansion,  $D_2/D_1 = 2$ , by solving the continuity and fully elliptic momentum equation by finite difference technique. The viscosity profiles as a function of Reynolds and yield numbers are reproduced in Figures 2.17 and 2.18. Reynolds and yield numbers,  $Y$  are defined with the equations

$$Re = \frac{\rho D_1^n V_1^{2-n}}{K} \quad (2.184)$$

$$Y = \frac{\tau_0 D_1^n}{K V_1^n} \quad (2.185)$$

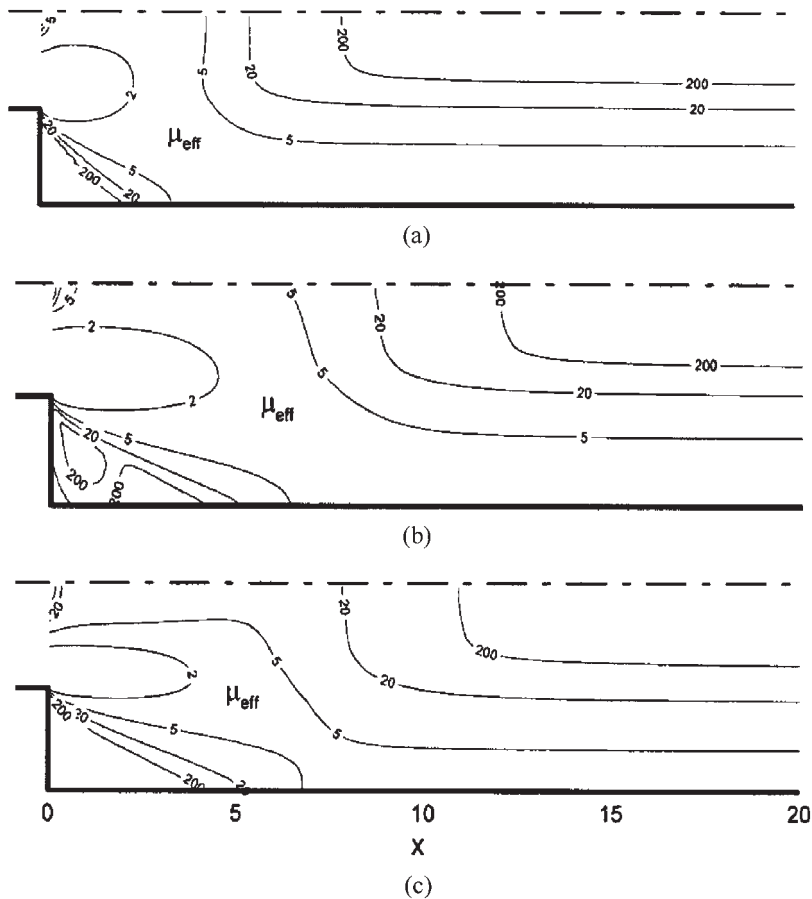


**Figure 2.18** Effective viscosity contours on sudden expansion as a function of Reynolds number (a)  $Y = 2$ ,  $Re = 50$ , and  $n = 1$ ; (b)  $Y = 2$ ,  $Re = 100$ , and  $n = 1$ ; (c)  $Y = 2$ ,  $Re = 100$ , and  $n = 0.6$ . (Hammad *et al.*, 2001. Figure 6 in the original, reproduced with permission of ASME.)

In these equations the subscript 1, denotes the upstream narrow pipe.  $K$  and  $n$  are the consistency and flow behavior index determined in a rheometer. Effective viscosity is equivalent to the apparent viscosity of Herschel–Bulkley fluids based on the viscosity in the upstream pipe.

Comparison of (a) and (b) in Figure 2.17 gives the effect of an increase in Reynolds number. Note the enlargement of the deformation zone denoted by the  $\mu_{\text{eff}} = 2$  area at the entrance and recession of the  $\mu_{\text{eff}} = 200$  contour signifying the plug flow region, on increase in shear rate at increased Reynolds numbers in Bingham fluids ( $n = 1$ ). Comparison of (b) and (c) in Figure 2.17 gives the effect of a decrease in flow behavior index as an advancement of the  $\mu_{\text{eff}} = 200$  contour in the plug area and recirculation region at the corners. Comparison of Figure 2.17(c), for Herschel–Bulkley fluids with Figure 2.16 for power-law fluids gives the effect of the yield stress at the same flow behavior index

$n = 0.6$ , as steeper gradients in viscosity and much higher viscosities in the relatively stagnant zones, in spite of a fivefold increase in the Reynolds number.

The cases are given in Figure 2.18, in the same order as in Figure 2.17, at an increased level of yield stress. The recession of the  $\mu_{\text{eff}} = 2$  area at the entrance and advancement of the  $\mu_{\text{eff}} = 200$  contour in comparison to their counterparts in Figure 2.16 is a direct result of an increase in yield stress. Comparison of (b) and (c) in Figure 2.18 gives the synergistic effect of the yield stress and the flow behavior index in converting the recirculation region into a stagnation zone, in addition to the advancement of the plug flow zone. Stagnation regions are also observed at low Reynolds and high yield numbers as in Figure 2.18(a).

### 2.3.3.3 Pressure losses in expansion

Variation in the expansion loss coefficient between Newtonian and non-Newtonian fluids become significant in laminar regime, when the loss coefficient is a function of the Reynolds number which in turn is a function of the rheological parameters of the fluid as given in Section 2.3.1.3.

A mechanical energy balance between any two points, 1 and 2 in Figure 2.15, located in the undisturbed, well-developed flow zones away from the expansion site in the upstream and downstream pipes, respectively, yields

$$P_1 - P_2 = \frac{\alpha_2 \rho V_2^2 - \alpha_1 \rho V_1^2}{2} + \left( 4f_2 \frac{L_2}{D_2} \frac{\rho V_2^2}{2} + 4f_1 \frac{L_1}{D_1} \frac{\rho V_1^2}{2} \right) + C_l \left( \frac{\rho V_1^2}{2} \right) \quad (2.186)$$

The first term on the RHS is the reversible kinetic energy variation on expansion corrected for velocity distribution within the pipes; the second term given in parenthesis is the irreversible frictional dissipation of mechanical energy in the well-developed flow sections of the downstream and upstream pipes, respectively. The third term is the dissipation of mechanical energy around the expansion site where the velocity profiles are severely distorted. The pressure loss coefficient on expansion,  $C_l$ , can be obtained from this equation after corrections are made for the kinetic energy and momentum distortions on the change in flow area.

#### 2.3.3.3.1 Correction for the variation due to non-Newtonian behavior

Pinho *et al.* (2003) found that the loss coefficient decreases monotonically with decreasing  $n$  in shear-thinning power-law fluids, if the loss coefficient  $C_l$  is plotted as a function of the modified Reynolds number defined as

$$Re_{\text{mod}} = \frac{\rho D_1^n V_1^{2-n}}{K} \quad (2.187)$$

as given in Figure 2.19 for a  $D_1:D_2 = 1:2.6$  expansion. The loss coefficient  $C_l$  varies linearly with the Reynolds number up to  $Re_{\text{mod}} \approx 10$ , and levels off to a constant value around  $Re_{\text{mod}} \approx 100$ .

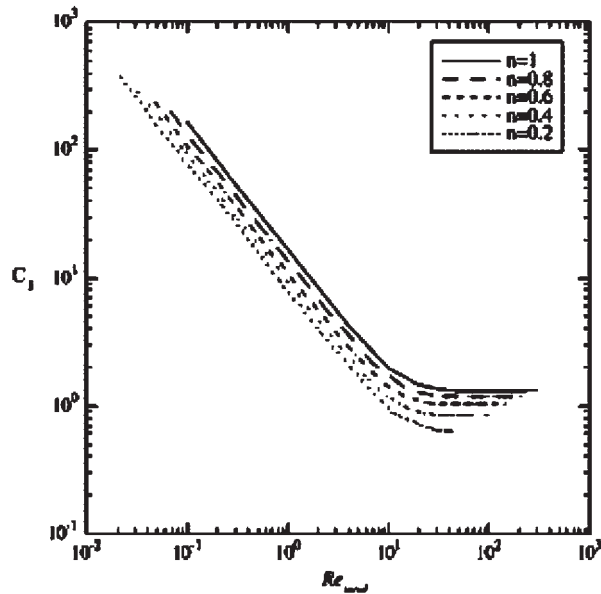


**Figure 2.19** Variation of the pressure loss coefficient in sudden expansion of shear-thinning fluids as a function of modified Reynolds number,  $Re_{mod}$  and flow behavior index  $n$ . (Pinho *et al.*, 2003. Figure 8b in the original, reproduced with permission of Elsevier.)

The value of the loss coefficient decreases with decreasing  $n$  for all Reynolds numbers. The flat velocity profiles observed in highly shear-thinning fluids brought about by the relatively high apparent viscosities resist further deformations related with the expansion, and the pressure losses decrease.

#### 2.3.3.4 Pressure losses in flow through fittings

Unfortunately there is no comprehensive literature covering the effect of rheological parameters, solids concentration and pipe diameter, or wall effects on pressure losses of non-Newtonian fluids in flow through fittings. In the work done by Turian *et al.* (1998), flow of laterite (3.6–12.7 v%) and gypsum (10.7–30.6 v%) slurries were investigated for two sizes (2.5 and 5 cm in diameter) of bends, elbows, and gate and globe valves. When pressure losses through the fittings including the effects of increased turbulence, secondary flows, flow separation, and recirculation in the adjacent pipes were correlated as a function of Metzner–Reed Reynolds number, eq. (2.135), an inverse variation with the Reynolds number of the form

$$K_L = \frac{A_F}{Re_{MR}} \quad (2.188)$$

was found for laminar regime. The constant  $A_F$  varied only with the type of the fitting, independent of its size. Transition Reynolds number from laminar to turbulent regimes was

found to be dependent on the size, increasing with an increase in the nominal diameter. A constant loss coefficient  $K_T$  was approached in fully developed turbulent flow, the value of which varied with the diameter and design of the fitting only, and was independent of the concentration of solids and the value of the flow behavior index  $n$ , as Reynolds number was no longer a parameter. Experimental determination of  $K_T$  is unavoidable due to the variations in the design of the fittings, but the experimental evidence presented in this work, that the  $K_T$  values for the suspensions are the same as that of water bears practical significance.

In another work on non-Newtonian flow of polymers through fittings (Etemad, 2004), a strong dependence of the loss coefficients on the flow behavior index  $n$ , in relation to increased concentration of polymer was found. Frictional losses correlated with the modified Reynolds number (eq. (2.187)), confirmed that the effect of the polymer concentration is exerted through variations in viscosity relations, stressing the importance of using the appropriate definition of the Reynolds number in correlating non-Newtonian flow.

## 2.4 FLOW THROUGH NONCYLINDRICAL CHANNELS

Cylindrical pipes, flow equations for which are given in Section 2.3, are most widely used in all processes. However, in specific applications ducts of noncircular cross-section are used also. Open channel and free flows of mud and debris are encountered in floods and volcano eruptions. Ditches, ducts, and even valleys can act as a natural open channel in mudflows after torrents and landslides. Mud can also flow freely over sloping land sites. Rectangular ducts through which phase change materials flow are important in cooling electronic circuits. They are also used in high-efficiency heat exchangers in processes of food technology. On the other hand, annuli serving as channels are encountered in double pipe heat exchangers, extruders, and discharge pipes in drilling. The last of these operations bears considerable economical significance in oil well drilling justifying the extensive research in this field. An extensive literature survey of research on flow through annular channels done until 2002 is provided by Escudier *et al.* (2002). In drilling pipes not only is mud a solid suspension in liquid, but the stone cuttings carried up by the mud also makes the subject significant for the contents of this book. A recent application of annular geometry is in purification of water and treatment of wastewater by heterogeneous photocatalysis, where a concentrated slurry of semiconductor photocatalyst  $\text{TiO}_2$  flows down the annular space around an ultraviolet light source in plug flow in the closed channel or in free fall as a thin film (Puma and Yue, 2001, 2003). As the viscosity of non-Newtonian fluids depend on the shear rate and velocity gradients within the channel, the above equations have to be revised to account for the noncircular cross-sections.

### 2.4.1 Flow through annular channels

Parameters which control flow through annular channels are the ratio of the radii of the inner cylinder and outer cylinders; and the relative positions of the centers of the inner and outer cylinders with respect to each other, defined as the eccentricity; magnitude and



direction of the velocity of inner and outer cylinders; the rheological model of the flowing fluid. The simplest case relevant to solid-liquid two phase flow is that of a non-Newtonian fluid flowing through a concentric annular space between two stationary cylinders, for which a general derivation will now be made.

#### 2.4.1.1 Flow through concentric annuli

A schematic drawing of a concentric annular channel is given in Figure 2.20 on which the relevant dimensions and the velocity and shear stress distributions of a yield-pseudoplastic fluid are given as the most general case of non-Newtonian fluid flow. The inner radius  $R_i$  is generally expressed as a fraction of the outer radius  $R_o$ , in an annular geometry

$$R_i = \kappa R_o \equiv \kappa R \quad (2.189)$$

In the most general case, a plug flow region may exist, due to the presence of a yield stress,  $\tau_0$ , or very low value of the flow behavior index,  $n$ . The inner and outer surfaces of the plug flow zone are located at distances of  $\lambda_i R$  and  $\lambda_o R$ , respectively. The width of this plug flow region is of prime importance in the characterization of flow through annuli. A cylindrical control volume over which a momentum balance can be made is located at an arbitrary distance,  $r$  from the center

$$r = \xi R \quad (2.190)$$

where  $\kappa < \xi < 1$ .

A momentum balance equation similar to the case of flow through pipes can now be written for flow in a concentric annulus under gravitational and pressure forces to obtain

$$\frac{d(r\tau_{rz})}{dr} = \left( \frac{P_0 - P_L}{L} + \rho g \right) r \quad (2.191)$$

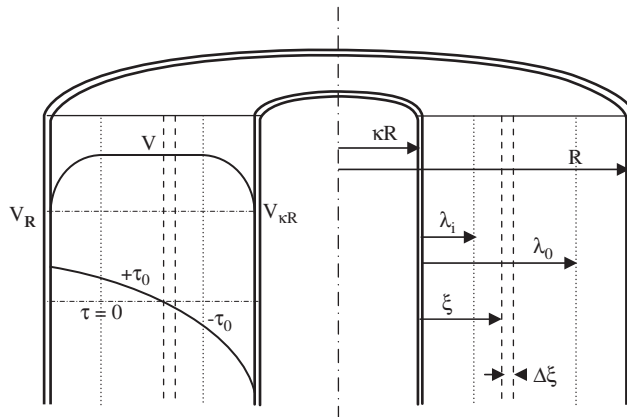


**Figure 2.20** Dimensions and velocity and shear stress distributions in a concentric annulus.

Using the relation  $\xi = r/R$  for scaling the radial distance and integrating the resulting equation with respect to  $\xi$  gives

$$\tau_{rz} = \left( \frac{P_0 - P_L}{L} + \rho g \right) R \frac{\xi}{2} + \frac{C_1}{\xi} \quad (2.192)$$

The integration constant  $C_1$  is evaluated at the radial distance  $\lambda R$  ( $\xi = \lambda$ ), the point of maximum velocity where the velocity gradient and the shear stress vanish. Then the shear distribution is obtained as

$$\tau_{rz} = \frac{R}{2} \left\{ \frac{P_0 - P_L}{L} + \rho g \right\} \left( \xi - \frac{\lambda^2}{\xi} \right) \quad (2.193)$$

The momentum generation terms in brackets on the RHS of the equation can be denoted by  $\Phi$ .  $\Phi$  multiplied by  $R/2$  can be used as a scaling factor in the nondimensionalization of the shear stress distribution equation

$$T_{rz} = \left( \xi - \frac{\lambda^2}{\xi} \right) \quad (2.194)$$

where  $T_{rz}$  is the nondimensional shear stress

$$T_{rz} = \frac{2\tau_{rz}}{\Phi R} \quad (2.195)$$

Eq. (2.194) is valid for all types of fluids. The velocity distribution depends on the rheological model which best describes the flow behavior. A general case is a fluid exhibiting a yield stress and nonlinear shear stress–shear rate relation. Herschel–Bulkley model could be suitable for the depiction of the general fluid behavior. A further complication could be the yield stress  $\tau_0$  being nonlinearly dependent on the initial shear rate exerted on the fluid, instead of having a constant value regardless of the magnitude of the initial strain

$$\tau_{rz} = K \dot{\gamma}_0^n + K \left( \frac{-dV_z}{dr} \right)^n \quad (2.196)$$

For mathematical simplicity, eq. (2.196) could be written in the form

$$\tau_{rz} = K \left( \frac{-dV_z}{dr} + \dot{\gamma}_0 \right)^n \quad (2.197)$$

which is in the form of the Robertson–Stiff model (eq. (2.56b)). With the use of dimensionless shear stress definition in eq. (2.195), eq. (2.197) becomes

$$T_{rz} = \frac{2K}{\Phi R} \left( \frac{-dV_z}{dr} + \dot{\gamma}_0 \right)^n \quad (2.198)$$

Taking the  $1/n$ th power of each term, the nondimensional eq. (2.199) is obtained after rearrangement

$$T_{rz} = \left( \frac{-d\phi_v}{d\xi} + T_0^{1/n} \right)^n \quad (2.199)$$

where the nondimensional velocity  $\phi_v$  and yield stress  $T_0$  are defined by eqs. (2.200) and (2.201), respectively.

$$\phi_v = \left( \frac{2K}{\Phi R} \right)^{1/n} (V_z / R) \quad (2.200)$$

$$T_0 = \left( \frac{2K}{\Phi R} \right) \dot{\gamma}_0^n \quad (2.201)$$

Equating the nondimensional equivalents of the yield stress in eqs. (2.194) and (2.199) yields

$$\left( -\frac{d\phi_v}{d\xi} + T_0^{1/n} \right)^n = \left( \xi - \frac{\lambda^2}{\xi} \right) \quad (2.202)$$

Plug flow is observed in yield-pseudoplastic fluids where the shear stress remains less than the yield stress at low flow rates. As a general case, a plug flow region with an inner boundary at  $r = \lambda_i R$ , and an outer boundary at  $r = \lambda_0 R$  could be considered with deformation regions in the interval  $\kappa R \leq r \leq \lambda_i R$  and  $\lambda_0 R \leq r \leq R$ , or equivalently,  $\kappa \leq \xi \leq \lambda_i$  and  $\lambda_0 \leq \xi \leq 1$ , respectively. In the inner deformation region  $\kappa R \leq r \leq \lambda_i R$ , the velocity gradient is positive if the inner tube is either stagnant, or moving with an axial velocity less than that of the outer tube. As yield stress is always nonnegative, the LHS of eq. (2.202) is always positive; whereas, the RHS is negative, since  $\xi \leq \lambda_i$ . To eliminate the inherent negativity, a minus sign is placed in front of the RHS parenthesis in eq. (2.202). Taking the  $1/n$ th power of each term, the differential velocity distribution

$$\frac{d\phi_v}{d\xi} = -T_0^s + (\lambda^2 - \xi^2)^s \xi^{-s} \quad \kappa < \xi < \lambda_i \quad (2.203)$$

is obtained where  $s = 1/n$ . In the outer deformation region  $\lambda_0 R \leq r \leq R$ , velocity decreases toward the outer wall making the velocity gradient negative. As the yield stress is a positive quantity, eq. (2.204) is obtained with a similar procedure, as above, for the outer region

$$-\frac{d\phi_v}{d\xi} = -T_0^s + (\xi^2 - \lambda^2)^s \xi^{-s} \quad \lambda_o < \xi < 1 \quad (2.204)$$

Integration of eqs. (2.203) and (2.204) with the boundary conditions of  $\phi_v(\kappa)$  at  $\xi = \kappa$  and  $\phi_v(1)$  at  $\xi = 1$  yield, respectively, eqs. (2.205) and (2.206) which still contain integral terms on their RHS which have to be solved numerically with any of the iterative solution techniques for known values of the rheological parameters and the ratio of the radii,  $\kappa$

$$\phi_v(\xi) = \phi_v(\kappa) + \int_{\kappa}^{\xi} (\lambda^2 - \xi^2)^s \xi^{-s} d\xi - \int_{\kappa}^{\xi} T_0^s d\xi \quad (2.205)$$

$$\phi_v(\xi) = \phi_v(1) + \int_{\xi}^1 (\xi^2 - \lambda^2)^s \xi^{-s} d\xi - \int_{\xi}^1 T_0^s d\xi \quad (2.206)$$

Before proceeding on with the solution techniques, an expression for a nondimensional flow rate  $Q^*$  has to be made starting with the definition of the flow rate  $Q$

$$Q = \pi(R^2 - \kappa^2 R^2) V_{av} = \left[ \pi(R^2 - \kappa^2 R^2) \frac{\int_{\kappa R}^R V_z 2\pi r dr}{\int_{\kappa R}^R 2\pi r dr} \right] \quad (2.207)$$

Replacing  $V_z$  by its nondimensional form  $\phi_v$  from eq. (2.200) and using nondimensional radii,  $\xi = r/R$ ,

$$\frac{Q}{\pi R^3 (R\Phi/2K)^s} = 2 \int_{\xi=\kappa}^{\xi=1} \phi_v(\xi) \xi d\xi \quad (2.208)$$

where the LHS of the equation is defined as the dimensionless flow rate  $Q^*$

$$Q^* = \frac{Q}{\pi R^3 (R\Phi/2K)^s} \quad (2.209)$$

$\phi_v$  from eqs. (2.205) and (2.206) must be replaced into eq. (2.208), to find the volumetric flow rate in the inner and outer deformation regions after the indicated integrations.

With the boundary conditions of eqs. (2.205) and (2.206), the region extends from an undefined arbitrary boundary  $\xi$ , to the inner and outer pipe wall, respectively, in these equations. If there is a plug flow region within the flow area it cannot be taken into account in this form. To integrate the shear surfaces at either sides of the plug flow region into the expression to be developed, the boundary conditions are initially replaced with  $\xi - \lambda$  and  $\lambda - \xi$  in eqs. (2.205) and (2.206), respectively. Here  $\lambda$  denotes the radial distance at which  $\tau_{rz} = 0$ . This distance can be a single plane where the velocity is maximum, or it may cover a radial range from  $\lambda_i$  to  $\lambda_o$  where the velocity is at its maximum value and  $\tau_{rz} = 0$  within a plug region depending on the relative magnitude of  $\Phi$  and  $T_0$ . Eqs. (2.205) and (2.206) with the new integration boundaries of  $\xi$  and  $\lambda$  are now placed into the integral at the RHS of eq. (2.208). The integration boundaries of eq. (2.208), in turn, are taken from  $\kappa$  to  $\lambda_i$  and  $\lambda_o$  to 1 for the two deformation regions, respectively. The resultant dimensionless flow rate equation still contains integral terms.

$$Q^* = \phi_v(\kappa)(\lambda_i^2 - \kappa^2) + \phi_v(1)(1 - \lambda_o^2) - \left(\frac{T_o^s}{3}\right)(1 + \kappa^3 - \lambda_i^3 - \lambda_o^3) \\ + T_o^s \lambda^2 (1 + \kappa - \lambda_i - \lambda_o) + \int_{\kappa}^{\lambda_i} (\lambda^2 - \xi^2)^{s+1} \xi^{-s} d\xi + \int_{\lambda_o}^1 (\xi^2 - \lambda^2)^{s+1} \xi^{-s} d\xi \quad (2.210)$$

To eliminate the integral terms in eq. (2.210), an alternative expression for  $Q^*$  may be obtained by integrating eq. (2.208) by parts as

$$Q^* = \phi_v(\xi) \xi^2 \Big|_{\kappa}^1 - \left[ \int_{\kappa}^1 \left( \frac{d\phi_v}{d\xi} \right) \xi^2 d\xi \right] \quad (2.211)$$

The integral covering plug flow is not included into this equation as the velocity gradient,  $d\phi_v/d\xi$  is assumed to be zero in this region. The dimensionless flow rate is

$$Q^* = \phi_v(1) - \phi_v(\kappa)\kappa^2 + \frac{T_o^s}{3}(\lambda_i^3 + \lambda_o^3 - \kappa^3 - 1) + \left(\frac{1}{2}\right)\left(\frac{1}{s+1}\right) \\ [(1 - \lambda^2)^{s+1} - \lambda_o^{1-s}(\lambda_o^2 - \lambda^2)^{s+1} + \lambda_i^{1-s}(\lambda^2 - \lambda_i^2)^{s+1} - \kappa^{1-s}(\lambda^2 - \kappa^2)^{s+1}] \\ - \left(\frac{1}{2}\right)\left(\frac{1-s}{s+1}\right) \left( \int_{\kappa}^{\lambda_i} (\lambda^2 - \xi^2)^s \xi^{-s} d\xi + \int_{\lambda_o}^1 (\xi^2 - \lambda^2)^{s+1} \xi^{-s} d\xi \right) \quad (2.212)$$

In this equation  $\phi_v(1)$  and  $\phi_v(\kappa)$  are the dimensionless velocities of the two walls and are equal to zero if the pipe walls are stationary. Since the integral terms in both eqs. (2.210) and (2.212) are in the same form, these equations are combined and

rearranged to obtain the analytical equation for the dimensionless volumetric flow rate of a fluid flowing through the annulus formed by two pipes moving with dimensionless velocities  $\phi_v(\kappa)$  and  $\phi_v(1)$

$$\begin{aligned} Q^* = & \phi_v(1) \left[ 1 - \left( \frac{1-s}{3+s} \right) \lambda_o^2 \right] + \phi_v(\kappa) \left[ \left( \frac{1-s}{3+s} \right) \lambda_i^2 - \kappa^2 \right] \\ & + \frac{T_o^s}{3} (\lambda_i^3 + \lambda_o^3 - \kappa^3 - 1) - \left( \frac{1-s}{3+s} \right) T_o^s \lambda^2 (\lambda_i + \lambda_o - \kappa - 1) \\ & + \left( \frac{1}{3+s} \right) \left[ (1 - \lambda^2)^{s+1} - \lambda_o^{1-s} (\lambda_o^2 - \lambda^2)^{s+1} + \lambda_i^{1-s} (\lambda^2 - \lambda_i^2)^{s+1} \right] \end{aligned} \quad (2.213)$$

When the pipe walls are stationary, eq. (2.213) is reduced to the form originally derived by Gücüyener and Mehmetoğlu (1992). This equation is also in agreement with that derived by Filip and David (2003) (eq. (41) in their paper) after redefining  $Q$  and setting the velocity of the outer pipe to zero. By setting the yield stress term  $T_o$  equal to zero, volumetric flow rate for power-law fluids is obtained in confirmation with Filip and David (2003) and Malik and Shenoy (1991). Fordham *et al.* (1991) derived similar equations for Herschel–Bulkley, Robertson–Stiff, and Casson models.

Eq. (2.213) interrelates flow parameters,  $Q^*$ ,  $\lambda$ ,  $\lambda_i$ ,  $\lambda_o$  and rheological parameters,  $T_o$ ,  $s$  ( $\equiv 1/n$ ). Eq. (2.194) written for the two shear surfaces of the plug flow region is equated, at inner and outer surfaces, respectively. Equating these two equations

$$\lambda^2 = \lambda_i \lambda_o \quad (2.214)$$

is obtained. Substituting  $\lambda^2$  from eq. (2.214) into eq. (2.194) written at the outer surface of the plug region,  $\lambda$  is eliminated and the plug width is related to the yield stress through

$$\lambda_i = \lambda_o - T_o \quad (2.215)$$

The velocities at the two surfaces ( $\lambda_i$  and  $\lambda_o$ ) of the plug flow region are assumed to be equal. Eqs. (2.205) and (2.206), giving dimensionless velocities, are rewritten for these plug surfaces by changing the integration boundaries to  $\kappa - \lambda_i$  and  $\lambda_o - 1$ , respectively, and equating to each other. The resulting equation in terms of  $\lambda_o$  is

$$\begin{aligned} & \int_{\kappa}^{\lambda_i} [(\lambda_o - T_o) \lambda_o - \xi^2]^s \xi^{-s} d\xi - T_o^s (\lambda_o - T_o - \kappa) + \phi_v(\kappa) \\ & = \int_{\lambda_o}^1 [\xi^2 - (\lambda_o - T_o) \lambda_o]^s \xi^{-s} d\xi - T_o^s (1 - \lambda_o) + \phi_v(1) \end{aligned} \quad (2.216)$$

For known values of  $\kappa$  (eq. (2.189)) and the yield stress  $T_o$  (eq. (2.201)) and flow behavior index  $n$  ( $\equiv 1/s$ ), this equation is solved by using any of the iteration methods.

Results of the numerical solution of eq. (2.216) in terms of  $\lambda_o = f(\kappa, n, T_o)$  for the case of stationary pipe walls are tabulated (see Appendix C) for Robertson–Stiff model by Güciyener and Mehmetoğlu (1992), and for Herschel–Bulkley model by Hanks (1979) for the evaluation of  $Q$  for a given  $\Delta P$ . The procedure for the design of laminar flow in annular channels by using these tables can be summarized as: For given rheological constants ( $n, K, \tau_o, \dot{\gamma}_o$ ), flow conditions ( $\Delta P$ ) and channel shape ( $\kappa$ ),  $\lambda_o$  is found from the tables.  $\lambda_i$  and  $\lambda$  are found from eqs. (2.215) and (2.214), respectively. Replacing these quantities in eq. (2.213), volumetric flow rate  $Q$  is found from the definition of  $Q^*$  in eq. (2.209). This type of solution is called the “direct” solution. Solution of the equation for  $\Delta P$  for a given  $Q$  is called an “inverse” solution. The results of such a solution by Fordham *et al.* (1991) is reproduced in Figure 2.21, where dimensionless pressure is plotted as a function of

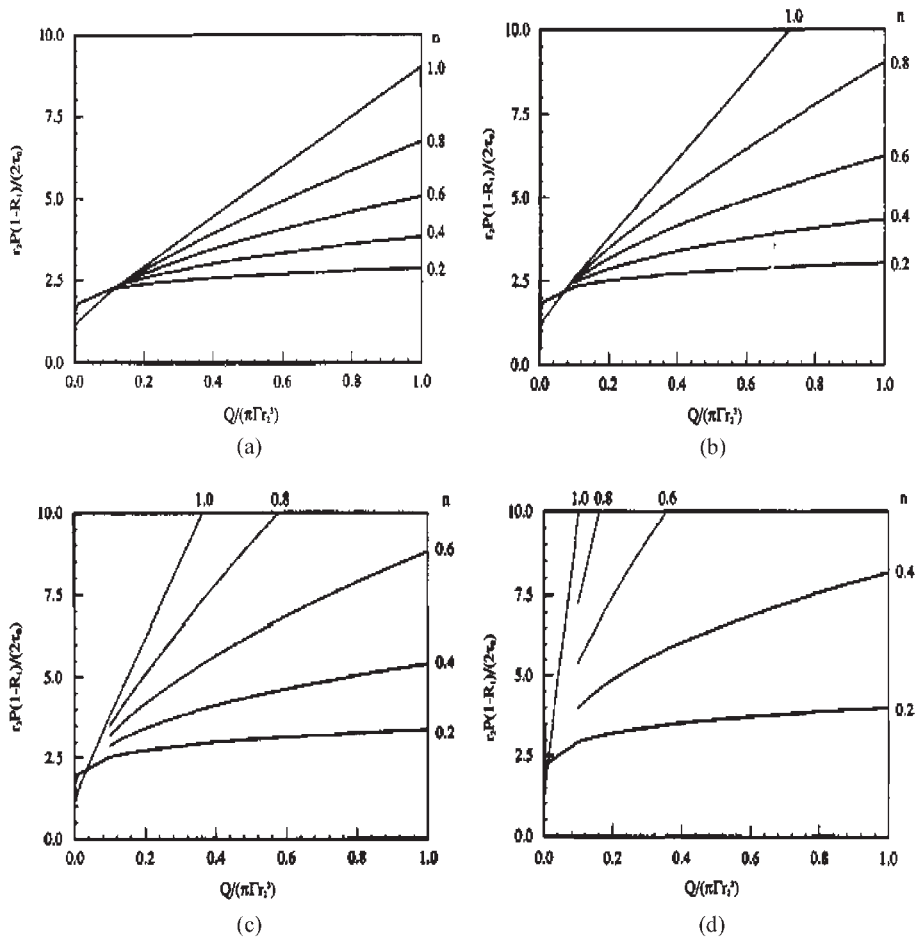


**Figure 2.21** Variation of dimensionless pressure with dimensionless flow rate in concentric annuli with  $\kappa$  equal to (a) 0.2, (b) 0.4, (c) 0.6, (d) 0.8 as a function of  $n$  values. (Fordham *et al.*, 1991. Figure 1 in the original, reproduced with permission of American Chemical Society.)

dimensionless flow rate, for different values of  $n$  and  $\kappa$ . The dimensionless pressure given as the ordinate of the plots,  $r_2 P(1 - R_1)/2\tau_0$  is equivalent to  $R(-dP/dz)(1 - \kappa)/2\tau_0 = (1 - \kappa)\tau_w/\tau_0$  with the notation of this book and inherently contains the yield stress  $\tau_0$  as a rheological parameter. The dimensionless flow rate,  $Q/(\pi\Gamma r_2^3)$  equivalent to  $Q/(\pi\Gamma R^3)$ , with the notation adopted here, inherently contains the shear rate, given as  $\Gamma$  in the general form. The value of  $\Gamma$  assumes the values

$$\Gamma^C = \frac{\tau_0}{\eta_0} \quad (2.217a)$$

$$\Gamma^{HB} = \left( \frac{\tau}{K} \right)^{1/n} \quad (2.217b)$$

$$\Gamma^{RS} = \dot{\gamma}_0 \quad (2.217c)$$

for the Casson, Herschel—Bulkley, and Robertson—Stiff models, respectively. The plots are given for the radii ratio  $\kappa = 0.2, 0.4, 0.6, 0.8$  in Figure 2.21(a)–(d), respectively. As the inner and outer pipes approach each other in diameter, that is, as the gap width decreases, the effect of flow behavior index,  $n$ , on pressure gradient increases. Pressure requirement for a given flow rate and diameter ratio decreases as  $n$  decreases because of a decrease in the apparent viscosity near the wall region that becomes more effective as the gap width decreases ( $\kappa$  increases).

#### 2.4.1.2 Flow through eccentric annuli

When the axis of the inner tube is displaced from the concentric position, the flow area varies in the azimuthal direction. The eccentricity is defined as the displacement of the axis of the inner pipe with respect to the outer pipe,  $d$ , scaled with the difference in the radii of the respective pipes

$$\varepsilon = \frac{d}{(R_o - R_i)} \quad (2.218)$$

The velocity and pressure variations concomitant with flow area variation result in a sequential change in the shear-dependent rheological behavior. Variation of fluid properties brought about along the azimuthal direction makes analytical solutions of mass and momentum balances possible only with thin slit approximations as  $\kappa \rightarrow 1$ . Such an analytical solution was made by Üner *et al.* (1988) approximating the annular area with a slit of variable height. Flow equations were derived for power-law, Bingham, and Sutterby models. A similar analytical treatment was made by Walton and Bittleston (1991) for flow of Bingham fluids through narrow-gap annular channels. Limitations on the gap width of annular channels and the need for information on the local values of shear stress and velocity for all values of radii ratio  $\kappa$  and eccentricity  $\varepsilon$  necessitates the use of numerical methods in flow analysis.



de Pina and Carvalho (2006) used lubrication approximation to solve the three-dimensional momentum conservation equations defining the flow of Newtonian fluids through an annulus with variable eccentricity and stationary walls. Their results showed that the ratio of maximum to the average velocity to decrease, the extent of secondary (vortex) flow in the wider section of the gap to increase and the pressure losses expressed as  $f \cdot Re$  to decrease as the eccentricity of the annulus is increased. For eccentricities less than 0.65, the radius ratio  $\kappa$  was found to have no effect on the ratio of maximum to average velocities.

Momentum equations for laminar flow of power-law fluids ( $0.2 \leq n \leq 1$ ) through eccentric annuli with annuli radius ratios in the range  $0.2 \leq \kappa \leq 0.8$  and inner pipe eccentricities in the range  $0 \leq \varepsilon \leq 0.8$  were numerically solved by Fang *et al.* (1999) using the method of finite differences. The variation of the velocity distributions with flow behavior index  $n$  were similar to those given in Figure 2.6(a): Flow rate varied in the azimuthal direction decreasing toward the narrow gap side and increasing toward the wider side. The maldistribution of flow rates increased with increasing eccentricity of the annulus. The plug-like velocity distributions observed in low values of  $n$ , coupled with increasing eccentricities cause the flow in the narrow gap side to be nearly stagnant, bringing with it the tendency of blockage. The combined effect of the geometrical parameters, radii ratio,  $\kappa$ , eccentricity,  $\varepsilon$ , and rheological property, flow behavior index  $n$ , on the pressure requirement for flow is given in Figure 2.22. In this figure,  $r^*$  and  $\varepsilon^*$  are equivalent to  $\kappa$  and  $\varepsilon$  with the notation of this book. Reynolds number in the  $f \cdot Re$  term is based on the

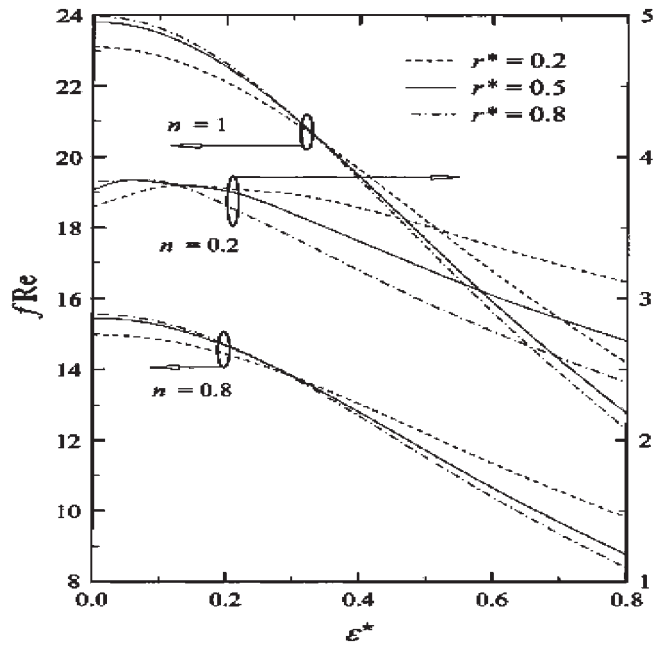


**Figure 2.22** Influence of annuli radius ratio  $r^*$ , eccentricity  $\varepsilon^*$  and flow behavior index  $n$  on the friction factor. (Fang *et al.*, 1999. Figure 8 in the original, reproduced with permission of Elsevier.)

hydraulic diameter of the annulus ( $D_h = 2(R_o - R_i)$ ) and the generalized viscosity expression for power-law fluids

$$Re = \frac{D_h \rho V_z}{K(V_z / D_h)^{n-1}} \quad (2.219)$$

Increased wall shear of power-law fluids cause the frictional losses to be less than the Newtonian fluids. The variation of the frictional losses of Newtonian fluids is more sensitive to increases in eccentricity than the power-law fluids. The circles around the groups of lines for a given  $n$ , indicate the critical eccentricities when the slope, or variation of pressure losses with the eccentricity becomes steeper.

#### 2.4.1.3 Helical flow in annuli

When the inner pipe rotates, while the outer pipe is stationary, the axial flow under an external force, such as a pressure gradient or gravity, follows a *helical* or *spiral* path. In addition to the Reynolds number, *Taylor number*  $Ta$

$$Ta = \left( \frac{\rho \omega}{\eta} \right)^2 R_o (R_o - R_i) \quad (2.220)$$

where  $\omega$  is the angular velocity of the inner cylinder also becomes effective. Escudier *et al.* (2002) generalized the results found by Fang *et al.* (1999) to helical flow through the ratio of velocities in the azimuthal and axial directions,  $\xi$  defined as

$$\xi = \frac{\omega R_i}{V} \quad (2.221)$$

The velocity ratio is related to the nondimensional shear rate  $\dot{\gamma}_F$  through,

$$\dot{\gamma}_F = \left( \frac{1}{2} \right) (1 + \xi^2)^{1/2} \quad (2.222)$$

The results of Fang *et al.* (1999) for stationary pipes are also relevant for  $\xi \leq 1$  when the effect of axial velocity on the direction of bulk flow is much greater than the effect of rotational velocity component. At high rotational velocities when  $\xi \geq 10$ ,  $f \cdot Re$  was found to depend on the recirculation region observed in the wider section of the gap at high rotational speeds and eccentricities greater than  $\varepsilon \geq 0.5$ .

Flow patterns in terms of axial velocity and streamlines in helical flow within concentric and eccentric annuli are obtained numerically by Hussain and Sharif (2000) using the finite volume technique in solving the momentum conservation equations. The results are reproduced in Figure 2.23 for eccentricities of  $\varepsilon = 0.25, 0.5, 0.75$  under a pressure gradient of  $25 \text{ Pa m}^{-1}$ , and rotational velocity of  $16.67 \text{ rad s}^{-1}$ ,  $\kappa = 0.5$  with  $R_o = 0.12 \text{ m}$ . The fluid was assumed to conform to power-law model with  $n = 0.75$  and  $K = 0.1 \text{ Pa s}^n$ .

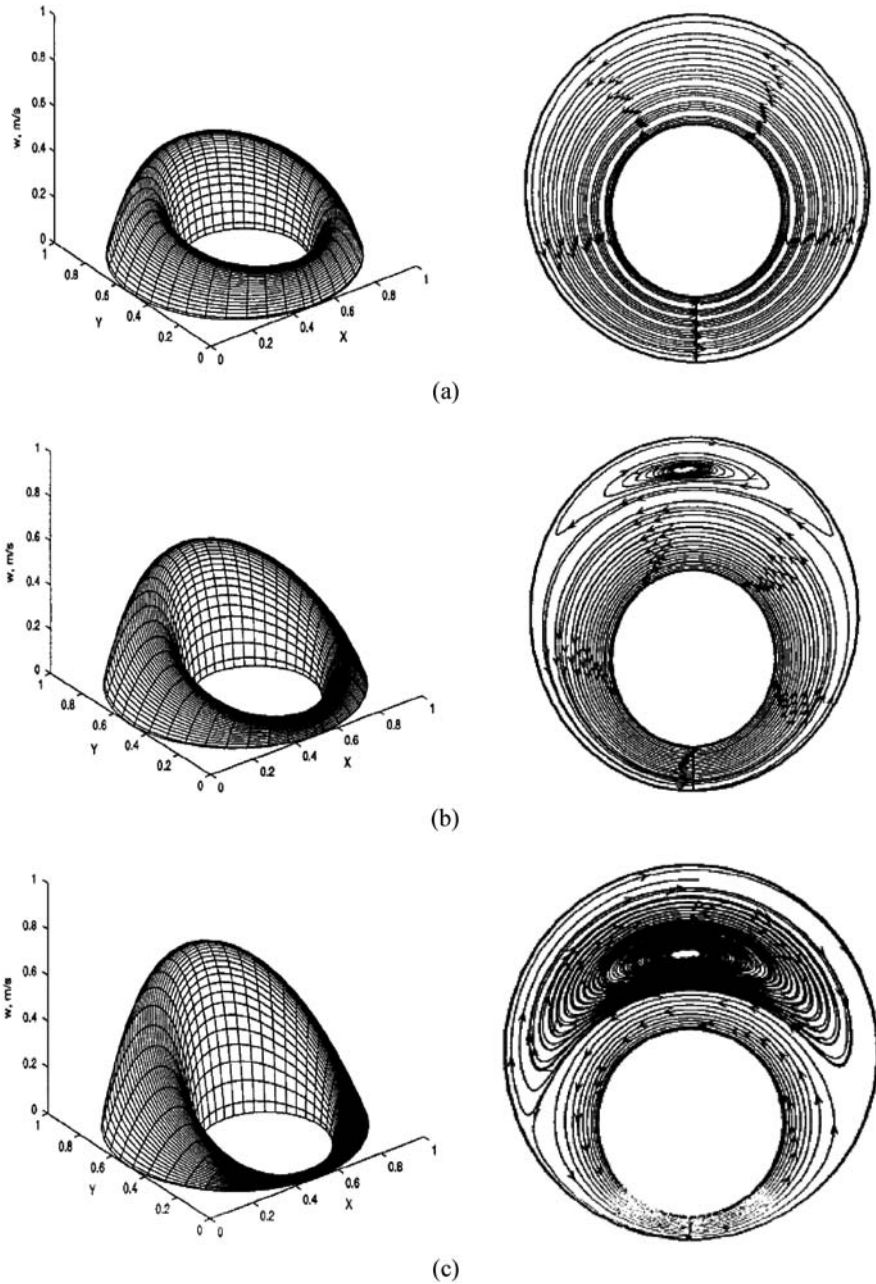


**Figure 2.23** Axial velocity distributions in the annulus for varying eccentricity and streamlines on the cross-sectional plane for varying eccentricity, (a)  $\varepsilon = 0.25$ , (b)  $\varepsilon = 0.5$ , (c)  $\varepsilon = 0.75$ ,  $P = 25 \text{ Pa m}^{-1}$ ,  $\omega = 16.67 \text{ rad s}^{-1}$ . (Hussain and Sharif, 2000. Figure 11 and 12 in the original, reproduced with permission of Taylor & Francis.)

The distortion of the velocity profiles in the azimuthal direction and enlargement of the recirculation zone at eccentricities greater than 0.5 are apparent in the figure.

As in the case observed with recirculation zones in sudden expansions (Section 2.3.3), the viscosity of the fluid becomes higher within the recirculation region in comparison with the high shear region around the inner rotating cylinder. As the volume fraction of fluid passing through the wider side of the gap is larger than that passing through the high shear zone, the friction factor increases. Only at very high values of the eccentricity or the rotational speed of the inner cylinder, do the velocities in the recirculation zone increase, leading to a decrease in the viscosities and the friction factor (Escudier *et al.*, 2002).

The effect of the flow behavior index is rather complicated in helical flow in parallel with the complexity of the flow. A decrease in  $n$  down to 0.6 increases the volumetric flow rate through the annulus. As  $n$  approaches very low values of around 0.2, the flattened velocity profiles stagnate the flow in the narrow section of the annulus and hinder the formation of recirculation patterns in the wider section.

## 2.4.2 Flow through rectangular channels

The parameters that control the flow of shear-thinning fluids are the Reynolds number, the height to width ratio (*aspect ratio*) of the channel, and the rheological parameters such as the flow behavior index, yield stress, and the normal stresses indicative of the viscoelasticity of the fluid. Literature on the flow of non-Newtonian fluids through noncircular channels is meager and fragmentary, and not all of the above parameters are fully investigated for any one rheological model.

### 2.4.2.1 Velocity distributions in rectangular channels

#### 2.4.2.1.1 Laminar flow

Velocity distribution in the laminar flow of yield stress fluids in square channels were found numerically by Huilgol and You (2005) by the application of the augmented Lagrangian method. Bingham, Casson, and Herschel–Bulkley models were investigated in this work. The results of the Herschel–Bulkley fluids with  $n = 0.75$  and  $n = 0.5$ , each at Oldroyd number,  $Od = \tau_0/[(\Delta P/L)R] = 0.2$  are reproduced in Figure 2.24 to show the effect of the flow behavior index,  $n$ . The almost circular inner contour constitutes the boundary of the plug flow zone. As the channel walls are approached, the contours become more rectangular in shape. A decrease in the flow behavior index  $n$  results in an extension of the plug flow zone at the center, with consequential steeper velocity gradients toward the walls, similar to cylindrical pipes.

As the Oldroyd number is increased, that is, either the yield stress is increased or the wall shear stresses are reduced, the plug zone at the center extends toward the corners. Similar to the case in sudden expansion (Figures 2.17–2.18), stagnant zones appear at the corners that extend in area as the Oldroyd number is increased.

The increase in the plug flow region and plug velocity in square pipes relative to that of cylindrical pipes of the same hydraulic diameter,  $D_h$ , were found to cause the average velocity to be greater in the former case.

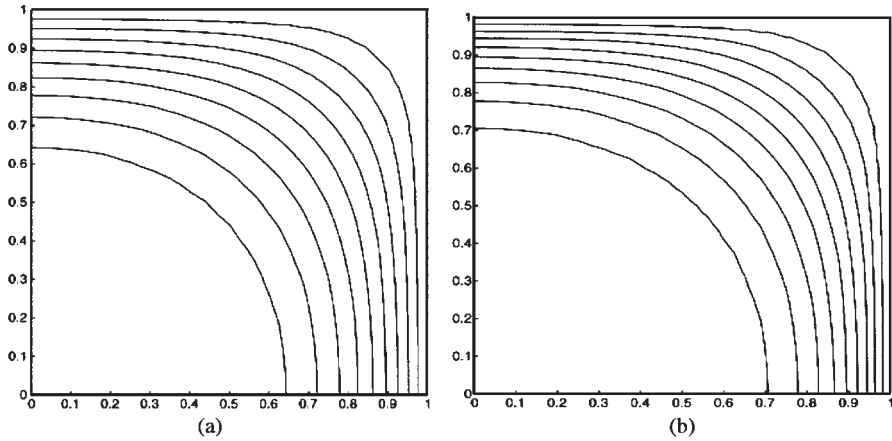


**Figure 2.24** Velocity contours in laminar flow of Herschel–Bulkley fluids in square pipes ( $Od = 0.2$ ) (a)  $n = 0.75$ , (b)  $n = 0.5$ . (Huigol and You, 2005. Figure 10 and 11 in the original, reproduced with permission of Elsevier.)

#### 2.4.2.1.2 Turbulent flow

Velocity distributions of shear-thinning fluids in turbulent flow are investigated experimentally by Escudier and Smith (2001). In experimental measurement of local velocity variations with the laser Doppler anemometer, requirement of transparency necessitates the use of polymers that introduce unavoidable complications of viscoelasticity in addition to shear thinning. The fluids used in this work, 0.1% w/w sodium carboxymethylcellulose (CMC) blended with an equal concentration of xanthan gum (XG), and 0.125% w/w polyacrylamide (PAA) showed both shear thinning and normal stresses representative of viscoelastic behavior. The rheological properties of the solutions were described by the Cross model. The equivalent power-law models at the inflection point of the flow curves, and the variation of normal stress ( $N_1$ ) with shear stress are given by  $\tau = 0.275\dot{\gamma}^{0.52}$ ,  $N_1 = 1.35\tau^{1.18}$  for the CMC/XG solution and  $\tau = 0.733\dot{\gamma}^{0.32}$ ,  $N_1 = 16.3\tau^{1.48}$  for the PAA solution, respectively.

The high values of the normal stress and the low values of the flow behavior index indicate that PAA is the more viscoelastic of the two solutions. The mean axial velocities scaled by the centerline velocity in each case are given in Figure 2.25 together with the velocity contours of water as the Newtonian fluid. These data were taken around the maximum Reynolds number that could be obtained in the channel, i.e.,  $Re^* = 43,000$ , 10,500, and 16,400 for water, CMC/XG, and PAA, respectively.  $Re^*$  is the Kozicki generalized Reynolds number defined as eq. (2.152) in Section 2.3.2.1. Momentum transport from the high velocity region at the center to the relatively stagnant regions at the corners cause secondary flows, which cause a diagonal distortion of the velocity contours. This motion is counteracted by the elasticity of the polymer solutions in proportion with the normal stresses generated as given in Figure 2.25(b) and (c). The plug flow region also extends as flow behavior index decreases, as in the case of laminar flow.

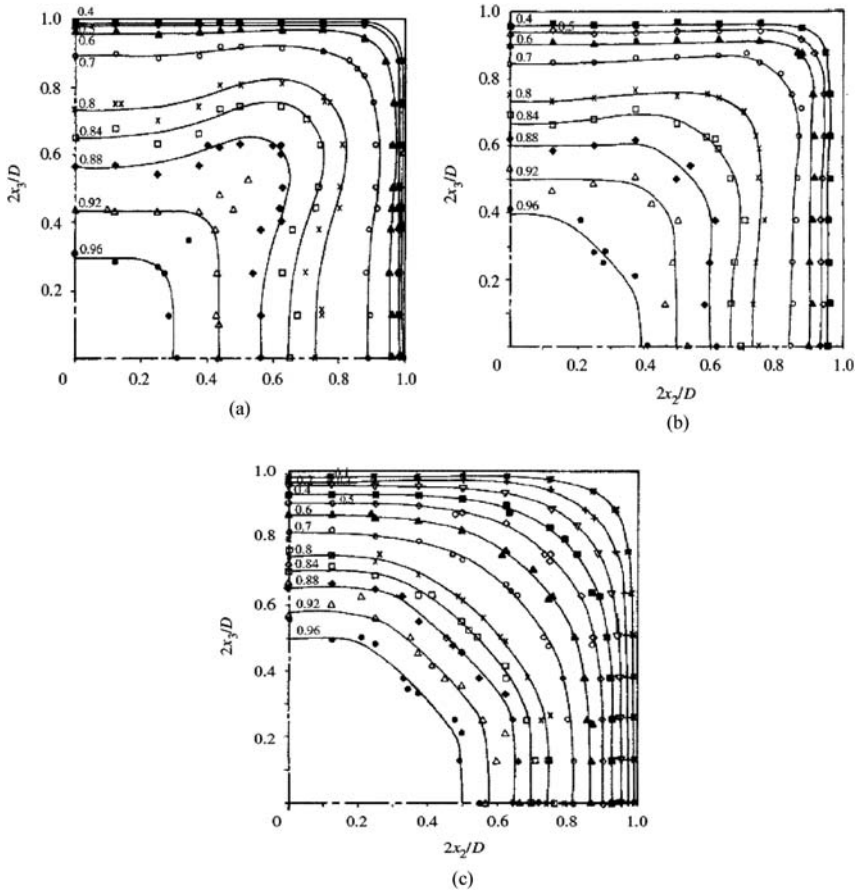


**Figure 2.25** Contours of mean axial velocity scaled by the centerline velocity in turbulent flow in square channels; (a) water, (b) CMC/XG, and (c) PAA. (Escudier and Smith, 2001. Figure 9 in the original, reproduced with permission of the Royal Society.)

The effect of the drag reduction at the channel walls is given by the experimentally determined boundary layer equations in the same work (Escudier and Smith, 2001): the velocity distribution of water are given by the equations

$$V_1^+ = y^+ \quad \text{for } y^+ < 10 \quad (2.223)$$

$$V_1^+ = 2.5 \ln y^+ + 5 \quad \text{for } y^+ > 10 \quad (2.224)$$

In the case of polymer solutions, the slope of the turbulent boundary layer equations were shown to increase in proportion with the degree of viscoelasticity and eq. (2.224) approach the asymptotic equation for drag reduction proposed by Virk *et al.* (1970)

$$V_1^+ = 11.7 \ln y^+ - 17 \quad (2.225)$$

A second proof of drag reduction at the wall was the reduction of the friction factors after the onset of turbulence as will be explicated below.

#### 2.4.2.2 Frictional losses in rectangular channels

Kozicki *et al.* (1966) proposed that the analog of Rabinowitsch–Mooney equation (eq. 2.114) could be applied to noncircular pipes with the introduction of two geometric parameters  $a$  and  $b$ .

$$\frac{8V_m}{D_h} = \frac{1}{a} \frac{1}{\tau_w^{b/a}} \int_0^{\tau_w} \tau_w^{(b/a)-1} f(\tau) d\tau \quad (2.226)$$

A practical method proposed by Mahfoud *et al.* (2005) which has good agreement with available correlations is obtained by taking the derivative of eq. (2.226)

$$\tau_w^{b/a} \frac{d(a8V_m/D_h)}{d\tau} + a \frac{8V_m}{D_h} \frac{b}{a} \tau_w^{(b/a)-1} = \tau_w^{(b/a)-1} f(\tau) \quad (2.227)$$

Rearrangement gives an expression for the function of shear stress at the wall

$$a\tau_w \frac{d(8V_m/D_h)}{d\tau_w} + b \frac{8V_m}{D_h} = f(\tau_w) \quad (2.228)$$

Eq. (2.226) in terms of maximum velocity were written as

$$\frac{8V_{\max}}{D_h} = \frac{1}{a} \frac{1}{\tau_w^{b/a}} \int_0^{\tau_w} f(\tau) d\tau \quad (2.229)$$

Taking the derivative of eq. (2.229) and rearrangement gives

$$a\tau_w \frac{d(8V_{\max}/D_h)}{d\tau_w} + a \frac{8V_{\max}}{D_h} = f(\tau_w) \quad (2.230)$$

Parameters  $a$  and  $b$  are independent of the rheological characteristics of the fluid and can be determined through the solution of eqs. (2.228) and (2.230)

$$a = \frac{\tau_w}{2\eta(8V_{\max}/D_h)} \quad (2.231a)$$

$$a + b = \frac{\tau_w}{2\eta(8V_m/D_h)} \quad (2.231b)$$

These parameters were experimentally determined by Mahfoud *et al.* (2005) through the measurement of pressure gradient,  $dP/dz$ , and  $V_{\max}$ , as a function of volumetric flow rate through rectangular tubes of aspect ratio (height/width of channel) 0.1 and 0.4.



Measurement of velocity at only a single point, at the centerline, by LDA is sufficient for the determination of the parameters. The parameters  $a$  and  $b$  can be determined from the slope of the pressure gradient versus volumetric flow rate and the maximum velocity for a given flow rate. These parameters are used in the general definition of the Reynolds number, eq. (2.152) in the correlations of friction factor, eq. (2.130) for laminar flow and Dodge–Metzner correlation (1959), eq. (2.181), for turbulent flow of inelastic power-law fluids in square channels as shown by Kostic and Hartnett (1987).

Appearance of elasticity reduces the friction factor in fully developed turbulent flow. Escudier and Smith (2001), experimentally showed that the friction factor of fluids with varying degrees of elasticity could be correlated with the general equation of Kostic and Hartnett (1987),

$$f = \frac{0.2}{Re^{*0.48}} \quad (2.232)$$

which is lower than the friction factor correlation of Blasius for Newtonian fluids in turbulent flow

$$f = \frac{0.0791}{Re^{*0.25}} \quad (2.233)$$

The peak value of  $f$  observed in the plot of friction factor  $f$  versus the generalized Reynolds number  $Re^*$  is taken to be an indication of the establishment of fully developed turbulence in Newtonian flow. Escudier showed that power-law fluids with varying degrees of elasticity show only a variation in slope from the linear plot, at the onset of turbulence. The peak value in the fluctuation intensity of axial flow, regarded to be an indication of the transition to turbulence (Park *et al.*, 1989), nearly coincides with the inflection of the friction factor. Experimental observations by Escudier and Smith (2001) showed that the flow is fully turbulent for  $Re^* > 7000$  for the polymer suspensions investigated.

### 2.4.3 Flow in microchannels

Channels with diameters of 1–1000  $\mu\text{m}$  are called microchannels. Microchannels are used along with miniaturized devices in developing microtechnologies as bioreactors and biological separations, biomedicine, micropower generation, micro-electromechanical systems (MEMS) covering communication and information systems, automotive, and aerospace. The increased efficiency in heat removal brought about by the high surface area to volume ratio of microchannels make them attractive in cooling of micro- and macro-electronic devices and other heat-exchange operations (Bayraktar and Pidugu, 2006). Development of manufacturing technologies of microchannels is still in its infancy stage, as are the underpinning technologies such as flow measurement.

Flow through a microchannels could be under a driving force of, (a) pressure gradient along the channel length, (b) electro-osmotic forces, (c) magnetic forces, or (d) surface forces.



Cross-sectional areas of microchannels can be of any geometrical shape, with varying aspect ratios. The minute dimensions of the microchannels causes parameters of negligible importance in the flow of non-Newtonian fluids in macrochannels to be a determining factor in this scale. As the manufacturing technologies are not fully developed, many parameters such as roughness cannot be kept under control for all of the materials from which the channels are manufactured. As a result, experimental results could be misinterpreted and relations that are not substantiated could be developed. This section will cover only those factors that are found to be effective in flow through microchannels.

#### 2.4.3.1 Flow under a pressure gradient

The Navier–Stokes equations are based on the assumption that fluids can be considered as a continuous medium, even though they are composed of individual molecules. This presumes that the dimensions of the molecules are negligible in comparison with the channel dimensions. In microchannels, where the channel dimensions may approach molecular scale, the Knudsen number,  $Kn = \lambda/L$  is taken as the criterion for deciding if the Navier–Stokes equations can be used.  $\lambda$  is the mean free path of the molecules, and  $L$ , a characteristic dimension of the microchannel. If  $Kn < 0.01$ , the fluid may be assumed as a continuum. This sets a limit to the dimensions of microchannels where the flow problems can be handled with conventional theories.

Considerable pressures are required to maintain flow in microchannels. Naturally, research effort is concentrated on pressure losses in flow through microchannels. Due to the very small diameter of the microchannels, the Reynolds numbers are quite low until very high velocities are approached. As in this stage of development only the flow of Newtonian fluids are considered, the friction factors, or equivalently,  $f \cdot Re$  compared with their equivalents in the macro size. Evaluation of correct pressure gradients required for flow depends on elimination of error due to parameters often overlooked in macro scale. These are the entrance effects, wall roughness scale, correct diameter assessment, slip, pressure measurement, flow rate determination, viscous dissipation, and pressure dependence of thermophysical properties.

Entrance effects arise due to variation of the velocity profiles along the entrance length until a fully developed velocity profile is established. The entrance length,  $L_e$ , is correlated with the diameter of the tube,  $D$ .

$$\frac{L_e}{D} = 0.055 Re \quad (2.234)$$

The Reynolds number is based on the inlet (average) velocity and the physical properties of the Newtonian fluid. At Reynolds numbers close to transition to turbulence, entrance length is around a hundred diameters, which represents a considerable fraction of the total pressure difference across the tube length in view of the short lengths of microchannels. The friction factor relation given by Shah and London (1978) is

$$f \cdot Re \approx \frac{3.44}{(\zeta)^{1/2}} + \frac{f_p Re + K_\infty / 4\zeta - 3.44(\zeta)^{1/2}}{1 + c/\zeta^2} \quad (2.235)$$

The Reynolds number is based on hydraulic diameter of the channel,  $D_h$ , average velocity at the entrance and physical properties. In this equation  $f_p Re = 14.23$ ,  $K_\infty = 1.43$ ,  $c = 0.00029$ , and  $\zeta = (z/D_h)/Re$  and  $z$  is the axial distance from the inlet. Not taking the entrance length into account, may be misleadingly interpreted as an early transition to turbulence (Kohl, 2005). Celata *et al.* (2006) took the entrance effects into account by using two tubes of different lengths and estimating the pressure gradient from the difference in pressure differences measured for the two tubes.

Accounting for losses outside of the channel could be another source of error in the measurement of pressure differences. This problem was successfully handled by Kohl *et al.* (2005) by integrating tap lines and pressure sensing membranes into a system of silicon chips, thus, measuring the pressure within the channel.

Roughness could be a factor in determining the frictional losses in the length scale of microchannels. However, deviation of the pipe perimeter from circularity is more effective in increasing  $f$  than roughness (Shah and London, 1978). With the existing procedures in manufacturing technology, it may be difficult to identify the roughness scale from the deviations in the geometry for different materials, and maintain uniformity in roughness scale. Therefore, any correlations with the roughness scale should be approached with caution. Similarly, incorrect measurements of diameter could be another source of error (Xu *et al.*, 2000)

In this scale, flow measurement could also introduce inaccuracies if evaporation cannot be controlled. The slip effect, which could be attributed to wall surface phenomena, is shown to be not the case. Celata *et al.* (2006) showed that slip is due to the lubrication effect of air bubbles of nanometer size range by eliminating the effect through using degassed water. The minimum diameter used in this work was  $70\mu\text{m}$ . The effect of surface forces at the lower limits of size range  $D \leq 50\mu\text{m}$  is yet to be discovered.

An effect, totally disregarded in flow through macroscale pipes is the effects of heat released by viscous dissipation and more important still is the transfer rate of this heat. As long as the released heat can be transferred away from the generation sight, the effect can be tolerated. Otherwise the rise in temperature affects the local viscosity and the friction factor through variations in the Reynolds number (Judy *et al.*, 2002; Koo and Kleinstreuer, 2004; Celata *et al.*, 2006).

High pressures are employed to maintain flow in microchannels. Pressure dependence of thermophysical properties might be considered under ultrahigh pressures. Specifically an increase in the viscosity due to high pressures may decrease  $f \cdot Re$  (Judy *et al.*, 2002).

Experiments in which the above sources of error are taken into consideration (Xu *et al.*, 2000; Judy *et al.*, 2002; Kohl, *et al.* 2005; Celata *et al.*, 2006) showed that there is no difference between micro and macro sized channels in terms of mechanism of momentum transfer. This is reflected as the validity of eq. (2.235) for the Fanning friction factor, and the same range ( $\approx 2000$ ) of critical Reynolds numbers for transition to turbulence.

#### 2.4.3.2 Velocity distributions in microchannels

Three different techniques for velocity measurement are developed to measure the velocities in microchannels:

Infrared thermal velocimetry (ITV) (Chung *et al.*, 2003) makes use of the transparency of silicon to infrared radiation. An infrared laser heats the flowing fluid in a silicon

microchannel and the thermal image of the heated moving liquid is used to determine the average velocity. Velocity distributions cannot be determined with this method and effect of temperature rise on the flow characteristics remains to be evaluated.

Particle image velocimetry (PIV), uses 200 nm diameter flow-tracing particles, a pulsed Nd:YAG laser, epi-fluorescent microscope, and a camera to record high-resolution particle image fields (Meinhart *et al.*, 1999; Li and Olsen, 2006). The spatial resolution of the PIV technique by the diffraction-limited resolution of the recording system. Measurements showed an agreement within 2% with the theoretical calculations.

Particle tracking velocimetry (PTV) uses the principle of electro-osmotic flow (Devasenathipathy and Santiago, 2002) in conjunction with PIV to measure velocity distributions in microchannels.

Techniques of flow measurement in microchannels have only been developed recently, so no parametric investigation of effects on the velocity distribution in microchannels could be done yet.

#### 2.4.4 Flow in open channels

The most widespread application of open channels is mudflows in constructed and natural trenches. Therefore, in the models developed for flow in open channels, the flowing fluid is taken as a clay–water mixture without the sedimenting debris usually dragged along with the mudflow (Coussot and Proust, 1996; Piau, 1996; Mei and Yuhi, 2001; Balmforth and Liu, 2004). Under these conditions, mud acts as a yield-plastic fluid that can be modeled with Bingham or Herschel–Bulkley equations.

Generally, the channel shape is given by a power-law relationship where the height of the channel,  $h$ , varies as

$$h = W y^m \quad (2.236)$$

where  $W$  is a scale parameter that indicates the steepness of the banks, and exponent  $m$  sets the shape of the channel. The origins,  $y = 0$ , is the centerline and  $h = 0$  is the base of the channel. When,  $m = 0$ , the open channel is a flat bed with a depth  $W$ , of flowing mud.  $m = 1$ , denotes a triangular channel and  $m = 2$ , a parabolic basin.

Flow in open channels differs from that in the previous channels in having a free surface open to the atmosphere. The velocity is a maximum with respect to the variation along the depth of the channel. Because of the limited width of the channel, a velocity gradient also exists in the  $y$ -direction along the width of the channel, giving the flow profile a tongue shape as in Figure 2.26. The arrows indicate the velocity at a distance  $\Delta y$  from the bank walls where the local velocity is equal to the length of the arrows. The velocity distribution profile can also be envisaged as a velocity profile in closed channels, sliced longitudinally at the center.

Since the channel is open to the atmosphere, flow is possible only under gravitational acceleration. The channel contents can flow under steady-state conditions provided the slope of the channel is sufficient for the resulting wall shear stress, to overcome the yield stress of the fluid. As pressure is not a parameter in open channel flow, deformation is

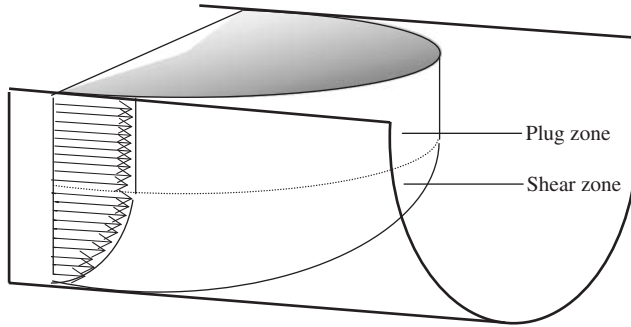


**Figure 2.26** Velocity profile in an open channel with vertical side walls and a parabolic basin.

dictated by the slope of the channel ( $\tan\theta$ ) in the flow direction and the height of the fluid in the channel. The critical height of mud slurry to start the flow,  $h_c$ , is given as

$$h_c = \frac{\tau_0}{\rho g \sin \theta} \quad (2.237)$$

This equation can be nondimensionalized by scaling with a characteristic dimension  $H$ , which could be defined as the height of a mud layer at the entrance (Mei and Yuhi, 2001). For steady flow, the height of the slurry should be larger than  $h_c$ .

Maximum velocity at the free surface is equivalent to zero-shear stress. A plug layer forms at the surface, given as the constant velocity region in Figure 2.26. The thickness of this layer is a function of  $\tau_w$  and  $\tau_0$ , which in turn depend on the slope of the channel and the solid content of the slurry, respectively. If the side walls of the channel deviate from the vertical, pockets of relatively stagnant fluid form between the plug layer and the side walls (banks), since the depth of fluid in this region is not sufficient to develop wall shear stresses greater than the yield stress. The existence of these regions keeps the plug layer intact and stabilizes the flow against small disturbances.

In shallow channels where the depth of the mud is not sufficient to sustain flow, the mud slurry is almost stagnant. If mud is surged into this channel, as in an outbreak, mud slurry advances in the form of roll waves along the channel. Similar waves also develop in steep channels at high volumetric flow rates of slurry. This issue is closely related with the concept of the yield stress phenomena given in Section 2.2.2. The three concepts of yield stress assume complete rigidity, plastic or elastic behavior with a high viscosity below the yield value, given by eqs. (2.42), (2.44), and (2.45), respectively. The capability of the plug layer in offsetting these roll waves depends on the rigidity of non-Newtonian fluids below the yield stress. In case elastic behavior below the yield value is accepted to be valid, then normal stresses are expected to evolve on straining this layer, such as in the case of a rough basin, or elongation of the surface layer on a sudden change of slope. The normal stresses can then contribute to increasing the stress level of the surface layer above the yield stress to obtain a deformable plug film. Elasticity may also help to restore the stability and prevent fracture formation in the plug layer.

How the system behaves depends very much on the composition of the mud and existing surface forces among the particles making up the slurry as will be taken up in Chapter 3.

## REFERENCES

- Alves, M.A., Oliveira, P.J., Pinho, F.T., 2004. On the effect of contraction ratio in viscoelastic flow through abrupt contractions. *Journal of Non-Newtonian Fluid Mechanics*, 122, 117–130.
- Aral, B.K., Kalyon, D.M., 1997. Viscoelastic material functions of noncolloidal suspensions with spherical particles. *Journal of Rheology*, 41(3), 599–619.
- Balmforth, N.J., Liu, J.J., 2004. Roll waves in mud. *Journal of Fluid Mechanics*, 519, 33–54.
- Başkurt, O.K., Tugral, E., Neu, B., Meiselman, H.J., 2002. Particle electrophoresis as a tool to understand the aggregation behavior of red blood cells. *Electrophoresis*, 23, 2103–2109.
- Bayraktar, T., Pidugu, S.B., 2006. Characterization of liquid flows in microfluidic systems. *International Journal of Heat and Mass Transfer*, 49, 815–824.
- Beşün, N., Peker, S., Köktürk, U., Yılmaz, H., 1996. Structure of starch-bentonite gels. *Colloid Polymer Science*, 275, 378–389.
- Bingham, E.C., 1922. *Fluidity and Plasticity*, McGraw-Hill, New York, 215.
- Bird, R.B., Dotson, P.J., Johnson, N.L., 1980. Polymer solution rheology based on finitely extensible bead-spring chain model. *Journal of non-Newtonian Fluid Mechanics* 7, 213–235.
- Bogue, D.C., Metzner, A.B., 1963. Velocity profiles in turbulent pipe flow: Newtonian and non-Newtonian fluids. *Industrial and Engineering Chemistry Fundamentals*, 2, 143–149.
- Carreau, J.P., DeKee, D., Daroux, M., 1979. Analysis of the viscous behavior of polymeric solutions. *Canadian Journal of Chemical Engineering*, 57(2), 135–140.
- Casson, N., 1959. A flow equation for pigment-oil suspensions of the printing ink type. In: *Rheology of Dispersed Systems* (ed. C. C. Mill), Pergamon Press, New York, 84–104.
- Celata, G.P., Cumo, M., McPhail, S., Zummo, G., 2006. Characterization of fluid dynamic behavior and channel wall effects in microtube. *International Journal of Heat and Fluid Flow*, 27, 135–143.
- Chhabra, R.P., Richardson, J.F., 1999. *Non-Newtonian Flow in the Process Industries*, Butterworth-Heinemann, Oxford. Chapter 3.
- Chilton, R.A., Stainsby, R., 1998. Pressure loss equations for laminar and turbulent non-Newtonian pipe flow. *Journal of Hydraulic Engineering*, 124(5), 522–529.
- Chung, J., Grigoropoulos, C.P., Greif, R., 2003. Infrared thermal velocimetry for nonintrusive flow measurement in silicon microfluidic devices. *Review of Scientific Instruments*, 74, 2911–2917.
- Clapp, R.M., 1961. Turbulent heat transfer in pseudoplastic non-Newtonian fluids. *International Developments in Heat Transfer, ASME Part III, Section A*, 652.
- Coussot, P., Proust, S., 1996. Slow, unconfined spreading of a mudflow. *Journal of Geophysical Research*, 101(B11), 25, 217–25, 230.
- Cross, M.M., 1965. Rheology of non-Newtonian fluids: A new flow equation for pseudoplastic systems. *Journal of Colloid Science*, 20, 417–437.
- Cruz, D.O.A., Pinho, F.T., Oliveira, P.J., 2005. Analytical solution for fully developed laminar flow of some viscoelastic liquids with a Newtonian solvent contribution. *Journal of non-Newtonian Fluid Mechanics*, 132, 28–35.
- de Pina, E.P.F., Carvalho, M.S., 2006. Three-dimensional flow of a Newtonian liquid through an annular space with axially varying eccentricity. *Journal of Fluids Engineering, Transactions of the ASME*, 128, 223–231.
- Devasenathipathy, S., Santiago, J.G., 2002. Particle tracking techniques for electrokinetic microchannel flows. *Analytical Chemistry*, 74, 3704–3713.

- Dodge, D.W., Metzner, A.B., 1959. Turbulent flow of non-Newtonian fluids. *AIChE Journal*. American Institute of Chemical Engineers, 5, 189–203.
- Escudier, M.P., Oliveira, P.J., Pinho, F.T., 2002. Fully developed laminar flow of purely viscous non-Newtonian liquids through annuli, including the effect of eccentricity and inner cylinder rotation. *International Journal of Heat and Fluid Flow*, 23, 52–73.
- Escudier, M.P., Poole, R.J., Presti, F., Dales, C., Nouar, C., Desaubry, C., Graham, L., Pullum, L., 2005. Observations of asymmetrical flow behaviour in transitional pipe flow of yield-stress and other shear-thinning liquids. *Journal of Non-Newtonian Fluid Mechanics*, 127, 143–155.
- Escudier, M.P., Presti, F., 1996. Pipe flow of a thixotropic liquid. *Journal of Non-Newtonian Fluid Mechanics*, 62, 291–306.
- Escudier, M.P., Smith, S., 2001. Fully developed turbulent flow of non-Newtonian liquids through a square duct. *Proceedings of the Royal Society of London Series A*, 457, 911–936.
- Etemad, S.G., 2004. Turbulent flow friction loss coefficients of fittings for purely viscous non-Newtonian fluids. *International Communications in Heat and Mass Transfer*, 31(5), 763–771.
- Fang, P., Manglik, R.M., Jog, M.A., 1999. Characteristics of laminar viscous shear-thinning fluid flows in eccentric annular channels. *Journal of Non-Newtonian Fluid Mechanics*, 84, 1–17.
- Filip, P., David, J., 2003. Axial Couette-Poiseuille flow of power-law viscoplastic fluids in concentric annuli. *Journal of Petroleum Science and Engineering*, 40, 111–119.
- Fordham, E.J., Bittleston, S.H., Tehrani, M.A., 1991. Viscoplastic flow in centered annuli, pipes and slots. *Industrial and Engineering Chemistry Research*, 30, 517–524.
- Güçüyener, H.I., Mehmetoğlu, T., 1992. Flow of yield-pseudo-plastic fluids through a concentric annulus. *AIChE Journal*. American Institute of Chemical Engineers, 38, 1139–1143.
- Hammad, K.J., Vradis, G.C., Ötügen, M.V., 2001. Laminar flow of a Herschel–Bulkley fluid over an axisymmetric sudden expansion. *Journal of Fluid Engineering*. Transactions of the American Society of Mechanical Engineers, 123, 588–594.
- Hanks, R.W., 1963. The laminar-turbulent transition for fluids with a yield stress. *AIChE Journal*. American Institute of Chemical Engineers, 9, 306–309.
- Hanks, R.W., 1978. In: *Proceedings of 5th International Conference on the Hydraulic Transport of Solids in Pipes (Hydrotransport 5)*, Paper C2, BHRA, UK.
- Hanks, R.W., 1979. The axial laminar flow of yield-pseudoplastic fluids in a concentric annulus. *Industrial and Engineering Chemistry Process Design and Development*, 18, 488–493.
- Herschel, W.H., Bulkley, R., 1926a. Measurement of consistency as applied to rubber–benzene solutions. *Proceedings of the American Society of Testing Materials*, 26, 621.
- Herschel, W.H., Bulkley, R., 1926b. Konsistenzmessungen von Gummi-Benzol-Lösungen, *Kolloid-Zeitschrift*, 39, 291–300.
- Holland, F.A., Bragg, R., 1995. *Fluid Flow for Chemical Engineers*, Edward Arnold, London (2nd edition.).
- Huilgol, R.R., You, Z., 2005. Application of the augmented Lagrangian method to steady pipe flows of Bingham, Casson and Herschel–Bulkley fluids. *Journal of Non-Newtonian Fluid Mechanics*, 128, 126–143.
- Hussain, Q.E., Sharif, M.A.R., 2000. Numerical modeling of helical flow of pseudoplastic fluids. *Numerical Heat Transfer, Part A*, 38, 225–241.
- Judy, J., Maynes, D., Webb, B.W., 2002. Characterization of frictional pressure drop for liquid flows through microchannels. *International Journal of Heat and Mass Transfer*, 45, 3477–3489.
- Kohl, M.J., Abdel-Khalik, S.I., Jeter, S.M., Sadowski, D.L., 2005. An experimental investigation of microchannel flow with internal pressure measurements. *International Journal of Heat and Mass Transfer*, 48, 1518–1533.
- Kök, M.V., Alikaya, V., 2005. Effect of polymers on the rheological properties of KCl/polymer type drilling fluids. *Energy Sources*, 27(5), 405–415.

- Koo, J., Kleinstreuer, C., 2004. Viscous dissipation effects in microtubes and microchannels. *International Journal of Heat and Mass Transfer*, 47, 3159–3169.
- Kostic, M., Hartnett, J.P., 1987. Pressure drop and heat transfer in viscoelastic duct flow—a new look. In: *Fundamentals of Convection in Non-Newtonian Fluids* (eds. J.L.S. Chen, T.M. Ehmman, G.P. Petersen), ASME, New York.
- Kozicki, W., Chou, C.H., Tiu, C., 1966. Non-Newtonian flow in ducts of arbitrary cross sectional shape. *Chemical Engineering Science*, 21, 665–679.
- Kozicki, W., Tiu, C., 1971. Improved parametric characterization of flow geometries. *Canadian Journal of Chemical Engineering*, 49(October), 562–569.
- Lam, C.K.G., Bremhorst, K.A., 1981. Modified form of the  $k$ - $\epsilon$  model for predicting wall turbulence. *Journal of Fluids Engineering*, 103, 456–460.
- Li, C., Mosyak, A., Hetsroni, G., 1999. Direct numerical simulation of particle-turbulence interaction. *International Journal of Multiphase Flow*, 25, 187–200.
- Li, H., Olsen, M.G., 2006. MicroPIV measurements of turbulent flow in square microchannels with hydraulic diameters from 200  $\mu\text{m}$  to 640  $\mu\text{m}$ . *International Journal of Heat and Fluid Flow*, 27, 123–134.
- Macosko, C.W., 1994. *Rheology Principles, Measurements and Applications*. VCH Publishers, New York.
- Madhav, M.T., Malin, M.R., 1997. The numerical simulation of fully developed duct flow. *Applied Mathematical Modelling*, 21, 503–507.
- Mahfoud, M., Benhadid, S., Lebouche, M., 2005. Frottements et pertes de pression des fluides non newtoniens dans des conduites non circulaires. *Comptes Rendus Mecanique*, 333, 513–520.
- Malik, S., Shenoy, U.V., 1991. Generalised annular Couette flow of a power law fluid. *Industrial and Engineering Chemistry Research*, 30, 1950–1954.
- Malin, M.R., 1997. The turbulent flow of Bingham plastic fluids in smooth circular tubes. *International Communications in Heat and Mass Transfer*, 24(6), 793–804.
- Malin, M.R., 1998. Turbulent pipe flow of Herschel-Bulkley fluids. *International Communications in Heat and Mass Transfer*, 25(3), 321–330.
- Matas, F.P., Morris, J.F., Guazzelli, E., 2003. *Philosophical Transactions of the Royal Society of London Series A*, 361, 911–919.
- Mei, C.C., Yui, M., 2001. Slow flow of a Bingham fluid in a shallow channel of finite width. *Journal of Fluid Mechanics*, 431, 135–159.
- Meinhart, C.D., Wereley, S.T., Santiago, J.G., 1999. PIV measurements of a microchannel flow. *Experiments in Fluids*, 27, 414–419.
- Metzner, A.B., 1965. Heat transfer in non-Newtonian fluids. In: *Advances in Heat Transfer*, 2nd edn. (eds. T.F. Irvine Jr., J.P. Hartnett), Academic Press, New York, 357.
- Metzner, A.B., Reed, J.C., 1955. Flow of non-Newtonian fluids—correlation of the laminar, transition, and turbulent-flow regions. *AIChE Journal. American Institute of Chemical Engineers*, 1(4), 434–440.
- Mooney, M.J., 1931. Explicit formulas for slip and fluidity. *Journal of Rheology*, 2, 210–222.
- Mosolov, P.P., Miasnikov, V.P., 1965. Variational methods in the theory of the fluidity of a viscous-plastic medium. *Journal of Applied Mathematics and Mechanics*, 29, 545–577.
- Moyers-Gonzales, M.A., Frigaard, I.A., 2004. Numerical solution of duct flows of multiple viscoplastic fluids. *Journal of Non-Newtonian Fluid Mechanics*, 122, 227–241.
- Nunez-Santiago, M.C., Santoyo, E., 2003. Rheological evaluation of non-Newtonian Mexican nixtamalized maize and dry processed masa flours. *Journal of Food Engineering*, 60, 55–66.
- Oliveira, P.J., 1992. Computer modelling of multidimensional multiphase flow and application to T-junctions. PhD Thesis, Imperial College, University of London.
- Oliveira, P.J., Pinho, F.T., 1999. Analytical solution for fully developed channel and pipe flow of Phan-Thien-Tanner fluids. *Journal of Fluid Mechanics*, 387, 271–280.



- Ooi, Y.W., Sridhar, T., 2004. Resistance to uniaxial extensional flow of fibre suspensions. *Rheologica Acta*, 43, 223–231.
- Papanastasiou, T.C., 1987. Flows of materials with yield. *Journal of Rheology*, 31(5), 385–404.
- Papanastasiou, T.C., 1994. *Applied Fluid Mechanics*. PTR PrenticeHall, USA.
- Park, J.T., Mannheimer, R.J., Grimmley, T.A., Morrow, T.B., 1989. Pipe flow measurement of a transparent non-Newtonian slurry. *Journal of Fluids Engineering*, 111, 331–336.
- Peixinho, J., Nouar, C., Desaubry, C., Theron, B., 2005. Laminar, transitional and turbulent flow of yield stress fluid in a pipe. *Journal of Non-Newtonian Fluid Mechanics*, 128, 172–184.
- Phan-Thien, N., Tanner, R.I., 1977. A new constitutive equation derived from network theory. *Journal of non-Newtonian Fluid Mechanics*, 387, 271–280.
- Phan-Thien, N., 1978. A non-linear network viscoelastic model. *Journal of Rheology*, 22, 259–283.
- Piau, J.M., 1996. Flow of a yield stress fluid in a long domain. Application to flow on an inclined plane. *Journal of Rheology*, 40, 711–723.
- Pinho, F.T., Oliveira, P.J., Miranda, J.P., 2003. Pressure losses in the laminar flow of shear-thinning power-law fluids across a sudden axisymmetric expansion. *International Journal of Heat and Fluid Flow*, 24, 747–761.
- Pinho, F.T., Whitelaw, J.H., 1990. Flow of non-Newtonian fluids in a pipe. *Journal of Non-Newtonian Fluid Mechanics*, 34, 129–144.
- Poole, R.J., Escudier, M.P., 2004. Turbulent flow of viscoelastic liquids through an axisymmetric sudden expansion. *Journal of Non-Newtonian Fluid Mechanics*, 117, 25–46.
- Puma, G.L., Yue, P.L., 2001. A novel fountain photocatalytic reactor : Model development and experimental validation. *Chemical Engineering Science*, 56, 2733–2744.
- Puma, G.L., Yue, P.L., 2003. Modelling and design of thin-film slurry photocatalytic reactors for water purification. *Chemical Engineering Science*, 58, 2269–2281.
- Quemada, D., 1978. Rheology of concentrated disperse systems Parts 2 and 3. *Rheologica Acta*, 17, 632–642 and 643–653.
- Rabinowitsch, B., 1929. Ueber die viskosität und elastizität von solen. *Zeitschrift für Physikalische Chemie-Abteilung A*, 145, 1–26.
- Robertson, R.E., Stiff, H.A., 1976. An improved mathematical model for relating shear stress to shear rate in drilling fluids and cement slurries. *Society of Petroleum Engineers Journal*, 261(Feb), 31–36.
- Rudman, M., Blackburn, H.M., Graham, L.J.W., Pullum, L., 2004. Turbulent pipe flow of shear-thinning fluids. *Journal of Non-Newtonian Fluid Mechanics*, 118, 33–48.
- Rueb, C.J., Zukoski, C.F., 1997. Viscoelastic properties of colloidal gels, *Journal of Rheology*, 41(2), 197–218.
- Schlichting, H., 1955. *Boundary Layer Theory*, McGraw-Hill, New York.
- Schramm, G., 1994. *A Practical Approach to Rheology and Rheometry*, HAAKE, Karlsruhe, Germany.
- Seth, J.R., Cloitre, M., Bonnecaze, R.T., 2006. Elastic properties of particle pastes. *Journal of Rheology*, 50(3), 353–376.
- Shah, R.K., London, A.L., 1978. *Laminar Flow Forced Convection in Ducts: A Source Book for Compact Heat Exchanger Analytical Data*, Academic Press, New York.
- Shook, C.A., Roco, M.C., 1991. *Slurry Flow*. Butterworth-Heinemann, Oxford.
- Sisko, A.W., 1958. The flow of lubricating greases. *Industrial Engineering Chemistry*, 50, 1789–1792.
- Slatter, P.T., 1995. In: *Proceedings of the 8th Conference on Transport and Sedimentation of Solid Particles*, Prague, Czech Republic, A3.
- Slatter, P.T., 1996. Turbulent flow of non-Newtonian slurries in pipes. *Journal of Hydrology and Hydromechanics*, 44(1), 24–38.



- Surve, M., Pryamitsyn, V., Ganesan, V., 2006. Universality in structure and elasticity of polymer-nanoparticle gels. *Physical Review Letters*, 96(17), 177805.
- Tanner, R.I., Hailgol, R.R., 1975. Progress in experimental rheology. *Rheology Acta* 14, 959–962.
- Thomas, A.D., Wilson, K.C., 1987. New analysis of non-Newtonian turbulent flow-yield-power-law fluids. *Canadian Journal of Chemical Engineering*, 65(2), 335–338.
- Trouton, F.T., 1906. On the coefficient of viscous traction and its relation to that of viscosity. *Proceedings of the Royal Society of London Series A*, 77, 426–440.
- Turian, R.M., Ma, T.W., Hsu, F.L.G., Sung, D.J., 1998. Flow of concentrated non-Newtonian slurries: 1. Friction losses in laminar, turbulent and transition flow through straight pipe. *International Journal of Multiphase Flow*, 24(2), 225–242.
- Üner, D., Özgen, C., Tosun, I., 1988. An approximate solution for non-Newtonian flow in eccentric annuli. *Industrial and Engineering Chemistry Research*, 27, 698–701.
- Virk, P.S., Mickley, H.S., Smith, K.A., 1970. The ultimate asymptote and mean-flow structure in Toms' phenomenon. *Trans. Journal of Applied Mechanics. Transactions of American Society of Mechanical Engineers*, 37, 488–493.
- Vlasak, P., Chara, Z., 2004. Laminar and turbulent transition of fine-grained slurries. *Particulate Science and Technology*, 22, 189–200.
- Vradis, G.C., Otügen, V., 1997. The axisymmetric sudden expansion flow of a non-Newtonian viscoplastic fluid. *Journal of Fluids Engineering*, 119(1), 193–200.
- Walton, I.C., Bittleston, S.H., 1991. The axial flow of a bingham plastic in a narrow eccentric annulus. *Journal of Fluid Mechanics*, 222, 39–60.
- Xu, B., Ooi, K.T., Wong, N.T., Choi, W.K., 2000. Experimental investigation of flow friction for liquid flow in microchannels. *International Communications in Heat and Mass Transfer*, 27, 1165–1176.
- Yasuda, K., Armstrong, R.C., Cohen, R.E., 1981. Shear flow properties of concentrated solutions of linear and star branched polystyrenes. *Rheologica Acta*, 20, 163–178.

# – 3 –

## Concentrated Suspensions

---

Concentrated suspensions have an immense significance, not only in the classical technologies, but also in the emerging technologies as well as in biological systems. In the classical technologies paints, coatings, cement slurries, coal slurries, mineral tailings, ceramic oxides, drugs, and food materials are only a few of the many diverse applications. Microstructure and flow behavior of concentrated suspensions is an underpinning science for nanotechnologies covering a wide scope of applications from electronics to “intelligent” materials. The aggregation and flow behavior of blood, a concentrated suspension, sustains the functioning of all organs.

The aim of this chapter is twofold: The first is to show how the surface forces reviewed in Chapter 1 affect the non-Newtonian behavior of solid–liquid suspensions, with the aim of having a deeper understanding of the rheological phenomena introduced in Chapter 2. The second aim is to show how an increase in the volume fraction of the solids affects the microstructure of the suspension and its rheology.

### 3.1 ORDERING IN CONCENTRATED SUSPENSIONS

Spatial organization of the particles within the suspension is called its *microstructure*. The microstructure of a suspension is determined by the freedom with which particles can wander around in the suspending medium, quantified by its *diffusivity*. The motion of the particle is given by a balance of forces acting on the particles known as the Langevin equation; i.e., the *interactive forces* ( $F_I$ ) between the particles, dispersive *Brownian forces* ( $F_B$ ) due to their thermal energy, and *hydrodynamic forces* ( $F_H$ ), mainly as shear exerted through the intermediary suspending medium.

$$m \frac{d^2 x}{dt^2} = F_p = F_B + F_H + F_I \quad (3.1)$$

The net effect of these three forces ( $F_p$ ) on the particle of mass  $m$ , causes a variation in the position of the particle, denoted by the second derivative of the position in space  $x$  with respect to time  $t$ . The extent and nature of this motion depend on the forces dominant in the system.

*Brownian forces* result from the internal energy of the molecules making up the suspending fluid, and appear as random isotropic motion of the particles. Brownian motion is significant only in the colloidal scale covering a size range from a few nanometers up to a few micrometers and very short time and length scales. In this scale of dimensions, the momentum of the particle is supplied by the thermal fluctuations of the surrounding liquid molecules that bombard it from all directions, as well as causing it to collide with other Brownian scale particles. The momentum delivered by these collisions cause the particle to overcome the inertia of the surrounding fluid molecules and displace them, altering the flow field, which appears as viscosity of fluid counteracting the Brownian motion. Naturally, the particle is diverted to regions where the resistance toward its motion is minimal. This tendency can be used to advantage in exploring the topography of structured materials such as polymers, and gels, by following up the particle's trajectory (Lukič *et al.*, 2005). Brownian forces are represented by the thermal energy of the fluid, given as a product of the Boltzman constant ( $k_B = 1.38 \times 10^{-23} \text{ JK}^{-1}$ ) and absolute temperature  $T$  [K] as  $k_B T$ . The diffusion coefficient  $D_0$  is related to the thermal energy through the Einstein (1906) equation,

$$D_0 = \frac{k_B T}{(6\pi\eta R)} \quad (3.2)$$

where  $R$  is the radius of the particle and  $\eta$  the viscosity of the suspending medium. To take into account the many-body interactions between the diffusing particle and the surrounding molecules, the viscosity of the suspension can also be used instead of the suspending medium. The random Brownian motion tends to disperse the particles and opposes their aggregation.

Contrary to Brownian forces which arise due to motion in the molecular scale, *hydrodynamic forces* are macroscopic forces arising due to shear stresses exerted by the fluid on the particles. In addition, shear forces push the particles toward each other favoring aggregation, counteracting the effect of Brownian forces. As the volumetric concentration of particles increases, the distance of separation between the particles is reduced to a fraction of their diameter. The motion of the fluid through these narrow spaces is then described by the lubrication equations.

*Interaction between particles can be through volume exclusion effects, through the mediation of polymers or through surface forces.* If the particles are completely inert with no attractive or repulsive forces between them, the only interaction can be through arrestment by physical obstruction of the escape ways of a particle by the neighboring particles. In concentrated suspensions, each particle is arrested, in turn, by its own circle of neighboring particles. These inert particles, called *hard-sphere* particles are an idealization: The closest approach to this ideal case is by steric stabilization of electrostatic charges and suspension in liquids of matching refractive index to equate the Hamaker constant and thus, the van der Waals forces to zero. These hard-structured particles behave as model hard-sphere particles, provided the additional excluded volume due to the polymer coating is accounted for. Under these conditions, the interactive forces are equivalent to the energy required to overcome the physical barriers of particles. In the second case, if there is an unadsorbed polymer in the suspending medium, the osmotic pressures created in the

excluded volume between the particles will create attractive *depletion forces*, even if the particles are neutral. In the third case, attractive forces due to bridging of polymers adsorbed on the particles, or attractive–repulsive forces due to DLVO forces constitute the interactive surface force,  $F_I$ .

Brownian forces exist under all conditions for all particle types, even in cases where they are dominated by other forces, such as hydrodynamic forces. Brownian forces tend to disperse and hence, stabilize the suspensions. Hydrodynamic forces are present only when an external force acts on the system and shears the fluid phase with respect to the particles. Interactive forces between the particles depend on the particle characteristics and composition making up the particulate phase, which can be grouped under the main headings of “hard sphere” and “soft” particles, denoting the conditions of absence and presence of surface forces, respectively.

### 3.1.1 Characterization of the particle size

Ordering of hard-sphere-like colloidal particles in Newtonian suspending media depend on the polydispersity index (PDI) of the particles defined as

$$PDI = \frac{\sum_i N_i |R_i - \bar{R}|}{N_T} \quad (3.3)$$

where  $N_i$  is the number of particles of radius  $R_i$ ,  $N_T$  the total number, and  $\bar{R}$  the average radius of particles in the sample.

Unlike the free hard-sphere particles, soft particles with attractive forces between them exist as aggregates or porous clusters. Either the *radius of gyration*  $R_g$ , or the *hydrodynamic radius*  $R_H$ , can be used for the radius of the aggregate,  $R$ , to take into account the porous structure.

$$R_g^2 = \frac{\sum_i M_{0i} r_i^2}{\sum_i M_{0i}} \quad (3.4)$$

$$R_H = \frac{k_B T}{6\pi\mu D_0} \quad (3.5)$$

where  $M_{0i}$  is the mass of the primary particles of size  $i$  of distance  $r_i$  from the center of mass of the aggregate,  $k_B$  the Boltzmann constant,  $T$  the absolute temperature,  $\mu$  the viscosity of the suspending medium, and  $D_0$  the Stokes–Einstein diffusion coefficient of the aggregated particles in the suspending Newtonian fluid, given by eq. (3.2), for a single particle.

In highly concentrated suspensions, the distinction between well dispersed and aggregated structures becomes vague due to the decreasing volume fraction of void space. In the case of particles sterically stabilized by adsorption of polymers or surfactants, the excluded volume of the adsorbed film also decreases the free interparticle space by the thickness of the adsorbed film. The volume fraction of the polymer-coated (structured)

particles  $\phi$  resides somewhere between the volume fraction of hard-sphere particles, calculated from their mass concentration,  $C_M$ , and density,  $\rho_p$ ,

$$\phi = \frac{C_M}{\rho_p} \quad (3.6)$$

and the effective volume fraction of the structured particles calculated from the product of the number concentration of the particles,  $n$ , and the volume of a single particle (Smith and Zukoski, 2004),

$$\phi = n \left( \frac{4\pi R^3}{3} \right) \quad (3.7)$$

Mass concentration,  $C_M$ , and the number concentration  $n$ , denote mass and the number of total particles per unit volume of suspension. In the case of soft particles and rather dilute systems such as gels, the fractal dimension  $d_f$  should be taken into account in the calculation of the volume of the aggregates, given by eq. (1.56).

### 3.1.2 Phases and states in concentrated suspensions

There are three equilibrium and two nonequilibrium states of colloidal dispersions. The equilibrium states are designated as gas, liquid, and crystal states, as shown in Figures 3.1(a), (b), and (c), respectively. At very low concentrations in a suspension, the particles act independent of each other reminiscent of molecules in the *gas state*, in random Brownian motion conferred by the isotropic bombardment of the solvent molecules. At higher concentrations, particles interact with each other through binary collisions without the formation of regular arrays, very much like molecular *liquids*. The state reached at higher concentrations depends on the attractive forces between the particles and their morphology. *Colloidal crystals* with regular array of particles form under strong attractive forces. In Figure 3.1(c), various sizes of crystal structures are depicted as separated out from the suspension phase. The attractions between the particles are so strong that aggregation results in a regular crystal structure, without need for further compaction. Liquid crystals form such regular textures under their phase transition temperatures. Colloidal particles with dielectric constant or magnetic susceptibility that is different from the solvent acquire a dipole moment parallel to an externally applied electric or magnetic field. Dipolar hard-spheres exhibit fluid, face-centered cubic (fcc), hexagonal-close-packed (hcp), body-centered tetragonal phases (bct) as a function of the dipole moment strength and packing fraction according to the phase diagram. Dipolar soft particles exhibit a body-centered orthorhombic (bco) phase in addition to the phases observed with hard spheres (Hynninen and Dijkstra, 2005). Formation of defect free, monodispersed colloid crystals has a significant technological application in optical band-gap adjustment (van Dillen *et al.*, 2004; Vermant and Solomon, 2005), but formation of crystal phases is outside the scope of this book.

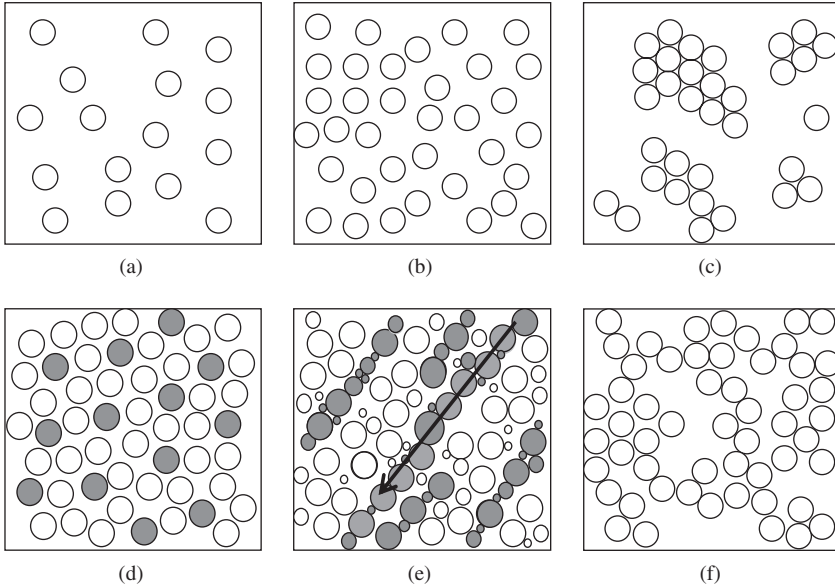


**Figure 3.1** Ordering in hard-sphere suspensions: Equilibrium structures of (a) the gas phase, (b) the liquid phase, (c) the solid crystal phase, (d) development of cages in concentrated suspensions, (e) glassy state with jamming of random particle chains shown in gray, (f) the gel state.

Ideal hard-sphere particle suspensions exist in a disordered fluid state up to volume fractions of  $\phi_f = 0.49$ , the so-called *freezing* point of the suspension manifested by the initial appearance of ordered clusters within a disordered suspension. The *melting* volume fraction of the hard-sphere suspension occurs around  $\phi_m = 0.55$  by the *Lindemann criterion*, which corresponds to  $\approx 1/3$  expansion by volume of the close-packed crystal structure at  $\phi_{\max} = 0.74$ . At this volumetric fraction of solids, the suspension loses its rigidity. If the thermal energy,  $k_B T$  of the particles is sufficient to overcome their mutual attraction, a dense liquid phase is possible, where particles are mutually caged-in by surrounding particles. In the melted state, average interparticle spacing is increased around 10%, according to the Lindemann criterion. If the range of attractive forces is about twice this interparticle distance, then the suspension will stay in this caged configuration (Segre *et al.*, 1995., Poon, 2002). Figure 3.1(d) depicts such a cage structure around the shaded reference particles. Some of the hard spheres, taken as references, are shown in gray to bring out the cage-like configuration of the particles. The configuration depicted in the Figure is still far from regular, as can be observed in the number of particles ranging from five to seven, surrounding a reference particle shaded gray for illustration. Nevertheless, a periodicity in the occurrence of gray reference particles in all directions is still observable. Within their cage, the particles can freely rotate and vibrate, but translation out of their locations is restricted by the barriers formed by the neighboring particles, which in turn, are arrested in their own cages. The only way the reference particle can escape from the cage is by hopping over the surrounding particle barriers to an unoccupied location. This process is well known from

the kinetic theory of liquids. The probability of occurrence of a hop is higher in the case of hard spheres as there are no interactive energy barriers to be overcome.

In this structural conformation, particles can undergo two types of diffusion with different time scales: short range within the cage and long range outside of the cages. The frequency of the collisions within the cage is in the timescale of Brownian motion,  $t_B \approx mD_0/k_B T \approx 10^{-8}$  s, time taken for the particle to transfer its extra momentum to the surrounding molecules. The hopping process out of this cage is more difficult than the diffusion process and therefore takes a longer time, depicted as the Péclet time (Verberg *et al*, 1997):

$$t_p = \frac{d_p^2}{4D_0} \approx 10^{-3} \text{ s} \quad (3.8)$$

The diffusion process then involves a *short-time Brownian diffusion* and a *long-time cage-hopping and translational* counterparts, the latter becoming more dominant as the volumetric fraction of solid particles increases.

The translation and diffusion mechanisms are linked with the Péclet number,

$$Pe = \frac{\dot{\gamma} R^2}{D_0} \quad (3.9)$$

which relates shear rate,  $\dot{\gamma}$ , in the scale of the hard-sphere radius  $R$  with the diffusion rate  $D_0$  given by the Stokes–Einstein relation at infinite dilution eq. (3.2). Another interpretation of the Péclet number is the ratio of energy of shearing to thermal energy or the shear rate with the thermal energy,

$$Pe = \frac{6\pi\mu\dot{\gamma}R^3}{k_B T} \quad (3.10)$$

where  $\mu$  is the viscosity of the Newtonian suspending medium and  $k_B T$  the thermal energy, which causes diffusion.

Particle dynamics discussed above are related to the equilibrium microstructure represented by the structure factor  $S(q)$ , determined by scattering techniques. The internal microstructure of colloidal suspensions can be probed with the static light scattering technique through the measurement of the intensity of light  $I(q)$ , scattered from the suspension as a function of wave vector  $q$ , defined as,

$$q = \frac{4\pi}{\lambda} \sin\left(\frac{\theta}{2}\right) \quad (3.11)$$

where  $\lambda$  is the wavelength of light in the suspension medium and  $\theta$  the scattering angle. The scattered light intensity  $I(q)$  is given by the relation,

$$I(q) = NI_0(qd_p)S(q) \quad (3.12)$$

where  $I_0(qd_p)$  is the scattering intensity from a single particle at infinite dilution, also known as the *form factor*;  $N$  the total number of particles, and  $S(q)$  the *intraparticle structure factor* which depends on the microstructure of the suspension (Ferretti *et al.*, 1998):

$$S(q) = 1 + 4\pi n \int_0^{\infty} [g(r) - 1] r^2 \frac{\sin(qr)}{qr} dr \quad (3.13)$$

In this equation,  $n$  is the number concentration of scattering particles,  $g(r)$  the *radial distribution function* or the *pair correlation function* at contact, and gives the probability of finding a particle at a distance  $r$  from the reference particle, taken as the origin. Plots of  $g(r)$  versus  $r$ , and  $S(q)$  versus  $(qd_p)$  are closely related with each other and indicate the configuration of particles, as shells surrounding the reference particle spaced in multiples of  $d_p$ . The magnitude of the first peak in the structure factor  $S(q)$  when plotted against  $(qd_p)$ , gives an indication of the compactness of the cage structure, or particles immediately surrounding a reference particle within the suspension.

As the volume fraction of the particles is increased above  $\phi = 0.35$ , the suspension becomes compacted. The resulting order in the configuration depends on the polydispersity of the suspension: Highly polydisperse particles retain the liquid-phase disorder while becoming more concentrated. The glass state portrayed in Figure 3.1(e) looks more like a supercooled liquid, with a more close-packed structure than the liquid state depicted in Figure 3.1(b). Albeit the retention of randomness, local or widespread ordering of particles is observed with nearly monodisperse particles as depicted in Figure 3.1(e). Glass transition is observed around  $\phi = 0.58$  when the particles are arrested by their neighbors in the process of crystallization. Crystallization, which requires short-range strong attractive forces, cannot proceed under these conditions, where the translations of the particles are hindered by the longer-range attractions of the surrounding particles. Only the short-range Brownian diffusion within the cages formed by surrounding particles is permitted for the individual particles. Glassy state is not an equilibrium state, for the space left in the cages prevent the particle to assume a position for close-packed conformation. If the arrestment were somehow loosened, the particles would tend to form close-packed regular structures, the equilibrium solid crystal state. But the glasses are so rigid that equilibrium cannot be achieved within practical time scales, unless the temperature exceeds the *glass transition temperature*,  $T_g$ , above which the glass melts and becomes a liquid in the case of molecular glasses. Hard-sphere glassy structures are not sensitive to temperature, but to the variations in the packing density of the suspension.

A similar nonequilibrium state of colloidal particles is the *gel* state. Gels are network of colloids spanning the available volume. Typical manifestation of gel formation is the development of a yield stress and viscoelastic behavior. Appearance of a yield stress indicates a self-supporting network, while elasticity requires free volume for relaxation. Colloidal gels are reversible, unlike the polymer gels with chemical bonds or attracted with bridging bonds given in Example 1 of Chapter 2, even though they exhibit similar properties. Typically, depletion forces supply the necessary reversible attractions. Consequently, gel behavior is observed in the presence of polymers used for steric stabilization, unadsorbed polymers, grafted polymers, or soft particles with DLVO forces. The greater the strength of attraction, the less is the requirement for an adequate volumetric fraction of



solids for supporting the gel structure. The gel structure depicted in Figure 3.1(f) involves the attachment of individual clusters through *percolation* (interconnectivity). *Percolation threshold* is a term used to denote the minimum solid particle concentration where a self-supporting continuous network is formed which can distribute an applied force within its components. Such a state is called *nonergodic* signifying that the structure is not homogeneous and any part taken out does not represent the configuration of the overall structure. This portrayal of the gel structure can be generalized as *localization* phenomena in colloidal suspensions. Localization can be brought about by local cage-like formations, fractal clusters, or simply aggregations in suspensions of inhomogeneous composition. They can be *thermodynamic* or *hydrodynamic* in origin (Foss and Brady, 2000; Gopalakrishnan and Zukoski, 2004). Clusters of thermodynamic origin signifying the effect of surface forces is presented in Chapter 1. Clusters of hydrodynamic origin result when the component of shear forces in the direction of flow dominates the interparticle and dispersive Brownian forces and compresses the particles into a cluster (Bossis and Brady, 1989). These clusters are called *hydroclusters* to indicate their origin. Clusters will be taken up again in the following sections on shear and viscoelastic behavior of concentrated suspensions.

Rheology of concentrated suspensions is not only affected by the volumetric fraction of solids,  $\phi$ , but also by the existence of interparticle attractive forces and the state of the suspension. Attractive forces among the particles lead to either uniform or localized high-density regions, increasing both the shear viscosity and the elastic modulus. Consequently, hard-sphere particle suspensions where no interactive forces exist, serve as a reference for the evaluation of the rheology of soft-particle suspensions. The states of the particle suspensions can be grouped as glassy state, gels, and concentrated pastes. In what follows concentrated hard-sphere suspensions will be given first, followed by the soft particle suspensions.

## 3.2 RHEOLOGY OF CONCENTRATED HARD-SPHERE SUSPENSIONS

Hard-sphere suspensions in the glassy state are peculiar in that they do not deform and show limited viscoelasticity even under very high external stresses. Therefore, the glassy state will be taken up first before going on to the rheology of other states of hard-sphere suspensions.

### 3.2.1 Colloidal glasses and jamming

As the particle concentration is increased, a transition to high-density glass state is observed around  $\phi = 0.58$  (Vanmegen and Underwood, 1994). If glass state is overpassed somehow, then the suspension reaches its maximum compaction as a randomly close-packed solid at  $\phi_m = 0.63$ . As the polydispersity of the suspension increases, it deviates from equilibrium behavior. Fluid–solid two-phase region contracts, disappearing completely above a polydispersity of around 10%, and a continuous transition from the fluid to the glass state is observed, instead.

Glassy state is characterized by the appearance of a yield stress and apparent solid behavior in spite of a random fluid microstructure. Even though the particles are not at their maximum compaction, and a certain free volume exists within the suspension, the particles are arrested within the network, as the interparticle space is not sufficient for the particles to exchange positions. Under an applied shear, the suspension has to dilate to open-up space to be able to deform. Dilation is prevented as long as there is an incompressible suspending fluid in the interparticle space, where *cohesive forces*,  $F_{\text{coh}}$  exist among fluid molecules, and *adhesive forces*,  $F_{\text{adh}}$ , act at the fluid–solid interface, regulated by surface and interfacial tensions, respectively. As a result, glasses cannot deform and are fragile.

A consequence of the inability to deform is *jamming* among the particles associated with the glassy state. A linear array of particles randomly formed within the glass structure delivers external stress acting in the collinear direction through the chain, and the suspension counteracts the stress like a stiff solid (Cates *et al.*, 1998). The shaded spherical particles in Figure 3.1(e) depict such random chains of particles collinear with the direction of the external stress acting on the suspension. Should the compressive strength change its direction, the suspension will react similarly if transmitting chains of particles are available (or could be formed by limited deformation in less concentrated suspensions) in the direction of the new force; otherwise, it will break apart unable to support the external stresses. The jamming mechanism in colloidal glasses is used advantageously in the process of *granulation* from highly concentrated pastes in high-shear mixers. The paste breaks down into irregular pieces that become uniform in size after repeated disintegration and aggregation steps. Granules are used in medicines, powder detergents, and fertilizers, among other applications. Granules have peculiar properties (Cates *et al.*, 2005): They are matt in appearance due to protruding colloidal particles at the surface, rearrange under vibration to smooth-surfaced spherical particles but become matt again under an external force due to jamming. The effect of vibration on jamming transition in opening up space is similar to the effect of temperature on molecular glasses, which melt and start to flow above the melting temperature.

Jamming may be observed at solid fractions below  $\phi = 0.35$  under dynamic conditions if particle chains form within the suspension, or in filled material composites, which are more important technologically. For example, oscillating behavior of vulcanized elastomers filled with hard-sphere particles such as carbon black used in automobile tires is a determining factor in the useful life of these tires. The behavior of these suspensions under oscillating strain was investigated in a model system below the compaction volume fraction of  $\phi = 0.35$  by Robertson and Wang (2005). Suspensions of polydispersed silica particles in the size range of  $10 < d_p < 500$  nm dispersed in oil at volume fractions of  $0.08 < \phi < 0.35$  was subjected to homogeneous oscillatory strain in a cone and plate rheometer at a temperature well above the glass transition temperature of the oil. The variation of dynamic elastic and viscous moduli as a function of percent strain ( $(\gamma \equiv \frac{\Delta L}{L}) \times 100$ ) is shown in Figure 3.2(a) for different volumetric fraction of hard spheres. At low strains, a strain-independent jammed state was observed with solid-like behavior characterized by an elastic modulus  $G'$ , much greater than the viscous modulus  $G''$ , depicted as the more or less horizontal initial section of the elastic modulus,  $G'$ . A breakup of the jammed state was found to occur just after the maximum point in the  $G''$  plot, which corresponded to the

initiation of a decrease in  $G'$ , to a value below that of the viscous modulus  $G''$ . In all the experiments with different volume fractions, the shear stress created in the suspension,  $\sigma$  ( $\equiv \tau$  in Figure 3.2) was found to decrease with an increase in the strain,  $\gamma$ . When the moduli were normalized with the elastic modulus at very low strains  $G'_0$  as  $G'/G'_0$ , and with the maximum in the viscous modulus,  $G''_{\max}$  as  $G''/G''_{\max}$  and plotted against the mechanical energy dissipated in straining a unit volume of suspension,  $\sigma\gamma$  ( $\equiv \tau\gamma$ ) ( $\text{J m}^{-3}$ ), the curves for different volume fractions were found to be superimposed on each other. This superimposition

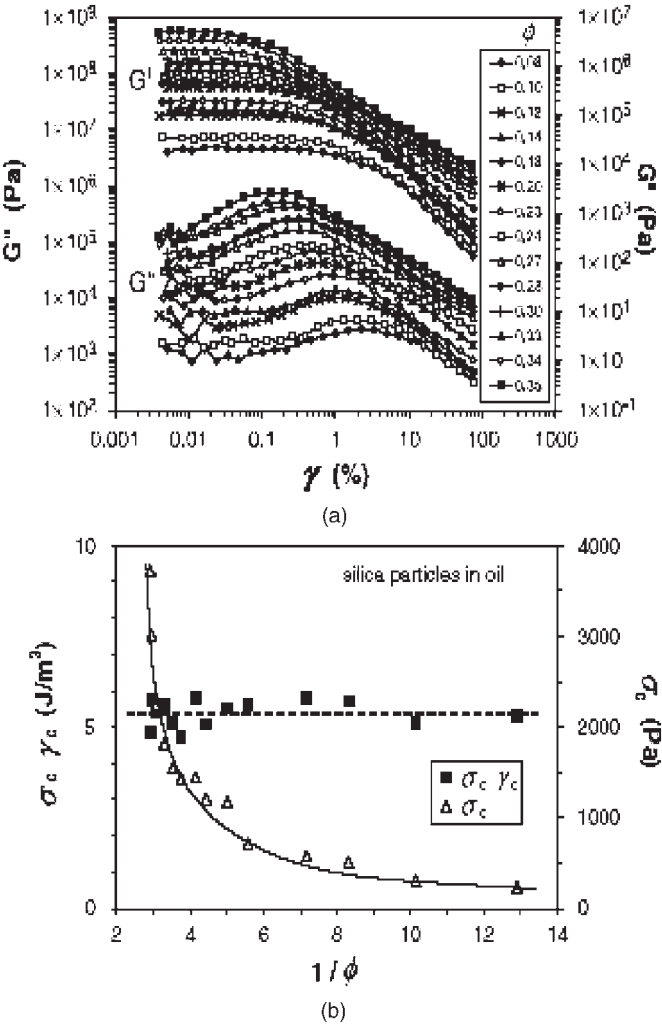


**Figure 3.2** Dynamic behavior of random solid-liquid mixtures, (a) Variation of elastic and viscous moduli with volume fraction of solids and percent strain, (b) Variation of the critical stress and energy with inverse volume fraction for oil-silica mixtures ( $\sigma \equiv \tau$ ). (Robertson and Wang, 2005. Reproduced with permission of The American Physical Society, Figures 1 and 3 in the original).

was taken as an indication of thermodynamic control of jamming transition, which was confirmed by the constant value of  $\sigma_c \gamma_c$  when plotted against  $1/\phi$  as given in Figure 3.2(b). The critical stress and strain values,  $\sigma_c$  and  $\gamma_c$  denote the transition from the jamming state, right after the maximum in  $G''$ . These results were in parallel with the results of Payne (1962), who first observed the phenomena, and show that jamming transition takes place at constant energy,  $\sigma_c \gamma_c$ . The rheology of the suspending phase, and size distribution and volume fraction of the particles do not change the trend but affect the absolute value of the constant,  $\sigma_c \gamma_c$ . The authors associated the onset of the nonlinearity in viscoelasticity at the jamming transition,  $\sigma_c \gamma_c$ , with the yield stress ( $\tau_0$ ) and yield strain ( $\gamma_0$ ) and proposed a scaling relation with the volume fraction of solids in filled materials as

$$\tau_0 \gamma_0 < \sigma_c \gamma_c < \phi^{a-2b} \quad (3.14)$$

Since the transition energy  $\sigma_c \gamma_c$  is independent of the volume fraction of solids, the exponent of  $\phi$  should be zero. From the experimental results, the authors found  $a = 3.3 \pm 0.2$  and  $b = 1.7 \pm 0.1$  in conformation with values found for other solid–liquid suspensions given in the literature.

### 3.2.2 Relative viscosity of colloidal suspensions

The viscosity of hard-sphere suspensions is a function of the volumetric concentration of the solids,  $\eta(\phi)$ , but as it also depends on the medium viscosity  $\mu_0$ , it is generally expressed in the form of relative viscosity,  $\eta_r = \eta(\phi)/\mu_0$ .

Einstein first derived the relative viscosity of dilute suspensions of hard spheres in a Newtonian fluid in 1906, based on the additional resistance of the suspension to shear by the change in the velocity field of the fluid due to a single hard-sphere particle placed in it:

$$\frac{\eta}{\mu_0} = 1 + \frac{5}{2} \phi \quad (3.15)$$

In this equation,  $\eta$  is the viscosity of the suspension,  $\mu_0$  the viscosity of the suspending medium, a Newtonian liquid, and  $\phi$  the volumetric concentration of solids. Rearrangement of the equation in terms of relative viscosity ( $\eta_r = \eta/\mu_0$ ) to the form

$$\frac{\eta_r - 1}{\phi} = 2.5 \quad (3.16)$$

converts the LHS of this equation to the *viscosity number* or *reduced specific viscosity* that is equated to a constant in Einstein's equation, known as the *intrinsic viscosity*  $[\eta]$  of the suspension at infinite dilution. Eq. (3.15) is extended to include moderately concentrated suspensions by the addition of nonlinear terms:

$$\eta_r = \frac{\eta}{\mu_0} = 1 + [\eta]\phi + k_H \phi^2 + O(\phi^3) \quad (3.17)$$

The first two terms describe the diffusion of a particle in a dilute suspension. The third term is used in the case of concentrated suspensions and its coefficient (called *Huggins coefficient*) is very sensitive to the structure of the suspension.

Viscosity of suspensions is closely related to their microstructure and the rate of diffusion of the particles through the microstructure. The microstructure of the suspensions are described by the pair correlation function,  $g(R, \phi)$ , the probability of finding two particles of radius  $R$  at contact in the suspension, which is an inverse function of the void fraction  $\phi_v$  in the suspension. The diffusion rate is also proportional to the free volume or void fraction  $\phi_v$  in the suspension,

$$\phi_v = \frac{(\phi_m - \phi)}{\phi_m} = 1 - \frac{\phi}{\phi_m} \quad (3.18)$$

where  $\phi_m$  is the maximum packing fraction of the suspension. As the Brownian contribution to the viscosity is inversely proportional to the diffusion rate, the viscosity of the suspension is inversely proportional to the *square* of void fraction, when the contributions of both the Brownian motion and microstructure are taken into account:

$$\eta \propto \frac{1}{(1 - \phi / \phi_m)^2} \quad (3.19)$$

Real suspensions show systematic deviations from this equation which are taken into account by more complicated functions of volumetric fraction of the solid particles,  $\phi$ , that can be increased up to the random close packing fraction of uniform hard spheres,  $\phi_m$ . Under low-shear rate, or *quasistatic* conditions,  $\phi_m = 0.63$ . Alignment of the particles at higher shear rates increases the maximum volumetric fraction of solids to  $\phi_m = 0.74$ , that of the face-centered cubic packing. This is the limiting compaction for particles acting as hard spheres, with the suspending medium preserving its continuity. The maximum volumetric fraction of solids,  $\phi_m$ , is a function of the shape and size distribution of the particles as well as the shear rate. Relative viscosity of real suspensions is correlated with the ratio of the solids to its maximum value, in the form of a dimensionless equation, to make it independent of the effects of shear in the correlations given in Table 3.1. Due to complexity of the interacting mechanisms,  $\phi_m$  is generally found as a fitting parameter and checked against experimental findings. Some of the semiempirical correlations for relative viscosity of hard-sphere suspensions are given in Table 3.1. Of the equations given, that of Krieger and Dougherty (1959) have found general acceptance as to its applicability for a wide range of noninteracting hard-sphere pastes. The term in square parenthesis,  $[\eta]$ , is the *intrinsic viscosity* or the *crowding factor* originally proposed by Mooney (1957), generally found as a curve fitting parameter. As the volumetric fraction of solid particles approach its maximum value,  $\phi_m$ , relative viscosity term  $\eta_r$  diverges, and the suspension viscosity approaches infinity.

### 3.2.3 Theoretical models of concentrated suspension viscosity

In summary, particles in concentrated suspensions with a microstructure such as given in Figure 3.1(d), interact through *Brownian*,  $F_B$ , *interparticle*,  $F_I$ , and *hydrodynamic*,  $F_H$ ,

**Table 3.1**

Empirical equations for the relative viscosity of suspensions

Equations	References	Equation numbers
$\eta_r = \exp\left(\frac{[\eta]\phi}{1 - (\phi/\phi_m)}\right)$	Mooney (1957)	(3.20)
$\eta_r = 1 + \frac{[\eta]\phi}{(1 - (\phi/\phi_m))}$	Robinson (1957)	(3.21)
$\eta_r = (1 - (\phi/\phi_m))^{-[\eta]\phi_m}$	Krieger and Dougherty (1959)	(3.22)
$\eta_r = [1 - (\phi/\phi_m)]^{-2}$	Quemada (1984)	(3.23)
$\eta_r = \left[1 + \frac{[\eta]\phi_m}{2} \left(\frac{\phi/\phi_m}{1 - (\phi/\phi_m)}\right)\right]^2$	Chong <i>et al.</i> (1971)	(3.24)
$\eta_r = \left(1 + \frac{[\eta]\phi_m}{2(1 - (\phi/\phi_m))}\right)^2$	Eilers (1941) modified by Wildemuth and Williams (1984)	(3.25)

forces. Langevin equation, eq. (3.1) gives the displacement  $\Delta x$  of the particle as a result of the forces acting on it. Brownian forces arise out of the thermal energy of the particles and are completely random, acting toward the dispersion of formed clusters. Interactive forces in terms of attraction and repulsion does not exist in hard-sphere particles: The only interactive forces possible are *volume exclusion* in terms of formation of barriers by the surrounding particles against long-range diffusive motion and depletion forces. Hydrodynamic forces are the effect of imposed forces on the suspension transmitted to the particles through the intermediacy of the liquid suspending medium, and arise in the presence of an applied external shear. Unfortunately, there is no comprehensive theory that takes into account the effect of all these forces, to date. Two theoretical developments will be presented below which take into account the thermal and interparticle forces (Verberg *et al.*, 1997; Cohen *et al.*, 1998), and that is based on thermal and hydrodynamic forces (Brady, 1993; Foss and Brady, 2000, and other publications cited in these references).

### 3.2.3.1 Theoretical model of viscosity based on suspension microstructure

When no external shear stresses or strains are applied to the system, the suspending medium does not take an active role in transferring momentum and hydrodynamic forces are not involved. The suspension is in equilibrium under the balance of interactive and Brownian forces. Verberg *et al.* (1997) developed a theoretical model that could correctly predict the experimental results given in Figure 3.3(a), in the range  $0 < \phi < 0.55$  encompassing both

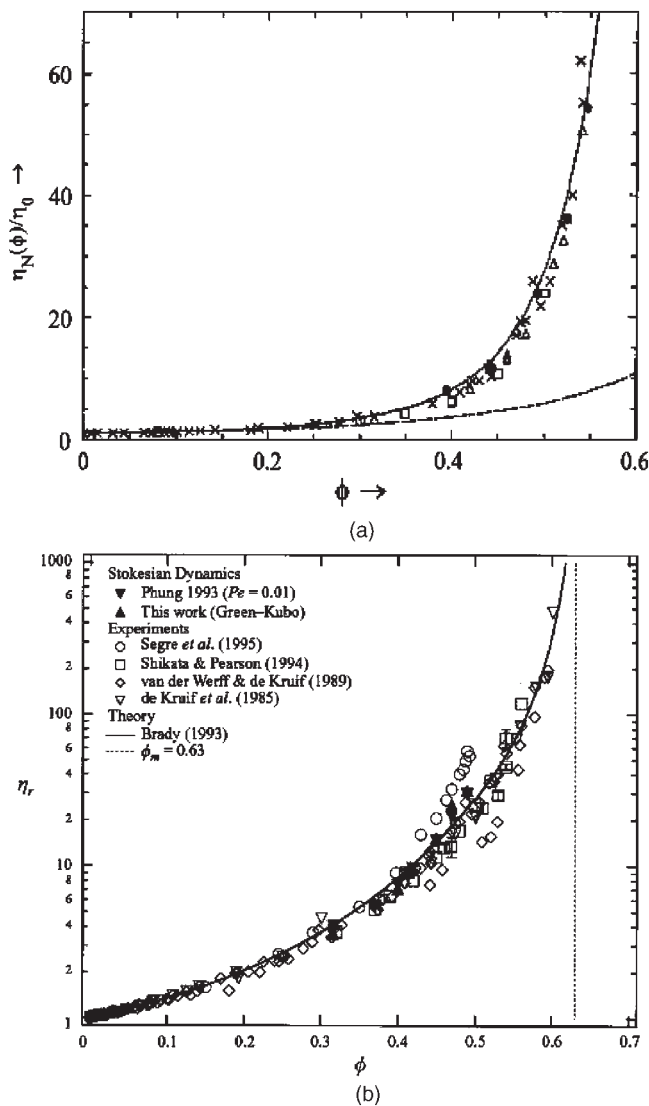


**Figure 3.3** Variation of the relative Newtonian viscosity of suspensions at zero shear rate with the volume fraction of solids. (a) Relation based on direct particle interactions of Verberg *et al.* (1997) Experimental points: Crosses (van der Werff and de Kruif, 1989), open triangles, (van der Werff *et al.*, 1989); circles, (Jones *et al.*, 1991, 1992); squares, (Papir and Krieger, 1970). (Reproduced with permission of The American Physical Society, Figure 3 in the original) (b) Relation based on Stokesian Dynamics simulations (Foss and Brady, 2000) (Reproduced with permission of Cambridge University Press, Figure 1 in the original).

the viscous and viscoelastic counterparts of hard-sphere suspension viscosities. The model is based on the microstructure depicted in Figure 3.1(d), with the reference particles (or equivalently cages formed by neighboring particles) recurring with a wave number,  $k$ . As the concentration of the suspensions increases, the distribution of particles become more homogeneous and the wave number approaches  $k \approx k^* = 2\pi/d_p$ , leaving a surface–surface clearance between the particles of only 10% of the particle diameter,  $d_p$ . The viscosity of the suspension is based on two processes, a short-time process,  $t \leq t_B$  when momentum is transferred by binary collisions among the particles, the probability of which is related to the equilibrium radial distribution, (the pair-correlation function at contact),  $g(r)$ , now a function of both the particle diameter and volumetric fraction of solids

$$g_{eq}(d_p, \phi) \equiv \chi(\phi) \quad (3.26)$$

and diffusion coefficient, given by the Stokes–Einstein relation, eq. (3.2).  $\chi(\phi)$  is the number concentration distribution function of the particles. At high-particle concentrations, momentum is transferred mainly by the particles jumping out of their cages, which occurs at relatively longer Péclet time scales  $t_p$ ,

$$t_p \approx t_c(k^*, \phi) = \frac{1}{D_c(k^*, \phi)k^{*2}} \quad (3.27)$$

where  $t_c$  and  $D_c$  are the time and diffusion coefficients associated with the hopping of the particles out of their cages, respectively.

The shear viscosity is defined by the authors in the most general terms, as the linear response of the suspension to an applied shear rate given as,

$$\dot{\gamma}(t) = \dot{\gamma}_0 e^{-i\omega t} \quad (3.28)$$

$\omega \rightarrow 0$ , gives the maximum amplitude of the shear rate  $\dot{\gamma} \rightarrow \dot{\gamma}_0$ . Very high frequencies, as  $\omega \rightarrow \infty$ , denote very short-time conditions where the suspension viscosity  $\eta_\infty$  increases above the suspending medium viscosity  $\mu_0$  as a function of the volumetric concentration of particles  $\chi(\phi)$  due to contact (collisions) between particles only,

$$\eta_\infty(\phi) = \mu_0 \chi(\phi) \quad (3.29)$$

where  $\mu_0$  is the viscosity of the Newtonian suspension medium. The self-diffusion of the particles,  $D_s$  decreases below the diffusion coefficient in the suspension medium,  $D_0$  by the same function as

$$D_s(\phi) = \frac{D_0}{\chi(\phi)} \quad (3.30)$$

Shear viscosity can also be defined in terms of the applied shear stress,  $\tau_{xy}$ . In the plane of the deformation  $x$ – $y$ , the component of the shear stress tensor  $\tau_{xy}$  has static,  $\tau_{xy,s}$ , and dynamic counterparts,  $\tau_{xy,d}$ , which are given in functional form as

$$\tau_{xy}(\phi, \omega, \dot{\gamma}_0, t) = \tau_{xy,s}(\phi, \dot{\gamma}_0, t) + \tau_{xy,d}(\phi, \omega, \dot{\gamma}_0, t) \quad (3.31)$$



The static contribution is obtained when the dynamic contribution is zero at  $\omega \rightarrow \infty$ :

$$\tau_{xy,s}(\phi, \dot{\gamma}_0, t) = -\eta_\infty(\phi) \dot{\gamma}(t) \quad (3.32)$$

The dynamic contribution to the shear stress is based on the Smoluchowski equation for the aggregation of an N-particle system under a shear rate  $\dot{\gamma}(t)$ :

$$\tau_{xy,d}(\phi, \omega, \dot{\gamma}_0, t) = -\frac{1}{2v} \left\langle \sum_{j \neq i=1}^N r_{ij,x} \frac{\partial U(r_{ij})}{\partial r_{i,y}} \right\rangle_{ne} \quad (3.33)$$

where  $v$  is the volume of the suspension,  $\mathbf{r}_i$  the position of particle  $i$  ( $i = 1, \dots, N$ ),  $\mathbf{r}_{ij} = \mathbf{r}_i - \mathbf{r}_j$ ,  $U(r_{ij})$  the interparticle potential between particles  $i$  and  $j$  at a distance  $r_{ij} = |\mathbf{r}_{ij}|$ , and the ensemble average of the summation function is taken with respect to a nonequilibrium (ne) distribution function.

The total shear stress can then be expressed as the sum of short-time static,  $t \leq t_B$  ( $\omega \rightarrow \infty$ ) and long-time dynamic,  $t \geq t_p$  contributions. In the first case, given by eqs. (3.29) and (3.32), the time allowed for any interaction is so short that viscosity can increase only by the dissipation of energy due to binary collisions, which increases with the number concentration of particles given by the function,  $\chi(\phi)$ . Generally, an extension of Einstein's equation is used for  $\chi(\phi)$ :

$$\chi(\phi) = 1 + \frac{5}{2}\phi + O(\phi^2) \quad (3.34)$$

the last term gives the remaining terms as a quadratic function of  $\phi$ . Another function, also used to describe the concentration distribution of solid particles, Carnahan–Starling approximation,

$$\chi(\phi) = \frac{1 - 0.5\phi}{(1 - \phi)^3} \quad (3.35)$$

given as the dotted line in Figure 3.3(a), was found to describe short-time experimental results (not given in the figure) in the range  $0 < \phi < 0.55$ , by the authors (Verberg *et al.*, 1997; Cohen *et al.*, 1998).

The potential term in the long-time dynamic contribution (eq. (3.33)) essentially gives the resistance due to the difficulty in overcoming the particle barriers in the cages. Therefore, the potential in the case of hard-sphere particles with no interactive forces can only be direct interaction associated with the structure of the suspension described by the structure factor  $S(q)$ . The resistance evolves from the highly reduced diffusion coefficient of the particles into and out of the cages,  $D_c$ , again associated with the microstructure of the suspension. The derivation that associates the structure is long and detailed, so only the basic equations will be given below. For the details of the derivations refer to (Verberg *et al.*, 1997; Cohen *et al.*, 1998).

The long-time resistance of the suspension has two counterparts: (1) Newtonian viscosity,  $\eta_N(\phi)$  observed by setting  $\omega = 0$ , (2) Complex viscosity  $\eta^*$ , with elastic and dynamic counterparts due to viscoelasticity of the suspension.

### 3.2.3.1.1 Newtonian viscosity of concentrated hard-sphere suspensions

The result of the derivations for long times and  $\omega = 0$  gives:

$$\eta_N(\phi) = \mu_0 \chi(\phi) \left[ 1 + \frac{1}{40\pi} \int_0^\infty \kappa^2 \frac{[S'_{eq}(\kappa, \phi)]^2}{S_{eq}(\kappa, \phi) d(\kappa)} d\kappa \right] \quad (3.36)$$

where  $S_{eq}$  is the equilibrium structure factor,  $\kappa = kd_p$  where  $k$  is the wave number,  $S'_{eq}$  is its derivative and  $d(\kappa)$  is the spherical Bessel function. Although eq. (3.36) is derived for solid particle volume fractions  $\phi > 0.35$ , it is also valid for smaller solid concentrations due to the first term in parenthesis. Evaluation of this equation gives an approximate equation that can be used in practical applications in the range,  $0 < \phi < 0.55$ , with a relative error less than 0.25%:

$$\eta_N(\phi) = \mu_0 \chi(\phi) \left[ 1 + \frac{1.44\phi^2 \chi(\phi)^2}{1 - 0.1241\phi + 10.46\phi^2} \right] \quad (3.37)$$

The plot of eq. (3.36) is drawn in Figure 3.3(a) as the solid line. The agreement with experimental results identified in the captions is remarkable, even though no hydrodynamic forces, for example, momentum transfer through the suspending liquid, was taken into account. This might be due to the dominance of direct interactions over hydrodynamic effect under nearly close packing conditions.

Microstructure-based predictions of zero-shear viscosity cannot go beyond a volumetric fraction of solids  $\phi \geq 0.50$  (Verberg *et al.*, 1997; Cohen *et al.*, 1998). Schweizer and Saltzman (2003a,b) incorporated the hopping time of the encaged particles as an additional diffusion time, enabling the model to predict the zero-shear viscosities of much more concentrated suspensions. Eq. (3.30) is then converted into

$$D_c^s = \frac{D_0}{S(q)[g(d_p)d(q)^{-1} + (\xi_{HOP}/\xi_0)]} \quad (3.38)$$

where the second term in the denominator gives the resistance due to hopping defined as  $\xi = k_B T/D_s$ , and  $D_c^s$  is the short time diffusion of the encaged particles.

### 3.2.3.1.2 Viscoelastic behavior of concentrated hard-sphere suspension

Spaces left between particles in random packing allow the suspension to exhibit limited ability to store an applied energy, and deform (at low-solid concentrations), making them viscoelastic. The resistance of the suspension toward dynamic shear can be expressed as

the complex viscosity,  $\eta^*$ , with the real ( $\eta'$ ) and imaginary ( $\eta''$ ) parts expressed in terms of dimensionless quantities,  $\eta_R^*$  and  $\eta_i^*$ , respectively:

$$\eta_R^*(\phi, \omega) = \frac{\eta'(\phi, \omega) - \eta(\phi, \infty)}{\eta(\phi, 0) - \eta(\phi, \infty)} = \frac{\eta'(\phi, \omega) - \eta_\infty(\phi)}{\eta_N(\phi) - \eta_\infty(\phi)} \quad (3.39a)$$

$$\eta_i^*(\phi, \omega) = \frac{\eta''(\phi, \omega)}{\eta_N(\phi) - \eta_\infty(\phi)} \quad (3.39b)$$

The authors (Verberg *et al.*, 1997) found good agreement between eqs. (3.39a) and (3.39b) with the limited number of experimental values. The real part of the complex viscosity  $\eta_R^*$  varies between 1 ( $\omega \rightarrow 0$ ) and 0 ( $\omega \rightarrow \infty$ ). The imaginary part,  $\eta_i^*$  equals zero at both limits and shows a maximum in the intermediate values of  $\omega$ .

### 3.2.3.2 Theoretical model of viscosity based on Stokesian Dynamics simulations

Stokesian Dynamics is a simulation technique similar to molecular dynamics applied to particles suspended in a Newtonian fluid. In the previous model Péclet number was taken into consideration in terms of time scales for diffusion processes taking relatively longer times for occurrence than the Brownian motion. In Stokesian Dynamics, it enters as a second parameter, besides the volume fraction of solid particles,  $\phi$ , to denote the ratio of hydrodynamic shear to thermal forces. The theory is based on hydrodynamic equations written for the suspending liquid and multiparticle solid phases, separately, that are linked to the Brownian forces through the Péclet number (Foss and Brady, 2000). Navier–Stokes equation of motion given in Appendix A3, describes the flow of the suspending liquid. Langevin equation (eq. (3.1)) for coupled N-body systems is used as the starting relation for the motion of the solid particle phase. In vector notation,

$$\mathbf{m} \cdot \frac{d\mathbf{V}}{dt} = \mathbf{F}_H + \mathbf{F}_I + \mathbf{F}_B \quad (3.40)$$

where  $\mathbf{m}$  is the generalized mass/moment of inertia tensor;  $\mathbf{V}$  the particle rotational/translational velocity vector for  $N$  particles in six directions;  $\mathbf{F}_H$ ,  $\mathbf{F}_B$ , and  $\mathbf{F}_I$  are the force/torque vectors of  $6N$  dimensions representing, respectively, hydrodynamic forces on the particles due to their motion relative to the fluid phase, Brownian forces and interactive forces among the particles. Since interactive forces do not exist in hard-sphere suspensions,  $\mathbf{F}_I \equiv 0$ . For small Reynolds numbers based on particle diameter,  $d_p$ ,

$$Re_p = \frac{\rho d_p^2 \dot{\gamma}}{\eta} \ll 1 \quad (3.41)$$

the hydrodynamic force/torque exerted on the particles of a suspension in linear flow is given as

$$\mathbf{F}_H = -\mathbf{R}_{FV} \cdot (\mathbf{V} - \langle \mathbf{V} \rangle) + \mathbf{R}_{FE} : \langle \mathbf{E} \rangle \quad (3.42)$$

The first term on the RHS of the equation gives the difference between the velocity of the particle  $\mathbf{V}$  in vector form, and the imposed bulk flow evaluated at the particle centers,  $\langle \mathbf{V} \rangle$  defined as,

$$\langle \mathbf{V} \rangle = (\langle \mathbf{E} \rangle + \langle \mathbf{\Omega} \rangle) \cdot \mathbf{x} \quad (3.43)$$

where  $\langle \mathbf{E} \rangle$  and  $\langle \mathbf{\Omega} \rangle$  are the bulk rate of strain and vorticity tensors, which take into account shear and rotational flows in the bulk suspension phase, respectively. The microstructure of the suspension is taken into account by the configuration-related tensors  $\mathbf{R}_{\text{FV}}(\mathbf{x})$  and  $\mathbf{R}_{\text{FE}}(\mathbf{x})$ , giving the hydrodynamic force (or torque) on the particles due to their velocity relative to the fluid, and due to an imposed external flow, respectively. The vector  $\mathbf{x}$  specifies the location and orientation of all  $N$  particles.

The Brownian motion arising from the thermal energy ( $k_{\text{B}}T$ ) of the fluid phase molecules are related to the component of hydrodynamic force  $\mathbf{R}_{\text{FV}}$  on the particles due to their velocity relative to the fluid through the time correlation function

$$\overline{\mathbf{F}_{\text{B}}(0)\mathbf{F}_{\text{B}}(t)} = 2k_{\text{B}}T\mathbf{R}_{\text{FV}}\delta(t) \quad (3.44)$$

The LHS of the equation gives the average amplitude of the correlation between random Brownian fluctuations at  $t = 0$  and  $t = t$ . The overbar denotes an average over the fluctuations of the solvent molecules.  $\delta(t)$  is the delta function, giving the displacement of the particle as a function of time.

Bulk stress,  $\tau_v$ , over a volume,  $v$ , containing  $N$  particles is given by the relation,

$$\tau_v = -\langle p \rangle \mathbf{I} + 2\eta \langle \mathbf{E} \rangle + \langle \tau_p \rangle. \quad (3.45)$$

The first term in the gives the pressure of the medium, the second term, stress contribution of the fluid stress to the total stress and the last term gives the total contribution of the particles including the components:

$$\langle \tau_p \rangle = -nk_{\text{B}}T\mathbf{I} + n\{\langle \mathbf{S}_{\text{H}} \rangle + \langle \mathbf{S}_{\text{P}} \rangle + \langle \mathbf{S}_{\text{B}} \rangle\} \quad (3.46)$$

where  $n$  is the number density of particles, the first term on the RHS is the isotropic stress associated with the Brownian motion of the particles due to their thermal energy. The stress terms  $\mathbf{S}$  in the parenthesis denote the mechanical stress transmitted by the suspending fluid in shear flow ( $\mathbf{S}_{\text{H}}$ ), stress due to interparticle forces ( $\mathbf{S}_{\text{P}}$ ), stress developed during Brownian motion ( $\mathbf{S}_{\text{B}}$ ).

Simulations based on eqs. (3.40)–(3.46) were performed in the range  $0.316 \leq \phi \leq 0.49$  and  $0 < Pe < 10000$  by Foss and Brady (2000). In the theoretical development of Brady and coworkers (Bossis and Brady, 1989; Brady, 1993; Foss and Brady, 2000), the Péclet number is used to relate the dispersive Brownian motion due to thermal energy, to the shear strain that distorts the structure of the suspension through eq. (3.10). Brownian forces dominate at  $Pe \leq 10$ : For comprehension in quantitative terms, this is equivalent to  $\dot{\gamma} \leq 17\text{s}^{-1}$  for particles  $1\text{ }\mu\text{m}$  in diameter, suspended in water at  $25^\circ\text{C}$ . Since there are no attractive or repulsive forces among hard-sphere particles, hydrodynamic forces dominate for  $Pe \geq 10$ . Viscosity by definition is the ratio of the stress created by these forces to the shear rate.

Assuming the viscosity of the suspending medium  $\mu_0$  to be constant, the relative viscosity of the suspension  $\eta_r$  can be designated as the sum of the contributions due to the molecules of the suspending medium, and due to the Brownian and hydrodynamic stresses:

$$\eta_r = 1 + \eta_r^B + \eta_r^H \quad (3.47)$$

The contributions of the reduced suspending medium viscosity ( $\mu_0/\mu_0 \equiv 1$ ) and the contribution of hydrodynamic viscosity,  $\eta_r^H$  can be equated to the high-frequency dynamic viscosity,  $\eta'_\infty$ , which represents the viscous contribution to the stress at equilibrium as Péclet number approaches zero. As Brownian motion creates a rapidly fluctuating stress, the Brownian contribution to the viscosity is calculated by integrating the autocorrelation function over a large time span, through the Green–Kubo formula:

$$\eta_0 = \eta'_\infty + \eta_r^B = \eta'_\infty + \frac{v}{k_B T} \int_0^\infty \langle \tau_{xy}(t) \tau_{xy}(0) \rangle dt \quad (3.48)$$

where  $v$  is the volume,  $\tau_{xy}$  the instantaneous shear stresses in the  $xy$  plane and  $\eta_0$ , the zero-shear viscosity of the suspension, the relative viscosity as  $Pe \rightarrow 0$ . The results of the zero-shear-rate viscosity calculations are redrawn in Figure 3.3(b). Comparison of Figure 3.3(a) and (b) shows that the results of the two theories are similar, even though the starting equations and models are different. This similarity holds for the “zero-shear rate” viscosities, the viscosity of suspensions at very low-shear rates when the hydrodynamic forces are not dominant. Localizations leading to cage formation as in the theory developed by Verberg *et al.* (1997) are confirmed in a recent article by Gopalakrishnan and Zukoski (2006), for volumetric fractions greater than  $\approx 0.40$  and are held responsible for the high viscosities observed in dense suspensions. On the other hand, the model developed based on Stokesian Dynamics correctly predicts the shear behavior of dense suspensions as will be given in the next section.

The variation of the viscosity contributions in eq. (3.47) with the Péclet number found by Foss and Brady (2000) is given in Figure 3.4(a). At  $Pe \leq 10$ , the hydrodynamic contribution to the viscosity remains approximately constant, equal to  $\eta'_\infty$ , and increases at  $Pe \geq 10$ . On the other hand, the Brownian contribution decreases with an increase in the Péclet number. The sum of these contributions bring about a minimum in the relative viscosity of the suspension, or equivalently the suspension shear thins from the level of zero-shear viscosity shown by the dotted lines on the figure to a minimum around  $Pe = 10$  after which shear thickening is observed. The variation of the extent of shear thinning and thickening expected with the variation in volumetric fraction of solids is given in Figure 3.4(b), together with the experimental data confirming the simulation results.

Brady and coworkers (Bossis and Brady, 1989; Foss and Brady, 2000) explain the shear-thinning behavior by the relative rates of deformation and relaxation of the equilibrium structures of concentrated suspensions. The distortion of equilibrium structures by flow-induced shear is relaxed by the back diffusion of particles under the action of thermal forces. At very low-shear rates, when the diffusion rate of the particles is equal to the deformation rate, the viscosity remains constant at the “zero-shear” viscosity value. As the shear rate, or equivalently Péclet number increases to a value greater than the Stokes–Einstein diffusion rate of particles  $D_0$  (eqs. (3.2) and (3.9)), the back diffusion of the particles to their

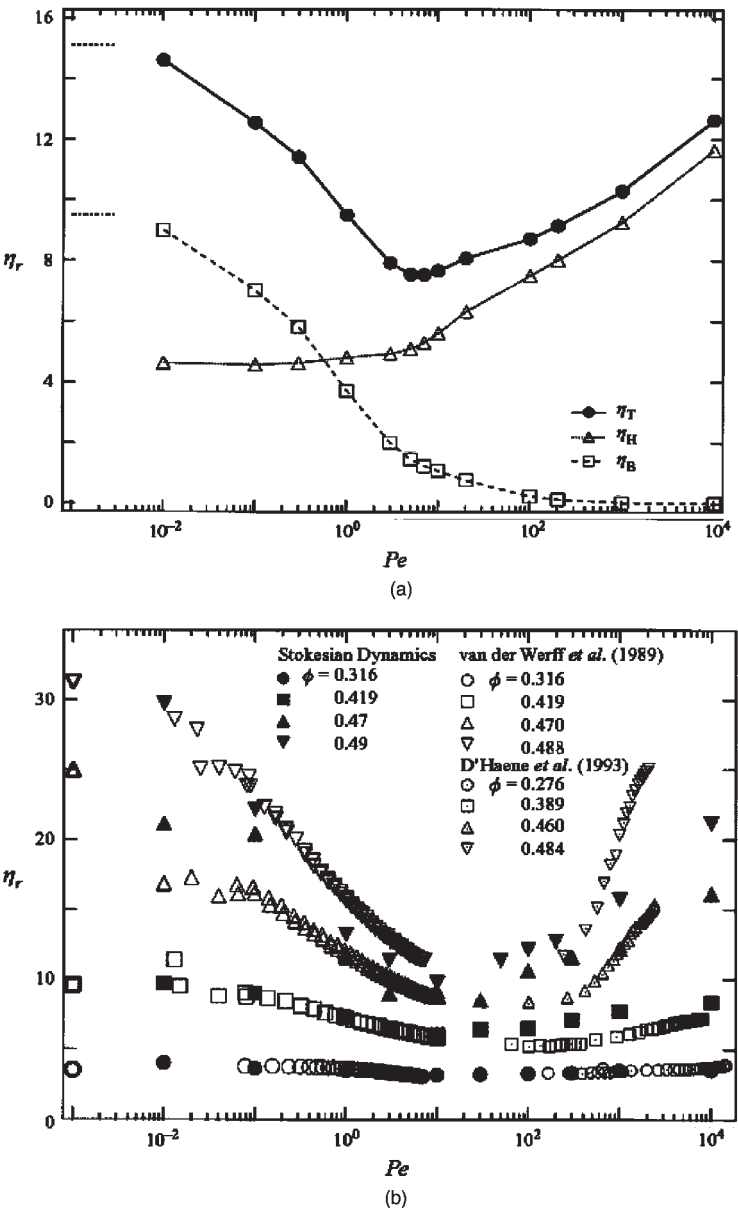


**Figure 3.4** Variation of the relative viscosities of concentrated hard-sphere suspensions with the Péclet number. (a) Contribution of Brownian,  $\eta_B$ , and hydrodynamic,  $\eta_H$ , counterparts to the total relative viscosity at  $\phi = 0.45$ , (b) variation of the relative viscosity with the volumetric concentration of solids  $\phi$  and the Péclet number. (Foss and Brady, 2000. Reproduced with permission of Cambridge University Press, Figures 2 and 3 in the original)

equilibrium configuration remains below the rate of deformation. Brownian viscosity then decreases inversely with the Péclet number. At high Péclet numbers, hydrodynamic forces dominate everywhere except within a thin boundary layer around the particles, where Brownian motion still exists. Lubrication flow takes place within this narrow channel. Component of shear in the direction of flow pushes the particles together to form reversible aggregates, called *hydroclusters*, when the separation distance between the particles is around one percent of their radius. The clusters grow as Péclet number increases. The Brownian motion, now unable to disrupt the cluster, determines the compaction and size of the clusters by breaking the connectivity of the cluster, preventing gel formation in the process. The simulations predict an increase in the rate of both shear thinning and shear thickening as volumetric concentration of solids increases.

### 3.2.4 Shear behavior of concentrated hard-sphere suspensions

It is now generally accepted that *hydrocluster* formation by the compression effect of shear stress component, acting in the flow direction proposed by Brady and coworkers (Bossis and Brady, 1989; Foss and Brady, 2000), is responsible for shear thickening. Shear thickening found by Stokesian Dynamics simulations described in the previous section is not the same as the shear thickening in dilatant power-law behavior observed when  $n > 1$  in power-law fluids given in Chapter 2 (eq. (2.34)): Dilatant behavior of non-Newtonian fluids is generally associated with an increase in the number of “particles” such as in the cleavage of clay platelets, breakup of drops in an emulsion or particles in a suspension, with an increase in the shear rate; whereas, shear thickening in concentrated suspensions is due to grouping of particles by hydrodynamic forces in the form of clusters. *Hydroclusters* are also different from the fractal clusters and aggregates formed by attractive forces, as given in Chapter 1, which for this reason are called *thermodynamic clusters*.

#### 3.2.4.1 Shear thinning and shear thickening behavior of suspensions

Hydroclusters are formed whenever hydrodynamic forces overcome the dispersive Brownian forces. The critical shear stress for the onset of shear thickening is found by a force balance between hydrodynamic forces,  $F_H$  and Brownian forces,  $F_B$  (Bender and Wagner, 1996; Maranzano and Wagner, 2001). As Brownian motion is instantaneous and random, averaging (mean field approximation) is made by multiplying the thermal energy,  $k_B T$  with the derivative of the equilibrium radial distribution function  $g(r)$ , to take into account the distribution of particles surrounding a given particle:

$$F_B = -k_B T \left[ \frac{\partial \ln g(r)}{\partial r} \right] \quad (3.49)$$

As any cluster formation starts with the collision of two particles, hydrodynamic force is taken as the force between two particles (Boersma *et al.*, 1992)

$$F_H = \frac{3\pi\mu_0 \dot{\gamma} R^3}{h} \quad (3.50)$$

where  $h$  is the interparticle separation distance defined in terms of the volumetric fraction of solids,

$$\frac{h}{2R} = \left( \frac{\phi}{0.71} \right)^{1/3} - 1 \quad (3.51)$$

The maximum volumetric fraction taken as 0.71 in this equation is the experimentally found value where monodisperse, hard-sphere suspensions do not flow (deKruif *et al.*, 1985). Interactions exist not only between two particles but also among many particles present in the concentrated suspension. Further correction is made for this many-body effect by using eq. (3.19) (Maranzano and Wagner, 2001). The critical stress at which hydrocluster formation starts is found by equating eqs. (3.49) and (3.50), and using the identity ( $\tau_{hc} = \eta \dot{\gamma}$ );

$$\frac{\tau_{hc}}{k_B T} \frac{R^3}{\mu_0} = -\frac{h}{3\pi} \frac{\eta}{\mu_0} \left( \frac{d \ln g(r)}{dr} \right) \quad (3.52)$$

The LHS of the equation is a dimensionless stress and  $\tau_{hc}$  is the critical stress for the onset of hydrocluster formation. As hard-sphere properties can also be maintained by steric stabilization and by electrostatic repulsive forces among particles, shear thickening will arise whenever hydrodynamic forces dominate the dispersive forces.

Gopalakrishnan and Zukoski (2004) used the well-defined system of silica particles of radius  $R = 103\text{nm}$ , stabilized with octadecanol, and suspended in decalin. The results of the experiments are redrawn in Figures 3.5(a) and (b), as the variation of relative viscosity,  $\eta_r$  with the nondimensional shear stress,  $\tau R^3/k_B T$  (in the abscissa (a) is used to denote  $R$ , the particle radius). The zero-shear viscosity at low-shear rates increases with an increase in the volumetric fraction of solids in Figure 3.5(a). The suspensions show shear thinning behavior up to  $\tau R^3/k_B T \leq 10$ . The minimum in the viscosity where shear thickening starts remains approximately constant with the volumetric fraction of hard-sphere solids,  $\phi$ . Gopalakrishnan and Zukoski (2004)] propose that the critical shear rate for the onset of shear thickening,  $\dot{\gamma}_c$ , should not be taken as the critical shear rate for the onset of hydrocluster formation  $\dot{\gamma}_{hc}$ , even though hydrocluster formation is a prerequisite for shear thickening. Equally important are the thermodynamic attractions, such as that brought about by depletion forces due to presence of nonadsorbing polymers in the suspension medium.

Even though the particles have no attractive or repulsive interactions, attractions can still arise as depletion forces due to nonadsorbed polymers in the suspending medium. Presence of nonadsorbing polymers creates different effects on the microstructure and rheology of concentrated hard-sphere suspensions depending on the molecular weight and radius of gyration of the polymer molecules and the ratio of the radius of gyration of the polymer to the hard-sphere radius of the particle. Radius of gyration of the polymer,  $R_{gp}$  determines the distance (range) over which attractive forces act. The concentration of the polymer affects the osmotic pressure between the bulk of the solution and the excluded



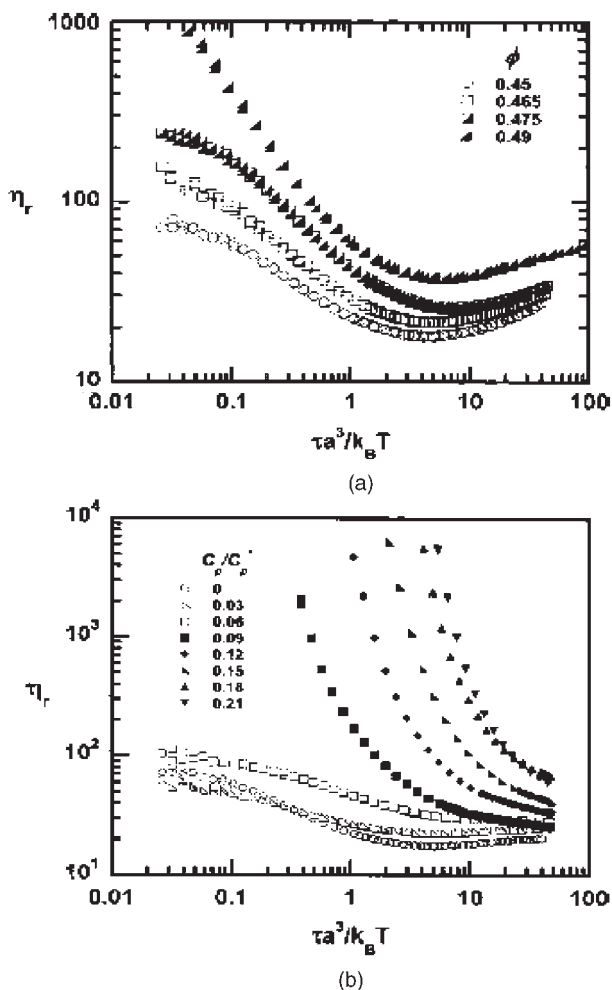


**Figure 3.5** Steady-state viscosity flow curves for hard-sphere suspensions, (a) at different volumetric fractions,  $\phi$ , for  $R = 103$  nm. (b) as a function of increasing polymer concentration for  $\phi = 0.45$  and  $R = 103$  nm ( $a \equiv R$ ) (Gopalakrishnan and Zukoski, 2004. Reproduced with permission of The Society of Rheology, Figures 2(a) and 4 in the original.)

volume among the particles. The greater the concentration, the greater the osmotic pressure and hence the strength of the depletion forces leading to localization.

Gopalakrishnan and Zukoski (2004, 2006) made in-depth studies of the effect of depletion forces on the shear behavior of hard-sphere-like suspensions of silica particles stabilized with octadecanol. The particles are suspended in decalin with varying concentrations of nonadsorbing polymer polystyrene. Decalin is a good solvent for polystyrene in which it can fully extend (theta solvent).

The concentration of the polymer  $C_p$  is nondimensionalized with the overlap concentration of the polymer  $C_p^*$ , defined as

$$C_p^* = \frac{M_w / N_A}{4\pi R_{gp}^3 / 3} \quad (3.53)$$

where  $M_w$  is the molecular weight of the polymer,  $N_A$ , the Avogadro's number and  $R_{gp}$  is the radius of gyration of the polymer defined with the general expression for the radius of gyration eq. (3.4) for a polymer made up of the same identical monomers (homopolymer) of equal mass as

$$\bar{R}_{gp}^2 = \frac{\left\langle \sum_{i=1}^{N_p} |\bar{r}_i - \bar{r}_{cm}|^2 \right\rangle}{N_p} \quad (3.54)$$

where  $N_p$  is the number of monomers in the polymer,  $r_{cm}$  the center of mass of the polymer, and  $r_i$  the distance of the  $i$ th monomer from the center of mass. As the polymer continuously changes its configuration, only the average distances are taken.  $R_{gp}$  is the radius of the shell that circumscribes the molecule. The radius of gyration of a polymer does not specify the shape or the configuration of the polymer.

At very low concentrations of the polymer, only weak attractions prevail between the hard-sphere particles. Similar to the melting of glasses described in Section 1.6.1, these weak attractions draw the particles closer together, opening up sufficient space for the encaged particles (Poon, 2002) to escape freely as shown schematically in Figure 3.6(a). The variation of the relative viscosity of the suspensions with the polymer concentration is drawn in Figure 3.6(b) as a function of dimensionless stress,  $\tau d_p^3 / 8k_B T = \tau R^3 / k_B T$ . The plot in the insert is actually a cross view of the figure at low values of the shear stress, the profile that would be observed if the data were plotted on a three-dimensional graph, the third axis being  $C_p / C_p^*$ . The breakup of the cage structure causes a large reduction in the zero shear viscosity: As the dimensionless polymer concentration increases, the zero-shear viscosity decreases to a minimum around  $C_p / C_p^* = 0.03$  and then increases again as shown in the insert of the figure. The increase in the zero-shear viscosity after the minimum shows that attractive forces due to increasing polymer concentration re-establish the cage-like structure, which is also reflected on the infinite shear viscosity as an increase.

Attractive depletion forces facilitate the formation of both the thermodynamic clusters leading to formation of gels, and the hydrodynamic clusters leading to shear thickening. As a result, either shear thickening or gel formation is observed at lower shear stresses and strains. The rheological behavior will be dictated by the dominant mechanism. In the case of high polymer concentrations, the strong thermodynamic attractive forces among the particles prevent formation of hydroclusters and shear thickening will not be observed after the minimum in relative viscosity. At low concentrations of polymer, attractive depletion forces are too weak to prevent hydrocluster formation at high-shear rates (or shear stresses) and shear thickening is observed.

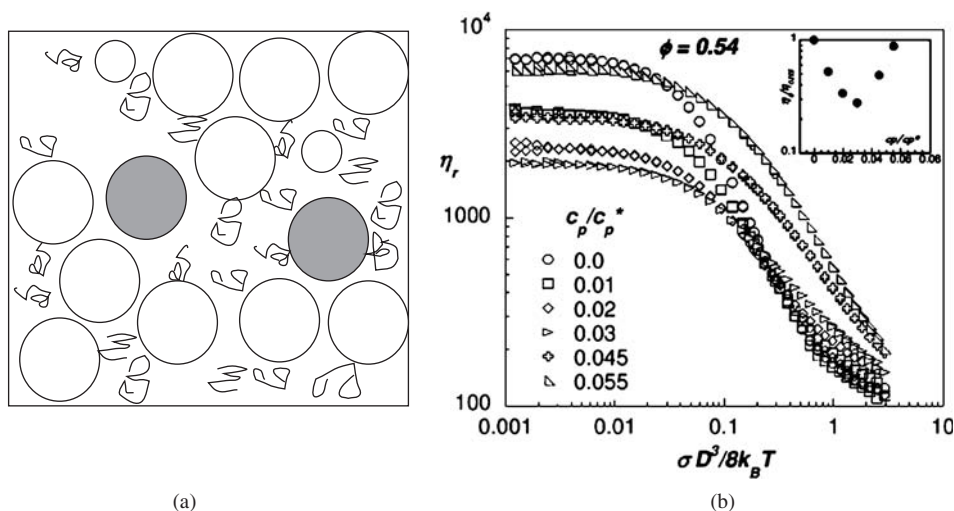


**Figure 3.6** Effect of nonadsorbing polymers on hard-sphere suspensions: (a) opening-up of the cage structure, (b) effect of structural variation on the relative viscosity plotted as a function of dimensionless shear, as in Figure 3.5. ( $\sigma$  is stress denoted as  $\tau$  in this text, and  $D$  is the particle diameter,  $d_p$ ).  $d_p = 48$ ,  $R_{gp} = 1.31$  nm,  $R_{gp}/R = 0.055$ . (Gopalakrishnan and Zukoski, 2006. Reproduced with permission of The American Chemical Society, Figure 6 in the original).

The relative viscosity of the same silica particle system but with lower particle concentration of  $\phi = 0.45$  and different particle radii  $R = 103$  nm, and polymer radius of gyration ( $R_{gp} = 5.53$  nm,  $R_{gp}/R = 0.05$ ) at  $\phi = 0.45$  is given in Figure 3.5(b). In the fluid state shown with open symbols, the relative viscosity goes through a constant zero-shear region at very low shear stresses. A minimum and subsequent shear thickening are observed only when  $C_p/C_p^* \leq 0.03$ . At higher concentrations, the minimum region could be observed at higher stresses, if slip flow and secondary flow could be eliminated.

Shear thickening is not observed also, in the case of irregular or rough particles as the asperities prevent the close approach of particles to the point of overlapping boundary layers, necessary for hydrocluster formation.

#### 3.2.4.2 Shear behavior of colloidal hard-sphere gels

Gopalakrishnan and Zukoski (2004, 2006) draw attention to the similarity of mechanisms in the formation of dense suspension gels, hydroclusters, and glasses. All of the three states are manifestations of localization phenomena, which destroy the uniformity and homogeneity of the suspension on all length scales, termed as *ergodicity*. Concentrated suspension gels consist of clusters with sizes of 3–8 particle diameters (Shah *et al.*, 2003). As shown in Figures 3.1(d) and (f), the particles encaged in the clusters of a gel have a limited freedom of Brownian motion. This freedom does not exist in glasses where the particles are much more closely spaced and the interparticle distance is reduced to the order of radius of gyration of polymer molecules. Hydroclusters are also cases of localization brought about by shearing. The rheological properties associated with localization in the

case of gels are development of yield stress, and elastic moduli ( $G'$  and  $G''$ ); and in the case of hydroclusters, is shear thickening. Both the elasticity and shear thickening arise when the clusters formed span all of the available volume as an interconnected network, termed as *percolation*.

Gels exhibit measurable viscosities in a very limited shear stress (or shear rate) range due to development of yield stresses as a result of strong attractive forces between the particles. Slip at the walls is also considerable because the attractive forces between the particles severely decrease the adherence of the suspension to the wall. The low-shear viscosities diverge to very high values indicating the appearance of yield stresses characteristic of gel behavior as shown by the filled symbols in Figure 3.5(b). The greater the yield stress, the narrower is the region where shear behavior could be measured. Shear viscosity measurements are limited in the high-shear regions, also, because of the secondary flows observed in the case of viscoelastic behavior (see Chapter 2, Figure 2.23). Within the narrow measurable region, gels are highly shear thinning.

### 3.2.5 Viscoelastic behavior of hard-sphere gels

Gels are nonequilibrium structures typically characterized by the formation of a continuous network structure extending over the available volume. Existence of attractive forces is a prerequisite for gel formation. The greater the strength of the attractive forces, the less is the particle concentration required for the continuity of the network. Another closely related phenomenon is localizations in the microstructure of the gels. If the attractions between particles are very strong, such as in the case of hydrophobic forces among particles the localizations are not observed. An example is the thermal gels obtained on cooling of a suspension of silica particles ( $d_p \approx 90\text{nm}$ ) in decalin that behaves as a hard-sphere suspension at elevated temperatures. Reversible clusters formed by the action of applied shear are reported to disintegrate with the recovery of the original nonlocalized structure on the cessation of shear (Ramakrishnan *et al.*, 2005; Ramakrishnan and Zukoski, 2006).

The ratio of the radius of gyration of the polymer to the radius of the hard-sphere particle determines the equilibrium and nonequilibrium states to be expected (Chen and Schweizer, 2004): In the case of high molecular weight polymers with  $R_{gp}/R \geq 0.3$  fluid–fluid phase separation is observed in the suspension. Either of the two states can be observed with the use of low molecular weight polymers,  $R_{gp}/R \leq 0.3$ : A transition from fluid to the solid state under equilibrium conditions or from fluid to gel states under nonequilibrium conditions. Particle gels are characteristically amorphous, nonergodic, have very long relaxation times, are viscoelastic with the modulus of elasticity weakly dependent on frequency of strain under low stresses and have an apparent yield stress above which they deform continuously, i.e., flow. As long as the attractive forces prevail, the gel structure will form again upon relaxation.

Gel microstructure has two counterparts: The backbone network that transmits the applied stresses throughout the gel network and the clusters which may or may not be viscoelastic themselves, depending on the compaction of their microstructure. The greater the concentration of the particles, the stronger will be the interlinking bonds among the clusters, the greater will be the yield stress and the magnitude of the modulus of elasticity.

The rheology of the gels depends largely on the cluster structure, which can be grouped under three broad classes:

### 3.2.5.1 Hard-sphere gels with a fractal microstructure

Gels in this group are formed when the fractal clusters grow sufficiently in size and overlap with each other to fill the available volume. There are several models proposed to relate the microstructure of the fractal gels to their rheological behavior. Russel *et al.* (1989) assumed all the primary particles are in aggregated form in clusters of characteristic size  $R_{\text{agg}}$ , with particle-free spaces among the clusters. The ratio of the size of clusters to that of the primary particles  $R_0$  is related to the volumetric fraction of solids,  $\phi$  through a relation in terms of the fractal dimension,  $d_f$  obtained by a mass balance using eq. (1.59),

$$\frac{R_{\text{agg}}}{R_0} = \left( \frac{\phi}{\phi_m} \right)^{1/(d_f-3)} \quad (3.55)$$

$\phi_m$  is the volumetric fraction of solids at random close packing,  $\phi_m = 0.64$ .

Shih *et al.* (1990) assumed that the cluster structure remained constant with an increase in the volumetric fraction of solids, but the number of bonds interlinking these clusters increased with  $\phi$ . The shear modulus of elasticity  $G'$  is related to the cluster size  $R_{\text{agg}}$  and volumetric fraction of solids  $\phi$  with a power-law relation of the form,

$$G' \propto R_{\text{agg}}^{-(2+d_{\text{fb}})} \quad (3.56)$$

$$G' \propto \phi^{(3+d_{\text{fb}})/(3-d_f)} \quad (3.57)$$

where  $d_{\text{fb}}$  is the fractal dimension of the backbone clusters of the gel, which bear the external shear stress, ( $1 \leq d_{\text{fb}} \leq d_f$ ) while  $d_f$  is the fractal dimension of the clusters. Rheological measurements of alumina gels in the range  $0.03 \leq \phi \leq 0.12$  led to an empirical relation of the form

$$G' = \phi^{4.1} \quad (3.58)$$

in agreement with the results of Buscall *et al.* (1986), who found the exponent as 4.5 under reaction limited conditions and 3.5, under diffusion limited conditions.

Overlapping fractal cluster model of hard-sphere particle gels are relevant at low values of the volumetric fraction of solids. At increasing solid fractions, overlapping becomes so extensive that identity of individual clusters becomes ambiguous.

### 3.2.5.2 Percolation gels

Percolation clusters grow at the sterically more favorable sites along the edges of the cluster resulting in a more porous structure. When clusters are linked at the edges to form a highly porous volume-spanning network, the suspension is said to *percolate*. As all the

fractal clusters are now interlinked, the gel structure behaves as an infinite-sized cluster, i.e., the cluster size diverges. Gels form when continuity within the network is maintained, after which an applied force can be transmitted throughout the gel. This volumetric fraction, denoted as  $\phi_G$ , marks the transition to gellation. As  $\phi$  increases, interlinking mechanism becomes stronger at the expense of decreasing porosity.

Carbon black particles of 30 nm diameter compacted into very dense clusters forming the primary particles of radius,  $R_0 \approx 0.25 \mu\text{m}$ , and fractal dimension  $d_f = 2.2 \pm 0.1$  stabilized with double-chained surfactants suspended in oil to simulate motor oils were investigated by Trappe and Weitz (2000). The system behaved nearly as a percolation gel when attractive interactions were kept under control. The appearance of the gels taken under an optical microscope and elastic behavior of the gels at three volumetric concentrations of 0.097, 0.064, and 0.033 are reproduced in Figure 3.7. The curves for different volumetric fractions were found to coincide for both  $G'$  and  $G''$  when the elastic and viscous moduli are normalized by dividing with the plateau value of the elastic modulus and the frequency, by the frequency where the elastic and storage moduli cross over. At the lowest volumetric fraction of  $\phi = 0.033$  the interconnectivity of the gel is lost and the gel flows like a fluid.

As the interlinking between the clusters increases, the gel behaves more like a viscoelastic solid. When the bonds between the clusters are not very strong, the gel behaves like a yield stress fluid, (Section 2.3.2 in Chapter 2) responding elastically to applied shear stress below the yield value and flowing as a Newtonian fluid at stresses above the yield stress value.

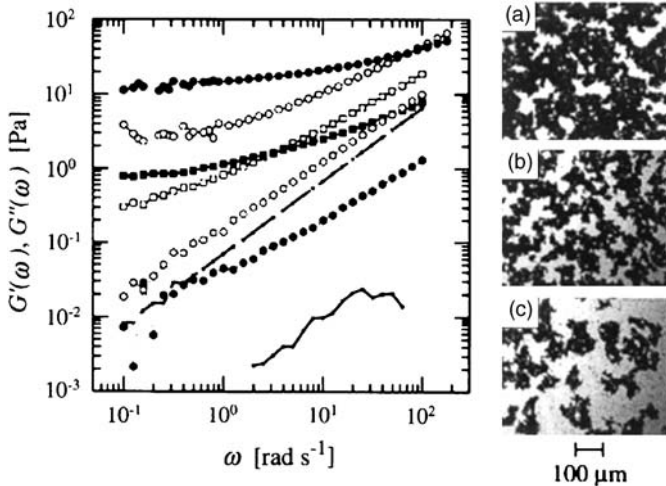


**Figure 3.7** Appearance and viscoelastic behavior of carbon black gels. Solid symbols denote  $G'(\omega)$  and open symbols  $G''(\omega)$  (a)  $\phi = 0.097$  denoted by squares, (b)  $\phi = 0.064$  denoted by hexagons (c)  $\phi = 0.033$  denoted by solid ( $G'(\omega)$ ) and dashed lines ( $G''(\omega)$ ). Circles with the highest values of  $G'$  (and)  $G''(\omega)$  denote the rheological behavior at  $\phi = 0.149$  where the gel is too dense for its microstructure to be visible. (Trappe and Weitz, 2000. Reproduced with permission of The American Physical Society, Figure 1 in the original.)

### 3.2.5.3 Locally densified nonfractal gels

In dense depletion gels approaching the glass transition volumetric fractions, the exponent of the power-law dependence of elastic modulus  $x$ ,  $G' = \phi^x$ , reaches very high values of  $5 \leq x \leq 8$  (Ramakrishnan *et al.*, 2005) implying very small changes in the local compaction will have very large effects on the elasticity of the gels. The interpenetrating clusters are very compact, unlike the ramified fractal clusters, and are small with a size range of  $R_{\text{agg}} \approx (3 - 5)R_0$ . The localization length, or the scale of freedom of particle motion,  $r_{\text{loc}}$  is found starting from the equation of motion. Given this length scale and the structure factor as inputs, an expression for the shear modulus of elasticity is obtained as

$$G' = \frac{\phi k_B T}{r_{\text{loc}}^2} \quad (3.59)$$

This relation can predict the elastic behavior of dense gels (Shah *et al.*, 2003): The elastic modulus  $G'$  increases with an increase in the volumetric fraction of solids  $\phi$ ; the energy of attraction that has to be overcome, expressed in terms of thermal energy,  $k_B T$ ; and with a decrease in the localization length,  $r_{\text{loc}}$ . Good agreement could be obtained with experimental results (Ramakrishnan *et al.*, 2005) when the predicted shear modulus  $G'_{\text{pr}}$  is scaled with the ratio of the primary particle to cluster dimension  $R_0/R_{\text{agg}}$

$$G' = G'_{\text{pr}} \left( \frac{R_0}{R_{\text{agg}}} \right)^3 \quad (3.60)$$

### Example 3.1: Viscoelastic behavior of sterically stabilized clay gels

*The case:* Nonswelling montmorillonite type of clays form unstable suspensions in water and settle in a short-time interval after dispersion. Adsorption of cationic surfactants, such as cetyl trimethyl ammonium bromide (CTAB) or double-chained surfactants on the clay platelets, sterically stabilizes the particles keeping them in suspension. Above a critical concentration, the particles form a volume spanning gel. Nonswelling montmorillonite type clay particles stabilized with CTAB are used in this example, to illustrate the rheological properties of the gels. Volumetric fraction of clay suspensions is  $\phi = 0.023$ ,  $\phi = 0.029$ ,  $\phi = 0.033$ . Rheological characterization is made under stress control with cone and plate sensors (35 mm in diameter, with a cone angle of  $1^\circ$ ) at  $25^\circ\text{C}$  to characterize the clay gels. The samples are not subjected to preshearing to illustrate the effects of structure formation on standing in thixotropy tests.

*Analysis of the Case:* Creep and recovery tests are used to characterize the viscoelastic behavior qualitatively under an applied shear stress. The results of the creep tests of clay suspensions stabilized with a 10% coverage of surfactants, run at a step increase in the shear stress of 1 Pa, are given in Figure 3.8(a). The common features for all the volumetric fractions are the initial jump in the strain, a region of gradual increase in strain and a final linear region. In the most concentrated suspension, the final linear region is horizontal; whereas, a linear region with a positive slope is observed in lower volume fractions.

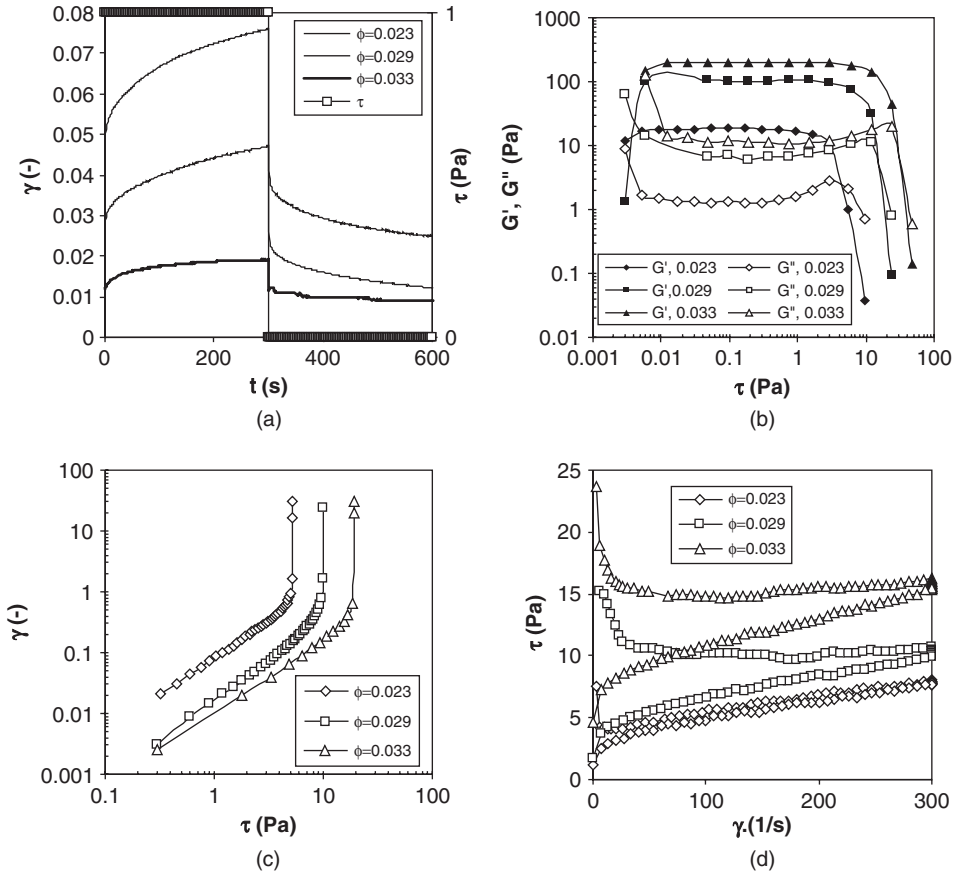


**Figure 3.8** Viscoelastic properties of clay suspensions stabilized by adsorption of a cationic surfactant: (a) creep and recovery tests, (b) viscoelastic properties under dynamic conditions, (c) yield stress analysis, (d) thixotropic behavior under shear.

The initial step in strain increases in the order 0.01, 0.03, 0.05 with a decrease in the volumetric fraction of solids 0.033, 0.029, 0.023. The immediate response to a sudden increase in stress is due to the elasticity of the gels, exhibiting Maxwell behavior. The inverse relation can be attributed to the restricted motion of the particles in concentrated suspensions. If the gel would deform linearly after this initial response, the fluid would be called a *Maxwell liquid*. However, instead of a linear increase, the rate of deformation of the gel decreases with the time during which it is subjected to the step increase in stress. This type of response is termed *Kelvin-Voigt* behavior, typically exhibited by viscoelastic solids. If the gels were Kelvin-Voigt solids, the rate of decrease in the strain response would end up with an equilibrium situation, whereby the gel would completely comply with the applied stress. This response is observed only in the case of most concentrated gels,  $\phi = 0.033$ . In the other cases, a linear increase in strain is observed, i.e., Maxwell behavior. It should be noted that Burger or Kelvin-Voigt model behavior could also have been observed



if the applied stress were much lower than 1 Pa. When the step stress is removed at the end of 300 s, all the gels react with a sudden jump back to their initial configuration equal in magnitude to the initial jump in the reverse direction. A nonlinear decrease in strain follows the step decrease during which the gel relaxes (recovers) from the effect of the stress. The longest relaxation time is observed with the least concentrated suspension that had undergone the severest deformation. The strain level where the relaxation ends up finally, is an indication of the frictional losses in the process. Since the starting points were the same (zero strain) in all cases, the level of strain remaining after the cessation of stress shows the equivalent energy that is lost through friction and cannot be used to return to the original configuration. Figure 3.8(a) shows that the frictional losses increase with the magnitude of the initial strain response to the applied stress. A fluid that shows a Kelvin–Voigt solid behavior linked in sequence with Maxwell liquid behavior is said to behave as a *Burger* fluid (Schramm, 1994). Burger model is very flexible and can be adjusted to fit the responses of most of the real fluids by adjusting the relative contribution of Maxwell and Kelvin–Voigt counterparts. The strain response of fluids to a step increase in stress is given in Table 3.2 for the Burger model and its counterparts, the Maxwell and Kelvin–Voigt models. The subscript (1) in eq. (3.63) denotes the Kelvin–Voigt and (o), the Maxwell contribution.

The dynamic response of the gels to oscillatory shear stress is given in Figure 3.8(b). In all of the cases, the storage modulus  $G'$  is greater than the loss modulus  $G''$  displaying gel behavior or a linear viscoelastic response in this interval. As the volumetric fraction of clay decreases below 0.023, the strength and stability of the gel decreases. Regression of the plateau values of storage modulus with the volumetric fraction of clay particles yield an expression

$$G' \propto \phi^{6.4} \quad \text{with} \quad r^2 = 0.996 \quad (3.64)$$

indicating a compact microstructure for the gels.

The shear stress values at which  $G'$  and  $G''$  curves cross over are closely related with the yield stress of the gels given in Figure 3.8(c). The stress values at which a sudden divergence in strain is observed are the yield stress values of the gels.

**Table 3.2**

Strain response in viscoelastic models

Model	Response to stress	Equation numbers
Kelvin–Voigt model (solid)	$\gamma(t) = \frac{\tau_0}{G} [1 - e^{(-t/\lambda)}]$	(3.61)
Maxwell model (Liquid)	$\gamma(t) = \left( \frac{\tau_0}{\eta} \right) t + \frac{\tau_0}{G}$	(3.62)
Burger model	$\gamma(t) = \frac{\tau_0 t}{\eta_0} + \frac{\tau_0}{G_0} + \frac{\tau_0}{G_1} [1 - e^{(-t/\lambda_1)}]$	(3.63)

The behavior of the gels under shear stresses above their yield value is presented in Figure 3.8(d). The variation of the shear stress with the rate of shear is given for the initially undisturbed gels to illustrate the thixotropy of the gels: The microstructure of the gel is formed by the clay platelets coated with surfactant. Under the effect of the applied shear, the microstructure is broken down and the particles are forced to assume a position parallel to the direction of the shear. The shear stress created in the gel is reduced as more and more particles assume a parallel direction with an increase in the shear rate. The upper curve (upflow curve) in each cycle represents the structural breakdown in the gels. The initial steep decrease in the shear stress is an indication of the structural break-down. The slope after the initial decrease gives the extent and difficulty in the reorientation of the particles. In the case of concentrated suspensions  $\phi = 0.029$ , and  $\phi = 0.033$ , the shear stress remains constant indicating that the viscosity decreases steadily in association with the reorientation. In the case of rather dilute suspension  $\phi = 0.023$ , the structural breakdown is completed at very low-shear rates, after which the shear stress increases in conformation with power-law behavior. The shear rate is reduced after the maximum shear rate set for the experiment at  $\dot{\gamma} = 300\text{s}^{-1}$ . All of the curves in downflow from high to low-shear rate levels (lower curves) are similar and represent power-law behavior. Fit to Herschel-Bulkley model eq. (2.48) through the regression of the downflow curves yields the equations

$$\tau = 1.37 + 0.39\dot{\gamma}^{0.482} \quad \text{with } r^2 = 0.9965 \quad \text{for } \phi = 0.023 \quad (3.65)$$

$$\tau = 1.78 + 0.69\dot{\gamma}^{0.426} \quad \text{with } r^2 = 0.9968 \quad \text{for } \phi = 0.029 \quad (3.66)$$

$$\tau = 4.19 + 1.17\dot{\gamma}^{0.394} \quad \text{with } r^2 = 0.9921 \quad \text{for } \phi = 0.033 \quad (3.67)$$

Eqs. (3.65)–(3.67) show an increase in the yield stress  $\tau_0$ , and consistency,  $K$ , and a decrease in the power-law index  $n$  with an increase in the volumetric fraction  $\phi$  of clay. Note the severe reduction in the yield stress  $\tau_0$  after structural break-down. The area remaining in between the upflow and downflow curves is called *thixotropy index* (TI) and gives the energy per unit time and unit volume ( $\text{J m}^{-3} \text{s}^{-1}$ ) expended for the breakdown of the network structure and reorientation of the particles

$$TI = \int_{\dot{\gamma}_{\min}}^{\dot{\gamma}_{\max}} (\tau d\dot{\gamma})_{\text{upflow}} - \int_{\dot{\gamma}_{\min}}^{\dot{\gamma}_{\max}} (\tau d\dot{\gamma})_{\text{downflow}} \quad (3.68)$$

Regression of the TI values for the thixotropic cycles given in Figure 3.8(d) yields a relation of the form

$$TI = 4 \times 10^{10} \phi^{5.1} \quad \text{with } r^2 = 0.9995 \quad (3.69)$$

implying both the strength of the network structure and the difficulty experienced by the particles in changing their orientation with an increase in the volumetric fraction of the solids.

### 3.3 RHEOLOGY OF SOFT-PARTICLE SUSPENSIONS

In Section 3.2 of this chapter, the particles were identified as “hard sphere”, meaning the interactions are zero at all separations except in contact when the repulsive forces rise up to infinity due to the inelasticity of the particles. This ideal case is approached through steric stabilization by short-chain hydrocarbons, with hydrocarbon chain length,  $l$ , being only a few percent of the particle radius,  $R_0$ ,  $l \ll R_0$ . Particles with interactive forces such as electrostatic or surface forces have a halo of charges or sections of hydrocarbon chains, respectively, surrounding their hard core. Neither the charges, nor the chains are impenetrable, as can be seen in Figures 1.2(c) and 1.5(a–c). The ionic, or hydrocarbon halo around the particle leads to an increase in the effective radius of the particle,  $R_{\text{eff}}$ , depending on the pair-interaction energy of the particle,  $U(r)$ , scaled with the dispersive thermal energy,  $k_B T$ , (Persello *et al.*, 1994),

$$R_{\text{eff}} = R_0 + \frac{1}{2} \int_{2R_0}^{\infty} \left[ 1 - \exp\left(\frac{-U(r)}{k_B T}\right) \right] dr \quad (3.70)$$

Pair-interaction function depends on the interactive forces effective on the particles. If only electrostatic forces are acting, as in the case of DLVO theory, then the pair-interaction function can be given by eq. (1.39), reorganized as

$$\frac{U(r)}{k_B T} = \frac{Z^2 L_B}{r} \frac{\exp(-\kappa h)}{(1 + \kappa R_0)^2} \quad (3.71)$$

where  $h$  is the surface-to-surface distance of the particles ( $h = r - 2R_0$ ) and  $r$ , the center–center distance. The number of free counterions in the diffuse ionic halo, is estimated by the so-called  $Z$  criterion of Persello *et al.* (1994),

$$Z = \frac{4R_0}{L_B} \quad (3.72)$$

in terms of the Bjerrum length  $L_B$ , which can be obtained from the ion–ion potential energy given in Chapter 1, eq. (1.2) by dividing with the thermal energy,  $k_B T$ .

$$L_B = \frac{e^2}{(4\pi\epsilon_0\epsilon_r k_B T)} \quad (3.73)$$

$R_{\text{eff}}$  found from eq. (3.70), is used with eqs. (3.71)–(3.73) to correct the volume fraction of hard-sphere particles,  $\phi$ , for the effective increase in volume due to presence of soft particles in the suspension,

$$\phi_{\text{eff}} = \phi \left( \frac{R_{\text{eff}}}{R_0} \right)^3 \quad (3.74)$$

With the ionic (or hydrocarbon) halo surrounding the particles, the soft-particle suspension reaches close-packed conditions at a number density of particles much lower than that of hard-sphere particles. Depending on the volumetric fraction of solid particles and extent of

the ionic (or hydrocarbon) halo, the soft-particle suspension can exist in three states: (1) *Gas state* where there is no interaction between the particles. In this state, both the viscoelastic and the shear response of the suspension are linear. (2) *Soft solids* at intermediate volumetric fractions, where the limited overlap between the halos confer rheological properties of a *gel* to the suspension, even though the particles repel each other. This state is marked with the appearance of a yield stress. (3) Rigid, concentrated suspensions that have a very high-yield stress, after which they either slip or fracture (Persello *et al.*, 1994).

Because of the elastic halo that surrounds these particles, soft particle pastes behave like elastic solids at low stresses but they can flow when the yield stress is exceeded. The nature of the flow after the yield depends on the microstructure of the fluid. The dependence of the flow on the deformation of the microstructure introduces the effects of shear thinning, memory or shear history dependence, normal stresses and migration, wall slip, and aging phenomena into the rheology and flow behavior of soft particle pastes (cloitre, 2005). The elastic nature of the particles is reflected onto the shear behavior by the scaling of the yield stress,  $\tau_0$  with the shear modulus of elasticity,  $G$ .

The existence of a yield stress is an indication of the role of attractive forces among the particles. The yield stress reflects the aggregation state and the attractive forces between the particles within the aggregates, given by the relation (Burns *et al.*, 2003).

$$\tau_0 = \phi \frac{n}{2} E_{\text{sep}} \frac{1}{(4\pi R_0^3 / 3)} \quad (3.75)$$

where  $\phi$  is the volumetric concentration of the primary particles within the suspension,  $R_0$  the radius of the primary particles,  $n$  the coordination number, or average number of contacts per particle (divided by two to show the contribution of each particle in a pair), and  $E_{\text{sep}}$  the energy required to separate the aggregate into single primary units.  $E_{\text{sep}}$  is closely associated with the total potential energy  $U(r)$ , through the radial distribution function  $g(r)$  and the strength of the attractive and repulsive forces bringing the primary particles together in the form of an aggregate.

$E_{\text{sep}}$  also determines the non-Newtonian flow behavior of the suspension and the constitutive equations given in Chapter 2. If the primary particles can be dispersed easily under shear, then the suspension will behave like a Newtonian fluid after the yield stress is exceeded, which can be modeled with the Bingham relation (eq. (2.46)). If the clusters do not disintegrate readily, then the suspension will shear-thin, which can be modeled with Herschel-Bulkley (eq. (2.48)) or Casson (eq. (2.50)) equations. If the particles cannot totally relax from their sheared positions after the reduction of the shear within the time scale of measurement, then the suspension will exhibit *thixotropy*.

These effects can be manipulated by varying the process conditions as explained below.

### 3.3.1 Control of rheology through manipulation of surface forces

In view that the states of soft particle suspensions are determined by surface forces (eqs. (3.70)–(3.74)), the rheology of the suspensions can be manipulated through the control of these forces. Rigid, concentrated suspension behavior determines the working

conditions in extrusion of ceramics, for example. Otherwise, such high-volumetric concentrations are not desirable since they cannot flow in the sense of other non-Newtonian fluids with a noninterrupted shear stress gradient in the radial direction of the channel. Readily flowable suspensions with a low-yield stress are aimed for in ordinary operations, where transfer of solids is the main concern. If the process aims to collect the particles, then attractive forces should be enhanced to increase the particle collection efficiency, such as in sedimentation. Two alternative routes are possible: The particles can coagulate as discrete aggregates or flocs that readily settle in an almost Newtonian medium; or, they can coagulate in the form of gels, which will be more difficult to handle due to development of yield stresses and increased viscosities. If the stability of the suspension is aimed for, then repulsive forces should be enhanced to keep the particles in suspension. The yield stress should be minimized to reduce the energy costs in transferring the suspension, and during filtration, and yet the yield stress should be high enough to reduce settling of the particles.

In a series of articles (Scales *et al.*, 1998; Franks *et al.*, 1999; Johnson *et al.*, 2000; Zhou *et al.*, 2001), surface forces affecting the rheological properties, particularly, the yield stress, are investigated, with applications to mineral-oxide suspensions. Table 3.3 on the manipulation of surface forces, and Figure 3.9 on the variation of zeta potential with pH, and Figure 3.10 on the effect of surface forces on the yield stress are redacted from the work of Johnson *et al.* (2000). Not all the parametric effects are fully understood at the present. Table 3.3 should be taken as a guide only, because the effects of the parameters and the underlying mechanisms through which they act may be very complicated.

To evaluate the effect of surface forces on the yield stress, Table 3.3 should be evaluated together with Table 1.2, Figures 1.2 and 1.5 of Chapter 1. Figure 3.9 gives the zeta potentials of two metal oxides  $\alpha$ -alumina and zirconia as a function of the pH of the suspending medium. The isoelectric point where there is no charge on the particles is  $\text{pH} \approx 9.5$  for  $\alpha$ -alumina, and  $\text{pH} \approx 7.8$  for zirconia. We know that the zeta potential is the nearest approximation for the surface potential,  $\Phi_0$  of the particles that can be measured experimentally, as given in Figure 1.2(a). The repulsive force  $F_R$  between two particles of radii  $R$  can be approximated in terms of the zeta potential,  $\zeta$ , with the equation of Hogg *et al.* (1966),

$$F_R = \frac{2\pi R \epsilon_0 \epsilon \kappa \zeta^2 e^{-\kappa h}}{1 + e^{-\kappa h}} \quad (3.76)$$

written with the notation identified in Chapter 1 (eqs. (1.1) and (1.33)). Then the total DLVO force,  $F_T$  between two spherical particles in terms of the zeta potential will be,

$$F_T = -\frac{H_{121}R}{12h^2} + \frac{2\pi R \epsilon_0 \epsilon \kappa \zeta^2 e^{-\kappa h}}{1 + e^{-\kappa h}} \quad (3.77)$$

The repulsion force term can become zero only under two conditions: very large distances between two particles  $h$ , as  $h \rightarrow \infty$ , or the isoelectric point where  $\zeta = 0$ . In concentrated suspensions, keeping the pH at the isoelectric point is the only way of eliminating the repulsive forces. Under these conditions, attractive van der Waals forces become dominant

**Table 3.3**

## Manipulation of surface forces

Force	Manipulated by
van der Waals	<ol style="list-style-type: none"> <li>1. Particle size</li> <li>2. Volume fraction of solids</li> </ol>
Double layer repulsion	<ol style="list-style-type: none"> <li>1. pH (zeta potential, <math>\zeta</math>)</li> <li>2. Electrolyte type and concentration</li> <li>3. Charged surfactants</li> <li>4. Size of particles</li> </ol>
Depletion	<ol style="list-style-type: none"> <li>1. Maintaining nonadsorbing conditions by the adjustment of pH and electrolytes</li> <li>2. Choice of polymer size</li> </ol>
Steric	<p>Selection of polymer with</p> <ol style="list-style-type: none"> <li>1. Good adsorption properties</li> <li>2. Concentration adequate for complete surface coverage</li> <li>3. Low molecular weight to prevent bridging selection of appropriate pH and ionic strength in the case of polyelectrolytes</li> </ol>
Bridging	<p>Selection of appropriate polymer or polyelectrolyte type in terms of</p> <ol style="list-style-type: none"> <li>1. Molecular weight of polymer</li> <li>2. Polymer concentration</li> <li>3. pH</li> <li>4. Electrolyte concentration</li> </ol> <p>The dissociation and conformation of polyelectrolytes are strongly affected by pH and electrolyte concentration.</p>
Hydrophobic	<p>Enhancing/preventing surfactant adsorption on the particles to regulate the attractive forces.</p>
Structural (hydration)	<ol style="list-style-type: none"> <li>1. Adsorbed ions at the surfaces of the particles to determine the strength and range of repulsion</li> <li>2. Type and concentration of electrolytes in solution to determine the strength and range of repulsion</li> <li>3. pH-induced changes of the surface charge</li> </ol>

and the yield stress reaches its peak value. As the pH of the suspending medium increases or decreases from the isoelectric point, the increasing absolute values of zeta potential, or equivalently,  $\zeta^2$ , causes an increase in the repulsive forces, and the yield stress declines from its maximum value toward either direction. The shape of the yield stress curves in Figure 3.10 reflects the combined effect of attractive van der Waals and repulsive electrical double-layer forces, as given by eq. (3.77).

The variation of yield stress with the volumetric concentration of solids (indicated on the curves) is given in Figures 3.10(a) and (b) as a function of pH. The zeta potential of alumina is much greater than that of zirconia, implying greater repulsion between alumina

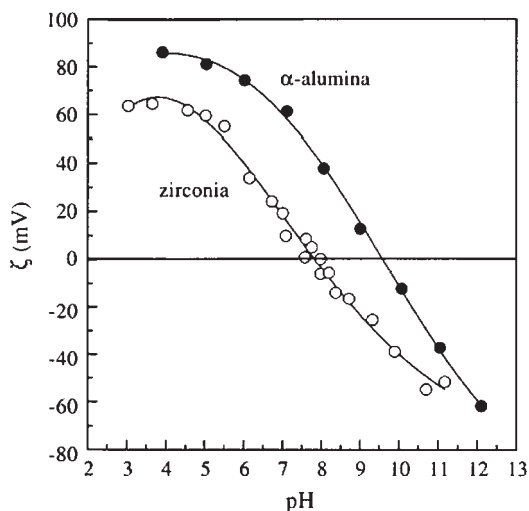


**Figure 3.9** Variation of the zeta potential with the pH of aqueous suspensions of zirconia and  $\alpha$ -alumina (Johnson *et al.*, 2000. Reproduced with permission of Elsevier Science Ltd., Figure 2 in the original).

particles. This is observed as a greater yield stress in the case of zirconia for equivalent volumetric solid fraction,  $\phi$ . These curves for different volumetric fractions coincide into a single curve, when the yield stress is scaled with the maximum yield stress at the isoelectric point,  $\zeta = 0$  (Scales *et al.*, 1998).

Another effective parameter is the thickness of the double layer, indicated by the Debye length,  $\kappa^{-1}$ . We know from Figure 1.1, that neutral (passive) electrolytes compress the double layer, causing the particles to come closer to each other. This is manifested in Figure 3.10(c) where the concentrations of the electrolyte KCl ( $\text{mol dm}^{-3}$ ) are indicated on the curves. The yield stress increases with an increase in the concentration of electrolyte wherever the repulsive forces are active, except around the maximum point, where only attractive van der Waals forces are active. Maximum yield stress also decreases, because of the repulsion created by hydrated  $\text{K}^+$  ions adsorbed on the surfaces of the particles keeping them apart. As a result the yield stress curve becomes flatter as the ion concentration increases.

The effect of particle size on the yield stress is given in Figure 3.10(d) at  $\phi = 0.250$ . The increase in the yield stress with decreasing particle size is due to the immense increase in the surface area that also impedes the creation of slip layers where the suspension yields. Decrease in the particle size also increases the coordination number of each particle, which means greater support among the particles. The effect of polymers is illustrated with the case of PAA (polyacrylic acid) with molecular weights of 2000 and 750,000 adsorbed on zirconia at  $\phi = 0.184$  in Figures 3.10(e) and (f), respectively. The numbers on the curves denote the concentration of the polymer in terms of dry weight percentage. Low molecular weight PAA strongly adsorbs on the surfaces, stabilizing the particles with *steric forces*.

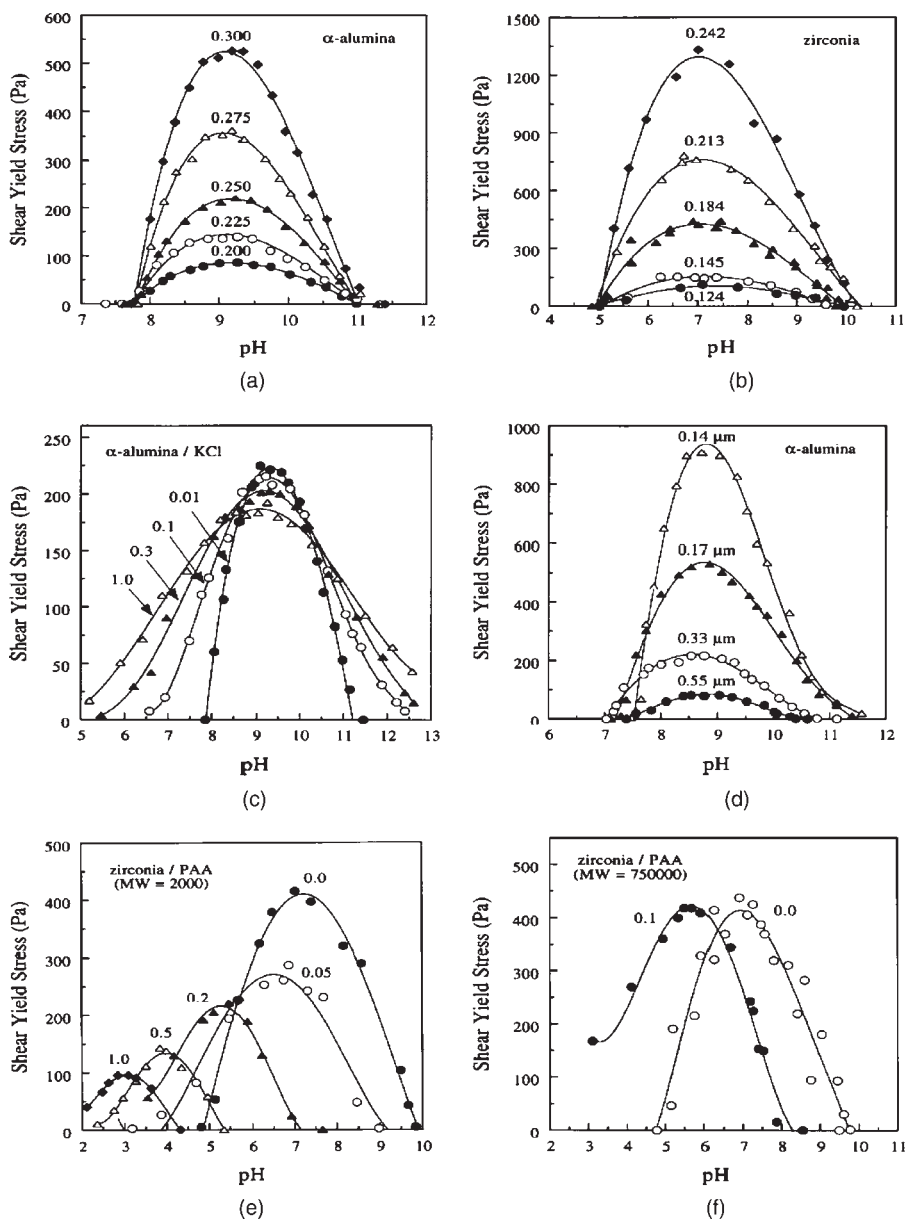


**Figure 3.10** Variation of yield stress with pH and (a) volumetric concentration of alumina, (b) volumetric concentration of zirconia, (c) electrolyte concentration, (d) particle size, (e) polyelectrolyte concentration at low molecular weights, (f) polyelectrolyte concentration at high molecular weights, (Johnson *et al.*, 2000. Reproduced with permission of Elsevier, Figures 3, 4, 8, 13, 17 and 21 in the original).



Since PAA is anionic, the isoelectric point of the composite particles decreases with an increase in the polymer concentration. The flat adsorption of PAA molecules on the surfaces increases the distance between the particles, decreasing the van der Waals forces, and hence the maximum yield stresses. When the molecular weight of the polymer is large as in Figure 3.10(f), not all of the polymer can be adsorbed on the particle surfaces. The dangling polymer pieces interact with each other, bridging the particles together. The polymer shifts the isoelectric point to lower pH values because of its charge. Even though polymer bridges attract particles together, the yield stress is not increased due to unavoidable repulsion brought about by the adsorbed portions of the polymers that sterically stabilize the particles.

### 3.3.2 Flow behavior of soft-particle suspensions under steady shear

Soft-particle suspensions can flow continuously only under limited conditions. These limitations are set by the interaction forces between the particles, volumetric fraction of particles, and for a given fraction, the shear stress the suspension can withstand. The interactions between particles are necessarily repulsive, for otherwise, gel formation and arrestment of particles would prevent continuous deformation. The repulsive forces can be steric, or more commonly electrostatic in origin. In either case, the particles with their increased diameter fill up the available volume at volumetric fractions much less than that of the hard-sphere particles. Only in the gaseous state, at extremely low particle fractions can the particles diffuse freely.

#### 3.3.2.1 Continuous flow of monodispersed suspensions

Under low-shear rates, the diffusivity of the particles is high enough to permit the particles to diffuse back to their minimum energy configuration. Under these conditions, the soft-particle suspension behaves like a Newtonian fluid.

Particles impede the free diffusion of each other at higher concentrations. The concentration at which this impediment becomes effective depends on the range of the repulsive forces, or equivalently the Debye length given in Chapter 1 and is controlled by the parameters effective on the Debye length. Monodispersed soft particles typically exhibit constant shear stresses spanning several orders of magnitude in shear rate, at very low values of shear rates. Since within this range the suspension can be sheared at any rate, the constant value of the shear stress is called *dynamic yield stress*. If the compaction of the suspension is still below the maximum, then the shear stress increases after the dynamic yield stress is exceeded. If the compaction is around the maximum, then shear localizations take place and the suspension fractures.

Typically, the viscosity of hard-sphere suspensions has a constant zero-shear value at low-shear rates, decreases with increasing shear rates (shear thinning region) and reaches again a constant value at very high-shear rates, the infinite shear-viscosity. On the other hand, soft-sphere suspensions exhibit different flow behavior with increasing shear rate. In the order of increasing shear rates the suspension (1) behaves elastically at small deformations, (2) behaves like a Newtonian fluid with “zero-shear viscosity”, (3) shear thins steadily under constant stress, (4) shear thins at a decreasing rate like a power-law fluid,

(5) behaves like a Newtonian fluid under extremely high rates of shear. Which of these regimes does the suspension undergo under a given range of shear rates depends completely on its microstructure.

### 3.3.2.2 Effect of polydispersity on the flow behavior of soft-particle pastes

One way to overcome the limitations in the flow of soft-particle pastes is to use mixtures of different particle sizes. In this way, it is possible to decrease the viscosity of a suspension and obtain a more flowable suspension at the same total volumetric fraction of solids. Bimodal suspensions are used industrially in inks, paints, and ceramics (Olhero and Ferreira, 2004 and references therein), low-calorie high solid content food products (Marti *et al.*, 2005) as well as in other suspensions.

Primary factors that control the flow behavior of monodispersed soft-sphere suspensions are the total volume fraction of solids and the particle size range (e.g., nanoscale or microscale). Other variables in bimodal mixtures of particles are (1) ratio of particle sizes, (2) ratio of volumetric fraction of each size range, and (3) the range of surface forces under the existing conditions of the suspending medium.

Another factor that also affects the performance of mixed suspensions but cannot be quantified easily is the *segregation* of particles. Segregation is a natural outcome of depletion forces when small-sized particles are present in the medium together with larger particles. As given in Chapter 1, small particles in the nanoscale range dispersed between larger particles create an osmotic pressure gradient if they are excluded from the spaces in between the particles, pushing the larger particles together. Under equilibrium conditions, regions of densely packed large diameter particle zones will exist within the less densely populated small-particle suspensions, creating zones with different local volumetric fraction of solids. Shear modulus of elasticity,  $G$  is related with the volumetric fraction of solids and will be higher in the densely packed large particle zones. In turn, small particle zones are more deformable (Hunt and Zukoski, 1999).

Osmotic pressure shows the same qualitative dependence on the volumetric fraction of solids,  $\phi$ , as the dynamic yield stress (Persello *et al.*, 1994). Under the action of shear, the equilibrium structure of the suspension will be distorted and free space will be opened up. This will create an imbalance of forces, which will cause the particles to jump to the new locations. The equilibrium microstructure and its distortion is characterized by the shear modulus of elasticity,  $G$ . Yield stress indicates the span of shear rates over which the system responds elastically and indicates the resistance shown by the liquid molecules toward the motion of the solid particles in the distorted microstructure. When yield stress is scaled with the shear modulus, the dimensionless yield stress,  $\tau_0/G$ , becomes independent of particle composition, volumetric fraction, ionic strength and depends only weakly on the particle size with values in the range,  $0.01 \leq \tau_0/G \leq 0.035$ . Shear rate is nondimensionalized with the rate of energy dissipation that is proportional to  $G/\eta$ , where  $\eta$  is the viscosity of the suspension medium. When dimensionless yield stress,  $\tau_0/G$  is plotted against the dimensionless shear rate,  $\dot{\gamma}\eta/G$ , the flow curves of both the monodispersed suspensions and the mixtures fall on a single master curve (Hunt and Zukoski, 1999).

Bimodal suspensions shear thicken at very low-shear rates and low volumetric fractions compared with the hard-sphere suspensions, whereas, monodispersed suspensions of soft

particle do not show any thickening. Since the suspensions do not flow below their yield stress and irreversible aggregation and shear localization take place above the critical shear stress where shear thickening is observed, bimodal suspensions of soft particles in the nanometer size range have a very narrow range of operation where flow can be sustained. Working with particles in the micrometer size range, Olhero and Ferreira (2004) found that the suspension shear thickens when the ratio of small to large particles increase, and shear thins when the ratio decreases.

### 3.3.2.3 Effect of aspect ratio on the flow behavior of soft-particle pastes

Spherical geometry is a simplification used to model the physical and rheological properties of particles. Many industrially important materials have particle geometries that are highly anisotropic and cannot be treated as spheres. Examples are some mineral crystals, clay, nanoparticles, fibers, polymers, and protein molecules. The dynamics and viscosity of these particles depend on their sizes, whether in the colloidal size range or larger, as well as their geometrical shape and aspect ratio.

#### 3.3.2.3.1 Characterization and microstructure of nonspherical particles

Anisotropic particles may be in the form of spheroids, rods, flakes, or discs. They are characterized by their *aspect ratio*,  $L/D$ , where  $L$  is the length and  $D$  is the diameter or the width of the particles. If there are large repulsive forces among the particles, they exist as individual entities. If there are attractive forces between the particles, they exist as aggregates. The specific orientation in the group depends on the localization of attractive forces. Clay platelets with negatively charged surfaces and positively charged edges group in the form of a card-house structure, or in the form of a ladder. As the volumetric concentration of solids increase, the network structure percolates, or spans the available volume and a gel is formed. The particles disperse under high shear. In the case of surfactants and polymers, lateral electrophilic groups (such as  $-\text{OH}$  groups) form hydrogen bonds, a form of van der Waals attractions, which causes the alignment of the colloids in the form of a nematic phase. Application of moderate shear enhances the alignment by bringing the particles together. In the absence of attractive forces, the dispersions are isotropic.

Besides the aspect ratio, the orientation of the particles with respect to the direction of flow is also important in determining the rheology of suspensions. A good review of the theoretical and experimental work on the viscosity of rod-shaped particles can be found in Wierenga and Philipse (1998).

#### 3.3.2.3.2 Physical basis for the deviation of viscosity from the hard-sphere case

In the particle-size range, where the Brownian motion is not negligible, the contribution of the translational motion of the particles to the viscosity is negligible in comparison with the rotational motion. So the Péclet number for translational flow, eq. (3.9) is replaced by its equivalent in terms of rotational diffusivity,  $\mathcal{D}_r$ ,

$$Pe_{\text{rot}} = \frac{\dot{\gamma}}{\mathcal{D}_r} \quad (3.78)$$

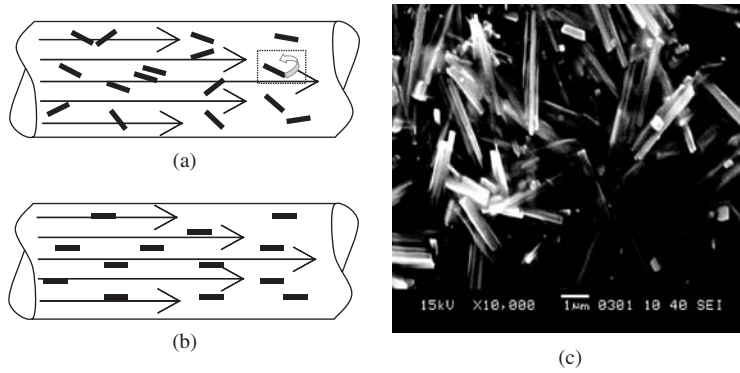


**Figure 3.11** Rod-shaped particles (a) randomly distributed in the flow field, (b) after alignment in the direction of flow, (c) Rod-shaped  $\text{Zn}(\text{C}_2\text{O}_4)$  particles (İkizler, 2005).

For flow in a channel in the  $z$  direction, a velocity gradient will exist in the  $r$  direction, forcing the particles to align parallel to the  $z$  direction, as shown in Figure 3.11(a) and in the fully aligned condition in Figure 3.11(b). This is possible for particles greater than the Brownian-size range. The Brownian particles rotate in the  $\phi$  direction under the action of shear induced by the velocity gradients. A rotating particle under the action of velocity gradients is shown in the square box in Figure 3.11(a).

Three factors contribute to the viscosity of anisotropic particles (Wierenga and Philipse, 1998): (1) Rotation of the particles, (2) the distribution of the orientations of the particles with respect to the flow direction, and (3) the thermal fluctuation of solvent molecules that induce Brownian particles to rotation. The aspect ratio is the single factor that causes the particles to rotate and change the flow field. As the concentration of the particles increase, they tend to entangle, decreasing the rotational freedom of the particles. For this reason, the viscosity relations are correlated in terms of the effective parameters of aspect ratio,  $L/D$ , and the volumetric fraction of solid particles,  $\phi$ .

### 3.3.2.3.3 Viscosity relations for elongated particles: Prolate spheroids and rods

Volumetric concentration of the particles can be expressed in terms of the number density of particles,  $n$ , and the maximum rotational volume of the particles that is proportional to  $L^3$ , as

$$\phi = nL^3 \quad (3.79)$$

Then eq. (3.17) can be written in the form

$$\eta_r = \frac{\eta}{\mu_0} = 1 + [\eta]nL^3 + k_H(nL^3)^2 + O((nL^3)^3) \quad (3.80)$$

The rotational motion of the particles under shear affects the intrinsic viscosity term,  $[\eta]$  in eq. (3.80). In very dilute dispersions where each particle can rotate freely, the shear rate

is very low with,  $Pe_{\text{rot}} \ll 1$  and particles are long with  $L/D \gg 1$ , the intrinsic viscosity is given by the Onsager equation

$$[\eta] = \frac{4}{15} \frac{(L/D)^2}{\ln(L/D)} \quad (3.81)$$

The Onsager equation can be used with both hard sphere and soft particles, whether they are rigid or flexible. It gives a good estimate of the intrinsic viscosity in the range of aspect ratios,  $20 \leq (L/D) \leq 1000$ , where particle dimensions of most materials fall (Wierenga and Philipse, 1998), as in the case of rod-shaped particles of  $\text{Zn}(\text{C}_2\text{O}_4)$  in Figure 3.11(c). For lower aspect ratios, end-effects become dominant and Onsager equation underestimates  $[\eta]$ .

At higher shear rates, the distribution of particle orientations also become important. Péclet number limits are given in terms of the aspect ratio, signifying the excluded volume allowed for an individual particle. In the high-shear region where  $Pe_{\text{rot}} \geq (L/D)^3$  and  $L/D \gg 1$ , the equation proposed by Hinch and Leal (1972) can be used to estimate the intrinsic viscosity:

$$[\eta] = 0.315 \frac{(L/D)}{\ln(L/D)} \quad (3.82)$$

Comparison of eqs. (3.81) and (3.82) shows that intrinsic viscosity at high-shear rates is lower than the viscosity at low-shear rates by a factor of  $\approx L/D$ . In between the two limits of Péclet number for low-and high-shear regions,  $1 \leq Pe_{\text{rot}} \leq (L/D)^3$ , intrinsic viscosity decreases in proportion with the cube root of Péclet number,  $[\eta] \propto Pe_{\text{rot}}^{1/3}$ .

#### 3.3.2.3.4 Effect of an increase in the volumetric concentration of particles

Comparison of eqs. (3.80), (3.81), and (3.82) shows that an increase in the shear rate affects the coefficient (intrinsic viscosity) of the second term of eq. (3.80). An increase in the concentration of the particles affects the microstructure of the suspension, and therefore, the coefficient of the third term in eq. (3.80), the Huggins coefficient will be affected. As the concentration of particles increases, a limiting concentration will be approached, where one particle will be present in each rotational volume, or in terms of the number concentration,  $n$ ,

$$n^* = \frac{1}{L^3} \quad (3.83)$$

where  $n^*$  is the overlap concentration, above which the particles will interfere with the rotation of each other. For particle concentrations less than the overlap concentration, the equation of Berry and Russell (1987) can be used to estimate the relative viscosity:

$$\eta_r = \frac{\eta}{\mu_0} = 1 + [\eta]\phi + k_H[\eta]^2\phi^2 \quad (3.84)$$

where the Huggins coefficient  $k_H$ , is given by the relation,

$$k_H = \frac{2}{5} \left( 1 - 0.00142 Pe_{\text{rot}}^2 \right) \quad (3.85)$$

For higher concentrations of particles Krieger–Dougherty (eq. (3.22)) or Quemada (eq. (3.23)) relations can better describe the variation of the relative viscosity with the volumetric concentration of particles. Although the two equations approach each other under certain conditions, Krieger–Dougherty equation gives better fit to Brownian particles and Quemada equation to non-Brownian particles. Examination of the equations in Table 3.1 shows that they differ in the exponent of the dimensionless volume fraction,  $\alpha$ . The exponent,  $(-2)$  in the Quemada model arises from the similar dependence (power of  $(-1)$ ) of diffusion coefficient and the radial distribution function on the volumetric fraction of solids (eqs. (3.18) and (3.19)). At high-aspect ratios, the rotational and translational diffusivities of rod-like suspensions are highly retarded due to the entanglement of the particles. Experimentally, Solomon and Boger (1998) found the exponent of the dimensionless volume fraction,  $\alpha$ , to increase with aspect ratio as  $\alpha = 1.7, 2.2$  and  $2.8$ , for aspect ratios of  $L/D = 1, 4.8$  and  $8.4$ , respectively.  $\alpha$  was not found to be a function of ionic strength, but maximum volumetric fraction,  $\phi_m$  was. As the concentration of electrolyte was increased,  $\phi_m$  increased also due to the decrease in the thickness of the diffuse ionic layer, or Debye length,  $\kappa^{-1}$ , leaving more space for compaction. Solomon and Boger, rescaled the effective volumetric fraction with the aspect ratio as

$$\phi_{\text{eff}} = \phi \left( \frac{L}{D} \right)^3 \quad (3.86)$$

This correction for the effective concentration was found to be valid for rather dilute suspensions of  $\phi/\phi_m < 0.6$ . For more concentrated suspensions around  $\phi/\phi_m \geq 0.6$ , overlapping starts between the particles, restricting the freedom to rotate in any direction. Thus, the excluded volume is reduced from a sphere to a cylinder in the direction of flow (Doi and Edwards, 1986) through which the particle can pass with only restricted rotation. Solomon and Boger (1998) found all their experimental values to fall onto a single curve regardless of ionic strength and aspect ratio when they rescaled the effective volume according to these restrictions.

An alternative correction for maximum volumetric fraction,  $\phi_m$  was proposed by Philipse and coworkers (Wierenga and Philipse, 1998; Philipse, 1996) in terms of average number of contacts experienced by a rod. Experiments showed that the microstructure of randomly packed rods is a glass state, which is highly probable in view of the entanglements restricting the free motion of particles.

### 3.3.2.3.5 Effect of surface forces

The effect of the surface forces on anisotropic particles is not much different from spherical particles. For the suspension to be able to flow under applied shear, the repulsive forces should be dominant, generally in the form of electrostatic forces. As in the case of spherical particles, ionic double layers increase the effective volume of the particles, decreasing

the volumetric fraction at maximum compaction. The effect of shear on the double layers of the anisotropic particles in a suspension is taken into account under three groups: (1) The primary electroviscous effect is due distortion of the ionic cloud and hence the potential under shear. This distortion directly affects the intrinsic viscosity, as it does not depend on the microstructure. (2) The secondary electroviscous effect is due to the overlapping of the double layers at high concentrations or under compressive stress. The information in this area is meager, especially as concerns the variation of the double-layer thickness with aspect ratio and locally over the particle surface. (3) The tertiary electroviscous effect is due to the flexibility of the polymer chains. The flexibility of the chain decreases the effective length and increases the effective diameter of the rod encasing the polymer. In addition, internal coil formation within the colloid may cause local repulsions due to overlapping of the ionic clouds.

Existence of attractive forces will generally result in gel formation, with similar properties as the gels of spherical particles if the aspect ratio is low or polymeric gels if the aspect ratio is very high. A particular form of attraction, leading to nematic phases is important in terms of viscosity: The aggregation and alignment of particles form larger particles above the Brownian range, which easily align in the direction of flow (shear). As a result, the viscosities of equilibrium crystalline phases are lower than isotropic suspensions of anisotropic particles.

### 3.4 MIGRATION, SLIP, AND DRAG REDUCTION

Migration, slip, and drag reduction are associated phenomena taking place along the solid wall boundaries in general, and along the pipe walls in flow through pipes. The latter case bears significance in relation to industrial applications, and used advantageously in reducing the pumping costs during the transfer of concentrated pastes. The same phenomena have a deterrent effect on the assessment of rheological properties in rheometers. Migration has significant consequences in bifurcational flow of the vascular system: The reduced hematocrit level and consequential reduction in viscosity in the capillaries is due to migration of red blood cells (RBCs) toward the central sections of the arteries.

#### 3.4.1 Migration

Migration results from the diffusion of particles from an area of high shear to a region of lower shear. Migration is especially severe in shear thinning suspensions and power-law fluids where there is a severe reduction in viscosity. The underlying physical phenomena could be the ease of diffusion of the particles in a medium of reduced viscosity. It could also result from the resistance of the particle toward deformation if the particles are viscoelastic. If particles exist in the form of aggregates, attractive surface forces could also resist disintegration, whereby migration to a low-shear area would be the easiest escape. If there is a microstructure in the flowing suspension, the equilibrium microstructure is deformed under high shear. The particles tend to diffuse back to their equilibrium position to minimize their potential energy. This can be done more conveniently in the central



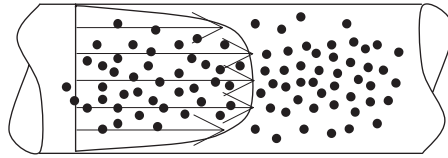


**Figure 3.12** Migration of solid particles to the regions of lower velocity gradient.

regions of the pipe where the velocity distribution is flatter as discussed in Section 2.4.1.1 of Chapter 2. Due to one or all of these reasons, particles migrate toward the central regions of the pipe leaving a more dilute suspension, and in the extreme, only the suspending medium along the walls as depicted in Figure 3.12.

One of the outcomes of migration is the evolution of slip flow, which will be discussed next. Another outcome is the effect on particle distribution.

### 3.4.2 Slip flow

Slip flow signifies a discontinuity in momentum transfer. It may arise due to absence or insufficiency of adhesion forces between the liquid and the solid molecules. In this case, the liquid will not adhere to the surface of the solid walls, invalidating the basic assumption in the derivation of velocity distribution equations (Chapter 2), that the velocity of the liquid is equal to that of the solid wall to which it adheres. This is called *true slip*.

Slip flow can also be *apparent* due to formation of a liquid-rich layer along the walls, such as in the case of migration. Since the viscosity of concentrated suspensions is very sensitive to solids concentration, the viscosity decreases and velocity increases in a very thin layer, observed as the *slip velocity*. Another mechanism operative in the apparent slip could be a fracture within the suspension causing layers of suspension to slip past each other.

Slip is generally encountered over smooth walls. When the walls are rough, slip is negligible or does not exist at all along the walls. This shows that slip flow is closely related with the flow conditions and rheology of a very thin layer along the wall. In the case of Couette flow, momentum is transferred from the wall to the fluid, creating homogeneous flow or deformation within the bulk of the suspension if the walls are rough. If slip is extensive, momentum transfer between the bulk of the fluid and the wall is interrupted. Then a constant stress is observed over a wide range of shear rates in measurements with a rheometer. Slip causes plug flow in the case of flow through pipes.

Rough walls can prevent slip formation along the walls, but if heterogeneities exist in the suspension, a fracture plane will develop if the microstructure of the suspension cannot sustain the applied stress. The fracture plane may form due to an irregularity of structure, due to presence of air bubbles, due to water (solvent) layer formed along the walls or at boundaries of clusters, or due to a random accumulation of void spaces in the microstructure. Slip can occur even in the absence of these defects. Persello *et al.* (1994) studied slip flow in suspensions of silica particles, 9 nm in diameter, stabilized with electrostatic repulsions, at a volume fraction of  $\phi = 0.329$  corresponding to an effective volume fraction of  $\phi_{\text{eff}} \geq 0.74$  together with the ionic cloud, forming a soft-particle paste.



Under a step strain in a rheometer, the stress increased linearly up to a maximum value and then decreased to a constant plateau level, just below the *dynamic yield stress* value, depending on the volumetric fraction of the solids. This maximum stress is called the *critical stress*, and the plateau is the stress that the suspension can withstand. Results of the flow visualization experiments and rheological measurements lead to the conclusion that if slip does not take place at the walls, then any plane could be transformed into a slip layer under these conditions: (1) Slip occurs at a threshold stress, called the dynamic yield stress, (2) Threshold stress is a function of volumetric fraction of solids only; it is not dependent on the shear history. (3) As long as the strain level is above the critical, the stress level is fixed by the existence of these slip planes that localize the strain, (4) Transformation of a plane into a slip layer is a reversible process: slip layer may form or an existing slip layer can be self-healed depending on the balance between the osmotic pressure and the magnitude of the shear stress. Variation in microstructure triggers a change in the osmotic pressure: If solvent (water) fills a layer, osmotic pressure will tend to redistribute the liquid among spaces between the particles. In general, heterogeneous flow (with slip layers) will occur in soft particle pastes exhibiting a yield stress. Similar heterogeneous flows were observed in laponite (Pignon *et al.*, 1996) and bentonite (Coussot *et al.*, 2002) pastes.

Meeker *et al.* (2004) studied the slip flow in microgel pastes by flow visualization and rheological measurements. Microgel pastes behaved like yield stress fluids under high-shear stresses conforming to the Herschel-Bulkley model ( $\tau = 24 + 6.7\dot{\gamma}^{0.48}$ ). Correlating flow visualization of slipping paste with the flow curves, they were able to identify three regimes of slip: Regime I is observed at stresses much greater than the yield stress ( $\tau/\tau_0 \geq 1.5$  for microgels): Slip is negligible compared to the bulk flow. Rheological properties are not affected by the presence of slip. Regime II is observed just above the yield stress ( $1 \leq \tau/\tau_0 \leq 1.5$ ) where the slip becomes significant and should be considered in the flow equations. Regime III is observed just below the yield stress, where deformation in the bulk is negligible and the suspension flows by sliding over the slip plane along the walls. In the case of soft particles, such as microgels, yield stress depends on the elastic shear modulus  $G_0$  through,

$$\tau_0 = G_0\gamma_0 \quad (3.87)$$

As the elastic shear modulus is increased, characteristic slip velocity of the paste,  $V^*$ , occurring at or just above the yield stress increases and the onset of slip is found to shift to higher shear rates,  $\dot{\gamma}^*$ . The characteristic slip velocity could be correlated with the paste properties through the relation

$$V^* \approx \frac{G_0 R}{\mu_0} \quad (3.88)$$

for all except the most concentrated pastes, where  $\mu_0$  is the suspending medium (solvent) viscosity and  $R$ , the particle radius. This relation implies that slip is affected by the bulk elasticity of the paste, which in turn is a function of the degree of compression of soft particles, or equivalently osmotic pressure of the solvent that compress the soft particles.

Since hard-sphere particles cannot be compressed, slip does not depend on the shear modulus of elasticity,  $G_0$ , in hard-sphere suspensions (Aral and Kalyon, 1994). Solvent viscosity enters into the relation through the lubrication effect: greater the viscosity, the less will be the probability of slip. That slip occurs readily in suspensions of large particles is generally accepted. The slip layer thickness  $\delta$  of soft-particle pastes is about 1% of the particle radii as inferred from different research work with different types soft particles (Meeker *et al.*, 2004 and references in Table 1 of the article).

Slip is an important phenomenon, both in large-scale operations such as extrusion, and in microscale operations such as flow through microelectromechanical devices. For this reason, slip phenomena is an area of extensive research. Experimental work on the slip of Newtonian fluids over solid surfaces is critically reviewed by Neto *et al.* (2005). The factors that may cause slip are given as surface wettability, surface smoothness, shear rate, formation of nanobubbles and gas films, adsorption of surfactants from solution, polarity, and viscosity of the liquid. The main conclusion was that slip is a surface phenomenon and needs a comprehensive study of solid surfaces on the molecular scale. In the realm of microfluidics, parameters affecting slip change scale also: For example, roughness in the macroscale is a protrusion or a crevice on the surface. In the microscale, patches of adsorbed surfactant on the surface produce a roughness.

### 3.4.3 Drag reduction by surfactants and polymers

Drag reduction is related with slip phenomena in that it is controlled by the mechanisms taking place in the turbulent boundary layer. Drag reduction has practical significance on all scales where it is observed. At the largest scale, it is observed in the flow of rivers: Under the action of constant gravitational force, the flow rate in a river is inversely proportional to the resistance of the basin (Wang and Larsen, 1994). In the industrial scale, polymer or surfactant solutions are injected to the pipelines to reduce the energy costs in delivering concentrated slurries over long distances.

Drag reduction is expressed as the percentage savings in power due to a use of additive, such as polymers or surfactants:

$$DR = \frac{\mathcal{P}_{o, \text{ slurry}} - \mathcal{P}_{o, \text{ with additive}}}{\mathcal{P}_{o, \text{ slurry}}} \times 100 \quad (3.89)$$

where  $\mathcal{P}_o$  is the power consumption in flow (the product of frictional losses and the volumetric flowrate). Drag reduction is achieved if the frictional losses could be decreased with the use of an additive.

The actual mechanism of drag reduction is not resolved yet. It is known that polymers of molecular weights in the range of  $\approx 10^6 \text{ g mol}^{-1}$  cause a drag reduction around 30% (Drappier *et al.*, 2006). Typically, around 60% reduction in power consumption can be obtained with the use of surfactants. Generally, a cationic (quaternary) surfactant is used with a salt of salicylic acid as the surfactant, which show birefringence properties. Cationic surfactants adsorb strongly on negatively charged surfaces. However, the mechanism of drag reduction is more complex than simple adsorption, when salicylic acid is used

together with the cationic surfactant. These two surfactants, when present above their critical micelle concentration, aggregate in the form of worm-like micelles, an extension of hexagonal micelles shown in Figures 1.12(c) and (d). The diameter of these micelles is around two times the length of a surfactant molecule, but the length spans thousands of molecules. In this way, they resemble long-chain polymers.

The mechanism of drag reduction is generally attributed to the elongational viscosity of long-chain structures that resists extensional flow. As given in Chapter 2, the greatest extension exists in the laminar sublayer due to the velocity gradient in turbulent flow through pipes, where these long-chain molecular structures partly adsorbed on the walls exert their full effect. They decrease the flow rate, prevent the formation and penetration of turbulent eddies, increasing the thickness of the sublayer and the entrance length of the pipe required for the establishment of steady-state velocity distributions. In this way, mechanical energy dissipation through turbulent eddies is reduced. However, two counter-acting mechanisms operate in the process: energy dissipation by turbulence is reduced, but viscosity is increased and velocity is decreased in the sublayer. Frictional losses are determined by the net effect of these mechanisms.

Under high-shear rates, polymers are observed to degrade. Surfactants are preferred in the drag reduction because of their stability and effectiveness. The mechanism through which they act involves shear-induced arrayed structures. With the formation of these structures, the surfactant solution shear thickens at low-shear rates, and then suddenly starts shear thinning. This behavior may be attributed to initial entanglement followed by dissociation of the micellar structure. Elongational viscosity also increases exponentially up to a maximum and then shows a sudden exponential decrease approaching the Newtonian limit at long times. Due to this peculiar rheology, surfactants exhibit superiority over polymers that cannot display these sudden changes. Drappier *et al.* (2006) suggest that drag reduction takes place through slip formed in the sublayer when the elongational and shear viscosities reach their maximum. Although they cannot submit evidence to explain the mechanism, they show that both the slip flow and the drag reduction show a maximum at the same surfactant concentration. In addition, instantaneous orthoradial velocities were measured with magnetic resonance imaging (resolution time, 0.1 s), in a couette-type flow cell with two counter-rotating discs at  $Re = \rho\omega R_{disc}^2/\mu = 5 \times 10^4$ . The data shows that pure water and polymer solutions are highly turbulent with root mean velocity fluctuations of 22.1 and 17.9 cm s<sup>-1</sup>, respectively. On the other hand, the surfactant solution appears iridescent showing that turbulence is greatly suppressed and an order has set in among the surfactant molecules, with a root mean square velocity of only 3.8 cm s<sup>-1</sup>. This is mainly due to inhibition of momentum transfer from the rotating disc to the bulk due to slip in the boundary layer, showing that drag reduction mechanism by surfactants involve the formation of a slip layer.

Clay platelets also show chain-like structures when they aggregate face-to-face, forming long ladders. When clay concentration exceeds 4%, a network structure is formed in the suspension, with shear-thinning properties and appearance of yield stress typical of gels. Wang *et al.* (1998) tested the existence of drag reduction in the flow of clay slurry in a wide channel of 23.5 m length and 0.6 m width to simulate river flow. The degree of roughness was set by using gravel or stones in the bed of the channel. Drag reduction was observed only in the case flow over the gravel bed under conditions where turbulent shear dominated

the resistance. Gel structure suppressed the fluctuating turbulent eddies, reducing the power requirement. Under all other conditions, the increase in the viscous resistance controlled the power requirement; therefore, no drag reduction was observed.

### 3.5 SHEAR FLOW OF VISCOELASTIC SUSPENSIONS

Viscoelastic behavior in concentrated suspensions may develop due to viscoelasticity of the suspension medium, the viscoelasticity of the suspended particles, or the existence of a microstructure of soft particles that deform under shear. In all cases, the effect of viscoelasticity is observed under dynamic conditions. These cases will be reviewed in the following sections.

#### 3.5.1 Effect of the viscoelasticity of suspending medium

Viscoelasticity of the suspension medium affects the overall viscoelastic properties of the suspension, as well as causing deviations in the microstructure under steady shear flow. Experimental evidence (Aral and Kalyon, 1997; Scirocco *et al.*, 2004) in the literature shows that string-like alignment of particles in the direction of flow under an applied continuous shear is due to the viscoelasticity of the suspending medium.

Aral and Kalyon (1997) conducted systematic investigations of highly filled suspensions in a viscoelastic medium. Glass beads of 6  $\mu\text{m}$  radius were suspended in a viscoelastic medium of poly dimethyl siloxane (PDMS) fluid of approximately equal density to obtain a neutrally buoyant suspension. In this particle size range, Brownian motions are dominated by hydrodynamic forces (high Péclet numbers), and variations in the microstructure are correlated with the rheological characteristics under imposed shear. The viscoelastic behavior was assessed through the response of the suspension 1) to an increase in the amplitude, and frequency of oscillations in strain, 2) to the time the suspension was subjected to dynamic and steady shear, 3) through the measurement of normal stresses and 4) through visual observation of the Weissenberg effect. Strain amplitude sweep tests showed that the storage modulus  $G'$  of the suspension medium remained constant throughout the measured range. Addition of particles caused a decrease in the range of strain amplitudes over which the viscoelastic response of the suspension is linear. As the volumetric fraction of the particles increased, the range of amplitudes where  $G'$  remained constant decreased, both in magnitude and in range. The value of  $G'$  decreased with a greater slope as the amplitude of oscillations increased in concentrated suspensions,  $\phi \geq 0.3$ . The response of the suspension to variations in the frequency of oscillations were found to differ with the volumetric fraction of solids,  $\phi$ : For  $\phi$  values approaching the compaction limit, 0.6, storage  $G'$  and loss  $G''$  moduli approached constant values at low values of frequency, indicating the development of yield stress. Time-dependent response observed for  $\phi \geq 0.4$  indicated structuring effects and thus deformation history under oscillatory shear. The breakup of the network structure is again associated with the yield stress. Concentrated suspensions took a longer relaxation time after an applied step-strain was removed.

Primary normal stress difference  $N_1$  (eq. (2.1)) indicates the development of normal forces in a direction perpendicular to the direction of flow, which is manifested as the Weissenberg effect, or climbing of the viscoelastic suspension around a rotating shaft. In the experiments of Aral and Kalyon, the suspension medium exhibited Weissenberg effect, but at increasing fraction of solids, this effect disappeared completely, leading instead to a depression of the fluid level around the rotating shaft, vortex formation, as in the case of Newtonian fluids. This effect was attributed to the formation of particle strings in the flow direction that lengthened up by capturing approaching particles.

Confirmation to the effect of medium viscoelasticity on particle alignment came through recent observations of polystyrene particles of diameter  $d_p = 2.7 \pm 0.1 \mu\text{m}$  suspended in fluids with a wide range of first normal stress differences and viscosities (Scirocco *et al.*, 2004). The string formation was confirmed by microscopic images and small-angle light scattering patterns of the suspension microstructure taken with a digital video camera. The flow behavior was investigated at the shear rates covering a range of particle Reynolds numbers,  $3 \times 10^{-11} \leq Re_p \leq 4 \times 10^{-8}$ . The interparticle distance between the particles in the strings,  $1.1 \mu\text{m}$  were constant in time. Compared with the particle diameters, interparticle distances are too long for the particle surfaces to be effective. Wall effects seemed to hinder rather than promote string formation. High-shear regions near the walls in non-Newtonian fluids were also thought to cause aggregation of strings into crystalline structures observed on the walls. The authors concluded that alignment into strings is determined by the rheology of the suspending fluid, with shear thinning as the prerequisite, and viscoelasticity as the necessary condition. In addition, time-dependent transient rheological behavior is also thought to be important in the capture mechanism into strings.

### 3.5.2 Effect of the viscoelasticity of the particles

Biological cells, vesicles, and microcapsules consist of surfactant–polymer membranes that envelope a liquid, generally with viscoelastic properties arising from their composition. The membrane undergoes undulatory motion under shear flow. If these particles were solid with rigid surfaces, shear gradient in a flow field would induce rotary motion to the particles, with an angular velocity  $\omega$ , equal to half of the local shear rate  $\omega = \dot{\gamma}/2$ . If these particles were liquid drops with mobile liquid–liquid interfaces, then the induced internal circulation and transmitted shear stress would deform the particle, which would move with a fixed orientation to the flow direction at steady state. Viscoelastic particles behave like solid particles under low-shear rates, and approach liquid-like behavior at high-shear rates. Even under pure shear flow of the suspending medium, these particles will behave elastically with a normal stress,

$$\tau_{xx} = \mu_0 \dot{\gamma} \sin 2\varphi(t) \quad (3.90)$$

$\varphi$  is the angle between the axis of the particle rotating in the positive or negative directions normal to the flow direction, with a maximum value of the angle of maximum deformation  $\varphi_m$ . For a fixed normal stress, at low-shear rates the viscoelastic particle would show a

similar behavior to solid particles, whereas at high-shear rates  $\varphi$  will approach a constant value. Snabre and Mills (1999) analyzed the rheology of viscoelastic particles under the conditions of hydrodynamic effects and inertial forces dominating the motion of the particles, i.e.,  $d_p > 1\mu\text{m}$  and  $Re_p = d_p^2 \dot{\gamma} \rho / \mu_0 \ll 1$ , where  $Re_p$  is the Reynolds number based on the particle diameter,  $d_p$ ;  $\dot{\gamma}$ , the shear rate in the medium where the particle is situated,  $\rho$ , and  $\mu_0$  are the density and viscosity of the suspending medium, respectively. Their analysis is outlined below with the nomenclature adopted in this book. In the analysis, Kelvin–Voigt model of viscoelasticity is assumed to describe the behavior of the viscoelastic particles:

$$\tau_{\theta y} = -G \frac{dy(t)}{d\theta(t)} - \eta_p \frac{dV_y}{d\theta(t)} \quad (3.91)$$

where  $\eta_p$  is the viscosity of the viscoelastic particle (intra particle viscosity) and  $dy(t)/d\theta(t) = \sin\varphi = (R-r)/R$ . For an element on the surface of a particle located at the origin of the axes, with  $y \equiv r$ ,  $x \equiv z$  and making a rotary motion in the  $\theta$  direction,

$$\tau_{\theta y} = -G \left( \frac{R-r}{R} \right) - \eta_p \frac{d}{d\theta} \left[ -\frac{dy}{dt} \right] \quad (3.92)$$

Equating the Kelvin–Voigt stress (eq. (3.92)) to the normal stress (eq. (3.90)) on the surface element

$$\mu_0 \dot{\gamma} \sin 2\varphi(t) = -G \left( \frac{R-r}{R} \right) + \eta_p \frac{d}{d\theta} \left[ \frac{dr}{dt} \right] \quad (3.93)$$

the time dependence of the radius of the particle was found by integrating eq. (3.93) with respect to  $\theta$

$$\frac{dr}{dt} = \frac{\mu_0 R \dot{\gamma} \sin 2\varphi(t)}{\eta_p} - \frac{R}{\lambda} \left( \frac{r-R}{R} \right) \quad (3.94)$$

where  $\lambda (\equiv \eta_p/G)$  is the relaxation time of the viscoelastic fluid inside of the particle. The angular position  $\varphi(t)$  is defined in terms of the angular frequency and shear rate as

$$\varphi(t) = \int_0^t \omega dt = \frac{\dot{\gamma} t}{2} + \varphi_0 \quad (3.95)$$

Eq. (3.94) is nondimensionalized with the use of the variables,  $\xi = (r-R)/R$ , giving the relative particle deformation;  $\theta = t/\lambda$ , the ratio of time to the relaxation time of the viscoelastic fluid in the interior of the particle,  $\lambda$ ;  $\Lambda = \eta_p/\mu_0$ , the ratio of the effective viscosity of the fluid inside the particle to the viscosity of the suspending medium, used to denote the continuity of shear stresses at the interface, or the ability of an external shear to sustain deformation within the particle;  $De = \lambda \dot{\gamma}$ , Deborah number, the product of the relaxation time and shear rate, relating the time scales of deformation,  $\dot{\gamma}$ , to that required

for the particle to recover from the effect of the deformation,  $\lambda$ , also called the characteristic time of the particle.

The resulting nondimensional equation relates the rate of deformation,  $d\zeta/d\theta$  of an initially spherical viscoelastic particle to its relaxation time  $\lambda$ , the ratio of intraparticle ( $\eta_p$ ) to suspending medium ( $\mu_0$ ) viscosities,  $\Lambda$ , and the shear rate through the Deborah number,

$$\frac{d\zeta}{d\theta} + \zeta = \frac{De}{\Lambda} \sin(De\theta + 2\varphi_0) \quad (3.96)$$

The general solution of this equation describes the motion of the particle,

$$\zeta(\theta) = \zeta_m \cos(2\varphi - 2\varphi_m) \quad (3.97)$$

In this equation  $\varphi_m$  is the angle of maximum deformation. The maximum relative deformation  $\zeta_m$  is related to the Deborah number and ratio of viscosities through,

$$\zeta_m = \frac{De}{\Lambda} [1 + (De)^2]^{1/2} \quad (3.98)$$

The normal  $\zeta_{xx}$  and shear  $\zeta_{xy}$  components of the strain tensor  $\zeta$  evaluated at  $\varphi = 0$  and  $\varphi = \pi/4$  then follow as,

$$\zeta_{xx} = \frac{(De)^2}{\Lambda(1 + (De)^2)} \quad (3.99)$$

$$\zeta_{xy} = \frac{(De)}{\Lambda(1 + (De)^2)} \quad (3.100)$$

The authors derived a hard-sphere model to be used as a reference for the relative viscosity of a suspension of viscoelastic particles (Mills and Snabre, 1988; Snabre and Mills, 1996),

$$\eta_r(\phi, \phi_0^*) = \frac{\eta(\phi, \phi_0^*)}{\eta_0} = \frac{1 - \phi}{(1 - \phi/\phi_0^*)^2} \quad (3.101)$$

Under low-shear rates, there is no orientation of particles and maximum packing fraction  $\phi_0^*$ , does not depend on the shear rate. When random packing fraction near the glass transition is taken as the maximum packing fraction,  $\phi_0^* = 4/7 \approx 0.57$ , eq. (3.101) could describe experimental values up to  $\phi \approx 0.50$ .

Eq. (3.101) has to be corrected for the effect of the shear rate, if it is to be used to give the shear viscosity of diluted suspensions of viscoelastic particles. This was done by expanding the maximum packing fraction  $\phi_0^*(\dot{\gamma})$  as a function of the shear strain gradient,  $\zeta_{xx}(\dot{\gamma})$  in the direction of flow

$$\phi^*(\dot{\gamma}) = \phi_0^*[1 + \beta \zeta_{xx}(\dot{\gamma}) + O(\zeta_{xx}^2)] \quad (3.102)$$



where  $\phi_0^*$  is the maximum packing concentration around the zero shear rate limit and  $\beta$  a constant related to the flow type.

Combining eqs. (3.99), (3.101), and (3.102), an expression for the relative viscosity of dilute viscoelastic suspensions can be obtained as

$$\eta_r(\phi, \xi_{xx}) = \frac{1 - \phi}{(1 - \phi/(\phi_0^*(1 + \beta\xi_{xx})))^2} \quad (3.103)$$

If the internal viscosity of the particles is much greater than the external viscosity of the suspension medium, and the suspension not too concentrated, then the viscous dissipation within the particle phase can be neglected in comparison with the external phase.

Snabre and Mills (1999) assumed that the viscoelastic particles in a concentrated suspension behave as isolated particles in a fluid with viscosity equal to the effective suspension medium viscosity  $\mu = \eta(\phi, \dot{\gamma})$  and experience an effective shear stress  $\tau = \eta(\phi, \dot{\gamma})\dot{\gamma}$ . Using eqs. (3.101) and (3.102), an equation giving the relative shear viscosity of concentrated suspensions of viscoelastic particles were obtained as

$$\eta_r(\phi, De) = \frac{1 - \phi}{(1 - (\phi/\phi_0^*)(1 + \eta_r(\phi, (De))(\beta\Lambda^{-1}(De)^2/(1 + (De)^2)))^{-1})^2} \quad (3.104)$$

This equation could capture the shear thinning behavior of the suspensions associated with the shear-induced deformation of viscoelastic spheres with  $\beta/\Lambda = 0.1$  and  $\phi_0^* = 0.57$ . At high-shear rates, the relative viscosity was found to reach a constant value of  $\eta_{r\infty}(\phi, \phi_0^*, \beta/\Lambda)$  which decreases with the maximal particle strain  $\xi_{xx}(De \rightarrow \infty) = 1/\Lambda = \mu_0/\eta_p$  in the flow direction.

### 3.5.3 Elastic behavior of soft particles with a microstructure

Under long-range interactions, solid suspensions behave like a soft solid with elastic properties, generally called, *soft-particle pastes*. Of special interest in this group are the microgel pastes, such as microemulsions, microgels, or polymer-coated particles, due to their technological importance. Contrary to hard-sphere particles, the “soft” particles can be compressed above their maximum packing fraction of  $\approx 0.64$ , due to the interpenetrability of their “halos” of diffuse ionic clouds, polymer coating, or surfactant hydrocarbon chains (see e.g., Figures 1.2 and 1.5). Up to this point, this overlapping was considered as a repulsive force among particles freely suspended in a medium. When the number concentration of particles within a fixed volume of suspending media is increased above the critical concentration of maximum compaction, these repulsive forces act as compressed springs and create another source of elasticity in addition to that arising from the microstructure of the gels (Figure 3.1(f)). The actual physical case is the interpenetration of the “halos”, but it may be simpler to visualize this compaction as a flattening of the contact points or faces, similar to the appearance of high internal phase ratio emulsions or polyhedral foams.

The elastic properties of these soft pastes were simulated by Seth *et al.* (2006) supported by experimental results, which will be presented below. The basis of the simulation study



is a model based on soft spheres arranged randomly, which on compression deform elastically up to 10% of their radii, so as to conform to the Hertz theory of elasticity (see Section 1.8.1.2 in Chapter 1). It is also assumed that the deformation due to a pair interaction does not affect the deformations in other directions due to surrounding particles. Under these conditions, the overlap distance  $h_{ij}$  between two compressed particles of radius  $R_i$  and  $R_j$  with their centers located at  $\mathbf{r}_i$  and  $\mathbf{r}_j$ , respectively, is given by

$$h_{ij} = R_i + R_j - |\mathbf{r}_i - \mathbf{r}_j| \quad (3.105)$$

The pair-wise elastic energy arising from this contact is given as

$$\begin{aligned} u_{ij} &= \frac{8}{15} E^* h_{ij}^{5/2} R_c^{1/2} & h_{ij} > 0 \\ u_{ij} &= 0 & h_{ij} \leq 0 \end{aligned} \quad (3.106)$$

based on Hertz theory. In this equation,  $E^*$  is the *elastic contact modulus* of the particles and gives the contribution of the particles to the total elasticity. The stiffer the particle, the greater the energy required for a given deformation and hence, greater the elastic contact modulus. This is similar to *Young's modulus*,  $E$  and the two moduli are related through the Poisson's ratio  $\nu$  by the relation

$$E^* = \frac{E}{2(1 - \nu^2)} \quad (3.107)$$

$R_c$  in eq. (3.106) is a composite radius related to the radii of the contacting particles  $i$  and  $j$  through

$$\frac{1}{R_c} = \frac{1}{R_i} + \frac{1}{R_j} \quad (3.108)$$

The total potential energy  $U$  for a random packing of  $N$  particles is the sum of pair-wise interaction energies of the particles

$$U = \sum_i^N \sum_{j>i}^N u_{ij} \quad (3.109)$$

Total energy  $U$  of the initial microstructure of the system is given in terms of the radial distribution function  $g(r)$  around a particle and the pair-wise interaction energy function  $u(r)$  as,

$$U = 4\pi n \int_0^{2R} r^2 u(r) g(r) dr \quad (3.110)$$

The function for a single particle is extended throughout the suspension by multiplying the integral with the number density of particles  $n$ .

The osmotic pressure  $\Pi$  is related to the stress tensor  $\tau$  through the relations,

$$\tau = \frac{1}{v} \sum \sum \mathbf{r}_{ij} \frac{du_{ij}}{d\mathbf{r}_{ij}} \quad (3.111)$$

$$\Pi = \frac{tr(\tau)}{3} \quad (3.112)$$

where  $v$  is the volume of the suspension and  $tr(\tau)$  is the transpose of the stress tensor. These relations arise from the variation of osmotic pressure as a function of local concentration of ions or polymers within the suspension. Local variations in concentration arise, in turn, from the action of stresses that compress the particles and their halos together. Osmotic pressure in an undeformed, isotropic suspension can be given in terms of the potential energy gradient and radial distribution function as

$$\Pi = -\frac{4\pi n}{6} \int_0^{2R} r^3 \frac{du(r)}{dr} g(r) dr \quad (3.113)$$

When an isotropic suspension is stretched uniaxially, the elastic energy per unit volume changes as a function of the shear modulus  $G$ . Deformation affects the microstructure, causing a variation in the particle density along the extended axis. The pair correlation function in the extended condition,  $g(r, \theta)$  is now a function of both the radial position from the particle and the angular distance from the stretched axis,  $\theta$ . When the shear modulus  $G$ , and the osmotic pressure  $\pi$  are scaled with the elastic contact modulus  $E^*$ , excellent agreement was obtained between the simulated and the analytical results. Figure 3.13 shows that the shear moduli at high ( $G_\infty$ ) and low frequencies ( $G_0$ ) are different for monodisperse random packings. Since the gel relaxes partially at low frequencies,  $G_0 < G_\infty$ ,

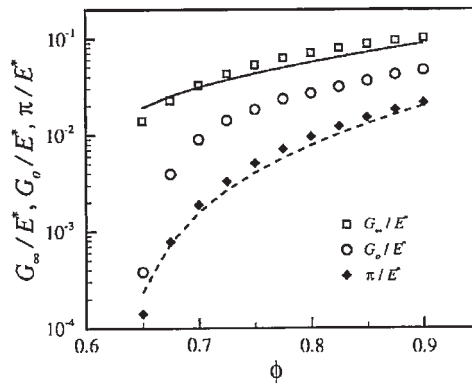


**Figure 3.13** Variation of shear moduli and osmotic pressure in soft particle gels as a function of packing fraction. Simulation results for monodispersed packings are shown with symbols and analytical results with the lines. (Seth *et al.*, 2006. Reproduced with permission of the Society of Rheology, Figure 1 in the original).

both moduli and the osmotic pressure are zero below the critical packing volume  $\phi_c = 0.64$  when the particles do not touch each other ( $C \leq C_m$ ). At concentrations above the critical, deformation begins at the contact surfaces and the moduli show an immediate step increase at  $\phi_c = 0.64$ . The increase in the moduli with  $\phi$  above the critical concentration is much greater than that of regular lattices, covering a range of two orders of magnitude, due to development of many facets as particles approach each other. Osmotic pressure does not show a jump but rather a sharp increase.

The other results of this work and related studies, (Borrega *et al.*, 1999; Cloitre, 2005) can be summarized as follows:

### 3.5.3.1 Rheological parameters

Elastic modulus  $G'$  becomes greater than the loss modulus  $G''$  and exhibits a plateau at low frequencies with the onset of solid-like behavior at  $\phi_c = 0.64$ . The polymer concentration at this volumetric fraction is taken as another criterion for the onset of solid-like behavior,  $C = C_m$ . The value of  $C_m$  increases with an increase in the cross-link density and electrolyte concentration. The shear modulus is found to depend on the concentration of the polymer with a power-law relation,  $G_0 \propto C^k$ , when  $C > C_m$ .  $k$  is found in the range of 6–7, experimentally, and  $G_0 \propto \phi^6$  through simulations. This power relation is in agreement with the results of Ramakrishnan *et al.* (2005) for hard-sphere gels given in Section 3.2.5.3, above. The rheology of concentrated dispersions of soft particles can be controlled through the adjustment of solvent viscosity  $\mu_0$  and the storage modulus of elasticity  $G'$  (Cloitre, 2005).

### 3.5.3.2 Assessment of the volumetric fraction of solids $\phi$

Volumetric fraction of solids in hard-sphere suspensions can be calculated from either the mass or the number concentration once the density and the size distribution are known. On the other hand, polyelectrolyte microgels are formed by emulsion polymerization with cross-linking. Even though the particle size is limited with the micelle size, the cross-linked polyelectrolyte globules swell at pH values above the isoelectric point coupled with dissociation of the ionic groups. Soft particle gels swell under the effect of osmotic pressure gradients within the gels. At high concentrations of the polymer, the reverse process of deswelling takes place both sterically (by the limitation of the available solvent for full swelling) and osmotically. In the latter case, the concentration of counterions is closely related to the concentration of the polyelectrolyte that produces osmotic pressure gradients between the inside and outside of the globules. The osmotic pressures can be counteracted by the addition of neutral electrolytes. At high concentrations above the critical where the globules become compressed, osmotic deswelling is not significant (Borrega *et al.*, 1999). When osmotic deswelling is suppressed, volumetric fraction varies in proportion with the polymer concentration,  $\phi \propto C$ . Since the critical volumetric concentration for randomly packed soft particle pastes is  $\phi_c = 0.64$ , the volumetric fraction can be calculated using the relation

$$\phi = \frac{\phi_c}{C_m} C \quad (3.114)$$

$C_m$  is the polymer concentration at the onset of solid-like behavior where the zero shear viscosity diverges.

### 3.5.3.3 Effect of polydispersity

Polydispersity was found to have no effect on  $G_0$  or  $\Pi$  up to 20% deviation in particle diameter, in agreement with experimental observations cited in the article (Seth, *et al.*, 2006). Percolation threshold where the network forms is not affected by the polydispersity within this range, either.

## 3.6 FLOW OF BIOLOGICAL FLUIDS: BLOOD FLOW IN THE CIRCULATORY SYSTEM

Blood flow as a complex solid–liquid two-phase flow system incorporates many of the issues given in this and the previous chapters for the flow of nonliving materials. Based on these properties, blood flow is chosen as a case to recapitulate this chapter.

Blood is a concentrated suspension with hematocrit levels  $\phi_H \geq 0.3$  ( $\phi_H \geq 0.4$  on the average). As introduced in Chapter 1, it is a mixture of particles and colloids of different dimensions and shapes. Red blood cells (RBCs), the main component of hematocrit, can form reversible aggregates that dissociate under high shear. RBCs have polymers integrated into the membrane: sections of these proteins dangle freely outside of the cell, contributing to the steric stabilization of the cells besides the electrostatic repulsion. The electrolytes of the serum further regulate the stabilization. Proteins present in the plasma such as fibrinogen and the globulins that are not adsorbed on the cells affect the local osmotic pressures, causing the depletion forces to become active. The RBCs are viscoelastic, deformable, soft particles. In addition, the presence of proteins (polymers) in blood confers viscoelastic properties to the suspension medium of the cells, the plasma. The viscoelastic suspension medium helps the RBCs to form string-like structures. In addition, the particles migrate to the central regions of the vessels due to the shear thinning rheological behavior of the plasma. The RBCs aggregate in the form of rouleaux (Figure 1.18(c)) in the low-shear regions of the blood vessels. The rouleaux act as flexible rod shaped particles. These properties cover almost all the topics given under Section 4 of this chapter.

No other flow system has been investigated as much as the circulatory system. Naturally, most of these are devoted to the effects of the disease conditions. Nevertheless, the system is so complex that no model developed up to the present can capture all the aspects of blood flow of even healthy individuals. Complexities are brought about by being in the control of the nervous system that regulates the flow rate, pressure, and even the composition of the blood and diameter of the vessels according to conditions existing in other tissues of the body. The complexities of the circulatory system can be classified under three groups: (1) *Flow conditions*: Pulsatile flow under periodically varying pressure, and variable flow rate with local changes in the flow regime. (2) *Vascular system*: Complex network of blood vessels with walls of varying flexibility and varying diameters. (3) *Rheology of Blood*: The nonlinearity introduced to the rheology of the suspension by the interactions between living cells and proteins.

### 3.6.1 Flow conditions of blood

The circulatory system can be modeled as a highly branched piping network consisting of pipes of decreasing diameter in the arteries (increasing diameter, in the venous part)

connected in series, which, in turn are connected in parallel, all within two closed cycles, *systemic* and *pulmonary*, attached to the two compression sides of a double-acting membrane pump the heart. The energy for recirculation of blood within the circulatory system is supplied by the heart that serves as a membrane type double-action positive displacement pump. In the *systemic cycle*, that recycles the blood in various organs of the body, maximum pressure of compression (systole) is 120 mm Hg and minimum pressure (diastole) is 80 mm Hg under normal conditions. These values change with the flexibility of the blood vessel walls, roughness produced by complex lipids and stenosis (blockage). The cyclic nature of the pressure averaging 100 mm Hg, persists through the aorta and the large arteries. The amplitude of the cyclic pressure decays in the small arteries and arterioles and does not exist in the capillaries (Guyton and Hall, 2006). The magnitude of the average gage pressure decreases significantly in the small arteries, arterioles, and capillaries connected in series. The average pressure in the capillaries is  $\approx 10$  mm Hg. The gage pressure is effectively zero in the veins and at the entrance to the atrium of the heart. The flow is again pulsatile in the *pulmonary circulation* through the lungs, with the pressure cycling between 25 mm Hg (systole) and 8 mm Hg (diastole), averaging 16 mm Hg. The magnitude as well as the amplitude of the fluctuations decays in the arterioles of the lungs reaching a minimum of 7 mm Hg (in place of zero as in the systemic cycle) in the venules and pulmonary veins. The same volumetric  $\approx 8.3 \times 10^{-5} \text{ m}^3 \text{ s}^{-1}$  ( $\approx 5 \text{ L min}^{-1}$ ) recycles through both the systemic and pulmonary system. The ratio of the maximum pressure difference between the exit of the heart and the capillaries in the systemic cycle to the pressure difference in the pulmonary system

$$\frac{\Delta P_{\text{systemic}}}{\Delta P_{\text{pulmonary}}} = \frac{(80 - 10)}{(25 - 8)} \approx 4 \quad (3.115)$$

is equal to the ratio of the frictional losses in the systemic and pulmonary blood vessel systems.

Flow rate,  $Q$ , and pressure, or more correctly pressure drop  $\Delta P$  are controlled by separate mechanisms in the circulatory system. Flow rate is controlled by the tissue requirements. The chemical composition of nutrients, wastes, and oxygen are monitored by the capillaries, arterioles, and venules in the tissues that dilate or constrict to meet the tissue requirements. In case, the local adjustments are not sufficient, the central nervous system sends a signal to the heart to increase its capacity, which can be increased four to seven times, in addition to controlling the diameter of the vessel through constrictions and expansions. Pressure of the blood is controlled by a stronger positive displacement of the heart, by contraction of the venous system (the blood reservoirs) to increase and by constricting the arteries to reduce the blood throughput (Guyton and Hall, 2006).

The flow regime is regulated by the mechanisms controlling the rheology of the blood, the cross-sectional area and the roughness of the blood vessels and velocity of the blood. The regime is generally laminar, with local turbulence arising when the vessel makes a sharp change in direction, in bifurcations, in case of internal wall surfaces highly roughened by lipid deposits and obstructions (stenosis) within the vessel.

### 3.6.2 The vascular system

The average diameters, wall thicknesses, and elasticities of various blood vessels are given in Table 3.4. The equivalent area in the table is the total cross-sectional area of a given type of blood vessel. The average velocities are based on the data given in Guyton and Hall (2006) with an average blood flow rate of  $83 \text{ mL s}^{-1}$  under resting conditions. The calculated velocities are based on the total material balance, or the continuity principle, which states that under steady-state conditions blood flow rate in both systems are equal. These values are valid under at-rest conditions only, as the self-regulatory system of the blood vessels (constriction and dilation) and the pulsation rate of the heart increase or decrease the volumetric flow rate of blood according to the necessities of the tissues.

The walls of the arteries are thicker because of the higher pressures and thicker muscle cells that provide the elasticity of the walls to convert the extra kinetic energy during the systole (pulse) to potential energy. This stored potential energy is then converted into lateral pressures during the diastole (flow in between the pulses). In this way, the pulsations are absorbed by the walls and blood is given to the tissues at a more or less constant rate.

The thinner elastic walls of the veins can dilate to store about 64% of the total amount of blood (Guyton and Hall, 2006). The inner walls of the blood vessels are lined with a layer of soft endothelium cells to reduce the frictional losses. The length of the capillaries varies in the range of  $0.2 < L < 0.8 \text{ mm}$ . Arteries and veins are much longer, but due to the highly branched vessel system, the length between bifurcations is generally too short to reach steady-state conditions.

With the variations of the diameters and velocities in the different section of the circulatory system, the Reynolds number is expected to be highly variable, determined largely by the local value of the viscosity under the prevalent shear conditions. As the diameter of

**Table 3.4**

Average properties of blood vessels

	Aorta	Arteries	Arterioles	Precapillaries
(a) Arteries				
Diameter (mm)	18	4	0.030	0.035
Wall thickness (mm)	2	1	0.020	0.030
Equivalent area ( $\text{cm}^2$ )	2.5	20	40	<sup>a</sup>
Average velocity ( $\text{cm sec}^{-1}$ )	33	4	2	
Elasticity <sup>b</sup>	H	M–H	M	L
	Capillaries	Venules	Veins	Venae Cavae
(b) Veins				
Diameter (mm)	0.008	0.020	5	31
Wall thickness (mm)	0.001	0.002	0.5	1.5
Equivalent area ( $\text{cm}^2$ )	2500	250	80	8
Average velocity ( $\text{cm sec}^{-1}$ )	0.03	0.33	1	10
Elasticity <sup>b</sup>	Not elastic	Not elastic	M–L	M

<sup>a</sup>Calculated together with the capillaries.

<sup>b</sup>H: high, M: medium, L: low.

the vessel walls decrease, the rouleaux disintegrate into smaller segments, until only single cells remain in the capillaries (see Section 1.9 in Chapter 1). Apparent viscosity of blood decreases as the capillary tube diameter decreases, reaching a minimum value around 6–8  $\mu\text{m}$ , corresponding to the diameter of RBCs. RBC deformability has a significant role in the disintegration of the rouleaux causing the appearance of this minimum in viscosity, which does not exist with rigidified RBC. The cells deform into thimble shapes to reduce the shear stress acting on the surfaces. Negative charge carried by both the RBC and the endothelial cells prevent contact of the cells with the walls facilitating the passage. Further decrease in the tube diameter causes a sharp increase in apparent viscosity known as the *Fahraeus–Lindquist* effect.

Another factor that contributes to the decrease in viscosity in small capillaries is branching (bifurcation) from the main arteries to the capillary blood vessels: Capillary vessels generally open up along the walls of the main blood vessels, where the shear rate is highest. Similar to the behavior of other colloids given in Figure 3.12 in Section 4.1 of this chapter, RBCs tend to migrate toward the axially central sections of the vessel, where the velocity distribution flattens signifying a low-shear region, leaving the plasma with decreased concentration of RBC along the walls of the vein. In bifurcations, this plasma layer with highly decreased hematocrit, enters the capillaries. Due to the reduced level of solids content, the viscosity of blood in the capillaries is less than that in the larger veins under the same shear rate (Baskurt and Meiselman, 2003).

### 3.6.3 Rheology of blood

The blood circulatory system is a case of solid–liquid two-phase flow with *hematocrit* as the solid phase and *plasma* as the liquid phase. Hematocrit is mainly composed of *erythrocytes* or RBCs, *leucocytes* or WBCs, and platelets (*thrombocytes*) at an approximate order of magnitude ratio of  $10^6:10^3:10^5$ , respectively, in terms of number per cubic millimeter. The liquid phase, plasma, is a solution of proteins (albumin, globulin, and fibrinogen), coagulation factors and electrolytes, mainly  $\text{Na}^+$ ,  $\text{K}^+$ , and  $\text{Ca}^{+2}$ . The presence of proteins causes nonlinearity in the rheological behavior of plasma, proportional with their concentration.

Rheology of blood is extremely complicated for reasons that can be grouped under three headings. (1) Aggregation behavior of RBC and other cells brought about by shear rate and interaction with other noncellular components. (2) The viscoelasticity of the particulate phase RBC, as the main component of hematocrit. (3) The viscoelasticity of the plasma, the suspending medium, due to the presence of proteins, which are complex polymers.

#### 3.6.3.1 Aggregation behavior of RBCs

Aggregation behavior of RBCs and platelets are discussed in Chapter 1, Section 9.1. Platelet aggregation takes place in case of injury to the vessel walls. Aggregation of RBCs controls the rheology of blood. In turn, the shear rate in a particular vessel and the concentration of proteins, or other polymers infused into the blood vessels. Polymers should play an important role in aggregation of RBCs as aggregation does not take place in saline solutions. How the polymers affect the aggregation is not clearly elucidated yet. Of the two



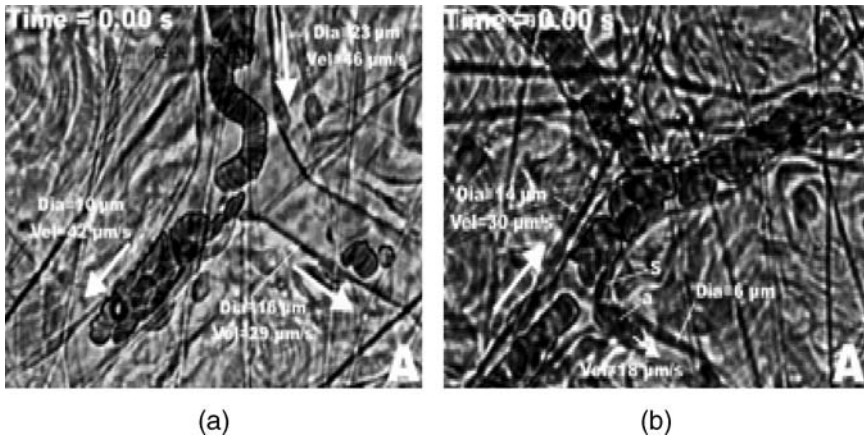


**Figure 3.14** Photographs of rat RBC aggregates (a) RBC aggregates flowing slowly through a precapillary bifurcation following administration of fibrinogen. (b) RBCs flowing through a precapillary bifurcation after the enhancement of aggregation by in vivo infusion of Dextran 500. (Pearson and Lipowsky, 2004. Reproduced with permission of Taylor & Francis, Figures 1(a) and 2(a) in the original.)

surface forces that could be effective, depletion and bridging, depletion mechanism seems to be more plausible, in regard to the reversibility of aggregation with respect to shear rate (blood flow rate) in healthy individuals with normal levels of plasma proteins. High molecular weight polymers like Dextran infused into the blood may bring about bridging forces into effect as given in Figure 3.14(b). The change in the mechanism of aggregation is evident from the shape of the RBC clusters in Figure 3.14(b), that are far different from the rouleaux shape observed in (a). The stability of these clusters under different flow disturbances as in the case of bifurcations also imply the stability of the bridging bonds formed in the aggregate, as given in the figure: The rouleaux deform into shapeless clusters after the bifurcation whereas clusters formed in the presence of Dextran are not affected at all.

Polymers also affect the aggregation mechanism by changing the rheology of plasma. Normal forces arising in the case of a viscoelastic suspending medium cause the particles to assume string-like shapes, as will be discussed in the sections below.

### 3.6.3.2 Viscoelasticity of blood cells

Biological cells and macromolecules are soft, viscoelastic particles, and behave as solid particles under low-shear conditions, and as liquid-like under high shear. That is, they try to rotate under the effect of the shear stresses acting on their external surfaces at low-shear rates, whereas; deform to assume the least resistive configuration under high-shear rates.

Cells are essentially Newtonian fluids wrapped up in a viscoelastic gel (as in the case of spectrin network beneath the membrane) that in turn is covered by the phospholipid bilayer, the membrane. The proteins embedded in the membrane attach the spectrin network to the membrane, besides serving other functions summarized in Chapter 1. The very strong van der Waals and hydrophobic forces among the phospholipid molecules resist



**Table 3.5**

Rheological constants of red blood cells

Property	Units	Values	References
Internal (cytosolic) viscosity, $\eta_i$	Pa s	$6 \times 10^{-3}$	Snabre and Mills (1999)
Surface viscosity of membrane, $\eta_s$	N s m <sup>-1</sup>	$6 \times 10^{-7}$	Waugh and Evans (1979) Hochmuth <i>et al.</i> (1979)
Shear modulus, $G$	N m <sup>-1</sup>	$6 \times 10^{-6}$	Waugh and Evans (1979) Hochmuth <i>et al.</i> (1979)
Relaxation time, $\lambda$	s	0.1	Chien <i>et al.</i> (1978)
Bending modulus, $K_b$	J	$1.8 \times 10^{-19}$	Evans (1983)
Modulus of elasticity, $K_{el}$ (modulus of isotropic dilatation)	N m <sup>-1</sup>	0.5	Chien <i>et al.</i> (1978)

stretching but allow deformation, in a way limiting the elastic strain that may be imposed on the cell, displayed through the relative magnitudes of the moduli given in Table 3.5.

Evans and coworkers (Waugh and Evans, 1979; Hochmuth *et al.*, 1979) experimentally investigated the viscoelastic properties of the cell membrane and found that the elastic shear modulus of the cell membrane remained constant  $\approx 6 \times 10^{-6} \text{ Nm}^{-1}$  independent of the degree of cell deformation. The experimental value of the elastic shear modulus found by Evans and coworkers were confirmed by further experimental and theoretical work (Stokke *et al.*, 1985, 1986) and was attributed to the ionic-gel network of spectrin. The relaxation time of the membrane was found to range in the interval,  $0.1 \leq \lambda \leq 0.01$ , decreasing with increasing deformation rate of the cell (Chien *et al.*, 1978). This again is expected from the strong intermolecular forces between the phospholipids of the bilayer that resists stretching (dilatation) in the lateral direction.

RBCs isolated under high shear deform into ellipsoids, and align at a certain angle to the direction of flow with a tank treading (undulatory) motion of the membrane at a frequency that depends on the shear rate,  $f \approx \gamma/2$  (Fisher *et al.*, 1978).

Snabre and Mills (1999) applied the analysis given in Section 3.5.2 above, to blood flow with RBCs as the viscoelastic particles. The Deborah number  $De$ , is related to the relaxation time of the cell membrane under small deformations ( $\lambda_0 \approx 0.1\text{s}$ ) with a power-law relationship,

$$De = (\lambda_0 \dot{\gamma})^{1-n} \quad (3.116)$$

$n$  varying in the range,  $0.7 \leq n \leq 0.8$ . The normal strain is related to the Deborah number through the relation

$$\varepsilon_{xx} = \eta_r(\phi, \varepsilon_{xx}) \Lambda^{-1} \frac{(\lambda_0 \dot{\gamma})^{(2-2n)}}{1 + (\lambda_0 \dot{\gamma})^{(2-2n)}} \quad (3.117)$$

Approximating the particle viscosity by the viscosity of the fluid inside the cell membrane (cytosolic viscosity)  $\eta_i$ , the authors found a relation that could describe the relative viscosity of blood:

$$\eta_r(\phi, De) = \frac{1 - \phi}{(1 - (\phi / \phi_0^*)(1 + \eta_r(\phi, De)((\beta \Lambda^{-1}(\lambda_0 \gamma)^{(2-2n)}) / (1 + (\lambda_0 \gamma)^{(2-2n)})))^{-1})^2} \quad (3.118)$$

The relative viscosity at high-shear rates was reduced to

$$\eta_{r\infty} = \frac{1 - \phi}{(1 - (\phi / \phi_0^*)(1 + \eta_{r\infty} \beta \Lambda^{-1})^{-1})^2} \quad (3.119)$$

The authors tested the model with experiments conducted with RBCs dispersed in saline solution. The variation of relative viscosity with volumetric fraction of solids (RBC) and shear rate is reproduced in Figure 3.17(a) within the context of Example 3.2.

### 3.6.3.3 Effect of the viscoelasticity of plasma

The suspending medium of the blood cells (hematocrit) is the plasma that contains proteins of different sizes and shapes in an ionic solution, the serum. When the concentration of the proteins is high, the rheology of the plasma can no longer remain linear. Viscoelasticity and shear thinning of plasma may be observed at high concentration of plasma proteins. The non-Newtonian behavior of the plasma has two effects on blood flow: a high-shear region develops along the walls, and normal forces develop perpendicular to the direction of flow. Particles orient in the form of strings under high-shear rates as given in Section 3.5.1. The Weissenberg number,  $Ws$ , the ratio of first normal stress difference to the shear stress controls the string formation. In a recent study performed with fluids of different viscoelasticity (Scirocco *et al.*, 2004), the formation of string-like structures of varying lengths were detected by microscopy and alignment of particles were evaluated by small-angle light scattering technique. The results showed that shear thinning is an essential factor in string formation. As the particles escape from the high-shear regions along the vessel walls, migration effects are stronger than in the case of Newtonian fluids. As a result, tendency of string formation in the central regions of the channel was observed. The critical Weissenberg number was not constant but varied in the range 0.5–16.5. These results support the well-known Fahreus and Fahreus-Lindqvist effects in blood rheology, that the viscosity and hematocrit value in micro blood vessels and capillaries that withdraw the blood from bifurcations along the wall of the main arteries are lower than their systemic values. In addition, an alternative effect on the agglomeration of RBCs in the form of rouleaux is suggested as a form of string-like formations. Basing on small-angle light scattering results, Scirocco *et al.* (2004) showed that the individual particles in a string do not touch each other. Similarities in the rheological properties of blood suggest that similar mechanisms may be involved during the reversible aggregation of RBCs. Further research is required to assess the effect of the suspending medium rheology on the aggregation behavior of RBCs.

**Example 3.2: Rheology of blood**

*The case:* Blood samples obtained by venipuncture are subjected to rheological analysis in a controlled stress/strain rheometer. Cone and plate sensors with diameter 35 mm and cone angle, 1°, are used in the tests. Tests are performed at 37 °C, normal body temperature, with the use of a solvent trap to prevent drying of the sample. The concentrations of the components in the blood analysis that may affect the rheology of blood are given in Table 3.6. Tests are conducted both with fresh blood, immediately after transpiration, and with blood mixed with EDTA at a ratio of 1.5 mg EDTA mL<sup>-1</sup> blood during transpiration. The clear serum remaining above the fresh blood samples after sedimentation and plasma remaining above the blood sample taken into EDTA is separated and subjected to the same tests. pH of fresh blood is 7.3 at 25 °C.

*Rheological analysis:* Blood viscosity is a highly variable property, varying not only between different individuals, but also with disease conditions and nutrition. The composition of blood is given in Table 3.6 to define the conditions under which the rheological behavior is observed. The variation of the viscosities of fresh blood are given in Figure 3.15 together with the blood withdrawn into a tube containing EDTA and mixed right after transpiration. Viscosities of the fresh blood are given together with its serum, and blood taken into EDTA with its plasma, respectively, for comparison over a range of shear rates,  $10^{-4} \leq \dot{\gamma} \leq 10^{+4}$  for full evaluation of blood rheology under different conditions, especially at very low-shear rates significant under prolonged inactivity (stasis). Range of shear rates encountered in blood flow is  $10^{-1} \leq \dot{\gamma} \leq 10^{+2}$  under normal conditions. The nominal values of blood viscosity reported by Baskurt and Meiselman (2003) are shown with crossed symbols corresponding to 10, 20, and 100 mPa s at the shear rates

**Table 3.6**  
Composition of blood samples in Example 3.2<sup>a</sup>

	Component	Units	Concentration	Reference range
Blood cells		Hematocrit	32.7	35.9–44.6
	Erythrocytes	mm <sup>-3</sup>	$5.57 \times 10^6$	$4.1\text{--}5.1 \times 10^6$
	Leucocytes	mm <sup>-3</sup>	$7.1 \times 10^3$	$4.5\text{--}11 \times 10^3$
	Thrombocytes	mm <sup>-3</sup>	$3.38 \times 10^5$	$1.5\text{--}4.5 \times 10^5$
	Hemoglobin	g L <sup>-1</sup>	105	120–156
Proteins	Total	g L <sup>-1</sup>	79	64–83
	Albumin	g L <sup>-1</sup>	46	35–52
	Globulin	g L <sup>-1</sup>	33	25–35
	Fibrinogen	g L <sup>-1</sup>	5.48	1.75–4
	IgG	g L <sup>-1</sup>	11.58	7–16
	IgA	g L <sup>-1</sup>	2.61	0.7–4
	IgM	g L <sup>-1</sup>	6.85	0.4–2.3
Ions	Ca	g L <sup>-1</sup>	0.105	0.086–0.102
	Na	meq L <sup>-1</sup>	140	136–145
	K	meq L <sup>-1</sup>	4.3	3.5–5

<sup>a</sup> The laboratory results are published with the permission of the Clinical Biochemistry Division of the Faculty of Medicine, Ege University.

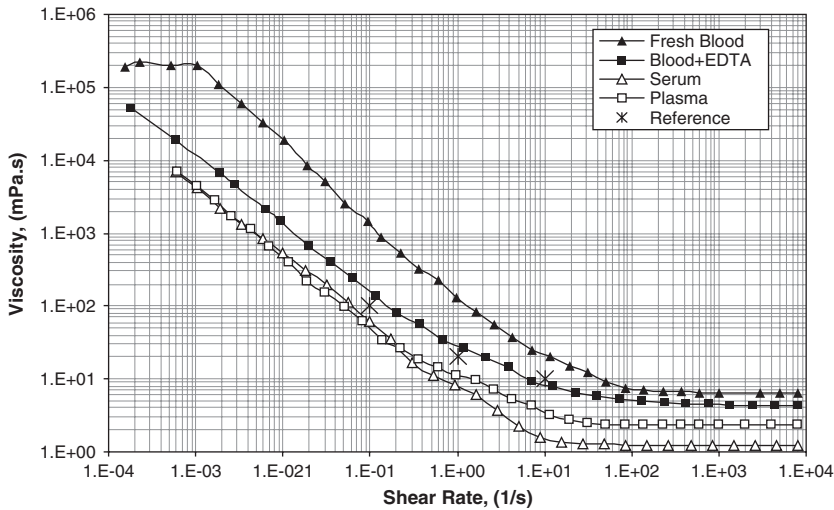


**Figure 3.15** Variation of blood and plasma viscosities with shear rate.

of 10, 1,  $0.1 \text{ s}^{-1}$ , respectively. Since blood coagulates rapidly, generally the blood viscosities in EDTA are reported. The serum viscosity is around  $1.2 \text{ mPa s}$  and plasma viscosity  $2.1 \text{ mPa s}$ , and the blood viscosities around  $5\text{--}6 \text{ mPa s}$  in the Newtonian region at high-shear rates in agreement with the accepted nominal values.

Evaluation of blood viscosities in qualitative terms brings the effect of platelets on blood viscosity. EDTA destroys the structure of platelets as discussed in Chapter 1 and greatly reduces blood coagulation. The effect of EDTA does not change the shape of the viscosity curve, except at very low-shear rates approaching zero shear, but creates an order of magnitude decrease, as evaluated at  $\dot{\gamma} \leq 1 \text{ s}^{-1}$ . At higher shear rates, the viscosities approach each other since the viscosity of fresh blood decreases more steeply with the shear rate. The more densely coagulated fresh blood drags along some of the plasma proteins during sedimentation leaving serum of lower viscosity. The effect of reduced polymer content is significant at  $\dot{\gamma} \geq 1 \text{ s}^{-1}$ , under stretched conditions. The most significant observation given in this plot is the shear thinning, or power-law behavior of all the samples, and the Newtonian viscosities observed at high-shear rates. Shear thinning in fresh blood results from the dissociation of RBC in addition to the effect of alignment of the proteins. The shear rate at which constant viscosity is observed decreases with a decrease in the colloid content. Fresh blood, richest in colloid and particle composition, approaches constant viscosity around  $200 \text{ s}^{-1}$ , whereas, serum with the lowest colloid content approaches constant viscosity around  $20 \text{ s}^{-1}$ . Within the measurement range, ( $10^{-4} \leq \dot{\gamma} \leq 10^{+4}$ ) only fresh blood approaches a constant value of zero-shear viscosity at low values of shear rate. This is to be expected, as only the fresh blood is a concentrated suspension of particles. Plasma and serum act more like polymeric solutions, the flow behavior of which is given in Chapter 2.

Variation of shear stress with shear rate given in Figure 3.16 gives further information about the mechanism of shear flow. Only in the case of fresh blood, a linear

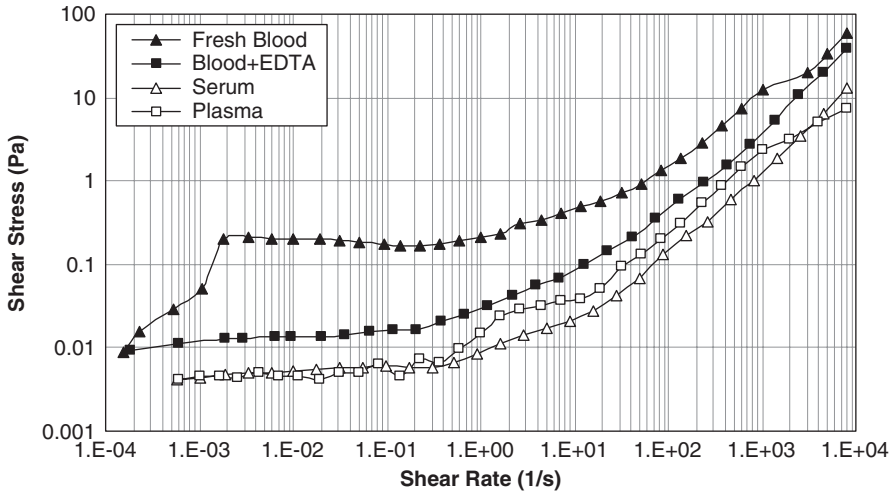


**Figure 3.16** Variation of shear stress with shear rate of blood components.

increase of shear stress with shear rate is observed corresponding to zero-shear viscosity, below the dynamic yield stress range of shear rates. The constant stress or dynamic yield stress region explained in Section 3.3.2.1 above for the shear-rate behavior of soft particles indicates the underlying mechanism for the steadily decreasing viscosities in this region. Effect of the platelets can be seen by comparing the relative magnitudes of the dynamic yield stress of fresh blood and that withdrawn into EDTA. Shear stress increases for all the blood components above the yield stress because the volumetric fraction of particles, the hematocrit is below the maximum compaction level,  $\phi_m$ . The polymers set the lowest level of the shear stress; in fact, the shear stress of plasma and serum does not remain constant, but increases slightly in accordance with a power-law relation with the shear rate.

Effect of the viscoelasticity of RBCs is observed with the analysis of Snabre and Mills (1999). The variation of the relative viscosity of RBCs suspended in saline solution with shear rate and volumetric concentration of cells is redrawn from the original article in Figure 3.17(a). Blood withdrawn into EDTA in this example is used for comparison, to approach similar conditions as in the original experiments. The relative viscosity of blood with hematocrit level of 32.7, corresponding to  $\phi = 0.327$  falls in between the curves for  $\phi = 0.35$  and  $0.25$  onto the correct place. This result is remarkable and shows that Snabre and Mills analysis is relevant even when the suspending medium shows non-Newtonian behavior, provided the viscosities corresponding to the same shear rates are used in the calculation of relative viscosity.

Presence of RBCs and rouleaux in the central regions of the blood vessels are mainly due to migration. But normal stress differences present in polymer solutions may also be effective in forcing the particles in a direction normal to the flow direction, i.e., radially, also causing the aggregation. The first normal stress difference  $N_1$ , eq. (2.1) is the

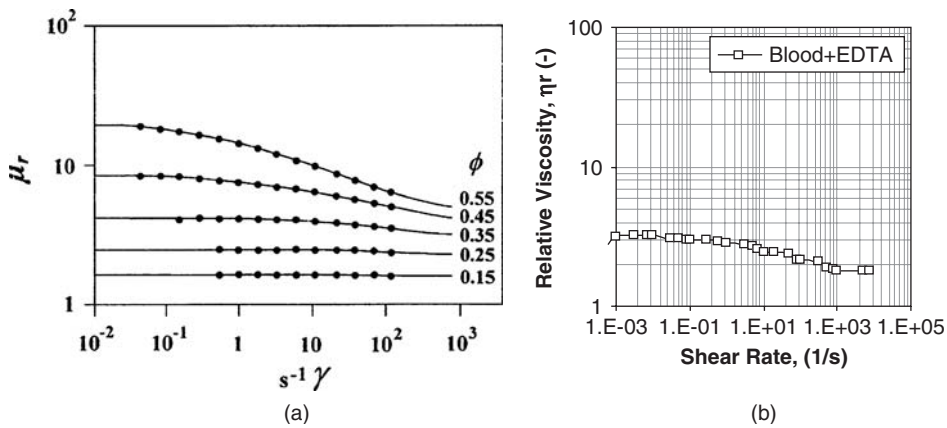


**Figure 3.17** Shear viscosity of RBC suspensions. (a) Relative shear viscosity as a function of shear rate for normal RBC suspended in saline solution (Snabre and Mills, 1999. Reproduced with permission of Elsevier, Figure 6 in the original) (b) The results obtained for the blood sample with  $\phi = 0.327$  in this example.

difference between the flow direction and the radial direction. When the normal stress in the radial direction is greater than the normal stress in the flow direction,  $N_1$  becomes negative. Figure 3.18 shows that the first normal stress difference of fresh blood is almost equal to that of serum. This signifies that the suspending medium also has viscoelastic properties, which may be one of the reasons for string (rouleaux) formation of RBC as predicted by the observations of Scirocco *et al.* (2004) in Section 3.3.5.1 above. Normal forces were not observed in blood mixed with EDTA.

Creep and recovery tests given in Figure 3.19 indicate the viscoelastic behavior under prolonged applied stress. Under a constant stress of 0.07 Pa, fresh blood behaves almost like a Burger fluid, if it were not for the decaying overshoots on relaxation. Similar overshoots were observed in concentrated soft-particle suspensions by Persello *et al.* (1994) and were interpreted as a fast linear response in the direction of the change and a slow relaxation back to the plateau value. It was taken as an indication of resistance to shear, if the shear rate is increased, and augmenting this resistance if the shear rate is reduced. Similar nonlinear response is observed in the case of serum, which essentially behaves like a fluid.

Dynamic tests give further support to the viscoelastic behavior observed in fresh blood and serum, as given in Figure 3.20. The storage modulus of elasticity  $G'$  is higher than the viscous modulus  $G''$  in fresh blood, indicating the dominance of elastic forces. The increasing moduli indicate that blood shows nonlinear viscoelastic behavior at low-shear rates approaching linearity in the range of physiological interest. On the other hand, serum acts like a liquid with the viscous modulus  $G''$  greater than the modulus of elasticity  $G'$  and shows a linear response over the shear-rate interval of physiological interest.

Various models are used to predict the shear behavior of blood. Within the context of this example Quemada model cannot be used, because the determination of maximum compaction of blood cells is outside the scope of this book. The fit to the Casson model

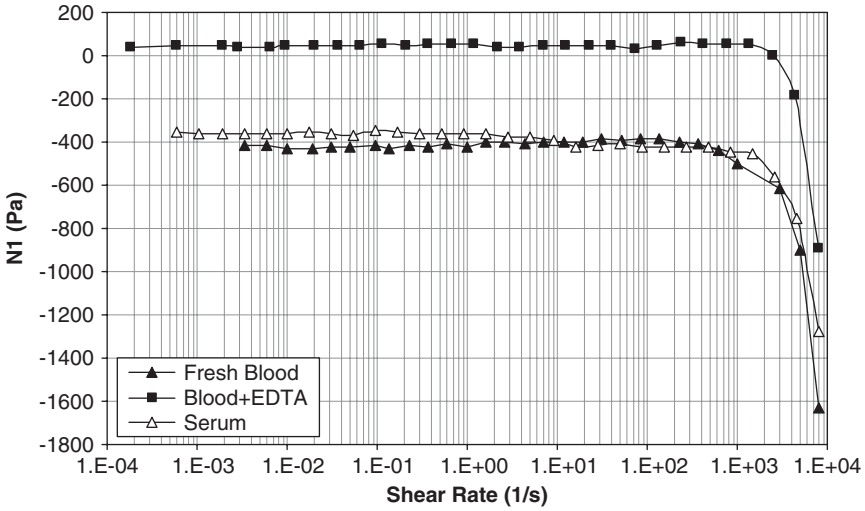


**Figure 3.18** First normal stress difference  $N_1$  of blood components.

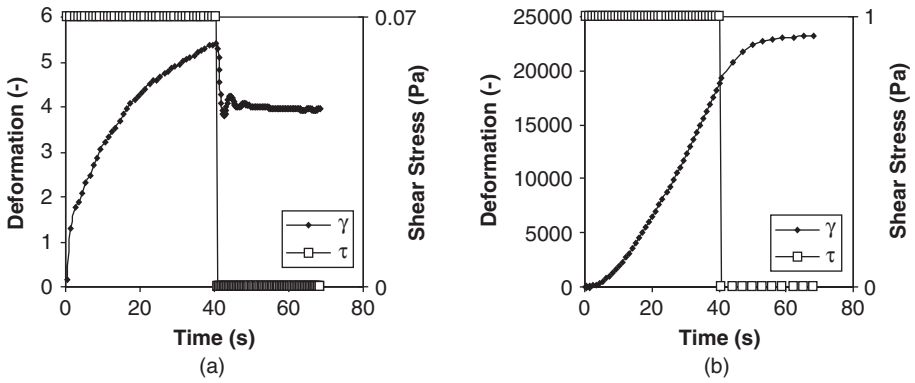


**Figure 3.19** Creep and recovery tests of (a) fresh blood at 0.07 Pa, (b) serum at 1 Pa.

(eq. (2.50) of fresh blood and serum is given in Figures 3.21(a) and (c), respectively. The regression equations for fresh blood,

$$\tau^{0.5} = (0.165)^{0.5} + (0.0067)^{0.5} \gamma^{0.5} \quad r^2 = 0.9972 \quad (3.120)$$

and serum,

$$\tau^{0.5} = (0.0041)^{0.5} + (0.0012)^{0.5} \gamma^{0.5} \quad r^2 = 0.9946 \quad (3.121)$$

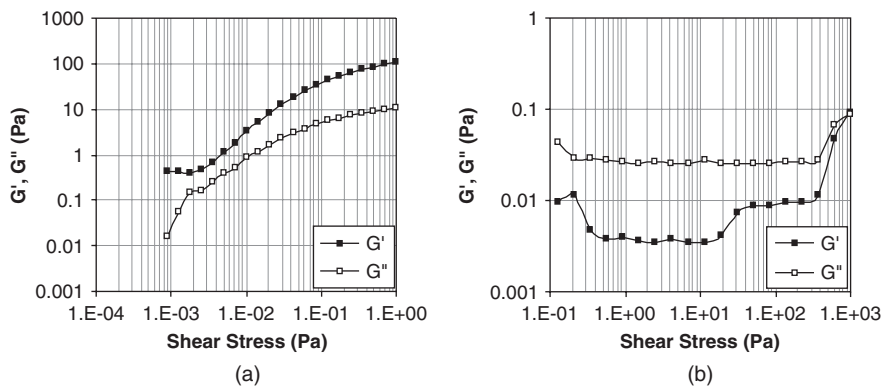


**Figure 3.20** Variation of modulus of elasticity  $G'$  and viscous modulus  $G''$  with the amplitude of shear-stress variations at a frequency of 1 Hz. (a) fresh blood, (b) serum.

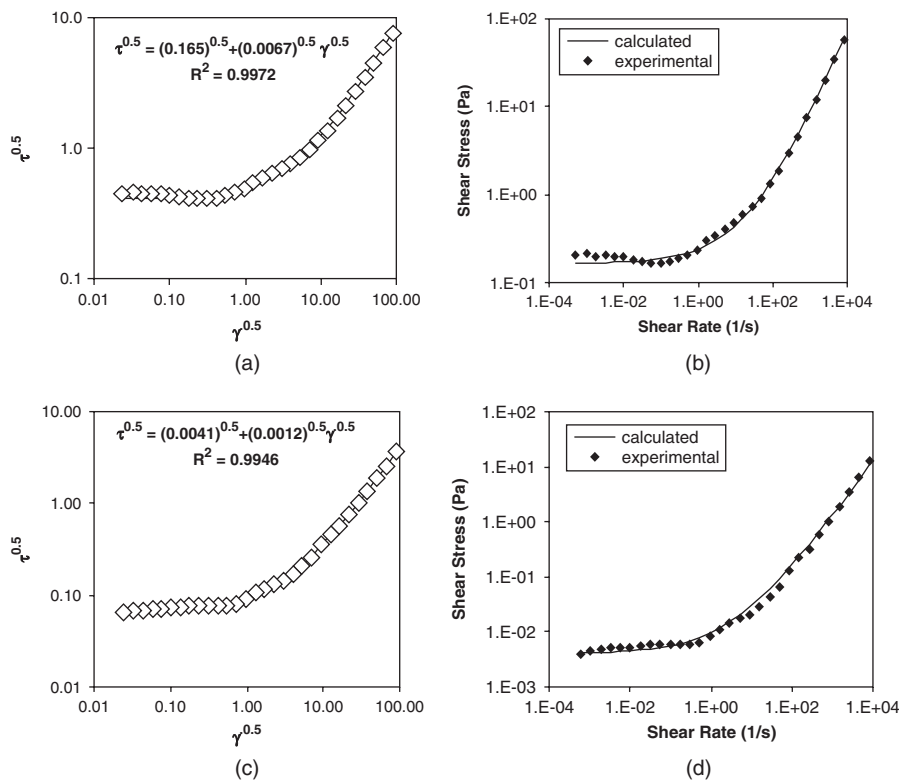


**Figure 3.21** Curve fitting to Casson's model. (a) Casson plot for fresh blood, (b) agreement between the experimental and calculated values for fresh blood, (c) Casson plot for serum, (d) agreement between the experimental and calculated values for serum.



The yield stress of the serum is equal to the yield stress reported for blood of 2–4 mPa (Baskurt and Meiselman, 2003) but the yield stress of the blood is much higher. The excess concentration of the polymers, fibrinogen, and Immunoglobulin M may be one reason for the increased yield stresses. The viscosity at infinite shear, 6.7 mPa s for blood and 1.2 mPa s for serum are in complete agreement with the values given in the same reference.

For colloidal suspensions with constant zero shear and infinite shear viscosities, the viscosity variation with shear stress is described by the equation,

$$\frac{\eta(\dot{\gamma}) - \eta_{\infty}}{\eta_0 - \eta_{\infty}} = \frac{1}{1 + (\tau / \tau_c)^{\beta}} \quad (3.122)$$

The viscosity at the critical stress  $\tau_c$  is defined by the equation,

$$\eta(\tau_c) = \frac{(\eta_0 - \eta_{\infty})}{2} \quad (3.123)$$

Dimensionless viscosity plotted against the dimensionless shear stress is given in Figure 3.22. The drop in the dimensionless viscosity by more than two orders of magnitude at the critical shear stress ( $\tau / \tau_c$ ) supports the existence of the dynamic yield stress observed in Figure 3.16. Viscosity of fresh blood within the measured shear rate range is fitted to eq. (3.122) giving

$$\frac{\eta - 6.4}{224000 - 6.4} = \frac{1}{1 + (\tau / 0.197)^{2.36}} \quad r^2 = 0.99 \quad (3.124)$$

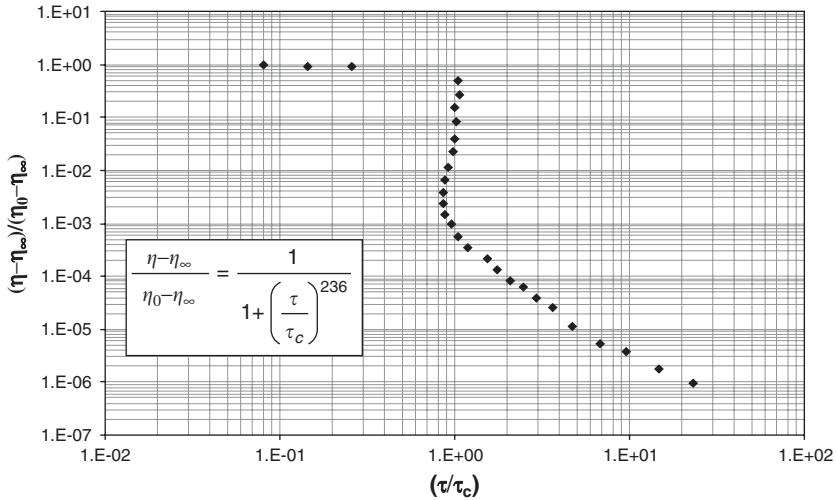


**Figure 3.22** Variation of the dimensionless viscosity of fresh blood with the dimensionless shear stress.

The exponent 2.36 is close to the range of typical values  $1 \leq \beta \leq 2$  (Russel *et al.*, 1989). The exponent indicates that the rouleaux length, formation, and disintegration are highly effective in determining the shear stress dependence of the viscosity, in accordance with experimental observations.

## REFERENCES

- Aral, B.K., Kalyon, D.M., 1994. Effects of temperature and surface roughness on time dependent development of wall slip in steady torsional flow of concentrated suspensions. *Journal of Rheology*, 38, 957–972.
- Aral, B.K., Kalyon, D.M., 1997. Viscoelastic material functions of noncolloidal suspensions with spherical particles. *Journal of Rheology*, 41, 599–620.
- Baskurt, O.K., Meiselman, H.J., 2003. Blood rheology and hemodynamics. *Seminars in Thrombosis and Hemostasis*, 29, 435–450.
- Bender, J., Wagner, N.J., 1996. Reversible shear thickening in monodisperse and bidisperse colloidal dispersions. *Journal of Rheology*, 40, 899–916.
- Berry, D.H., Russel, W.B., 1987. The rheology of dilute suspensions of slender rods in weak flows. *Journal of Fluid Mechanics*, 180, 475–494.
- Boersma, W.H., Laven, J., Stein, H.N., 1992. Viscoelastic properties of concentrated shear thickening dispersions. *Journal of Colloid and Interface Science*, 149, 10–22.
- Borrega, R., Cloitre, M., Betremieux, I., Ernst, B., Leibler, L., 1999. Concentration dependence of the low-shear viscosity of polyelectrolyte micronetworks: From hard spheres to soft microgels. *Europhysics Letters*, 47, 729–735.
- Bossis, G., Brady, J.F., 1989. The rheology of Brownian suspensions. *Journal of Chemical Physics*, 91, 1866–1874.
- Brady, J.F., 1993. The rheological behavior of concentrated colloidal dispersions. *Journal of Chemical Physics*, 99, 567–581.
- Burns, J.L., Yan, Y., Jameson, G.J., Biggs, S., 2003. The rheology of concentrated suspensions of depletion-flocculated latex particles. *Colloids and Surfaces A: Physicochemical Engineering Aspects*, 214, 173–180.
- Buscall, R., Mills, P.D.A., Yates, G.E., 1986. Viscoelastic properties of strongly flocculated polystyrene latex dispersions. *Colloids and Surfaces*, 18, 341–358.
- Cates, M.E., Haw, M.D., Holmes, C.B., 2005. Dilatancy, jamming, and the physics of granulation. *Journal of Physics: Condensed Matter*, 17, S2517–S2531.
- Cates, M.E., Wittmer, J.P., Bouchaud, J.P., Claudin, P., 1998. Jamming, force chains, and fragile matter. *Physical Review Letters*, 81, 1841–1844.
- Chen, Y.L., Schweizer, K.S., 2004. Microscopic theory of gelation and elasticity in polymer-particle suspensions. *Journal of Chemical Physics*, 120, 7212–7222.
- Chien, S., Sung, K.L.P., Skalak, R., Usami, S., Tözeren, A., 1978. Theoretical and experimental studies on viscoelastic properties of erythrocyte membrane. *Biophysics Journal*, 24, 463–487.
- Chong, J.S., Christiansen, E.B., Baer, A.D., 1971. Rheology of concentrated suspensions. *Journal of Applied Polymer Science*, 15, 2007–2021.
- Cloitre, M., 2005. Tailoring the flow properties of soft colloidal dispersions. *Macromolecules Symposium*, 229, 99–106.
- Cohen, E.G.D., Verberg, R., de Schepper, I.M., 1998. Viscosity and diffusion in hard-sphere-like colloidal suspensions. *Physica A*, 251, 251–265.

- Coussot, P., Raynaud, J.S., Moucheron, P., Guilbaud, J.P., Huynh, H.T., Jarny, S., Lesueur, D., 2002. Coexistence of liquid and solid phases in flowing soft glassy materials. *Physical Review Letters*, 88, 218311 (1–4).
- deKruif, C.G., van Iersel, E.M.F., Vrij, A., Russel, W.B., 1985. Hard sphere colloidal dispersions: Viscosity as a function of shear rate and volume fraction. *Journal of Chemical Physics*, 83, 4717–4725.
- Doi, M., Edwards, S.F., 1986. *The Theory of Polymer Dynamics*. Clarendon Press, Oxford.
- Drappier, J., Divoux, T., Amarouchene, Y., Bertrand, F., Rodts, S., Cadot, O., Meunier, J., Bonn, D., 2006. Turbulent drag reduction by surfactants. *Europhysics Letters*, 74, 362–368.
- Eilers, H., 1941. Die Viskosität von emulsionen hochviskoser Stoffe als funktion der konzentration. *Kolloid Zhurnal*, 97, 313–321.
- Einstein, A., 1906. Calculation of the viscosity-coefficient of a liquid in which a large number of small spheres are suspended in irregular distribution. *Annalen der Physik*, 19, 286–306.
- Evans, E.A., 1983. Bending elastic modulus of red blood cell membrane derived from buckling instability in micropipette aspiration tests. *Biophysics Journal*, 43, 27–30.
- Ferretti, R., Zhang, J., Buffle, J., 1998. Flocculation of hematite with polyacrylic acid: Fractal structures in the reaction- and diffusion-limited aggregation regimes. *Journal of Colloid and Interface Science*, 208, 509–517.
- Fisher, T.M., Stohr-Liesen, M., Schmid-Schonbeim, H., 1978. The red cell as a fluid droplet. Tank tread like motion of the human erythrocyte membrane. *Science*, 202, 894.
- Foss, D.R., Brady, J.F., 2000. Structure, diffusion and rheology of Brownian suspensions by Stokesian Dynamics simulation. *Journal of Fluid Mechanics*, 407, 167–200.
- Franks, G.V., Johnson, S.B., Scales, P.J., Boger, D.V., Healy, T.W., 1999. Ion-specific strength of attractive particle networks. *Langmuir*, 15, 4411–4420.
- Gopalakrishnan, V., Zukoski, C.F., 2004. Effect of attractions on shear thickening in dense suspensions. *Journal of Rheology*, 48, 1321–1344.
- Gopalakrishnan, V., Zukoski, C.F., 2006. Viscosity of hard-sphere suspensions: Can we go lower? *Industrial Engineering and Chemistry Research*, 45, 6906–6914.
- Guyton, A.C., Hall, J.E., 2006. *Textbook of Medical Physiology*, 11th edition., Elsevier Saunders, Philadelphia (Chapter 14).
- Hinch, E.J., Leal, L.G., 1972. The effect of Brownian motion on the rheological properties of a suspension of non-spherical particles. *Journal of Fluid Mechanics*, 52, 683.
- Hochmuth, R.M., Worthy, P.R., Evans, E.A., 1979. Red cell relaxation and the determination of membrane viscosity. *Biophysics Journal*, 26, 101–114.
- Hogg, R., Healy, T.W., Fuerstenau, D.W., 1966. Mutual coagulation of colloidal dispersions. *Journal of Chemical Society, Faraday Transactions*, 62, 1638–1651.
- Hunt, W.J., Zukoski, C.F., 1999. The rheology of bimodal mixtures of colloidal particles with long-range, soft repulsions. *Journal of Colloid and Interface Science*, 210, 343–351.
- Hynninen, A.P., Dijkstra, M., 2005. Phase behavior of dipolar hard and soft spheres. *Physical Review E*, 72, 051402, 1–10.
- İkizler, B., 2005. *Production of ZnO Nanoparticles Using Microemulsion Method*, MS Thesis, Ege University.
- Johnson, S.B., Franks, G.V., Scales, P.J., Boger, D.V., Healy, T.W., 2000. Surface chemistry-rheology relationships in concentrated mineral suspensions. *International Journal of Mineral Processing*, 58, 267–304.
- Jones, D.A.R., Leary, B., Boger, D.V., 1991. The rheology of a concentrated colloidal suspension of hard spheres. *Journal of Colloid and Interface Science*, 147, 479.
- Jones, D.A.R., Leary, B., Boger, D.V., 1992. The rheology of a sterically stabilized suspension at high concentration. *Journal of Colloid and Interface Science*, 150, 84.

- Krieger, I.M., Daugherty, T.J., 1959. A mechanism for non-Newtonian flow in suspensions of rigid spheres. *Transactions of The Society of Rheology*, 3, 137–152.
- Lukič, B., Jeney, S., Tischer, C., Kulik, A.J., Forró, L., Florin, E.L., 2005. Direct observation of non-diffusive motion of a Brownian particle. *Physical Review Letters*, PRL 95, 16060, 1–4.
- Maranzano, B.J., Wagner, N.J., 2001. The effects of interparticle interactions and particle size on reversible shear thickening: Hard-sphere colloidal dispersions. *Journal of Rheology*, 45, 1205–1222.
- Marti, I., Höfler, O., Fischer, P., Windhab, E.J., 2005. Rheology of concentrated suspensions containing mixtures of spheres and fibres. *Rheologica Acta*, 44, 502–512.
- Meeker, S.P., Bonnecaze, R.T., Cloitre, M., 2004. Slip and flow in pastes of soft particles: Direct observation and rheology. *Journal of Rheology*, 48, 1295–1320.
- Mills, P., Snabre, P., 1988. The fractal concept in the rheology of concentrated suspensions. *Rheologica Acta*, 26, 105–108.
- Mooney, M., 1957. The viscosity of a concentrated suspension of spherical particles. *Journal of Colloid Science*, 6, 162–170.
- Neto, C., Evans, D.R., Bonaccorso, E., Butt, H.J., Craig, V.S.J., 2005. Boundary slip in Newtonian liquids. *Reports in Progress of Physics*, 68, 2859–2897.
- Olhero, S.M., Ferreira, J.M.F., 2004. Influence of particle size distribution on rheology and particle packing of silica based suspensions. *Powder Technology*, 139, 69–75.
- Papir, Y.S., Krieger, I.M., 1970. Rheological studies on dispersions of uniform colloidal spheres-2-Dispersions in nonaqueous media. *Journal of Colloid and Interface Science*, 34, 126.
- Payne, A.R., 1962. The dynamic properties of carbon black-loaded natural rubber vulcanizates. *Journal of Applied Polymer Science*, 6, 57.
- Pearson, M.J., Lipowsky, H.H., 2004. Effect of fibrinogen on leukocyte margination and adhesion in postcapillary venules. *Microcirculation*, 11, 295–306.
- Persello, J., Magnin, A., Chang, J., Piau, J.M., Cabane, B., 1994. Flow of colloidal aqueous silica dispersions. *Journal of Rheology*, 38, 1845–1870.
- Philippe, A.P., 1996. The random contact equation and its implications for (colloidal) rods in packings, suspensions, and unisotropic powders. *Langmuir*, 12, 1127–1133.
- Pignon, F., Magnin, A., Piau, J.M., 1996. Thixotropic colloidal suspensions and flow curves with minimum: Identification of flow regimes and rheometric consequences. *Journal of Rheology*, 40, 573–587.
- Poon, W.C.K., 2002. The physics of a model colloid-polymer mixture. *Journal of Physics: Condensed Matter*, 14, R859–R880.
- Quemada, D., 1984. Models for rheological behavior of concentrated disperse media under shear. In: *Advances in Rheology* (eds. B. Mena, A. Garcia-Rejon, C. Rangel –Nafaile), Universidad Nacional Autonoma de Mexico, Mexico City (pp. 571–582).
- Ramakrishnan, S., Gopalakrishnan, V., Zukoski, C.F., 2005. Clustering and mechanics in dense depletion and thermal gels. *Langmuir*, 21, 9917–9925.
- Ramakrishnan, S., Zukoski, C.F., 2006. Microstructure and rheology of thermoreversible nanoparticle gels. *Langmuir*, 22, 7833–7842.
- Robertson, C.G., Wang, X., 2005. Isoenergetic jamming transition in particle-filled systems. *Physical Review Letters*, PRL 95, 075703, 1–4.
- Robinson, J.V., 1957. The viscosity of suspension of spheres: sediment volume as a determining parameter. *Transactions of The Society of Rheology*, 1, 15.
- Rueb, C.J., Zukoski, C.F., 1998. Rheology of suspensions of weakly attractive particles: Approach to gelation. *Journal of Rheology*, 42, 1451–1476.
- Russel, W.B., Saville, D.A., Schowalter, W.R., 1989. *Colloidal Dispersions*. Cambridge University Press, Cambridge.

- Scales, P.J., Johnson, S.B., Healy, T.W., Kapur, P.C., 1998. Shear yield stress of partially flocculated colloidal suspensions. *AIChE Journal*, 44, 538–544.
- Schramm, G., 1994. A Practical Approach to Rheology and Rheometry, HAAKE, Karlsruhe, Germany.
- Schweizer, K.S., Saltzman, E.J., 2003a. Entropic barriers, activated hopping, and the glass transition in colloidal suspensions. *Journal of Chemical Physics*, 119, 1181–1196.
- Schweizer, K.S., Saltzman, E.J., 2003b. Transport coefficients in glassy colloidal fluids. *Journal of Chemical Physics*, 119, 1197–1202.
- Sciocco, R., Vermant, J., Mewis, J., 2004. Effect of viscoelasticity of the suspending fluid on structure formation in suspensions. *Journal of Non-Newtonian Fluid Mechanics*, 117, 183–192.
- Segre, P.H., Meeker, S.P., Pusey, P.N., Poon, W.C.K., 1995. Viscosity and structural relaxation in suspensions of hard-sphere colloids. *Physical Review Letters*, 75, 958.
- Seth, J.R., Cloitre, M., Bonnecaze, R.T., 2006. Elastic properties of soft particle pastes. *Journal of Rheology*, 50, 353–376.
- Shah, S.A., Chen, Y.L., Schweizer, K.S., Zukoski, C.F., 2003. Viscoelasticity and rheology of depletion flocculated gels and fluids. *Journal of Chemical Physics*, 119, 8747–8760.
- Shih, W.H., Shih, W.Y., Kim, S.I., Liu, J., Aksay, I.A., 1990. Scaling behaviour of the elastic properties of colloidal gels. *Physical Review A*, 42, 4722–4778.
- Smith, W.E., Zukoski, C.F., 2004. Flow properties of hard structured particle suspensions. *Journal of Rheology*, 48, 1375–1388.
- Snabre, P., Mills, P., 1996. Rheology of weakly flocculated suspensions of rigid particles. *Journal of Physics III* 6, 1811–1834.
- Snabre, P., Mills, P., 1999. Rheology of concentrated suspensions of viscoelastic particles. *Colloids and Surfaces A: Physicochemical and Engineering Aspects*, 152, 79–88.
- Solomon, M.J., Boger, D.V., 1998. The rheology of aqueous dispersions of spindle-type colloidal hematite rods. *Journal of Rheology*, 42, 929–949.
- Stokke, B.T., Mikkelsen, A., Elgsaeter, A., 1985. Some viscoelastic properties of human erythrocyte spectrin networks end-linked in vitro. *Biochimica et Biophysica Acta*, 816, 111–121.
- Stokke, B.T., Mikkelsen, A., Elgsaeter, A., 1986. The human erythrocyte membrane skeleton may be an ionic gel. I. Membrane mechanochemical properties. *European Biophysics Journal*, 13, 203–218.
- Suzuki, H., Fuller, G.G., Nakayama, T., Usui, H., 2004. Development Characteristics of drag-reducing surfactant solution flow in a duct. *Rheologica Acta*, 43, 232–239.
- Trappe, V., Weitz, D.A., 2000. Scaling of the viscoelasticity of weakly attractive particles. *Physical Review Letters*, 85, 449–452.
- van der Werff, J.C., de Kruif, C.B., 1989. Hard-sphere colloidal dispersions: The scaling of rheological properties with particle size, volume fraction, and shear rate. *Journal of Rheology*, 33, 421–454.
- van der Werff, J.C., de Kruif, C.B., Blom, C., Mellema, J., 1989. Linear viscoelastic behavior of dense hard-sphere suspensions. *Physical Review A*, 39, 795.
- van Dillen, T., van Blaaderen, A., Polman, A., 2004. Shaping colloidal assemblies. *Materials-today*, July/August, 40–46.
- Vanmegen, W., Underwood, S.M., 1994. Glass-transition in colloidal hard spheres—Measurement and mode-coupling-theory analysis of the coherent intermediate scattering function. *Physical Reviews E*, 49, 4206.
- Verberg, R., de Schepper, I.M., Cohen, E.G.D., 1997. Viscosity of colloidal suspensions. *Physical Review E*, 55, 3143–3158.
- Vermant, J., Solomon, M.J., 2005. *Journal of Physics: Condensed Matter*, 17, R187–R216.

- Wang, Z.Y., Larsen, P., 1994. Turbulent structure of flows of water and clay suspensions with bed load. *Journal of Hydraulic Engineering*, ASCE, 120, 577–600.
- Wang, Z.Y., Larsen, P., Nestmann, F., Dittrich, A., 1998. Resistance and drag reduction of flows of clay suspensions. *Journal of Hydraulic Engineering*, 124, 41–49.
- Waugh, R., Evans, E.A., 1979. Thermoelasticity of red blood cell membrane, *Biophysics Journal*, 26, 115–132.
- Wierenga, A.M., Philipse, A.P., 1998. Low shear viscosity of isotropic dispersions of (Brownian) rods and fibres; a review of theory and experiments. *Colloids and Surfaces A: Physicochemical and Engineering Aspects*, 137, 355–372.
- Wildemuth, C.R., Williams, M.C. 1984. Viscosity of suspensions modeled with a shear-dependent maximum packing fraction. *Rheologica Acta*. 23, 627–635.
- Zhou, Z., Scales, P.J., Boger, D.V., 2001. Chemical and physical control of the rheology of concentrated metal oxide suspensions. *Chemical Engineering Science*, 56, 2901–2920.

This page intentionally left blank

# – 4 –

## Motion of Particles in Fluids

---

Motion of particles other than Brownian motion will be the subject of this chapter. There will be a relative motion between the particles and the suspending fluid unless: (a) the particles form a gel and become captured within the network structure; or (b) interact strongly with each other and with the suspending fluid to form a single-phase non-Newtonian fluid; or (c) have the same density as the suspending fluid so their moment of inertia cannot be identified from that of the fluid. The aims and conditions of the process determine the desirability of this relative motion: if a stable and homogeneous suspension is the aim, then measures are taken to prevent the relative motion, such as stabilization by repulsive surface forces coupled with introduction of turbulent convection to enhance random motion of particles and prevent settling. Convective motion may disperse the weak aggregations; but may also be used to enhance aggregation if surface forces are adjusted accordingly. On the other hand, motion of particles in fluids is the basis of all separation processes and the design of the separation equipment is based on enhancing or manipulating the relative motion. Under all conditions, the motion of particles should be under control for proper and efficient operation of the processes. The parameters that affect velocity of particles in Newtonian fluids, namely, the forces acting on the particles, and the particle characteristics that affect the motion of particles will be presented in this chapter, which will form the basis for flow of settling slurries taken up in Chapter 6, mixing of solid-liquid mixtures, in Chapter 7 and separation of solids from liquids, in Chapter 8.

### 4.1 MOTION OF THE FLUID PHASE

The drag force on the particle, or equivalently Stokes' law for the shear force, expressed as energy of shearing in the definition of Peclet number in eq. (3.10), is of prime importance in determining the rheological behavior of concentrated suspensions. Stress distribution on the surfaces of the solid particles created by the velocity distribution of the flowing liquid will affect the motion of the particles even if the suspension is not concentrated. The effect of fluid flow on the particle should then be taken up first, before an analysis of the other forces acting on the particles.



### 4.1.1 Creeping flow

Creeping motion, also known as Stokes' flow, takes place when the velocity of the flowing fluid is very low, or when the viscosity of fluids is very high and/or size of the particles small. In creeping flow the Reynolds number is very small ( $Re \ll 1$ ) such that the inertial effects can be ignored in comparison with the viscous resistance.

Motion of the fluids is described with the help of streamlines and stream functions. A *streamline* is defined as a path within a fluid across which no flow occurs and the tangent of which gives the direction of the local velocity at that point. Velocity in creeping flow regime is so slow that the streamlines can diverge as the particle approaches, flow around the surface of the particle and then converge again downstream of the particle as depicted in Figure 4.1(a). As the Reynolds number increases, vortices start to appear in the wake of the sphere indicating the separation of the boundary layer from the surface as in Figure 4.1(b). The separation point of the boundary layer moves down to the equator of the sphere, with an increase in the velocity of the fluid to much higher values.

*Stream functions*,  $\psi$ , are used to define and plot streamlines. Lines of constant  $\psi$  are streamlines of the flow; i.e., they are everywhere parallel to the local velocity vector. Thus, selected  $\psi$  lines can be interpreted as boundaries of the flow. Velocity components in any coordinate system at a given point are described by the partial derivatives of  $\psi$  at that point. The stream function is generally defined for two-dimensional flow through or around various geometries as  $\psi = (x, y)$ .

### 4.1.2 Velocity distribution around a sphere in creeping flow

Flow of an incompressible Newtonian fluid around a stationary sphere of radius  $R_p$  will be taken as an example for creeping flow. Fluid with a uniform free stream velocity  $V_\infty$  approaches a fixed sphere of diameter  $d_p$  vertically upward in the  $z$ -direction as shown in

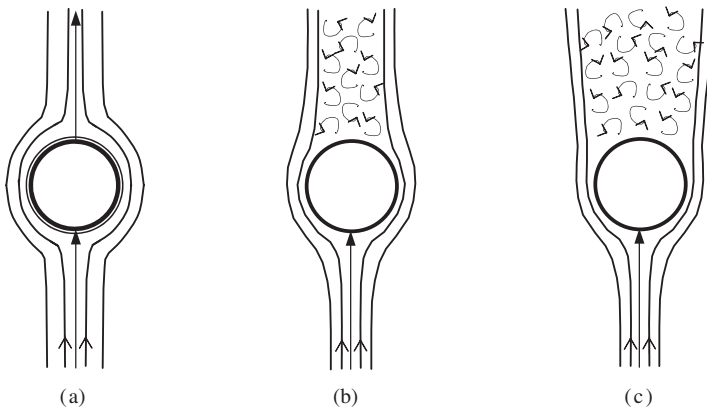


**Figure 4.1** Flow patterns for the flow around a sphere (a) for creeping flow condition; (b) as the Reynolds number increases; (c) for high Reynolds numbers.

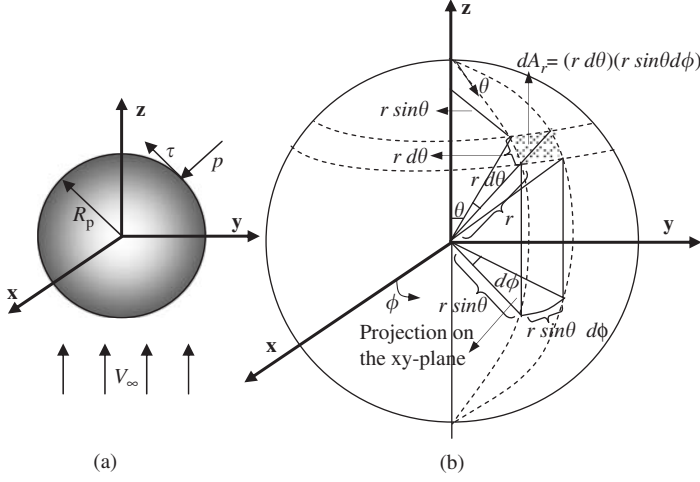


**Figure 4.2** (a) Schematic representation of a sphere, to which fluid approaches with a velocity  $V_\infty$  in the  $z$ -direction; (b) surface element taken on the sphere,  $dA_r$ , shown as shaded area.

Figure 4.2(a). Creeping flow conditions are valid provided Reynolds number based on free stream velocity  $V_\infty$  and particle diameter  $d_p$  is less than one,

$$Re = \frac{\rho V_\infty d_p}{\mu} \leq 1 \quad (4.1)$$

where  $\rho$  and  $\mu$  are the density and viscosity of the fluid, respectively.

Spherical coordinates  $(r, \theta, \phi)$  will be used to analyze the system with the origin at the center of the sphere and with the velocity components of the form

$$V_r = V_r(r, \theta), \quad V_\theta = V_\theta(r, \theta), \quad V_\phi = 0 \quad (4.2)$$

Solutions of the equation of motion (Navier–Stokes' equations) in three dimensions are difficult to obtain because of the dependence of both velocity and pressure on the variables. Hence, the solution is simplified with the assumption of axisymmetric flow around the  $z$ -axis, for which  $\partial/\partial\phi = 0$  and  $V_\phi = 0$ . With the elimination of variation in the third direction, it becomes possible to solve the equation of motion in two-dimensional flow by introducing the stream function,  $\psi(r, \theta)$ . Velocity components ( $V_r$  and  $V_\theta$ ) of the flow first will be presented as derivatives of  $\psi$ . Then,  $r$ - and  $\theta$ -components of the Navier–Stokes' equations of motion are combined into one equation using stream functions. Velocity components can thus be obtained after  $\psi$  is found (Bird, et al., 2002).

*Equation of continuity* for the two-dimensional incompressible flow in spherical coordinates can be rewritten from eq. (A3.1.3) as

$$\frac{1}{r^2} \frac{\partial}{\partial r} (r^2 V_r) + \frac{1}{r \sin \theta} \frac{\partial}{\partial \theta} (V_\theta \sin \theta) = 0 \quad (4.3)$$

Multiplying the above equation with  $r^2 \sin \theta$  gives

$$\frac{\partial}{\partial r}(-V_r r^2 \sin \theta) = \frac{\partial}{\partial \theta}(V_\theta r \sin \theta) \quad (4.4)$$

Stream function must automatically satisfy the continuity equation and it is also an exact differential:

$$\frac{\partial^2 \psi}{\partial r \partial \theta} = \frac{\partial^2 \psi}{\partial \theta \partial r} \quad (4.5)$$

Comparing eqs. (4.4) and (4.5) gives the expressions for velocity components in terms of the stream function as

$$V_r = -\frac{1}{r^2 \sin \theta} \frac{\partial \psi}{\partial \theta} \quad (4.6)$$

$$V_\theta = \frac{1}{r \sin \theta} \frac{\partial \psi}{\partial r} \quad (4.7)$$

The equation of continuity is automatically satisfied by replacing eqs. (4.6) and (4.7) into eq. (4.3).

The Navier–Stokes' equations for spherical coordinates with incompressible flow are given in Table A3.5. These equations can be written in operator notation as

$$\rho \frac{D\mathbf{V}}{Dt} = \rho \left( \frac{\partial \mathbf{V}}{\partial t} + \mathbf{V} \cdot \nabla \mathbf{V} \right) = -\nabla p + \mu \nabla^2 \mathbf{V} + \rho \mathbf{g} \quad (4.8)$$

where  $\mathbf{V}$  is the velocity vector of the fluid at a fixed point in space in three-dimensional form,  $D\mathbf{V}/Dt$  gives the total derivative of  $\mathbf{V}$ , and  $\mathbf{V} \cdot \nabla \mathbf{V}$  term indicates the inertial term.

The  $r$ -component (eq. (A3.5.7)) and  $\theta$ -component (eq. (A3.5.8)) of the Navier–Stokes' equations are first written in terms of  $\psi$  by substituting eqs. (4.6) and (4.7). Then, differentiation operations, i.e., the  $\theta$ -equation with respect to  $r$  and  $r$ -equation with respect to  $\theta$ , are carried out and equating the second derivatives of the pressure gives (Slattery, 1978; Bird *et al.*, 2002)

$$\begin{aligned} \frac{\partial}{\partial t}(E^2 \psi) + \frac{1}{r^2 \sin \theta} \frac{\partial(\psi, E^2 \psi)}{\partial(r, \theta)} \\ - \frac{2E^2 \psi}{r^2 \sin^2 \theta} \left( \frac{\partial \psi}{\partial r} \cos \theta - \frac{1}{r} \frac{\partial \psi}{\partial \theta} \sin \theta \right) = \nu E^4 \psi \end{aligned} \quad (4.9a)$$

where  $\nu$  is the kinematic viscosity and equals  $\nu = \mu/\rho$ , and the Jacobian notation  $\partial(\psi, E^2\psi)/\partial(r, \theta)$  can be expressed as

$$\frac{\partial(\psi, E^2\psi)}{\partial(r, \theta)} = \begin{vmatrix} \frac{\partial\psi}{\partial r} & \frac{\partial\psi}{\partial\theta} \\ \frac{\partial(E^2\psi)}{\partial r} & \frac{\partial(E^2\psi)}{\partial\theta} \end{vmatrix} \quad (4.9b)$$

and also  $E^2$  represents the second derivatives with respect to  $r$  and  $\theta$  in the form of:

$$E^2 \equiv \left[ \frac{\partial^2}{\partial r^2} + \frac{\sin\theta}{r^2} \frac{\partial}{\partial\theta} \left( \frac{1}{\sin\theta} \frac{\partial}{\partial\theta} \right) \right] \quad (4.9c)$$

If the creeping flow conditions are satisfied, the term  $\mathbf{V} \cdot \nabla \mathbf{V}$  can be neglected and for steady state, i.e.,  $\partial/\partial t = 0$ , the LHSs of eqs. (4.8) and (4.9a) become zero. Hence, the Navier–Stokes' equation in terms of stream function for creeping flow becomes

$$E^4\psi = 0 \quad \text{or} \quad E^2(E^2\psi) = 0 \quad (4.10a)$$

$$\left[ \frac{\partial^2}{\partial r^2} + \frac{\sin\theta}{r^2} \frac{\partial}{\partial\theta} \left( \frac{1}{\sin\theta} \frac{\partial}{\partial\theta} \right) \right]^2 \psi = 0 \quad (4.10b)$$

The boundary conditions (BC) are:

$$\text{BC1: at } r = R_p, V_r = -\frac{1}{r^2 \sin\theta} \frac{\partial\psi}{\partial\theta} = 0 \quad (4.11)$$

$$\text{BC2: at } r = R_p, V_\theta = \frac{1}{r \sin\theta} \frac{\partial\psi}{\partial r} = 0 \quad (4.12)$$

$$\text{BC3: as } r \rightarrow \infty, \psi \rightarrow -\frac{1}{2} V_\infty r^2 \sin^2\theta \quad (4.13)$$

BC1 and BC2 describe the nonslip condition at the sphere surface. The third condition arises from the assumption of semi-infinite medium where  $V_z \rightarrow V_\infty$  as  $r \rightarrow \infty$ . The last boundary condition suggests that  $\psi(r, \theta)$  is of the form

$$\psi = f(r) \sin^2\theta \quad (4.14)$$

Although  $\psi(\theta) \propto \sin^2\theta$ ,  $\psi(r)$  is not as straightforward as  $\psi(r) \propto r^2$  due to the velocity constraints on the surface of the sphere. Substituting eq. (4.14) into eq. (4.10b), and

separating the variables leads to a linear, homogenous and fourth order differential equation in terms of function  $f$  in eq. (4.14):

$$\frac{d^4 f}{dr^4} - \frac{4}{r^2} \frac{d^2 f}{dr^2} + \frac{8}{r^3} \frac{df}{dr} - \frac{8}{r^4} f = 0 \quad (4.15)$$

A solution of the form  $f(r) = C_n r^n$  is assumed to exist, where  $C_n$  is a constant. Repeated differentiation of  $f(r)$  and substitution of these derivatives into eq. (4.15) gives solutions for  $n = -1, 1, 2, 4$ . Therefore,  $f(r)$  has a general solution of the form

$$f(r) = \frac{C_1}{r} + C_2 r + C_3 r^2 + C_4 r^4 \quad (4.16)$$

Using BC3, constants  $C_3$  and  $C_4$  are found as

$$C_3 = -\frac{1}{2} V_\infty \quad \text{and} \quad C_4 = 0 \quad (4.17)$$

and also using the boundary conditions BC1 and BC2 at  $r = R_p$ , one can evaluate the constants  $C_1$  and  $C_2$  after some mathematical manipulations as

$$C_1 = -\frac{1}{4} V_\infty R_p^3 \quad \text{and} \quad C_2 = \frac{3}{4} V_\infty R_p \quad (4.18)$$

Hence, the stream function expression takes the form

$$\psi = \left[ -\frac{1}{4} \frac{R_p^3}{r} + \frac{3}{4} R_p r - \frac{1}{2} r^2 \right] V_\infty \sin^2 \theta \quad (4.19)$$

The velocity components within the fluid are obtained after substituting the stream function definition of the above equation into eqs. (4.6) and (4.7) giving, respectively

$$\frac{V_r}{V_\infty} = \left[ 1 - \frac{3}{2} \left( \frac{R_p}{r} \right) + \frac{1}{2} \left( \frac{R_p}{r} \right)^3 \right] \cos \theta \quad (4.20)$$

$$\frac{V_\theta}{V_\infty} = - \left[ 1 - \frac{3}{4} \left( \frac{R_p}{r} \right) - \frac{1}{4} \left( \frac{R_p}{r} \right)^3 \right] \sin \theta \quad (4.21)$$

Equations confirm the zero velocity at the surface of the sphere and also show that for  $r \rightarrow \infty$ , the fluid velocity is in the  $z$ -direction as  $V_z \rightarrow V_\infty$  ( $V_r = V_\infty \cos \theta$  and  $V_\theta = -V_\infty \sin \theta$ ).

### 4.1.3 Pressure and shear stress distribution on the surface of a sphere

The pressure distribution within the fluid under creeping flow conditions is found by substituting the velocity components into the  $r$ - and  $\theta$ -components of the Navier–Stokes' equations (eq. (4.8)) reduced to

$$\nabla p = \mu \nabla^2 \mathbf{V} + \rho \mathbf{g} \quad (4.22)$$

After some mathematical manipulation, the pressure distributions within the fluid in the  $r$ - and  $\theta$ -directions are given as

$$\frac{\partial P}{\partial r} = 3\mu V_\infty \frac{R_p}{r^3} \cos \theta \quad (4.23)$$

$$\frac{\partial P}{\partial \theta} = \frac{3}{2} \mu V_\infty \frac{R_p}{r^2} \sin \theta \quad (4.24)$$

where  $P$  is the modified pressure and equals  $P = p + \rho g z$ .

The pressure distribution is determined after integration of eqs. (4.23) and (4.24) with the condition that as  $r \rightarrow \infty$  the modified pressure equals  $p_0$  (ambient pressure, the pressure in the plane  $z = 0$  far from the sphere)

$$p = p_0 - \rho g z - \frac{3}{2} \mu V_\infty \frac{R_p}{r^2} \cos \theta \quad (4.25)$$

where  $\rho g z$  denotes the hydrostatic pressure resulting from weight of the fluid and the last term represents the contribution of the fluid motion. The pressure distribution on the surface of the solid particles is found by evaluating eq. (4.25) at  $r = R_p$  and  $z = R_p \cos \theta$

$$(p)|_{r=R_p} = p_0 - \rho g R_p \cos \theta - \frac{3}{2} \mu V_\infty \frac{\cos \theta}{R_p} \quad (4.26)$$

The shear stress  $\tau$ , acting tangentially on the sphere, as shown in Figure 4.2(a), is obtained by substituting the velocity components into eq. (A3.4.11) as

$$\tau_{r\theta} = \frac{3}{2} \frac{\mu V_\infty}{R_p} \left( \frac{R_p}{r} \right)^4 \sin \theta \quad (4.27)$$

The normal ( $p$ ) and tangential ( $\tau$ ) forces exerted by the flowing fluid act at every point on the sphere surface. The net force  $F_p$  acting on the sphere will be in the  $z$ -direction because of the axisymmetric flow around the  $z$ -axis. So, the net force is obtained by

integrating the  $z$ -components of the normal and tangential forces over the surface of the sphere ( $r = R_p$ ) as

$$F_p = F_n + F_t = \int_0^{2\pi} \int_0^\pi (-p)|_{r=R_p} \cos \theta R_p^2 \sin \theta d\theta d\phi + \int_0^{2\pi} \int_0^\pi ((\tau_{r\theta})|_{r=R_p} \sin \theta) R_p^2 \sin \theta d\theta d\phi \quad (4.28)$$

where  $((-p)|_{r=R_p} \cos \theta)$  and  $((\tau_{r\theta})|_{r=R_p} \sin \theta)$  denote the  $z$ -components of the normal and tangential forces, respectively. A differential surface element of the system is shown in Figure 4.2(b) that equals  $dA_r = R_p^2 \sin \theta d\theta d\phi$  at the sphere surface. The pressure (eq. (4.26)) and shear stress (eq. (4.27)) distributions are substituted into eq. (4.28) at  $r = R_p$  and the net force of the fluid on the sphere is obtained as

$$F_p = \frac{4}{3} \pi R_p^3 \rho g + 2\pi \mu R_p V_\infty + 4\pi \mu R_p V_\infty \quad (4.29)$$

The first term on the right is the buoyancy force that the fluid exerts on the sphere, the second term corresponds to the *form drag* as a result of the normal forces and the third term gives *friction drag* as a result of the tangential forces. So, the total drag force,  $F_D$ , acting on the particle due to motion of the fluid is

$$F_D = 6\pi \mu V_\infty R_p \quad (4.30)$$

which is known as *Stokes' law*.

## 4.2 FORCES ACTING ON PARTICLES

Force could be briefly described as an influence on a body, which causes it to accelerate. In this way, force is defined through Newton's laws of motion. Newton's laws of motion have two fundamental principles, which form the basis of classical mechanics. *The first law*, also called the law of inertia, states that if a body is at rest or moving at constant speed, it will continue to do so unless it is acted upon by another force. *The second law* states that the force  $F_p$  acting on a body is equal to the mass  $m$  of the body times its acceleration  $a$ , as

$$F_p = ma = \rho_p v_p \frac{dV}{dt} \quad (4.31)$$

where  $\rho_p$  is the density and  $v_p$  the volume of the body.

Force can also be defined in terms of an energy gradient as

$$F_p = -\frac{dU}{dx} \quad (4.32)$$

Of special interest is the gradient in potential energy, which is called potential, in short. Any particle captured within a field is subjected to a force acting on it. Field strength describes a measure of the force that a field exerts on a mass. Examples are gravitational, magnetic, and electrostatic forces acting under gravitational, magnetic, and electric fields, respectively.

It is misleading to classify the forces according to their range as “short” and “long” ranges without denoting the length scale. Surface forces act on the length scale of molecules and colloidal particles; therefore, their effect is observed in such processes as aggregation of particles as presented in Chapter 1. The forces that will be presented in this chapter are effective over much greater distances than the particle or aggregate dimensions.

### 4.2.1 Gravitational force

The gravitational field strength (in vector notation) is defined as the force per unit mass acting on a body

$$\mathbf{g} = \frac{\mathbf{F}}{m} \quad (4.33)$$

The gravitational force,  $F_g$ , of a particle is expressed in terms of volume of the particle as

$$F_g = \rho_p v_p g \quad (4.34)$$

where  $\rho_p$  is the density of the particle,  $v_p$  the volume of the particle ( $v_p = \pi d_p^3/6$  for spherical particles of diameter  $d_p$ ) and  $g$  the acceleration due to gravity ( $9.81 \text{ m s}^{-2}$ ) at the Earth's surface. For small particles with a low terminal velocity, motion under the effect of gravity will be slow. To speed-up the process, the acceleration can be increased by rotation in a centrifugal field at an angular velocity,  $\omega$

$$F_c = m r \omega^2 = \rho_p v_p r \omega^2 \quad (4.35)$$

where  $r$  is the distance between the particle and the axis of rotation. Under a centrifugal field, the particles move radially outwards.

### 4.2.2 Buoyancy force

Buoyancy is caused by the pressure difference on the lower portion of an object being higher than the portion on the top. The result is a force that points in the opposite direction of gravity. It is calculated using Archimedes' Principle, which states that the magnitude of the buoyant force is equal to the weight of the displaced fluid. So, the buoyancy force,  $F_b$ , is proportional to the volume of liquid that it displaces, the gravitational acceleration, and the density of the liquid; and can be written as

$$F_b = \rho v_p g \quad (4.36)$$



Both the gravitational and buoyancy forces depend on the volume of the particle and act on a particle whether it is stagnant or moving in a fluid. Buoyancy under a centrifugal field is expressed with an analogous equation

$$F_{cb} = \rho v_p r \omega^2 \quad (4.37)$$

### 4.2.3 Magnetic force

Magnetic fields can be produced by magnetic materials or by electric currents. Magnetic particles can be classified as ferromagnetic, paramagnetic, and diamagnetic based on magnetic susceptibility of particle's material,  $\chi_m$ . Ferromagnetic materials have a very high susceptibility to magnetic forces. Magnetic force acting on a magnetic particle in the presence of a nonuniform magnetic field is given by

$$\mathbf{F}_M = \chi_m \mu_0 v_p (\mathbf{H} \cdot \nabla) \mathbf{H}_0 = \chi_m \mu_0 v_p \frac{3}{2 + \mu_{mp}} (H_0 \nabla H_0) \quad (4.38)$$

where  $\mu_0$  is the magnetic permeability of vacuum [ $4\pi \times 10^{-7} \text{ TmA}^{-1}$ ],  $\mu_{mp}$  relative magnetic permeability of the material,  $\mathbf{H}$  the magnetic field strength inside the particle, and  $\mathbf{H}_0$  the external magnetic field strength at a given point (Svoboda and Fujita, 2003; Smolkin and Smolkin, 2006). The magnetic force acting on a particle becomes zero in a homogeneous magnetic field.

Freely moving charged particles also experience a magnetic force when passing through a magnetic field. The magnetic force,  $\mathbf{F}_M$ , acting on a single charged particle is written as

$$\mathbf{F}_M = q \mathbf{V} \times \mathbf{B} \quad (4.39)$$

where  $q$  is the charge of the particle,  $\mathbf{V}$  the velocity vector of the particle, and  $\mathbf{B}$  the magnetic induction. The magnetic force is perpendicular to the plane formed by the velocity vector and the magnetic field vector.

### 4.2.4 Electrostatic force

An electric field (in the vicinity of charged surfaces or charged particles) at any point in space causes a charged particle in this space to experience a force, the electrostatic force. The strength of electric field,  $\mathbf{E}$ , is defined as the force  $\mathbf{F}_E$  per unit charge ( $q$ )

$$\mathbf{E} = \frac{\mathbf{F}_E}{q} \quad (4.40)$$

A charged particle in the presence of both an electric field  $\mathbf{E}$  and a magnetic field  $\mathbf{B}$  will feel a force, given by the Lorentz equation

$$\mathbf{F} = q(\mathbf{E} + \mathbf{V} \times \mathbf{B}) \quad (4.41)$$

Electrostatic force acts in the direction of the electric field, but the magnetic force acts perpendicular to the magnetic field. In addition, the electrostatic force acts on a moving or stationary charged particle, whereas the magnetic force acts only on a moving charged particle.

#### 4.2.5 Acoustic force

A colloidal particle with dimensions comparable to the wavelength of sound ( $kR_p \ll 1$ ) will be subjected to a force  $\mathbf{F}_{ac}$

$$\mathbf{F}_{ac} = \frac{2\pi(kR_p)^3(2\bar{E}_{st})}{k^2} \Phi\left(\frac{\rho_p}{\rho}, \frac{c_p}{c}\right) \sin(2k\mathbf{r}_0) \quad (4.42)$$

with

$$\Phi\left(\frac{\rho_p}{\rho}, \frac{c_p}{c}\right) = \frac{1}{3} \left[ \frac{5(\rho_p/\rho) - 2}{2(\rho_p/\rho) + 1} - \frac{1}{(\rho_p/\rho)(c_p/c)^2} \right] \quad (4.43)$$

when a standing wave field is set up in the fluid, in which the particle is suspended (Kapishnikov *et al.*, 2006). In this equation,  $\bar{E}_{st}$  is the time averaged acoustic energy density of the standing waves,  $c_p/c$  the ratio of the velocity of sound in the particle to that in the fluid,  $R_p$  the particle radius,  $k$  the wave-number ( $k = 2\pi/\lambda$ ),  $\lambda$  being the wavelength, and  $\mathbf{r}_0$  the vector normal to the force node. Acoustic forces are proportional to the volume of the particle in the expression and the frequency of the ultrasound waves,  $f$  ( $f = kc/2\pi$ ).

#### 4.2.6 Shear force

Forces presented above have a common characteristic of being dependent on the body (mass or volume) of the particle. As a result, they act on the particles even under static conditions. On the other hand, shear forces are dynamic forces and act on the surface area to deform a particle

$$F_s = \tau_{xy}S \quad (4.44)$$

where  $S$  is the surface area of the particle. An analogous force, the drag force, is again area dependent, and acts on the cross-sectional area,  $A$ , of the particle. Shear forces exist wherever there is a relative motion and adhesive/cohesive forces acting between the molecules (no-slip condition). In the absence of adhesive forces, the fluid and the solid velocities are not equal at the interface and there is no shear force, so the fluid *slips* past the particle. Shear forces exist between fluid layers as well as between a solid boundary and a fluid flowing past it.

#### 4.2.7 Drag force

The resistance of the particle to motion is called the drag force. The magnitude of the drag force exerted on a body moving in a fluid depends on the velocity of the body relative to the medium, the viscosity and density of the medium, the shape and cross-sectional area

of the body, and the roughness of its surface. Drag force always acts opposite to the direction of the particle's velocity, and is expressed as

$$F_D = \frac{C_D A \rho V^2}{2} \quad (4.45)$$

where  $C_D$  is the drag coefficient,  $A$  the projected area of the particle onto the flow direction, and  $V$  the velocity of the particle relative to the medium. The drag coefficient  $C_D$  depends on the velocity of the particle, viscosity of the medium, the shape of the particle, and the roughness of the particle's surface. The particle *Reynolds number*,  $Re_p$ , is found to be a useful dimensionless number that can characterize the drag coefficient's dependence on the velocity. Within this context, the Reynolds number is the ratio of the inertial force of the particle to the viscous force, on the length scale of the particle

$$Re_p = \frac{\rho V_t d_p}{\mu} \quad (4.46)$$

where  $V_t$  is the terminal velocity of the particle which will be given in detail in the next section.

The drag force for a spherical particle is defined as

$$F_D = \frac{C_D \pi d_p^2 \rho V^2}{8} \quad (4.47)$$

There are three regimes for the drag coefficient in flow around a spherical particle:

- *Laminar regime* ( $Re_p < 1$ ): Creeping flow conditions are valid for small values of the Reynolds number, where inertial effects are negligibly small compared to the viscous forces. Stokes derived the total resisting force on a spherical particle for this flow condition as shown in Section 4.1. Eq. (4.30) can be rewritten in terms of particle diameter as

$$F_D = 3\pi\mu d_p V \quad (4.48)$$

One-third of this drag force is a *form drag* coming from normal stresses on the sphere, and the remaining 2/3 is a *friction drag* coming from shear stresses on the sphere. The total drag force acting on the particle is obtained by integrating the normal and the tangential forces over the surface of the particles (Section 4.1.3). The drag coefficient for spherical particles in Stokes' regime can be expressed by combining eqs. (4.47) and (4.48) as,

$$C_D = \frac{24}{Re_p} \quad (4.49)$$

- *Intermediate regime* ( $1 < Re_p < 1000$ ): When the inertial effects cannot be neglected, the drag coefficient cannot be predicted theoretically, and so an approach has to be developed to correlate data for  $C_D$  and  $V$ .
- *Turbulent regime* ( $Re_p > 1000$ ): When the flow is turbulent, the drag coefficient  $C_D$  is approximately constant, independent of velocity or  $Re$ . Drag coefficient of a spherical particle in turbulent flow (known as Newton's regime) becomes

$$C_D \cong 0.44 \quad (4.50)$$

At  $Re_p \sim 2 \times 10^5$  the drag coefficient decreases abruptly due to boundary layer separation in the form of vortices carried by the fluid downstream, reducing the friction on the particle.

### 4.3 MOTION OF SPHERICAL PARTICLES

Uniform particle motion through a fluid confined within a chamber is the result of the action of two groups of forces: a constant external force ( $F_{ext}$ ) such as gravity, buoyancy, electrostatic, or magnetic forces and the resistance of the fluid to particle motion. The type of fluid involved, flow regime, the size and shape of the particles, and the dimensions of the chamber are also important factors affecting the motion. In a gravitational field, motion of spherical particles is governed by Newton's law of motion, where all the affecting forces sum up to the net force,  $F_p$ , as:

$$F_p = F_g - F_b - F_D \quad (4.51)$$

with the direction of gravity taken as the positive direction and where  $F_g > F_b$ . When the particles are charged, electrostatic (eq. (1.3)) or double layer repulsion (eq. (3.76)) should also be included into the force balance. The force balance equation can be written in terms of particle characteristics as

$$\rho_p v_p \frac{dV}{dt} = \rho_p v_p g - \rho v_p g - \frac{1}{2} C_D A \rho V^2 \quad (4.52)$$

The velocity of spherical particles as a function of time under the action of gravitational, buoyancy and drag forces in Stokes' regime ( $Re_p < 1$ ) is:

$$\left( \rho_p \frac{\pi d_p^3}{6} \right) \frac{dV}{dt} + 3\pi\mu d_p V = (\rho_p - \rho) \frac{\pi d_p^3}{6} g \quad (4.53)$$

The solution of this differential equation is

$$V(t) = \frac{(\rho_p - \rho)gd_p^2}{18\mu} \left[ 1 - \exp\left(-\frac{18\mu}{\rho_p d_p^2} t\right) \right] \quad (4.54)$$

This is a decaying function of time approaching the term outside of the parenthesis at a rate dependent on the particle characteristics and viscosity of the medium.

The solution to the differential equation, eq. (4.52), under the same forces in the Newton's regime (taking  $C_D$  as constant) gives a more complex function of time for the decay rate

$$V(t) = \sqrt{\frac{2(\rho_p - \rho)v_p g}{\rho A C_D}} \tanh\left(\sqrt{\frac{(\rho_p - \rho)g\rho A C_D}{2\rho_p^2 v_p}} t\right) \quad (4.55)$$

Eqs. (4.54) and (4.55) imply that there are two stages during the motion of the particle: the acceleration and then constant velocity, known as the *terminal velocity* or *free settling velocity*,  $V_t$ , stages. The terminal velocity of a particle is the constant speed it reaches when all the forces exerted on it are in equilibrium:

$$F_g - F_b - F_D = 0 \quad (4.56)$$

Substitution of eqs. (4.34), (4.36), and (4.45) into the above equation gives

$$(\rho_p - \rho)v_p g - \frac{1}{2}C_D A \rho V_t^2 = 0 \quad (4.57)$$

Eqs. (4.54) and (4.55) then reduce to eq. (4.58) for Stokes' regime ( $V_{ts}$ ) and eq. (4.59) for Newton's regime ( $V_{tN}$ ), respectively, for spherical particles

$$V_{ts} = \frac{(\rho_p - \rho)gd_p^2}{18\mu} \quad (4.58)$$

$$V_{tN} = 1.75 \sqrt{\frac{gd_p(\rho_p - \rho)}{\rho}} \quad (4.59)$$

The terminal velocity of particles in the intermediate regime can be written in the general form of

$$V_t = \left[ \frac{2(\rho_p - \rho)v_p g}{\rho A C_D} \right]^{1/2} \quad (4.60)$$

which reduces to the following equation for spherical particles:

$$V_t = \left[ \frac{4}{3} \frac{(\rho_p - \rho)gd_p}{\rho C_D} \right]^{1/2} \quad (4.61)$$

In the case of charged particles settling in an electrolyte solution, fluid flowing around the particle distorts the electrical double layer and gives rise to an induced electrical field. Keh and Liu (1997) and Liu and Keh (1998) found that the presence of fixed charge reduces the settling velocity of the charged particle in comparison with uncharged particles given by eq. (4.61).

### 4.3.1 Correlations for drag coefficient

The drag coefficient,  $C_D$ , is not a constant and decreases linearly with increasing Reynolds number. Hence, it is dependent on the flow regime of the fluid.  $C_D$  in the laminar ( $Re_p < 1$ ) and turbulent regimes ( $Re_p > 1000$ ) can be calculated by Stokes' (eq. (4.49)) and Newton's equations (eq. (4.50)), respectively. Except in the Newton's regime, the terminal velocity appears in the equations of both the drag coefficient and the particle Reynolds number. No closed form solutions are possible for the intermediate region of  $1 < Re_p < 1000$ . Numerous sphere drag correlations have been proposed in the literature relating  $C_D$  to the particle

Reynolds number and some of these are listed in Table 4.1. Brown and Lawler (2003) analyzed all the correlations in the list using 480 experimental data points, which were corrected for wall effects. They suggested a model, which is the modification of Haider and Levenspiel (1989), that fits to  $\sim 82\%$  of the data lying within  $\pm 5\%$  of the correlation. The correlation of Clift *et al.* (1978) appears to model the drag on spheres the best. As more than one correlation is used to describe the drag coefficients in the different ranges of Reynolds numbers, it includes slight discontinuities at the transitions from one Reynolds number range to another.

### 4.3.2 Correlations for terminal velocity

Determination of the terminal velocity,  $V_t$ , from any of the proposed equations for  $C_D$  versus  $Re_p$  requires a trial and error procedure, since  $V_t$  is present in both variables, and also the relation between the drag coefficient and the Reynolds number is highly nonlinear. This difficulty, however, can be circumvented by introducing a new dimensionless group as *dimensionless terminal velocity*,  $V^*$ , as a function of a *dimensionless sphere diameter*,  $d^*$  (Brown and Lawler, 2003).

The terminal velocity of rigid spheres can be directly predicted using these dimensionless numbers:

$$V^* = V_t \left[ \frac{\rho^2}{g\mu(\rho_p - \rho)} \right]^{1/3} = \left( \frac{4}{3} \frac{Re_p}{C_D} \right)^{1/3} \quad (4.68)$$

$$d^* = d_p \left[ \frac{g\rho(\rho_p - \rho)}{\mu^2} \right]^{1/3} = \left( \frac{3}{4} C_D Re_p^2 \right)^{1/3} \quad (4.69)$$

The third power of  $d^*$  is called the *Archimedes number*,  $Ar$ .

$$Ar = d_p^3 \left[ \frac{g\rho(\rho_p - \rho)}{\mu^2} \right] \quad (4.70)$$

The terminal velocity can be written in terms of dimensionless terms in Stokes' regime as

$$V^* = \frac{(d^*)^2}{18} \quad (4.71)$$

and

$$V^* = 1.75\sqrt{d^*} \quad (4.72)$$

in Newton's regime. Terminal velocity correlations in terms of dimensionless functions developed by various authors are given in Table 4.2. For moderate Reynolds numbers ( $Re_p \leq 5000$ ), terminal velocity can be calculated by introducing a new factor to eq. (4.71), that gives the deviation of the terminal velocity from that of Stokes' velocity. Eqs. (4.76) and (4.77) are obtained in this manner.

**Table 4.1**

Drag coefficient correlations for spherical particles

References	$Re_p$ range	Correlation	
Clift <i>et al.</i> (1978)	$0.01 \leq Re_p \leq 20$	$C_D = \frac{24}{Re_p} [1 + 0.1315 Re_p^{0.82-0.05w}]$	(4.62a)
	$260 \leq Re_p \leq 1500$	$\log C_D = 1.6435 - 1.1242w + 0.1558w^2$	(4.62b)
	$1500 \leq Re_p \leq 1.2 \times 10^4$	$\log C_D = -2.4571 + 2.5558w - 0.9295w^2 + 0.1049w^3$	(4.62c)
	$4.4 \times 10^4 \leq Re_p \leq 3.38 \times 10^5$	$\log C_D = -4.3390 + 1.5809w - 0.1546w^2$ , where $w = \log Re_p$	(4.62d)
Flemmer and Banks (1986)	$Re_p < 8.6 \times 10^4$	$C_D = \frac{24}{Re_p} 10^E$ , where	(4.63)
		$E = 0.261 Re_p^{0.369} - 0.105 Re_p^{0.431} - \frac{0.124}{1 + (\log Re_p)^2}$	
Turton and Levenspiel (1986)	$Re_p < 2.6 \times 10^5$	$C_D = \frac{24}{Re_p} (1 + 0.173 Re_p^{0.657}) + \frac{0.413}{1 + 16,300 Re_p^{-1.09}}$	(4.64)
Khan and Richardson (1987)	$0.01 < Re_p < 3 \times 10^5$	$C_D = (2.25 Re_p^{-0.31} + 0.36 Re_p^{0.06})^{3.45}$	(4.65)
Haider and Levenspiel (1989)	$Re_p < 2.6 \times 10^5$	$C_D = \frac{24}{Re_p} (1 + 0.1806 Re_p^{0.6459}) + \frac{0.4251}{1 + (6880.95 / Re_p)}$	(4.66)
Brown and Lawler (2003)	$Re_p < 2 \times 10^5$	$C_D = \frac{24}{Re_p} (1 + 0.15 Re_p^{0.681}) + \frac{0.407}{1 + (8710 / Re_p)}$	(4.67)

**Table 4.2**

Terminal velocity correlations in dimensionless form

References	Correlation	
Zigrang and Sylvester (1981)	$V^* = \frac{[(14.51 + 1.83(d^*)^{3/2})^{1/2} - 3.81]^2}{d^*}$	(4.73)
Khan and Richardson (1987)	$V^* = \frac{(2.33(d^*)^{0.054} - 1.53(d^*)^{-0.048})^{13.3}}{d^*}$	(4.74)
Turton and Clark (1987)	$V^* = \left[ \left( \frac{18}{(d^*)^2} \right)^{0.824} + \left( \frac{0.321}{d^*} \right)^{0.412} \right]^{-1.214}$	(4.75)
Nguyen <i>et al.</i> (1997)	$V^* = \frac{(d^*)^2/18}{1 + ((d^*)^3/96)(1 + 0.079(d^*)^{2.247})^{-0.755}}$	(4.76)
Brown and Lawler (2003)	$V^* = \frac{(d^*)^2(22.5 + (d^*)^{2.046})}{0.0258(d^*)^{4.046} + 2.81(d^*)^{3.046} + 18(d^*)^{2.046} + 405}$	(4.77)

#### 4.3.2.1 Wall effect on terminal velocity

Wall effect refers to the retardation of the motion of a particle due to the opposing motion of the displaced fluid. When the diameter of the particle approaches the length scale of the container, the retardation effect of the walls is quantified by introducing a quantity called *wall factor*,  $f$ . The wall factor is defined as the ratio of the terminal velocity of a sphere in a bounded fluid medium ( $V_{tw}$ ) to that in an unbounded fluid ( $V_t$ ), i.e.,  $f = V_{tw}/V_t$ . Wall factor is a function of Reynolds number and the spherical particle-to-tube diameter ratio,  $\lambda = d_p/D$ .

In the laminar flow region, the empirical equations obtained by Francis (1933)

$$\frac{V_{tw}}{V_t} = \left[ \frac{1 - \lambda}{1 - 0.475\lambda} \right]^4 \quad (4.78)$$

and theoretical expression due to Haberman and Sayre (1958)

$$\frac{V_{tw}}{V_t} = \frac{1 - 2.105\lambda + 2.0865\lambda^3 - 1.7068\lambda^5 + 0.7260\lambda^6}{1 - 0.7586\lambda^5} \quad (4.79)$$

were found to be satisfactory for  $\lambda < 0.9$  and  $Re_p \leq 0.2$ .

In the turbulent region, wall factor again becomes independent of  $Re_p$ . Munroe's (1888) equation is the most satisfactory for  $1000 < Re_p < 3000$  and  $\lambda \leq 0.8$

$$\frac{V_{tw}}{V_t} = 1 - \lambda^{1.5} \quad (4.80)$$



Newton's correlation, eq. (4.81), also gives the best prediction in Newton's regime especially at around  $Re_p \sim 10^4$

$$\frac{V_{tw}}{V_t} = (1 - \lambda^2)(1 - 0.5\lambda^2)^{0.5} \quad (4.81)$$

Wall factor values depend only on the diameter ratio in both laminar and turbulent regimes while they are a function of both the diameter ratio and Reynolds number in the intermediate regime. For the intermediate flow regime, Fidleris and Whitmore (1961) reported the effect of the column diameter on a single particle settling velocity in the range of Reynolds numbers,  $0.05 < Re_p < 20,000$  and diameter ratios  $0 < \lambda < 0.6$ . They presented wall effect correction factors given in Figure 4.3, based on 3000 experimental velocity measurements, plotted as  $(V_{tw}/V_t)$  versus the Reynolds number,  $Re_p$  ( $Re_p$  is calculated at  $V_t$ ), for various diameter ratios. They found that the retarding effect of the wall on a falling sphere is reduced on transition from laminar to turbulent flow and decreases with increasing  $Re_p$  to an approximately constant value. They showed that the wall effect is greatest at low  $Re_p$  and high  $\lambda$  values. For small  $\lambda$  values ( $< 0.1$ ), wall effect becomes negligible for  $Re_p > 30$ . Di Felice (1996) gives another relation for the wall effect over the whole range of flow conditions, in conformation with the results of Fidleris and Whitmore (1961) as

$$\frac{V_{tw}}{V_t} = \left( \frac{1 - \lambda}{1 - 0.33\lambda} \right)^{\alpha} \quad (4.82)$$

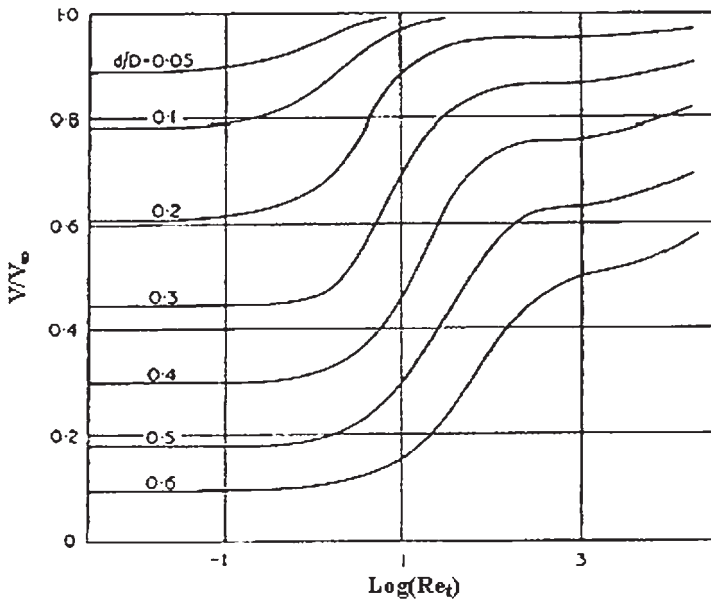


**Figure 4.3** Wall effect correction factors for different particle-to-tube diameter ratio ( $d/D$ ) falling in a cylindrical vessel.  $V/V_\infty = V_{tw}/V_t$  and  $Re_t = Re_p$  (Fidleris and Whitmore, 1961. Figure 4 in the original, reproduced with the permission of *British Journal of Applied Physics*).

where  $\alpha$  is a function of  $Re_p$  and can be given as

$$\frac{3.3 - \alpha}{\alpha - 0.85} = 0.1Re_p \quad (4.82a)$$

## 4.4 MOTION OF NONUNIFORM PARTICLES

The relations for drag force and terminal velocity in Section 4.3 are valid for spherical geometries even though very few processes involve perfectly spherical particles. The correlations for spheres serve as a basis to develop expressions/correlations for nonspherical particles. In this section, motion of nonspherical particles and porous particles including fractal aggregates and clusters, motion of particles with nonhomogenous density distribution will be presented. Since the settling velocity of a particle depends strongly on its drag coefficient, correlations for the drag coefficient of these irregular particles are required for the understanding of the processes and the design of equipments. Also, motion of particles with nonhomogenous density distribution, will be presented at the end of this section, for the case of microorganisms in motion.

### 4.4.1 Motion of nonspherical particles

The terminal velocity and the drag coefficient of a particle are dependent on many parameters: particle size, shape and orientation, the viscosity of the medium, densities of the particle and the fluid medium. Although the development of a single correlation for all shapes and orientation of nonspherical particles is very difficult, the correlations can be improved using various shape factors and parameters.

#### 4.4.1.1 Shape factors and parameters

The basic equations for drag coefficient  $C_D$  (eq. (4.45)) and terminal velocities  $V_t$  (eq. (4.60)) have terms related with particle cross-sectional area and volume. For an irregularly shaped particle, it is difficult to assess these quantities, such as in a natural sponge settling in the sea. Various expressions are developed to define an equivalent diameter on which the effective cross-sectional area and volume calculations will be based. Some of these expressions are presented below:

- *Equivalent-volume sphere diameter,  $d_v$* , is the diameter of a sphere having the same volume as the particle. It can be defined as  $d_v = \sqrt[3]{6v_p/\pi}$ , where  $v_p$  is the particle volume and is widely used as the characteristic size to calculate Reynolds number,  $Re_{np}$ , of nonspherical particles

$$Re_{np} = \frac{\rho V_t d_v}{\mu} \quad (4.83)$$

- *Equivalent projected area diameter,  $d_A$* , is the diameter of a sphere having the same projected area as the particle. It can be written as  $d_A = \sqrt{4A/\pi}$ .

- *Equivalent surface area diameter*,  $d_s$ , is defined as the diameter of a sphere having the same surface area as the particle and is expressed as  $d_s = \sqrt{S_{ns}/\pi}$ , where  $S_{ns}$  is the surface area of nonspherical particles.
- *Sphericity*,  $\Psi$ , is a dimensionless number for characterizing the shape of isometric or close-to-isometric nonspherical particles. It is defined as the ratio of the surface area of the equivalent-volume sphere,  $A_s$ , to the actual surface area of the particle having the same volume:

$$\Psi = \left( \frac{A_s}{S_{ns}} \right)_{\text{equal volume}} = \frac{\pi d_v^2}{S_{ns}} = \frac{d_v^2}{d_s^2} \quad (4.84)$$

Thus,  $\Psi = 1$  for perfect spheres and 0.846 for octahedrons, 0.806 for cubes, 0.67 for tetrahedrons, and  $<0.67$  for disks are examples of commonly encountered sphericity values for nonspherical particles (Hartman *et al.*, 1994). However,  $\Psi$  is difficult to determine for strongly irregular particles because it requires a measure of the surface area, which is not easy to accomplish in every case.

- *Circularity*,  $C$ , is another shape factor, which is easier to determine for irregular particles and can be written as follows:

$$C = \frac{\pi d_A}{P_p} \quad (4.85)$$

where  $P_p$  is the projected perimeter of the particle in the direction of motion. A disadvantage of the difficulties of using the circularity,  $C$ , is that rarely it yields the same value for three-dimensional and two-dimensional objects. For example, cubes and squares that fall on their flat sides have the same circularity.

- *Corey shape factor*,  $Co$ , is another approach for characterizing the shape of three-dimensional irregular particles and defined as the ratio of the shortest particle axis ( $c$ ) to the square root of the product of the other two axes ( $a$  and  $b$ ). The Corey shape factor seems to be appropriate to characterize the flatness of particles that exhibit a compact shape. One of the disadvantages of using this shape factor is that  $Co = 1$  for spheres as well as for noncompact particles having three perpendicular axes of the same length, such as star-shaped particles

$$Co = \frac{c}{\sqrt{ab}}, \quad \text{where } a > b > c \quad (4.86)$$

- *Aspect ratio* ( $L/D$ ) is defined as the ratio of particle length along the symmetry axis to the largest diameter of the cross-section. It is used to account for the particle elongation and conveniently describes axisymmetric shapes.
- *Skin factor*,  $\aleph$ , is another approach, which takes into account the surface roughness, defined as  $\aleph = d_s/d_v$ .

#### 4.4.1.2 Drag coefficients of nonspherical particles

Experimental results show that the departure of a particle from the spherical shape causes a decrease in its terminal velocity in a fluid. This implies a higher  $C_D$  for the nonspherical particles. Numerous forms of expressions for relating the particle shape factor to the drag

coefficient are available in the literature. Only the widely used correlations are included in Table 4.3. Chhabra *et al.* (1999) reported a comparison of available expressions for the drag of nonspherical particles by using 1900 data points covering a range of Reynolds numbers ( $10^{-4} < Re_{np} < 10^5$ ), geometrical shapes of particles, and sphericity values of  $0.09 < \Psi < 1$ . Based on the discussion by Chhabra *et al.* (1999), expressions derived by Haider and Levenspiel (1989) and Ganser (1993) give more accurate results with an average error of 16.3%. Tran-Cong *et al.* (2004) reported drag coefficient measurements of six different geometrical shapes, including isometric, axisymmetric, orthotropic, plane, and elongated conglomerates of spheres.

Table 4.3 shows that calculations of drag coefficient involve the use of Reynolds number, which is a function of terminal velocity. Therefore, the estimation of the terminal velocity corresponds to a given shape factor and physical properties of a system, and requires an iterative solution of one of the  $C_D$  equations in Table 4.3 and eq. (4.60), simultaneously.

Eq. (4.96) can further be simplified and written in terms of  $C_D$  by defining  $v_p$  and  $A$  in terms of the generally used equivalent-volume sphere diameter  $d_v$ ,

$$C_D = \frac{4}{3} d_v \frac{(\rho_p - \rho)g}{\rho V_t^2} \quad (4.96)$$

Instead of the equivalent-volume sphere diameter  $d_v$ , the equivalent volume can be divided by the actual projected area (Tran-Cong *et al.*, 2004):

$$C_{DA} = \frac{4}{3} \frac{d_v^3}{d_A^2} \frac{(\rho_p - \rho)g}{\rho V_t^2} \quad (4.97)$$

#### 4.4.1.3 Motion of cylindrical particles

Cylindrical particles ranging from short rods to fibers and wires have a wide range of applicability. The determining shape factor in cylindrical particles is the aspect ratio,  $L/D$ . Instead of using the concept of sphericity, the drag coefficient of cylindrical particles can be correlated with the orientation and the Reynolds number, based on the diameter of the cylinder,  $D$ . The Reynolds number increases with an increase in the aspect ratio, in the settling of cylindrical particles, and terminal velocity of particles approach a constant value when their aspect ratio is high enough.

It is found that (Fan *et al.*, 2004; Jianzhong *et al.*, 2003; Yin *et al.*, 2003) cylinders tend to exhibit preferential orientation during settling and the torque induced, causes the particle to rotate until it assumes a stable position with its axis of symmetry aligned horizontally, no matter what the aspect ratio is. High and low-pressure regions located at the ends of a cylindrical particle at any tilt angle away from the vertical causes the center of pressure to shift from the location of the center of mass of the body, and a torque is generated.

Two types of torque act on particle in rotational motion. A torque ( $\mathbf{T}_1$ ) arises when the center of pressure does not coincide with the center of mass (Yin *et al.*, 2003) of the particle:

$$\mathbf{T}_1 = \mathbf{x}_{cp} \times \mathbf{F}_p$$

**Table 4.3**

Drag coefficient correlations for nonspherical particles

References	$Re_{np}$ range	Correlation	
Haider and Levenspiel (1989)	$Re_{np} < 25,000$ $0.026 < \Psi < 1.0$	$C_D = \frac{24}{Re_{np}} [1 + \exp(2.3288 - 6.4581\Psi + 2.4486\Psi^2) Re_{np}^{0.0964+0.5565\Psi}]$ $+ \frac{Re_{np} \exp(4.905 - 13.8944\Psi + 18.4222\Psi^2 - 10.2599\Psi^3)}{Re_{np} + \exp(1.4681 + 12.2584\Psi - 20.7322\Psi^2 + 15.8855\Psi^3)}$	(4.87)
Ro and Neethling (1990)	$15 < Re_{np} < 87$ $S_F = \frac{d_A}{d_v} < 1$	$C_D = \frac{24\aleph}{Re_{np}} + 21.55 S_F^2 Re_{np}^{-0.518}$	(4.88)
Thompson and Clark (1991)	$Re_{np} < 10^4$ $\Im = \frac{C_D}{C_{Ds}}$	$C_D = \frac{24}{Re_{np}} [1 + (0.178 \times 10^{0.056\Im}) Re_{np}^{0.677\Im - 0.208}]$ $+ \frac{Re_{np} (0.101 + 0.366\Im)}{Re_{np} + 5732.1\Im^{-1.96}}$	(4.89)
Swamee and Ojha (1991)	$1 < Re_{np} < 10^4$ $0.3 < Co < 1.0$	$C_D = \frac{48.5}{(1 + 4.5Co^{0.35})^{0.8} Re_{np}^{0.64}}$ $+ \frac{1}{Co^{18} + 1.05Co^{0.8}} \left( \frac{Re_{np}}{Re_{np} + 100 + 100Co} \right)^{0.32}$	(4.90)
Ganser (1993)	$Re_{np} K_1 K_2 < 10^5$	$\frac{C_D}{K_2} = \frac{24}{Re_{np} K_1 K_2} [1 + 0.1118 (Re_{np} K_1 K_2)^{0.6567}] + \frac{0.4305}{1 + (3305 / Re_{np} K_1 K_2)}$	(4.91)

$$0.026 < \Psi < 1.0 \quad K_1 = \left[ \left( \frac{1}{3} \right) + \left( \frac{2}{3} \right) \Psi^{-0.5} \right]^{-1}, \quad \text{for isometric particles} \quad (4.91a)$$

$$K_2 = 10^{1.8148(-\log \Psi)^{0.5743}}$$

$$\begin{array}{ll} \text{Chien (1994)} & Re_{np} \leq 5000 \\ & 0.2 \leq \Psi \leq 1.0 \end{array} \quad C_D = \left( \frac{30}{Re_{np}} \right) + 67.289 \exp(-5.03\Psi) \quad (4.92)$$

$$\begin{array}{ll} \text{Hartman} & 10^{-2} < Re_{np} < 16,000 \\ \text{et al. (1994)} & \end{array} \quad \log C_D(Re_{np}, \Psi) = \log C_D(Re_p, 1) + P(Re_{np}, \Psi) \quad (4.93)$$

$$\begin{array}{ll} & 0.67 < \Psi < 1.0 \end{array} \quad \begin{aligned} P(Re_{np}, \Psi) = & -0.03874(1 - \Psi) \log Re_{np} + 0.09238(1 - \Psi)(\log Re_{np})^2 \\ & + 0.06003(1 - \Psi)(\log Re_{np})^3 + 0.01005(1 - \Psi)(\log Re_{np})^4 \\ & - 0.003571(1 - \Psi)(\log Re_{np})^5 - 0.005697(1 - \Psi)^2(\log Re_{np})^5 \end{aligned} \quad (4.93a)$$

see eq. (4.64) for  $\log C_D(Re_p, 1)$

$$\begin{array}{ll} \text{Xie and} & Re_{np} < 1 \\ \text{Zhang (2001)} & 0.2 < \Psi < 1.0 \end{array} \quad C_D = \frac{24}{Re_{np}} \Psi^{0.83} \quad (4.94)$$

$$\begin{array}{ll} \text{Tran-Cong} & 0.15 < Re_{np} < 1500 \\ \text{et al. (2004)} & \end{array} \quad C_D = \frac{24}{Re_{np}} \frac{d_A}{d_v} \left[ 1 + \frac{0.15}{\sqrt{C}} \left( \frac{d_A}{d_v} Re_{np} \right)^{0.687} \right] + \frac{0.42(d_A/d_v)^2}{\sqrt{C}(1 + 4.25 \times 10^4 (Re_{np} d_A/d_v)^{-1.16})} \quad (4.95)$$

$$0.8 < \frac{d_A}{d_v} < 1.5$$

$$0.4 < C < 1.0$$

---

<sup>a</sup> $C_D$  and  $C_{Ds}$  are drag coefficients of the particle and sphere having equal volumes at  $Re = 10^4$ .

Here,  $\mathbf{F}_p$  is the total pressure force acting on the particle and  $\mathbf{x}_{cp}$  the distance between the points of action of net pressure and body forces (gravity, buoyancy) that act at the center of mass of the particle. Another type of torque ( $\mathbf{T}_2$ ) is caused by the viscous resistance shown by the liquid suspending medium to rotation when the particle has an angular velocity,  $\omega$  (Rosendahl, 2000):

$$\mathbf{T}_2 = K_w \mu v_p \left( \frac{1}{2} \nabla \times \mathbf{u}_f - \boldsymbol{\omega} \right)$$

where  $K_w$  is a constant, of the order of unity, and  $\mathbf{u}_f$  the fluid undisturbed velocity at the center of mass of the particle.

Through the joint action of two torques, the cylindrical particle rotates, oscillates, and stabilizes in a horizontal position. Under the action of random disturbances, the particle oscillates vertically in either direction while falling in a horizontal position.

#### 4.4.2 Motion of porous aggregates

##### 4.4.2.1 Fractal aggregates and their permeability models

Theory of fractals, structure of aggregates, and parameters affecting fractal dimension,  $d_f$ , were given in Chapter 1 and Appendix B. Three-dimensional fractal dimension,  $d_f$ , is used to quantify the porosity of an object. The fractal dimension of an aggregate is related to packing of the particles forming the aggregate and will reflect the aggregate packing factor. In summary, the significant properties of such clusters are their irregular shape and porous structures, self-similarity, and scale-independence. A fractal aggregate cluster mass,  $M$ , varies with the radius of the aggregate,  $R_{agg}$ , as

$$M \propto R_{agg}^{d_f} \quad (4.98)$$

The fractal dimension of an aggregate is  $d_f \leq 3$ , with the value of 3 corresponding to a solid spherical structure. Thus, the effective density of the cluster,  $\rho_{eff}$ , varies with the radius as:

$$\rho_{eff} \propto R_{agg}^{d_f-3} \quad (4.99)$$

The settling behavior of aggregates is dependent on the drag force and the permeability of the aggregates, due to their porous structure. The porosity of the fractal aggregates,  $\varepsilon$ , is defined as the fraction of void space of interconnected pores with respect to the bulk volume. It is expressed in terms of the number of primary particles in the aggregate,  $N$ , volume of a primary particle,  $v_0$ , and the volume of the aggregates,  $v_{agg}$ , as:

$$1 - \varepsilon = \frac{N v_0}{v_{agg}} \quad (4.100)$$

Porosity can also be related to the effective density as

$$\rho_{eff} = \rho_{agg} - \rho = (1 - \varepsilon)(\rho_p - \rho) \quad (4.101)$$

where  $\rho_{\text{agg}}$ ,  $\rho_p$ , and  $\rho$  are density of aggregates, primary particles, and suspending liquid, respectively. Calculation of porosity based on eqs. (4.100) and (4.101) assumes aggregates have homogenous pore distribution. However, fractal aggregates in reality have nonhomogenous distribution of primary particles due to the aggregation mechanism (Appendix B). So, the size of the pores of the aggregates tends to increase with an increase in aggregate size and the pores are larger around the peripheries of the aggregates. Hence, equations based on the homogenous distribution assumption will not correctly describe the settling behavior of fractal aggregates. Veerapaneni and Wiesner (1996) express the non-homogenous distribution of particles by assuming that the porosity of fractal aggregates varies radially from the center of gyration, and increases with the distance away from the center of the aggregate. They define the porosity in terms of the diameter of primary particles,  $d_p$ , diameter of the aggregates,  $d_{\text{agg}}$ , and fractal dimension,  $d_f$ , as

$$\varepsilon = 1 - \left( \frac{d_{\text{agg}}}{d_p} \right)^{d_f - 3} \quad (4.102)$$

Although the porosity of aggregates does not necessarily vary in the radial direction, the above equation might give better results in porosity determination because it does not assume homogenous distribution of particles within the aggregate.

The permeability through the aggregates can be described as a function of porosity. Various models have been developed for expressing the permeability of an aggregate,  $\kappa$ , where the most commonly used correlations are listed in Table 4.4 (Li and Logan, 2001). These models consider aggregates of spherical primary particles under creeping flow conditions.

Permeability models indicate that increasing the aggregate diameter or decreasing the fractal dimension would also increase the permeability. The disadvantage of the Carman–Kozeny model is that it is only valid when the porosity is less than 0.5. So, it cannot be used to predict permeability for highly porous aggregates. Brinkman and Happel models are the most appropriate models based on simulation and experimental results in the literature (Lee *et al.*, 1996; Veerapaneni and Wiesner, 1996; Li and Logan, 2001). A combination of Stokes' law with permeability models, such as Brinkman or Happel, may be used to describe the settling behavior of permeable aggregates.

**Table 4.4**

Aggregate permeability functions

Correlation	Permeability, $\kappa$
Carman–Kozeny	$\kappa = \frac{d_p^2}{180} \left[ \frac{\varepsilon^3}{(1 - \varepsilon)^2} \right] \quad (4.103)$
Brinkman	$\kappa = \frac{d_p^2}{72} \left[ 3 + \frac{4}{1 - \varepsilon} - 3 \sqrt{\frac{8}{1 - \varepsilon}} - 3 \right] \quad (4.104)$
Happel	$\kappa = \frac{d_p^2}{18} \left[ \frac{3 - 4.5(1 - \varepsilon)^{1/3} + 4.5(1 - \varepsilon)^{5/3} - 3(1 - \varepsilon)^2}{(1 - \varepsilon)(3 + 2(1 - \varepsilon)^{5/3})} \right] \quad (4.105)$



#### 4.4.2.2 Terminal velocity of fractal aggregates

The resistance experienced by a permeable sphere with a high porosity is much lower than that of an impermeable sphere due to the internal flow through the aggregates. As a result, flow through the interior of an aggregate can increase the settling velocity of an aggregate compared with an identical impermeable particle. Terminal velocity of fractal aggregates depends both on the flow regime of the suspending medium along the particle boundaries and the porous structure of the aggregates. In this section, the terminal velocity considerations are presented in two groups based on the flow regime of the suspending liquid: (a) under creeping flow conditions and (b) above creeping flow conditions.

##### 4.4.2.2.1 Motion of fractal aggregates under creeping flow conditions

*Impermeable spherical aggregates* The terminal settling velocity of a spherical impermeable aggregate under gravity can be calculated from a force balance (eq. (4.56)) as

$$\frac{1}{2} \rho V_t^2 A C_D = v_{\text{agg}} (\rho_{\text{agg}} - \rho) g \quad (4.106)$$

Terminal velocity of impermeable aggregates is obtained when the geometrical relations of  $v_{\text{agg}} = \pi d_{\text{agg}}^3 / 6$  and  $A = \pi d_{\text{agg}}^2 / 4$  for spheres are used:

$$V_t = \left[ \frac{4}{3} \frac{g(\rho_{\text{agg}} - \rho) d_{\text{agg}}}{\rho C_D} \right]^{1/2} \quad (4.107)$$

Drag coefficient,  $C_D$ , is a function of the Reynolds number

$$Re_{\text{agg}} = \frac{\rho V_t d_{\text{agg}}}{\mu} \quad (4.108)$$

where  $V_t$  is the actual settling velocity. Under creeping flow conditions ( $Re < 1$ ), the substitution of eqs. (4.49) and (4.101) for the density differences into eq. (4.107) gives

$$V_{\text{ts,agg}} = \left[ \frac{g(1 - \varepsilon)(\rho_p - \rho) d_{\text{agg}}^2}{18\mu} \right] \quad (4.109)$$

which is equivalent to the conventional form of the Stokes' law. For an aggregate made up of  $N$  particles, each of volume  $v_0$ , the porosity term in the above equation can be written as in eq. (4.100) yielding

$$V_{\text{ts,agg}} = \left[ \frac{g(\rho_p - \rho) N v_0}{3\pi \mu d_{\text{agg}}} \right] \quad (4.110)$$

Stokes' law is the fundamental equation describing the settling behavior of an aggregate (Johnson *et al.*, 1996; Li and Yuan, 2002). However, this equation is only applicable when

the particle is spherical and relatively impermeable. As the nonsphericity and porous structure alter the settling behavior of real aggregates, Stokes' law should be improved to take into account these deviations. The developments that can be made are: (1) assuming homogenous distribution of particles in the aggregate; and (2) describing the porosity in terms of fractal size and dimension.

*Homogenous permeable spherical aggregates* When a permeable sphere settles, part of the displaced liquid will move up from the open pores of the particle or the aggregate. The drag will then be exerted on the fraction of the total cross-sectional area occupied by the solid. The total drag force exerted on a porous particle will then be lower compared with an impermeable sphere of the same diameter. The reduction of the drag force is taken into account by the use of a correction factor,  $\Omega$ , defined as the ratio of resistance experienced by a permeable sphere of diameter  $d_{\text{agg}}$  to the resistance experienced by an impermeable sphere of the same diameter. Hence, the drag force exerted on the aggregate takes the form:

$$F_D = \left( \frac{\pi}{4} d_{\text{agg}}^2 \right) \left( \frac{1}{2} \rho V_t^2 \right) C_D \Omega \quad (4.111)$$

Brinkman model is one of the widely used models to describe the fluid velocity within the porous sphere by taking into account the viscous effects and high porosity of the aggregates. Under creeping flow conditions, the correction factor,  $\Omega$ , based on Brinkman model is found analytically with the equation (Naele *et al.*, 1973):

$$\Omega = \frac{2\beta^2 [1 - (\tanh \beta) / \beta]}{2\beta^2 + 3[1 - (\tanh \beta) / \beta]} \quad (4.112)$$

where  $\beta$  is a dimensionless permeability factor of porous aggregates and is related to the size and permeability of the aggregate,  $\kappa$ , through

$$\beta = \frac{d_{\text{agg}}}{2\sqrt{\kappa}} \quad (4.113)$$

Brinkman model is suitable in the description of the sedimentation of highly porous homogenous aggregates, in laminar flow (Naele *et al.*, 1973).

Flow through an aggregate decreases its drag force compared to impermeable aggregates. So, a settling velocity, that is faster than that of identical impermeable sphere (calculated using Stokes' law ( $V_{t,\text{agg}}$ ) of eq. (4.110)), is expected. The settling velocity of a permeable aggregate,  $V_t$ , can be related to that predicted by Stokes' law  $V_{t,\text{agg}}$  (Matsumoto and Suganuma, 1977; Johnson *et al.*, 1996; Lee *et al.*, 1996) through a function of  $\beta$ ,

$$\Gamma = \frac{V_t}{V_{t,\text{agg}}} = \frac{\beta}{\beta - \tanh \beta} + \frac{3}{2\beta^2} \quad (4.114)$$

based on Brinkman model where  $\Gamma$  is the settling velocity ratio. As the aggregate permeability increases,  $\beta$  as given in eq. (4.113) decreases and  $\Gamma$  increases.  $\Gamma = 1$  for relatively impermeable particles as  $\beta$  approaches infinity.

Johnson *et al.* (1996) showed that fractal aggregates composed of inorganic microspheres could settle on the average 4–8.3 times faster than predicted by calculations for impermeable or permeable spheres of homogenous distribution of identical mass, cross-sectional area, and primary particle density. The experiments were done for the three different fractal dimensions. Experimentally found settling velocities of aggregates are compared with the impermeable sphere settling velocity (eq. (4.110)) in Figure 4.4 and compared with the settling velocity of aggregates having homogenous porosity distribution (eq. (4.114)) in Figure 4.5. These differences in settling velocities should be a consequence of the nonhomogenous distribution of primary particles and hence of the pores in a fractal aggregate. Pores become larger as fractal aggregates increase in size. The permeability of the macropores between clusters is much greater than the permeability inside the smaller clusters. These pores then operate as pipes connected in parallel, with flow through the large cross-sectional area pipe much greater than others. This results in a greater flow through the aggregate interior than possible for homogenous permeable spherical aggregates. These large pores must produce a smaller overall drag per total cross-sectional area of the fractal aggregate, part of the drag force being converted to shear of lesser magnitude in flowing through the pores.

Many expressions for drag coefficient  $C_D$  are derived to cover a wide range of Reynolds numbers and many different irregular shapes. The correlations given in Table 4.3 applicable to impermeable individual particles may not be applicable for fractal aggregates, which have macrosized pores in addition to micropores of the particles. Drag coefficients of porous aggregates developed by Masliyah and Polikar (1980) can be given as an example of one of the empirical  $C_D$  correlations. It is derived using regression analysis based on the settling experiments assuming the shape of the aggregates to be spherical and valid for the range  $15 < \beta < 33$ .

$$C_D = \frac{24\Omega}{Re_{agg}} [1 + 0.1315 Re_{agg}^{0.82 - 0.05 \log Re_{agg}}], \quad \text{for } 0.1 < Re_{agg} \leq 7 \quad (4.115)$$

$$C_D = \frac{24\Omega}{Re_{agg}} [1 + 0.0853 Re_{agg}^{1.093 - 0.105 \log Re_{agg}}], \quad \text{for } 7 < Re_{agg} < 120 \quad (4.116)$$

*Modification of porosity terms* The calculation method of settling velocity or  $\Gamma$  can be generalized by including the fractal dimension  $d_f$  that determines the permeability of an aggregate. In order to incorporate the structure of fractal aggregates into the expressions of aggregate permeability, Li and Logan (2001) introduced two new porosity definitions using single-particle-fractal model or cluster-fractal model.

- (a) *Single-particle-fractal model*: Porosity is calculated based on a uniform distribution of primary particles in the aggregate. The number of primary particles,  $N$ , in this model is defined as (Li and Logan, 2001):

$$N = c \left( \frac{d_{agg}}{d_p} \right)^{d_f} \quad (4.117)$$

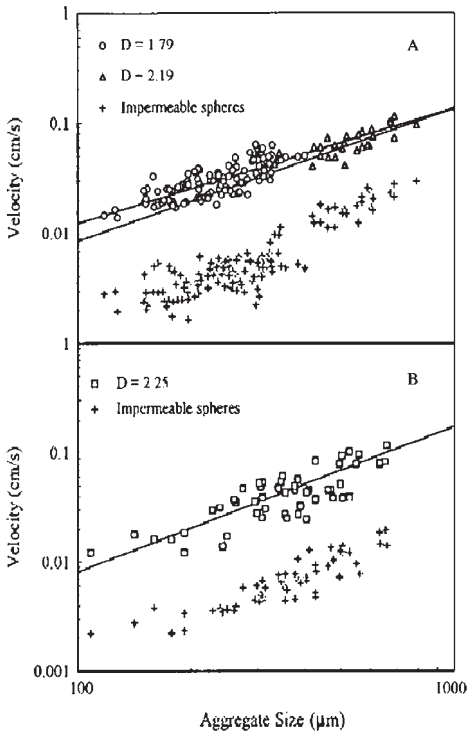


**Figure 4.4** Settling velocities of aggregates versus aggregate size. Comparison of experimental results of (A)  $d_f = 1.79$  ( $\circ$ ) and  $2.19$  ( $\Delta$ ); and (B)  $d_f = 2.25$  ( $\square$ ) with the predicted for impermeable spheres using Stokes' law ( $+$ ).  $D$  denotes  $d_f$  in figures (Johnson *et al.*, 1996. Figure 4 in the original, reproduced with permission of *The American Chemical Society*).

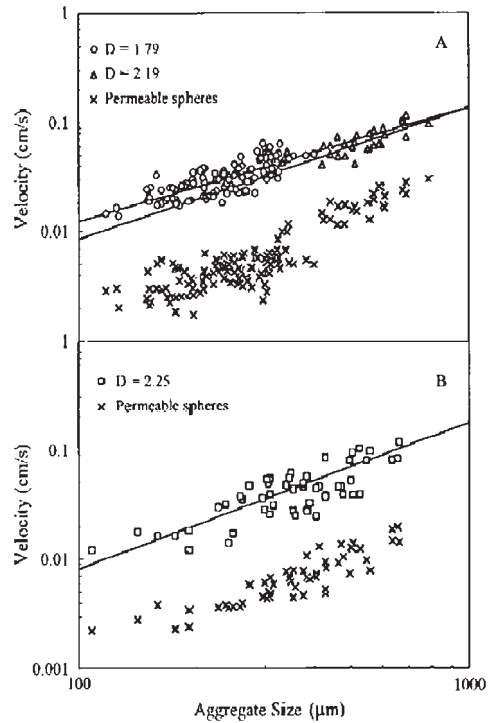


**Figure 4.5** Settling velocities of aggregates versus aggregate size. Comparison of experimental results of (A)  $d_f = 1.79$  ( $\circ$ ) and  $2.19$  ( $\Delta$ ); and (B)  $d_f = 2.25$  ( $\square$ ) with the predicted for homogeneous permeable spherical aggregates using eq. (4.114) ( $\times$ ).  $D$  denotes  $d_f$  in figures (Johnson *et al.*, 1996. Figure 6 in the original, reproduced with permission of *The American Chemical Society*).

So, the porosity of the aggregate,  $\varepsilon$ , is calculated by combining eqs. (4.100) and (4.117) using  $v_0 = \pi d_p^3/6$  and  $v_{\text{agg}} = \pi d_{\text{agg}}^3/6$ , as

$$\varepsilon = 1 - c \left( \frac{d_{\text{agg}}}{d_p} \right)^{d_f - 3} \quad (4.118)$$

where  $c$  is a packing coefficient. Once the aggregate ( $d_{\text{agg}}$ ) and primary particle ( $d_p$ ) sizes are determined experimentally, the settling velocity of porous fractal aggregates  $V_t$  can be calculated by using eq. (4.118) for  $\varepsilon$ , Table 4.4 for  $\kappa$ , eq. (4.113) for  $\beta$  and eq. (4.114).

- (b) *Cluster-fractal model*: In this approach, aggregates are composed of clusters with a range of sizes, with each subcluster formed by successively smaller clusters having the same self-similar shape. The largest cluster is defined as the principle cluster. The pores between the largest clusters control the overall aggregate permeability (Li and Logan, 1997). With the assumption that all of the largest clusters forming an aggregate have the same size and an aggregate has  $k$  number of principal clusters, one can write

$$k = c \left( \frac{d_{\text{agg}}}{d_c} \right)^{d_f} \quad (4.119)$$

where  $d_c$  is the size of the principle cluster and volume of clusters equals  $v_c = \pi d_c^3/6$ . The porosity of a fractal cluster aggregate  $\varepsilon_c$  can be written as

$$1 - \varepsilon_c = \frac{kv_c}{v_{\text{agg}}} \quad (4.120)$$

Rearrangement of the above equation gives the porosity of cluster aggregate as

$$\varepsilon_c = 1 - c \left( \frac{d_{\text{agg}}}{d_c} \right)^{d_f - 3} = 1 - c \left( \frac{n}{c} \right)^{(d_f - 3)/d_f} \quad (4.121)$$

The settling velocity of porous aggregates of clusters  $V_t$  are calculated by using eq. (4.114), eq. (4.113) for  $\beta$ , eq. (4.121) for  $\varepsilon$  and Table 4.4 with  $d_p$  and  $\varepsilon$  replaced by  $d_c$  and  $\varepsilon_c$ , respectively.

Settling experiments on aggregates of latex microspheres are compared with the calculated values of the two models in Figure 4.6. The cluster-fractal model was found to fit the experimental data well for  $d_f = 1.81$  but estimated lower values for  $d_f = 2.33$ . However, experimental results were much larger than the calculated ones with the single-particle-fractal model. Results showed that the overall permeability of the aggregate and settling velocity were controlled by the largest holes formed by the principal clusters, even though there is relatively little flow within the small clusters.

#### 4.4.2.2.2 Motion of fractal aggregates above creeping flow conditions

If the creeping flow conditions are not valid, modified Stokes' law correlations are used regardless of the aggregate Reynolds number. Lee *et al.* (1996) express that owing to the advection flow through the floc interior, boundary layer separation and the after-sphere wake might not occur as in the nonporous case, so correlations like Stokes' law can be used even under high Reynolds numbers. Wu and Lee (1998) found that boundary layer separation and wake formation, mainly responsible for the deviation of Stokes' law at elevated  $Re$ , had not occurred for a highly porous sphere even at  $Re \sim 40$  from the results of their simulation studies. The expressions using modified Stokes' law are given in Table 4.5.

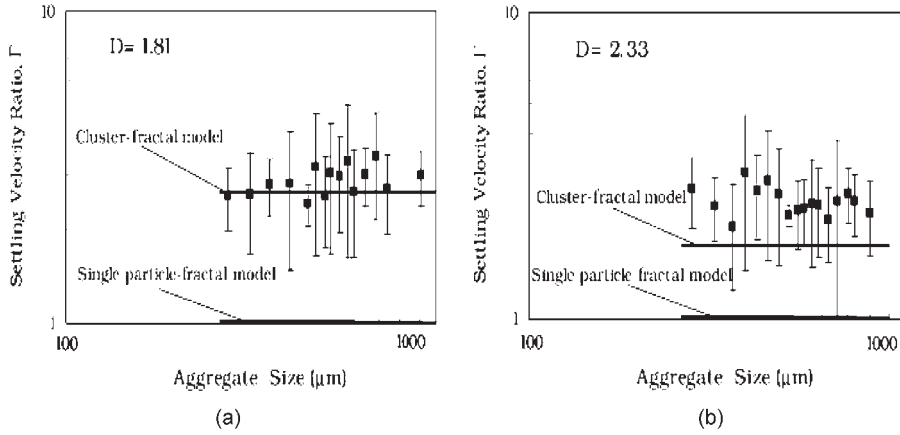


**Figure 4.6** Settling velocity ratios of the aggregates. Comparison of experimental data of (a)  $d_f = 1.81$  (■) and (b)  $d_f = 2.33$  (■) with the estimations from the cluster-fractal model and the single-particle fractal model (—) taking  $c = 0.15$ .  $D$  denotes  $d_f$  in figure (Li and Logan, 2001. Figure 5 in the original, reproduced with permission of Elsevier Science Ltd.).

*Settling velocity of flocs* Flocs are defined as highly porous, irregularly shaped, and loosely connected aggregates composed of smaller primary particles that exhibit a fractal dimension ranging between 1.4 and 2.8 (Li and Ganczarczyk, 1989; Wu *et al.*, 2002). Sedimentation rate is one of the most important methods used in measuring floc size and structure (Jarvis *et al.*, 2006). The drag force exerted on the floc can be expressed as in eq. (4.111). The product of  $C_D \Omega$  for flocs can be roughly taken as inversely proportional to the floc's Reynolds number (Wu and Lee, 1998; Wu *et al.*, 2002; Jarvis *et al.*, 2006), as

$$C_D \Omega = \frac{a(\beta)}{Re_{agg}} \quad (4.127)$$

where  $a(\beta)$  is the correction factor accounting for the advection flow through the interior of aggregate over a wide range of  $Re_{agg}$ . Also, the effective density of flocs can be expressed by scaling relations, with the diameter and fractal dimension of the aggregates:

$$\rho_{eff} = \rho_{agg} - \rho = C d_{agg}^{d_f-3} \quad (4.128)$$

where  $C$  is a proportionality constant. Eq. (4.128) states that the density of a fractal aggregate decreases with increasing floc size. The terminal velocity of flocs can be written after a force balance between drag force and net gravity force (eq. (4.56)) (Wu and Lee, 1998; Wu *et al.*, 2002; Jarvis *et al.*, 2006) as

$$V_t = \frac{4Cg}{3a(\beta)\mu} d_{agg}^{d_f-1} \quad (4.129)$$

If the correction factor  $a(\beta)$  can be regarded as a constant over the range of  $Re_{agg}$  investigated, then the log-log plot of the floc terminal velocity versus the floc size is a line of slope “ $d_f - 1$ ”

**Table 4.5**

Modified Stokes' law expressions for aggregate settling

Reference	Assumptions	Correlation*
Tambo and Watanabe (1979)	$V_t$ and $d_{agg}$ were measured experimentally. $\Psi$ is constant at 0.8. Aggregates were assumed to be impermeable	$V_t = \frac{8\rho_{eff}d_{agg}^2}{34\mu}$ (4.122)
Adachi and Kamiko (1993)	Shape of the flocs is taken as an ellipse. Homogenous distribution of pores within the aggregate	$V_t = \frac{\rho_{eff}gd_p^2}{14.4\Omega\mu} \left( \frac{D_{max}}{d_p} \right)^{d_f-1}$ $D_{max} = 3.27R_p$ (4.123)
Gmachowski (1996)	Overall shape of the fractal aggregate is spherical. The settling velocity of a single aggregate increases by a factor of $N v_0/v_{agg}$ from settling velocity of a single primary particle obeying Stokes' law	$V_t = \frac{2\rho_{eff}gR_p^2}{9\mu} N^{(d_f-1)/d_f}$ (4.124)
Allain <i>et al.</i> (1996)	$V_0$ represents the settling velocity of primary particles. $V_t$ and $R_{agg}$ were measured experimentally	$V_t = V_0 \left( \frac{R_{agg}}{R_p} \right)^{d_f-1}$ $V_0 = \frac{2\rho_{eff}gR_p^2}{9\mu}$ (4.125)
Johnson <i>et al.</i> (1996)	$V_t$ and $d_{agg}$ were measured experimentally. Spherical particles are assumed. $d_{f2} = 2$ when $d_f \geq 2$ , and $d_{f2} = d_f$ when $d_f < 2$ . In creeping flow ( $Re_{agg} < 1$ ), $b = 1$ , and when $0.1 < Re_{agg} < 10$ , $b = 0.871$	$V_t \propto d_{agg}^{d_f-1}$ $V_t \propto d_{agg}^{d_f-d_{f2}+1}$ $V_t \propto d_{agg}^{(d_f-d_{f2}+b)/(2-b)}$ (4.126)

\* $R_p$ : radius of primary particles;  $D_{max}$ : maximum distance between primary particles in the projected aggregate;  $R_{agg}$ : radius of aggregate;  $d_{f2}$ : two-dimensional fractal dimension.

as in Figures 4.4 and 4.5. The slope of the line in Figure 4.4(A) is nearly 1.3, so  $d_f$  can be calculated as 2.3, which is in good agreement with the  $d_f$  value (2.25) in Figure 4.4(A).

#### 4.4.3 Motion of particles with nonuniform density distribution

Microorganisms (i.e. algae, *Paramecium*, ciliate and flagellate protozoa, and planktonic larvae) have asymmetry in their internal density. A torque is generated as a result of the nonuniform density distribution within them to orient the organism either upwards or downwards.

The external forces acting on a microorganism in an aqueous medium are gravitational, buoyancy and the drag force and are described as given in Section 2 of this chapter with the force balance of eq. (4.56). Gravitational force,  $F_g$  acts at the center of mass but buoyancy force,  $F_b$  and drag force,  $F_D$  act at the volumetric center of the particle. Motion of the microorganisms are in the Stokes regime since the Reynolds number is considerably low (in the order of  $\sim 10^{-2}$ ), so the drag force is directly proportional to the velocity. When a microorganism, having a uniform density distribution within its body, falls in a liquid, all the three forces act at the same point as in Figure 4.7(a), so no torque will be generated within the organism to rotate it. If the density is not equally distributed within the particle, the three forces will act at different centers; hence, a difference in distance ( $L_g$ ) between the centers of action of the forces appears as shown in Figure 4.7(b). A torque will be generated because of the region of higher density within the microorganism.

The torque resulting under the action of gravity is given as

$$T_v = F_g L_g \sin \theta \quad (4.130)$$

where  $L_g$  is the distance between the centers of action and  $\theta$  the orientation angle of the fore-aft axis of the body to the vertical. If the Reynolds number of rotational motion is adequately small, all torques can be expressed as proportional to the first power of rotational velocity ( $d\theta/dt$ ). In such a case, rotational motion can be written as

$$-K\mu \frac{d\theta}{dt} = T_v \quad (4.131)$$

where  $K$  is the coefficient of resistance for rotational motion. Consequently, the rotational velocity can be given as

$$\frac{d\theta}{dt} = \frac{-F_g L_g \sin \theta}{K\mu} \quad (4.132)$$

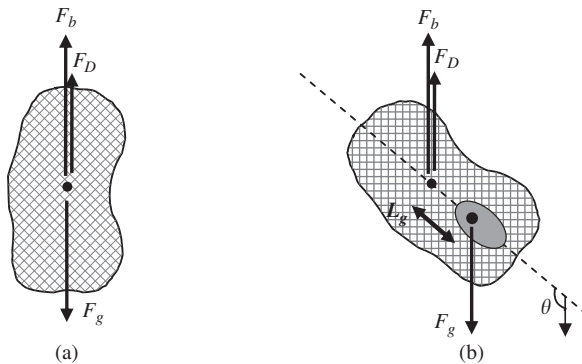


**Figure 4.7** Illustrative drawing of a microorganism having a (a) homogenous density distribution and (b) nonuniform density distribution.



if gravitational force,  $F_g = \rho_p v_p g$  is placed into the above equation;

$$\frac{d\theta}{dt} = B_v \sin \theta \quad (4.133)$$

a differential equation in terms of  $\theta$  is obtained where  $B_v = \rho_p v_p g L_g / K \mu$  is a constant specific to the microorganism and its environment.

The Reynolds number of rotational motion ( $Re_r$ ) of the microorganisms with a characteristic body length of  $l$  and an angular velocity of rotation,  $\omega$ , is defined (Happel and Brenner, 1973) as

$$Re_r = \frac{l^2 \omega \rho}{\mu} \quad (4.134)$$

Mogami *et al.* (2001) found that  $Re_r \approx 2 \times 10^{-3}$  for the *Paramecium* or sea urchin larvae and also found that *Paramecium* oriented upwards in a medium of lower density ( $\rho < \rho_p$ ) during sinking due to gravity, while they oriented downwards during floating up in a denser medium ( $\rho > \rho_p$ ). Fukui and Asai (1985) proposed that the upward orientation of *Paramecium* is strongly influenced by the torque resulting from the higher density of the posterior part of the organism due to the accumulation of food vacuoles.

#### 4.5 HINDERED SETTLING

The free settling behavior of a single solid sphere in a Newtonian fluid media is given in Section 4.3. The settling velocity of single particles can be predicted by equating net gravitational force and drag force using an appropriate drag coefficient for spheres. As the concentration of solids in the suspension increases, interaction between the particles becomes significant. Consequently, the settling velocity of a particle in a liquid suspension is affected by the presence of nearby particles and the drag force created by the settling particles will affect the movement of nearby particles, and settling will be hindered.

Sedimentation velocity of a particle in a concentrated suspension is significantly less than its terminal falling velocity under free settling conditions and depends on the volumetric fraction of particles,  $\phi$ . The density of a suspension,  $\rho_s$ , is given as

$$\rho_s = \phi \rho_p + (1 - \phi) \rho \quad (4.135)$$

from which the volumetric fraction of particles is obtained

$$\phi = \frac{\rho_s - \rho}{\rho_p - \rho} \quad (4.136)$$

When many particles fall simultaneously, the displaced fluid will create an upwards flow with a velocity  $V_f$  against the downward motion of the solid particles, and of the fluid dragged along with them. Collisions between particles and other interactions are also factors, which effectively decrease the free fall terminal velocity of particles. This terminal

velocity of the particles under hindered settling conditions is denoted by  $V_{ht}$ . In a closed system such as a sedimenting tank, downward flow of the solid must be balanced by the upward flow of suspending liquid for conservation of mass in a system:

$$\phi V_{ht} + (1 - \phi)V_f = 0 \quad (4.137)$$

Settling velocity of the particles relative to a fluid (relative velocity),  $V_r$ , is expressed as the difference between the downward velocity of the particles ( $V_{ht}$ ) and the velocity of displaced fluid ( $V_f$ ) as

$$V_r = V_{ht} - V_f = \frac{V_{ht}}{1 - \phi} \quad (4.138)$$

This velocity definition is used especially in batch settling.

Dilute suspensions with fine particles, however, tend to behave quite differently from concentrated suspensions. Experimental results of Kaye and Boardman (1962) and Koglin (1971) demonstrated that the settling velocity of particles at very low volume fractions is higher than the single particle free fall velocity,  $V_t$ . They also found that settling velocity of particles in very dilute suspensions ( $\phi \approx 0.01$ ) was 1.5 times greater than  $V_t$  due to the cluster formation of particles. The flocculation behavior of fine particles can be the results of interaction between the charged regions on the particle surfaces (Smith, 1998). The effect is less significant for concentrated suspensions because of the increase in interparticle collisions and aforementioned reasons.

Sedimentation of suspensions will be analyzed in this section giving hindered settling correlations available in the literature, for both monodisperse and polydisperse particles, and mainly for spherical particles to simplify experimental and theoretical analyses.

#### 4.5.1 Sedimentation of monodisperse suspensions

Settling of monodisperse suspensions involves nearly uniform spheres having the same physical characteristics. The settling velocity,  $V_{ht}$ , of the solid particles is determined experimentally by observing the rate of fall of the suspension–supernatant interface during constant-rate sedimentation (Triant *et al.*, 1997).

The settling velocity (or the relative velocity of particles) is defined as a function of

$$\frac{V_{ht}}{V_t} = f(\phi, Re_p) \quad \text{or} \quad \frac{V_r}{V_t} = f((1 - \phi), Re_p) \quad (4.139)$$

where  $V_t$  is the terminal velocity of a single particle, falling through the same fluid and container in any flow regime.  $Re_p$  is the particle Reynolds number (eq. (4.46)) based on  $V_t$ , which can be calculated by eq. (4.61) using the solid–fluid properties. Settling velocity also depends on the size of the sedimentation tank, mainly to the particle-to-tube diameter ratio ( $\lambda$ ). The effect is more significant for higher  $\lambda$  values.

Suspensions generally settle in the Stokes' regime. Then, terminal velocity of single particles,  $V_t$  in eq. (4.139), is replaced with Stokes' velocity,  $V_{ts}$ , given in eq. (4.58) in Stokes'

regime. Various relations are proposed to predict hindered settling velocity. One of them is to express  $V_{ht}$  by introducing a correction factor,  $h(\phi)$  (Richardson and Zaki, 1954; Batchelor, 1972; Davis and Gecol, 1994; Di Felice, 1999), into the Stokes' equation as

$$V_{ht} = \frac{(\rho_p - \rho)gd_p^2}{18\mu} h(\phi) = V_{ts} h(\phi) \quad (4.140)$$

where  $h(\phi)$  is called the hindered settling function, a function of volumetric fraction of particles,  $\phi$ . Another approach accounting for the multiparticle effect is to modify the Stokes' equation by replacing liquid viscosity,  $\mu$ , by suspension viscosity,  $\eta_s$ , as

$$V_r = \frac{(\rho_p - \rho)gd_p^2}{18\eta_s} \quad (4.141)$$

This approach takes into account the particle collisions during settling. Frequent collisions between particles in concentrated suspensions appear in effect as an increase in the viscosity of the suspending medium. The suspension viscosity is a function of the volume fraction of particles given by various correlations based on Einstein equation (eq. (3.15)) for dilute suspensions ( $\phi \leq 0.02$ ) and eq. (3.17) for moderately concentrated suspensions (see also Table 3.1 for more correlations). These correlations express  $\eta_s$  in the form of relative viscosity  $\eta_r$  as

$$\eta_r = \frac{\eta_s}{\mu} \quad (4.142)$$

Hence, the hindered settling velocity,  $V_{ht}$ , can be defined in terms of suspension viscosity as (Shojaei and Arefinia, 2006)

$$V_r = \frac{V_{ht}}{1 - \phi} = \frac{(\rho_p - \rho)gd_p^2}{18\eta_s} = V_{ts}\eta_r^{-1} \quad (4.143)$$

#### 4.5.1.1 Settling of dilute suspensions

When the volumetric fraction of solids is not high enough to be considered as concentrated and yet low enough for flocculation to occur, the case is referred as dilute suspension where settling velocity can be expressed in terms of hindered settling functions.

Batchelor (1972) expresses the hindered settling function  $h(\phi) = 1 - n\phi$  and gives settling velocity of randomly dispersed spheres in suspensions with this linear relation of  $\phi$  in Stokes' regime as

$$V_{ht} = V_{ts}(1 - n\phi) \quad (4.144)$$

where  $n$  is an empirical parameter,  $n = 6.55$  for perfectly spherical monosized suspensions, but a function of the Peclet number for a suspension made up from particles of the same

density but with slightly polydisperse size distribution. Peclet number ( $Pe$ ) gives the magnitude of the motion due to gravity relative to the motion due to Brownian diffusion. Batchelor and Wen (1982) proposed  $n$  values for negligible interparticle forces as  $n \approx 5.5$  for suspensions with very large  $Pe$  and  $n \approx 6.5$  for suspensions with very small  $Pe$ . In experimental studies  $n$  was found to vary from 5.1 (Cheng and Schachman, 1955) to 7.5 (Al-Naafa and Selim, 1992).

Di Felice (1999) measured the settling velocity of dilute suspensions of spheres ( $\phi \leq 5\%$ ) in the Reynolds number range of  $0.01 < Re_p < 1000$  and proposed a linear function of  $\phi$ , similar to Batchelor's approach. The coefficient  $n$  is given as

$$\frac{6.5 - n}{n - 3} = 0.1Re_t^{0.74} \quad (4.145)$$

where  $n \approx 6.5$  for  $Re_t < 1$  and  $n \approx 3$  for  $Re_t > 980$ .

Hindered settling velocity can be given as a function of the particle volume concentration to the power of  $1/3$  as an alternative approach

$$V_{ht} = V_t \left( \frac{1}{1 + n\phi^{1/3}} \right) \quad (4.146)$$

Happel and Epstein (1954) give the  $n$  value of eq. (4.146) as 1.5 for dilute suspensions. Barnea and Mizrahi (1973) reported  $n$  values varying in the range of 1–2.1 dependent on the system.

Di Felice and Parodi (1996) experimentally showed that the settling velocity of spheres of  $\phi > 0.1$  in viscous flow regime was not affected by the wall, even for  $d_p/D > 0.2$ .

#### 4.5.1.2 Settling of concentrated suspensions

Richardson and Zaki (1954) equation is the most widely used semi-empirical correlation for high volume fraction of particles ( $0.05 < \phi < 0.50$ ) and for slightly polydisperse suspensions:

$$V_{ht} = V_t(1 - \phi)^n \quad (4.147)$$

Richardson and Zaki (1954) defined the hindered settling function as  $h(\phi) = (1 - \phi)^n$  and used uniform spherical particles ( $d_p > 100 \mu\text{m}$ ) in their research, that could be assumed to be sufficiently large for viscosity effects and flocculation to be negligible. The variation of  $n$  was derived based on experiments in all flow regimes and is expressed in terms of wall effects by including the particle-to-tube diameter ratio ( $d_p/D$ ) as given in Table 4.6.

Rowe (1987) gives the index  $n$  of eq. (4.147) in a compact form as a function of flow regime as

$$\frac{4.65 - n}{n - 2.35} = 0.175Re_p^{0.75} \quad (4.148)$$

The most frequently encountered equations in detailed reviews on the settling velocity in sedimentation are given in Table 4.7.

**Table 4.6***n* values of Richardson and Zaki equation

$Re_p$ range	$n$ values	
$Re_p \leq 0.2$	$4.65 + 19.5 \left( \frac{d_p}{D} \right)$	(4.147a)
$0.2 < Re_p < 1$	$\left[ 4.35 + 17.5 \left( \frac{d_p}{D} \right) \right] Re_p^{-0.03}$	(4.147b)
$1 \leq Re_p < 200$	$\left[ 4.45 + 18 \left( \frac{d_p}{D} \right) \right] Re_p^{-0.1}$	(4.147c)
$200 \leq Re_p < 500$	$4.45 Re_p^{-0.1}$	(4.147d)
$Re_p \geq 500$	2.4	(4.147e)

### 4.5.2 Sedimentation of polydisperse suspensions

Settling of polydisperse particles requires a separate definition of the volume fraction and densities of each species in the suspension. Sedimentation of these particles can be described by assuming  $K$  number of species of spherical particles and low Reynolds number hydrodynamics. The net flux in batch sedimentation can be defined as

$$(1 - \phi)V_f + \phi_1 V_1 + \dots + \phi_K V_K = 0 \quad (4.153)$$

where  $\phi_i$  and  $V_i$  are the volume fraction and the velocity of solids species  $i$ , respectively, with  $i = 1, \dots, K$  and  $\phi = \phi_1 + \dots + \phi_K$  (Berres *et al.*, 2005).

The behavior of concentrated suspensions during sedimentation and the interparticle forces are usually analyzed with Kynch's (1952) theory, in which sedimentation is approximated by multiplying the Stokes' velocity of the particles ( $V_{ts,i}$ ) by the hindered settling functions,  $h_i(\phi)$ . Settling velocity of solid particles can then be written in the form of

$$V_{ht,i} = V_{ts,i} h_i(\phi) \quad (4.154)$$

where  $V_{ts,i}$  is the settling velocity of species  $i$  at infinite dilution ( $\phi \rightarrow 0$ ). If the retardation effects of container walls are negligible,  $V_{ts,i}$  will be the same as Stokes' equation of a single particle:

$$V_{ts,i} = \frac{(\rho_i - \rho)gd_i^2}{18\mu} \quad (4.155)$$

Table 4.7

Hindered settling velocity correlations for monodisperse suspensions

References	$Re_p$ range	Correlation
Letan (1974)	$1.5 \leq Re_p \leq 2200$ $\phi < 0.50$	$\frac{V_r}{V_t} = \frac{(1 + 0.1Re_p^{0.687})(1 - \phi)^{3.5}}{1 + 0.15Re_p^{0.687}(V_r/V_t)^{0.687}(1 - \phi)^{1.72}}$ (4.149)
Garside and Al-Dibouni (1977)	$10^{-3} \leq Re_p \leq 3 \times 10^4$ $0.10 < \phi < 0.60$	$\frac{V_r}{V_t} = (1 - \phi)^{n-1}$ $\frac{5.1 - n}{n - 2.7} = 0.1Re_p^{0.9}$ (4.150) Or
	$B = 0.8(1 - \phi)^{1.28}$ for $\phi > 0.15$ ; $B = (1 - \phi)^{2.65}$ for $\phi < 0.15$	$\frac{(V_r/V_t) - (1 - \phi)^{4.14}}{B - (V_r/V_t)} = Re_p^{(1-\phi)+2}$ (4.151)
Concha and Almendra (1979)	$d_p^* = \frac{d_p}{(3\mu^2/(4(\rho_p - \rho)\rho g))^{1/3}}$	$V_r = \frac{20.52}{d_p^*} f_1(\phi) [(1 + 0.0921[d_p^*]^{3/2} f_2(\phi))^{1/2} - 1]^2$ $f_1(\phi) = \frac{(1 - \phi)^2 (1 + 0.75\phi^{1/3})}{(1 - 1.45\phi)^{1.83} (1 - \phi + 1.2\phi^{2/3})^{3/2}}$ (4.152) $f_2(\phi) = \frac{(1 - 1.45\phi)^{1.83} (1 - \phi + 1.2\phi^{2/3})^{3/4}}{(1 - \phi)(1 + 0.75\phi^{1/3})}$
Chong <i>et al.</i> (1979)	$Re_p < 0.2$ $0.10 < \phi < 0.35$ $V_t$ was obtained by linearly extrapolating $V_{ht}$ as $\phi \rightarrow 0$ on a log-log plot of $V_{ht}$ versus $(1 - \phi)$	$V_{ht} = V_t(1 - \phi)^n$ $n \sim 4.8$ for smooth spheres; $\sim 5.4$ for cubic shapes; $\sim 5.8$ for brick-like and angular particles (4.147)

If the wall effect cannot be neglected, a correction factor of Khan and Richardson (1989) may be used as

$$V_{\text{tw},i} = V_{\text{ts},i} \left( 1 - 1.15 \left( \frac{d_i}{D} \right)^{0.6} \right) \quad (4.156)$$

The hindered settling function  $h_i(\phi)$  of eq. (4.154) proposed by Batchelor and Wen (1982), (eq. (4.157)), is generally applied to dilute suspensions only and by Davis and Gecol (1994) (eq. (4.158)) to concentrated suspensions.

Batchelor and Wen (1982) expressed the hindered settling function,  $h_i(\phi)$ , for the poly-disperse suspensions as

$$h_i(\phi) = 1 + \sum_{j=1}^K S_{ij} \phi_j, \quad i = 1, \dots, K \quad (4.157)$$

The settling coefficients  $S_{ij}$  depend on size ratio  $\lambda = d_j/d_i$  and buoyant density ratio  $\gamma = (\rho_j - \rho)/(\rho_i - \rho)$ , where  $d_i$  and  $\rho_i$  are the size and the density of species  $i$ , respectively, and  $\rho$  the density of the fluid.  $S_{ij}$  are calculated by Batchelor and Wen (1982) as  $S_{ii} = -6.55$  for  $\lambda = 1$  and  $\gamma = 1$ ;  $S_{ii} = -5.6$  for  $\lambda \approx 1$  and  $\gamma = 1$ ; and  $S_{ii} = -2.6$  for  $\lambda = 1$  and  $\gamma \approx 1$ . Batchelor's theory for dilute suspensions predicts the settling velocity in the presence of other spheres that differ in size or density. However, this theory is based on the assumption that identical spheres have identical velocities, and leads to significantly differing results for spheres that differ only slightly in size or density. Batchelor's equation (with  $S_{ii} = -6.5$  for  $\lambda \approx 1$  and  $\gamma \approx 1$ ) appears to work well at small Peclet numbers in the absence of interparticle forces. In this case, Brownian motion ensures that the random distribution of sphere centers remains uniform. Hydrodynamic diffusion is very important at large Peclet numbers, but is not taken into account in the Batchelor–Wen analysis (Höfler *et al.*, 1999; Berres *et al.*, 2005).

Davis and Gecol (1994) assumed that Batchelor's results could be extended to higher concentrations as

$$h_i(\phi) = (1 - \phi)^{-S_{ii}} \left[ 1 + \sum_{j=1}^K (S_{ij} - S_{ii}) \phi_j \right], \quad i = 1, \dots, K \quad (4.158)$$

The sedimentation coefficients  $S_{ij}$  are given by the theory of Batchelor and Wen (1982). For very small values of  $\phi$ , second order terms can be neglected, and eq. (4.158) reduces to eq. (4.157). The equation also takes the same form as Richardson and Zaki (1954) equation for monodisperse suspensions (with  $n = -S_{ii}$ ).

Settling velocity of solid particles can also be written in a different form of eq. (4.154) in terms of relative velocity  $V_{\text{ht},i} = (1 - \phi)V_{\text{r},i}$ ,

$$V_{\text{ht},i} = h_i(\phi) V_{\text{ts},i} \frac{\rho_i - \rho_s}{\rho_i - \rho} - \sum_{j=1}^K \phi_j h_j(\phi) V_{\text{ts},j} \frac{\rho_j - \rho_s}{\rho_j - \rho} \quad (4.159)$$

where  $(1 - \phi)$  is calculated from eq. (4.136). This equation is not as straightforward as in the former case (Xue and Sun, 2003).  $\rho_s$  is the density of the suspension given as

$$\rho_s = \rho(1 - \phi) + \sum_{i=1}^K \rho_i \phi_i \quad (4.159a)$$

If  $\rho_1 = \rho_2 = \dots = \rho_K$ , then the above equation becomes

$$V_{ht,i} = (1 - \phi) \left[ h_i(\phi) V_{ts,i} - \sum_{j=1}^K \phi_j h_j(\phi) V_{ts,j} \right] \quad (4.160)$$

The above equation reduces to Richardson–Zaki equation when only a single species is present.

The most commonly used  $h_i(\phi)$  functions for the approach given in eq. (4.159) are proposed by Masliyah (1979) as

$$h_i(\phi) = (1 - \phi)^{n-2} \quad (4.161)$$

and Patwardhan and Tien (1985) as

$$h_i(\phi) = \left[ 1 - \left( \frac{1 + d_e}{d_i} \right)^{-3} \right]^{n-2} \quad (4.162)$$

where

$$d_e = \frac{\sum_{j=1}^K d_j \phi_j}{\phi} (\phi^{-1/3} - 1) \quad (4.162a)$$

As in the Richardson–Zaki equation, the value of  $n$  can be chosen to fit the experimental data and can be taken as 4.65 for creeping flow conditions (Xue and Sun, 2003; Berres *et al.*, 2005).

## REFERENCES

- Adachi, Y., Kamiko, M., 1993. Sedimentation of a polystyrene latex floc. *Powder Technology*, 78, 129–135.
- Al-Naafa, M.A., Selim, M.S., 1992. Sedimentation of monodisperse and bidisperse hard-sphere colloidal suspensions. *AIChE Journal*, 38, 1618–1630.



- Allain, C., Cloitre, M., Parisse, F., 1996. Settling by cluster deposition in aggregation colloidal suspension. *Journal of Colloid and Interface Science*, 178, 411–416.
- Barnea, F., Mizrahi, J., 1973. A generalized approach to fluid dynamics of particulate system. Part I. General correlation for fluidization and sedimentation in solid multiparticle systems. *Chemical Engineering Journal*, 5, 171–189.
- Batchelor, G.K., 1972. Sedimentation in a dilute dispersion of spheres. *Journal of Fluid Mechanics*, 52, 245–268.
- Batchelor, G.K., Wen, C.-S., 1982. Sedimentation in a dilute polydisperse system of interacting spheres. Part 2. Numerical results. *Journal of Fluid Mechanics*, 124, 495–528.
- Berres, S., Bürger, R., Tory, E.M., 2005. Applications of polydisperse sedimentation models. *Chemical Engineering Journal*, 111, 105–117.
- Bird, R.B., Stewart, W.E., Lightfoot, E.N., 2002. *Transport Phenomena*, 2nd edn., Wiley, USA (Chapter 4).
- Brown, P.P., Lawler, D.F., 2003. Sphere drag and settling velocity revisited. *Journal of Environmental Engineering*, 129(3), 222–231.
- Cheng, P.Y., Schachman, H.K., 1955. Studies on the validity of the Einstein viscosity law and Stokes' law of sedimentation. *Journal of Polymer Science*, 16, 19–30.
- Chhabra, R.P., Agarwal, L., Sinha, N.K., 1999. Drag on non-spherical particles: an evaluation of available methods. *Powder Technology*, 101, 288–295.
- Chien, S.F., 1994. Settling velocities of irregularly shaped particles. *SPE Drilling and Completion*, 9, 281.
- Chong, Y.B., Ratkowsky, D.A., Epstein, N., 1979. Effect of particle shape on hindered settling in creeping flow. *Powder Technology*, 23, 55–66.
- Clift, R., Grace, J.R., Weber, M.E., 1978. *Bubbles, Drops, and Particles*, Academic Press, New York, NY.
- Concha, F., Almendra, E.R., 1979. Settling velocities of particulate systems, 2. Settling velocities of suspensions of spherical particles. *International Journal of Mineral Processing*, 6, 31–41.
- Davis, R.H., Gecol, H., 1994. Hindered settling function with no empirical parameters for polydisperse suspensions. *AIChE Journal*, 40, 570–575.
- Di Felice, R., 1996. A relationship for the wall effect on the settling velocity of a sphere at any flow regime. *International Journal of Multiphase Flow*, 22(3), 527–533.
- Di Felice, R., 1999. The sedimentation velocity of dilute suspensions of nearly monosized spheres. *International Journal of Multiphase Flow*, 25, 559–574.
- Di Felice, R., Parodi, E., 1996. Wall effects on the sedimentation velocity of suspensions in viscous flow. *AIChE Journal*, 42, 927–931.
- Fan, L., Mao, Z-S, Yang, C., 2004. Experiment on settling of slender particles with large aspect ratio and correlation of the drag coefficient. *Industrial and Engineering Chemistry Research*, 43, 7664–7670.
- Fidleris, V., Whitmore, R.L., 1961. Experimental determination of the wall effect for spheres falling axially in cylindrical vessels. *British Journal of Applied Physics*, 12, 490–494.
- Flemmer, R.L.C., Banks, C.L., 1986. On the drag coefficient of a sphere. *Powder Technology*, 48, 217–221.
- Francis, A.W., 1933. Wall effect in falling ball method for viscosity. *Physics*, 4, 403–406.
- Fukui, K., Asai, H., 1985. Negative geotactic behavior of *Paramecium caudatum* is completely described the mechanism of buoyancy-oriented upward swimming. *Biophysical Journal*, 47, 479–482.
- Garside, J., Al-Dibouni, M.R., 1977. Velocity–voidage relationships for fluidization and sedimentation in solid–liquid systems. *Industrial and Engineering Chemistry Process Design and Development*, 16, 206–214.
- Ganser, G.H., 1993. A rational approach to drag prediction of spherical and non-spherical particles. *Powder Technology*, 77, 143–152.

- Gmachowski, L., 1996. Hydrodynamics of aggregated media. *Journal of Colloid and Interface Science*, 178, 80–86.
- Haberman, W.L., Sayre, R.M., 1958. David Taylor Model Basin. Department of Navy, Washington, Report No. 1143.
- Haider, A., Levenspiel, O., 1989. Drag coefficient and terminal velocity of spherical and non-spherical particles. *Powder Technology*, 58, 63–70.
- Happel, J., Brenner, H., 1973. *Low Reynolds Number Hydrodynamics*, Noordhoff International Publishing, Leyden.
- Happel, J., Epstein, N., 1954. Viscous flow in multiparticle systems: cubical assemblage of uniform spheres. *Industrial and Engineering Chemistry*, 46, 1187–1194.
- Hartman, M., Trnka, O., Svoboda, K., 1994. Free settling of nonspherical particles. *Industrial and Engineering Chemistry Research*, 33, 1979–1983.
- Höfler, K., Schwarzer, S., Wachman, B., 1999. Simulation of hindered settling in bidisperse suspensions of rigid spheres. *Computer Physics Communications*, 121–122, 268–269.
- Jarvis, P., Jefferson, B., Parsons, S.A., 2006. Floc structural characteristics using conventional coagulation for a high doc, low alkalinity surface water source. *Water Research*, 40, 2727–2737.
- Jianzhong, L., Xing, S., Zhenjiang, Y., 2003. Effects of the aspect ratio on the sedimentation of a fiber in Newtonian fluids. *Aerosol Science*, 34, 909–921.
- Johnson, C.P., Li, X., Logan, B.E., 1996. Settling velocities of fractal aggregates. *Environmental Science and Technology*, 30, 1911–1918.
- Kapishnikov, S., Kanster, V., Steinberg, V., 2006. Continuous particle size separation and size sorting using ultrasound in a microchannel. *Journal of Statistical Mechanics: Theory and Experiment*. P01012, 1–15.
- Kaye, B.H., Boardman, R.P., 1962. Symposium on the Interaction between Fluids and Particles. 3rd Congress of the European Federation of Chemical Engineering, London, UK, 17.
- Keh, H.J., Liu, Y.C., 1997. Sedimentation velocity and potential in a dilute suspension of charged composite spheres. *Journal of Colloid and Interface Science*, 195, 169–191.
- Khan, A.R., Richardson, J.F., 1987. The resistance to motion of a solid sphere in a fluid. *Chemical Engineering Communications*, 62, 135–150.
- Khan, A.R., Richardson, J.F., 1989. Fluid–particle interactions and flow characteristics of fluidized beds and settling suspensions of spherical particles. *Chemical Engineering Communications*, 78, 111–130.
- Koglin, B., 1971. Statistical distribution of sedimentation rate in suspensions of low concentration. *Chemie Ingenieur Technik*, 43, 761–764.
- Kynch, G.J., 1952. A theory of sedimentation. *Transactions of Faraday Society*, 48, 166.
- Lee, D.J., Chen, G.W., Liao, Y.C., Hsieh, C.C., 1996. On the free-settling test for estimating activated sludge floc density. *Water Research*, 30, 541–550.
- Létan, R., 1974. On vertical dispersed two-phase flow. *Chemical Engineering Science*, 29, 621–624.
- Li, D.H., Ganczarczyk, J.J., 1989. Fractal geometry of particle aggregates generated in water and wastewater treatment process. *Environmental Science and Technology*, 23, 1385–1389.
- Li, X.Y., Logan, B.E., 1997. Collision frequencies of fractal aggregates with small particles by differential sedimentation. *Environmental Science and Technology*, 31, 1229–1236.
- Li, X.Y., Logan, B.E., 2001. Permeability of fractal aggregates. *Water Research*, 35(14), 3373–3380.
- Li, X.Y., Yuan, Y., 2002. Settling velocities and permeabilities of microbial aggregates. *Water Research*, 36, 3110–3120.
- Liu, Y.C., Keh, H.J., 1998. Sedimentation velocity and potential in a dilute suspension of charged porous spheres. *Colloids and Surfaces A: Physicochemical and Engineering Aspects*, 140, 245–259.
- Masliyah, J.H., 1979. Hindered settling in a multi-species particle system. *Chemical Engineering Science*, 34, 1166–1168.

- Masliyah, J.H., Polikar, M., 1980. Terminal velocity of porous spheres. *Canadian Journal of Chemical Engineering*, 58, 299–302.
- Matsumoto, K., Suganuma, A., 1977. Settling velocity of a permeable model floc. *Chemical Engineering Science*, 32, 445–447.
- Mogami, Y., Ishii, J., Baba, S.A., 2001. Theoretical and experimental dissection of gravity-dependent mechanical orientation in gravitactic microorganisms. *Biological Bulletin*, 201, 26–33.
- Munroe, H.S., 1888. The English versus the continental system of jigging—is close sizing advantageous?. *Transactions of the American Institute of Mining Engineers*, 17, 637.
- Naele, G., Epstein, N., Nader, W., 1973. Creeping flow relative to permeable spheres. *Chemical Engineering Science*, 28, 1865–1874.
- Nguyen, A.V., Stechemesser, H., Zobel, G., Schulze, H.J., 1997. An improved formula for terminal velocity of rigid spheres. *International Journal of Mineral Processing*, 50, 53–61.
- Patwardhan, V.S., Tien, C., 1985. Sedimentation and liquid fluidization of solid particles of different sizes and densities. *Chemical Engineering Science*, 40(7), 1051–1060.
- Richardson, J.F., Zaki, W.N., 1954. Sedimentation and fluidisation. Part I. *Transactions of the Institution of Chemical Engineers*, 32, 35–53.
- Ro, K.S., Neethling, J.B., 1990. Terminal settling characteristics of bioparticles. *Research Journal of the Water Pollution Control Federation*, 62, 901–906.
- Rosendahl, L., 2000. Using a multi-parameter particle shape description to predict the motion of non-spherical particle shapes in swirling flow. *Applied Mathematical Modelling*, 24, 11–25.
- Rowe, P.N., 1987. A convenient empirical equation for estimation of the Richardson–Zaki exponent. *Chemical Engineering Science*, 43, 2795–2796.
- Shojaei, A., Arefinia, R., 2006. Analysis of the sedimentation process in reactive polymeric suspensions. *Chemical Engineering Science*, 61, 7565–7578.
- Slattery, J.C., 1978. *Momentum, Energy, and Mass Transfer in Continua*, Krieger Publishing Company, New York, NY (Chapter 3).
- Smith, T.N., 1998. A model of settling velocity. *Chemical Engineering Science*, 53(2), 315–323.
- Smolkin, M.R., Smolkin, R.D., 2006. Calculation and analysis of the magnetic force acting on a particle in the magnetic field of separator: analysis of the equations used in the magnetic methods of separation. *IEEE Transactions on Magnetics*, 11(42), 3682–3693.
- Svoboda, J., Fujita, T., 2003. Recent developments in magnetic methods of material separation. *Minerals Engineering*, 16, 785–792.
- Swamee, P.K., Ojha, C.P., 1991. Drag coefficient and fall velocity of non-spherical particles. *Journal of Hydraulic Engineering*, 117, 660–669.
- Tambo, N., Watanabe, Y., 1979. Physical characteristics of flocs—I. The flocs density function and aluminium floc. *Water Research*, 13, 409–419.
- Thompson, T.L., Clark, N.N., 1991. A holistic approach to particle drag prediction. *Powder Technology*, 67, 57–66.
- Tran-Cong, S., Gay, M., Michaelides, E.E., 2004. Drag coefficients of irregularly shaped particles. *Powder Technology*, 139, 21–32.
- Triantafyllidis, R.M., Ma, T.W., Hsu, F.L.G., Sung, D.J., 1997. Characterization, settling and rheology of concentrated fine particulate mineral slurries. *Powder Technology*, 93, 219–233.
- Turton, R., Clark, N., 1987. An explicit relationship to predict spherical particle terminal velocity. *Powder Technology*, 53, 127–129.
- Turton, R., Levenspiel, O., 1986. A short note on the drag correlation for spheres. *Powder Technology*, 47, 83–86.
- Veerapaneni, S.A., Wiesner, M.R., 1996. Hydrodynamics of fractal aggregates with radially varying permeability. *Journal of Colloid and Interface Science*, 177, 45–57.

- Wu, R.M., Lee, D.J., 1998. Hydrodynamic drag force exerted on a moving floc and its implication to free-settling tests. *Water Research*, 32(3), 760–768.
- Wu, R.M., Lee, D.J., Waite, T.D., Guan, J., 2002. Multilevel structure of sludge flocs. *Journal of Colloid and Interface Science*, 252, 383–392.
- Xie, H.Y., Zhang, D.W., 2001. Stokes shape factor and its application in the measurement of sphericity of non-spherical particles. *Powder Technology*, 114, 102–105.
- Xue, B., Sun, Y., 2003. Modelling of sedimentation of polydisperse spherical beads with a broad size distribution. *Chemical Engineering Science*, 58, 1531–1543.
- Yin, C., Rosendahl, L., Kaer, S.K., Sorensen, H., 2003. Modelling the motion of cylindrical particles in a nonuniform flow. *Chemical Engineering Science*, 58, 3489–3498.
- Zigrang, D., Sylvester, N., 1981. An explicit equation for particle settling velocities in solid–liquid systems. *AIChE Journal*, 6, 1043–1044.

This page intentionally left blank

## Modeling the Flow of Settling Suspensions

---

Flow of settling particles differs substantially from the flow of nonsettling particles in three basic aspects: need for averaging, flow pattern formation, and extension of the concept of interface. Since the particles tend to settle during transport through the pipe, different packing densities exist in the radial direction of the pipe in horizontal flow. Averaging techniques have to be developed to be able to use Navier–Stokes equations to model the flow behavior. Variation of compaction densities of the particles in the radial direction causes the formation of different flow behaviors of particles to arise within the same cross-sectional area. The segregation of particles into different sections necessitates an extension of the concept of the interface. Along with the solid–liquid interfaces on the surface of the particles, interfaces also exist between layers of different compactions in the pipe. The variations in these interfaces should also be taken into account in the momentum balance equation. The mathematical methods and models used in describing two-phase flow will be taken up in this chapter.

### 5.1 BASIC CONCEPTS IN MODELING OF TWO-PHASE FLOW

Whatever the flow pattern that exists in solid–liquid two-phase flow an interface between the solid particles and the liquid is always present. Besides the phase interface between the solids and the liquid, another type of interface is defined between layers of a flowing suspension with different compaction levels.

There are two main approaches used in flow models, the *Lagrangian* and *Eulerian* approaches. These approaches are initially explained for a single-phase (fluid) flow and then for homogeneous solid–liquid suspension flow.

#### 5.1.1 Eulerian and Lagrangian approaches for single-phase flow

In the *Eulerian approach*, a control volume is fixed in space (constant  $x$ ,  $y$ , and  $z$ ) through which the fluid flows. However, the control volume moves with the fluid in the *Lagrangian approach* with a velocity equal to that of the fluid stream  $\mathbf{V}$ .

The difference in the Eulerian and Lagrangian approaches can best be illustrated with the continuity equation. The continuity equation in Eulerian form is derived by using a

control element of constant volume and variable mass at a fixed position in space and given as

$$\frac{\partial \rho}{\partial t} = -\nabla \cdot \rho \mathbf{V} \quad (5.1)$$

where  $\rho$  is density,  $t$  the time, and  $\mathbf{V}$  the velocity vector. The Lagrangian form of the continuity equation for a control element of variable volume and constant mass moving with the velocity of the stream is defined in terms of substantial derivative as

$$\frac{D\rho}{Dt} = -\rho \nabla \cdot \mathbf{V} \quad (5.2)$$

The above equation can be written as in eq. (5.3) using the substantial derivative definition given in Appendix A1

$$\frac{\partial \rho}{\partial t} = -\mathbf{V} \cdot \nabla \rho - \rho \nabla \cdot \mathbf{V} \quad (5.3)$$

The RHS of the above equation can also be expressed as  $-\mathbf{V} \cdot \nabla \rho - \rho \nabla \cdot \mathbf{V} = -\nabla \cdot \rho \mathbf{V}$ , using the vectorial relations in Appendix A1, reducing to eq. (5.1). This proves the mathematical equivalency of the Eulerian and Lagrangian forms of the continuity equation.

Other transport equations such as momentum, energy, and mass can also be expressed in the Eulerian and Lagrangian forms, which are mathematically equivalent (Bird et al., 2002; Fahein, 1983). The Eulerian form of the equation of motion (momentum equation) in vectorial form is

$$\frac{\partial(\rho \mathbf{V})}{\partial t} = -\nabla \cdot \boldsymbol{\tau} - \nabla \cdot \rho \mathbf{V} \mathbf{V} - \nabla p + \rho \mathbf{g} \quad (5.4)$$

where  $\boldsymbol{\tau}$  is shear stress tensor,  $\mathbf{g}$  the acceleration vector, and  $p$  the pressure. The Eulerian form of the equation of motion is converted to the Lagrangian form by the same procedure with the use of the equation of continuity:

$$\frac{\rho D\mathbf{V}}{Dt} = -\nabla \cdot \boldsymbol{\tau} - \nabla p + \rho \mathbf{g} \quad (5.5)$$

### 5.1.2 Eulerian and Lagrangian approaches in solid–liquid suspension flow

In modeling of solid–liquid suspension flow, both the Lagrangian and the Eulerian approaches can be used for the dispersed particle phase, whereas only the Eulerian approach is used for the continuous fluid phase (Zhang and Prosperetti, 1997; Marchioro *et al.*, 2000; Patankar and Joseph, 2001a,b; Rani and Balachandar, 2004; Gudmundsson, 2005). Selection of the approach to be used for the dispersed phase depends on the size of particles,  $d_p$ ; or particle response time,  $t_{pr}$ , compared to the characteristic time-scale of the continuous liquid phase,  $t_c$ ; and the particle volume fraction,  $\phi(t, \mathbf{x})$ .

The particle response time,  $t_{pr}$ , is the time that a particle takes to respond to a change in suspending liquid flow velocity.  $t_{pr}$  is generally defined in terms of velocity vectors and the drag coefficient (Rani *et al.*, 2004) as

$$t_{pr} = \left( \frac{4}{3} \right) \left( \frac{\rho_p}{\rho} \right) \frac{d_p}{C_D V_t} \quad (5.6)$$

where  $C_D$  is drag coefficient, and  $V_t$ ,  $d_p$ , and  $\rho_p$  the terminal velocity, diameter, and density of the particle, respectively. If the particles are small, the particle Reynolds number  $Re_p$  is less than unity, so the particles move in the Stokes regime. Using  $C_D$  (eq. (4.49)) and  $V_t$  (eq. (4.58)) expressions for this regime, the particle response time,  $t_{pr}$ , is

$$t_{pr} = \frac{\rho_p d_p^2}{18\mu} \quad (5.7)$$

The characteristic time-scale of the continuous liquid phase,  $t_c$ , is taken as the time the liquid passes through a system of length  $L$

$$t_c = \frac{L}{V_c} \quad (5.8)$$

where  $V_c$  is superficial velocity of the liquid based on the free cross-sectional area for fluid flow.

The ratio of the particle response time to the characteristic time of the liquid is known as Stokes number,  $St$

$$St = \frac{t_{pr}}{t_c} \quad (5.9)$$

When  $St < 0.1$ , the particles have sufficient time to respond to the changes in the liquid velocity and the particle velocity approaches the liquid velocity. In cases where  $St > 10$ , the particles do not have sufficient time to respond to changing liquid velocity, so the particle velocity shows small variations.

As an example, the general case summarized in Table 5.1, is taken up to show the selection of the approaches for modeling the dispersed phase with the conditions of  $\rho_p/\rho \gg 1$  and very low solid volume fractions,  $\phi \approx 10^{-4}$ .

- When the particle size is extremely small with  $\phi \approx 10^{-4}$ , then solid particles cannot have relative motions with respect to the liquid phase. So, the mixture is considered as a single-phase or a homogeneous mixture and a *single fluid (mixture)* model is selected for modeling the suspension flow. This model is based on Eulerian approach. If the particles are too small, evaluation of the particle velocity,  $\mathbf{V}_p(t, x)$ , becomes hard. In this case, smaller time-steps than used in the fluid phase are taken to determine the Eulerian velocity distribution of the particulate phase. In cases where a particulate phase shows a wide size



Table 5.1

Example to select a suitable approach for modeling suspension flow

Particle dispersion	Particle size	Approach for dispersed phase	Model	Basis of model (approach of model)
Conditions: $\rho_p/\rho \gg 1, \phi \approx 10^{-4}$				
Monodisperse	$St < 0.1$	– (not considered as a separate phase)	Single fluid (mixture)	Eulerian
	$St > 10$	Eulerian	Two-fluid	Eulerian–Eulerian
Polydisperse	Very small	Fast (equilibrium) Eulerian	Two-fluid	Eulerian–fast (equilibrium) Eulerian
	Small, medium, large	Lagrangian	Dispersed phase	Lagrangian Eulerian
	Very large	Superparticle Lagrangian	Dispersed phase	Eulerian–superparticle Lagrangian

- distribution of very small particles, the particle velocity is found by *fast* or *equilibrium Eulerian approach*.
- If the particle size is large, particles are considered as a separate phase from that of the liquid phase. In this situation, *two-fluid model* based on *Eulerian–Eulerian* approach can be used. The constitutive equations required to define particle–particle interactions can be defined by empirical formulas or from kinetic theory (Ni and Xia, 2003; Wang and Ni, 2003; Fu *et al.*, 2005). In two-fluid model, distributions of the particle volume fraction,  $\phi(t, \mathbf{x})$ , and particle velocity,  $\mathbf{V}_p(t, \mathbf{x})$ , are evolved along the liquid flow that has a velocity distribution is  $\mathbf{V}_c(t, \mathbf{x})$ . This approach cannot be used when the number density of particles is too low which may result in an interruption of the continuity of the system.
  - In a polydisperse system, distributions of the particle volume fraction and particle velocity must be defined separately for each particle size. So, *Lagrangian approach* can be used to model the dispersed phase, where the particles are treated individually through force balances. However, the evaluation of the effect of the particles on the liquid phase is not so simple in this approach.
  - For very large particles, neither of the two approaches is appropriate in modeling the system. So, a new approach called *superparticle Lagrangian method* is suggested (Dukowicz, 1980). This approach assumes that particle groups (parcels), having same characteristics (size and concentration) interact with the liquid phase and their position is calculated by Newton’s equation of motion. Hence, the number of parcels describes the total particle phase.

5.1.2.1 Eulerian–Lagrangian approach

Eulerian–Lagrangian approach (also called *dispersed phase model*) considers the motion of each particle separately and the equation of motion is written for each individual particle.

The effect of particles on the flow field of the continuous phase is studied by the momentum transferred from each particle to the continuous phase. The momentum transfer is obtained by computing the change in the momentum when an individual particle passes through each control element.

In the Lagrangian approach the position of the particle,  $\mathbf{x}_p$ , is found as

$$\frac{d\mathbf{x}_p}{dt} = \mathbf{V}_p \quad (5.10)$$

and the particle velocity vector,  $\mathbf{V}_p$ , is determined after solving the Newton's equation of motion. The most general form of the equation of motion in differential form (Ferry and Balachandar, 2001) is given under unsteady-state conditions for the Stokes regime as

$$\begin{aligned} m_p \frac{d\mathbf{V}_p}{dt} = & 6\pi d_p \mu (\mathbf{V}_c - \mathbf{V}_p) + m_c \frac{D\mathbf{V}}{Dt} + \frac{1}{2} m_c \left( \frac{D\mathbf{V}_c}{Dt} - \frac{D\mathbf{V}_p}{Dt} \right) + (m_p - m_c) \mathbf{g} \\ & + \left( \frac{6\pi d_p^2 \mu}{(\mu/\rho_p)^{1/2}} \right) \frac{d^{1/2}}{dt^{1/2}} (\mathbf{V}_c - \mathbf{V}_p) + \left( \frac{9J_\infty}{\pi} \right) d_p^2 \left( \frac{\mu\rho}{|\omega|} \right)^{1/2} (\mathbf{V}_c - \mathbf{V}_p) \times \omega \end{aligned} \quad (5.11)$$

where  $m_p$  and  $m_c$  denote the mass of the particle and continuous phase, respectively, and  $J_\infty$  is called Saffman lift function taken as  $\approx 2.255$  (Ferry and Balachandar, 2001). The terms at the RHS of the equation give Stokes drag, fluid acceleration, virtual (added) mass, gravity, Basset history, and Saffman lift (Saffman, 1965) forces, respectively. Basset history and Saffman lift forces originate from collision of a particle with other particles and pipe wall resulting in a slip velocity. Saffman force furthermore causes a rotational motion of the particle, which results in vorticity ( $\omega$ ) of the liquid flowing around the particle. For other particle flow regimes or for high particle Reynolds numbers the drag force term (first term) needs modification. The fluid acceleration force (second term on the RHS) is effective in the absence of particles.

The equation of motion (eq. (5.11)) is also defined in terms of the density parameter,  $\beta$ , in a more compact form

$$\beta = \frac{3}{2(\rho_p/\rho) + 1} \quad (5.12)$$

The density parameter  $\beta$  covers all particles: for the dense particles  $\rho_p/\rho \gg 1$ ,  $\beta$  approaches zero; and  $\beta = 3$  for light particles  $\rho_p/\rho \ll 1$  (Rani and Balachandar, 2004). Eq. (5.11) is written in terms of  $\beta$  as

$$\frac{d\mathbf{V}_p}{dt} = \frac{1}{t_{pr}} (\mathbf{V}_c - \mathbf{V}_p) + \beta \frac{D\mathbf{V}_c}{Dt} + (1 - \beta) \mathbf{g} + \left( \frac{\beta}{t_{pr}} \right)^{1/2} t [\mathbf{V}_c - \mathbf{V}_p] \quad (5.13)$$

where  $\ell[\mathbf{V}_c - \mathbf{V}_p]$  is a linear operator and defined as

$$\ell[\mathbf{V}_c - \mathbf{V}_p] = \left( \sqrt{3} \frac{d^{1/2}}{dt^{1/2}} (\mathbf{V}_c - \mathbf{V}_p) + \frac{3\sqrt{3}J_\infty}{2\pi^2 \sqrt{|\omega|}} (\mathbf{V}_c - \mathbf{V}_p) \times \omega \right) \quad (5.14)$$

### 5.1.2.2 Eulerian–Eulerian approach

This approach can be applied when the particle size is small enough to move with the fluid flow. So, the model considers the dispersed (particle) phase as a continuous (fluid) phase, interpenetrating and interacting with the fluid phase (Gidaspow, 1994). Local equations for the instantaneous changes in each phase are introduced together with the local instantaneous conditions at the interface. Mass, momentum, and energy balance equations are also expressed in integral form for both phases. These equations must be averaged either in volume, in space, in time, or as an ensemble (Sections 5.2 and 5.5). Additional equations, known as the constitutive equations (closure laws), are required to describe particle–particle interactions as well. The constitutive equations are derived under empirical assumptions or kinetic theory describing granular-matter or flow.

The number of model equations is also affected by the particle size and size distribution. If the particles forming the dispersed phase have a wide size distribution, the number of model equations describing velocity and concentration profiles for the particulate phase increases as a result of the simultaneous consideration of all particles. Besides, the solution of the momentum equations for the particle phase becomes difficult for very small particles.

The *fast or equilibrium Eulerian approach* is proposed to find the Eulerian velocity distribution of the particulate phase  $\mathbf{V}_p(t, \mathbf{x})$  for small particle time-scales,  $t_{pr}$  (eq. (5.7)). This approach eliminates the additional momentum equations arising from the small particle size and/or wide size distribution of particles. When  $t_{pr}$ , time-scale, is small,  $\mathbf{V}_p = \mathbf{V}_p(t, \mathbf{x})$  is solved in terms of  $\mathbf{V}_c = \mathbf{V}_c(t, \mathbf{x})$ . If  $\beta = 1$ ,  $\mathbf{V}_p(t, \mathbf{x})$  equals  $\mathbf{V}_c(t, \mathbf{x})$ , the equation of the particle velocity becomes:

$$\mathbf{V}_p = \mathbf{V}_c + (1 - \beta) \left( -\mathbf{a} t_{pr} + \sqrt{\beta} \ell \mathbf{a} t_{pr}^{3/2} + \left( \frac{D\mathbf{a}}{Dt} + \mathbf{a} \cdot \nabla \mathbf{V}_c - \beta \ell^2 \mathbf{a} \right) t_{pr}^2 \right) + O(t_{pr}^{5/2}) \quad (5.15)$$

where  $\mathbf{a}$  includes the substantial derivative of the liquid phase and gravitational acceleration term, as

$$\mathbf{a} = \frac{D\mathbf{V}_c}{Dt} - \mathbf{g} \quad (5.16)$$

and  $d^{1/2}/dt^{1/2}$  in the definition of  $\ell[\mathbf{V}_c - \mathbf{V}_p]$  in eq. (5.14) is replaced with  $D^{1/2}/Dt^{1/2}$  collecting the difference into the  $O(t_{pr}^{5/2})$  term in eq. (5.15), the general expansion for the equilibrium Eulerian velocity distribution of the particle phase. For instance, when the gravitational force is dominant,  $\mathbf{V}_t = (1 - \beta)t_{pr} \mathbf{g}$ , the general equation is reduced to eq. (5.17) given in Table 5.2. Other simplifications are also given in the same table (Ferry and Balachandar, 2001).

**Table 5.2**

Simplified forms of particle velocity distribution based on fast Eulerian approach

Gravitational force is dominant:

$$\mathbf{V}_p = \mathbf{V}_c + \mathbf{V}_t - \sqrt{\beta\ell}\mathbf{V}_t t_{pr}^{1/2} - \left( (1-\beta)\frac{D\mathbf{V}_c}{Dt} + \frac{D\mathbf{V}_t}{Dt} \right) t_{pr} - (\mathbf{V}_t \cdot \nabla (\mathbf{V}_c + \mathbf{V}_t) - \beta\ell^2 \mathbf{V}_t) t_{pr} + O(t_{pr}^{3/2}) \quad (5.17)$$

Generally  $\mathbf{g}$  and, consequently,  $\mathbf{V}_t$  are constant over space and time, so the Basset force component of  $\ell\mathbf{V}_t = 0$  and the Saffman lift force becomes dominant:

$$\mathbf{V}_p = \mathbf{V}_c + \mathbf{V}_t + \frac{3J_\infty}{2\pi^2} \sqrt{\frac{3\beta t_{pr}}{|\omega|}} \omega \times \mathbf{V}_t + O(t_{pr}) \quad (5.18)$$

In the dense particles  $\beta \rightarrow 0$ , the Saffman lift force is not effective:

$$\mathbf{V}_p = \mathbf{V}_c + \mathbf{V}_t - \left( \frac{D\mathbf{V}_c}{Dt} + \mathbf{V}_t \cdot \nabla \mathbf{V}_c \right) t_{pr} + O(t_{pr}^2) \quad (5.19)$$

For too small particles, Basset and Saffman lift forces are omitted,  $\ell$  is ignored.

$$\mathbf{V}_p = \mathbf{V}_c + (1-\beta) \left( -\mathbf{a} t_{pr} + \left( \frac{D\mathbf{a}}{Dt} + \mathbf{a} \cdot \nabla \mathbf{V}_c \right) t_{pr}^2 \right) + O(t_{pr}^3) \quad (5.20)$$

Drag force, gravitational force, and collisional effects are omitted (Rani and Balachandar, 2004):

$$\mathbf{V}_p(t, \mathbf{x}) \approx \mathbf{V}_{p,eq} = \mathbf{V}_c - (1-\beta) t_{pr} \frac{D\mathbf{V}_c}{Dt} + O(t_{pr}^2) \quad (5.21)$$

## 5.2 AVERAGING TECHNIQUES FOR MODEL EQUATIONS

In a flow system, properties of solid–liquid suspensions change in all directions due to its heterogeneous nature. So, the corresponding transport equations are averaged and written in terms of time, volume/area, or ensemble averages depending on the used averaging technique to simplify the variables of the system.

### 5.2.1 Time averaging techniques

Macroscopic properties are generally expressed as the averages of molecular properties with respect to time and/or position. Statistical averaging techniques are used to obtain useful property calculations from molecular states, since they are realistic and consistent with experiment. A time-averaged value of a molecular property,  $\bar{g}_{pf}$ , is described using the local instantaneous values of a property,  $g_{pf}$ , which may be in scalar, vector, or tensor form.

$\bar{g}_{\text{pf}}$  can be written (at around the fluctuation values of local property,  $g_{\text{pf}}$ ) in terms of continuous function as in eq. (5.22) or in terms of discrete function as in eq. (5.23)

$$\bar{g}_{\text{pf}} = \lim_{t \rightarrow \infty} \frac{1}{t} \int_0^t g_{\text{pf}} dt' \quad (5.22)$$

where  $t'$  is time and  $t$  the total time.

$$\bar{g}_{\text{pf}} = \lim_{t \rightarrow \infty} \frac{1}{t} \sum_i g_{\text{pf},i} \Delta t_i \quad (5.23)$$

where  $g_{\text{pf},i}$  is local instantaneous value of a property,  $g_{\text{pf}}$ .

### 5.2.2 Volume and area averaging techniques

*Volume averaging* is done around a fixed point,  $x$ , in space at a certain time. The mean (volume-averaged) value of a property at position  $x$  is defined in terms of the continuity function as

$$\bar{g}_{\text{pf}} \Big|_{x, v_T} = \frac{1}{v_T} \int_{v_T} g_{\text{pf}} dv \quad (5.24)$$

where  $v$  denotes volume and  $v_T$  the total volume or in terms of discrete function as

$$\bar{g}_{\text{pf}} \Big|_{x, v_T} = \frac{1}{v_T} \sum_i g_{\text{pf},i} \Delta v_i \quad (5.25)$$

The averaging procedures have some limitations because of the dimension of the control element. In the case of the volume averaging technique, the dimension of the selected control volume must be larger than that of the particle size and less than that of the physical system.

*Area averaging* is done similarly around a fixed point  $x$  at a certain time along an area and can be calculated in terms of continuity function as

$$\bar{g}_{\text{pf}} \Big|_{x, A_T} = \frac{1}{A_T} \int_{A_T} g_{\text{pf}} dA \quad (5.26)$$

where  $A$  is area and  $A_T$  the total area. The area-averaged property is also defined as a function of discrete function as

$$\bar{g}_{\text{pf}} \Big|_{x, A_T} = \frac{1}{A_T} \sum_i g_{\text{pf},i} \Delta A_i \quad (5.27)$$

The relation between the area- and volume-averaged values of a property is given as in the following equation in the form of continuous functions:

$$\bar{g}_{\text{pf}}|_{x,v_T} = \frac{1}{A_T L} \int_L \int_{A_T} g_{\text{pf}} dA dx = \frac{1}{v_T} \int_L \int_{A_T} g_{\text{pf}} dA dx = \frac{1}{v_T} \int_L \bar{g}_{\text{pf}}|_{x,A_T} dx \quad (5.28)$$

or given in terms of discrete function as

$$\begin{aligned} \bar{g}_{\text{pf}}|_{x,v_T} &= \frac{1}{A_T L} \sum_i \left( \sum_i g_{\text{pf},i} \Delta A_i \right) \Delta x_i = \frac{1}{v_T} \sum_i \left( \sum_i g_{\text{pf},i} \Delta A_i \right) \Delta x_i \\ &= \frac{1}{v_T} \sum_i \bar{g}_{\text{pf}}|_{x,A_T} \Delta x_i \end{aligned} \quad (5.29)$$

where  $L$  is the length of the system in the flow direction.

### 5.2.2.1 Averages of volume-averaged properties

Volume and area averages of a volume-averaged property are written in eqs. (5.30) and (5.31), respectively. If the dimensions of the particulates forming the phase are too small compared to the characteristic length of the system (i.e., pipe diameter in the pipeline), the RHS of eq. (5.30) is defined by eq. (5.24) to find the volume average of the local volume-averaged property and hence,  $\bar{g}_{\text{pf}}|_{x,v_T,v_T} = \bar{g}_{\text{pf}}|_{x,v_T}$ . Similarly, eq. (5.26) is used to define the RHS of eq. (5.31) under the same conditions and then, the area average of the local volume-averaged property is found to be  $\bar{g}_{\text{pf}}|_{x,v_T,A_T} = \bar{g}_{\text{pf}}|_{x,A_T}$  (Slattery, 1978)

$$\bar{g}_{\text{pf}}|_{x,v_T,v_T} = \frac{1}{v_T} \int_{v_T} \bar{g}_{\text{pf}}|_{x,v_T} dv = \frac{1}{v_T^2} \int_{v_T} \int_{v_T} g_{\text{pf}} dv dv \quad (5.30)$$

$$\bar{g}_{\text{pf}}|_{x,v_T,A_T} = \frac{1}{A_T} \int_{A_T} \bar{g}_{\text{pf}}|_{x,v_T} dA = \frac{1}{A_T v_T} \int_{A_T} \int_{v_T} g_{\text{pf}} dv dA \quad (5.31)$$

The volume and space averaging can also be considered as approximations of ensemble averaging, because it can be viewed as the statistical average.

## 5.2.3 The ensemble averaging techniques

A macrosystem or state constituted of atoms, molecules, or particles is statistically considered to be formed of a large number of distinct microstates (or microsystems) at any time under the same macroscopic conditions.

The microstates at any time are defined by specifying the instantaneous positions ( $x_i$ ) and momenta ( $p_i$ ) of all particles depending on the three dimensions of the coordinate system. If  $N$  number of particles exist in the system, a  $6N$ -dimensional space, called *phase space*, is

identified by the  $3N$  positions (i.e.,  $x_1, x_2, \dots, x_{3N}$ ) and  $3N$  momenta (i.e.,  $p_1, p_2, \dots, p_{3N}$ ) coordinates. So, a representative *phase point* defined by  $x_i$  and  $p_i$  coordinates for a microstate,  $(x_i, p_i)$ , continuously changes as time passes. The changes form a path of the microstate moving under given forces, so a *trajectory* is taken from the microstate. At any time, the direction of the trajectory is determined by the generalized velocity,  $\dot{x}_i$  ( $\dot{x}_i = dx_i/dt$ ), and the corresponding generalized momentum,  $\dot{p}_i$ , known as *conjugate momenta* (one corresponding momentum for each generalized velocity).

A statistical collection of representative phase points for all microstates through which the macrosystem would pass in time is called an *ensemble* (a set of motions possible in the system). So, expected value of a property ( $g_{pf}$ ) found statistically from this local instantaneous representation and its probability is called the *ensemble average*,  $\bar{g}_{pf,E}$ .

$$\bar{g}_{pf,E}(x,t) = \sum_i P_i(\zeta) g_{pf,i}(x,t;\zeta) \quad (5.32)$$

where  $P_i$  is the probability of the quantity ( $g_{pf}$ ), found in a particular region of the phase space. Ensemble average in terms of probabilities can be written as a continuous function (Drew and Passman, 1999; Tiwari *et al.*, 2006):

$$\bar{g}_{pf,E}(x,t) = \int_E g_{pf}(x,t;\zeta) dP(\zeta) \quad (5.33)$$

where  $dP(\zeta)$  is the probability density function obtained by observing the quantity ( $g_{pf}$ ) for some particular collection (realization)  $\zeta$ , on the ensemble,  $E$ , that is the set of all possible motions in the system.

### 5.3 MATHEMATICAL REQUIREMENTS FOR AVERAGING TRANSPORT EQUATIONS

In a mixture where more than one phase exists, the volume averaging of a property in any phase  $k$  can be defined similar to eq. (5.24) over the whole volume,  $v_T$ , as in eq. (5.34) or over the volume of phase  $k$ ,  $v_k$ , as in eq. (5.35) (Wörner, 2003; Munkejord, 2006)

$$\bar{g}_{pf,k} \Big|_{x,v_T} = \frac{1}{v_T} \int_{v_T} g_{pf,k} X_k dv \quad (5.34)$$

$$\bar{g}_{pf,k} \Big|_{x,v_k} = \frac{1}{v_k} \int_{v_T} g_{pf,k} X_k dv \quad (5.35)$$

where  $X_k$  is a factor known as a *phase indicator function* or *characteristic function* that depends on position,  $x$ , and time,  $t$ . The phase indicator function,  $X_k$ , theoretically separates

each phase and identifies the presence of  $k^{th}$  phase. If the position vector,  $\mathbf{x}$ , is in the phase  $k$  at time  $t$ ,  $X_k$  becomes 1 and equals 0 for other states

$$X_k = \begin{cases} 1, & \text{if } \mathbf{x} \in k \text{ phase} \\ 0, & \text{otherwise} \end{cases} \quad (5.36)$$

In ensemble averaging,  $X_k$  is defined (Munkejord, 2006; Tiwari *et al.*, 2006) by

$$X_k(\mathbf{x}, t; \zeta) = \begin{cases} 1, & \text{if } \mathbf{x} \in k \text{ phase in realization, } \zeta \\ 0, & \text{otherwise} \end{cases} \quad (5.37)$$

If eq. (5.34) is compared with eq. (5.35)

$$\frac{\bar{g}_{pf,k} \big|_{x, v_T}}{\bar{g}_{pf,k} \big|_{x, v_k}} = \frac{v_k}{v_T} = \bar{\phi}_k \quad (5.38)$$

The ratio obtained signifies that these averages are linearly related to each other through the volume fraction of the phase  $k$ ,  $\bar{\phi}_k$ . The local average of the volumetric fraction of phase  $k$  can similarly be expressed by the phase indicator function as  $\bar{\phi}_k = \bar{X}_{k,E}(\mathbf{x}, t; \zeta)$  according to the ensemble averaging technique (eq. (5.33)) at the interface of the phases (Munkejord, 2006; Tiwari *et al.*, 2006) as

$$\bar{\phi}_k = \bar{X}_{k,E}(x, t) = \int_E X_k(x, t; \zeta) dP(\zeta) \quad (5.39)$$

Derivation of model equations for two- or multi-phase flows requires the use of both volume and ensemble averaging techniques. Mathematical operations, used in averaging techniques, are the averages of derivatives, topological equation, and Gauss and Leibniz rules. In addition to these, Reynolds rules are necessary in ensemble averaging to derive the averaged model equations.

The average of derivatives based on position is defined by the *Slattery volume averaging theorem* (1978) of a gradient as

$$\begin{aligned} \overline{\nabla g_{pf,k}} &= \frac{1}{v_T} \int_{v_k} \nabla g_{pf,k} dv = \nabla \left( \frac{1}{v_T} \int_{v_k} g_{pf,k} dv \right) + \frac{1}{v_T} \int_{S_k} g_{pf,k} \mathbf{n}_k dS \\ &= \nabla \bar{g}_{pf,k} + \frac{1}{v_T} \int_{S_k} g_{pf,k} \mathbf{n}_k dS \end{aligned} \quad (5.40)$$

where  $\mathbf{n}_k$  is the normal vector and  $S_k$  the surface area of volume,  $v_k$ . A special case of eq. (5.40), known as the *theorem for the volume average of a divergence* (Slattery, 1978), is

$$\overline{\nabla \cdot \mathbf{g}_{pf,k}} = \frac{1}{v_T} \int_{v_k} \nabla \cdot \mathbf{g}_{pf,k} dv = \nabla \cdot \bar{\mathbf{g}}_{pf,k} + \frac{1}{v_T} \int_{S_k} \mathbf{g}_{pf,k} \cdot \mathbf{n}_k dS \quad (5.41)$$



where the property  $g_{\text{pf},k}$  is considered as vector or tensor field. The volume average of time derivatives is determined by the *Reynolds transport theorem* (Munkejord, 2006) as

$$\overline{\frac{\partial g_{\text{pf},k}}{\partial t}} = \frac{\partial \overline{g_{\text{pf},k}}}{\partial t} - \frac{1}{v_T} \int_{S_k} g_{\text{pf},k} \mathbf{V}_i \cdot \mathbf{n}_k dS \quad (5.42)$$

where  $\mathbf{V}_i$  is the velocity vector at the interface and  $\mathbf{V}_i \cdot \mathbf{n}_k$  the rate of displacement of the interface.

The *Gauss rule* (Wörner, 2003; Munkejord, 2006) is written as

$$(\overline{X_k \nabla g_{\text{pf},k}})_J = (\nabla \overline{X_k g_{\text{pf},k}})_J - (\overline{g_{\text{pf},k,i} \nabla X_k})_J, \quad J = v, E \quad (5.43)$$

where  $g_{\text{pf},k}$  may be scalar or vector quantity and  $g_{\text{pf},k,i}$  is the value of this quantity on the  $k$  phase side of the interface. Subscript  $J$  in this equation becomes  $v$  in volume averaging and  $E$  in ensemble averaging. In volume averaging, Gauss rule is also written as

$$(\overline{X_k \nabla g_{\text{pf},k}})_{v_T} = (\nabla \overline{X_k g_{\text{pf},k}})_{v_T} - \frac{1}{v_T} \int_{(S_i \cap v_T)} \mathbf{n}_k g_{\text{pf},k,i} dS \quad (5.44)$$

where  $(S_i \cap v_T)$  shows the part of the interface which remains inside the averaging volume,  $v_T$ .

Similar to eq. (5.43), the averages involving the time averages are given by

$$X_k \frac{\partial \overline{g_{\text{pf},k}}}{\partial t} = \frac{\partial}{\partial t} \overline{X_k g_{\text{pf},k}} - \overline{g_{\text{pf},k} \frac{\partial X_k}{\partial t}}, \quad J = v, E \quad (5.45)$$

$\partial X_k / \partial t$  in the above equation can be expressed from the topological equation, given as

$$\frac{\partial X_k}{\partial t} + \mathbf{V}_i \cdot \nabla X_k = 0 \quad (5.46)$$

The above equation is the substantial derivative of  $X_k$  at the interface and this derivative is zero due to constant jump in  $X_k$  for a point moving with the interface velocity. Substitution of  $\partial X_k / \partial t$  definition in eq. (5.46) into eq. (5.45) gives the *Leibniz rule* (Wörner, 2003; Munkejord, 2006) as

$$\left( \overline{X_k \frac{\partial g_{\text{pf},k}}{\partial t}} \right)_J = \left( \frac{\partial}{\partial t} \overline{X_k g_{\text{pf},k}} \right)_J + (\overline{g_{\text{pf},k,i} \mathbf{V}_i \cdot \nabla X_k})_J, \quad J = v, E \quad (5.47)$$

The above equation can be used for both volume and ensemble averaging. Leibniz rule for volume averaging is also written as

$$\left( \overline{X_k \frac{\partial g_{\text{pf},k}}{\partial t}} \right)_{v_T} = \left( \frac{\partial}{\partial t} \overline{X_k g_{\text{pf},k}} \right)_{v_T} + \frac{1}{v_T} \int_{(S_i \cap v_T)} \mathbf{n}_k \cdot \mathbf{V}_i g_{\text{pf},k,i} dS \quad (5.47a)$$

The *Reynolds rules*, required in the development of the model equations for the multiphase flow, are related to linearity property (Munkejord, 2006) as explained before. If collections of the property  $g_{\text{pf}}$  in phases (fields) 1 and 2 ( $g_{\text{pf},1}$  and  $g_{\text{pf},2}$ , respectively) are in the same ensemble,  $E$ , or in different ensembles such as  $E_1$  and  $E_2$ , the Reynolds rule is

$$\overline{(C_1 g_{\text{pf},1} + C_2 g_{\text{pf},2})_E} = C_1 \overline{g_{\text{pf},1}} + C_2 \overline{g_{\text{pf},2}} \quad (5.48)$$

where  $C_1$  and  $C_2$  are constants. Furthermore, if collections are in the same ensemble, another Reynolds rule definition can be used as

$$\overline{g_{\text{pf},1} g_{\text{pf},2}} = (\overline{g_{\text{pf},1}})(\overline{g_{\text{pf},2}}) \quad (5.49)$$

## 5.4 BASIC EQUATIONS FOR SOLID–LIQUID SUSPENSION FLOWS

The continuity and momentum equations for a single-phase flow were given in eqs. (5.1) and (5.4), respectively. The continuity equation can be rewritten for any phase  $k$  in a suspension flow as

$$\frac{\partial \rho_k}{\partial t} + \nabla \cdot (\rho_k \mathbf{V}_k) = 0 \quad (5.50)$$

where  $\rho_k$  is the density and  $\mathbf{v}_k$  the velocity vector of  $k$  phase. Also, the momentum equation for any phase  $k$  becomes

$$\frac{\partial(\rho_k \mathbf{V}_k)}{\partial t} + \nabla \cdot (\rho_k \mathbf{V}_k \mathbf{V}_k) = -\nabla p_k - \nabla \cdot \boldsymbol{\tau}_k + \rho_k \mathbf{g} \quad (5.51)$$

or is written in terms of total stress tensor,  $\mathbf{T}_k$ , as

$$\frac{\partial(\rho_k \mathbf{V}_k)}{\partial t} + \nabla \cdot (\rho_k \mathbf{v}_k \mathbf{v}_k) = \nabla \cdot \mathbf{T}_k + \rho_k \mathbf{g} \quad (5.52)$$

where  $p_k$  and  $\boldsymbol{\tau}_k$  are the pressure and the shear stress in  $k$  phase. The total stress tensor is defined as

$$\mathbf{T}_k = -\mathbf{I}p_k + \boldsymbol{\tau}_k \quad (5.53)$$

where  $\mathbf{I}$  is the unit tensor.

Due to existence of more than one phase, an interface formed between the two phases necessitates additional relations, which are derived by considering two control volumes given in Figure 5.1: one of the control volumes includes more than one phase (i.e., suspension— $s$  phase) and the other one corresponds to interacting phase  $k$  (i.e., particulate or suspending liquid phase). The control volume of  $s$  phase is  $v_s$  and its total volume,  $v_T$ . The volume of  $k$  phase remaining inside the control volume,  $v_s$ , in Figure 5.1 is  $v_k$ . The interface

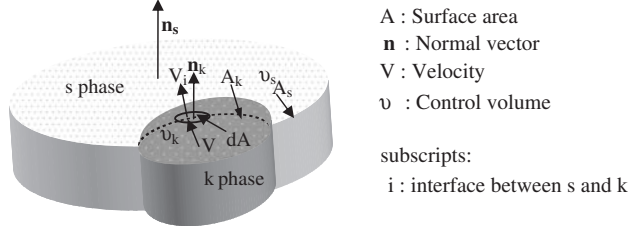


**Figure 5.1** Schematic presentation of control volumes of interacting  $s$  and  $k$  phases.

mass balance is written on the interface (denoted by curved dash line in Figure 5.1) between  $k$  and  $s$  phases and expressed as

$$\rho_k (\mathbf{V}_k - \mathbf{V}_i) \cdot \mathbf{n}_k + \rho_s (\mathbf{V}_s - \mathbf{V}_i) \cdot \mathbf{n} = 0 \quad (5.54)$$

where  $\mathbf{V}_i$  is the velocity vector at the interface of  $s$  and  $k$  phases, and  $\rho_s$  and  $\mathbf{V}_s$  the density and the velocity vector of  $s$  phase. Eq. (5.54) states that the mass transfer from  $k$  to  $s$  phase equals that from  $s$  to  $k$  phase and they are opposite to each other. If  $(\mathbf{V}_k - \mathbf{V}_i) \cdot \mathbf{n}_k = 0$  or  $\mathbf{V}_k = \mathbf{V}_i = \mathbf{V}_s$ , the mass transfer at the interface does not take place.

The most general form of the momentum balance at the interface can be written as

$$\begin{aligned} & -\rho_k \mathbf{V}_k (\mathbf{V}_k - \mathbf{V}_i) \cdot \mathbf{n}_k - \rho_s \mathbf{V}_s (\mathbf{V}_s - \mathbf{V}_i) \cdot \mathbf{n}_s + (-\mathbf{I}p_k + \boldsymbol{\tau}_k) \cdot \mathbf{n}_k \\ & + (-\mathbf{I}p_s + \boldsymbol{\tau}_s) \cdot \mathbf{n}_s - (\nabla \sigma)_i + \sigma K \mathbf{n} = 0 \end{aligned} \quad (5.55)$$

where  $\sigma$  is the interfacial tension and  $K$  the mean curvature along the interface. The first two terms in this equation only take place in the presence of mass transfer between  $s$  and  $k$  phases. The third and fourth terms show the momentum due to pressure and shear stresses in  $k$  and  $s$  phases, respectively. The fifth term indicates the momentum arising due to changes in the interfacial tension along the interface, since variations in temperature, pressure, and the composition of the material at the interface affect the interfacial tension. The interfacial tension related the curvature of the interface causes the appearance of a force normal to the interface and causes a momentum defined by the last term in eq. (5.55).

In cases where there is no mass transfer at the interface between the phases, the forces due to interfacial tension are balanced by the pressure and shear stress forces and eq. (5.55) becomes

$$(-\mathbf{I}p_k + \boldsymbol{\tau}_k) \cdot \mathbf{n}_k + (-\mathbf{I}p_s + \boldsymbol{\tau}_s) \cdot \mathbf{n}_s - (\nabla \sigma)_i + \sigma K \mathbf{n} = 0 \quad (5.56)$$

In addition to the absence of mass transfer, if interfacial tension is negligible, the pressure and shear stresses of each phase become equal at the interface and eq. (5.55) is reduced to

$$(-\mathbf{I}p_k + \boldsymbol{\tau}_k) \cdot \mathbf{n}_k + (-\mathbf{I}p_s + \boldsymbol{\tau}_s) \cdot \mathbf{n}_s = 0 \quad (5.57)$$

## 5.5 ENSEMBLE AVERAGED EQUATIONS FOR TWO-FLUID MODEL

One of the convenient ways of averaging is to integrate the differential conservation equations of the  $k^{th}$  phase, eqs. (5.50) and (5.52), over a control volume,  $v$ , that is known as *volume averaging*. The other way is to integrate the differential equations over an ensemble,  $E$ , so it is called *ensemble averaging*. Ensemble averaging technique is taken up in this section.

### 5.5.1 Ensemble averaging of the generalized equation

Both the continuity and momentum equations (eqs. (5.50) and (5.52)) of phase  $k$  can be reduced to a single equation (eq. (5.58)) by introducing new variables such as  $\mathbf{g}_{pf,k}$ ,  $\mathbf{T}$ , and  $\mathbf{G}$

$$\frac{\partial(\rho_k \mathbf{g}_{pf,k})}{\partial t} + \nabla \cdot (\rho_k \mathbf{V}_k \mathbf{g}_{pf,k}) = \nabla \cdot \mathbf{T}_k + \rho_k \mathbf{G} \quad (5.58)$$

In continuity equation,  $\mathbf{g}_{pf,k} = 1$ , and  $\mathbf{T}$  and  $\mathbf{G}$  equal to zero, whereas  $\mathbf{g}_{pf,k} = \mathbf{V}_k$ ,  $\mathbf{T} = \mathbf{T}_k$ , and  $\mathbf{G} = \mathbf{g}$  in the momentum equation of the  $k^{th}$  phase.

Each term of eq. (5.58) is then multiplied by the density probability function of  $\mathbf{g}_{pf,k}$  for some particular realization,  $\zeta$  on the ensemble  $E$ ,  $dP(\zeta)$ , and integrated over  $E$  as

$$\int_E \frac{\partial}{\partial t} (\rho_k \mathbf{g}_{pf,k}) dP(\zeta) + \int_E \nabla \cdot (\rho_k \mathbf{V}_k \mathbf{g}_{pf,k}) dP(\zeta) - \int_E (\nabla \cdot \mathbf{T}_k) dP(\zeta) - \int_E (\rho_k \mathbf{G}) dP(\zeta) = 0 \quad (5.59)$$

All the terms in the above equation conform to the definition of the ensemble averaging similar to eq. (5.33) and the resultant equation is

$$\left( \overline{\frac{\partial}{\partial t} (\rho_k \mathbf{g}_{pf,k})} \right)_E + \overline{(\nabla \cdot (\rho_k \mathbf{V}_k \mathbf{g}_{pf,k}))}_E - \overline{(\nabla \cdot \mathbf{T}_k)}_E - \overline{(\rho_k \mathbf{G})}_E = 0 \quad (5.60)$$

The ensemble averaged equation (eq. (5.60)) is averaged once more to take the effect of the portion of the phase  $k$  in  $s$  phase into consideration: each term of eq. (5.60) is multiplied by the phase indicator function  $X_k$  and  $dP(\zeta)$  and then integrated for the ensemble averaging; the equation becomes

$$\int_E X_k \left( \overline{\frac{\partial}{\partial t} (\rho_k \mathbf{g}_{pf,k})} \right)_E dP(\zeta) + \int_E X_k \overline{(\nabla \cdot (\rho_k \mathbf{V}_k \mathbf{g}_{pf,k}))}_E dP(\zeta) - \int_E X_k \overline{(\nabla \cdot \mathbf{T}_k)}_E dP(\zeta) - \int_E X_k \overline{(\rho_k \mathbf{G})}_E dP(\zeta) = 0 \quad (5.61)$$

Integration of the above equation yields

$$\begin{aligned} & \left( \overline{X_k \left( \frac{\partial}{\partial t} (\rho_k \mathbf{g}_{pf,k}) \right)} \right)_E + \overline{(X_k (\nabla \cdot (\rho_k \mathbf{V}_k \mathbf{g}_{pf,k}))}_E - \overline{(X_k (\nabla \cdot \mathbf{T}_k))}_E \\ & - \overline{(X_k (\rho_k \mathbf{G} X_k))}_E = 0 \end{aligned} \quad (5.62)$$

Applying the Reynolds rule (eqs. (5.49)) to the above equation gives

$$\begin{aligned} & (\overline{X_k})_E \left( \overline{\frac{\partial}{\partial t} (\rho_k \mathbf{g}_{pf,k})} \right)_E + (\overline{X_k})_E \overline{(\nabla \cdot (\rho_k \mathbf{V}_k \mathbf{g}_{pf,k}))}_E - (\overline{X_k})_E \overline{(\nabla \cdot \mathbf{T}_k)}_E \\ & - (\overline{X_k})_E \overline{(\rho_k \mathbf{G})}_E = 0 \end{aligned} \quad (5.63)$$

Each term in this equation comprises the local average of the phase indicator function,  $(\overline{X_k})_E$ . Multiplication of two averaging quantities can be collected in the same averaging sign as

$$\left( \overline{X_k \frac{\partial}{\partial t} (\rho_k \mathbf{g}_{pf,k})} \right)_E + \overline{(X_k \nabla \cdot (\rho_k \mathbf{V}_k \mathbf{g}_{pf,k}))}_E - \overline{(X_k (\nabla \cdot \mathbf{T}_k))}_E - \overline{(X_k \rho_k \mathbf{G})}_E = 0 \quad (5.64)$$

Using eq. (5.45), the first term in the above equation is defined as

$$\left( \overline{X_k \frac{\partial \rho_k \mathbf{g}_{pf,k}}{\partial t}} \right)_E = \frac{\partial}{\partial t} \overline{(\rho_k \mathbf{g}_{pf,k} X_k)}_E - \left( \overline{\rho_k \mathbf{g}_{pf,k} \frac{\partial X_k}{\partial t}} \right)_E \quad (5.45a)$$

The change in phase indicator function with respect to time in the above equation is described by using the topological equation, eq. (5.46). Then, the Leibniz rule is obtained as

$$\left( \overline{X_k \frac{\partial \rho_k \mathbf{g}_{pf,k}}{\partial t}} \right)_E = \frac{\partial}{\partial t} \overline{(X_k \rho_k \mathbf{g}_{pf,k})}_E + \overline{(\rho_k \mathbf{g}_{pf,k,i} \mathbf{V}_i \nabla X_k)}_E \quad (5.47b)$$

The second and third terms in eq. (5.64) are written by applying the Gauss rule (eq. (5.43)) as

$$\overline{(X_k \nabla \cdot \rho_k \mathbf{V}_k \mathbf{g}_{pf,k})}_E = \overline{(\nabla X_k \rho_k \mathbf{V}_k \mathbf{g}_{pf,k})}_E - \overline{(\rho_k \mathbf{V}_k \mathbf{g}_{pf,k,i} \nabla X_k)}_E \quad (5.44a)$$

$$\overline{(X_k (\nabla \cdot \mathbf{T}_k))}_E = \overline{(\nabla \cdot (X_k \mathbf{T}_k))}_E - \overline{(\mathbf{T}_{ki} (\nabla \cdot X_k))}_E \quad (5.44b)$$

where  $\mathbf{T}_{ki}$  is the value of tensor,  $\mathbf{T}_k$ , at the interface of the continuous and dispersed phases. Substitution of eqs. (5.47b), (5.44a), and (5.44b) into eq. (5.64) gives

$$\begin{aligned} \frac{\partial}{\partial t} (\overline{X_k \rho_k \mathbf{g}_{pf,k}})_E + (\overline{\rho_k \mathbf{g}_{pf,ki} \nabla X_k})_E + (\overline{\nabla X_k \rho_k \mathbf{V}_k \mathbf{g}_{pf,k}})_E \\ - (\overline{\rho_k \mathbf{V}_k \mathbf{g}_{pf,ki} \nabla X_k})_E - (\overline{\nabla \cdot (X_k \mathbf{T}_k)})_E + (\overline{\mathbf{T}_{ki} (\nabla \cdot X_k)})_E - (\overline{X_k \rho_k \mathbf{G}})_E = 0 \end{aligned} \quad (5.65)$$

Rearrangement of the above equation yields the ensemble averaged conservation equation

$$\begin{aligned} \frac{\partial}{\partial t} (\overline{X_k \rho_k \mathbf{g}_{pf,k}})_E + (\overline{\nabla X_k \rho_k \mathbf{V}_k \mathbf{g}_{pf,k}})_E - (\overline{\nabla \cdot (X_k \mathbf{T}_k)})_E - (\overline{X_k \rho_k \mathbf{G}})_E \\ - (\overline{[\rho_k \mathbf{g}_{pf,ki} (\mathbf{V}_k - \mathbf{V}_i) - \mathbf{T}_{ki}] \nabla X_k})_E = 0 \end{aligned} \quad (5.66)$$

The ensemble average of the phase indicator function,  $(\bar{X}_k)_E$  (or  $\bar{X}_{k,E}$ ), equals the local average of volume fraction of the  $k^{\text{th}}$  phase ( $\bar{\phi}_k$ ) (eq. (5.39)) as explained in Section 5.3 and the general ensemble averaged equation becomes

$$\begin{aligned} \frac{\partial}{\partial t} (\overline{\phi_k \rho_k \mathbf{g}_{pf,k}})_E + (\overline{\nabla \phi_k \rho_k \mathbf{V}_k \mathbf{g}_{pf,k}})_E - (\overline{\nabla \cdot (\phi_k \mathbf{T}_k)})_E - (\overline{\phi_k \rho_k \mathbf{G}})_E \\ - (\overline{[\rho_k \mathbf{g}_{pf,ki} (\mathbf{V}_k - \mathbf{V}_i) - \mathbf{T}_{ki}] \nabla \phi_k})_E = 0 \end{aligned} \quad (5.67)$$

### 5.5.2 Ensemble averaged continuity equations

The ensemble averaged continuity equation for  $k$  phase from eq. (5.67) is derived by neglecting the bulk motion of the  $k^{\text{th}}$  phase (the phase indication function  $\mathbf{g}_{pf,k}=1$ ), pressure, shear stress and gravitational effects ( $\mathbf{T} = \mathbf{G} = 0$ ) as

$$\frac{\partial}{\partial t} (\overline{\phi_k \rho_k})_E + (\overline{\nabla \phi_k \rho_k \mathbf{V}_k})_E - (\overline{[\rho_k (\mathbf{V}_k - \mathbf{V}_i)] \nabla \phi_k})_E = 0 \quad (5.68)$$

or

$$\frac{\partial}{\partial t} (\bar{\phi}_k \bar{\rho}_k) + \nabla \cdot (\bar{\phi}_k \bar{\rho}_k \bar{\mathbf{V}}_k) - \mathbf{M}_{ms,k} = 0 \quad (5.68a)$$

where  $\mathbf{M}_{ms,k}$  is the ensemble averaged mass source of  $k$  phase at the interface of  $k$  and  $s$  phases, defined by

$$\mathbf{M}_{ms,k} = (\overline{[\rho_k (\mathbf{V}_k - \mathbf{V}_i)] \nabla \phi_k})_E \quad (5.69)$$

This term takes place in continuity equation in the presence of the mass transfer at the interface due to phase change. Sum of the ensemble averaged mass sources of dispersed (particle) and continuous (liquid) phases at the interface of these phases satisfies the conservation of the mass (eq. (5.54)), known as the jump conditions for mass transfer as

$$\mathbf{M}_{ms,p} + \mathbf{M}_{ms,c} = (\overline{[\rho_p (\mathbf{V}_p - \mathbf{V}_i)] \nabla \phi_p})_E + (\overline{[\rho_c (\mathbf{V}_c - \mathbf{V}_i)] \nabla \phi_c})_E = 0 \quad (5.70)$$

**Table 5.3**

Ensemble averaged continuity and momentum equations for suspension flow

Equation	Dispersed phase ( $k = p$ )
Continuity	$\frac{\partial(\bar{\phi}_p \rho_p)}{\partial t} + \nabla \cdot (\bar{\phi}_p \rho_p \bar{\mathbf{V}}_p) = 0 \quad (5.68b)$
Momentum	$\begin{aligned} \frac{\partial(\bar{\phi}_p \rho_p \bar{\mathbf{V}}_p)}{\partial t} + \nabla \cdot (\bar{\phi}_p \rho_p \bar{\mathbf{V}}_p \bar{\mathbf{V}}_p) = & -\bar{\phi}_p \nabla \bar{p}_p \\ & -(\bar{p}_p - \bar{p}_{pi}) \nabla \bar{\phi}_p + (\bar{\boldsymbol{\tau}}_p - \bar{\boldsymbol{\tau}}_{pi}) \cdot \nabla \bar{\phi}_p \\ & + \bar{\phi}_p (\nabla \cdot \bar{\boldsymbol{\tau}}_p) + \bar{\phi}_p \rho_p \mathbf{g} - \mathbf{F}_{Dc} - \mathbf{F}_{o,c} \\ & + \bar{\phi}_p (\nabla \cdot \bar{\boldsymbol{\tau}}_{ci} - \nabla \cdot \bar{\boldsymbol{\tau}}_{pi}) - \bar{\phi}_p \nabla (\bar{p}_{ci} - \bar{p}_{pi}) \end{aligned} \quad (5.77a)$
Continuous phase ( $k = c$ )	
Continuity	$\frac{\partial(\bar{\phi}_c \rho_c)}{\partial t} + \nabla \cdot (\bar{\phi}_c \rho_c \bar{\mathbf{V}}_c) = 0 \quad (5.68c)$
Momentum	$\begin{aligned} \frac{\partial(\bar{\phi}_c \rho_c \bar{\mathbf{V}}_c)}{\partial t} + \nabla \cdot (\bar{\phi}_c \rho_c \bar{\mathbf{V}}_c \bar{\mathbf{V}}_c) = & -\bar{\phi}_c \nabla \bar{p}_c \\ & -(\bar{p}_c - \bar{p}_{ci}) \nabla \bar{\phi}_c + (\bar{\boldsymbol{\tau}}_c - \bar{\boldsymbol{\tau}}_{ci}) \cdot \nabla \bar{\phi}_c \\ & + \bar{\phi}_c (\nabla \cdot \bar{\boldsymbol{\tau}}_c) + \bar{\phi}_c \rho_c \mathbf{g} + \mathbf{F}_{Dc} + \mathbf{F}_{o,c} \end{aligned} \quad (5.77b)$
	$\mathbf{F}_{o,c} = \mathbf{F}_{L,c} + \mathbf{F}_{VM,c} + \mathbf{F}_{T,c} + \dots \quad (5.75a)$

In the absence of the mass transfer at the interface, the velocity at the interface is continuous and hence,  $\mathbf{V}_p = \mathbf{V}_c = \mathbf{V}_i$  and  $\mathbf{M}_{ms,p} = \mathbf{M}_{ms,c} = 0$ .

In solid–liquid suspension flow, application of the continuity equation related to multi-phase flow (eq. (5.68) or (5.68a)) gives two different continuity equations: the first one is for the dispersed phase and the other for the continuous phases. These equations are summarized in Table 5.3 for the case of no mass transfer at the interface.

### 5.5.3 Ensemble averaged momentum equations

The ensemble averaged momentum equation is derived from eq. (5.67) by considering the effects of the bulk motion of the  $k^{\text{th}}$  phase ( $\mathbf{g}_{pf,k} = \mathbf{V}_k$ ), gravitational ( $\mathbf{G} = \mathbf{g}$ ), pressure and shear stresses ( $\mathbf{T}_k$  as in eq. (5.53)).

$$\begin{aligned} \frac{\partial}{\partial t} (\overline{\phi_k \rho_k \mathbf{V}_k})_E + (\nabla \cdot \overline{\phi_k \rho_k \mathbf{V}_k \mathbf{V}_k})_E - (\nabla \cdot (\overline{\phi_k (-\mathbf{I} p_k + \boldsymbol{\tau}_k)}))_E - (\overline{\phi_k \rho_k \mathbf{g}})_E \\ - (\overline{[\rho_k \mathbf{V}_{ki} (\mathbf{V}_k - \mathbf{V}_i) - (-\mathbf{I} p_{ki} + \boldsymbol{\tau}_{ki})] \nabla \phi_k})_E = 0 \end{aligned} \quad (5.71)$$

The third and fifth terms of the above equation are written using Reynolds rule (eq. (5.48)) as

$$\begin{aligned} & \frac{\partial}{\partial t} (\overline{\phi_k \rho_k \mathbf{V}_k})_E + (\nabla \overline{\phi_k \rho_k \mathbf{V}_k \mathbf{V}_k})_E + (\nabla \cdot (\overline{\phi_k \mathbf{I} p_k}))_E - (\nabla \cdot (\overline{\phi_k \boldsymbol{\tau}_k}))_E \\ & - (\overline{\phi_k \rho_k g})_E - (\overline{[\rho_k \mathbf{V}_{ki} (\mathbf{V}_k - \mathbf{V}_i)] \nabla \phi_k}) - [-(\overline{(-\mathbf{I} p_{ki} + \boldsymbol{\tau}_{ki}) \nabla \phi_k})_E] = 0 \end{aligned} \quad (5.72)$$

where the sixth term points out the averaged interfacial momentum transfer  $\mathbf{F}_{k,ms,i}$ , due to mass transfer at the interface between the phases and is also defined using eq. (5.69) by

$$\begin{aligned} \mathbf{F}_{k,ms,i} &= (\overline{[\rho_k \mathbf{V}_{ki} (\mathbf{V}_k - \mathbf{V}_i)] \nabla \phi_k})_E \\ &= (\overline{[\rho_k (\mathbf{V}_k - \mathbf{V}_i)] \nabla \phi_k})_E (\bar{\mathbf{V}}_{ki})_E = \mathbf{M}_{ms,k} \bar{\mathbf{V}}_{ki} \end{aligned} \quad (5.73)$$

The last term in eq. (5.72) gives the averaged interfacial momentum transfer or interfacial force per unit volume due to pressure and shear stress. It can be written in terms of  $\mathbf{T}_{ki}$  as

$$\mathbf{F}_{ki} = -(\overline{(-\mathbf{I} p_{ki} + \boldsymbol{\tau}_{ki}) \nabla \phi_k})_E = -\bar{\mathbf{T}}_{ki} \cdot \nabla \bar{\phi}_k \quad (5.74)$$

The interfacial force per unit volume,  $\mathbf{F}_{ki}$  (or interfacial force density) generally includes additional two terms in addition to the terms given in eq. (5.74), that corresponds to the drag and other interfacial (lift, virtual mass, turbulent dispersion etc) forces. Using the ensemble averaging concepts for these drag and other interfacial force densities such as  $\mathbf{F}_{Dk}$  and  $\mathbf{F}_{o,k}$ , respectively, eq. (5.74) becomes

$$\mathbf{F}_{ki} = \bar{p}_{ki} \nabla \bar{\phi}_k - \bar{\boldsymbol{\tau}}_{ki} \cdot \nabla \bar{\phi}_k + \mathbf{F}_{Dk} + \mathbf{F}_{o,k} \quad (5.75)$$

where  $\mathbf{F}_{o,k}$  term covers the lift,  $\mathbf{F}_{Lk}$ , virtual (added) mass,  $\mathbf{F}_{VM,k}$ , turbulent dispersion,  $\mathbf{F}_{T,k}$ , and other effects

$$\mathbf{F}_{o,k} = \mathbf{F}_{Lk} + \mathbf{F}_{VM,k} + \mathbf{F}_{T,k} + \dots \quad (5.76)$$

The averaged momentum balance (eq. (5.72) is also written by using the definitions given in eqs. (5.73)–(5.75) as

$$\begin{aligned} & \frac{\partial (\bar{\phi}_k \bar{\rho}_k \bar{\mathbf{V}}_k)}{\partial t} + \nabla \cdot (\bar{\phi}_k \bar{\rho}_k \bar{\mathbf{V}}_k \bar{\mathbf{V}}_k) + \nabla (\bar{\phi}_k \bar{\mathbf{I} p_k}) - \nabla \cdot (\bar{\phi}_k \bar{\boldsymbol{\tau}}_k) - \bar{\phi}_k \bar{\rho}_k g \\ & - \mathbf{F}_{k,ms,i} - \underbrace{[\bar{p}_{ki} \nabla \bar{\phi}_k - \bar{\boldsymbol{\tau}}_{ki} \cdot \nabla \bar{\phi}_k + \mathbf{F}_{Dk} + \mathbf{F}_{o,k}]}_{\mathbf{F}_{ki}} = 0 \end{aligned} \quad (5.77)$$

The sum of the momentum transfers of any two phases at the interface satisfies the interface momentum balance, known as the momentum jump. Substituting the equations of the averaged interfacial forces due to the mass transfer taking place at the interface ( $\mathbf{F}_{k,ms,i}$ ,  $\mathbf{F}_{s,ms,i}$ ) and due to the total stresses ( $\mathbf{F}_{k,i}$ ,  $\mathbf{F}_{s,i}$ ) for the phases  $k$  and  $s$  into eq. (5.55), the jump condition at the interface becomes

$$\mathbf{M}_{ms,k} \bar{\mathbf{V}}_{ki} + \mathbf{M}_{ms,s} \bar{\mathbf{V}}_{si} + \mathbf{F}_{ki} + \mathbf{F}_{si} + \mathbf{F}_\sigma = 0 \quad (5.78)$$



where similar to eqs. (5.73) and (5.74)  $\mathbf{F}_{s,ms,i} = \mathbf{M}_{ms,s} \bar{\mathbf{V}}_{si}$  and  $\mathbf{F}_{si} = -\bar{\mathbf{T}}_{si} \cdot \bar{\nabla} \bar{\phi}_s$ , respectively.  $\mathbf{F}_\sigma$  is the interfacial force due to surface tension. If the surface tension is independent of position, the ensemble averaged force due to surface tension equals  $\mathbf{F}_\sigma = \sigma \bar{K}$ .

Momentum equations for the dispersed and continuous phases are defined using eq. (5.77) together with eqs. (5.73) and (5.78) in the absence of mass transfer at the interface and summarized in Table 5.3, where  $\bar{p}_c$  and  $\bar{p}_p$  are the ensemble averaged pressures of the continuous and dispersed phases, respectively.  $\bar{p}_{ci}$  and  $\bar{p}_{pi}$  are the interfacial pressures of the corresponding phases. Similarly,  $\bar{\tau}_c$  and  $\bar{\tau}_p$  are the ensemble averaged shear stresses of the continuous and dispersed phases.  $\bar{\tau}_{ci}$  and  $\bar{\tau}_{pi}$  are interfacial shear stresses of the phases. The last two terms in eq. (5.77a) denote the jump conditions across the interface.

The relation between the pressures of the phases and their pressures at the interface depends on the rigidity of the particles forming the dispersed phase: for deformable particles such as liquid droplets or gas bubbles, an interfacial pressure jump in eqs. (5.77a) and (5.77b) occurs due to surface tension

$$\bar{p}_{pi} - \bar{p}_{ci} = \sigma \bar{K} \quad (5.79)$$

where  $\bar{K}$  is the curvature of ensembled particle. When the particles are rigid, the pressures within the solid particle and on its surface are the same, so  $\bar{p}_p = \bar{p}_{pi} = \bar{p}_{ci}$ . The effect of the pressure jump is neglected for small rigid solid particles, so  $\bar{p}_{pi} \approx \bar{p}_{ci}$ . If the deformation of the particles is very small, the shear stress across the particle–liquid interface maintains continuity, and  $\bar{\tau}_p = \bar{\tau}_{pi} = \bar{\tau}_{ci}$ .

Due to the equivalence of pressures at the interfaces of the particles, the terms giving the pressure and shear stress differences between the interface and the particle, and their gradients vanish. Hence, eq. (5.77a) is reduced to the following equation:

$$\frac{\partial(\bar{\phi}_p \rho_p \bar{\mathbf{V}}_p)}{\partial t} + \nabla \cdot (\bar{\phi}_p \rho_p \bar{\mathbf{V}}_p \bar{\mathbf{V}}_p) = -\bar{\phi}_p \nabla \bar{p}_p + \bar{\phi}_p (\nabla \cdot \bar{\boldsymbol{\tau}}_p) + \bar{\phi}_p \rho_p \mathbf{g} - \mathbf{F}_{Dc} - \mathbf{F}_{o,c} \quad (5.80)$$

The shear stress term for the liquid phase in eq. (5.77b) refers to the total shear stress including viscous, turbulent (Reynolds), particle-induced-turbulent, and the interfacial shear stresses. Eqs. (5.77b) and (5.80) are satisfied for fully developed flows if the condition  $\bar{\tau}_p = \bar{\tau}_{pi} = \bar{\tau}_{ci} = \bar{\tau}_c$  is valid, indicating that there is no direct contact between particles in dilute particle suspensions.

Forces effective on the suspension flow, which arise from particle–particle and particle–liquid interactions (Chapters 3 and 6), are given with eqs. (5.75a) and (5.78) in ensemble averaged form. The equivalent expression of the terms in these equations is presented below in terms of velocities.

### 5.5.3.1 Averaged pressure difference

The local flow conditions affect the pressure difference ( $\bar{p}_c - \bar{p}_{ci}$ ) in eq. (5.77b). Drew and Passman (1999) defined the pressure difference by assuming potential flow around an individual spherical particle, as

$$\bar{p}_c - \bar{p}_{ci} = C_p \rho (\bar{\mathbf{V}}_p - \bar{\mathbf{V}}_c) \cdot (\bar{\mathbf{V}}_p - \bar{\mathbf{V}}_c) \quad (5.81)$$

where  $C_p$  is the interfacial continuous phase pressure parameter and is suggested as 0.25 (Drew and Passman, 1999).

### 5.5.3.2 Averaged drag force

If solid particles in a dilute suspension are less than 100  $\mu\text{m}$  in diameter, the interfacial drag has a dominant effect as described by Ishii and Zuber (1979):

$$\mathbf{F}_{Dc} = -\mathbf{F}_{Dp} = \frac{1}{8} C_D \rho |\bar{\mathbf{V}}_p - \bar{\mathbf{V}}_c| (\bar{\mathbf{V}}_p - \bar{\mathbf{V}}_c) A_{ip} \quad (5.82)$$

where  $|\bar{\mathbf{V}}_p - \bar{\mathbf{V}}_c|$  is the absolute value of the slip velocity (or difference between the velocities of solid and liquid phases) and  $A_{ip}$  the total particle interfacial area per unit particle volume, given as

$$A_{ip} = \frac{\pi d_p^2 \phi_p}{\pi d_p^3 / 6} = \frac{6 \phi_p}{d_p} \quad (5.83)$$

where  $d_p$  is the diameter of a spherical particle and calculated from the particle volume of  $v_p$ . For two phase flows of very small dispersed particles, which moves in Stokes' regime, the interfacial drag force is defined by eq. (5.82) with the help of  $A_{ip}$  (eq.(5.83)) and  $C_D$  (eq. (4.49)) equations:

$$\mathbf{F}_{Dc} = -\mathbf{F}_{Dp} = \frac{18\eta(\bar{\mathbf{V}}_p - \bar{\mathbf{V}}_c)\phi_p}{d_p^2} \quad (5.84)$$

As shown in Stokes' regime,  $C_D$  in Eq. (5.82) depends on particle Reynolds number,  $Re_{pi}$  in all particle flow regime and solid volume fraction. Particle Reynolds number,  $Re_{pi}$ , used in the interfacial drag force is defined as

$$Re_{pi} = \frac{\rho |\bar{\mathbf{V}}_p - \bar{\mathbf{V}}_c| d_p}{\eta} \quad (5.85)$$

which is based on the slip velocity ( $\bar{\mathbf{V}}_p - \bar{\mathbf{V}}_c$ ) (Section 5.7) and the solid-liquid suspension viscosity,  $\eta$ . Slip velocities are taken instead of terminal velocities in the calculation of interfacial drag force, in all the expressions used for the drag coefficient.

### 5.5.3.3 Averaged interfacial forces

The turbulent dispersion force,  $\mathbf{F}_{T,c}$ , becomes zero in laminar flow and the other interfacial forces for the continuous phase  $\mathbf{F}_{o,c}$ , only consists of lift and virtual (added) mass forces. Hence, eq. (5.75a) becomes

$$\mathbf{F}_{o,c} = \mathbf{F}_{L,c} + \mathbf{F}_{VM,c} \quad (5.86)$$

The lift force acting on spherical particles in shear flow is in opposite direction to the flow and it is expressed (Arnold *et al.*, 1989) as

$$\mathbf{F}_{L,c} = C_L \phi_p \rho [(\bar{\mathbf{V}}_p - \bar{\mathbf{V}}_c) \times (\nabla \times \bar{\mathbf{V}}_c)] \quad (5.87)$$

where  $C_L$  is the lift coefficient that depends on particle Reynolds number (Asakura *et al.*, 1997) and  $C_L = 0.25$  for dilute suspension flows including spherical particles. The term  $(\nabla \times \bar{\mathbf{V}}_c)$  in the equation is the liquid flow vorticity due to rotational motion of particles and is proportional to the lift force.

The motion of an object immersed in a fluid may cause acceleration of the surrounding fluid. This results in an interfacial force on the object, which is called the virtual (added) mass force. This hydraulic force exerted on a particle in time and/or position depends on velocities in each phase and is given by

$$\mathbf{F}_{VM,c} = C_{VM} \phi_p \rho \left[ \left( \frac{\partial \bar{\mathbf{V}}_c}{\partial t} + \bar{\mathbf{V}}_c \cdot \nabla \bar{\mathbf{V}}_c \right) - \left( \frac{\partial \bar{\mathbf{V}}_p}{\partial t} + \bar{\mathbf{V}}_p \cdot \nabla \bar{\mathbf{V}}_p \right) \right] \quad (5.88)$$

where  $C_{VM}$  is the virtual mass coefficient and  $C_{VM} = 0.5$  for dilute suspensions of spherical particles (Drew and Passman, 1999).

## 5.6 EULERIAN SINGLE FLUID MODEL: MIXTURE MODEL

Single-fluid model based on mixture theory, one of the approaches in modeling the suspension flow, assumes that both solid and liquid phases forming the suspension exist at each point in the mixture, the properties of the suspension depend on the properties of each individual phase and on their concentrations. This mixture model can be applied to suspensions flowing in turbulent regime since the turbulence models (i.e. differential stress, linear or non-linear eddy viscosity models such as  $k-\varepsilon$  models) can readily be introduced into the model.

### 5.6.1 Mixture model in laminar flow

A three-dimensional two-phase mixture model is based on a single fluid two-phase flow. In this case, a slurry system consisting of dispersed and continuous phases is considered as a single phase, and continuity and momentum equations are derived (Ling *et al.*, 2003; Xu *et al.*, 2004) as

$$\frac{\partial \rho_s}{\partial t} + \nabla \cdot (\rho_s \mathbf{V}_s) = 0 \quad (5.89)$$

$$\frac{\partial \rho_s \mathbf{V}_s}{\partial t} + \nabla \cdot (\rho_s \mathbf{V}_s \mathbf{V}_s) = -\nabla p - \nabla \cdot \left[ \phi_p \rho_p \left( 1 - \frac{\phi_p \rho_p}{\rho_s} \right) (\mathbf{V}_p - \mathbf{V}_c)(\mathbf{V}_p - \mathbf{V}_c) \right] + \nabla \cdot \boldsymbol{\tau}_{Gs} + \rho_s \mathbf{g} + S_M \quad (5.90)$$

Second term on the RHS of eq. (5.90) denotes the momentum transfer due to slip velocity. In this equation,  $\tau_{Gs}$  is the generalized stress and  $S_M$  is the momentum source defined by

$$S_M = \frac{\rho_s V_s^2}{L} \quad (5.91)$$

Here,  $L$  is the length of the conduit and  $V_s$  the local suspension velocity. The density of the suspension,  $\rho_s$ , and its velocity vector,  $V_s$ , are given with the equations

$$\rho_s = \sum_{k=1}^n \phi_k \rho_k \quad (5.92)$$

$$V_s = \left( \sum_{k=1}^n \phi_k \rho_k V_k \right) \left( \frac{1}{\rho_s} \right) \quad (5.93)$$

where  $\phi_k$ ,  $\rho_k$ , and  $V_k$  are the volume fraction, density, and velocity vector of the  $k^{\text{th}}$  phase, respectively. The volume fraction of particles,  $\phi_p$ , is determined by writing a continuity equation for the dispersed phase in the presence of slip velocity as

$$\frac{\partial \phi_p}{\partial t} + \nabla \cdot (\phi_p V_s - D_{Mp} \nabla \phi_p) = -\nabla \cdot \left( \phi_p \phi_c \frac{\rho}{\rho_s} (V_p - V_c) \right) \quad (5.94)$$

where  $D_{Mp}$  is the turbulent dispersion (diffusion) coefficient and  $(V_p - V_c)$  the relative velocity of the dispersed phase over the liquid phase which is called the slip velocity (Section 5.7). The slip velocity is defined by

$$|V_p - V_c| (V_p - V_c) = \frac{4d_p}{3C_D} \left( \frac{\rho_p - \rho_s}{\rho} \right) \left[ \mathbf{g} - (V_s \cdot \nabla) V_s - \frac{\partial V_s}{\partial t} \right] \quad (5.95)$$

$\nabla \cdot \tau_{Gs}$  and  $D_{Mp} \nabla \phi_p$  terms in the mixture momentum (eq. (5.90)) and the dispersed phase continuity (eq. (5.94)) equations, respectively, indicate the effect of turbulence.  $\tau_{Gs}$  includes both viscous and turbulent shear stresses in each phase as

$$\tau_{Gs} = (\eta + \eta_t) [\nabla V_s + (\nabla V_s)^T] - \frac{2}{3} \rho_s k_s \mathbf{I} \quad (5.96)$$

where  $\eta_t$  and  $k_s$  are the turbulent viscosity and turbulent kinetic energy of the suspension, respectively.  $\eta_t$  is defined by eq. (5.101) for  $k-\varepsilon$  model (Section 5.6.2), and  $(\nabla V_s)^T$  is the transpose of  $\nabla V_s$ .

The equations given above are used to model two-phase flow in laminar regime by dropping  $D_{Mp} \nabla \phi_p$  term in the continuity equation of dispersed phase and describing  $\tau_{Gs}$  in the momentum equation from eq. (5.96) as

$$\tau_{Gs} = \eta [\nabla V_s + (\nabla V_s)^T] \quad (5.97)$$

### 5.6.2 Mixture model in turbulent flow

The general model equations given in the above section are directly used to model the solid–liquid suspension flow in turbulent regime. However, additional definitions and equations are required for the turbulent flow. One of them is the turbulent diffusion coefficient,  $D_{Mp}$ , which describes the effects of all turbulent stresses existing in the two-phase flow.  $D_{Mp}$  is given for dense suspensions as

$$D_{Mp} = \frac{d_p \sqrt{k_s}}{18 \phi_p} \quad (5.98)$$

and will be covered in Section 6.3 in detail.

Turbulent flow of solid–liquid suspensions can be computed in two ways: (1) the averaged Navier–Stokes equations with suitable turbulent flux models are solved which will be given in this section and (2) computation of fluctuating quantities. Turbulent flux models are linear eddy viscosity ( $k$ – $\varepsilon$  and  $k$ – $\omega$ ) models, nonlinear eddy viscosity, and differential stress models (Aspley, 1995, 2006; Aspley and Leschziner, 1998).  $k$ ,  $\varepsilon$  and  $\omega$  denote kinetic energy of turbulence, dissipation and specific dissipation rates, respectively.  $\omega$  relates to  $k$  and  $\varepsilon$  as  $\omega = \varepsilon / (C_\mu k)$  where  $C_\mu$  is an empirical constant of  $k$ – $\varepsilon$  linear eddy viscosity model, widely used. So, the Navier–Stokes equations including  $k$ – $\varepsilon$  model are given as an example in this section. As the density ratio ( $\rho_p / \rho$ ) is almost unity, the use of mixture properties and velocities is appropriate to describe the features of the turbulent flow. The transport equations of  $k$ – $\varepsilon$  model are based on the solution of the conservation of the kinetic energy of turbulence,  $k_s$ , and its dissipation rate,  $\varepsilon$ , and are given by eqs. (5.99) and (5.100) for multiphase flow

$$\frac{\partial(\rho_s k_s)}{\partial t} + \nabla \cdot (\rho_s \mathbf{V}_s k_s) = \nabla \cdot \left( \frac{\eta_t}{\sigma_k} \nabla k_s \right) - \eta_t (\nabla \mathbf{V}_s + (\nabla \mathbf{V}_s)^T) : \nabla \mathbf{V}_s - \rho_s \varepsilon \quad (5.99)$$

$$\frac{\partial(\rho_s \varepsilon)}{\partial t} + \nabla \cdot (\rho_s \mathbf{V}_s \varepsilon) = \nabla \cdot \left( \frac{\eta_t}{\sigma_\varepsilon} \nabla \varepsilon \right) + \frac{\varepsilon}{k_s} (C_{1\varepsilon} \eta_t (\nabla \mathbf{V}_s + (\nabla \mathbf{V}_s)^T) : \nabla \mathbf{V}_s - C_{2\varepsilon} \rho_s \varepsilon) \quad (5.100)$$

where  $C_{1\varepsilon}$ ,  $C_{2\varepsilon}$ ,  $\sigma_k$ , and  $\sigma_\varepsilon$  are empirical constants of the  $k$ – $\varepsilon$  model (Aspley, 1995, 2006; Aspley and Leschziner, 1998).  $\eta_t$  is the turbulent viscosity defined by

$$\eta_t = \rho_s C_\mu k_s^2 \varepsilon^{-1} \quad (5.101)$$

Non-Newtonian suspension flow in laminar and turbulent regimes are generally modeled by this single fluid (mixture) model as given in Chapters 2.

Mixture model can also be applied to the flow of settling suspensions having different flow patterns in which different layers exist (Chapter 6). Each layer is considered as a separate mixture with different properties and the model is applied to each layer. A set of the model equations can be developed on both micro- and macro-scales. In the case of microscale modeling, the general equations given in this section are applied to each layer separately. The mixture model is widely used on macroscale for layered flow, so the general

balance equations independent of flow geometry are developed for heterogeneous settling suspension flow in Section 5.7.

## 5.7 MIXTURE MODEL ON MACROSCALE: GENERAL BALANCE EQUATIONS

Heterogeneous flow (Figure 6.1) is a characteristic behavior of solid–liquid suspension flows and a distribution of particle volume fraction ( $\phi$  or  $\phi_p$ ) occurs along the cross-sectional area and in the flow direction. The heterogeneous flow is schematically portrayed in Figure 5.2 at steady-state conditions with flow of solid particles,  $Q_p$ , and fluid,  $Q_c$ , through the cross-sectional area of an inclined hydraulic transportation line. The velocities and volume fractions of the phases are usually not equal and may vary. Therefore, total mass, momentum, and energy balances for the system given in Figure 5.2 are written independent of flow geometry to define the flow behavior of suspensions.

The properties of the suspension flow vary across the cross-sectional area (sections A, B, C, and  $SS'$ ) and throughout the flow path due to the settling of the particles during flow. A differential cross-sectional area,  $dA$ , is defined as shown in Figure 5.2 to take into account the variations across the cross-sectional area and along the flow path. The local values of particle volume fraction, the particle and liquid velocities on this differential area are taken as  $\phi$ ,  $V_p$ , and  $V_c$ , respectively.

General balance equations on macroscale between any two sections such as A and C given in Figure 5.2 can be written by representing the inlet and outlet properties for the whole cross-section, so the area-averaged properties must be used. Therefore, the local values are integrated along the cross-sectional area to describe the area-averaged properties (eq. (5.26)) as explained in Section 5.2. If a property is required to define the whole system from inlet to outlet in any balance equation i.e., density used in the gravitational force term in a force balance, volume-averaged properties are used. To describe the volume-averaged property, eq. (5.24) is applied to the local values of this property. Besides, if the area-averaged form of this property is known, its area-averaged form is converted into volume-averaged property using eq. (5.28).

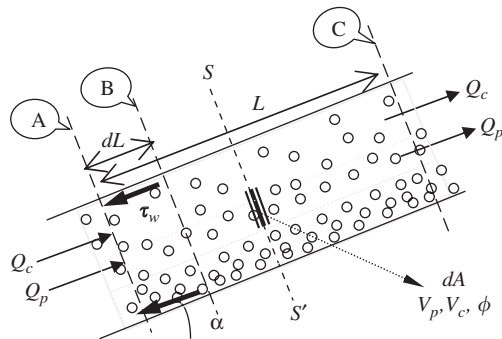


**Figure 5.2** Flow of solid liquid suspensions in an inclined channel.  $V$  is local velocity and  $\phi$  is the local particle volume fraction. The subscripts  $p$  and  $c$  denote particle and liquid phases. This system makes an angle  $\alpha$  with the horizontal.

### 5.7.1 Total mass balance

Total mass balance for suspension flow from inlet section A to outlet section C under steady state conditions, so the suspension mass flow rate is constant between Section A and C in

$$\dot{m}_{sA} = \dot{m}_{sC} = \dot{m}_s \quad (5.102)$$

The suspension mass flow rate,  $\dot{m}_s$ , can be written in terms of the solid,  $\dot{m}_p$ , and liquid,  $\dot{m}_c$ , components of flow as

$$\dot{m}_s = \dot{m}_p + \dot{m}_c \quad (5.102a)$$

or

$$\dot{m}_s = \rho_s Q_s = \rho_p Q_p + \rho Q_c \quad (5.103)$$

in terms of volumetric flow rate,  $Q$ . The subscripts s, p, and c denote suspension, particle (dispersed), and liquid (continuous) phases, respectively. Here, the suspension density,  $\rho_s$ , is written from eq. (5.92) as a function of the densities of solid particles and liquid as

$$\rho_s = \phi_d \rho_p + (1 - \phi_d) \rho \quad (5.104)$$

where  $\phi_d$  (widely used as  $C_{vd}$  in literature) is the delivered volume fraction of the solid phase in this suspension flow system.  $\phi_d$  is defined as the ratio of the volumetric flow rate of solid particles to the total volumetric flow rate of the suspension:

$$\phi_d = \frac{Q_p}{Q_s} \quad (5.105)$$

The delivered solid concentration  $\phi_d$  should be less than 0.30 for dispersed (fully suspended) flow where rather high velocities are used.  $\phi_d$  can be as high as 0.5 in the transportation of dense suspensions at relatively low velocities (*two layer flow*).

The volumetric flow rates in two-phase flow can also be written in terms of superficial velocity,  $V_{i,av}$ , based on the cross-sectional area,  $A$ , of the transportation line as

$$Q_i = V_{i,av} A \quad (5.106)$$

where subscript  $i$  may be p, l, or s denoting particulate and liquid phases and their mixture (suspension), respectively. A relation between the superficial solid and suspension velocities can be given using eqs. (5.105) and (5.106) as

$$\phi_d = \frac{V_{p,av} A}{V_{s,av} A} = \left( \frac{V_{p,av}}{V_{s,av}} \right) \quad (5.107)$$

To find the area-averaged properties of the liquid and particle phases, the cross-sectional area,  $A$ , can also be expressed in terms of the particle volume fraction as

$$A = \phi A + (1 - \phi)A \quad (5.108)$$

**Table 5.4**

Mean quantities of dispersed phase based on  $dA$  on  $SS'$  line in Figure 5.2

Quantity	Dispersed phase	
Area-averaged volume fraction	$\phi_t = \frac{1}{A} \int_A \phi dA$	(5.109)
Mass flow rate	$\dot{m}_p = \int_A \rho_p V_p \phi dA$	(5.110)
	$\dot{m}_p = \rho_p \bar{V}_p \phi_t A$	(5.110a)
Volumetric flow rate	$Q_p = \int_A V_p \phi dA = \bar{V}_p \int_A \phi dA$	(5.111)
	$Q_p = \bar{V}_p \phi_t A$	(5.111a)
Mean velocity	$\bar{V}_p = \frac{1}{A} \int_A V_p dA$	(5.112)
	$\bar{V}_p = \frac{Q_p}{\phi_t A}$	(5.112a)
Momentum	$\bar{J}_{Mp} = \dot{m}_p V_p = \int_A \rho_p V_p^2 \phi dA$	(5.113)
	$\bar{J}_{Mp} = \rho_p \bar{V}_p^2 \phi_t A = \dot{m}_p \bar{V}_p$	(5.113a)
Kinetic energy	$\bar{E}_{Kp} = \int_A \rho_p V_p \phi \left( \frac{V_p^2}{2} \right) dA$	(5.114)
	$\bar{E}_{kp} = \rho_p \bar{V}_p \phi_t A \left( \frac{\bar{V}_p^2}{2} \right) = \dot{m}_p \left( \frac{\bar{V}_p^2}{2} \right)$	(5.114a)



and the differential cross-sectional area,  $dA$ , on a section  $SS'$  in Figure 5.2 normal to the suspension flow is given as

$$dA = \phi dA + (1 - \phi)dA \quad (5.108a)$$

$dA$  does not cover the whole cross-sectional area since the volume fraction of solid particles shows variations across this area (normal to flow direction). Thus, the local values such as the local volume fraction,  $\phi$ , and the local velocities ( $V_p$ ,  $V_c$ ) on  $dA$  are used to define area-averaged quantities (mean volume fractions,  $\phi_t$ , and mean velocities of the solid,  $\bar{V}_p$ , and liquid,  $\bar{V}_c$ , phases and their flow rates) using eq. (5.24). For example, integration of the local volumetric fraction of solids across the cross-sectional area gives the area-averaged volume fraction,  $\phi_t$ . The resultant area-averaged equations for the dispersed and continuous phases are summarized in Tables 5.4 and 5.5, respectively.

In a similar way, substitution of eq. (5.111a) to define  $Q_p$  into the equation of the delivered volume fraction of the solid phase,  $\phi_d$  (eq. (5.105)), gives a relation between area-averaged solid particle and superficial suspension velocities

$$\phi_d = \frac{1}{V_{s,av}A} \int_A V_p \phi dA \quad (5.120)$$

or

$$\phi_d = \frac{A\phi_t \bar{V}_p}{V_{s,av}A} = \left( \frac{\bar{V}_p}{V_{s,av}} \right) \phi_t \quad (5.120a)$$

Eq. (5.120) indicates that there is slip between the phases, so that  $\bar{V}_p \neq V_{s,av}$ , and the average and delivered volume fractions are different. The slip velocity is expressed as the difference between the velocities of solid and liquid phases. The local ( $V_c - V_p$ ) and mean ( $\bar{V}_c - \bar{V}_p$ ) slip velocities are defined at an incremental area  $dA$  and across the cross-section  $SS'$ , respectively. The equations in Tables 5.4 and 5.5 are used to derive the following equation, the equation of *mean slip velocity*, which shows that there is no simple relation between local and mean velocities:

$$\bar{V}_c - \bar{V}_p = \frac{Q_c}{(1 - \phi_t)A} - \frac{Q_p}{\phi_t A} = \frac{\int_A V_c (1 - \phi) dA}{\int_A (1 - \phi) dA} - \frac{\int_A V_p \phi dA}{\int_A \phi dA} \quad (5.121)$$

However, sometimes the *slip velocity* (or *lag*) and the dimensionless slip velocity (*lag ratio*),  $\lambda_{slip}$ , are defined as the velocity difference between the suspension and the solid phase ( $V_{s,av} - \bar{V}_p$ ) and given by

$$\lambda_{slip} = \frac{V_{s,av} - \bar{V}_p}{\bar{V}_p} \quad (5.122)$$

**Table 5.5**Mean quantities for continuous phase based on  $dA$  across  $SS'$  line in Figure 5.2

Quantity	Continuous phase	
Mass flow rate	$\dot{m}_c = \int_A \rho V_c (1 - \phi) dA$	(5.115)
	$\dot{m}_c = \rho \bar{V}_c (1 - \phi_t) A$	(5.115a)
Volumetric flow rate	$Q_c = \int_A V_c (1 - \phi) dA$	(5.116)
	$Q_c = \bar{V}_c (1 - \phi_t) A$	(5.116a)
Mean velocity	$\bar{V}_c = \frac{1}{A} \int_A V_c dA$	(5.117)
	$\bar{V}_c = \frac{Q_c}{(1 - \phi_t) A}$	(5.117a)
Momentum	$\bar{J}_{Mc} = \dot{m}_c V_c = \int_A \rho V_c^2 (1 - \phi_t) dA$	(5.118)
	$\bar{J}_{Mc} = \rho \bar{V}_c^2 (1 - \phi_t) A = \dot{m}_c \bar{V}_c$	(5.118a)
Kinetic energy	$\bar{E}_{Mc} = \int_A \rho V_c (1 - \phi) \left( \frac{V_c^2}{2} \right) dA$	(5.119)
	$\bar{E}_{Kc} = \rho \bar{V}_c (1 - \phi_t) A \left( \frac{\bar{V}_c^2}{2} \right) = \dot{m}_c \left( \frac{\bar{V}_c^2}{2} \right)$	(5.119a)

In addition, substituting  $V_{s,av}/\bar{V}_p = 1 + \lambda_{slip}$  into eq. (5.120a), the delivered volume fraction of the solid phase  $\phi_d$  in terms of dimensionless slip velocity  $\lambda_{slip}$  is obtained as

$$\phi_d = \frac{\phi_t}{1 + \lambda_{slip}} \quad (5.123)$$

$\lambda_{slip}$  decreases with decreasing slip velocity and  $1/(1 + \lambda_{slip})$  ratio in the above equation increases. Thus, the difference between the area-averaged and the delivered volume fractions decreases and they become identical under no-slip conditions.

### 5.7.2 Linear momentum balance

The linear momentum balance for the suspension flow is written as a difference of area-averaged inlet and outlet quantities in the volume element (from section A to B) in Figure 5.2 under steady-state conditions

$$[(\bar{J}_{Ms})_B - (\bar{J}_{Ms})_A] + A(P_B - P_A) + A(\Delta L)\rho_{s,av}g \sin \alpha + S\tau_w = 0 \quad (5.124)$$

where  $\bar{J}_{Ms}$  is area-averaged momentum of the suspension,  $P$  the pressure,  $\alpha$  the angle of inclination,  $S$  the peripheral area of the transportation line (conduit) which is parallel to the flow direction,  $A$  is the area perpendicular to the suspension flow, and  $\rho_{s,av}$  the volume-averaged suspension density in the control volume since the density of the suspension changes depending on the solid volume fraction along the flow (from section A to B and across the cross-sectional area) in heterogeneous flow.

The terms in square bracket in the equation show the area-averaged total momentum flow rates (eqs. (5.127)–(5.127c) in Table 5.6), the second and third terms give the momentum

**Table 5.6**

Mean quantities for suspension based on  $dA$  on  $SS'$  line used in Figure 5.2

Area-averaged quantities	Suspension	
Density	$\bar{\rho}_s = \phi_t \rho_p + (1 - \phi_t)\rho$	(5.125a)
Mass flow rate	$\dot{m}_s = \rho_p \bar{V}_p \phi_t A + \rho \bar{V}_c (1 - \phi_t) A$	(5.126)
Momentum	$\bar{J}_{Ms} = \int_A \rho_p V_p^2 \phi dA + \int_A \rho V_c^2 (1 - \phi) dA$	(5.127)
	$\bar{J}_{Ms} = [\rho_p \bar{V}_p^2 \phi_t A + \rho \bar{V}_c^2 (1 - \phi_t) A]$	(5.127a)
	$\bar{J}_{Ms} = \dot{m}_p \bar{V}_p + \dot{m}_c \bar{V}_c$	(5.127b)
	$\bar{J}_{Ms} = \bar{J}_{Mp} + \bar{J}_{Mc}$	(5.127c)
Kinetic energy	$\bar{E}_{Ks} = \int_A \rho_p V_p \phi \left( \frac{V_p^2}{2} \right) dA + \int_A \rho V_c (1 - \phi) \left( \frac{V_c^2}{2} \right) dA$	(5.128)
	$\bar{E}_{Ks} = \dot{m}_p \left( \frac{\bar{V}_p^2}{2} \right) + \dot{m}_c \left( \frac{\bar{V}_c^2}{2} \right)$	(5.128a)
	$\bar{E}_{Ks} = \bar{E}_{Kp} + \bar{E}_{Kc}$	(5.128b)

due to external forces (pressure and gravity), and the fourth term is associated with the momentum loss due to shear stresses at the walls. Eq. (5.124) in differential form is

$$\left( \frac{d\bar{J}_{Ms}}{dL} \right) = -A \left( \frac{dP}{dL} \right) - A\rho_{s,av} g \sin \alpha - \frac{S\tau_w}{dL} \quad (5.124a)$$

The suspension density  $\rho_s$  is given in terms of the local solid volume fraction and the densities of each phase as

$$\rho_s = \phi \rho_p + (1 - \phi) \rho \quad (5.125)$$

across the differential cross-sectional area,  $dA$ . The area-averaged suspension density,  $\bar{\rho}_s$ , is expressed by eq. (5.125a) in Table 5.6 replacing the local solid volume fraction,  $\phi$ , with the area-averaged volume fraction,  $\phi_t$ . Area-averaged quantities related to suspension flow such as mass, momentum, and kinetic energy flow rates are summarized in Table 5.6.

The area-averaged suspension density,  $\bar{\rho}_s$ , is converted into volume-averaged quantities through

$$\rho_{s,av} = \frac{\int_{L_A}^{L_B} \bar{\rho}_s dL}{\int_{L_A}^{L_B} dL} \quad (5.129)$$

An expression for the volume-averaged suspension density  $\bar{\rho}_{s,av}$  is obtained by substituting eq. (5.125a) into eq. (5.129), then taking the integral and applying the integral boundaries:

$$\rho_{s,av} = \frac{(\int \rho_p \phi_t + \rho(1 - \phi_t))L)_B + (\int \rho_p \phi_t + \rho(1 - \phi_t))L)_A}{\Delta L} \quad (5.130)$$

The rearrangement of the above equation gives

$$\rho_{s,av} = \frac{(\rho_p - \rho)((\phi_t L)_B - (\phi_t L)_A)}{\Delta L} + \rho \quad (5.130a)$$

With the inclusion of the expressions for averaged quantities into the momentum equation (eq. (5.124a)), a general linear momentum balance equation describing the pressure drop along the hydraulic transportation line is derived at steady-state conditions for both homogeneous and heterogeneous flows

$$\left( \frac{dP}{dL} \right) = -\frac{S\tau_w}{A dL} - \left[ \frac{(\rho_p - \rho)((\phi_t L)_B - (\phi_t L)_A)}{\Delta L} + \rho \right] g \sin \alpha - \left( \frac{\dot{m}_p}{A} \frac{d\bar{V}_p}{dL} + \frac{\dot{m}_c}{A} \frac{d\bar{V}_c}{dL} \right) \quad (5.131)$$

where the first term denotes *shear stresses at the wall*, the second term the *gravitational effect* due to the weight of the suspension, and the third term the *acceleration* of the two

flowing phases. In the case of multilayered flow,  $\tau_w$  in the first term denotes the summation of shear stresses at upper and lower boundaries of each layer.

The linear momentum balance equation (eq. (5.131)) can be simplified in the following cases:

*Fully developed heterogeneous flow:* There is no change in the area mean velocities of the two phases along the pipe and the acceleration term is zero in this type of flow. In this case, the equation simplifies to

$$\left( \frac{dP}{dL} \right) = - \frac{S\tau_w}{A dL} - \left[ \frac{(\rho_p - \rho)((\phi_t L)_B - (\phi_t L)_A)}{\Delta L} + \rho \right] g \sin \alpha \quad (5.131a)$$

*Fully developed homogeneous flow:* The volume fraction of the phases across sections A and B normal to the flow of the suspension remains constant through the transportation line, so  $\phi_{tA} = \phi_{tB} = \phi_t$  and, consequently, the second term in eq. (5.131a) is reduced to a simpler form:

$$\left( \frac{dP}{dL} \right) = - \frac{S\tau_w}{A dL} - [\rho_p \phi_t + (1 - \phi_t)\rho] g \sin \alpha \quad (5.131b)$$

These equations are general and can be used for any inclination angle,  $\alpha$ , of the pipeline from horizontal to vertical position. In the equation,  $\sin \alpha = 0$  for horizontal flow and 1 for vertical flow.

### 5.7.3 Total mechanical energy balance

The total mechanical energy balance between the sections A and B in Figure 5.2 is

$$(P + \bar{P}_{KE} + \rho_{s,av} L g \sin \alpha)_A = (P + \bar{P}_{KE} + \rho_{s,av} L g \sin \alpha)_B + \Delta P_{loss} \quad (5.132)$$

where  $P$  is the pressure,  $\bar{P}_{KE}$  the area-averaged kinetic energy in pressure units, and  $\Delta P_{loss}$  is the *pressure or frictional losses* due to energy dissipation in the transportation line. The area-averaged kinetic energies of the dispersed and continuous phases on  $SS'$  line in Figure 5.2 in terms of local and area-averaged quantities are given in Tables 5.4 and 5.5, respectively. The area-averaged kinetic energy of the suspension on the same section is also given in Table 5.6. The suspension kinetic energy in terms of pressure unit can be expressed as

$$\bar{P}_{KEs} = \frac{\bar{E}_{Kp}}{\bar{V}_p \phi_t A} + \frac{\bar{E}_{Kc}}{\bar{V}_c (1 - \phi_t) A} = \rho_p \left( \frac{\bar{V}_p^2}{2} \right) + \rho \left( \frac{\bar{V}_c^2}{2} \right) \quad (5.133)$$

Eq. (5.132) can also be rewritten in differential form:

$$- \frac{dP_{loss}}{dL} = - \frac{dP}{dL} - \frac{d(\bar{P}_{KEs})}{d \Delta L} - \rho_{s,av} g \sin \alpha \quad (5.134)$$

Eq. (5.134) defines the total mechanical energy per unit volume. To express the total mechanical energy based on the total volume, eq. (5.134) is written by replacing  $\bar{P}_{\text{KEs}}$  with  $\bar{E}_{\text{Ks}}$ ,  $\rho_{\text{s,av}}$  with  $(\dot{m}_p + \dot{m}_c)$ , and multiplying  $dP/dL$  and  $dP_{\text{loss}}/dL$  terms with the total volumetric flow rate,  $Q_s$ , as

$$-Q_s \frac{dP_{\text{loss}}}{dL} = -Q_s \frac{dP}{dL} - \frac{d}{dL}(\bar{E}_s) - (\dot{m}_p + \dot{m}_c)g \sin \alpha \quad (5.135)$$

The rearrangement of the above equation by substituting  $Q_s = Q_p + Q_c$  and by using eq. (5.128a) yields

$$-\frac{dP_{\text{loss}}}{dL} = -\frac{dP}{dL} - \frac{1}{Q_p + Q_c} \left( \dot{m}_p \bar{V}_p \frac{d\bar{V}_p}{dL} + \dot{m}_c \bar{V}_c \frac{d\bar{V}_c}{dL} \right) - \left( \frac{\dot{m}_p + \dot{m}_c}{Q_p + Q_c} \right) g \sin \alpha \quad (5.136)$$

where the ratio of  $(\dot{m}_p + \dot{m}_c)$  to  $(Q_p + Q_c)$  in the last term gives the density, known as the mean delivered suspension density,  $\rho_{\text{s,av}}$

$$\rho_{\text{s,av}} = \left[ \frac{\dot{m}_p + \dot{m}_c}{Q_p + Q_c} \right] \quad (5.137)$$

Further substitution of eqs. (5.131) and (5.137) into eq. (5.136) gives

$$\begin{aligned} -\frac{dP_{\text{loss}}}{dL} = & + \frac{S\tau_w}{A dL} + \left[ \frac{(\rho_p - \rho)((\phi_t L)_B - (\phi_t L)_A)}{\Delta L} + \rho - \rho_{\text{s,av}} \right] g \sin \alpha \\ & + \left[ \left( \frac{\dot{m}_p}{A} - \frac{\dot{m}_p \bar{V}_p}{Q_p + Q_c} \right) \frac{d\bar{V}_p}{dL} + \left( \frac{\dot{m}_c}{A} - \frac{\dot{m}_c \bar{V}_c}{Q_p + Q_c} \right) \frac{d\bar{V}_c}{dL} \right] \end{aligned} \quad (5.138)$$

where first, second, and third terms indicate *shear stress at the wall*, *gravity effect*, and the *acceleration* of the dispersed and continuous phases, respectively. Thus, the terms designate the same quantities as eq. (5.131). In the case of *fully developed heterogeneous flow*, the third term becomes zero and the total mechanical energy balance becomes

$$-\frac{dP_{\text{loss}}}{dL} = + \frac{S\tau_w}{A dL} + \left[ \frac{(\rho_p - \rho)((\phi_t L)_B - (\phi_t L)_A)}{\Delta L} + \rho - \rho_{\text{s,av}} \right] g \sin \alpha \quad (5.138a)$$

For *fully developed homogeneous flow*, the second term in the above equation is simplified when there is no change in the volume fraction of the dispersed phase throughout the system and the total mechanical energy balance reduces to

$$-\frac{dP_{\text{loss}}}{dL} = + \frac{S\tau_w}{A dL} + [\rho_p \phi_t + \rho(1 - \phi_t) - \rho_{\text{s,av}}] g \sin \alpha \quad (5.138b)$$

The terms in square brackets show the difference between the area-averaged (eq. (5.125a)) and the mean delivered suspension densities, so the average slurry density is taken into account.

### 5.7.3.1 Effect of slip on total mechanical energy balance

The density difference given by the square brackets in eq. (5.138b) can also be defined by using eqs. (5.125a) and (5.123) in terms of dimensionless slip velocity,  $\lambda_{\text{slip}}$

$$\bar{\rho}_s - \rho_{s,\text{av}} = (\rho_p + \rho)(\phi_t - \phi_d) = (\rho_p - \rho)\phi_d \lambda_{\text{slip}} \quad (5.139)$$

If the suspension can flow upwards, this means that the superficial suspension velocity is greater than the area mean velocity of the particles,  $V_{s,\text{av}} > \bar{V}_p$ , and the dimensionless slip velocity,  $\lambda_{\text{slip}}$ , becomes positive. Hence, the density difference from eq. (5.139) used in the second term of the total mechanical energy balance equation (eq. (5.138b)) becomes positive. This indicates mechanical energy dissipation, since eq. (5.138b) has a negative sign. In the case of downward flow,  $\sin \alpha$  becomes negative and  $V_{s,\text{av}} < \bar{V}_p$  which causes the dimensionless slip velocity,  $\lambda_{\text{slip}}$ , and the density difference in eq. (5.139) to be negative. As a consequence, slip of the dispersed phase causes mechanical energy dissipation in both upward and downward flows of suspensions.

## 5.8 Drift Flux Model

The presence of relative motion between the solid and liquid phases in a mixture with respect to each other and with respect to the average flow of the mixture in a solid-liquid suspensions necessitates modelling the suspension flow by using the two-fluid (Section 5.4), mixture (Sections 5.6) or drift-flux models depending on the degree of the coupling of the motion of the phases. Two-fluid model that takes the relative motion of all phases with respect to each other is the most general form. If the phases move with the same velocity that indicate the existence of mechanical equilibrium between the phases, the slip velocity vanishes and the most simple model called the homogeneous model can be used. Therefore, there is only one velocity ( $\bar{\mathbf{V}}_p = \bar{\mathbf{V}}_c = \bar{\mathbf{V}}_m$ ) in the homogeneous model and a momentum equation is written based on the mixture properties. In addition, continuity equations for particulate (eqs.(5.68b) and (5.68c)) for liquid phases or only a single continuity equation for the suspension (eq. (5.89)) can be used.

The two-fluid model is appropriate for modeling the suspension flow when the velocities of the solid and liquid phases are different. However, the two momentum equations used in the model causes significant difficulties due to mathematical complications together with uncertainties to specify the interactions between the solid and liquid phases at the interface. Improper selection of the interactive relations causes numerical instabilities in the solution of the model equations. These difficulties in the modeling of the two-phase flow can be reduced by using a new approach called *drift-flux model* (Munkejord, 2006). In the drift flux model, the mixture is considered as a whole rather than as solid and

liquid phases and the slip velocity  $\bar{\mathbf{V}}_{ls}$ , is approximated by an algebraic expression that is a function of flow variables.

$$\bar{\mathbf{V}}_{ls} = (\bar{\mathbf{V}}_p - \bar{\mathbf{V}}_c) = f(\rho_p, \rho, \mu, \eta, \phi_p \bar{\mathbf{V}}_c) \quad (5.140)$$

The drift-flux model provides a constitutive equation for the *drift-flux velocity*  $\mathbf{J}_{ls}$ , of the dispersed phase (Zuber and Findley, 1965), that is the velocity of the phase relative to the volume averaged velocity of the mixture (Zuber and Findley, 1965; Wörner, 2003). The volumetric flux density of the mixture  $\mathbf{J}_m$  is given as

$$\mathbf{J}_m = \mathbf{J}_c + \mathbf{J}_p = (1 - \phi_p) \bar{\mathbf{V}}_c + \phi_p \bar{\mathbf{V}}_p \quad (5.141)$$

where  $\mathbf{J}_c$  and  $\mathbf{J}_p$  are the volumetric flux densities of the continuous and disperse phases, respectively. The drift velocities of the phases related to the slip velocity  $\bar{\mathbf{V}}_{ls}$ , are

$$\bar{\mathbf{V}}_c = \phi_p \bar{\mathbf{V}}_{ls} \quad (5.142)$$

$$\bar{\mathbf{V}}_p = (1 - \phi_p) \bar{\mathbf{V}}_{ls} \quad (5.143)$$

The drift-flux model is derived by considering the two fluid model in two ways: In the first way, the interfacial pressure is assumed to be the same for the solid and liquid phases ( $\bar{P}_p = \bar{P}_{pi} = \bar{P}_{ci}$ ) and the interfacial momentum source terms ( $\bar{\tau}_p = \bar{\tau}_{pi} = \bar{\tau}_{ci} = \bar{\tau}_c$ ) are neglected in the momentum equations (eqs. (5.77a) and (5.77b)). Then the mixture momentum equation is obtained by adding the momentum equation for the liquid phase (eq.(5.77b)) to that for the solid phase (eq. (5.77a)):

$$\begin{aligned} \frac{\partial}{\partial t} (\bar{\phi}_p \rho_p \bar{\mathbf{V}}_p + \bar{\phi}_c \rho_c \bar{\mathbf{V}}_c) + \nabla \cdot (\bar{\phi}_p \rho_p \bar{\mathbf{V}}_p \bar{\mathbf{V}}_p + \bar{\phi}_c \rho_c \bar{\mathbf{V}}_c \bar{\mathbf{V}}_c) = & -\bar{\phi}_p \nabla \bar{p}_p \\ & -\bar{\phi}_c \nabla \bar{p}_c + \bar{\phi}_p \rho_p \mathbf{g} + \bar{\phi}_c \rho_c \mathbf{g} \end{aligned} \quad (5.144)$$

For the two-phase flow, the gradient of the volume fraction is equal and opposite, so  $\bar{p}_i \nabla \bar{\phi}_i$  (where  $i = p, c$ , or  $i$ ) does not appear in the above equation. In addition to this momentum equation, the drift-flux model incorporates two continuity equations (eqs.(5.68b) and (5.68c)).

The second way is to formulate the drift-flux model is by mixture momentum (eq.(5.144) and mixture continuity equations (eq.(5.89), together with the continuity equation for the dispersed phase (eq.(5.68b)).

When the motion of two phases are strongly coupled, it is more appropriate to use the drift-flux model instead of the more complex two-fluid model. It is usually applied its one dimensional form that is obtained from time-averaging of the three dimensional drift- flux model (Hibiki and Ishii, 2003).



## REFERENCES

- Arnold, G., Drew, D.A., Lahey, R.T., Jr, 1989. Derivation of constitutive equations for interfacial force and Reynolds stress for a suspension of spheres using ensemble averaging. *Chemical Engineering Communications*, 86, 43–54.
- Asakura, K., Asari, T., Nakajima, I., 1997. Simulation of solid–liquid flows in a vertical pipe by collision model. *Powder Technology*, 94, 201–206.
- Aspley, D.D., 1995. Numerical Modelling of Neutral and Stably Stratified Flow and Dispersion in Complex Terrain, PhD Thesis, University of Surrey.
- Aspley, D.D., 2006. <http://personalpages.manchester.ac.uk/staff/david.d.aspley/lecture.htm>.
- Aspley, D.D., Leschziner, M.A., 1998. A new low-Reynolds-number nonlinear two equation turbulence model for complex flows. *International Journal of Heat and Fluid Flow*, 19, 209–222.
- Bird, R.B., Stewart, W.E., Lightfoot, E.N., 2002. *Transport Phenomena*, 2nd edn., Wiley, New York, NY (Chapter 3, appendices).
- Drew, D.A., Passman, S.L., 1999. *Theory of Multicomponent Fluids*, Applied Mathematical Science Series Vol. 135, Springer-Verlag, New York, NY (Chapter 9).
- Dukowicz, J.K., 1980. A particle-fluid numerical model for fluid sprays. *Journal of Computational Physics*, 35, 229–253.
- Faheien, R.W., 1983. *Fundamentals of Transport Phenomena*, McGraw-Hill, Inc., New York, NY (Chapter 9).
- Ferry, J., Balachandar, S., 2001. A fast Eulerian method for disperse two phase flow. *International Journal of Multiphase Flow*, 27, 1199–1226.
- Fu, X.D., Wang, G.Q., Shao, X.E., 2005. Vertical dispersion of fine and coarse sediments in turbulent open-channel flows. *Journal of Hydraulic Engineering*, 131, 877–888.
- Gidaspow, D., 1994. *Multiphase Flow and Fluidization Continuum and Kinetic Theory Descriptions*, Academic Press, Boston, MA.
- Gudmundsson, R.L., 2005. A Numerical Study of the Two-Fluid Models for Dispersed Two Phase Flow, PhD Thesis, Stockholm, Sweden.
- Hibiki, T., Ishii, M., 2003. One-dimensional drift model and constitutive equations for relative motion between phases in various two phase flow regimes. *International Journal of Heat and Mass Transfer*, 46, 4935–4948.
- Ishii, M., Zuber, N., 1979. Relative motion and interfacial drag coefficient in dispersed two-phase flow of bubbles, drops and particles. *AIChE Journal*, 25, 843.
- Ling, J., Skudarnov, P.V., Lin, C.X., Ebadian, M.A., 2003. Numerical investigations of liquid–solid slurry flows in a fully developed turbulent flow region. *International Journal of Heat and Fluid Flow*, 24, 389–398.
- Marchioro, M., Tanksley, M., Prosperetti, A., 2000. Flow of spatially non-uniform suspensions. Part I—Phenomenology. *International Journal of Multiphase Flow*, 26, 783–831.
- Munkejord, S.T., 2006. Analysis of the Two Fluid Model and the Drift Flux Model for Numerical Calculation of Two Phase Flow, PhD Thesis, Norwegian University of Science and Technology, Trondheim, Norway.
- Ni, J.R., Xia, J.X., 2003. Particle fluctuation intensities in sediment-laden flows. *Mechanics Research Communications*, 30, 25–32.
- Patankar, N.A., Joseph, D.D., 2001a. Modeling and numerical simulation of particulate flows by the Eulerian–Lagrangian approach. *International Journal of Multiphase Flow*, 27, 1659–1684.
- Patankar, N.A., Joseph, D.D., 2001b. Lagrangian numerical simulation of particulate flows. *International Journal of Multiphase Flow*, 27, 1685–1706.

- Rani, S.L., Balachandar, S., 2004. Preferential concentration of particles in isotropic turbulence: A comparison of the Lagrangian and the equilibrium Eulerian approaches. *Powder Technology*, 141, 109–118.
- Rani, S.L., Winkler, C.M., Vanka, S.P., 2004. Numerical simulations of turbulence modulation by dense particles in a fully developed pipe flow. *Powder Technology*, 141, 80–99.
- Saffman, P.G., 1965. The lift on small sphere in a slow shear flow. *Journal of Fluid Mechanics*, 22, 385–400.
- Slattery, J.C., 1978. *Momentum, Energy, and Mass Transfer Continua*, Robert E. Krieger Publishing Company, Huntington, NY (Chapter 4).
- Tiwari, P., Antal, S.P., Podowski, M.Z., 2006. Three-dimensional fluid mechanics of particulate two-phase flows in U-bend and helical conduits. *Physics of Fluids*, 18, 043304.1–043304.18.
- Wang, G.Q., Ni, J.R., 2003. The kinetic theory for dilute solid/liquid two-phase flow. *International Journal of Multiphase Flow*, 17, 273–281.
- Wörner, M., 2003. *A Compact Introduction to the Numerical Modeling of Multiphase Flow*, FZKA 6932, Forschungszentrum Karlsruhe GmbH, Karlsruhe, Germany.
- Xu, J., Rouelle, A., Smith, K.M., Celik, D., Hussaini, M.Y., Van Sciver, S.W., 2004. Two-phase flow of solid hydrogen particles and liquid helium. *Cryogenics*, 44, 459–466.
- Zhang, D.Z., Prosperetti, A., 1997. Momentum and energy equations for disperse two-phase flows and their closure for dilute suspensions. *International Journal of Multiphase Flow*, 23, 425–453.
- Zuber, N., Findlay, J.A., 1965. Average volumetric concentration in two phase flow systems. *Journal of Heat Transfer*, 87, 453–468.

This page intentionally left blank

# – 6 –

## Flow of Settling Slurries

---

Solid–liquid suspensions may consist of solid particles in different size ranges such as particles in nano-, micro-, and milli-meter scales and different densities: If densities of particles and liquid forming a suspension are approximately the same or the sizes of the particles are too small, the particles do not settle. Nonsettling suspensions can be treated as pseudofluids with effective rheological properties and their flow through circular and noncircular pipes can be evaluated as single-phase flow. First group of nonsettling suspensions is non-Newtonian slurries covered in Chapter 2. The other group of nonsettling suspensions shows Newtonian behavior and will be taken up in this chapter as a *fully suspended (homogeneous) flow* together with the *settling slurry flow*.

The slurries comprising small and coarser particles or particles having higher density than that of liquid tend to settle from the suspending liquid. These particles accumulate at the bottom of the channel, resulting in the emergence of different flow patterns depending on the flow homogeneity and velocity. The internal structures of the flow patterns of settling slurries are effective in determining the pressure drop due to friction over the length of the slurry transportation system.

Various aspects of suspension flow such as flow patterns, flow regimes, transition velocities, and the flow behavior in pipes of different geometries based on experimental and model studies will be covered in this chapter, as a function of concentration, shape, size, and size distribution of particles. Model equations for fully suspended, two- and three-layered flow patterns derived in this chapter are based on the general balance equations given in Section 6 of Chapter 5.

### 6.1 FLOW PATTERNS AND FLOW REGIMES

Flow patterns are defined with respect to the dispersed phase to describe the flow behavior of settling slurries. Depending on the suspension flow rate, the dispersed phase may form a homogeneous or heterogeneous single-phase flow, or a layered flow such as two- or three-layer flow.

6.1.1 Flow patterns

Settling slurries exhibit different flow patterns based on visual observations of the dispersed phase flow as shown in Table 6.1. A general classification of the flow patterns based on the solid distribution in the transportation line can be made as (Doron and Barnea, 1996): (1) fully suspended flow with two sub patterns—pseudohomogeneous and -heterogeneous flow, (2) flow with moving bed, and (3) flow with a stationary bed including saltation.

6.1.1.1 Fully suspended flow

This type of suspension flow is single phased and generally observed at high suspension flow rates. All solid particles are uniformly suspended across the flow cross-section at any position throughout the flow direction resulting in a *pseudohomogeneous suspension flow* (Figure 6.1(a-1)). If the solid particles are randomly distributed in the normal direction to

Table 6.1

Classification of flow patterns

Nomenclature for flow patterns in the literature	References	Flow pattern classification of this book
Nondeposit flow regime	Durand (1953)	Fully suspended flow
Flow regime with deposits	Condolios and Chapus (1963)	Two-layer flow
Saltation $\equiv$ Moving bed	Bain and Bonnington (1970) Turian and Yuan (1977)	Two-layer flow
Homogeneous flow		Fully suspended flow
Heterogeneous flow	Vocaldo and Charles (1972)	Fully suspended flow
Heterogeneous and sliding flow	Goedde (1978)	Two-layer flow
Saltation and stationary bed	Parzonka <i>et al.</i> (1981)	Three-layer flow
Saltation and stationary bed	Ayazi Shamlau (1970)	Three-layer flow
Fully segregated flow regime		Layered flow
Heterogeneous flow regime	Brown (1991)	Fully suspended flow
Homogeneous flow		Fully suspended flow
Pseudohomogeneous flow		Fully suspended flow
Heterogeneous flow		Fully suspended flow
Fully moving bed	Lazarus and Neilson (1978)	Two-layer flow
Part stationary bed		Three-layer flow
Stationary bed		Three-layer flow
Pseudohomogeneous flow		Fully suspended flow
Heterogeneous flow		Fully suspended flow
Moving/stationary bed	Ercolani <i>et al.</i> (1979)	Three-layer flow
Moving dunes		Two-layer flow
Stationary bed		Three-layer flow

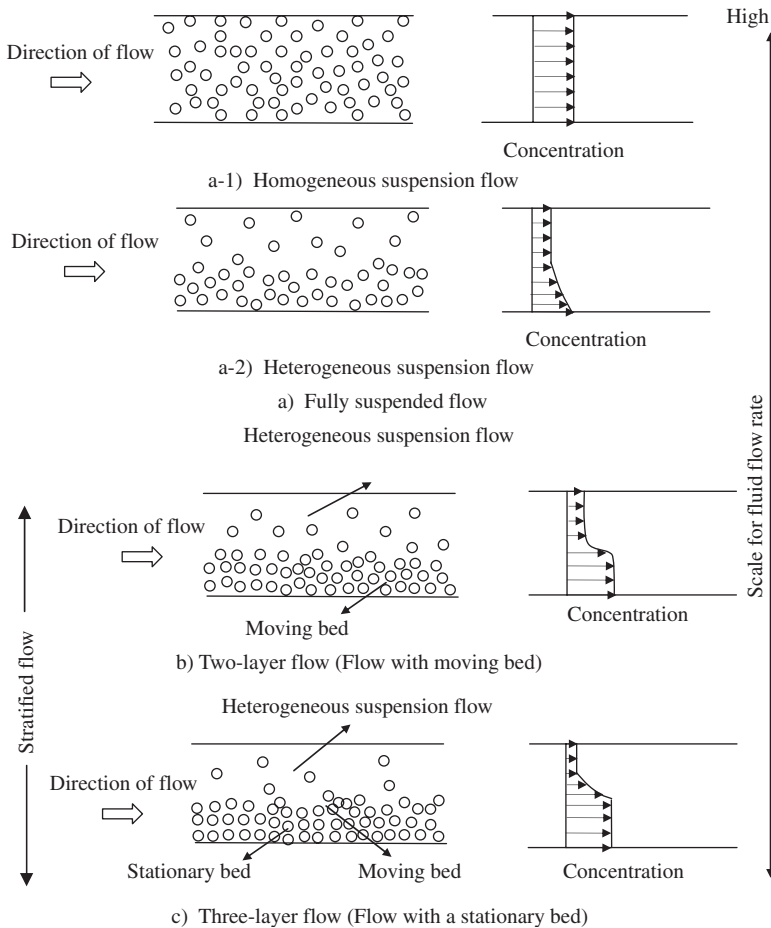


**Figure 6.1** Schematic presentation of flow patterns and concentration distributions in normal direction to flow (a) fully suspended flow, (b) two-layer flow (flow with moving bed), (c) three-layer flow (flow with a stationary bed).

flow, a particle concentration gradient is formed, causing a *heterogeneous suspension flow* (Figure 6.1(a-2)). The absence or presence of a particle concentration gradient in fully suspended flow does not change the number of phases.

#### 6.1.1.2 Flow with a moving bed

Solid particles accumulate at the bottom of ducts resulting in a dense packed layer at low suspension flow rates. The packed layer moves along the lower wall, and a heterogeneous suspension forming the upper layer flows in the rest of the duct (Figure 6.1(b)). This type of the suspension flow with a moving particle bed is defined as *two-layer flow*.

### 6.1.1.3 Flow with a stationary bed

A stationary bed is observed at the bottom of the duct (Figure 6.1(c)) since the suspension flow rate is too low to move all the immersed particles. There is a separate moving layer on the top of this bed. In many cases a phenomenon known as *saltation*, that is the formation of dune-like forms on the surface of the bed, can also be observed. The rest of the flow system is filled with heterogeneous suspension flow where the solid concentration profile is much steeper than in the other flow patterns. This flow pattern of heterogeneous suspension together with stationary and moving bed layers can also be interpreted as *three-layer flow*.

These three main flow patterns will be mentioned as fully suspended, two- and three-layer flows in this book. The flows including more than one layer such as two- and three-layers are also generalized as stratified flow as given in Figure 6.1. The flow patterns given in the literature are regrouped as fully suspended, two- and three-layer flows in the last column of Table 6.1.

The transitions between flow patterns are usually determined by visual observations. The definition of the transition velocity varies with a change in the definition of the flow patterns. However, summary of the definition of transition velocities given in Table 6.2 shows that there are two fundamental transition velocities, *limit deposit* and *suspending velocities* as shown in the last column of the table. Limit deposit velocity is the velocity that marks the lowest velocity required for a fully suspended flow. The limit deposit velocity conditions in slurry flow comprise stationary bed flow with a stagnant lower zone. Prevention of this limit deposit velocity is essential for the avoidance of the partial blockage of the pipes that reduces the efficiency of the pipelines, enhancing pipe wear in industrial applications.

## 6.1.2 Particle support mechanisms in the flow of settling slurries

The solid particles forming slurries tend to settle under the action of gravity due to density difference with the suspension medium during slurry flow. Particles are supported by several mechanisms depending on the flow patterns to overcome the gravitational force.

The suspended weight of particles in homogeneous and heterogeneous flow is supported by *the turbulent diffusive action of the conveying fluid*. However, the concentration of solid particles along the bottom of the pipe increases in all types of flow patterns in heterogeneous suspension flow shown in Figure 6.1. With increasing solid concentration, packing of particles and interactions among the solid particles also increase, so the *interparticle contact* opposes the effect of gravity and is the dominant mechanism for particle support. Particle–particle and particle–fluid interactions taken up in Chapter 1 have an important bearing on the flow of settling slurries and will be used in related sections of this chapter.

### 6.1.3 Parameters describing the flow of slurries

Density and viscosity of solid–liquid suspensions are effective parameters controlling the flow of slurries. The density of slurries  $\rho_s$  is defined by eq. (5.125). Viscosity of the solid–liquid suspensions,  $\eta$  depends on the viscosity of the suspending medium,  $\mu$  and the densities of

**Table 6.2**

Transition velocities

Transition velocity	Definition	References	Definition used in this book
Limit deposit velocity	Marks the separation between the deposit and nondeposit flow regimes	Durand (1953)	Limit deposit velocity
Limit deposit velocity	Limit velocity for the stationary bed	Wilson (1976, 1984); Toda <i>et al.</i> (1980)	
Critical deposition velocity	Transition velocity between the deposit and nondeposit flow regimes	Doron and Barnea (1996); Graf <i>et al.</i> (1970); Bain and Bonnington (1970); Stevens and Charles (1972); Kazanskij (1979)	
Deposit velocity	Limit velocity for the stationary bed	Wood (1979); Parzonka <i>et al.</i> (1981)	
Deposition velocity	Limit velocity for the stationary bed	Shook and Roco (1991)	
Critical velocity	Velocity below which there are deposited particles	Zandi and Govatos (1967); Vocaldo and Charles (1972); Ercolani <i>et al.</i> (1979); Oroskor and Turian (1980); Goedde (1978); Turian <i>et al.</i> (1987)	Suspending velocity
Settling velocity	Velocity above which fully suspended flow is observed	Smith (1955)	
Minimum velocity Suspending velocity		Spell (1955) Doron and Barnea (1996)	

the phases forming the suspension and is defined in the form of relative viscosity,  $\eta_r$  as (Kofanov, 1964; Stokes and Evans, 1997)

$$\eta_r = \frac{\eta}{\mu} = 1 + 2.5 \left( \frac{\rho_s - \rho}{\rho_p - \rho} \right) \quad (6.1)$$

where  $\rho_p$  is the density of the particle and  $\rho$ , the density of the suspending medium. This equation is used for dilute suspensions formed by uniform fine or coarse spherical particles. The density ratio in eq. (6.1) refers to the solid volume fraction,  $\phi$  as defined by



eq. (4.136). Replacing the density ratio with the solid volume fraction  $\phi$  converts eq. (6.1) into eq. (3.15). There is a linear relation between the suspension viscosity and the volume fraction of dispersed phase in eq. (6.1). However, viscosity–volumetric fraction relation is not linear in concentrated suspensions and eq. (6.1) becomes inadequate with increasing concentrations. Additional terms of order two or higher are required to describe the interactions between particles such as

$$\frac{\eta}{\mu} = [1 + 2.5\phi + C_1\phi^2 + C_2 \exp(C_3\phi)] \quad (6.2)$$

where  $C_1$ ,  $C_2$ , and  $C_3$  are constants, which are given in the same order as 10, 0.0019, and 20 by Gillies *et al.* (1999), 10.05, 0.00273, and 16.6 by Shook (1993) and Fangary *et al.* (1997). The suspension viscosity can also be defined in terms of the solid mass fraction,  $\phi_w$  (Shook, 1993; Choi and Cho, 2001)

$$\frac{\eta}{\mu} = \left[ 1 + 2.5 \left( \frac{\rho_s}{\rho_p} \right) \phi_w + 10.05 \left( \frac{\rho_s}{\rho_p} \right) \phi_w^2 + 0.00273 \exp \left( 16.6 \left( \frac{\rho_s}{\rho_p} \right) \phi_w \right) \right] \quad (6.3)$$

where  $\phi_w$  is given as

$$\phi_w = \phi \left( \frac{\rho_p}{\rho_s} \right) \quad (6.4)$$

Krieger and Dougherty (1959) equation given in eq. (3.22) can also be used to define the relative viscosity of settling slurries. The power of eq. (3.22),  $[\eta] \cdot \phi_m$  (Krieger, 1972) is taken as 1.82 and  $\phi_m = 0.6$  (Averbakh *et al.*, 1997; Shauly *et al.*, 1997).

Liu and Masliyah (1996) proposed an equation similar to eq. (3.17) that can be used to estimate the viscosity of both dilute and concentrated suspensions,

$$\eta_r = \frac{\eta}{\mu} = \left[ \left( 1 - \frac{\phi}{\phi_m} \right)^{-2} + \left( 2.5 - \frac{2}{\phi_m} \right) \phi + \left( k_H - \frac{6}{\phi_m^2} \right) \phi^2 \right] \quad (6.5)$$

where  $k_H$  is the Huggins constant and  $\phi_m$  is the volume fraction at the maximum packing. Both  $\phi_m$  and  $k_H$  are strong functions of shear rate. Under low shear rates, or *quasistatic* conditions,  $\phi_m = 0.63$  and  $k_H = 6$ . At higher shear stresses  $\phi_m = 0.74$  due to the alignment of the particles and  $k_H = 7.1$ .

## 6.2 GENERAL BALANCE EQUATIONS FOR FLOW OF SLURRIES THROUGH PIPES

Flow patterns observed during flow of settling suspensions through cylindrical pipes are similar to those given in Section 6.1 and schematically illustrated in Figure 6.2. Starting with the most general forms of the balance equations given in Chapter 5 for a fully suspended flow, balance equations for all flow patterns in Figure 6.2 will be derived.

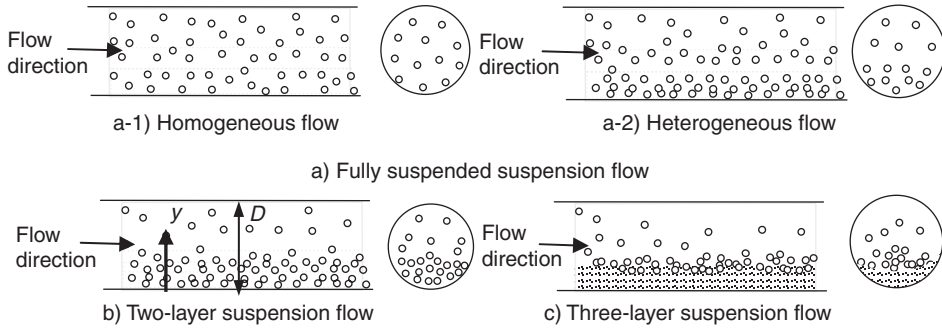


**Figure 6.2** Schematic presentation of flow patterns in cylindrical pipes.

### 6.2.1 Fully suspended flow

*Homogeneous fully suspended flow* illustrated in Figure 6.2(a) occurs when the sizes of particles making up the suspension are too small or when the average velocity  $V_{s,av}$  is sufficiently high. Hence, the area-averaged solid volume fraction of the suspension  $\phi_t$  is uniformly distributed throughout the pipe cross-section. The total mechanical energy balance for fully suspended homogeneous suspension flow through a cylindrical pipe of any inclination, vertical, or horizontal is expressed by eq. (5.131b).  $A$  and  $S$  are replaced with  $A = (\pi D^2/4)$  and  $S = \pi D(dL)$ , respectively, and the shear losses at wall,  $\tau_w$  with Darcy–Weisbach expression

$$\tau_w = \frac{1}{2} f_s \rho_s V_s^2 \quad (6.6)$$

where  $f_s$  is friction factor,  $V_s$  is the superficial velocity of the suspension and equals  $V_{s,av}$  in Chapter 5. Hence, the total mechanical energy balance for fully suspended flow is defined as

$$\left( -\frac{dP}{dL} \right) = \frac{4f_s \rho_s V_s^2}{2D} + [\rho_p \phi_t + \rho(1 - \phi_t)] g \sin \alpha \quad (6.7)$$

where  $dP/dL$  is the pressure loss per unit length of pipe,  $g$  the acceleration of gravity, the expression in square brackets is the area averaged effective density of the suspension,  $\bar{\rho}_s$  is defined by eq. (5.125a), and  $\alpha$  is the angle of inclination of the pipeline. Under no-slip conditions,  $\bar{\rho}_s$  becomes identical to the volume averaged suspension density,  $\rho_s$  according to eq. (5.139).

Depending on the type of the fluid and the flow regime of the suspension, several relationships are used to find the friction factor,  $f_s$ . For Newtonian fluids,  $f_s$  for laminar flow is given by

$$f_s = \frac{16}{Re_s} \quad (6.8)$$

and for turbulent flow (Doron *et al.*, 1987; Kelessidis and Bandelis, 2004)

$$f_s = \frac{0.046}{Re_s^{0.2}} \quad (6.9)$$

where  $Re_s$  is the Reynolds number of the suspension flow defined as

$$Re_s = \frac{D\rho_s V_s}{\eta} \quad (6.10)$$

where  $D$  is the diameter of the pipe.

In *heterogeneous fully suspended flow* (Figure 6.2(b)), solid particles are nonuniformly distributed over the pipe cross-section, which necessitates the use of an area-averaged solid volume fraction,  $\phi_t$  throughout the pipeline. Thus, total energy balance for fully developed heterogeneous flow in a pipeline at any position is derived by using eq. (5.138a)

$$\left(-\frac{dP}{dL}\right) = \frac{2f_s \rho_s V_s^2}{D} + \left[ \frac{(\rho_p - \rho)((\phi_t L)_B - (\phi_t L)_A)}{\Delta L} + \rho - \rho_s \right] g \sin \alpha \quad (6.11)$$

$\phi_t$  is constant in the normal direction to flow and changes along the pipeline.

## 6.2.2 Two-layer flow

Suspension flow may change its flow pattern from fully suspended to two-layer flow (Figures 6.2(c) and 6.3(a)) with a decrease in average suspension velocity,  $V_{s,av}$ . In this type of flow, the solid–liquid mixtures in each layer are considered to have the solid and liquid phases in different volume fractions, so that continuity equations for solid and liquid phases are separately written. The upper layer is the heterogeneous dispersed phase denoted by **1** and the moving bed by **2** in Figure 6.3. The flow in each layer has distinct properties, which are defined by means of the averaged quantities such as mean velocity,  $\bar{V}$ , and concentration,  $\phi_d$ . If the area-averaged mean velocity of the solid particles,  $\bar{V}_p$  equals that of the liquid,  $\bar{V}_c$  in each layer, or  $\bar{V}_p = V_s$ , this is an indication that there is no slip between the two phases as explained in Section 5.7.3 in Chapter 5. Momentum transfer due to shear forces between the layers takes place at the interface, which characterizes the thickness of the interface. Continuity equation for each phase and force (linear momentum) balance on each layer are written under no-slip conditions at steady state using the notations given in Figure 6.3.

### 6.2.2.1 Continuity equations

The continuity equation for the solid phase is

$$\bar{V}_1 \phi_{d,1} A_1 + \bar{V}_2 \phi_{d,2} A_2 = V_s \phi_0 A \quad (6.12)$$

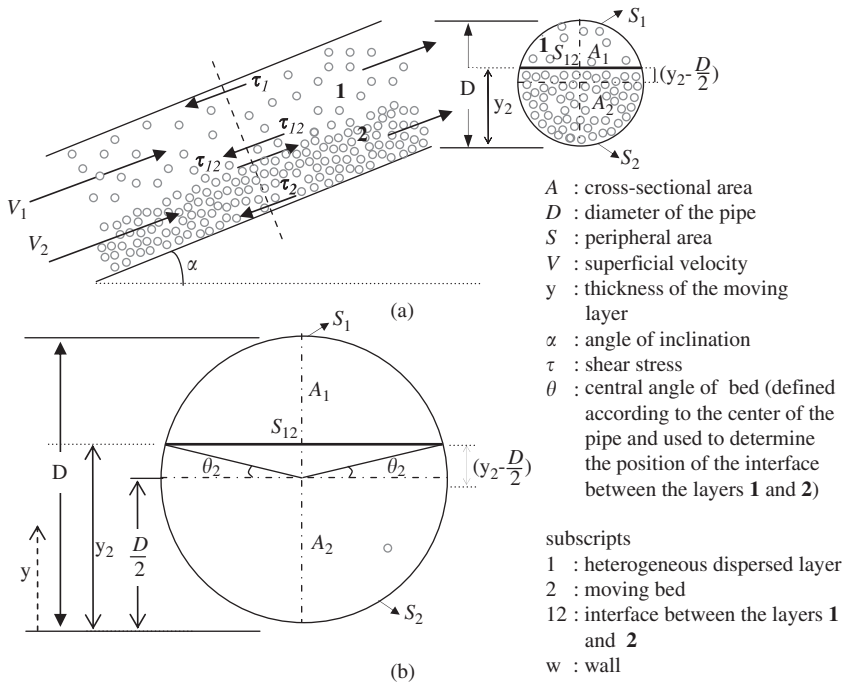


**Figure 6.3** Two-layer flow: (a) velocities and shear stresses, (b) area definitions (bold line below  $S_{12}$  indicates the interface between dispersed and moving bed layers).

and for the liquid phase

$$\bar{V}_1(1 - \phi_{d,1})A_1 + \bar{V}_2(1 - \phi_{d,2})A_2 = V_s(1 - \phi_0)A \quad (6.13)$$

where  $\bar{V}_1$  and  $\bar{V}_2$  are the area-averaged mean velocities of the upper and the moving bed layers.  $\phi_0$  is the mean concentration (volume fraction) of the suspension at the inlet,  $\phi_{d,1}$  and  $\phi_{d,2}$  are the solid concentrations of the upper and moving bed layers in succession.  $A$ ,  $A_1$ , and  $A_2$  are the cross-sectional area of the pipe, upper and moving bed layers, respectively.

#### 6.2.2.2 Linear momentum balances

Linear momentum balance on each layer in Figure 6.3(a) is defined by eq. (5.131a) or eq. (5.131b). Forces due to shear stress,  $S\tau_w$  and cross-sectional areas,  $A$  for the two-layer flow in eqs. (5.131a) or (5.131b) are replaced with the related definitions given in Table 6.3. As the heterogeneous upper layer is considered as pseudohomogeneous liquid with effective properties, eq. (5.131b) for the upper layer under no-slip conditions is reduced to

$$\left( \frac{dP}{dL} \right) = - \left( \frac{S_1\tau_1 + S_{12}\tau_{12}}{A_1 dL} \right) - \rho_{s,1}g \sin \alpha \quad (6.14)$$

**Table 6.3**

First terms of eqs. (5.108a) and (5.108b) for two-layer flow

Layers in two-layer flow	$S\tau_w$	$A$
Upper layer	$(S_1\tau_1 + S_{12}\tau_{12})$	$A_1$
Moving bed layer	$(F_2 + A_2\tau_2 - S_{12}\tau_{12})$	$A_2$

where  $\tau_1$  is the upper layer shear stress at the pipe wall,  $\tau_{12}$  the interfacial shear stress acting on the interface between the upper and moving bed layers, and  $\rho_{s,1}$  is the averaged density, based on the delivered solid volume fraction,  $\phi_{d,1}$  of the upper layer.

The upper layer shear stress at the pipe wall,  $\tau_1$  is found by Darcy–Weisbach equation (eq. (6.6))

$$\tau_1 = \frac{1}{2} f_1 \rho_{s,1} \bar{V}_1^2 \quad (6.15)$$

where  $f_1$  is the friction factor. In the calculation of the friction factor for Newtonian fluids, eqs. (6.8) and (6.9) are used depending on the flow regime. However, the Reynolds number,  $Re_s$  in these equations are defined in terms of hydraulic diameter,  $D_{h,1}$  and the suspension viscosity,  $\eta_1$  as

$$Re_1 = \frac{\rho_{s,1} \bar{V}_1 D_{h,1}}{\eta_1} \quad (6.16)$$

The hydraulic diameter of the upper layer is defined by

$$D_{h,1} = \frac{4A_1}{(S_1/dL) + (S_{12}/dL)} \quad (6.17)$$

where  $S_1$  is a portion of the peripheral area of the pipe corresponding to the upper layer and  $S_{12}$  the area of the interface between the upper and moving bed layers. To find  $D_{h,1}$ , the required cross-sectional and peripheral areas of the upper-layer are described in Table 6.4 in terms of pipe diameter, height of the moving bed,  $y_2$  and central angle to the edge of the moving bed,  $\theta_2$ .  $\theta_2$  is required to determine the position of the interface between the particle bed and the heterogeneous upper layer or the size of the deposition region of the particles and is defined according to the center of the pipe as shown in Figure 6.3(b). Using the hydraulic diameter definition together with the area equations of the upper layer given in Table 6.4,  $D_{h,1}$  is found to be

$$D_{h,1} = D \left( \frac{(\pi/2) - \theta_2 - [(2y_2/D) - 1] \cos \theta_2}{(\pi/2) - \theta_2 + \cos \theta_2} \right) \quad (6.18)$$

**Table 6.4**

Cross-sectional area and peripheral area equations for two-layer flow

Cross-sectional area		
Upper-layer flow	$A_1 = \frac{D^2}{4} \left( \frac{\pi}{2} - \theta_2 - \left( \frac{2y_2}{D} - 1 \right) \cos \theta_2 \right)$	(6.19)
Moving bed	$A_2 = \frac{D^2}{4} \left( \frac{\pi}{2} + \theta_2 + \left( \frac{2y_2}{D} - 1 \right) \cos \theta_2 \right)$	(6.20)
Peripheral area		
Upper-layer flow	$S_1 = D \left( \frac{\pi}{2} - \theta_2 \right) dL$	(6.21)
Interface of the upper layer and the moving bed	$S_{12} = D \cos \theta_2 dL$	(6.22)
Moving bed	$S_2 = D \left( \frac{\pi}{2} + \theta_2 \right) dL$	(6.23)

The interfacial shear stress,  $\tau_{12}$  at the interface between the two layers is expressed in terms of the relative velocity between the layers.

$$\tau_{12} = \frac{1}{2} f_i \rho_{s,1} (\bar{V}_1^2 - \bar{V}_2^2) \quad (6.24)$$

where  $f_i$  is friction factor at the interface between the upper and moving bed layers which is estimated by the Colebrook equation with an effective interfacial roughness, assumed to be equal to the particle diameter,  $d_p$ . The collisions of suspended particles with the bed and their deposition at the interface are effective on the friction factor  $f_i$ . These effects are taken into consideration by multiplying the friction factor by 2 (Televantos *et al.*, 1979; Doron *et al.*, 1987).

$$\frac{1}{\sqrt{2f_i}} = -0.86 \ln \left( \frac{(d_p/D_{h,1})}{3.7} + \frac{2.51}{\text{Re}_1 \sqrt{2f_i}} \right) \quad (6.25)$$

The linear momentum equation for moving bed layer under no-slip conditions is

$$\left( \frac{dP}{dL} \right) = \frac{-F_2 - S_2 \tau_2 + S_{12} \tau_{12}}{A_2 dL} - \rho_{s,2} g \sin \alpha \quad (6.26)$$

where  $\rho_{s,2}$  is the effective density of the suspension in the moving bed and  $\tau_2$  the hydrodynamic shear stress acting at the surface of the moving bed contacting with the pipe wall.

$\tau_2$  is caused by the liquid film (viscous sublayer) between the wall and the particles adjacent to the wall. Similar procedure used to find the shear stress at the pipe wall,  $\tau_1$  is applied to find the shear stress,  $\tau_2$  in the moving bed with the properties of the suspension in this bed. However, the effect of the concentration of the particles on the viscosity (Section 6.1.3) depends on the particle size and the thickness of the viscous sublayer: If the particles are coarser or larger than the thickness of the viscous sublayer, the apparent viscosity is not affected by these particles. Hence, the viscosity of the solid-liquid suspension is taken to be equal to that of the suspending liquid; otherwise, the suspension viscosity must be used in the calculations of  $\tau_2$ . Models, based on this approximation, are known as the *equivalent liquid model* (ELM) (Matoušek, 2002). The hydraulic diameter of the moving bed,  $D_{h,2}$  is defined by

$$D_{h,2} = \frac{4A_2}{(S_2/dL) + (S_{12}/dL)} \quad (6.27)$$

where  $S_2$  is a part of the peripheral area of the pipe along the moving bed layer. Using  $A_2$ ,  $S_{12}$  and  $S_2$  given in Table 6.4, the hydraulic diameter is obtained as

$$D_{h,2} = D \left( \frac{(\pi/2) + \theta_2 + [(2y_2/D) - 1] \cos \theta_2}{(\pi/2) + \theta_2 + \cos \theta_2} \right) \quad (6.28)$$

$F_2$  in eq. (6.26) is the mechanical (or Coulombic) friction force acting on the bottom of the pipe, which occurs due to contact of particles moving within the bed layer with the pipe wall. It is defined according to Coulomb's law as

$$F_2 = f_{cf} F_{N,2} \quad (6.29)$$

where  $F_{N,2}$  is the total normal force applied by the solid particles forming the bed on the pipe wall.  $f_{cf}$  is the mechanical or dry-state friction factor between the particles and the wall of the channel, which is constant for a given solid particle and depends on the flow conditions.

The total normal force,  $F_{N,2}$  has two components: normal forces due to the submerged weight of the solid particles,  $F_{Nw,2}$ ; and normal forces due to the conduction of normal stresses resulting from the shear on the bed-suspension interface,  $F_{N\tau,2}$ ;

$$F_{N,2} = F_{Nw,2} + F_{N\tau,2} \quad (6.30)$$

Substitution of eq. (6.29) into eq. (6.30) gives

$$F_2 = f_{cf} (F_{Nw,2} + F_{N\tau,2}) \quad (6.31)$$

where the normal,  $F_{Nw,2}$  and shear,  $F_{N\tau,2}$  stresses are multiplied by the dry-state friction factor,  $f_{cf}$  to find the friction force,  $F_2$ . The normal force at the pipe wall due to submerged weight of the particles,  $F_{Nw,2}$ , is determined by the bed-wall friction model of Wilson (Wilson, 1970; Matoušek, 2002). Wilson's method assumes that the normal force  $F_{Nw,2}$

shows a hydrostatic variation in the vertical direction through a solid bed and can be integrated to give

$$F_{Nw2} = (\rho_p - \rho)g\phi_{d,2} \cos \alpha \frac{D^2}{2} \left[ \left( \frac{2y_2}{D} - 1 \right) \left( \theta_2 + \frac{\pi}{2} \right) + \cos \theta_2 \right] \quad (6.32)$$

over the bed perimeter.  $\phi_{d,2}$  is the delivered solid volume fraction in the moving bed layer.  $F_{Nw2}$  can also be defined in terms of only the central angle of the bed  $\theta_2$ .

$$F_{Nw2} = F_{w2} \cos \alpha \left[ \frac{2(\sin \theta_2 - \theta_2 \cos \theta_2)}{\theta_2 - \sin \theta_2 \cos \theta_2} \right] \quad (6.33)$$

where  $F_{w2}$  is due to the submerged weight of the particles in the bed given as

$$F_{w2} = g(\rho_p - \rho)\phi_{d,2}A_2 \quad (6.34)$$

and  $A_2$  is the cross-sectional area of the bed, illustrated in Figure 6.3 and defined by eq. (6.20) in Table 6.4.

The normal forces arising from the transmission of normal stresses from the interface between the upper and moving bed layers through the particles in the bed,  $F_{N\tau 2}$ , is observed whenever a fluid flows over a deposit of solid particles (Bagnold, 1954). It is dependent on the shear stress at the interface,  $\tau_{12}$  and the peripheral area of the interface,  $S_{12}$  through

$$F_{N\tau 2} = \frac{\tau_{12}(S_{12}/dL)}{\tan \sigma} \quad (6.35)$$

where  $\sigma$  is the *angle of internal friction* (repose) between the particles.  $\sigma$  is determined experimentally by introducing sufficient amount of solid particles to form a bed in the lower half of the horizontal pipe. With a gradual increase in the inclination of the pipe, the first movement of a few individual particles is evaluated as the relocation of the individual particles. The angle of inclination at which many particles move is taken as the angle of the internal friction. Depending on the type of flow and the particle characteristics, the angle of internal friction varies in the interval  $0.35 < \tan \sigma < 0.75$  (Doron *et al.*, 1987).

Thus, the two-layer flow is described by a set of four conservation equations (eqs. (6.12)–(6.14) and (6.26)). The six unknown parameters are the mean velocities ( $\bar{V}_1, \bar{V}_2$ ) and the mean concentrations ( $\phi_{d,1}, \phi_{d,2}$ ) of the upper and the moving bed layers, respectively, the height of the moving bed ( $y_2$ ) and the pressure gradient ( $dP/dL$ ). The particles are generally assumed to be in close contact in the moving bed. Thus,  $\phi_{d,2}$  is taken as 0.52, which is the maximum cubic packing of the deposited particles. With five remaining unknowns, there are still four equations. This necessitates an additional equation to estimate the concentration distribution of solid particles,  $\phi_1$  in the upper heterogeneous layer. The equation that describes the dispersion of solid particles in the layer, is the *diffusion equation* (Section 6.3, in this chapter). The set of five equations together with additional expressions and constitutive relations is solved to describe the concentration profiles, the flow patterns and their transitions.



6.2.3 Three-layer flow

Three layers exist when the flow rate is too low to move all immersed particles in suspension flow through horizontal or slightly inclined pipes: a stationary bed over the pipe wall, a moving bed above this stationary bed, and a heterogeneous mixture at the top of the moving bed (Figures 6.2(c) and 6.4(a)). The continuity equations are obtained by assuming uniform velocities in the three layers and no changes in their thicknesses. The continuity equations, similar to eqs. (6.12) and (6.13), for solid and liquid phases and

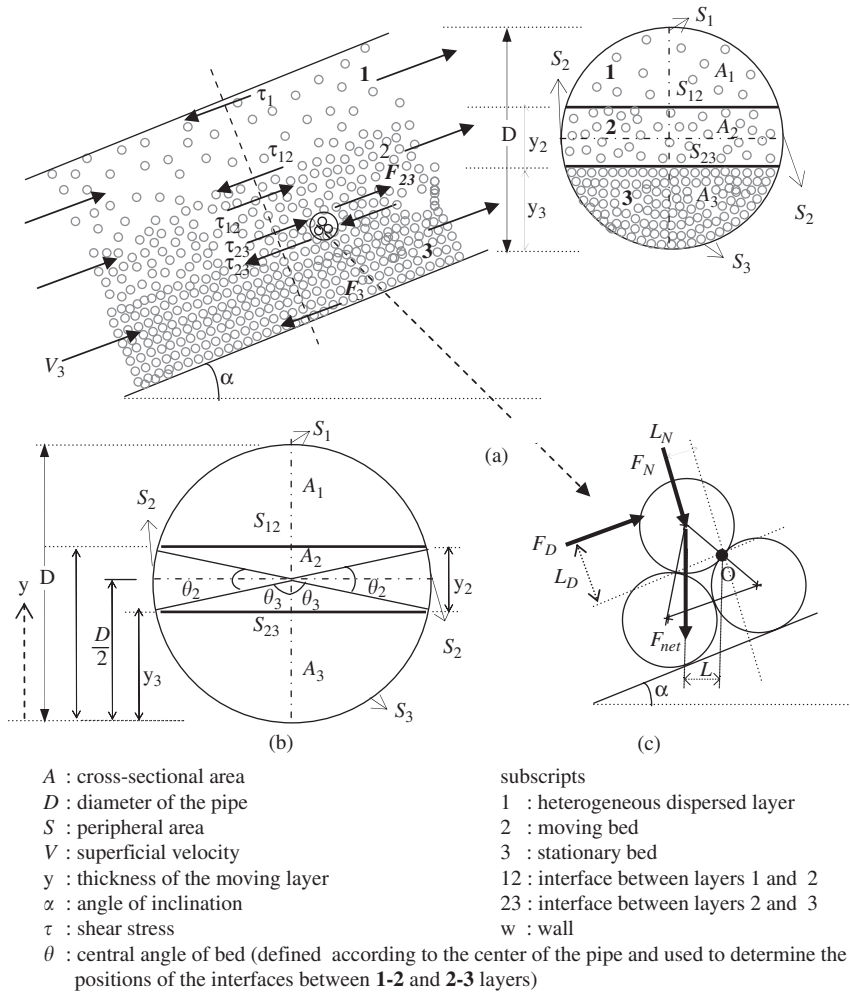


**Figure 6.4** Three-layer flow: (a) velocities and shear stresses, (b) area definitions, (c) forces acting at the interface between the moving and stationary bed layers (bold lines below  $S_{12}$  indicate the interface between the upper and moving bed layers, and the bold lines above  $S_{23}$  indicate the interface between the moving bed and stationary bed layers).

the force (linear momentum) balances on each layer are written under no-slip conditions at steady state using the notations given in Figure 6.4.

The momentum balance equation, eq. (6.14) derived for the heterogeneous upper layer in the two-layer flow is also used for the upper layer in the three-layer flow. For the moving bed layer, the momentum balance similar to eq. (6.26) is written as

$$\left(\frac{dP}{dL}\right) = \left(\frac{-F_2 - S_2\tau_2 + S_{12}\tau_{12}}{A_2 dL}\right) - \left(\frac{F_{23} + S_{23}\tau_{23}}{A_2 dL}\right) - \rho_{s,2} g \sin \alpha \quad (6.36)$$

where  $F_2$  is the friction force effective at the upper and moving bed layer interface. The cross-sectional,  $A_2$  and the peripheral,  $S_i$  areas are defined in Table 6.5 for the three-layer

**Table 6.5**

Cross-sectional area and peripheral area equations for three-layer flow

Cross-sectional area, $A_i$	
Upper-layer flow	$A_1 = \frac{D^2}{4} \left( \theta_3 + \left( \frac{2y_3}{D} - 1 \right) \sin \theta_3 \right) = \frac{D^2}{4} \left( \theta_3 + \left( \frac{2y_3}{D} - 1 \right) \cos \theta_2 \right) \quad (6.39)$
Moving bed	$A_2 = \left( \frac{D^2}{2} \right) \left( \theta_2 + \left( 1 - \frac{2y_3}{D} \right) \sin \theta_3 \right) = \left( \frac{D^2}{2} \right) \left( \theta_2 + \left( 1 - \frac{2y_3}{D} \right) \cos \theta_2 \right) \quad (6.40)$
Stationary bed	$A_3 = \frac{D^2}{4} \left( \theta_3 + \left( \frac{2y_3}{D} - 1 \right) \sin \theta_3 \right) = \frac{D^2}{4} \left( \theta_3 + \left( \frac{2y_3}{D} - 1 \right) \cos \theta_2 \right) \quad (6.41)$
Peripheral area, $S_i$	
Upper-layer flow	$S_1 = D\theta_3 dL = D \left( \frac{\pi}{2} - \theta_2 \right) dL \quad (6.42)$
Interface of the upper layer and the moving bed	$S_{12} = D \sin \theta_3 dL = D \sin \left( \frac{\pi}{2} - \theta_2 \right) dL = D \cos \theta_2 dL \quad (6.43)$
Moving bed	$S_2 = D\theta_2 dL \quad (6.44)$
Interface of the moving bed and the stationary bed	$S_{23} = S_{12} \quad (6.45)$
Stationary bed	$S_3 = D\theta_3 dL = D \left( \frac{\pi}{2} - \theta_3 \right) dL \quad (6.46)$

flow.  $F_{23}$  is the friction force acting at the interface between the moving bed and the stationary bed, and  $\tau_{23}$ , the hydrodynamic shear stress acting on that interface. Both  $F_{23}$  and  $\tau_{23}$  are caused by the presence of a stationary bed adjacent to the moving bed layer. Consequently the two friction forces,  $F_2$  and  $F_{23}$ , exist in three-layer flow due to presence of the two interfaces. Although  $F_2$  is defined by eq. (6.31), a definition different from that of eq. (6.32) is required for its normal force component  $F_{Nw2}$  because it is due to the submerged weight, is affected by the presence of the stationary bed:

$$F_{Nw2} = \eta(\rho_p - \rho)g\phi_{d,2} \cos \alpha \frac{D^2}{2} \left[ \left( \frac{2(y_2 + y_3)}{D} - 1 \right) \theta_2 + \cos(\theta_3 + \theta_2) - \cos \theta_3 \right] \quad (6.37)$$

In this equation,  $y_3$  is the thickness of the stationary bed,  $\theta_3$  is the central angle of the stationary bed layer required to determine the position of the interface between stationary and moving bed layers as shown in Figure 6.4(b). Similar to  $\theta_2$ , it is defined according to the center of the pipe. The friction force,  $F_{23}$  is expressed in terms of the total normal force,  $F_{N,3}$

$$F_{23} = f_{Cf} F_{N,3} \quad (6.38)$$

$F_{N,3}$  consists of two components: the force due to the submerged weight of the particles,  $F_{Nw3}$  and the force due to the stress at the interface between the moving and stationary bed layers,  $F_{Nr3}$ . Hence, eq. (6.38) becomes

$$F_{23} = f_{Cf} (F_{Nw3} + F_{Nr3}) \quad (6.47)$$

$F_{Nw3}$  is defined (Doron *et al.*, 1997) as

$$F_{Nw3} = f_{Cf} (\rho_p - \rho) g \phi_{d,2} y_2 S_{23} \cos \alpha \quad (6.48)$$

and is effective at the interface between the moving and stationary bed layers and through the stationary bed. The force arising from the shear stress ( $\tau_{23}$ ) at the interface between the moving and stationary beds  $F_{Nr3}$ , is defined similar to eq. (6.35) as

$$F_{Nr3} = \frac{\tau_{23} (S_{23}/dL)}{\tan \sigma} \quad (6.49)$$

where  $S_{23}$  is the peripheral area of the interface given in Table 6.5.

The presence of the stationary layer is verified by a force balance written on the stationary bed in an inequality form.

$$\left( \frac{dP}{dL} \right) + \left( \frac{F_{23} + S_{23} \tau_{23}}{A_3 dL} \right) \leq \left( \frac{F_3}{A_3 dL} \right) \quad (6.50)$$

where  $F_3$  is the dry-state friction force acting on the perimeter of the stationary bed. It is described by eq. (6.31) with its components, the normal hydrostatic force distribution,

$F_{Nw2}$  (eq. (6.37)) and the normal force based on the normal shear stress,  $F_{Nr2}$  (eq. (6.36)) using the area definitions given in Table 6.5.

$A_3$  is the cross-sectional area of the stationary bed based on the hydraulic diameter. The hydraulic diameters are defined by eqs. (6.18) and (6.28) for the upper and moving bed layers, respectively. The hydraulic diameters of the upper,  $D_{h,1}$  and the stationary bed,  $D_{h,3}$  layers are found to be identical as  $D_{h,1} = D_{h,3} = D_h$ . Thus,  $D_h$  is given as

$$D_h = D \left[ \frac{\theta_3 + (2y_3/D - 1)\sin\theta_3}{\theta_3 + \sin\theta_3} \right] = D \left[ \frac{(\pi/2 - \theta_2) + (2y_3/D - 1)\cos\theta_2}{(\pi/2 - \theta_2) + \cos\theta_2} \right] \quad (6.51)$$

The hydraulic diameter of the moving bed layer,  $D_{h,2}$  is expressed as

$$D_{h,2} = D \left[ \frac{2\theta_2 + 2(1 - 2y_3/D)\sin\theta_3}{\theta_2 + 2\sin\theta_3} \right] = D \left[ \frac{2\theta_2 + 2(1 - 2y_3/D)\cos\theta_2}{\theta_2 + 2\cos\theta_2} \right] \quad (6.52)$$

The particles at the interface between the moving and stationary bed layers are at the border of rolling (Figure 6.4(c)). Under this condition, the drag exerted by the moving bed layer on a particle causes a torque,  $F_D L_D$ . This torque should be equal to an opposing torque acting on that particle to prevent rolling. The opposing torque consists of two components: One of its components is  $F_w L$  arising from the submerged weight of the particle and the other,  $F_N L_N$  due to the solid particles in the moving bed layer pressing on that particle. By writing a balance between the torque due to drag and the opposing torques, the minimum velocity of the moving bed,  $V_{min,23}$  is derived as (Doron *et al.*, 1997)

$$V_{min,23} = \left\{ \frac{1.56(\rho_p - \rho)gd_p}{\rho C_D} \left[ \sin\left(\frac{\pi}{6} + \alpha\right) + \frac{\cos\alpha}{2} \left(\frac{y_2}{d_p} - 1\right) \right] \right\}^{1/2} \quad (6.53)$$

where  $C_D$  is the particle drag coefficient based on  $V_{min,23}$ . In any two-layer flow, a stationary bed layer forms at the lower section of the pipe if the velocity of the moving bed is less or equal to the minimum velocity,  $V_{min,23}$ . Selection of the velocity of the moving bed as  $V_{min,23}$ , signifies the formation of a stationary bed and as a consequence three-layer formation.

The three-layer flow is described by a set of five equations, eqs. (6.12), (6.13), (6.26), (6.36), and (6.53) with seven unknowns: the mean concentrations ( $\phi_{d,1}$ ,  $\phi_{d,2}$ ) and mean velocities ( $\bar{V}_1$ ,  $\bar{V}_2$ ) of the upper and the moving bed layers, respectively, the heights of the moving bed ( $y_2$ ), and the stationary bed ( $y_3$ ) layers, and the pressure gradient ( $dP/dL$ ).  $\phi_{d,2}$  is taken as equal to the maximum packing of the deposited particles ( $\phi_{d,2} = \phi_m = 0.52$ ). Hence, the number of unknowns becomes six with five equations. An additional equation, covered in Section 6.3, is required to estimate the concentration distribution of solid particles in the upper heterogeneous layer,  $\phi_1$ . The conservation and the diffusion equations are simultaneously solved using additional expressions and constitutive relations given in this section to predict the flow patterns, and concentration distributions.

### 6.3 DISPERSION MECHANISMS OF SOLID PARTICLES

Distribution of the particles carried by the liquid in suspension flow is taken into account by writing a mass balance. The related balance equation is based on the averaged properties due to the heterogeneous nature of the suspensions, since their properties change in all directions. In the case of settling suspensions, the effect of the gravity on the sedimentation flux is considered by an averaged unsteady state mass-balance equation (Liu, 1999).

$$\frac{d\phi}{dt} + \nabla \cdot \mathbf{J}_p = 0 \quad (6.54)$$

where  $t$  is the time,  $\mathbf{J}_p$  the total particle flux. The total particle flux mainly covers two types of particle motion as

$$\mathbf{J}_p = \mathbf{V}_p \phi + \mathbf{J}_D \quad (6.55)$$

where  $\mathbf{V}_p$  is the particle velocity vector.  $\mathbf{V}_p \phi$  denotes the convective transport of particles caused by their bulk motion and  $\mathbf{J}_D$ , the dispersive transport of particles in vectorial form. Substitution of eq. (6.55) into eq. (6.54) gives

$$\frac{d\phi}{dt} + \nabla \cdot \mathbf{V}_p \phi + \nabla \cdot \mathbf{J}_D = 0 \quad (6.56)$$

The particle-dispersion flux,  $\mathbf{J}_D$  generally covers the motion of particles from high to low concentration regions leading to isotropic flow. Dispersion flux consists of three components due to (1) shear-induced particle migration,  $\mathbf{J}_{si}$ , (2) flow-induced particle dispersion,  $\mathbf{J}_{fi}$ , and (3) Brownian diffusion of particles,  $\mathbf{J}_{pb}$ . Thus,  $\mathbf{J}_D$  is expressed as the summation of these three particle dispersions:

$$\mathbf{J}_D = \mathbf{J}_{si} + \mathbf{J}_{fi} + \mathbf{J}_{pb} \quad (6.57)$$

Depending on the properties of suspensions, one or more than one of these dispersion mechanisms may be effective. For example, the Brownian motion is less effective on the dispersion of coarse particles.

The bulk velocity of the particle,  $\mathbf{V}_p$  is the sum of the average suspension velocity,  $\mathbf{V}_s$  and hindered settling velocity of uniform particle mixtures,  $\mathbf{V}_{ht}$ .

$$\mathbf{V}_p = \mathbf{V}_s + \mathbf{V}_{ht} \quad (6.58)$$

The average suspension velocity in vectorial form is defined as

$$\mathbf{V}_s = (1 - \phi)\mathbf{V} + \phi\mathbf{V}_p \quad (6.59)$$

where  $\mathbf{V}$  is the velocity vector of the suspending liquid. Substitution of the average suspension velocity into the particle velocity equation yields

$$\mathbf{V}_p = \mathbf{V} + \frac{\mathbf{V}_{ht}}{(1 - \phi)} \quad (6.60)$$

where  $(\mathbf{V}_{ht}/(1 - \phi))$  indicates the settling velocity of the particles relative to the suspending liquid, which is known as relative velocity,  $V_r$  and defined by eq. (4.138) in Chapter 4. The random fluctuations of the two velocities,  $V$  and  $V_{ht}$  are independent of each other. Substitution of eqs. (6.60) and (6.56) into eq. (6.46) gives

$$\frac{d\phi}{dt} + \nabla \cdot \left[ \left( \mathbf{V} + \frac{\mathbf{V}_{ht}}{(1 - \phi)} \right) \phi + \mathbf{J}_{si} + \mathbf{J}_{fi} + \mathbf{J}_{pb} \right] = 0 \quad (6.61)$$

Eq. (6.61) shows that the particle dispersion increases as the fluid velocity or the settling velocity of the particles increases. This equation is the most general form of particle-mass balance equation and can be applied to all types of solid-liquid suspensions using appropriate definitions related to hindered settling velocity given in Section 4.4 in Chapter 4 under several conditions. For the concentrated suspension,  $(\mathbf{V}_{ht}/(1 - \phi))$  term is replaced by  $(\mathbf{V}_{ht} - \mathbf{V})$  according to eq. (4.138) and eq. (6.61) is written as

$$\frac{d\phi}{dt} + \nabla \cdot [(\mathbf{V}_{ht}\phi) + \mathbf{J}_{si} + \mathbf{J}_{fi} + \mathbf{J}_{pb}] = 0 \quad (6.62)$$

### 6.3.1 Shear-induced particle migration

In settling slurries, particles migrate from the higher-shear region near the wall to the low-shear region in the center of the pipe similar to concentrated suspensions. As a consequence, the concentration of the particles becomes higher in the center and lower near the wall region. The motion of the particles induced by shear is known as *shear-induced particle migration*, and defined by the product of the shear rate,  $\dot{\gamma}$  (velocity gradient,  $dV/dy$ ), and the square of the particle diameter,  $d_p^2$  in eqs. (6.63) and (6.64). The particle diameter is taken as the length scale of the dispersion (Leighton and Acrivos, 1987).

In the shear-induced particle migration, the particle-dispersion flux consists of three components: (1) dispersion flux due to shear-induced particle-particle collision,  $J_{si,c}$

$$J_{si,c} = -D_{si,c} d_p^2 \phi \nabla(\phi \dot{\gamma}), \quad (6.63)$$

(2) dispersion flux due to viscosity gradient in the shear field,  $J_{si,\eta}$

$$J_{si,\eta} = -D_{si,\eta} \frac{\dot{\gamma} d_p^2 \phi^2}{\eta} \frac{d\eta}{d\phi} \nabla(\phi), \quad (6.64)$$

and (3) the self-diffusion flux due to Brownian motion,  $J_{pb}$  (Phillips *et al.*, 1992)

$$J_{pb} = -\mathcal{D}_p \nabla(\phi) \quad (6.65)$$

where  $D_{si,c}$  and  $D_{si,\eta}$  are adjustable parameters in eqs. (6.63) and (6.64), which are estimated using the experimental data. Phillips *et al.* (1992) determined these parameters as  $D_{si,c} = 0.1075$  and  $D_{si,\eta} = 0.1625$  using the Krieger's equation for the suspension viscosity,  $\eta$  given in Chapter 3 with  $\phi_m = 0.68$ .  $\mathcal{D}_p$  in eq. (6.65) is the diffusion coefficient of the particle or aggregates.

The particle dispersion due to both shear-induced particle–particle collision and viscosity gradient takes place in the shear field. The variation in the shear rate and changes in the viscosity gradient in this field affect the migration of particles, so the particle distribution. Therefore, the first two fluxes arising from shear can also be represented as a single flux for the shear field in terms of the adjustable parameter of the dispersion flux of the shear-induced particle–particle collision,  $C_{si,c}$ .

$$J_{si} = J_{si,c} + J_{si,\eta} = -D_{si,c} \frac{d_p^2 \phi^2}{\eta^{1.5}} \nabla(\eta^{1.5} \phi \dot{\gamma}) \quad (6.66)$$

The shear-induced particle migration can also be described in a general form based on the volume- and time-averaging techniques (Liu, 1999)

$$\mathbf{J}_{fi} = -D_s \frac{d_p^2}{\eta} \nabla \left( \left( 1 - \frac{\mu}{\eta} \right) \mu \gamma \right) \quad (6.67)$$

where  $D_s$  is the shear-induced particle migration coefficient, which is a function of the particle volume fraction defined by

$$D_s = 7.09 \phi^{2/3} (1 - \phi)^{11/3} \quad (6.68)$$

and  $\gamma$  is the absolute value of the shear rate matrix and described in terms of the vectorial operation of the suspending liquid velocity vector and its transpose as

$$\gamma = 10.5 [\nabla \mathbf{V} + (\nabla \mathbf{V})^T] : [\nabla \mathbf{V} + (\nabla \mathbf{V})^T]^{0.5} \quad (6.69)$$

The equations given in this section show that an increase in particle diameter or the particle concentration increases the effect of the shear-induced migration.

### 6.3.2 Flow-induced particle dispersion: turbulent diffusion

The bulk flow of the particle itself and its rotation give rise to the distribution of the particles due to its random movement in concentrated suspensions. Hence, the fluctuations in particle velocity causes the flow-induced dispersion mass flux,  $\mathbf{J}_{fi}$  (Liu, 1999) and is described by

$$\mathbf{J}_{fi} = -d_p \left( |\mathbf{V}| + \frac{|\mathbf{V}_{ht}|}{(1 - \phi)} \right) D_N \delta_L \nabla \phi - C_r d_p^2 \left| \nabla \times \left( \mathbf{V} + \frac{\mathbf{V}_{ht}}{(1 - \phi)} \right) \right| D_N \delta_L \nabla \phi \quad (6.70)$$

where the first term shows the translational flow of the particle, which is directly proportional to the particle diameter,  $d_p$  and the second term, its rotational flow, proportional to its square,  $d_p^2$ .  $C_t$  is a constant which is estimated as 2.4 (Liu, 1999).  $D_N$  is the flow-induced dispersion coefficient for the particle transport in the normal direction to the flow.  $\delta_L$  is the ratio of dispersivity in flow direction to that in the normal direction, which is found to change in the range of 14 and 40 for sedimenting suspensions (Ladd, 1993, 1994, 1997). However, there is no experimental data related to  $\delta_L$  for the suspension flow.  $D_N\delta_L$  is the axial-dispersion coefficient which is approximated by Liu (1999) as

$$D_N\delta_L = 320\phi^{2/3}(1-\phi)^{11/3} \quad (6.71)$$

Eq. (6.70) together with eq. (6.71) indicates that the flow-induced dispersion is a strong function of particle volume fraction,  $\phi$ . The particle dispersion due to bulk flow becomes zero when  $\phi = 0$  and increases with increasing particle concentration up to a maximum value, the random packing limit,  $\phi_m$ . Due to the dependence of the translational and rotational motions of the particles on the particle diameter, the influence of the flow-induced dispersion on the total mass flux increases with increasing particle size.

### 6.3.3 Particle-dispersion mechanisms in settling suspensions

In stratified solid–liquid suspension flow, the displacements of solid particles are generally controlled by the large eddies in a turbulent diffusion process. Upward movement of particles is counteracted by the gravitational force, which causes the particles to settle to the bottom of the pipe.

#### 6.3.3.1 Particle dispersion in two-/three-layer flow

To determine the distribution of the particle concentration (solid volume fraction) in any layered flow (Section 6.2) at steady-state conditions, eq. (6.62) is used by neglecting the unsteady-state, and the shear- and flow-induced particle-dispersion terms. The term  $\mathbf{J}_{pb}$  in this equation only covers the molecular motion of particles based on their Brownian motion. To take into account the turbulent diffusion of the particles in the balance equation, the particle Brownian diffusion coefficient,  $\mathcal{D}_p$  is replaced by the mean particle diffusion coefficient,  $D_{pM}$ . Hence eq. (6.62) is reduced and written for the turbulent flow as

$$\nabla \cdot [(\mathbf{V}_{ht}\phi) - D_{pM}\nabla\phi] = 0 \quad (6.72)$$

The particle concentration generally shows a distribution in the vertical ( $y$ ) direction to the flow in any inclined pipeline transportation. Assuming constant particle settling velocity that is independent of the position, the governing equation becomes

$$-V_{ht,y} \frac{\partial\phi_1(y)}{\partial y} - D_{pM} \frac{\partial^2\phi_1(y)}{\partial y^2} = 0 \quad (6.73)$$

where  $\phi_1(y)$  is the local volumetric fraction of the solid particles in the upper layer,  $y$  is the distance in the normal direction to the flow as shown in Figures 6.3(b) and 6.4(b),  $V_{ht,y}$  is



the component of the mean hindered terminal settling velocity in  $y$  direction ( $V_{ht,y} = V_{ht} \cos \alpha$ ). The negative sign in front of  $V_{ht,y}$  in eq. (6.73) shows the direction of the settling velocity is opposite to that of the suspending liquid velocity (or opposite to the flow direction). As the volumetric fraction depends only on the vertical direction  $y$ , integration of eq. (6.73) gives the distribution of the particle concentration in the upper heterogeneous layer using the moving bed volumetric fraction,  $\phi_{d,2}$  as the boundary condition

$$\phi_1(y) = \phi_{d,2} \exp\left(-\frac{V_{ht} \cos \alpha}{D_{pM}}(y - y_2)\right) \quad (6.74)$$

Eq. (6.74) can also be written in terms of the central angle of the bed,  $\theta$ :  $y$  and  $y_2$  defined in Figure 6.3(b) for the two-layer and Figure 6.4(b) for three-layer flows can be expressed as

$$y = \frac{D}{2}(1 + \sin \theta) \quad (6.75)$$

$$y_2 = \frac{D}{2}(1 + \sin \theta_2) = \frac{D}{2}(1 + \sin \theta_B) \quad (6.76)$$

where  $\theta_B = \theta_2$  and  $\theta_B = \theta_3 + \theta_2$  for the two- and three-layer flows, respectively. Then, the integration of eq. (6.74) over the cross-sectional area of the upper layer gives the area-averaged mean concentration,  $\phi_{t,1}$

$$\phi_{t,1} = \frac{\phi_{d,2} D^2}{2A_1} \int_{\theta_B}^{\pi/2} \exp\left(-\frac{V_{ht} D \cos \alpha}{2D_{pM}}[\sin \theta - \sin(\theta_B)]\right) \cos^2 \theta d\theta \quad (6.77)$$

The mean hindered settling terminal velocity in eq. (6.77),  $V_{ht}$  can be calculated from semi-empirical Richardson and Zaki correlation (1954) given in eq. (4.147) in Chapter 4.

The mean diffusion coefficient,  $D_{pM}$  can be evaluated according to Taylor (1954) or Prandtl (1952) approach, which assumes that the coefficient of the mass transfer is almost equal to that of the momentum transfer,  $D_M$  and it is described by

$$D_{pM} = D_M = 0.052 V_* r_{h,1} \quad (6.78)$$

where  $r_{h,1}$  is the hydraulic radius of the upper-layer cross-section (Doron *et al.*, 1987, 1997; Doron and Barnea, 1996) and  $V_*$  is the shear or friction velocity defined by

$$V_* = \bar{V}_{s,1} \sqrt{\frac{f_1}{2}} \quad (6.79)$$

The mean diffusion coefficient,  $D_{pM}$  in equations given above is also considered to be independent of solid concentration, particle size, and shape for the monodispersed suspensions. However, the effect of these particle properties on  $D_{pM}$  and the variation of the particle diffusivity must be taken into account (Kaushal and Tomita, 2002; Kaushal *et al.*, 2002a, b;

Kumar *et al.*, 2003) in suspensions including multisized particles. For polydispersed suspensions, Karabelas (1977) considered the variation in the particle diffusivity, which is defined as

$$D_{pM} = \beta D_M \quad (6.80)$$

where  $\beta$  is the dimensionless particle diffusivity defined as a function of the area-averaged solid volume fraction,  $\phi_t$  and the static-settling volume fraction,  $\phi_{ss}$  (Kaushal and Tomita, 2002).

$$\beta = 1 + 0.125 \exp\left(\frac{4.22\phi_t}{\phi_{ss}}\right) \quad (6.81)$$

in which  $\phi_{ss}$  exhibits the highest concentration obtained from the settling of particles under the effect of gravity. However, the variation in particle concentration may affect the dimensionless particle diffusivity along the cross-sectional area of the pipe and thus, it is considered by Kaushal (1995) as

$$\beta = 1 + 0.09322 \exp\left(\frac{5.5423\phi(y)}{\phi_{ss}}\right) \quad (6.82)$$

The variation of the momentum diffusivity along the cross-sectional area of the pipe due to the turbulent motion affects the particle diffusivity, although, both the particle and momentum diffusivities are assumed to be constant across the cross-section (Karabelas, 1977). The variation of  $D_M$  depends on many parameters such as pipe diameter and the flow conditions. Hence,  $D_M$  is defined in turbulent flow (Longwell, 1977) as

$$D_M = 0.369RV_* \frac{y}{R} \left(1 - \frac{y}{R}\right) \quad 0 \leq \frac{y}{D} \leq 0.337 \quad (6.83)$$

$$D_M = 0.0775RV_* \quad 0.337 \leq \frac{y}{D} \leq 0.663 \quad (6.83a)$$

$$D_M = 0.369RV_* \frac{y}{R} \left(\frac{y}{R} - 1\right) \left(2 - \frac{y}{R}\right) \quad 0.663 \leq \frac{y}{D} \leq 1 \quad (6.83b)$$

where  $R$  is the radius of the pipe.

### 6.3.3.2 Particle dispersion in fully suspended flow

In heterogeneous suspensions flowing at higher velocities than the limit deposition velocity, the concentration distribution of the solid particles is approximated by the Rouse–Schmidt turbulent diffusion model across the entire pipeline cross-section. Hence, the mass flux of the solid particles due to gravity is balanced by the mass flux of particles moving upward in vertical ( $y$ ) direction due to the turbulent diffusion

$$D_{pM} \frac{d\phi(y)}{dy} = -V_{ht} \phi(y) \quad (6.84)$$

This model can be applied both to dilute and concentrated suspensions: The hindered settling terminal velocity,  $V_{ht}$  is used in concentrated suspensions, whereas, the settling terminal velocity of single particles,  $V_t$  is directly used in dilute monodispersed suspensions due to negligible effect of particle concentration on the particle motion. In the case of dilute polydispersed suspensions, the hindered settling velocity,  $V_{ht}$  is defined by eq. (4.147) with the exponent  $n = 4.7(1 + 0.15Re_p^{0.687})/(1 + 0.253Re_p^{0.687})$  (Matoušek, 2002).

The particle diffusion equation, eq. (6.84) can also be written in the form of force balance by taking the square of the both sides of this modified diffusion equation and replacing  $V_{ht}$  with  $V_t(1 - \phi)^n$  where  $V_t$  is defined by eq. (4.61) as  $V_t = \{(4/3)[(\rho_p - \rho)d_p g / (C_D \rho)]\}^{1/2}$ . Its rearrangement gives

$$\left( \frac{D_{pM}}{\phi(y)(1 - \phi(y))^n} \right)^2 \left( \frac{4d_p}{3C_D \rho} \right)^{-1} \frac{\partial \phi(y)}{\partial y} \left| \frac{\partial \phi(y)}{\partial y} \right| = -(\rho_p - \rho)g \quad (6.85)$$

The LHS of this equation denotes the turbulent diffusion and mixing effects whereas its RHS indicates the submerged weight of the particles in the absence of interparticle contact. The sign of the LHS term is conserved by using one of  $(\partial \phi(y)/\partial y)$  terms in absolute form. The dispersive stress due to turbulent diffusion depends on the solid volume fraction as shown in eq. (6.85).

In cases where the interparticle contact occurs, the submerged weight of the particle is conducted to the pipe wall by mechanical friction causing stresses due to this contact as explained in Section 6.2. In this case, the Bagnold dispersive stress is effective in determining the distribution of the particle volume fraction. The submerged weight of the particle at the RHS of eq. (6.85) is balanced by the Bagnold dispersive stress difference,  $(\partial \tau_{yy}/\partial y)$ ,

$$(\rho_p - \rho)g\phi(y) = \frac{\partial \tau_{yy}}{\partial y} = \frac{\partial}{\partial y} \left( -\eta \frac{dV}{dy} \right) \quad (6.86)$$

Substitution of this balance equation in eq. (6.85) gives

$$\left( \frac{D_{pM}}{\phi(y)(1 - \phi(y))^n} \right)^2 \left( \frac{4d_p}{3C_D \rho} \right)^{-1} \frac{\partial \phi(y)}{\partial y} \left| \frac{\partial \phi(y)}{\partial y} \right| = \left( \frac{-1}{\phi(y)} \right) \left( \frac{\partial \tau_{yy}}{\partial y} \right) \quad (6.87)$$

As the viscosity of the suspension,  $\eta$  strongly depends on the solid particle concentration, the changes in viscosity are effective on the particle dispersion. Thus, the higher-order terms in the viscosity equation (eq. (6.2) in Section 6.1.3) should be taken into account in the definition of the repulsive stress,  $\tau_{yy}$  as shown in eq. (6.64). Its derivative used in eq. (6.87) is evaluated by considering this effect, so a dispersion equation is developed for the shear-induced particle migration due to velocity and viscosity gradient in the presence of the turbulent effects.

## 6.4 MECHANISM OF FRICTIONAL LOSSES

The pressure drop due to friction over the length of the pipeline is related with the internal structure of the suspension flow. To elucidate the basis of all types of frictional losses in any suspension flow, interactions of solid particles with (1) each other, (2) the suspending liquid, and (3) the boundary of the flow must be known.

The fundamental assumption is that the friction is confined to the boundary of the suspension flow. Solid particles affect the total friction of the suspension flow through friction due to permanent, temporary or zero contact of particles with pipe wall, and friction at the interface of the granular bed and heterogeneous suspension layer. The frictions due to the interactions of the particles with the wall are related to the layers of the suspending liquid formed near the pipe wall region. The friction at the top of the bed is related with the boundary layers formed by the liquid around the solid particles. These liquid layers cause *viscous friction*, which also affects the friction arising from the contact of the solid particles with the pipe wall. Therefore, the liquid boundary layers and the shear stresses formed will be given first.

### 6.4.1 Frictional losses due to viscous flow

A very thin liquid film over the pipe wall is formed in the flow of a settling suspension through a pipeline similar to liquid flow. The thin liquid film between the wall and the particles adjacent to the pipe wall always shows laminar flow behavior independent of the flow regime of the suspension, since its velocity is too low for inertial forces, so turbulent effects to exist. The liquid film is called *laminar sublayer*.

The flow of liquid in the laminar sublayer is affected by the roughness of the pipe causing a resistance to flow. To estimate this resistance to the flow a parameter known as the relative roughness,  $(k_s/\delta_s)$  is defined as the ratio of the height of the wall roughness,  $k_s$  to the thickness of the laminar sublayer,  $\delta_s$ . The wall roughness completely remains within the sublayer. The relative roughness becomes negligible with an increase in the laminar sublayer and a decrease in the roughness of the wall.

The flow regimes for a liquid flowing in a pipe and the parameters effective on the friction factor are determined based on the experiments carried out in pipes roughened with sand (Nikuradse, 1930, 1933). The flow regimes are found to be related to the relative roughness,  $(k_s/\delta_s)$  (or Reynolds number) formed with the sand size of roughness and the friction velocity,  $V_*$  as

$$Re_{k_s} = \frac{k_s}{\delta_s} = \frac{k_s V_*}{(\mu/\rho)} \quad (6.88)$$

where the thickness of the laminar sublayer is  $\delta_s \approx (\mu/(V_*\rho))$ ,  $k_s$  denotes the sand size in Nikuradse's sand roughness. The flow regimes and the related parameters effective on the friction factor in Darcy–Weisbach equation (eq. (6.6)) are determined for (1) hydraulically smooth regime,  $0 \leq Re_{k_s} \leq 5$  where the friction factor only depends on  $Re_{k_s}$ , (2) transition regime,  $5 \leq Re_{k_s} \leq 70$  where both  $Re_{k_s}$  and  $k_s/R$  are effective in

the estimation of the friction factor. Here  $R$  is the radius or hydraulic radius in circular and noncircular ducts, respectively. The roughness extends partly outside of the laminar sublayer and part of the roughness remaining in the boundary layer forms an additional resistance to flow due to form drag, (3) Completely rough regime,  $Re_{ks} > 70$  where only  $k_s/R$  is effective on the friction factor. In this regime, roughness height extends outside the laminar sublayer and the largest amount of the resistance to flow arises from form drag acting on the roughnesses (Schlichting, 1979).

When a solid–liquid suspension flows instead of a single-phase liquid through a pipe, the suspending liquid forms a boundary layer around the solid particles in addition to the boundary layer along the pipe wall. Thus, the ratio of the Nikarudse particle roughness height to the size of the particles forming the suspension ( $k_s/d_p$ ) becomes an important parameter instead of ( $k_s/R$ ) in deciding the flow regime. This ratio will be taken up in Section 6.4.3.

## 6.4.2 Frictional losses due to particle–pipe wall interactions

### 6.4.2.1 Friction due to contact of solid particles with pipe wall

The presence of solid particles in the suspending liquid adjacent to the pipe wall causes viscous friction as the particles are not in contact with the pipe wall. The continuous contact of particles with the pipe wall causes the formation of stress with normal and shear components. The normal,  $F_{N,i}$  and shear stresses,  $F_{\tau,i}$  related through the dry-state friction factor,  $f_{Cf}$  was given in Section 6.2. If the suspended particles temporarily contact with the pipe wall, frictional losses due to interactions between the particles, suspending liquid and pipe wall occur.

The diameters of suspended coarse and fine particles cannot be differentiated clearly in the suspension. However, their friction behavior is essentially different and is considered to be related to the thickness of the viscous sublayer near the pipe wall. If the diameter of the solid particles is smaller than the thickness of the sublayer, the particles in the sublayer change the properties of the suspending liquid forming the sublayer, so the suspension properties are used to find the frictional losses. The description of the viscous shear stress as a function of the mixture properties is considered in equivalent liquid model (ELM). (Matoušek, 2002).

The particles larger than the thickness of the laminar sublayer do not affect the viscous friction: The larger particles always tend to move outside of the laminar sublayer and migrate toward the interior to escape from the large shear existing in this region. The particles outside of the laminar sublayer have no effect on the properties of the suspending liquid forming the sublayer. Hence, the properties of the suspending liquid are used to define the wall shear stress. The suspending liquid may form a sharp velocity gradient in coarse-particle suspensions at high flow rates. The coarse particles existing near the wall region cause *collisional* (or *mutual collisions*) and *turbulent dispersive actions*.

In collisional dispersive action, particles with different local velocities collide with each other and with the wall. The particles are impelled in the direction of the pipe wall. They generate stress acting against the pipe wall, which is known as the *Bagnold dispersive stress*. The Bagnold dispersive stress,  $\tau_{p,B}$  is defined for two different flow regimes, viscous

and turbulent flows (Bagnold, 1954). To distinguish the flow regimes, a dimensionless number,  $B$  is defined as

$$B = \frac{\rho_p d_{50}^2 \lambda^{1/2} \dot{\gamma}}{\mu} \quad (6.89)$$

where  $d_{50}$  is the median particle diameter, which is found from the cumulative size distribution of the particles,  $\lambda$  a parameter known as the linear concentration of the particles and given as

$$\lambda = \left( \left( \frac{\phi_m}{\phi_i} \right)^{0.3} - 1 \right)^{-1} \quad (6.90)$$

where  $\phi_i$  is the local volume fraction of the particles, and  $\phi_m$  the volume fraction at the maximum packing.

The dispersive stress,  $\tau_{p,B}$  in viscous regime ( $B < 40$ ) is described as a function of fluid viscosity as

$$\tau_{p,B} = \mu \left[ \frac{\phi^2 (2 - \phi)}{(1 - \phi)^3} \right] \dot{\gamma} \quad (6.91)$$

and  $\tau_{p,B}$  in turbulent regime ( $B > 450$ ) for the sheared flow is

$$\tau_{p,B} = K_B \rho_p d_{50}^2 \lambda^2 \left( \frac{dV_c}{dy} \right)^2 \quad (6.92)$$

where,  $K_B$  is a proportionality constant, found to be 0.013 by Bagnold's measurements.

The Bagnold-type solid shear stress can also be defined in the absence of contact of the particles with the pipe wall. In this case, the dry-state friction is neglected and stress is defined as

$$\tau_{p,B} = K_B \lambda^2 V_{s,av}^2 \quad (6.93)$$

where  $K_B$  is a proportionality constant.

$\tau_{p,B}$  in the presence and absence of contact of the particles with the pipe wall are calibrated using the pressure drop data in vertical pipe flows. The relations are summarized in Table 6.6. The results for horizontal flow obtained by neglecting the dry-state friction are also given in the same table.

The solids stress,  $\tau_{p,B}$  arising from these particle collisions with the pipe wall can be decreased by removing the coarse particles from the region near the pipe wall. Their removal is brought about by the liquid stream due to its lift (buoyancy) effect and this force is called as *hydrodynamic off-wall lift*.

#### 6.4.2.2 Frictional losses due to particle–liquid interaction: hydrodynamic lift

The liquid flows across the particles with a steep velocity gradient near the pipe wall. The particles rotate and a pressure gradient over the particles, known as the hydrodynamic (lift)

Table 6.6

Modified expressions for Bagnold's dispersive stress

Dry-state friction <sup>a</sup>	$d_p$ (mm)	References	
Vertical flow			
E	1.4–3.4	Shook and Bartosik (1994); Bartosik (1996)	$\tau_{p,B} = \left( \frac{8.3018 \times 10^7}{Re^{2.317}} \right) D^2 \rho_p d_{50}^2 \lambda^{1.5} \left( \frac{\tau_{l,w}}{\mu} \right)^2 \quad (6.94)$ <p>where <math>Re = \rho D V_{s,av} / \mu</math> and <math>\tau_{l,w} = (1/2) f_l \rho V_{s,av}^2</math></p>
E	1.8–4.6	Ferre and Shook (1998)	$\tau_{p,B} = \left( \frac{0.0214}{Re_p^{0.36}} \right) \left( \frac{d_{50}}{D} \right)^{0.99} \rho_p \lambda^{1.31} V_{s,av}^2 \quad (6.95)$ <p>where <math>Re_p = V_{s,av} \rho_p d_{50} / \mu</math></p>
NE	0.37	Matoušek (2005)	$\tau_{p,B} = 0.991 \lambda^{0.81} V_{s,av}^{0.99} \quad (6.96)$
Horizontal flow			
NE	0.175	Gillies and Shook (2000)	$\tau_{p,B} = 0.00002 \lambda^2 V_{s,av}^2 \quad (6.97)$
NE	0.37	Matoušek (2005)	$\tau_{p,B} = 0.499 \lambda^{1.36} V_{s,av}^{1.02} \quad (6.98)$

<sup>a</sup>Contact of the particles with the wall, E: exist, NE: nonexistent.

force is created normal to the pipe wall due to this velocity gradient. It repels the particle from the wall of the horizontal pipe and decreases the collisional stress (dry-state friction) at the wall. The lift force is found to be effective in a certain portion of the turbulent region, but not in the transition layers. The lift diminishes throughout the transition layer range ( $5 < y^+ < 30$ ) and drops to a negligible value on reaching the laminar sublayer ( $y^+ = 5$ ).

The lift force,  $F_L$  for a solid particle interacting with water in the horizontal direction can be expressed as

$$\left( \frac{F_L}{[(\rho_p - \rho)g\pi d_{50}^3/8]} \right)_{\max} = \frac{0.27 f_l \rho V_{s,av}^2}{8(\rho_p - \rho)g d_{50}} \quad y^+ > 30 \quad (6.99)$$

where  $f_l$  is the Darcy–Weisbach friction factor for the liquid flow over the pipe wall and  $y^+$  is the dimensionless distance from the wall. In horizontal flows at high velocities (Matoušek, 2002), there is no effect on solid volume fraction. The same trend is also observed in the vertical flow of fine and coarse particles at low and moderate solid concentrations (Newitt *et al.*, 1961; Matoušek, 2005). The lift force increases with increasing particle diameter, therefore, is not effective in fine suspensions. Particle size range, in which the lift force is effective, is found to be in the range of 0.15–0.40 mm for sand–water slurries (Wilson and Sellgren, 2003).

In heterogeneous suspension flow, the vertical pressure distribution across the channel is measured to detect a lift force: The pressure observed may be positive or negative relative to the hydrostatic head of water (Campbell *et al.*, 2004). In dilute region near the top of the channel, the pressure is positive, which shows that the particles are supported by the turbulent eddies of the liquid. The pressure is negative near the wall region at the lower section of the channel indicating that the negative lift force moves the particles toward the wall.

#### 6.4.2.3 Friction at the top of the granular bed

The upper boundary of the granular bed consists of mobile particles and causes frictional losses in the flow of settling suspensions in stratified flow patterns. The shear stress at this boundary,  $\tau_{B,top}$  (equivalent to  $\tau_{12}$  in two- and  $\tau_{23}$  in three-layer flow) for closed conduits is defined by Wilson and Pugh (1995) as

$$\tau_{B,top} = \left( \frac{f_B}{8} \right) \rho \bar{V}_{s,top}^2 \quad (6.100)$$

where  $f_B$  is the friction factor, defined in terms of Darcy–Weisbach friction factor as  $f_B = 4f_i$ , and  $\bar{V}_{s,top}$  is the mean velocity of suspension above the contact bed. For pressure gradient ratio,  $(H_s \rho / (\rho_p - \rho)) > 0.0167$ ,  $f_B$  is experimentally determined as

$$f_B = 0.87 \left( \frac{H_s \rho}{\rho_p - \rho} \right)^{0.78} \quad (6.101)$$

where  $H_s$  is the hydraulic gradient of the suspension flow.

In the determination of the shear stress at the top of the bed, the upper boundary has a roughness height related to the particle size in a nondistorted bed given in eq. (6.25). However, the particle size is not a proper boundary roughness parameter for distorted beds. Another characteristic size that can be used as a boundary roughness parameter is the thickness of the sheared portion of the bed.

A rough-boundary concept based on Nikuradse particle roughness height,  $k_s$  is used to determine the shear stress,  $\tau_{B,top}$  (Wilson, 1989; Sumer *et al.*, 1996; Ribberink, 1998; Matoušek, 2005). The roughness height is given as

$$\frac{k_s}{d_{50}} = f(Sh_B) \quad (6.102)$$

The LHS of this equation indicates the relative bed roughness, which depends on the Shield number (particle mobility),  $Sh_B$ , defined as the square of the ratio of the shear velocity at the upper surface of the bed,  $V_{*,B}$  to the *characteristic velocity*,  $V_{ch}$ .

$$Sh_B = \left( \frac{V_{*,B}}{V_{ch}} \right)^2 = \left[ \frac{V_{*,B}}{[(\rho_p - \rho)/\rho] g d_{50}^{1/2}} \right]^2 \quad (6.103)$$



Table 6.7

RHS of eq. (6.118) for the Nikuradse’s friction equation

$f(Sh_B)$	$Sh_B$ range	Comments	References
$5Sh_B$		Wilson’s close conduit data	Wilson (1989)
$1 + 6(Sh_B - 1)$	$1 < Sh_B < 7$	Wilson’s close conduit data in given $Sh_B$ range	Ribberink (1998)
$k_s/d_{50}$	$0.8 < Sh_B < 5$	Acryl particle $V_t^* = V_t/V_{ch} = 0.72$	Sumer <i>et al.</i> (1996)
with $\bar{V}_{s,top}/V_{*,B} = \sqrt{8/f_B'} = 2.46 \ln[14.8(D_{h,B}/4)/k_s]^a$			
$0.13(Sh_B + 1.38)^{2.34}$	$4 < Sh_B < 25$	0.2–25 mm sand particles	Matoušek (2004, 2005)

<sup>a</sup> $D_{h,B}$ : Hydraulic diameters (hydraulic diameter of the upper layer,  $D_{h,1}$  and of the moving bed in three-layer flow,  $D_{h,2}$ ).  $\bar{V}_{s,top}$ : Mean suspension velocity at the surface of the bed (mean suspension velocity of the upper layer,  $\bar{V}_{s,1}$  and of the moving bed in three-layer flow,  $\bar{V}_{s,2}$ ).

The characteristic velocity of the particle  $V_{ch}$ , the counterpart for settling particles of the friction velocity in pipe flow  $V_{*,B}$ , is given by

$$V_{ch} = \left( \left[ \frac{\rho_p - \rho}{\rho} \right] g d_{50} \right)^{1/2}$$

(6.104)

and the shear velocity,  $V_{*,B}$  is related to  $f_i$  through eq. (6.79). Using eqs. (6.102) and (6.103), the shear stress at the upper surface of the bed is calculated by taking the roughness of the boundary into consideration.

Function of  $f(Sh_B)$  given at the RHS of eq. (6.102) is formulated by using the data obtained from closed conduits and the results are summarized in Table 6.7. Eq. (6.102) can be generalized as the ratio of Nikuradse equivalent roughness size to any sediment particle size as  $k_s/d_x$ . Here  $d_x$  is the diameter of particles with percentage in a cumulative particle size distribution of x%. Using one of these particle sizes in determining  $k_s/d_x$ , resistance to flow of settling suspensions due to formation of a bed with a boundary consisting of movable particles are reported in both pipes and channels (Yen, 1991; Yen and Asce, 2002).

6.5 PRESSURE LOSSES IN PIPE FLOW

In the flow of solid–liquid suspensions through a pipe, the solid particles at any concentration may form a homogeneous or heterogeneous single-phase flow or layered flow such as two-layer (Figures 6.2(b) and 6.3) or three-layer (Figure 6.4) flow depending on the flow rate, causing a particle concentration distribution along the vertical direction across the cross-section of the pipe as illustrated in Figure 6.1. These flow patterns affect the pressure losses along the pipe. Superficial particle and suspension velocities also change with delivered particle volume fraction due to variation in flow pattern of the suspension flow.

**Table 6.8**

Models used in flow patterns

Flow	Model used for				
	Momentum		Particle dispersion	Related sections	Figure numbers
	Model	Wall–particle interaction <sup>a</sup>			
Fully suspended	ELM <sup>b</sup>	NE		6.2.1, 6.4	6.7
Two-layer	Two-LFM	E	Rouse–Schmidth model, eq. (6.84)	6.2.2, 6.3.3, 6.4	6.8, 6.11
Fully suspended	Bartosik–Shook (eq. (6.110))	E		6.2.1, 6.4	6.9
Three-layer	Three-LFM	E		6.2.3, 6.4	6.10, 6.15

<sup>a</sup>E: exist, NE: nonexistent.<sup>b</sup>ELM: Equivalent liquid model.

Therefore, plots of these parameters can be used as a tool to show the flow patterns such as, frictional losses against the mean suspension velocity (Section 6.5), particle concentration distribution along the vertical distance,  $y$  above the pipe wall (Section 6.6), and superficial suspending liquid velocity against the particle superficial velocity or suspension velocities as a function of delivered solid volume fraction (Section 6.9). All of these plots show the flow patterns of suspensions flowing through horizontal and inclined pipes whereas only the plot of frictional losses against the mean suspension velocity is used to indicate the flow patterns of the suspensions in vertical pipes. Due to gravitational force, only homogeneous or heterogeneous fully suspended flow is observed in vertical flow and a bed never forms.

Flow patterns both estimated theoretically and based on experimental measurements are given in this section, Sections 6.6 and 6.9. Models used in the estimation of theoretical flow patterns and related sections in this chapter are summarized in Table 6.8.

In Figure 6.5, the general relation between the pressure loss and suspension velocity is given as a function of solid volume fraction. In the case of pure liquids, which do not contain any particles, the pressure loss changes linearly with velocity. At high velocities where a homogeneous region is formed, the pressure drop of the suspensions approaches that of the pure liquid. As the suspension velocity decreases, the relation between the pressure loss and velocity becomes nonlinear. The velocity at this transition point is called *suspending* (or *homogeneous suspension*) velocity,  $V_{\text{susp}}$ . A further decrease in velocity causes a decrease in pressure loss which shows a minimum at a point, called *limit deposit velocity*,  $V_{\text{dep}}$ . The velocities below the  $V_{\text{dep}}$  cause formation of the moving bed (bedload), which results in an increase in pressure loss due to the increase in hydrostatic head and particle–particle, particle–wall, and particle–liquid interactions. The velocity at which the pressure loss

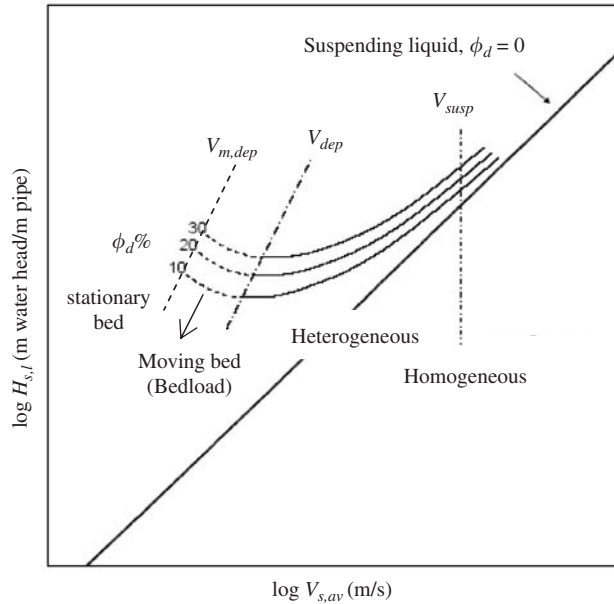


**Figure 6.5** Flow regimes in solid–liquid two-phase flow and transition velocities. (Almedeij and Algharaib, 2005. Figure 1 in the original. Redrawn with permission of Elsevier.)

increases and the velocity below which there is no flow is called *minimum deposition velocity*,  $V_{m,dep}$ . A stationary bed forms since the velocity is not sufficient to cause particle motion.

Initial formation of a stationary bed below the moving bed causes an opposing torque acting on the moving particles that helps the particles to overcome gravitational force, minimizing the pressures losses. The particles move with a minimum velocity at this condition. Hence, the minimum velocity can theoretically be based on the initial formation of a stationary bed. The velocity corresponding to the minimum energy gradient for a given solid volume fraction is expressed as *limit deposit velocity*,  $V_{dep}$  (Matoušek, 2002, 2005; Wilson *et al.*, 2002; Almedeij and Algharaib, 2005; Kaushal *et al.*, 2005).

An increase in solid volume fraction increases pressure losses due to increase in interactions among the particles in the bed region, so both minimum deposition and limit deposit velocities increase. The homogeneous suspension velocity remains constant since the homogeneous phase is always dilute, and independent of the particle concentration.

The other parameters affecting pressure losses are pipe inclination, pipe diameter, density and diameter of the solid particles, properties of the liquid phase, and dry-state friction factor.

### 6.5.1 Pressure losses in horizontal flow of suspensions

Variation of pressure losses with mean velocity as a function of area averaged solid volume fraction are given in Figure 6.6 (a)–(c) for spherical glass beads of sizes 125 and 440  $\mu\text{m}$  and their mixture on an equal mass basis (Kaushal *et al.*, 2005).

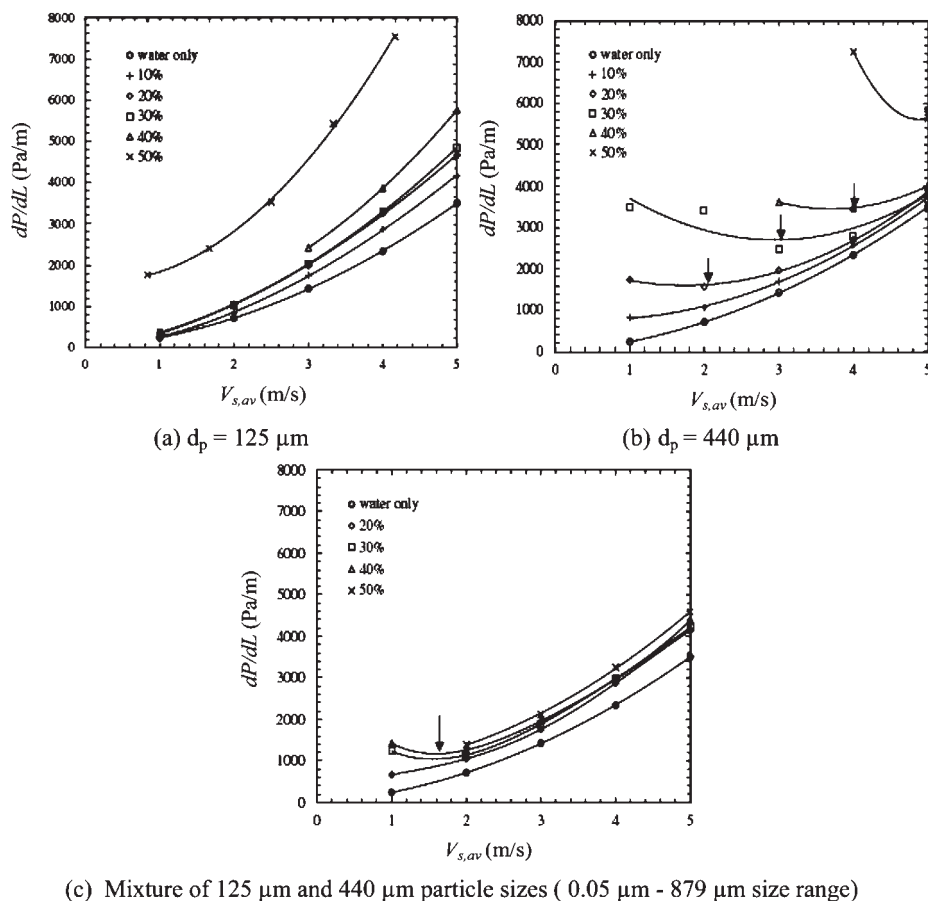


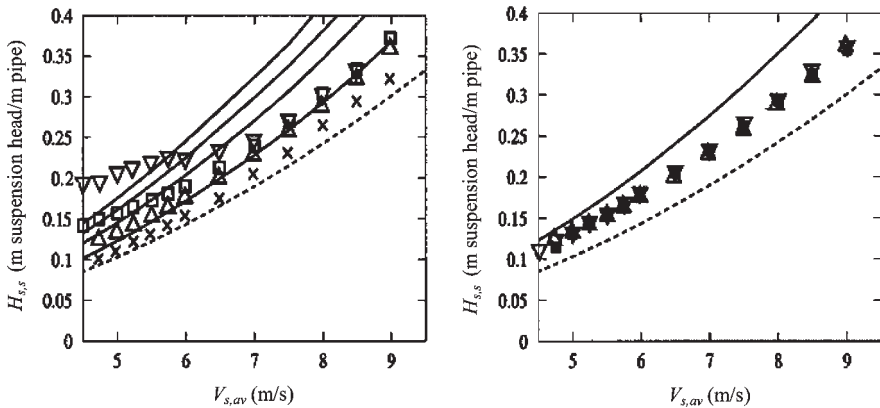
**Figure 6.6** Effect of particle size distribution on pressure gradient in the flow of highly concentrated slurries with specific gravity of 2.47 in 54.9 mm diameter horizontal pipe. (Kaushal *et al.*, 2005. Figures 3–5 in the original, Redrawn with permission of Elsevier.)

Pressure gradients of  $125 \mu\text{m}$  particle suspensions increase with increasing solid volume fraction at any suspension velocity as given in Figure 6.6(a). The rate of increase in frictional losses is greater at high velocities than at low velocities. No minimum is observed in the pressure gradients for any of the volume fractions. The nonlinear pressure loss suspension velocity relationship together with Figure 6.5 can be interpreted as an indication of fully suspended heterogeneous flow pattern. A similar relation between the pressure gradient and solid volume fraction is observed for  $440 \mu\text{m}$  particles as a function of velocity (Figure 6.6(b)) for all particle concentrations, except 50% by volume. The pressure gradient curves corresponding to different solid particle concentrations converge to a single curve as the velocity increases above  $4 \text{ m s}^{-1}$ . At solid concentrations equal or greater than 20%, a minimum is observed in the pressure gradient (pointed out by arrows), which signifies the formation of stratified flow in Figure 6.6(b). The velocity corresponding to

the minimum pressure is the limit deposit velocity as presented in Figure 6.5. Due to the effect of gravity, the amount of coarse particles in the bed increases as suspension velocities decrease below the limit deposit velocity in Figure 6.6(b) and, so does the height of the bed. This causes an increase in hydrostatic head and in the interactions among the particles causing the pressure losses to increase. The increase in the thickness of the bed reduces the pipe free cross-sectional area and the pipeline is choked. These trends show the significance of the limit deposit velocity as an important parameter in the design of solid–liquid suspension pipelines. Above the limit deposit velocity the pressure losses for suspensions of coarse particles is less than that of the fine particles since the viscous frictional forces arising from the liquid film near the pipe wall is only dependent on the properties of the suspending liquid in the flow of the coarse particles larger than the thickness of the laminar sublayer (Section 6.4.2).

For mean velocities greater than  $5 \text{ m s}^{-1}$ , the frictional losses, determined experimentally and predicted by ELM, in horizontal flow for medium and fine sands and their mixtures are given in Figures 6.7(a) and (b) as a function of solid volume fraction (Matoušek, 2002). Both the size and the specific gravity of the particles are in the range of the particles studied by Kaushal *et al.* (2005). Although the diameter of the pipe is large ( $D = 150 \text{ mm}$ ), the mean velocities are higher than that of given in Figure 6.6, because of the high volumetric flow rates.

In Figure 6.7, ELM explained in Sections 6.2 and 6.4 gives good results in agreement with the experimental results at low solid volume fractions (up to 0.43) and low mean suspension velocities (up to  $5 \text{ m s}^{-1}$ ) independent of the particle size. Both an increase in



(a) effect of solid volume fraction (b) effect of particle size at  $\phi_d = 0.27$   
 symbols: (---) : water, (—) : ELM model, (x):  $\phi_d = 0.13$ , ( $\Delta$ ):  $\phi_d = 0.26$ , ( $\square$ ):  $\phi_d = 0.35$ , ( $\nabla$ ):  $\phi_d = 0.43$  in (a) and fine sand in (b), ( $\blacksquare$ ): medium sand  $\phi_d = 0.12$  + fine sand  $\phi_d = 0.15$

**Figure 6.7** Frictional losses measured and predicted in horizontal flow for medium and fine sands and their mixtures. (Matoušek, 2002. Figures 5(a) and (b) in the original. Redrawn with permission of Elsevier.)

volume fraction and mean velocity cause an increase in the difference between the experimental and model results due to extremely thin sublayers near the wall at high velocities which prevents the remaining of particles in the sublayer. However, the ELM model uses the suspension properties as that of the sublayer as explained in Sections 6.2 and 6.4. Thus, the ELM model overpredicts the experimental results and is not appropriate to predict the pressure losses at high velocities in horizontal flow.

The nonlinear relation between the pressure gradient and mean velocity in Figure 6.7 is both theoretically and experimentally observed. Lack of a minimum indicates fully suspended heterogeneous flow. In Figure 6.7(a), the increase in pressure loss as a function of solid volume fraction is observed up to the mean velocity of  $7 \text{ m s}^{-1}$ , above which solid volume fraction has no effect on pressure loss, except  $\phi_d = 0.13$ . The pressure losses given in Figure 6.7(b) for medium, fine and their mixture shows that there is no effect of the particle size on the pressure loss at constant solid volume fraction  $\phi_d = 0.27$  for all mean suspension velocities.

Pressure losses in flow of coarse and coarse-fine suspension mixtures, are given in Figure 6.8. The experimental pressure losses showing a minimum around  $3\text{--}4 \text{ m s}^{-1}$  points out a transition from a heterogeneous single- to two-phase flow. Therefore, two-layer flow model together with particle-dispersion equation is considered in modeling the flows of coarse particles and their mixture with fine particles. Model results in Figure 6.8 are obtained using two-layer flow equations (Section 6.2.2) together with solid concentration equation (eq. (6.84)) with Richardson–Zaki exponent given in Section 6.3.3 and the bed wall friction model of Wilson (solids friction due to permanent contact of the particles with a pipe wall is taken into consideration) (Section 6.4.2). In coarse–fine suspensions, the suspending liquid is considered as pseudohomogeneous fine particle–water mixture. A reasonable agreement between the model and measured results is observed in Figure 6.8 with the

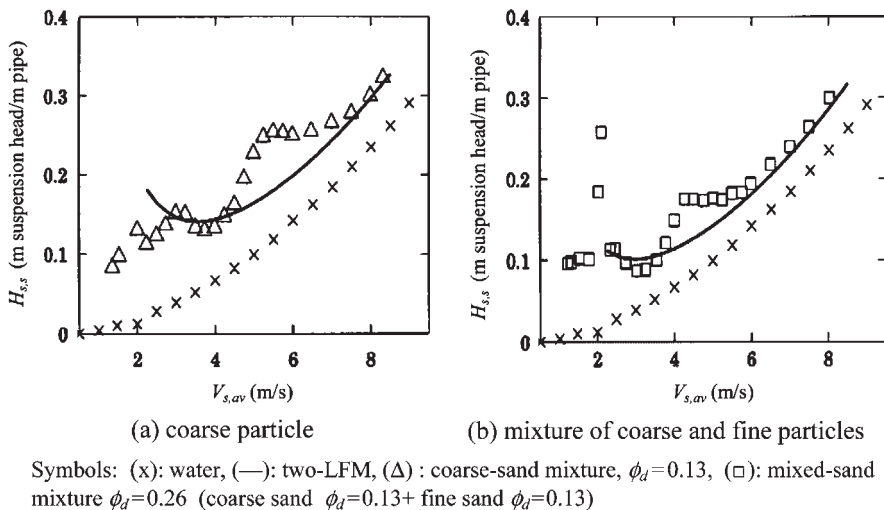


**Figure 6.8** Frictional losses measured and predicted in horizontal flow for coarse and coarse–fine sand particles. (Matoušek, 2002. Figure 7 in the original. Redrawn with permission of Elsevier.)

addition of fine sand to coarse sand flow in the range of velocity from 2 to 4 ms<sup>-1</sup> (Matoušek, 2002).

The evaluation of the pressure losses measured in horizontal pipes can be summarized as: the size of particle is effective on the pressure losses and the flow patterns at low and moderate velocities; the pressure losses are independent of the particle size at high velocities where a heterogeneous, fully suspended flow is observed.

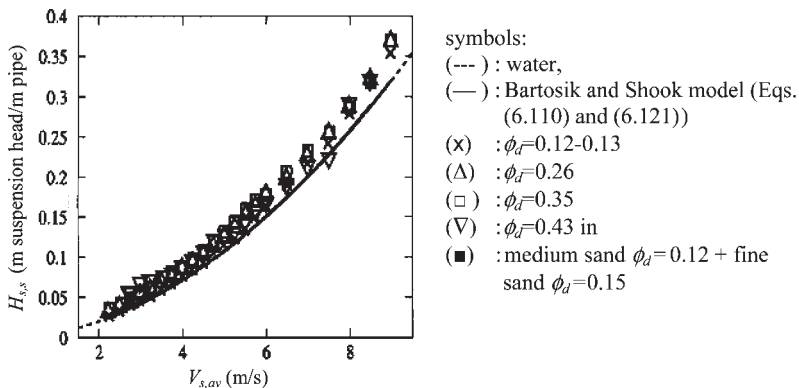
### 6.5.2 Pressure losses in vertical flow of suspensions

In vertical pipes, solid–liquid suspension flowing under the effect of gravity only forms homogeneous or heterogeneous flow, without a bed formation. The flow behavior of sand suspensions of medium size range ( $d_{50} = 0.37$  mm) through a vertical pipe is given in Figure 6.9 in terms of pressure losses at different solid volume fractions (Matoušek, 2002). The solid effects due to Bagnold dispersive stress acting against the pipe wall are taken into account with the use of eq. (6.94) (the Bartosik and Shook model). In this model, the frictional head loss,  $H_{s,l}$  equation for the vertical pipe is obtained from the force balance at equilibrium in terms of liquid,  $\tau_{w,l}$  (eq. (6.6)) and solid,  $\tau_{p,B}$  shear stresses (Section 6.4.2.1) at the pipe wall as

$$H_{s,l} = \frac{4(\tau_{w,l} + \tau_{p,B})}{D} \quad (6.105)$$

where the unit of  $H_{s,l}$  is given in the units of (m liquid head/m pipe length).

The model underpredicts the pressure losses of the suspensions at different solid volume fractions in Figure 6.9 and coincides with that of water. Thus, it can be concluded that the solids effect due to Bagnold stress is negligible in medium-sized particle flow through a vertical pipe. Application of Bartosik and Shook model to the suspensions with different particle size also gives the same results observed in Figure 6.9, so there is no effect of Bagnold stress on suspension flow. The pressure losses determined experimentally in this



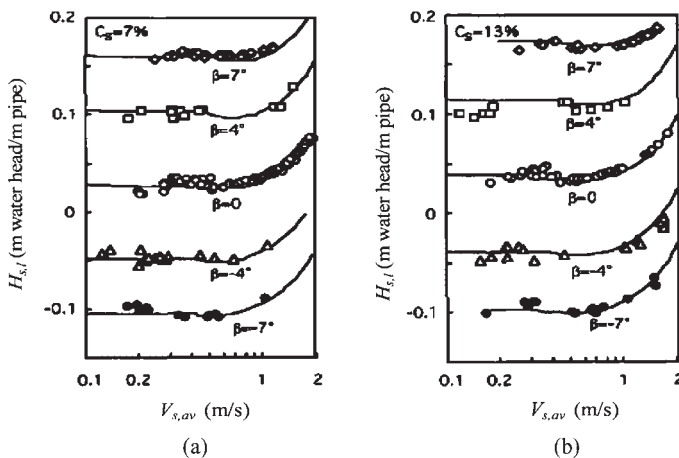
**Figure 6.9** Pressure losses measured and predicted in vertical flow for medium sand. (Matoušek, 2002. Figure 4(a) in the original. Redrawn with permission of Elsevier.)

figure do not exhibit a difference depending on the particle volume fraction and they are very close to those of water. This shows that the suspension behaves as a viscous liquid with the physical properties of the suspension up to a mean velocity of  $5 \text{ m s}^{-1}$ . Above  $5 \text{ m s}^{-1}$ , a slight increase in pressure loss is observed with increasing velocity. It is found to be independent of solid volume fraction and particle size (Matoušek, 2002).

### 6.5.3 Pressure losses in flow through inclined pipes

Inclination of a transportation line is effective on the pressure losses given by the momentum balance equations (i.e., eqs. (6.7), (6.14), (6.36)). As the suspension flows upward, an increase in inclination causes an increase in pressure loss due to increase in the effect of gravity in reverse direction. In the downward flow of the suspension, the gravity acts as a driving force. Consequently, the pressure losses increase with increasing inclination relative to horizontal flow ( $\alpha = 0^\circ$ ) in both positive and negative scales for up- and down-flows, respectively.

Results of experiments conducted in an experimental setup, which could be tilted up to an angle of  $7^\circ$  from the horizontal position, together with the related model studies are given in Figure 6.10. The inclination of the pipe affects the magnitude of the pressure losses but not the trends in the pressure loss curves in Figure 6.10. When suspension velocity is too low to move the solid particles, a stationary bed forms at the lower part of the pipe over the pipe wall. The change in the pressure losses is insignificant, at these low velocities. As the mean suspension velocity increases, the pressure losses decrease and a minimum appears in the pressure drop curve denoting a transition to flow with a moving bed. Beyond this minimum, the head losses increase with increasing velocity and fully



Symbols: data measured, lines: Three LFM,  $\rho_p = 1240 \text{ kg/m}^3$ ,  $d_p = 3 \text{ mm}$ ,  $D = 50 \text{ mm}$

**Figure 6.10** Effect of angle of inclination on frictional head loss measured and predicted; (a)  $C_s = \phi_d = 7\%$ , (b)  $C_s = \phi_d = 13\%$ ,  $\beta = \alpha$ : Angle of inclination. (Doron *et al.*, 1997. Figure 4 in the original. Redrawn with permission of Elsevier.)



suspended flow sets in. The experimental results show the presence of a three-layer flow. Therefore, three-layer flow model (Section 6.2.3), considering the effect of inclination on the pressure loss, is used and the model results of pressure loss are found to be in good agreement with the measured data (Doron *et al.*, 1997) in Figure 6.10.

Both model and experimental results indicate that the pressure losses increase with increasing inclination in positive or negative scale depending on the direction of the suspension flow. As in horizontal pipes, higher solid volume fractions also bring about higher-pressure losses in inclined pipes (Figure 6.10(a) and (b)).

## 6.6 PARTICLE CONCENTRATION DISTRIBUTIONS IN DIFFERENT FLOW PATTERNS

Another way to elucidate the flow patterns in settling suspensions is to plot distribution of particle concentration against the vertical distance above the pipe wall (Figure 6.11(a)). The particle distribution can both experimentally and theoretically be determined. Its theoretical estimation is based on solution of a particle-dispersion equation derived depending on the flow conditions (Section 6.3 in this chapter). Experimental observations of the effect of particle size, flow velocity, and addition of the fine particles on the particle concentration distributions will be given in this section.

### 6.6.1 Effect of particle size on flow pattern

Concentration distributions, determined experimentally, for fine ( $d_{50} = 0.37$  mm) and coarse ( $d_{50} = 1.85$  mm) sand particles suspended in water flowing through a 150 mm pipe are given in terms of the volume fraction in Figure 6.11 (Matoušek, 2002). In Figure 6.11b, fine sand particles indicate that there is no contact bed at  $6 \text{ m s}^{-1}$  mean suspension velocity that is higher than the limit deposit velocity in a horizontal pipe whereas a contact bed occupies at around  $\phi_d = 0.4$  volume fraction at the bottom of the pipe in the flow of medium sands.

Analysis of the experimental data given in this figure shows that the solid-dispersion coefficient  $D_{pM}$  remains constant throughout the turbulent suspension flow for both fine and medium sand particles. The ratio of the solid-dispersion coefficient to the shear velocity,  $(D_{pM}/V_*)$  defined by eqs. (6.78) or (6.83) is taken as 0.009 and 0.0115 for fine and medium sands, respectively. Theoretical concentration distributions illustrated in the same figure are based on Rouse–Schmidt turbulent diffusion model (eq. (6.84)). However, this model can only be applicable in the absence of the contact bed at mean velocities higher than the limit deposit velocity in a heterogeneous suspension flow. Therefore, the modeled concentration distribution in medium-sized sand particles is linked to the contact bed at the bottom of the pipe in Figure 6.11c. The results of the model are in good agreement with the experimental distributions of fine, medium (up to contact bed) and mixtures of fine–medium sands.

In the flow of coarse sands ( $d_{p,50} = 1.85$  mm), the experimental concentration distribution in Figure 6.11(c) indicates a sharp decrease but not the distribution found by the turbulent diffusion model in which  $D_{pM}/V_*$  is taken as 0.0115. This shows that the shearing

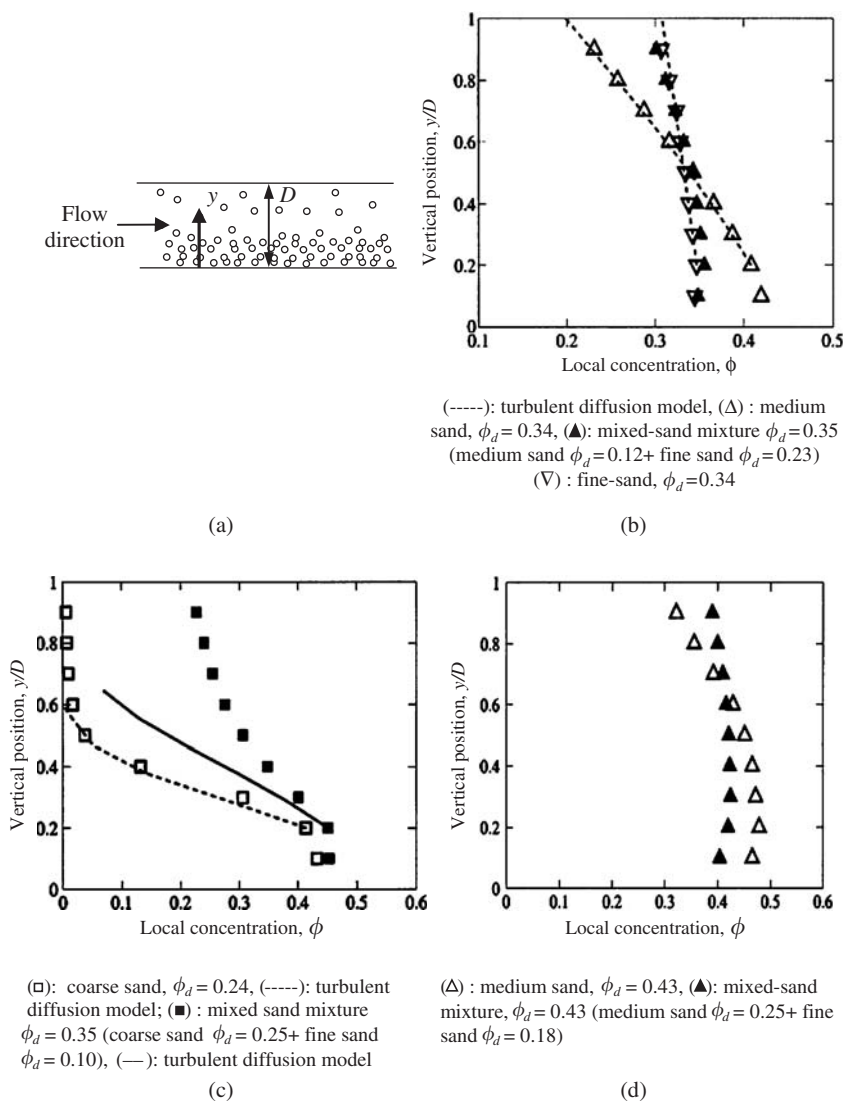


**Figure 6.11** Particle concentration distribution measured and predicted by the Rouse-Schmidt turbulent diffusion model at mean velocity  $6 \text{ m s}^{-1}$  in 150 mm pipe (Matoušek, 2002. Figures 2 and 3 in the original. Redrawn with permission of Elsevier.)

of the upper surface of the contact bed is more effective than the support of the sand particles due to turbulent diffusion of the suspension in the development of the concentration distribution above the contact bed. The turbulent eddies formed in the suspending liquid cannot suspend the coarse and heavy particles completely and a large shear stress at the upper surface of the contact bed is produced by the pressure gradient acting along the

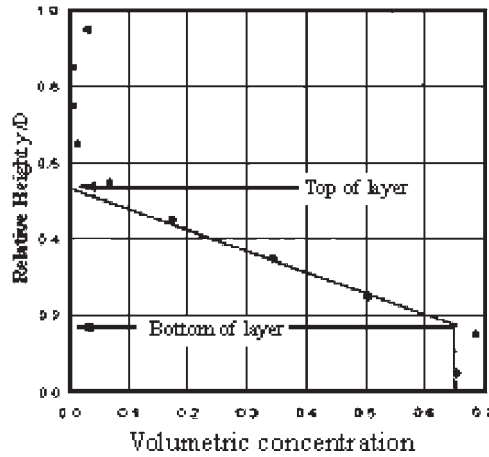


**Figure 6.12** Concentration profile due to the shearing of the upper surface of the bed and shear layer between the suspended and dense phases: Silica particles ( $d_p = 0.56$  mm,  $SG_p = 2.65$  in a 10 cm pipe at  $1.5 \text{ m s}^{-1}$ ). (Pugh and Wilson, 1999. Figure 2 in the original, with permission of Elsevier).

pipeline. Hence, the shear stress causes the development of a shear layer with the characteristic shape of a concentration distribution illustrated in Figure 6.12. When the shear stress at the top of the bed is effective, a concentration distribution similar to Figures 6.12 and 6.11(c) is observed. Thus, the turbulent diffusion model seems to be appropriate in the shear layer and the distribution of particle concentration found by the model is linked to the contact bed.

Results in Figure 6.11(b) and (c) show that flow patterns of sand–water suspensions gradually change from fully suspended heterogeneous flow to stratified flow based on the formation of the contact bed with increasing particle diameter at constant mean suspension velocity that is higher than the limit deposit velocity. The concentration profiles, determined experimentally, show that the solid particle volume fraction in the stationary bed at the lower portion of the pipe is about 0.43–0.45 in Figure 6.11(c) and 0.65 in Figure 6.12, respectively. An interfacial ramp exists above this stationary bed that denotes a linear decrease of solid volume fraction with height along the diameter of the pipe.

In Figure 6.11(c), the region between bottom of the fully suspended region and top of the stationary bed (the interface between top and bottom layers in Figure 6.12) shows two types of behavior: In the case of mixed-sand mixture, the interface is sharp, which denotes that the effective interfacial roughness depends on the particle size (Section 6.4.3). However, the interfaces in coarse particles and in Figure 6.12 form a ramp, which indicates an interfacial thickness (height) of many grain diameters.

In Figure 6.12, the solid concentration above the ramp is smaller and the concentration profile is curved which can be interpreted as particles supported by eddies. In Figure 6.12, height of the ramp corresponding to the nearly linear portion of the profile is known as the *shear layer thickness*,  $\delta_s$ . At the bottom of the ramp, the shear stress (or Bagnold shear force) and the submerged weight of the contact bed (Sections 6.2.2 and 6.4.2) are always effective resisting the motion of the particles. Thus, the shear layer thickness,  $\delta_s$  is proportional to the

shear stress, which signifies that the interfacial friction factor depends on the pressure gradient ratio ( $[H_{s,l} \rho / (\rho_p - \rho)]$ ), but not on the particle size.

### 6.6.2 Effect of flow velocity on flow pattern

Another parameter affecting the flow pattern is the flow velocity, which signifies the asymmetric distribution of particles with respect to the degree of asymmetry, increasing with decreasing flow velocity for the same overall solid volume fraction as shown in Figure 6.13. A decrease in flow velocity causes a decrease in turbulent energy that keeps the solids in suspended form in the liquid. An increase in delivered solid volume fraction,  $\phi_d$  reduces the asymmetry due to an increase in particle–particle interactions that are extremely strong at lower velocities, and at higher concentrations (Figures 6.13(a) or (b)). With an increase in the particle size, the asymmetry in the distribution also increases due to the gravity effect for a given delivered solid volume fraction (i.e.,  $\phi_d = 0.10$  or  $0.30$  in Figures 6.13(a) and (b)). It can be concluded that solid particle concentration distribution depends on the flow velocity, overall concentration of the suspension, and the particle size.

The maximum solid concentration at the bottom of the pipe does not change. It expands up to the center of the pipeline and then suddenly drops at the upper half of the pipeline at  $\phi_d = 0.30$  in  $440\mu\text{m}$  coarse particles whereas it remains constant along the vertical direction above the pipe wall in  $125\mu\text{m}$  particles. This difference in the concentration distribution can be attributed to the moving bed regime for coarse particles.

The mixed suspension including both  $125\mu\text{m}$  and  $440\mu\text{m}$  particles show solid concentration distributions similar to those of  $125\mu\text{m}$  particles and the solid concentration at the bottom of the pipe is also comparable with that in  $125\mu\text{m}$  particles (Figure 6.13(c)). With increasing  $\phi_d$  for a given suspension velocity in the same figure, the distributions become steep and the flow exhibits the lower stratification. However, the distributions are wider than those in  $125\mu\text{m}$  particles, since the particle size range of the suspension increases and becomes broad. Comparison of the distributions in Figure 6.13 shows that the solid volume fraction, the size of particles making up the suspension, and their size range are effective on flow pattern.

### 6.6.3 Effect of fine particles on flow pattern

Addition of fine sand particles to medium and coarse particles changes the properties of the suspending liquid, and the flow pattern. In this case, the larger particles will move in a fine-particle suspension instead of liquid water. The density difference between the suspending medium and the sand particles decreases, resulting in a decrease of the settling velocity of the particles, hence, a decrease in stratification.

The added fine sands decrease the stratification behavior of the medium sands in Figures 6.11(b) and (d) at the same delivered solid volume fraction. Increasing this fraction increases the solid concentration at the wall and reduces the asymmetry in the concentration distribution due to the interference effect between solid particles.

In contrary to the coarse particles, the flow of mixed particles shows a lower stratification behavior due to the hindered settling effect on the coarse particles in the mixed flow, hence a decrease in the solid effect, which is the difference between the pressure losses of

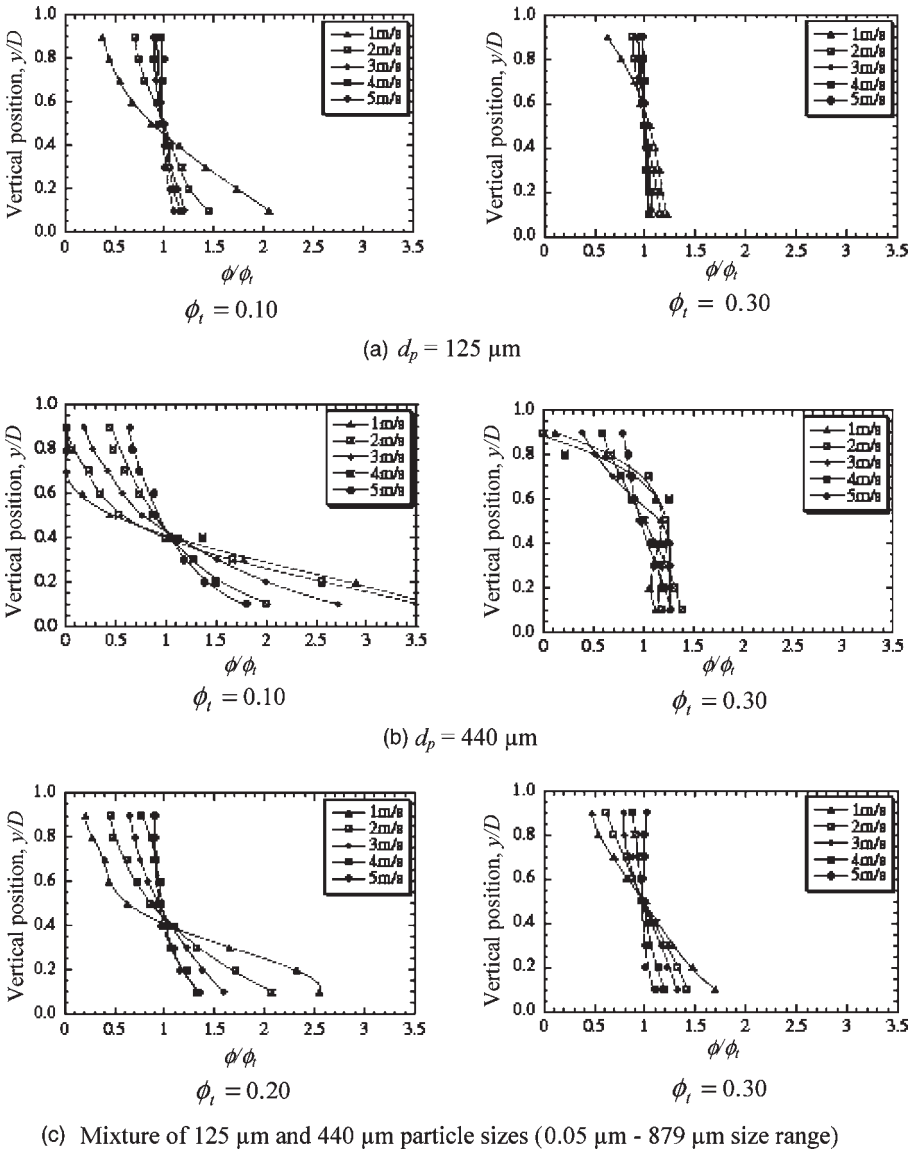


**Figure 6.13** Effect of flow velocity and particle size on concentration profiles in the flow of concentrated slurries in 54.9 mm diameter horizontal pipe (Kaushal *et al.*, 2005. Figures 6(a) and (b), 7(a) and (c), and 8(a) and (b) in the original. Redrawn with permission of Elsevier)

the suspension,  $H_{s,l}$  and the suspending liquid,  $H$ , ( $H_{s,l} - H$ ). Thicknesses of the contact beds formed in the flows of both mixed coarse and coarse particles are the same. The authors attributed the decrease in the solid effect in the mixed flow to buoyancy effect on the coarse particles forming the contact bed. This effect is predicted by two-layer flow model in Figure 6.8 in Section 6.5.1.

## 6.7 DEPOSITION VELOCITY

Deposition limit is a critical parameter in the formation of stationary bed of solids in the pipe. For trouble-free operation, stationary bed formation is generally avoided in industrial applications.

Due to stratified behavior of settling suspensions, a lower, particle rich and an upper, particle-lean zones generally exist in a pipeline. Therefore, the equations related with the two-layer flow model (Section 6.2.2) are applied to find the limit deposit velocity. Two driving forces are considered, one is related to the pressure gradient in the pipe,  $H_{s,l}$  and the other, the shear force at the interface. As the driving force just exceeds the resisting force produced by the contact of the particles with the pipe wall, the lower, particle-rich layer is set in motion. The resisting force is proportional to the dry-state friction factor,  $f_{Cf}$  and the submerged weight of the solid particles through the bed as explained in Section 6.2.2. The shear stress at the interface, is calculated using an equivalent roughness which is proportional to the size of solid particles in prior applications of two-LFM (Section 6.4.2).

Pugh and Wilson (1999) prepared the nomogram in Figure 6.14 to determine the limit deposit velocity. In Figure 6.14, the vertical line at the center of the nomograph corresponds to the limit deposit velocity,  $V_{dep}$  (equivalent to  $V_{sm}$  in the figure) for particles of specific gravity  $SG_p = 2.65$ , narrow particle grading and  $f_{Cf} = 0.4$ . The vertical axis at LHS of  $V_{dep}$  axis shows the internal pipe diameter,  $D$  and the particle size,  $d_p$  is located on the curved axis in this region. Hence LHS of the  $V_{dep}$  axis is used to find the limit deposit velocity for particles with  $SG_p = 2.65$ . The curved  $d_p$  axis located in this region has two sides: Its RHS shows sizes of small particles and the LHS, large particles. As an example, if the pipe and particle diameters for the particles with  $SG_p = 2.65$  are taken as 0.3 m and 5 mm, respectively, the limit deposit velocity,  $V_{dep}$  at this condition is determined joining the pipe and particle diameters with a straight line at RHS of the vertical  $V_{dep}$  line at the center of the nomogram and then, taking the intercept of this straight line with the vertical line at the center. This intercept gives the limit deposit velocity as  $2.65 \text{ m s}^{-1}$ . If the specific gravity of the particles is different from  $SG_p = 2.65$  and if it is, i.e.,  $SG_p = 1.6$  under the same conditions,  $2.65 \text{ m s}^{-1}$  limit deposit velocity and  $SG_p = 1.6$  on the relative density line are joined by a straight line and the intercept of this line with the vertical line at LHS is located and the actual limit deposit velocity is read as  $1.52 \text{ m s}^{-1}$ .

If the particle diameter,  $d_p > 0.006D$ , the nomographic chart should be used to obtain  $V_{dep}$ . If  $d_p < 0.006D$  and  $d_p > 0.3 \text{ mm}$ , eq. (6.106) should be used to find  $V_{dep}$ .

$$\frac{V_{dep}}{[2gD(SG_p - 1)]^{1/2}} = \left( \frac{0.018}{f} \right)^{0.13} \quad (6.106)$$

The Darcy–Weisbach friction factor,  $f$  in eq. (6.106) is defined as a function of the pressure gradient,  $H_{s,l}$  and the superficial liquid velocity,  $V_{s,av}$  and is given by

$$f = \frac{2gH_{s,l}}{V_{s,av}^2} \quad (6.107)$$

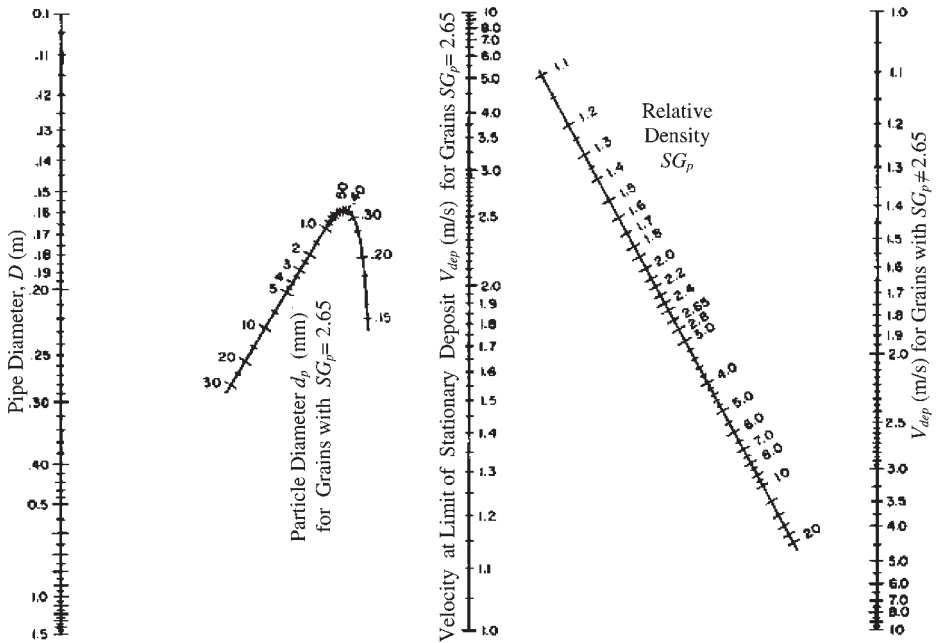


**Figure 6.14** Nomographic chart for limit deposition velocity; (Pugh and Wilson, 1999. Figure 1 in the original, with permission of Elsevier).

## 6.8 SETTLING FLOW OF SOLID-LIQUID SUSPENSIONS WITH STATIONARY BED

Suspension flow with solid deposits can be employed in some practical applications. Although the presence of solid bed leads to instabilities with a danger of blockage, this flow regime can be preferred in noncritical applications for economical reasons. In this case, the pressure gradient  $H_s$  for flows with stationary beds can be modeled in terms of pressure-gradient ratio, the *Durand velocity parameter*,  $Dr$ , and the delivered volumetric solid fraction for the conditions where eq. (6.106) is applicable.  $Dr$  is a modification of the Froude number, corrected for the density of the particles.

$$Dr = \frac{V_{s,av}}{[2gD(SG_p - 1)]^{1/2}} \quad (6.108)$$

The Durand parameter is used to define the other parameters effective in pressure drop correlations, such as, the dimensionless velocity,  $\psi$ ,

$$\psi = \frac{V_{s,av}^2}{gD(SG_p - 1)} \sqrt{C_D} \quad (6.109)$$

the characteristic velocity,  $V_{ch}$  of a particle defined by eq. (6.104) is given in terms of particle diameter  $d_p$  as

$$V_{ch} = [gd_p(SG_p - 1)]^{1/2} \quad (6.104a)$$

and the drag coefficient for spherical particles,  $C_D$  in eq. (6.109) is defined by

$$C_D = \frac{4}{3} \frac{gd_p(SG_p - 1)}{V_t^2} \quad (6.110)$$

### 6.8.1 Pressure drop correlations

Pressure losses can be expressed in dimensionless form as the ratio of the dimensionless solid effects to the amount of solid particles.

$$\Phi = \frac{(H_{s,l} - H)/H}{\phi_d} \quad (6.111)$$

Dimensionless pressure drop in settling suspensions are expressed by correlations based on Durand parameter in the literature. Durand's correlation is based on experimental data of sand and gravel slurries covering all flow regimes, with particle size ranging from 0.2 to 25 mm, in pipes changing from 3.8 to 58 cm in diameter and solids volume fraction up to 0.60. The other conditions of the correlations are given in Table 6.9. Although eq. (6.115) is used for all flow patterns, its constants change depending on the flow pattern and they are summarized in Table 6.10. In Table 6.10, the flow patterns are also numbered in the second column, which are used in Table 6.11 to show briefly the transitions from one to another flow pattern. Eq. (6.117) in Table 6.11 is used to calculate the friction factor at any transition between two flow patterns.

### 6.8.2 Limit deposition velocity correlations

The most general form of the dimensionless limit deposit velocity, which is the ratio of the limit deposition velocity,  $V_{dep}$  to the characteristic velocity,  $V_{ch}$  is

$$\frac{V_{dep}}{[gd_p(SG_p - 1)]^{1/2}} = A_c \quad (6.118)$$

where  $A_c$ , the correlation term for the limit deposit velocity, is a function of  $(d_p/D)$ , Reynolds number,  $Re_m$  and solid particle volume fraction,  $\phi$ . Reynolds number is defined in terms of the characteristic velocity as

$$Re_m = \frac{D\rho[gd_p(SG_p - 1)]^{1/2}}{\mu} = \frac{D\rho V_{ch}}{\mu} \quad (6.119)$$



Table 6.9

Pressure drop correlations for flow of settling suspensions in pipelines

References	Equations		Comments	$\overline{D}^a$
Durand and Condolios (1952), Durand (1953)	$\Phi = K\psi^m$	(6.112)	$K = 81, m = -1.5$	10.7–49.3
Newitt <i>et al.</i> (1955)	$\Phi = 0.6(SG_p - 1)$	(6.113)	Hom. FSF <sup>b</sup> Het. FSF <sup>b</sup>	6.12–26.4
	$\Phi = 1100\left(\frac{gDV_t}{V_{s,av}^2}\right)(SG_p - 1)$	(6.113a)	Two-LF <sup>b</sup>	
	$\Phi = 66\left(\frac{gD}{V_{s,av}^2}\right)(SG_p - 1)$	(6.113b)		
Zandi and Govatos (1967)	$\Phi = 280\psi^{-1.93}$	(6.114)	$\psi < 10, (\psi/\phi_d) > 40$	7.6–59.9
	$\Phi = 6.3\psi^{-0.354}$	(6.114a)	$\psi < 10, (\psi/\phi_d) > 40$	
Turian and Yuan (1977)	$f_s - f = A_1\phi_d^{A_2}f^{A_3}C_D^{A_4}\psi^{A_5}$	(6.115)	constants $A_1, A_2 \dots A_5$ given in Table 6.10	4.9–26.7
where	$f_s = \left[(-\Delta P)_s \frac{D}{2\rho LV_{s,av}^2}\right] = \left[\frac{\rho g H_s D}{2\rho LV_{s,av}^2}\right]$	(6.116)		

<sup>a</sup> $\overline{D}$ : The absolute average percent deviation, which changes from Hom. FSF to Two-LF as given.  
<sup>b</sup>FSF: Fully suspended flow, Hom. FSF: Homogeneous fully suspended flow, Het. FSF: Heterogeneous fully suspended flow, Two-LF: Two-layer flow.

Table 6.10

Constants of eq. (6.115) (Turian and Yuan, 1977; Oroskar and Turian, 1980)

Flow pattern	Pattern numbers	Constants				
		$A_1$	$A_2$	$A_3$	$A_4$	$A_5$
Hom. FSF	0	0.8444	0.5024	1.428	0.1516	−0.3531
Het. FSF	1	0.5513	0.8687	1.200	−0.1677	−0.6938
Two-LF	2	0.9857	1.018	1.046	−0.4213	−1.354
Three-LF <sup>a</sup>	3	0.4036	0.7389	0.7717	−0.4054	−1.096

<sup>a</sup>Three-layer flow.

**Table 6.11**

Constants of eq. (6.117) for transition between flow patterns

Equation							
$R_{NT} = \frac{V_{s,av}^2}{A_{R1} \phi^{A_{R2}} f^{A_{R3}} C_D^{A_{R4}} gD(SG_d - 1)} \quad (6.117)$							
Constants							
Transition from pattern	$R_{NT}^a$	$A_{R1}$	$A_{R2}$	$A_{R3}$	$A_{R4}$	Critical velocities	References
3–0	$R_{NT,30}$	0.3703	0.3183	−0.8837	−0.7496	$V_{dep}$	Oroskar and Turian (1980)
3–1	$R_{NT,31}$	0.4608	−0.3225	−1.065	−0.5906		
3–2	$R_{NT,32}$	31.93	1.083	1.064	−0.0616		
2–0	$R_{NT,20}$	1.167	0.5153	−0.3820	−0.5724	$V_{sus}$	Turian and Yuan (1977)
2–1	$R_{NT,21}$	2.411	0.2263	−0.2334	−0.3840		
1–3	$R_{NT,13}$	0.2859	1.075	−0.6700	−0.9375	$V_{dep}$	

<sup>a</sup> $R_{NT,ij} = 1$  at any transition point between two flow patterns.  $R_{NT,ij} > 1$  and  $R_{NT,ij} < 1$  correspond to turbulent and laminar regimes, respectively.

There are several correlations related to the limit deposit velocity in the literature. Some correlations for  $A_c$  and their application ranges are summarized in Table 6.12. In some cases, the limit deposit velocity correlation can be described by the Durand coefficient defined in terms of  $V_{dep}$ . The relation between the Durand coefficient and the dimensionless limit deposit velocity (eq. (6.112)) is obtained by replacing  $V_{s,av}$  with  $V_{dep}$  in eq. (6.108) and multiplying it by  $(d_p/d_p)$ :

$$\frac{V_{dep}}{[gD(SG_p - 1)]^{1/2}} = \frac{V_{dep}}{[gd_p(SG_p - 1)]^{1/2}} \left( \frac{d_p}{D} \right)^{1/2} \quad (6.120)$$

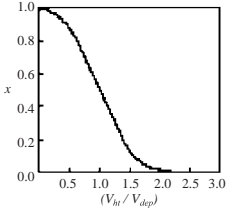
Eq. (6.120) shows that the Durand coefficient and the dimensionless limit deposit velocity are interconvertible. Turian *et al.*'s correlation (1987) based on the definition given in eq. (6.121) is

$$\frac{V_{dep}}{[gD(SG_p - 1)]^{1/2}} = \chi_1 \phi^{\chi_2} (1 - \phi^{\chi_3}) \left\{ \frac{D\rho[gD(SG_p - 1)]^{1/2}}{\mu} \right\}^{\chi_4} \left( \frac{d_p}{D} \right)^{\chi_5} \quad (6.121)$$

Various forms of eq. (6.121) are considered and the related values of adjustable constants,  $\chi_i$ , are determined by fitting the 864 limit deposit velocity data using multiple regressions with the linearized log form of the equation. The regression results are given in Table 6.13 together with the standard errors.

Table 6.12

Deposition velocity correlations

$A_c$	Comments	$SD^{a\%}$	References
$\sqrt{2}F_L(d_p/D)^{-1/2}$	$F_L = 0.7-1.3 \ d_p \leq 2.3 \text{ mm}$ $F_L = 1.3 \ d_p \leq 2.3 \text{ mm}$	51.3	Durand and Condolois (1952)
$[(8/3)\alpha\beta^2]^{1/2} (d_p/D)^{1/n} (d_p/D)^{-1/2}$	$\alpha = 2^{2n+2} n/(1+n)(2+n)$ , $\beta = (2n+1)(n+1)/2n^2, 7 < n < 10$	61.9	Kao and Wood (1974)
$34/(3C_D)^{1/2}$		73.2	Newitt <i>et al.</i> (1955)
$[0.025(DV_{s,av} \rho_p/\mu)^{0.775}]^{1/2}$		62.0	Spells (1955)
$[A_{R1}\phi^{A_{R2}}f^{A_{R3}} C_D^{A_{R4}} (D/d_p)]^{1/2}$	$A_{R1}, A_{R2}, A_{R3}, A_{R4}$ (see Table 6.10)	67.3	Turian and Yuan (1977)
$\sqrt{2}F_{L'}(d_p/D)^{-1/3}$	$F_{L'} = 3.4\phi^{0.22}$	49.8	Wasp <i>et al.</i> (1977)
$(40\phi/\sqrt{C_D})^{1/2} (d_p/D)^{-1/2}$		58.9	Zandi and Govatos (1967)
$b1.85\phi^{0.1536} (1 - \phi)^{0.3564} \times (d_p/D)^{-0.378} Re_m^{0.09} x^{0.30}$		21.8	Oroskar and Turian (1980)
<p>where <math>V_{ht} = V_t(1 - \phi_d)^n</math> <math>Re_m</math> is defined by eq. (6.119)</p>			
			
$x \text{ vs } (V_{ht}/V_{dep})$			

Source: Oroskar and Turian (1980). Reproduced with permission of the American Institute of Chemical Engineers, Figure 6 in the original.

<sup>a</sup> $SD$ : Standard deviation.

<sup>b</sup> $x$ : Fraction of eddies with velocities exceeding  $V_t$ .

$F_L$  and  $F_{L'}$ : Factors used in critical velocity correlations.  $\phi_d$ : delivered volume fraction of solid particles. Range of data evaluated in these correlations:  $SG_p = 1.30-5.25$ ,  $SG = 0.98-1.35$ ,  $\mu = 0.98-38\text{cP}$ ,  $d_p = 100-2040 \text{ }\mu\text{m}$ ,  $D = 2.67-31.52 \text{ cm}$ ,  $\phi = 0.01-0.50$ .

6.9 FLOW PATTERN MAPS IN PIPE FLOW

The hydrodynamic characteristics of the flow of the solid-liquid suspensions are influenced by operational conditions, i.e., pipe diameter and inclination, solid-liquid suspension flow rate, delivered concentration and superficial velocities, the physical properties of the solid and liquid phases, i.e., particle size and density, density and viscosity of the liquid, dry friction coefficient and angle of internal friction.

**Table 6.13**

Limit deposition velocity correlations (eq. (6.137)) using regression

Assumption	Parameter	Estimate	SE <sup>a</sup>	$\bar{D}^a$	RMS <sup>a</sup>
1. Estimate all $\chi_i$	$\chi_1$	1.7951	1.0878	20.53	0.3416
	$\chi_2$	0.1087	0.01610		
	$\chi_3$	0.2501	0.09870		
	$\chi_4$	0.00179	0.00767		
	$\chi_5$	0.06623	0.00958		
2. Assume $\chi_5 = 0$	$\chi_1$	1.8471	1.091	21.54	0.3447
	$\chi_2$	0.1126	0.01652		
	$\chi_3$	0.03421	0.1004		
	$\chi_4$	-0.03093	0.00621		
3. Assume $\chi_4 = 0$	$\chi_1$	1.8176	1.0665	20.57	0.3412
	$\chi_2$	0.1086	0.01608		
	$\chi_3$	0.2525	0.09812		
	$\chi_5$	0.06486	0.00754		
4. Assume $\chi_4 = \chi_5 = 0$	$\chi_1$	1.3213	1.0564	21.04	0.3552
	$\chi_2$	0.1182	0.01671		
	$\chi_3$	0.3293	0.1018		
5. Assume $\chi_3 = \chi_4 = \chi_5 = 0$	$\chi_1$	1.1228	1.0223	21.35	0.3559
	$\chi_2$	0.07367	0.00954		

Source: Turian *et al.* (1987). Redrawn with permission of Elsevier, Table 4 in the original.<sup>a</sup>SE: Standard error of estimate,  $\bar{D}$ : The absolute average percent deviation, RMS: The root mean square deviation

The effects of the operational conditions on the flow of solid–liquid suspensions are displayed in flow pattern maps. These maps may be in terms of superficial velocities of the two phases, solid–liquid suspension superficial velocity versus delivered concentration, solid–liquid suspension flow rate versus delivered concentration or in terms of mass flow rates of the two phases. One form given in Figure 6.15(a), similar to the map presentations in gas–liquid two-phase flows, employs log–log scale in terms of superficial velocities of the solid,  $V_{p,av}$  and liquid,  $V_{av}$  phases equivalent to the volumetric flow rates. Figure 6.15(b) indicates another type of the flow pattern map in which the superficial velocity of the solid–liquid suspension,  $V_{s,av}$  is plotted against the delivered concentration,  $\phi_d$ . The coordinates on the two types of presentation are interrelated and described by eqs. (5.103)–(5.105) as

$$V_{p,av} = V_{s,av} \phi_d \quad (6.122)$$

$$V_{av} = V_{s,av} (1 - \phi_d) \quad (6.123)$$

$$V_{s,av} = V_{p,av} + V_{av} \quad (6.124)$$

$$\phi_d = \left[ \frac{V_{p,av}}{V_{p,av} + V_{av}} \right] \quad (6.125)$$

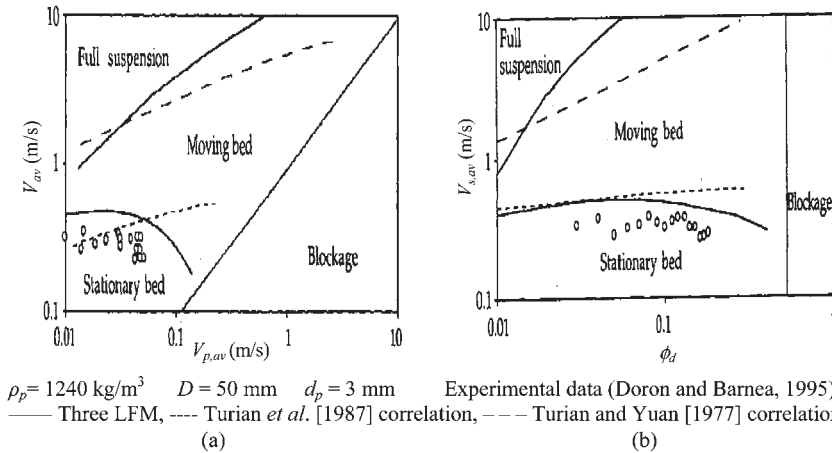


**Figure 6.15** Flow pattern maps in terms of (a) superficial velocities, (b) solid–liquid suspension velocity–delivered volume fraction. (Doron and Barnea, 1996. Figures 2 and 3 in the original with permission of Elsevier).

The flow pattern maps are obtained for any set of operational conditions from the results of both experiments and theoretical models. The transition between the flow-patterns is estimated using the flow pattern equations given in Section 6.2.3.

In Figure 6.15(a), the boundary between the stationary and moving beds is experimentally determined by Doron and Barnea (1996). In addition, this boundary is also predicted by three-LFM and Turian *et al.*'s correlations (1987). Both experimental and model results are in good agreement in this figure. The model prediction of the shape of the boundary is better than the results of the Turian *et al.*'s (1987) correlation. The transition from two-layer (flow with moving bed) to fully suspended flow is theoretically presented using both three LFM and Turian and Yuan (1977) correlation in Figure 6.15(a). The range of existence of the moving bed flow pattern increases with increasing solids superficial velocity.

The flow pattern map in Figure 6.15(b) is given in terms of suspension superficial velocity and delivered concentration. The variation of both the Turian *et al.* (1987) correlation and the three-LFM is insignificant in the range of  $\phi_d$  investigated experimentally. This shows that the transition from flow with a stationary bed to the moving bed is independent of the delivered concentration,  $\phi_d$ . The region of two-layer flow (flow with a moving bed) becomes larger with increasing  $\phi_d$  indicated by the greater slope of Turian and Yuan (1977) correlation and three-LFM. With increasing particle concentration, the suspension needs extremely high flow rates to achieve fully suspended flow. As the delivered concentration around  $\phi_d = 0.52$ , the whole pipe is filled by solid particles, hence a stationary bed is formed which is known as *blockage*.

#### *Effect of particle density*

Transitions from the stationary to moving bed and moving bed to fully suspended flow take place at higher suspension velocities with an increase in the particle density. The transition

from the stationary to the moving bed is independent of the delivered solids even though the value of the suspension velocity increases with the density of the particles. On the other hand, transition from moving bed to fully suspended flow is independent on both the density,  $\rho_p$ , and the solid volume fraction,  $\phi_d$ , of the particle.

#### *Effect of particle diameter*

The limit deposit velocity is predicted by the correlations to be independent of particle size. However, the transition to the fully suspended flow is affected by the particle size, as higher velocities are required to suspend larger particles.

#### *Effect of pipe diameter*

The pipe diameter affects the transitions from stationary to moving beds through the total mass and mechanical energy relations.

## REFERENCES

- Almedeij, J.H., Algharaib, M.K., 2005. Influence of sand production on pressure drawdown in horizontal wells: Theoretical evidence. *Journal of Petroleum Science and Engineering*, 47, 137–145.
- Averbakh, A., Shauly, A., Nir, A., Semiat, R., 1997. Slow viscous flows of highly concentrated suspensions—Part I: Laser-Doppler velocimetry in rectangular ducts. *International Journal Multiphase Flow*, 23(3), 409–424.
- Ayazi Shamlou, P., 1970. Hydraulic transport of particulate solids. *Chemical Engineering Communications*, 62, 233–249.
- Bagnold, R.A., 1954. Experiments on the gravity free dispersion of large solid particles under shear. *Proceedings of the Royal Society*, A225, 49–64.
- Bain, A.G., Bonnington, S.T., 1970. *The Hydraulic Transport of Solids by Pipeline*, Pergamon Press, Oxford.
- Bartosik, A.S., 1996. Modelling the Bagnold stress effects in vertical slurry flow. *Journal of Hydrology and Hydromechanics*, 44(1), 49–58.
- Brown, N.P., 1991. Flow regimes of settling slurries in pipes. In: *Slurry Handling Design of Solid–Liquid Systems*, Elsevier, London, pp. 41–52.
- Campbell, C.S., Avila-Segura, F., Liu, Z., 2004. Preliminary observations of a particle lift force in horizontal slurry flow. *International Journal of Multiphase Flow*, 30, 199–216.
- Choi, M., Cho, K., 2001. Effect of the aspect ratio of rectangular channels on the heat transfer and hydrodynamics of paraffin slurry flow. *International Journal of Heat Mass Transfer*, 44, 55–61.
- Condolios, E., Chapus, E.E., 1963. Designing solids-handling pipelines. *Chemical Engineering*, 131–138.
- Doron, P., Barnea, D., 1996. Flow pattern maps for solid-liquid flow in pipes. *International Journal of Multiphase Flow*, 22(2), 273–283.
- Doron, P., Granica, D., Barnea, D., 1987. Slurry flow in horizontal pipes—experimental and modeling. *International Journal of Multiphase Flow*, 13(4), 535–547.
- Doron, P., Simkhis, M., Barnea, D., 1997. Flow of solid–liquid mixtures in inclined pipes. *International Journal of Multiphase Flow*, 23(2), 313–323.

- Durand, R., 1953. Basic relationships of the transportation of solids in pipes-experimental research. In: *Proceedings of the Fifth Minneapolis International Hydraulics Convention*, Minneapolis, MN, pp. 89–103.
- Durand, R., Condolios, E., 1952. Communication de R. Durand et E. Condolios, *Compte Rendu des Deuxiemes Journees de L'Hydraulique* (Paris, Societe Hydrotechnique de France), pp. 29–55, June 1952.
- Ercolani, D., Ferrini, F., Arrigoni, V., 1979. Electric and thermic probes for measuring the limit deposit velocity. In: *Proceedings of the Sixth International Conference on the Hydraulic Transport of Solids in Pipes*, Canterbury, England, Paper A3, pp. 27–42.
- Fangary, Y.S., Abdel Ghani, A.S., El Haggag, S.M., Williams, R.A., 1997. The effect of fine particles on slurry transport processes. *Minerals Engineering*, 10(4), 427–439.
- Ferre, A.L., Shook, C.A., 1998. Coarse particle wall friction in vertical slurry flows. *Particulate Science and Technology*, 16, 125–133.
- Gillies, R.G., Hill, K.B., McKibben, M.J., Shook, C.A., 1999. Solids transport by laminar Newtonian flows. *Powder Technology*, 104, 269–277.
- Gillies, R.G., Shook, C.A., 2000. Modelling high concentration settling slurry flows. *Canadian Journal of Chemical Engineering*, 78, 709–716.
- Goedde, E., 1978. To the critical velocity of heterogeneous hydraulic transport. In: *Proceedings of the Fifth International Conference on the Hydraulic Transport of Solids in Pipes*, Hanover, Germany, Paper B4, 81–98.
- Graf, W.H., Robinson, M., Yucel, O., 1970. The critical deposit velocity for solid-liquid mixtures. In: *Proceedings of the First International Conference on the Hydraulic Transport of Solids in Pipes*, Warwick, England, Paper H5, 77–87.
- Kao, T.Y., Wood, D.J., 1974. Incipient motion of solids in solid liquid transport system, *Transactions of the Society of Mining Engineers, AIME*, 255, 39–44.
- Karabelas, A.J., 1977. Vertical distribution of dilute suspensions in turbulent pipe flow. *American Institute of Chemical Engineers Journal*, 23(4), 426–434.
- Kaushal, D.R., 1995. Prediction of Particle Distribution in the Flow of Multisized Particulate Slurries through Closed Ducts and Open Channels, Ph.D. Thesis, Department of Applied Mechanics, I.I.T. Delhi, India.
- Kaushal, D.R., Sato, K., Toyota, T., Funatsu, K., Tomita, Y., 2005. Effect of particle size on pressure drop and concentration profile in pipeline flow of highly concentrated slurry. *International Journal of Multiphase Flow*, 31, 809–823.
- Kaushal, D.R., Seshadri, V., Singh, S.N., 2002a. Prediction of concentration and particle size distribution in the flow of multi-sized particulate slurry through rectangular duct. *Applied Mathematical Modelling*, 26, 941–952.
- Kaushal, D.R., Tomita, Y., 2002. Solids concentration profiles and pressure drop in pipeline flow of multisized particulate slurries. *International Journal of Multiphase Flow*, 28, 1697–1717.
- Kaushal, D.R., Tomita, Y., Dighade, R.R., 2002b. Concentration at the pipe bottom at deposition velocity for transportation of commercial slurries through pipeline. *Powder Technology*, 125, 89–101.
- Kazanskij, I., 1979. Critical velocity of depositions for fine slurries—new results. In: *Proceedings of the Sixth International Conference on the Hydraulic Transport of Solids in Pipes*, Canterbury, England, Paper A4, 43–56.
- Kelessidis, V.C., Bandelis, G.E., 2004. Flow patterns and minimum suspension velocity for efficient cuttings transport in horizontal and deviated wells in coiled-tubing drilling. *SPE Drilling and Completion*, December, 213–227.
- Kofanov, V.J., 1964. Heat transfer and hydraulic resistance in a flowing liquid suspension in pipes. *International Chemical Engineering*, 4, 426–430.

- Krieger, I.M., 1972. Rheology of monodisperse lattices. *Advances Colloid Interface Science*, 3, 111–136.
- Krieger, I.M., Dougherty, T.J., 1959. A mechanism for non-Newtonian flow in suspensions of rigid spheres. *Transactions of the Society of Rheology*, 3, 137–152.
- Kumar, U., Mishra, R., Singh, S.N., Seshadri, V., 2003. Effect of particle gradation on flow characteristics of ash disposal pipelines. *Powder Technology*, 132, 39–51.
- Ladd, A.J.C., 1993. Dynamic simulations of sediment spheres. *Physics of Fluids A*, 5, 299–310.
- Ladd, A.J.C., 1994. Dynamic simulations of particular suspensions via a discretized Boltzmann equation. *Journal of Fluid Mechanics*, 271, 285–310, 311–339.
- Ladd, A.J.C., 1997. Sedimentation of homogeneous suspensions of non-Brownian spheres. *Physics of Fluids*, 9, 491–499.
- Lazarus, J.H., Neilson, I.D., 1978. A generalized correlation for friction head losses of settling mixtures in horizontal smooth pipelines. In: *Proceedings of the Fifth International Conference on the Hydraulic Transport of Solids in Pipes*, Hanover, Germany, Paper B1, 1–32.
- Leighton, D., Acrivos, A., 1987. The shear induced migration of particles in concentrated suspensions. *Journal of Fluid Mechanics*, 181, 415–439.
- Liu, S., 1999. Particle suspension for dispersion flow. *Chemical Engineering Science*, 54, 873–891.
- Liu, S., Masliyah, J.H., 1996. Rheology of suspensions. In: Schramm L.L. (Ed.), *Suspensions, fundamentals and applications in the petroleum industry* (eds.), ACS Advances in Chemistry, 251, 107–176.
- Longwell, P.A., 1977. *Mechanics of Fluid Flow*, McGraw Hill, New York.
- Matoušek, V., 2002. Pressure drops and flow patterns in sand-mixture pipes. *Experimental Thermal and Fluid Science*, 26, 693–702.
- Matoušek, V., 2004. Erosion of plane bed by sand slurry current in pipe. *Journal of Hydrology and Hydromechanics*, 52(3), 156–161.
- Matoušek, V., 2005. Research developments in pipeline transport of settling slurries. *Powder Technology*, 156, 43–51.
- Newitt, D.M., Richardson, J.F., Abbott, M., Turtle, R.B., 1955. Hydraulic conveying of solids in horizontal pipes. *Transactions of the Institution of Chemical Engineers*, 33, 93–110.
- Newitt, D.M., Richardson, J.F., Gliddon, B.J., 1961. Hydraulic conveying of solids in vertical pipes. *Transactions of the Institution of Chemical Engineers*, 39, 93–100.
- Nikuradse, J., 1930. Turbulente Strömung in nichtkreisförmigen rohren. *Ingenier-Archiv*, 1, 306–332.
- Nikuradse, J., 1933. Strömungsgesetze in rauhen rohren. *Forsch Arb Ing –Wes No. 361.*, also 1950 Technical report, NACA Technical Memo 1292. National Advisory Commission for Aeronautics, Washington, DC.
- Oroskar, A.R., Turian, R.M., 1980. The critical velocity in pipeline flow of slurries. *AIChE Journal*, 26(4), 550–558.
- Parzonka, W., Kenchington, J.M., Charles, M.E., 1981. Hydrotransport of solids in horizontal pipes: Effects of solids concentration and particle size on the deposit velocity. *Canadian Journal of Chemical Engineering*, 59, 291–296.
- Phillips, R.J., Armstrong, R.C., Brown, R.A., Graha, A.L., Abbott, J.R., 1992. A constitutive equation for concentrated suspensions that accounts for shear-induced particle migration. *Physics of Fluids A*, 4, 30–40.
- Prandtl, L., 1952. *Essentials of Fluid Dynamics*, Blackie, London.
- Pugh, F.J., Wilson, K.C., 1999. Role of the interface in stratified slurry flow. *Powder Technology*, 104, 221–226.
- Ribberink, J.S., 1998. Bed-load transport for steady flows and unsteady oscillatory flows. *Coastal Engineering*, 38, 59–82.



- Richardson, J.F., Zaki, W.N., 1954. Sedimentation and fluidization, part I. Transactions of the Institution of Chemical Engineers, 32, 35–53.
- Schlichting, H., 1979. Boundary Layer Theory, 7th edn., McGraw-Hill, New York (Chapter 20).
- Shauly, A., Averbakh, A., Nir, A., Semiat, R., 1997. Slow viscous flows of highly concentrated suspensions—Part II: Particle migration, velocity and concentration profiles in rectangular ducts. International Journal of Multiphase Flow, 23(4), 613–629.
- Shook, C.A., 1993. Slurry pipeline flow. In: Processing of Solid Liquid Suspensions (ed. P.A. Shamlou), Butterworth-Heinemann, Oxford, pp. 287–309.
- Shook, C.A., Bartosik, A.S., 1994. Particle-wall stresses in vertical slurry flows. Powder Technology, 81, 117–124.
- Shook, C.A., Roco, M.C., 1991. Slurry Flow: Principles and Practice, Butterworth-Heinemann, Boston, MA.
- Smith, R.A., 1955. Experiments on the flow of sand-water slurries in horizontal pipes. Transactions of the Institution of Chemical Engineers, 33, 85–92.
- Spells, K.E., 1955. Correlations for use in transport of aqueous suspensions of fine solids through pipes. Transactions of the Institution of Chemical Engineers, 33, 79–84.
- Stevens, G.S., Charles, M.E., 1972. The pipeline flow of slurries: Transition velocities. In: Proceedings of the Second International Conference on the Hydraulic Transport of Solids in Pipes, Coventry, England, Paper E3, 37–62.
- Stokes, R.J., Evans, D.F., 1997. Fundamentals of Interfacial Engineering. Wiley VCH, New York (Chapter 3).
- Sumer, B.M., Kozakiewicz, A., Fredsøe, J., Deigaard, R., 1996. Velocity and concentration profiles in sheet flow layer of movable bed. Journal of Hydraulic Engineering, 122(10), 549–558.
- Taylor, G., 1954. The dispersion of matter in turbulent flow through a pipe. Proceedings of the Royal Society, A223, 446–468.
- Televantos, Y., Shook, C.A., Carleton, A., Street, M., 1979. Flow of slurries of coarse particles at high solids concentrations. Canadian Journal of Chemical Engineering, 57, 255–262.
- Toda, M., Konno, H., Saito, S., 1980. Simulation of limit-deposit velocity in horizontal liquid-solid flow. In: Proceedings of the Seventh International Conference on the Hydraulic Transport of Solids in Pipes, Sendai, Japan, Paper J2, 347–358.
- Turian, R.M., Hsu, F.L., Ma, T.W., 1987. Estimation of the critical velocity in pipeline flow of slurries. Powder Technology, 51, 35–47.
- Turian, R.M., Yuan, T.F., 1977. Flow of slurries in pipelines. AIChE Journal, 23(3), 232–243.
- Vocaldo, J.J., Charles, M.E., 1972. Prediction of pressure gradient for the horizontal turbulent flow of slurries. In: Proceedings of the Second International Conference on the Hydraulic Transport of Solids in Pipes, Coventry, England, Paper C1, 1–12.
- Wasp, E.J., Kenny, J.P., Gandhi, R.L., 1977. Solid liquid flow—Slurry pipeline transportation. Trans. Tech. Publ., Rockport, MA, 1977.
- Wilson, K.C., 1976. A unified physically-based analysis of solid-liquid pipeline flow. In: Proceedings of the Fourth International Conference on the Hydraulic Transport of Solids in Pipes, Banff, Alberta, Canada, Paper A1, 1–16.
- Wilson, K.C., 1970. Slip points of the beds in solid-liquid pipeline flow. Proceedings ASCE, Journal of Hydraulics Division, 96, 1–12.
- Wilson, K.C., 1984. Analysis of contact-load distribution and application to deposition limit in horizontal pipes. Journal of Pipelines, 4, 171–176.
- Wilson, K.C., 1989. Mobile-bed friction at high shear stress. Journal of Hydraulic Engineering, 115(6), 825–830.
- Wilson, K.C., Cliff, R., Sellgren, A., 2002. Operating points for pipelines carrying concentrated heterogeneous slurries. Powder Technology, 123, 19–24.

- Wilson, K.C., Pugh, F.J., 1995. Real and virtual interfaces in slurry flows. In: Proceedings of Eighth International Conference on Transport and Sedimentation of Solid Particles, Prague, A4-1–A4-10.
- Wilson, K.C., Sellgren, A., 2003. Interaction of particles and near-wall lift in slurry pipelines. *Journal of Hydraulic Engineering*, 129(1), 73–76.
- Wood, D.J., 1979. Pressure gradient requirements for re-establishment of slurry flow. In: Proceedings of the Sixth International Conference on the Hydraulic Transport of Solids in Pipes, Canterbury, England, Paper D4, 217–228.
- Yen, B.C., 1991. Hydraulic resistance in open channels. In: *Channel Flow Resistance: Centennial of Manning's Formula* (ed. B.C. Yen), Water Resource Publications, Highlands Ranch, CO., pp. 1–135.
- Yen, B.C., Asce, F., 2002. Open channel flow resistance. *Journal of Hydraulic Engineering*, 128(1), 20–39.
- Zandi, I., Govatos, G., 1967. Heterogeneous flow of solids in pipelines. *Proceedings ASCE, Journal of Hydraulics Division*, 91, 145–159.

This page intentionally left blank

## Mixing in Solid–Liquid Systems

---

Mixing in solid–liquid systems is used for dispersing agglomerates, keeping the solid particles in suspension, blending various solid particles and colloids in a liquid, blending two liquids as in the case of paints and foods. Mixers are also used as stirred tank reactors, bioreactors, fermentors, crystallizers, and in the melting and phase change of solids. The aim in mixing is to produce a homogeneous mixture efficiently in terms of time and power consumption, if there is no other restriction imposed on the conditions of mixing, such as shear sensitivity. Recent advances in materials technology brought up the concept of structured mixtures of polymer blends and nanoparticles in the production of composites for a desired end use. This necessitates the use of programmed blender operation for flexibility in the structure of the blended product. Recent advances in micro-technologies necessitated development of microscale mixing, generally associated with other microscale operations.

Mixing operation in general involves the wetting and dispersion of solid particles, discharge of these particles into the liquid medium and incorporation into the liquid, and then mixing for the end result of homogenization, dissolution, or reaction while being suspended in the liquid medium. These topics will be taken up in this chapter, as indispensable operations in processes involving solid–liquid systems.

### 7.1 THE ROLE OF SURFACE TENSION IN WETTING OF SOLIDS

Penetration of the suspending liquid into clusters of colloidal and micrometer size range of particles, spreading over the surfaces, and wetting of the particles is the critical step in the dispersion of dry particles within a liquid medium. The particles may remain dispersed or aggregate after being suspended, depending on the effective surface forces introduced in Chapter 1.

#### 7.1.1 Phenomena involving surface and interfacial tensions

A molecule located within a bulk phase will be in equilibrium with respect to the interactive forces between the neighboring molecules. The number of these interaction sites (coordination number) will depend on the compaction of the phase, or the distribution

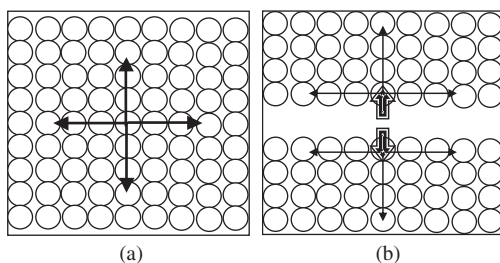


**Figure 7.1** Interactive forces acting on a molecule: (a) in equilibrium in the bulk phase, (b) at a free surface under equivalent surface tension.

function, of the molecules. In the two-dimensional space sketched in Figure 7.1(a), the interactive forces are shown to exist in four directions. This number will increase to six in three-dimensional space. When this material is cleaved to leave a free surface at the cleavage plane, the interactive forces will be left unbalanced. The remaining forces in the three directions will act to deform the surface into a sphere, the geometrical shape with the minimum surface to volume ratio. The force per unit length of surface acting on the surface layers is called the *surface tension*,  $\gamma$  [ $\text{Nm}^{-1} \equiv \text{Jm}^{-2}$ ]. Note that the same surface tension is exerted on both of the cleaved surfaces in Figure 7.1(b). The surface tension can also be interpreted in terms of energy required to create a unit area of free surface. With this interpretation, the sum of the surface tensions or equivalently *surface energies* will give the *work of cohesion*,  $W_{\text{coh}}$ .

$$W_{\text{coh}} = 2\gamma \quad (7.1)$$

As the surface tension is a positive quantity due to attractive forces within the aggregate of molecules, cohesion work will be positive, meaning energy must be given to the system to increase the surface area, as in the formation of drops in liquids or size reduction of solid particles.

#### 7.1.1.1 Interfacial energy

Except for solid surfaces in vacuum, all surfaces are actually interfaces between gas, solid, and liquid phases. Assuming the solids to be compact molecular aggregates, solid–gas, solid–liquid, and liquid–gas interfaces and the effective forces acting at the interfaces are shown schematically in Figures 7.2(a)–(c), respectively. Comparison of the forces in the lower bulk phases shows the forces in the solid phase to be greater than that in liquids due to compaction of the molecules. In the figure, all the molecules are shown as compact hard spheres. If the solids were polymers with ample free space in between the polymer chains, then the expected surface tension would be much lower. Solid surfaces are classified as “*high-energy*” and “*low-energy*” surfaces according to compaction of the molecules making up the bulk phase. For example, silicon and steel are high-energy surfaces with surface tensions of  $1240$  and  $1560 \text{ mNm}^{-1}$ , respectively. Polyethylene and polytetrafluoroethylene (PTFE = Teflon) are low-energy surfaces with surface tensions of  $30$  and  $18 \text{ mNm}^{-1}$ , respectively. The surface energy is a determining factor in the wetting of surfaces as explained below.

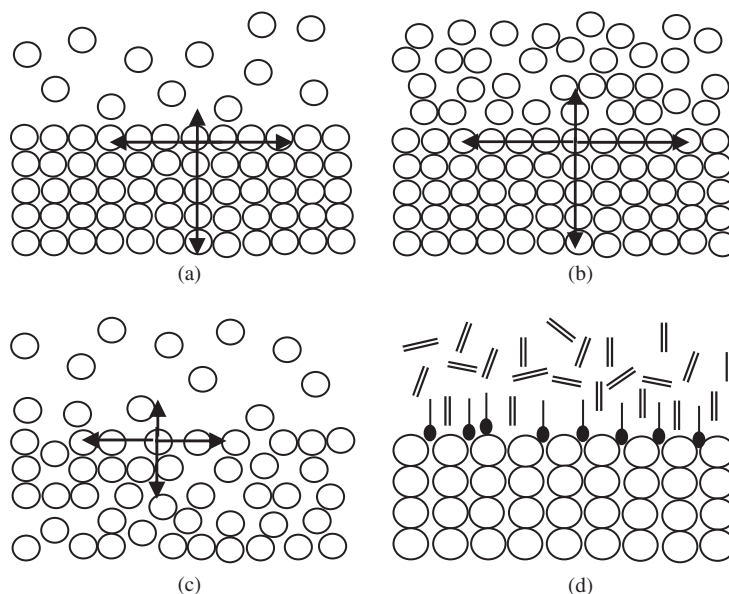


**Figure 7.2** Interactive forces between molecules: (a) at a solid–gas interface, (b) at a solid–liquid interface, (c) at a liquid–gas interface. (d) Role of surfactants in reducing the interfacial tension.

The magnitude of the solid–liquid interfacial tension, i.e., the interactive force across the interface, depends on the compaction of the molecules as well as on their shape, polarity, chemical composition, and molecular configuration. The interactive forces with gases are the minimum, as the gas phase is effectively void space under normal temperatures and pressures. For the same reason the interfacial tension with gases is effectively called the surface tension. Surfactants adsorbed at the interface reduce the interfacial energy, by acting as a bridge, preventing a sharp change in the magnitude of interactive forces across the phase boundaries, as shown schematically in Figure 7.2(d) for the case of a hydrophilic solid–hydrocarbon liquid interface. The orientation of the surfactants at the interface would be reversed in the case of a hydrophobic solid in contact with an aqueous solution.

### 7.1.1.2 Contact angle

The spreading of a liquid drop on a solid surface will be determined by a balance of forces (interfacial tensions) acting at the junction of the three interfaces as shown in Figure 7.3. In the figure, the subscripts S, L, and V denote the solid, liquid, and vapor phases, respectively, and  $\theta$  is the angle the liquid–vapor interfacial tension vector makes with the surface of the solid, called the *contact angle*.  $\gamma_{SV}$ ,  $\gamma_{LV}$ , and  $\gamma_{SL}$  are the solid–vapor, liquid–vapor, and solid–liquid interfacial tensions, respectively. These tensions are in equilibrium for a stagnant drop and, a force balance at the junction yields,

$$\gamma_{SV} = \gamma_{SL} + \gamma_{LV} \cos \theta \quad (7.2)$$

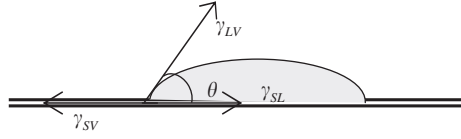


**Figure 7.3** Direction of interfacial tensions at the solid–liquid–vapor interfaces and the contact angle.

Suppose the surface area of the drop as shown in Figure 7.3 is  $A$ . The liquid drop has to increase its surface area by an amount  $dA$ , to be able to spread on the solid surface. Extension of the area will change the contact angle (in the limit to zero) and the balance of forces at the junction point. Keeping in mind the energy interpretation of interfacial tension, the spontaneous increase in the interfacial area will be possible only if there is free energy  $\Delta G$  available to do so:

$$\Delta G = [(\gamma_{SL} + \gamma_{LV} \cos\theta) - \gamma_{SV}]dA \quad (7.3)$$

If the liquid completely covers the surface of the solid, then the solid–vapor interface will be replaced by a solid–liquid interface below the liquid film and by the liquid–vapor interface at the upper surface.  $\Delta G$  has to be positive for a process to be spontaneous, implying the energies of the newly formed interfaces given within the parenthesis to be greater than the initial interfacial energy,  $\gamma_{SV}dA$ . This leads to the important conclusion that decreasing the contact angle,  $\theta \approx 0$ , such as through adsorption of surfactants will facilitate wetting of solid surfaces. The ease of wetting of high and low-energy surfaces will depend on the variation of  $\gamma_{SL}$  as well as on the magnitude of  $\gamma_{SV}$ .

#### 7.1.1.3 Young–Laplace equation and capillary forces

To relate the pressure difference across a curved interface with the surface tension, suppose a spherical drop of radius  $R$  is expanded to a new radius,  $R + dR$ , increasing its original volume by an increment,  $dv = 4\pi R^2 dR$ , and area by an increment,  $dA = 8\pi R dR$ . This expansion creates a  $Pdv$  work that is counteracted by the resistance to expansion, or the free energy requirement for the creation of a new surface area,  $\Delta G = \gamma dA$ :

$$\gamma 8\pi R dR = (\Delta P) 4\pi R^2 dR \quad (7.4)$$

The difference in pressure between the interior and exterior of the spherical drop,  $\Delta P$ , is then,

$$P_{\text{in}} - P_{\text{out}} = \Delta P = \frac{2\gamma}{R} \quad (7.5)$$

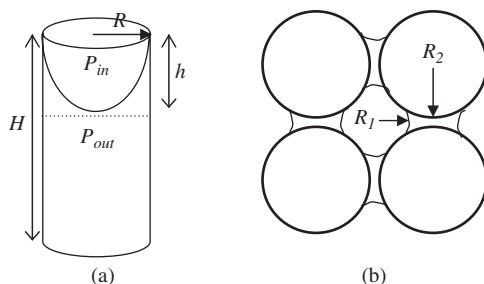


**Figure 7.4** Effect of capillary forces: (a) Capillary rise; (b) Bridging of particles by capillary forces.

In addition, for a generalized curved surface defined by two radii of curvature,  $R_1$  and  $R_2$ , the pressure difference is given by the Young–Laplace equation:

$$\Delta P = \left( \frac{1}{R_1} + \frac{1}{R_2} \right) \gamma \quad (7.6)$$

Young–Laplace equation is used to relate the capillary radius  $R$  to the hydrostatic pressure of a liquid climbing up a vertical capillary pipe to a height  $h$  (Figure 7.4(a)). Since  $P_{\text{out}} \leq P_{\text{in}}$  and the pressures are equal at any horizontal plane, the liquid will climb up the walls until the hydrostatic pressure of the meniscus equals  $\Delta P = P_{\text{in}} - P_{\text{out}}$ :

$$\Delta P = \rho g H = \frac{2\gamma \cos \theta}{R} \quad (7.7)$$

Another effect created by capillary forces is the capillary bridges formed by liquid remaining in between particles. The narrow channels (crevices) in between the particles are shaped like capillaries defined by two radii of curvature. As the pressure below the curved meniscus is lower than the pressure outside, the particles are pushed toward each other, forming a cluster. Cluster formation by capillary forces takes place if the liquid in the crevices is immiscible with the bulk of the suspending fluid, such as in the case of pigments prepared in an aqueous solution dispersed in an organic binder (Patton, 1979). Thorough spreading of the binding solution over drugs in powder form and bridging by capillary forces is also important in the preparation of dense granules of drugs by wet granulation (Zhang *et al.*, 2002).

#### 7.1.1.4 Adhesion, wetting, penetration, and spreading

Cohesion work defined by eq. (7.1) involved only interactions between the same kinds of molecules. When two phases, such as a liquid and a solid come into contact, the adhesion of the two different kinds of molecules at the interface involves work of adhesion per unit area basis, defined by,

$$W_{\text{adh}} = E_1 - E_2 = (\gamma_{\text{LV}} + \gamma_{\text{SV}}) - \gamma_{\text{SL}} \quad (7.8)$$



In this equation,  $E_1$  and  $E_2$  denote the initial and final energy states of the solid-liquid system in terms of energy per unit area. The two interfacial energy terms in the parenthesis denote the free state of the liquid and solid phases when they were exposed to the vapor or gas phase only, and the last term is the interfacial energy of the solid-liquid interface. A positive work of adhesion implies a decrease in the energy levels, therefore, spontaneous adhesion, whereas, a negative work indicates the requirement of the application of an external energy for adherence to take place.

Three closely related phenomena are based on the work of adhesion. *Spreading* is the coverage of a liquid or a solid surface by another liquid surface. Spreading of a finishing layer of paint over a base layer, oil on seas, or oil on soup are some of the examples. *Wetting* is a consequence of spreading and involves the attachment of the liquid layer onto the solid substrate without slipping. *Penetration* is the ability of a liquid to advance in the intra- and inter-particle pores and crevices of solid particles. Work of wetting and adhesion are defined by the same equation, eq. (7.8). Work of spreading and penetration are again expressed as a difference in energy between their final and initial states with eqs. (7.9) and (7.10), respectively.

$$W_{\text{spr}} = E_1 - E_2 = \gamma_{\text{SV}} - (\gamma_{\text{LV}} + \gamma_{\text{SL}}) \quad (7.9)$$

$$W_{\text{pen}} = E_1 - E_2 = \gamma_{\text{SV}} - \gamma_{\text{SL}} \quad (7.10)$$

Note that there is no liquid-vapor interfacial energy term in eq. (7.10) implying smooth solid surfaces are involved and there is no entrainment of air bubbles.

### 7.1.2 Surface tension related phenomena in particulate systems

The phenomena related with interfacial tensions introduced in Section 7.1.1 are basic principles under equilibrium or stagnation conditions. Three complications arise in the case of particulate systems: (1) Particles in powder form do not have extensive surfaces for the measurement of contact angles; (2) The particles may be in motion or under dynamic conditions; (3) The surfaces of the particles may be rough, or the particles themselves create this roughness, as in the case of penetration into dense solid particle clusters.

#### 7.1.2.1 Contact angles of powders

Sessile drop method of contact angle measurement requires the use of areas large in comparison to the dimensions of particulate solids. To determine the contact angle of liquids with solids that never exist in the form of plates, such as solid drugs in powder form, either the powders are compressed into pellets, or other methods such as the capillary penetration of liquids into bulk powders and the inverse chromatography methods are used.

Contact angle measurements on compressed pellets are reported to give good results (Zhang *et al.*, 2002) provided the profile of the drop is recorded within a small fraction of a second, the solid is not soluble in the liquid drop, and the solid powders are hydrophobic. Furthermore, the authors could estimate the surface energy of the solid surfaces from

the solid–liquid interfacial tension,  $\gamma_{SL}$ . Liquid molecules are bound to the solid molecules through dispersion forces (induced dipole–induced dipole interactions, eq. (1.13)) or polar interactions between dipoles or ions. The interfacial energies of both the liquid and the solid counterparts can be broken down to the polar (p) and dispersion (d) interactions (Zografi and Tam, 1976).

$$\gamma_{SL} = \gamma_{SV} + \gamma_{LV} - 2[(\gamma_{LV}^d \gamma_{SV}^d)^{1/2} + (\gamma_{LV}^p \gamma_{SV}^p)^{1/2}] \quad (7.11)$$

Employing two liquids with known properties, the solid surface energy could be obtained from the summation of the dispersive and polar components.

In the *penetration method of contact angle determination*, a jar with a porous bottom plate is packed up to a certain height with the solid particles, is hung to the arm of a balance and immersed into the liquid up to the upper level of the porous plate. The rise in the liquid level, equivalent to an increase in the weight of the packed bed is recorded as a function of time. If all the pores of the packed bed could be taken as a single capillary, then the height of the liquid would be found by replacing the pressure difference term in Hagen–Poiseuille equation with the Young–Laplace equation to obtain the expression known as the Washburn equation:

$$h^2 = \frac{\bar{R} \gamma_{LV} \cos \theta}{2\eta} t \quad (7.12)$$

Since the capillaries of the packed bed are not all of the same dimension and orientation, it is taken into account by multiplying the average radius of the capillaries  $\bar{R}$  by a factor  $C$ ,

$$\kappa = C\bar{R} \quad (7.13)$$

The height of capillary rise is difficult to observe externally. To follow up the rate of rise through measurement of weight  $m$ ,  $h$  in eq. (7.12) is replaced by  $m$  through  $h = m / \rho A$ ,

$$m^2 = \frac{\rho^2 (\kappa A^2) \gamma_{LV} \cos \theta}{2\eta} t = \frac{\rho^2 K \gamma_{LV} \cos \theta}{2\eta} t \quad (7.14)$$

where  $K$  is the capillary constant that depends on the packing conditions.  $K$  is determined by using a completely wetting liquid with  $\cos \theta = 1$ . Then the tube has to be packed again for the determination of the contact angle and the results plotted as  $m^2$  versus time. A linear rise is observed followed by a plateau when complete wetting is reached. The accuracy of the method depends on the reproducibility of  $K$  every time the tube is packed. By standardizing the methods of packing, and experimental conditions reasonable reproducibility could be maintained in the contact angle determination of drugs (Teipel and Mikonsaari, 2004; Heng *et al.*, 2006).

*Inverse gas chromatography* is used to obtain information on the interfacial energy of solids in powder form. Contrary to gas chromatography, the solid particulate phase is

investigated using probe liquids of known properties. The time required for the probe liquid to pass through the column is taken to be an indication of the interactions at the interface. To eliminate the effect of flow rate through the column, the quantity of solid used and the packing conditions, net retention volume  $v_n$  is used instead of the retention time and a relative comparison is made between the net retention times of probe liquids used. To find the dispersive component of the interaction (eq. (7.11)) nonpolar liquids such as hexane and octane are used whereas, polar liquids such as chloroform are used to find the polar counterpart of the interaction between the liquids and the solid surfaces. The interaction interfacial surface area of the solid and the dispersive component of the surface energy of the probe liquid should be known to determine the dispersive component of the surface energy of the solid,  $\gamma_{SV}^d$  through the relation of Schultz and Lavielle (1989).

$$R_G T \ln v_n = a(\gamma_{LV}^d)^{1/2} 2N_A (\gamma_{SV}^d)^{1/2} + C \quad (7.15)$$

In this equation,  $a$  is the interaction surface area,  $N_A$  the Avogadro number,  $R_G$  the universal gas constant,  $T$  the absolute temperature, and  $C$  a constant.  $\gamma_{SV}^d$  is found from the slope of the line when  $R_G T \ln v_n$  is plotted against  $a(\gamma_{LV}^d)^{1/2}$ , the energies of the probe liquids used (For more information on the use of inverse gas chromatography in the analysis of pharmaceutical powders: Grimsey *et al.* (2002)).

#### 7.1.2.2 Effect of dynamic conditions

The property affected the most by dynamic conditions is the contact angle. The contact angle determination by direct measurement with a goniometer as shown in Figure 7.3 is called the *sessile drop technique* and is pertinent under static, equilibrium conditions, where both of the phases are initially at rest. When, either the liquid or the solid phase is in motion, equilibrium is set by the balance of free energy for spreading, dynamic energy in terms of pressure and energy dissipated as friction. Dynamic contact angle  $\theta_d$  is always greater than the static contact angle  $\theta_s$ :

$$\cos \theta_d = \cos \theta_s - 2(1 + \cos \theta_s) \left( \frac{\mu V}{\gamma_{LV}} \right)^{1/2} \quad (7.16)$$

The last term in parenthesis is the *capillary number*  $Ca$  ( $Ca = \mu V / \gamma_{LV}$ ) where  $\mu$  is the viscosity of the liquid and  $V$  is the relative velocity between the solid and the liquid phases. Since the contact angle is dependent on the velocity of the fluid through the capillary, extent of wetting will not be equal in all the capillaries of a packed bed of particles that have different radii, length, and orientation. Under a constant pressure gradient, velocities and wetting in larger pores will be greater and entrained air will be driven to pores where the velocities are lower.

Dynamic contact angle is measured by the capillary technique using eq. (7.7) or the Wilhelmy plate technique where a plate of width  $a$  and thickness  $b$  is immersed and withdrawn from the solution at a constant rate. The contact angle in advancing the plate

into the solution involves penetration into a liquid and is greater than the contact angle in receding (pulling the plate up from the solution). The receding angle is much less than the advancing angle, generally approaching zero. The advancing contact angle is found from the ratio of net force acting on the plate during advancing  $F_A$  to that during receding,  $F_R$ .

$$\cos\theta_A = \frac{F_A}{F_R} \quad (7.17)$$

These forces are determined by the balance of surface forces acting around the perimeter where the liquid clings to the surface of the solid, and the net weight of the immersed section of the plate:

$$F = (2a + 2b)\gamma_{LV} \cos\theta - v_{\text{imm}}(\rho_p - \rho)g \quad (7.18)$$

$v_{\text{imm}}$  is the volume of the immersed section of the plate.

### 7.1.2.3 Effect of surface roughness

The actual surface area  $A_i$  of a solid is equal to the geometrical surface area  $A_g$ , in only a few materials. Generally, the surfaces are rough with protrusions and indentations, so that  $i = A_i/A_g \geq 1$ , as given in Figure 7.5 (Patton, 1979). In the figure,  $A_g$  represents a flat plate of unit width,  $A_i$ , the total surface area of the protrusions and  $A_a$ , the actual solid–liquid interfacial area. The work terms in eqs (7.8)–(7.10) are based on the geometrical area  $A_g$  whereas the interfacial energy terms are based on the total area  $A_i$ , so that for a rough surface, the equations are converted to,

$$W_{\text{adh}} = \gamma_{LV} + i(\gamma_{SV} - \gamma_{SL}) \quad (7.19)$$

$$W_{\text{spr}} = i(\gamma_{SV} - \gamma_{SL}) - \gamma_{LV} \quad (7.20)$$

$$W_{\text{pen}} = i(\gamma_{SV} - \gamma_{SL}) \quad (7.21)$$

Wetting takes place spontaneously when the surface tension of the solid is greater than the surface tension of the liquid,  $\gamma_{SV} \geq \gamma_{LV}$ . Comparison of Figures 7.2(a) and (b) shows that the solid–liquid interfacial tension is always lower than the solid–vapor interface because of the higher molecular number density in liquids. Summing up, eqs. (7.19)–(7.21) are always greater in magnitude than their counterparts for smooth surfaces, eqs. (7.8)–(7.10), denoting that roughness enhances spreading and wetting.

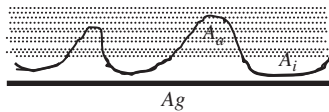


**Figure 7.5** Roughness on a flat surface.

## 7.2 DISCHARGE OF SOLIDS INTO LIQUIDS

Many industrial operations involve coarse particles of sizes ranging in the interval of micrometers to centimeters. The flow rate of particle suspensions in the upper size range is also high, so that the solids are introduced either through a hopper or by dropping the solids directly into the liquid. When the density difference between the liquid and the solid particles is high, then the main concern is to disperse the particles rapidly, so that there will be no local accumulations. On the other hand, there is a large class of particulate solids, called “*neutrally buoyant solids*,” that tend to float rather than settle due to a very small density difference with the suspending medium. They flow through channels homogeneously as a single-phase fluid, when the suspension velocity is high enough to disperse the particles radially by turbulent convection. When the liquid medium into which they are introduced is stagnant or flowing at a low velocity, the particles tend to collect near the surface of the liquid. An example from the metallurgical industry is the dropping of solid particles such as steel and alloying agents such as aluminum into molten liquid (Smith *et al.*, 2000). Another example comes from the food industry in the feeding and dispersion of granular foods to be processed, such as fruits, peas, beans, and chopped vegetables (Faderani *et al.*, 1998, a,b). Further examples to floating solids are microorganisms in bioreactors, fermentors, polymer globules in polymerization reactions and solids in wastewater treatment. The discharge and dispersion characteristics of these solids will be taken up in this section and mixing behavior in Section 7.3.

### 7.2.1 Discharge of solid–liquid suspensions from hoppers

Solids are introduced in suspension form to equipment through a standpipe connected to a hopper. The aim in such an operation is to convey a high ratio of solids for a given flow rate of liquid without damage to the solid particles. Depending on the flow rate and volumetric ratio of solids to liquids within the hopper and the standpipe, the suspension may be in the form of a highly packed bed; solid–liquid fluidized bed; non-settling or a settling suspension. The state of the suspension is determined by the inter-particle space filled with the liquid, or volumetric fraction of voids,  $\epsilon$ . Faderani *et al.* (1998, a,b) observed for the first time the variation of void spaces during flow of suspensions of imitation foods by scanning an acrylic hopper and standpipe with  $\gamma$ -ray tomography. A sketch of a hopper is given in Figure 7.6 to help presenting their model. Evaluation of tomographic measurements displayed a zone of high voidage above and below the hopper orifice and a gradual transition from a packed bed to a settling suspension in going down the hopper, and a transition in the reverse direction, back to a packed bed, in going down the standpipe. In the packed bed region the liquid velocity was higher than the particle velocity, signifying percolation of water within the packed bed. Transition to a high voidage region caused the solid particle velocities to increase above the liquid phase velocities, signifying settling of the particles. Experimental results showed that to maintain packed-bed flow conditions within the hopper, the mixture discharge velocity  $V_{\text{mix}}$  had to be greater than the terminal velocity of particles in free settling,  $V_t$ . However increasing the mixture velocity, caused an approach to a limiting value that is a function

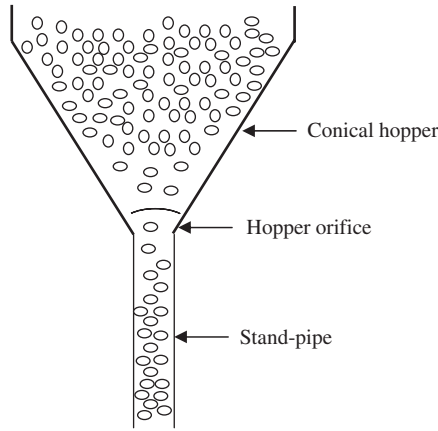


**Figure 7.6** Discharge of solids through a hopper.

of the ratio of volume of liquid to mixture volume,  $\alpha (\alpha \equiv (1 - \phi))$ ,  $\phi$  being the volumetric fraction of solids,

$$\frac{V_{\text{mix}}}{V_t} = ae^{bz} \quad (7.22)$$

The constants,  $a$  and  $b$  are found from the limiting values of  $\alpha = 0$  for solids only ( $a = V_{\text{mix},s}/V_t$ ) and  $\alpha = 1$  for liquids only ( $b = \ln(V_{\text{mix},l}/V_{\text{mix},s})$ ). Volumetric ratio of liquid in the mixture  $\alpha$  was related to the mixture velocity  $V_{\text{mix}}$  only at the orifice plane, so for a given mixture discharge rate, there was a single value of  $\alpha$ . However, both  $V_{\text{mix}}$  and the ratio of voids to the total volume,  $\varepsilon$  changed along the height of the hopper and the standpipe.  $V_{\text{mix}}$  is the velocity of the suspension with respect to fixed coordinates and does not give much information on the configuration of solid particles and mechanism of transport of the solid particles. So the drift-flux model, proposed by Wallis (1969) was adapted to model the flow through the hopper. This model gives the relative flux between the two phases,  $J_{\text{ls}}$ , in terms of volumetric fractions of solids  $\phi$  and relative velocity between the solid and liquid phases,  $V_{\text{ls}}$ :

$$J_{\text{ls}} = (1 - \phi)\phi V_{\text{ls}} = (1 - \phi)\phi(V_l - V_s) \quad (7.23)$$

where  $V_l$  and  $V_s$  are liquid and solid velocities, respectively.  $V_s$  is also equivalent to  $\bar{V}_p$  in Chapter 5.

Relative velocity,  $V_{\text{ls}}$ , can be expressed by the hindered settling velocity of particles in a concentrated suspension  $V_{\text{ht}}$ . Richardson-Zaki correlations (1954) relate  $V_{\text{ht}}$  to the terminal velocity  $V_t$  of the particles and the  $n$ th power of the volumetric fraction of solids  $\phi$ , under different flow regimes represented by the value of the exponent  $n$ . (eq. (4.147))

$$V_{\text{ls}} = V_t(1 - \phi)^{(n-1)} \quad (7.24)$$

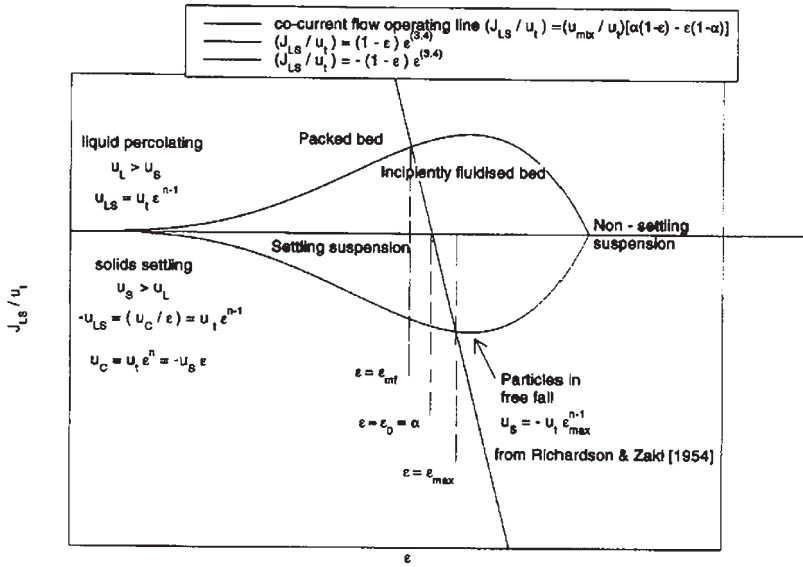


**Figure 7.7** Variation of normalized drift flux with voidage,  $\varepsilon$ . ( $\varepsilon = 1 - \phi$ ,  $U_L = V_1$ ,  $U_S = V_s$ ) (Faderani *et al.*, 1998. Reproduced with permission of Elsevier, Figure 15(b) in the original.)

Multiplying both sides of eq. (7.24) by  $\phi(1 - \phi)$  a drift flux between the liquid and particles is obtained as,

$$\frac{J_{ls}}{V_t} = \phi(1 - \phi)^n \quad (7.25)$$

defining the possible regimes in a hopper. For  $V_1 \geq V_s$ , eq. (7.25) is positive and defines the dividing line between the packed and fluidized beds in Figure 7.7, above the nonsettling region,  $V_1 = V_s$ . When  $V_1 \leq V_s$ , solids settle in the void spaces of the suspension moving down the hopper, eq. (7.25) becomes negative, forming the lower boundary of the settling suspension region in Figure 7.7. The variation of drift flux with porosity in a hopper is defined by the operating line, relating the velocities of the phases with the flow rates and the fraction of voidage. Liquid and solid velocities in terms of volumetric flow rates,  $Q$  are given by eqs. (7.26) and (7.27), respectively.

$$V_1 = \frac{Q_1}{A(1 - \phi)} \quad (7.26)$$

$$V_s = \frac{Q_s}{A\phi} \quad (7.27)$$

Substitution of eqs. (7.26) and (7.27) into eq. (7.23) gives,

$$J_{ls} = \frac{Q_l \phi}{A} - \frac{Q_s(1-\phi)}{A} = \frac{Q\phi}{A} - \frac{Q_s}{A} \quad (7.28)$$

In this equation,  $Q_l$  and  $Q_s$  are the flow rates of the liquid and solid components, together making up the total flow rate  $Q$ . This equation can be written in terms of the liquid volumetric fraction,  $\alpha$ , and becomes the equation of the operating line after rearrangement:

$$\frac{J_{ls}}{V_t} = \left( \frac{V_{mix}}{V_t} \right) [\alpha\phi - (1-\phi)(1-\alpha)] \quad (7.29)$$

The straight line in Figure 7.7 is the operating line. Its intersection with non-settling suspension ( $V_l = V_s$ ) line gives  $\alpha$ . The intersection with the upper and lower curve gives the minimum voidage  $\varepsilon_{mf}$  (at minimum fluidization velocity) and maximum voidage, respectively. Maximum value of the voidage remains below  $\varepsilon \leq 0.8$ . Increase in the volumetric fraction of liquid,  $\alpha$ , increases the slope of the operating line. Particle size and shape is effective through the terminal velocity. Particle elasticity becomes a factor only in very concentrated suspensions, where particles directly contact and compress each other.

## 7.2.2 Dispersion of solids upon introduction into the liquid

A thorough dispersion of solids in liquids in a very short duration is desirable to assist the maintenance of other operation conditions in heat and mass transfer, such as dissolution and melting. Dispersion becomes a problem when the liquid is stagnant, and when the particles are neutrally buoyant as in the extreme case of dropping aluminum into ladle of molten metal. Smith *et al.* (2000) simulated the dispersion of spherical, neutrally buoyant solids into a stagnant molten liquid utilizing an Eulerian–Eulerian, two-dimensional finite volume approach. The starting equations are the mass (eqs. (5.68a) and (5.68b)) and momentum (eqs. (5.77a) and (5.77b)) conservation equations, given generally in Chapter 5. Solid volume fraction  $\phi$  will rise above 0.2, in case of an undispersed cluster within the liquid. The authors used Ergun equation, to calculate the momentum transfer between the phases for  $\phi \geq 0.2$ :

$$\frac{\Delta P}{\rho V^2} \frac{d_p}{L} \frac{\varepsilon^3}{(1-\varepsilon)} = \frac{150}{Re_p} \frac{(1-\varepsilon)}{\varepsilon} + 1.75 \quad (7.30)$$

modified for the slip velocity in the drag function of the momentum conservation equation,  $K(V_l - V_s)$ ,

$$K = 150 \frac{(1-\varepsilon)^2 \mu}{\varepsilon d_p^2} + 1.75 \frac{\rho |V_l - V_s|}{d_p} (1-\varepsilon) \quad (7.31)$$



With the notation of this book eq. (7.31) can be rewritten as,

$$K = 150 \frac{\phi^2 \mu}{(1-\phi) d_p^2} + 1.75 \frac{\rho |V_l - V_s|}{d_p} \phi \quad (7.32)$$

Drag relations for single particles corrected for low-density packing were used for  $\phi \leq 0.2$ :

$$K = \frac{3}{4} C_D \frac{\phi(1-\phi) |V_l - V_s| \rho}{d_p} (1-\phi)^{-2.7} \quad (7.33)$$

The drag coefficient  $C_D$  is given by,

$$C_D = \frac{24}{Re_p} (1 + 0.15 Re_p^{0.687}) \quad (7.34)$$

under laminar conditions and by eq. (4.50) under turbulent conditions, or whichever is greater under given operating conditions. The Reynolds number based on the particle diameter and relative velocity and is defined by,

$$Re_p = \frac{|V_l - V_s| d_p (1-\phi) \rho}{\mu} \quad (7.35)$$

Volumetric fraction of solids rising above the maximum compaction value of 0.63 was prevented by incorporating an extra term for inter-particle forces on contact (Bouillard *et al.*, 1989),

$$F_s = e^{-600[(1-\phi)-0.37]} \nabla(1-\phi) \quad (7.36)$$

Simulation results were compared with experimental observation, as given in the right and left sides of Figure 7.8, respectively as a function of time. There is a good agreement between the simulation results and experimental observations. The solid lines on the RHS show the boundaries of the region with a solids volumetric fraction of 0.02, and the dashed lines,  $\phi = 0.10$ . The region with a volumetric fraction of solids  $\phi \leq 0.02$  expands with time as particles disperse into the liquid phase. Dispersion of individual particles, not taken into account in the model, helps to reduce concentration buildup of the solid particles in the inner plume. Even a low drift velocity, such as in horizontal channels modeled in Figure 7.9, helps to disperse the particles and reduces the local volumetric concentrations. Particles never reach the bottom of the channel, no matter how high the initial downward velocity is, because of their low density.

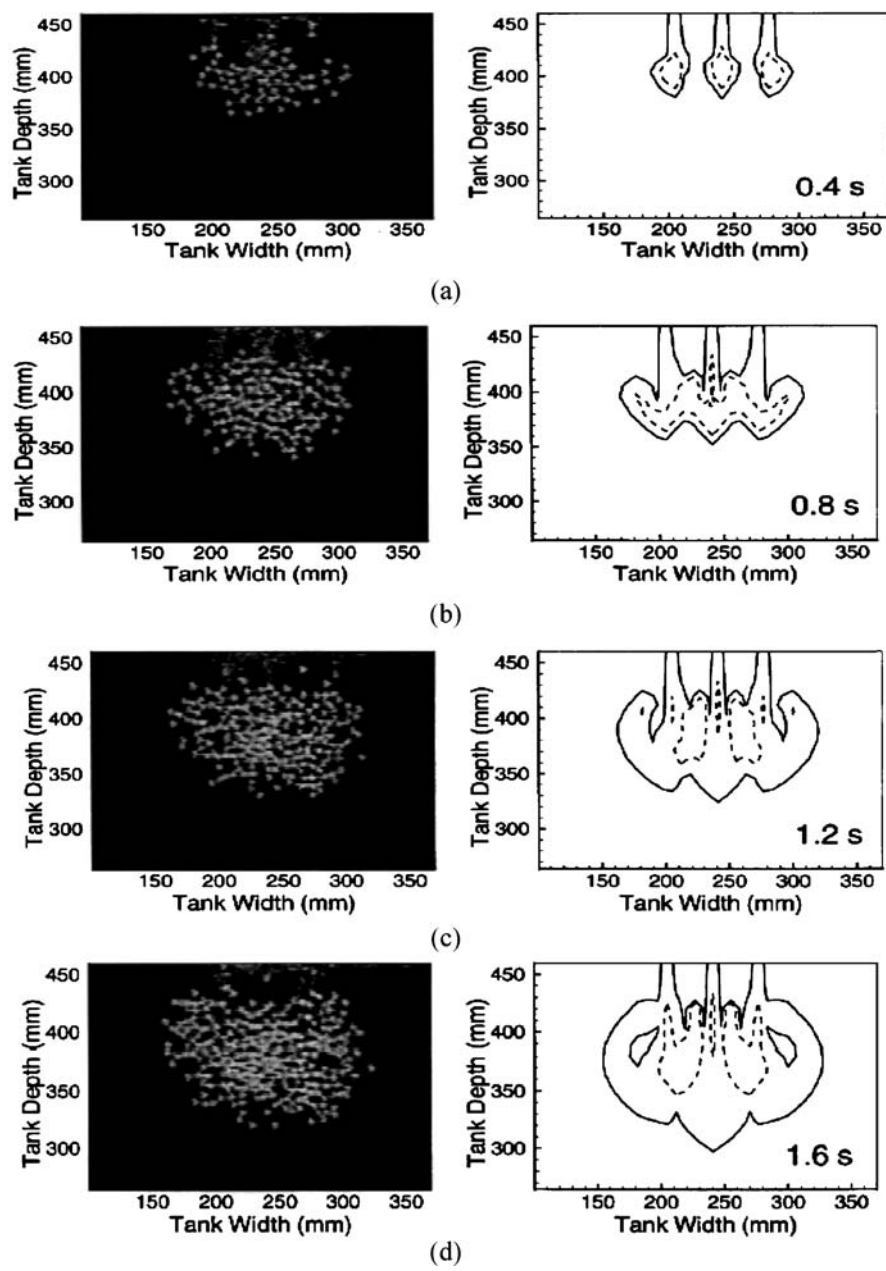


**Figure 7.8** Dispersion of solid particles in stagnant media as a function of time. Figures on the LHS are the experimental observations and on the right, simulation results. (Smith *et al.*, 2000. Redrawn with permission of Elsevier, Figures 3 and 4 in the original.)

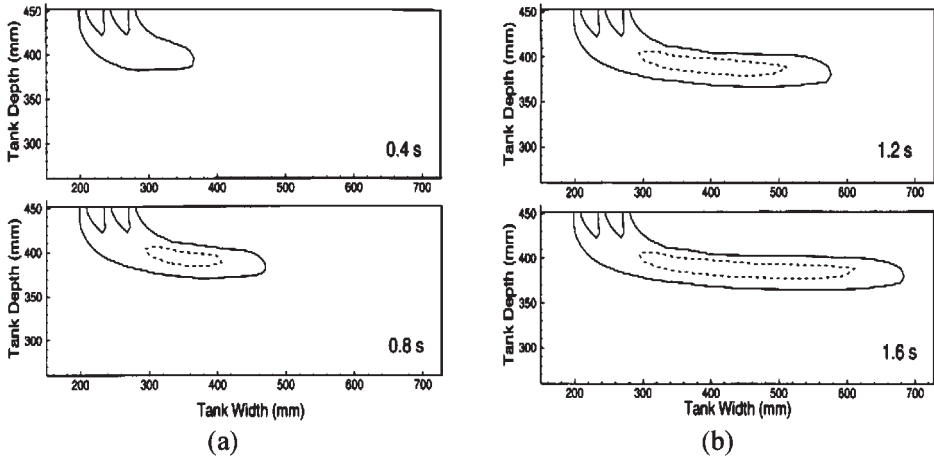


**Figure 7.9** Drift of solids as a function of time with flow upon introduction.  $V = 0.25 \text{ m s}^{-1}$ . (Smith *et al.*, 2000. Redrawn with permission of Elsevier, Figure 8 in the original.)

### 7.3 MECHANISMS OF MIXING

Agglomerates of particles can be dispersed by shear stresses in laminar flow, turbulent stresses created by velocity fluctuations, or elongational flow. These in turn depend on the dynamic shear viscosity  $\mu(\eta$ , in the case of non-Newtonian liquids), elongational viscosity  $\eta_e$ , and density  $\rho$  of the suspending liquid. In any case, the deformative forces created in the liquid phase should be strong enough to overcome the attractive forces between the many particles making up the aggregates. Complete dispersion of the aggregate into the component primary particles results in an increase of surface area proportional with the number of particles. For the same dispersion duty, elongational stresses are much more effective in disintegrating the aggregates than the shear forces. For the same reason the mixers which create shear flow only are much less efficient and require more power than the mixers which create elongational flow for the same mixing duty. Since, most of the commercial mixers can be designed to create both shear and elongational flows, a quantitative criteria, the *flow number*  $\lambda$  is used (Yao *et al.*, 2001) for the evaluation of the design of a mixer:

$$\lambda = \frac{|\mathbf{D}|}{|\mathbf{D}| + |\mathbf{\Omega}|} = \frac{\dot{\gamma}}{\dot{\gamma} + \omega} \quad (7.37)$$

$\dot{\gamma}$  and  $\omega$  are the magnitudes of the deformation rate  $\mathbf{D}$  and vorticity  $\mathbf{\Omega}$  tensors, respectively. The flow number varies in the range,  $0 \leq \lambda \leq 1$ .  $\lambda = 0$  denotes purely rotational flow without any mixing.  $\lambda = 0.5$  signifies simple shear flow, while  $\lambda = 1$  denotes pure elongational flow. When  $\lambda \geq 0.7$ , elongational flow also exists along with the shear flow.

In the case of concentrated suspensions with strong attractive forces between the particles making up the aggregates or in the case of two fluids with a large difference in density and viscosity, thorough mixing cannot be achieved with a single treatment of shear or

elongational flow; multiple passes through high shear rate or elongational flow regions are required. Multiple passes through high shear regions are maintained in different ways depending on the mechanism of mixing and the design of the mixer. For example, fluid is recirculated in agitated mixers: radially outwards and axially inwards with turbine type mixers and in the axial direction with propellers. Multiple passes are maintained using many baffles connected in series in static mixers and with the use of successive 90° turns or oscillating flow in micromixers.

In mixing solids suspended in liquids, mechanisms such as shear and elongation act through the agency of the suspending liquid. There are three basic fluid flow mechanisms through which mixing proceeds: turbulent convection; lamination and recombination of the layered liquid; and chaotic advection. Various designs of mixers are possible with the use of these mechanisms, and means of introducing shear or elongational flow with multiple recurrences through the mixer.

### 7.3.1 Mixing through turbulent convection

Mixing is carried out by breaking up the liquid bulk phases into small pieces in the form of turbulent eddies, that intermix to form an isotropic mixture. The break up of large drops depends on the balance between the kinetic energy and the surface energy of the drop. Large drops break up into smaller drops as long as their kinetic energy is greater than the surface energy requirement related with the interfacial area increase in the process. The size of the drops range between the Kolmogoroff's length scale of energy dissipating eddies in isotropic turbulence,  $l_K$ , and the length scale of the energy carrying eddies,  $l_e$ ,  $l_K \leq d_p \leq l_e$ . The Kolmogoroff length scale is a function of the viscosity  $\eta$ , and the density  $\rho$  of the liquid medium and the power input into a unit mass of agitated liquid,  $\varepsilon$ , through the equation,

$$l_K = \left( \frac{\eta^3}{\rho^3 \varepsilon} \right)^{1/4} \quad (7.38)$$

Isotropic turbulence is approached around the periphery of the impeller tips where the velocity is maximum under fully developed turbulence conditions. Local velocities decrease predominantly at the surface and the bottom of the stirred liquid during recirculation in the mixer, with a concomitant increase in the eddy size. Reaggregation of the solid particles may or may not occur depending on the viscosity of the liquid film separating the particles.

### 7.3.2 Mixing through lamination

When a barrier is placed parallel to the streamlines, the liquid flow will separate to go around the barrier and recombine at the rear. Repeated separations and recombinations will combine different layers of flow. Change in the direction of consecutive blades will enhance blending by further subdividing the lamella. If the blades of the barrier are flat with minimum cross-sectional projected area, only shear forces will exist along the wide

surfaces. If the blade shapes conform to the hydrodynamics of fluid flow, then the streamlines will extend and stretch as they go around the barrier, introducing elongation along with the shear flow with minimum turbulence losses. Another way to introduce elongational flow around a barrier is to twist the flow during passage over a barrier through 90°, similar to the flow in screw type of channels.

### 7.3.3 Mixing by chaotic advection

Concept of chaotic advection first introduced by Aref (1984) is formally defined as generation of a chaotic response in the distribution of a Lagrangian marker by simple Eulerian velocity field (Stremmer, *et al.*, 2004). In effect, it encompasses the two mechanisms of stretching of a liquid film, followed by folding over on itself, in a way analogous to the convective motion in turbulence. Advection results in response to a periodic oscillatory motion of the fluid under an external force or is brought about by the periodic change in the direction of the bounding surfaces. Its significance resides in the possibility of creating this motion in laminar flow at Reynolds numbers around or less than one, with a large contribution of elongational flow. Chaotic advection can be maintained by controlling the velocity of the bounding surfaces as in the case of smart blenders, by stretching the fluid over 90° bends as in the case of passive micromixers, or by oscillating the fluid by the action of pressure, magnetic, or electrical fields, as in the case of active micromixers.

Even though the liquid motion is laminar, chaos is created among the particles aggregated as clusters. Furthermore, any structural orientation and shape can be given to the scattered particles within the liquid suspending medium by controlling the stretching of local liquid sections through a predetermined protocol for the motion of the bounding surfaces (Zumbrunnen *et al.*, 2006 and the references therein).

### 7.3.4 Quantification of mixing efficiency

Theoretically mixing efficiency is quantified by the increase in the interfacial area between the two phases that are mixed or equivalently by the inter-material area created in the cases of blending or dispersion of solids within a liquid. Statistical concepts are invariably used in taking averages over the mixed volume.

In the case of liquid blending, interfacial boundaries cannot be readily visible. Mixing efficiency is then evaluated through the observation of color development or color variation, reaction products, pH, or fluorescence. Mixing a colored substance with an uncolored one and evaluation of the homogenization of color is one method. Instantaneous neutralization reaction with an indicator that changes color, such as phenolphthalein can also be used. Mixing is evaluated with images captured through a microscope with a charge-coupled device (CCD) camera. The intensity of color integrated over a captured image is proportional to the extent of reaction in the imaged volume (Liu *et al.*, 2000). The color intensity of an image is the sum of the intensities of the individual pixels:

$$I = \sum_{i=1}^N I_i \quad (7.39)$$

where the subscript  $i$  indicates an individual pixel, with  $N$  pixels in an image.  $I_{av} = I/N$  is the average color intensity of a pixel. To make the intensity measurements independent of the optical devices used, all the intensities are normalized by the maximum intensity observed in any pixel. Uniformity in mixing is evaluated by the standard deviation  $D_I$  from the maximum intensity:

$$D_I = \left[ \frac{1}{N} \sum_{i=1}^N (I_i - I_{\max})^2 \right]^{1/2} \quad (7.40)$$

Standard deviation is similarly normalized by the maximum intensity (Liu *et al.*, 2000). Similar evaluations can be done for the measurement of other properties used as probes, such as pH, and ionic concentration.

In multiple-impeller mixers where the height of the liquid,  $H$  is much greater than the diameter of the mixer tank,  $D_T$  (designed as  $H = n_i D_T$ , where  $n_i$  is the number of impellers connected to the same shaft), homogeneity in the axial  $z$ -direction also becomes a factor in determining the mixing efficiency. Montante *et al.* (2003) suggest the use of a dimensionless concentration profile along the axial direction,

$$\frac{C(z/H)}{C_{av}} = \frac{Pe_s}{1 - \exp(-Pe_s)} \exp\left(\frac{-zPe_s}{H}\right) \quad (7.41)$$

that incorporates the simultaneously occurring process of axial dispersion and sedimentation during mixing into a single parameter, the modified Péclet number ( $Pe_s$ ):

$$Pe_s = \frac{HV_s}{D_{pM}} \quad (7.42)$$

$V_s$  is the sedimentation velocity of the particles and  $D_{pM}$  the mean dispersion coefficient of the particles, represent the effects of sedimentation in the downward direction and lifting up by convective currents in the upward direction, respectively.  $C_{av}$  in eq. (7.41) is the mass concentration of solids [ $\text{kg m}^{-3}$ ] in the mixer and  $C$ , the mass concentration at any level  $z$ . In an ideal mixer, eq. (7.41) should equal to 1.0, with a constant concentration throughout the mixer.

## 7.4 MECHANICALLY AGITATED MIXERS

The main concern in agitated mixers is to keep the solid particles in suspended form, preventing accumulation in any part of the mixer volume with minimum power requirement.

### 7.4.1 General concepts in the design of mixers

Design of an agitated mixer for a given duty proceeds through the steps: (1) Selection of an impeller type according to the rheological properties of the suspension and process

requirements; (2) determination of the impeller speed depending on the physical properties of the particles and the suspension medium; (3) determination of the dimensions of the mixer according to the volume (or volumetric flow rate in the case of continuous mixers) of suspension to be mixed and required retention time in the mixer and shape factors. The distribution of particles within the stirred suspension medium and the power requirement for a given duty in a mixer are then determined basing on these selected parameters.

#### 7.4.1.1 Selection of impellers for a given duty

Impeller in a mixer determines the circulation pattern created within the suspension and the direction and magnitude of shear gradient around the periphery of the impeller tips. Impellers can be classified as axial flow, radial flow, mixed flow, and distributed flow. In axial flow impellers, the fluid is pumped in one direction and sucked from the opposite direction parallel to the axis of the shaft. Hydrofoil impellers, pitched blade with diagonally folded blades and marine propellers are examples of axial flow impellers. In radial flow impellers, such as the Rushton turbine, the fluid is pumped radially outwards and sucked in from both sides in the axial direction. In mixed flow impellers, such as the pitched blade turbine (PBT) the blades make an angle with the vertical and pump the fluid in both the radial and the axial directions and sucking from the reverse side in either direction. Distributed flow impellers, such as the ribbon and helical type of impellers, are used where the normal to the area of the blades change along the length of the impeller to distribute the shear plane over an angle of  $2\pi$  radians and the shear gradient in all directions to prevent the *Weissenberg* effect in viscoelastic fluids. They are also used in mixing high-viscosity pastes. These impellers are shown schematically in Figure 7.10.

Since the main duty of impellers in mixing solid–liquid suspensions is lifting up or drawing down of solid particles, axial flow impellers are generally used in mixing suspensions. Based on numerous experimental studies, it is generally agreed that hydrofoil type of impellers are the most efficient in terms of less energy expenditure at the same volumetric throughput, or equivalently, more liquid delivery (pumping) capacity for the same energy expenditure. The efficiency of hydrofoil impellers are due to their hydrodynamic profile that starts with a blade angle of  $45^\circ$  at the hub folding over an arch and ending up with a blade angle of  $22^\circ$  at the tips. The best substitute for hydrofoil impellers are pitched blade impellers (PB) with diagonally folded blades. Design of mixers is based on selection of impellers that require the minimum power for raising the particles off the bottom of the mixer tank and the critical impeller speed to keep the particles in suspension. The efficiency of impellers in suspending solid particles can be compared by means of a dimensionless power consumption criterion  $\Pi_s$ , (Rieger, 1999)

$$\Pi_s = Po(Fr')^{3/2} \left( \frac{D_i}{D_T} \right)^{7/2} \quad (7.43)$$

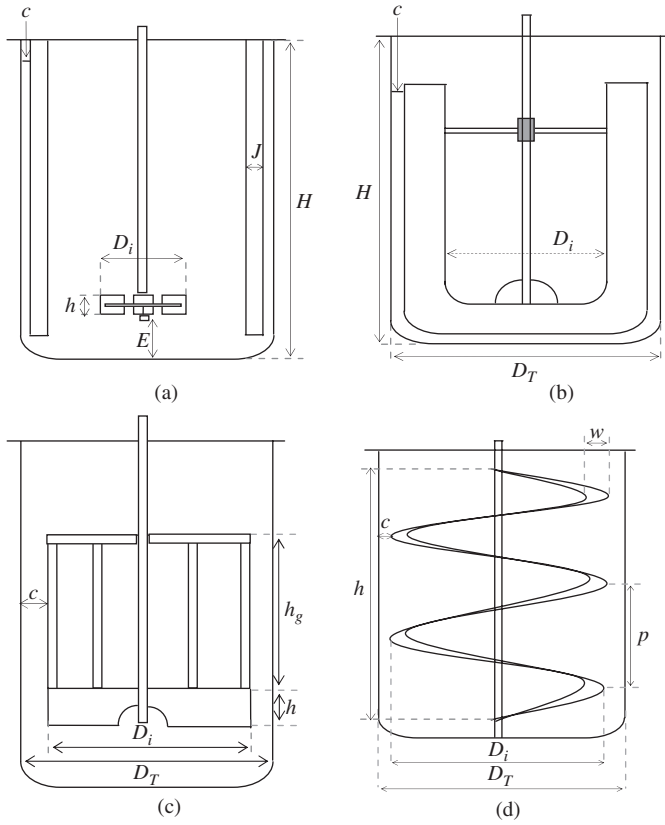


**Figure 7.10** Types of impellers used in mixing suspensions: (a) turbine, (b) anchor, (c) gate, (d) ribbon.

where  $Po$  is Power number,  $Fr'$  is Froude number,  $D_i$  and  $D_T$  are impeller and tank diameters, respectively. Rieger (2000, 2002) revised the Froude number  $Fr'$ :

$$Fr' = \frac{N_{js}^2 D_i \rho}{g(\rho_p - \rho)} \quad (7.44)$$

in eq. (7.43) to be used with a range of particle sizes including both fine and large sized particles with a single correlation,

$$Fr' = \frac{C_1(d_p/D_T)}{\left\{ 1 + \left[ \frac{C_1}{C_2} \left( \frac{d_p}{D_T} \right)^{\gamma_1 - \gamma_2} \right]^{10} \right\}^{1/10}} \quad (7.45)$$



$N_{JS}$  in eq. (7.44) is the *just-suspended stirring rate*. The constants  $C_i$  and  $\gamma_i$  are correlated with the volumetric concentration of solids  $\phi$ , with the use of experimentally determined constants  $A$  and  $B$ , and  $\alpha$  and  $\beta$  in each case:

$$C_i = A_i \exp(B_i \phi) \quad (7.46)$$

$$\gamma_i = \alpha_i + \beta_i \phi \quad (7.47)$$

Rieger found that when diagonally folded pitched blade turbine type of impellers are used, number of blades (3, 4, or 6) do not affect the dimensionless power consumption,  $\Pi_s$ , but the just-suspended stirring rate  $N_{JS}$  decreases and torque increases with an increase in the number of blades, independent of the size and volumetric concentration of particles. Energy requirement increases and the just-suspended stirring rate  $N_{JS}$  decreases with an increase in the pitch angle.

#### 7.4.1.2 Determination of the impeller speed

The intensity of kinetic energy supplied to the mixer varies with the process requirements as well as the viscosity, or in general, rheology of the suspending medium. However, even if the suspending medium is Newtonian, the stirred suspension will behave as a non-Newtonian fluid when the particle size is small and volumetric concentration in the mixer is high. When the suspension behaves as a Bingham or a power law fluid with a low viscosity index  $n$ , nearly stagnant regions may appear at the bottom and top surface of the suspension. When the viscosity of the suspending medium and the volumetric concentration of the solids are low, resistance to settling is greatly reduced. Then the density difference becomes a determining factor. If the density of the solid particles is much higher than that of the liquid, then the particles tend to settle to the bottom of the mixer where the velocity of the liquid is much lower than the linear tip velocity of the impeller. *Off-bottom lifting* then becomes the main concern and the critical speed of the impeller is the off-bottom speed,  $N_{BL}$ . On the other hand, if the particles are self-buoyant, then they tend to collect at the surface and need to be withdrawn into the bulk of the suspension. The critical speed is then the *just-draw-down* speed,  $N_{JD}$  in large tanks, with proportionally large diameter impellers, small clearances with the walls and relatively low speeds, keeping the solid particles in suspension becomes the critical process. The impeller speed under this *just-suspended condition* becomes the critical speed,  $N_{JS}$ . The last factor determining the intensity of mixing comes up in bioreactors: Intense agitation damages the microorganisms. The intensity of agitation should be high enough for thorough dispersion but not too high to prevent inactivation.

#### 7.4.1.3 Shape factors and dimensions of the mixer

Geometrical similarity between mixers is maintained by keeping the ratios of certain critical dimensions identical. These ratios are called *shape factors* denoted by  $S$ . The determinative shape factors of a mixer used for geometrical similarity in power calculations are

the ratios of the impeller diameter  $D_i$  and the height of the stirred fluid  $H$  in the mixer to the tank diameter  $D_T$ :

$$S_1 = \frac{D_i}{D_T} \quad (7.48)$$

$$S_2 = \frac{H}{D_T} \quad (7.49)$$

The distance between the horizontal center-line of the impeller,  $E$  and the bottom of the tank is critical in determining the dispersion quality and the power consumption and is given by the third shape factor,  $S_3$ :

$$S_3 = \frac{E}{D_i} \quad (7.50)$$

The ratio of the width of the baffles, used to break the vortex flow, to the tank diameter is the fourth shape factor,

$$S_4 = \frac{J}{D_T} \quad (7.51)$$

The generally employed values of these shape factors for Rushton turbines and other single axial or mixed flow impellers are:  $S_1 = 1/3$ ,  $S_2 = 1$ ,  $S_3 = 1/2 - 1$ ,  $S_4 = 1/10$ . The other shape factors which must be kept identical in value for geometrical similarity are:  $S_5$ , the clearance (the distance from the wall) of the baffles to the tank diameter;  $S_6$ , the distance between the baffle and the bottom of the tank to the tank diameter;  $S_7$ , radius of curvature of the tank bottom to the tank diameter;  $S_8$ , ratio of the length and  $S_9$ , the width of the impeller to the impeller diameter. Once, the tank diameter is determined, all the dimensions of the mixer is set by the accepted values of the shape factors. The general trend in the design of mixers is to equate the height of the suspension in the mixer,  $H$  to the diameter of the tank,  $D_T$ . The volume of the mixer tank is determined by taking  $S_2 = 1$ , and making an allowance for free space above the suspension. For deep tanks, one impeller is used for every incremental increase in height equivalent to one tank diameter, for example, when the depth of the fluid  $H$  is equal to three times the tank diameter  $D_T$  ( $H = 3D_T$ ), three impellers connected to the same shaft should be used.

### 7.4.2 Dispersion of solids in mixers

Mixing in agitated mixers is mainly based on the turbulent convections described in Section 7.3.1. Fluid leaving the tips of the rotating impeller undergoes two kinds of

motion: (1) Small scale convective motion: the turbulent eddies, that move randomly within the fluid and carry a large amount of kinetic energy due to their velocities; (2) superimposed on the convective turbulent eddy motion, recirculation around the mixer volume, the pattern of which is dictated by the shape of the impeller blades. Decision on the intensity of turbulence that should be created and the related power consumption depends on the ability of the solid particles and aggregates to be dispersed. Archimedes number (eq. (4.70)), is used as a criterion for the general homogeneity of the suspension medium. The particles tend to settle when  $Ar \geq 100$ , and behave as a non-Newtonian fluid at values much below this limit. The power requirement for the intended mixing is evaluated as the *specific power input*,  $P_{ov}$ , power per unit volume of fluid to be mixed, or energy expended per unit time and unit volume of fluid,

$$P_{ov} = \phi V_{ht} g \frac{(\rho_p - \rho)}{\rho} \quad (7.52)$$

Specific power input is a function of the volumetric fraction  $\phi$  of the particles, the hindered settling velocity of the particles,  $V_{ht}$ , and the densities of the particle  $\rho_p$ , and the liquid medium  $\rho$ , in which it is suspended.

#### 7.4.2.1 Theoretical derivation of the dispersion conditions for settling solids

A theoretical derivation of the minimum stirrer speed in mechanically agitated suspensions is made by Mersmann *et al.* (1998), which will be outlined below.

The derivation starts with a force balance on a single particle incorporating gravitational, buoyancy and drag forces, as given in Chapter 4. The net force acting on a suspended particle in the direction of gravity is converted into an energy form in the scale of a single particle by multiplying with the diameter,  $d_p$  of the particle:

$$E_p = \frac{\pi d_p^3}{6} (\rho_p - \rho) g d_p \quad (7.53)$$

This energy that causes the particle to settle must be counteracted by the kinetic energy of turbulence fluctuations in the scale of the particle,

$$E' = m_l \frac{V'^2}{2} = \frac{\pi d_p^3}{6} \rho \frac{V'^2}{2} \quad (7.54)$$

An expression for the fluctuation velocity is obtained in terms of a single particle velocity by equating the energies in eqs. (7.53) and (7.54) and incorporating the force balance into the equation:

$$V'^4 = 3C_D d_p g \frac{(\rho_p - \rho)}{\rho} V_t^2 \quad (7.55)$$

This analysis is extended to the bulk of the suspension by relating the particle velocity  $V_i$  to the suspension velocity  $V_s$  through the volumetric fraction of particles (eq. (4.147) for concentrated suspensions).

The exponent  $n$  in eq. (4.147) is a function of the Archimedes number and decreases from a constant value of 4.65 for  $Ar \leq 1$  to 2.4 for  $Ar \geq 10^5$ . The time averaged fluctuation velocity for the volume element incorporating monodispersed particles of diameter  $d_p$  is obtained by combining eqs. (7.52), (7.55), and (4.147):

$$V'^4 = 3C_D d_p V_i^2 \phi (1 - \phi)^n g \frac{(\rho_p - \rho)}{\rho} \quad (7.56)$$

Fluctuation velocity  $V'$  is proportional to the stirrer tip speed  $V_{tip}$ , so the turbulence parameters are expressed in terms of  $V'/V_{tip}$ . Volumetric average of the mean fluctuation velocities depends on the ratio of the impeller diameter  $D_i$  to the tank diameter  $D_T$ . The smaller is the ratio  $D_i/D_T$ , the broader is the distribution of the fluctuating velocities  $V'$ . The median of the fluctuating velocity,  $V'_{0.5}$  is proportional to  $D_i/D_T$ , as,

$$V'_{0.5} \propto \left( \frac{D_i}{D_T} \right)^{3/4} \quad (7.57)$$

The magnitude of the average fluctuation velocities is maximum around the impeller discharge that decrease in value as the solid-liquid boundary layers along the walls and the bottom of the mixer are approached. The relation between the fluctuating velocities and the Power number supported both by theoretical considerations and experimental observations is given by eq. (7.58):

$$\frac{V'_{0.5}}{V_{tip}} = 0.158 Po^{7/18} \left( \frac{D_i}{D_T} \right)^{3/4} \quad (7.58)$$

This equation can be generalized for all scales of turbulence fluctuations as,

$$\frac{V'}{V_{tip}} = a Po^{7/18} \left( \frac{D_i}{D_T} \right)^b \quad (7.59)$$

where the constants  $a$  and  $b$  are related through a curve fitting of the theoretical data in the range of  $0 \leq b \leq 3$ :

$$a = 0.18 \exp(-0.1772b) \quad (7.60)$$

as given in Figure 7.11. The fluctuation velocity near the bottom of the mixer bears significance in relation to lifting of the settled particles off the ground level. The relation

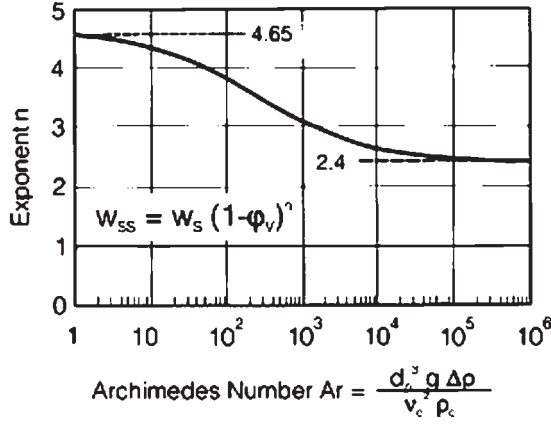


**Figure 7.11** Variation of exponent  $n$  in eq. (7.57) with the Archimedes number ( $W_s \equiv V_t$ ,  $W_{ss} \equiv V_{ht}$ ,  $\phi_v \equiv \phi$ ). (Mersmann *et al.*, 1998. Reproduced with permission of Elsevier, Figure 1 in the original.)

for the minimum fluctuating velocity based on the results of theoretical derivations of Mersmann and coworkers is,

$$\frac{V'_{\min}}{V_{\text{tip}}} = 0.088 Po^{7/18} \left( \frac{D_i}{D_T} \right)^{3/2} \quad (7.61)$$

which shows a very good agreement with experimental results. Minimum fluctuation velocity  $V'_{\min}$  can be used to relate the tip velocity of the impeller,  $V_{\text{tip}}$  and the settling velocity of the solids,  $V_t$  by replacing eq. (7.56) into eq. (7.61):

$$\left[ 3C_D d_p V_t^2 \phi (1 - \phi)^n g \frac{(\rho_p - \rho)}{\rho} \right]^{1/4} = 0.088 Po^{7/18} \left( \frac{D_i}{D_T} \right)^{3/2} V_{\text{tip}} \quad (7.62)$$

$$\frac{V_t^{1/2}}{V_{\text{tip}}} = \frac{0.088 Po^{7/18} (D_i/D_T)^{3/2}}{[3C_D d_p \phi (1 - \phi)^n g ((\rho_p - \rho)/\rho)]^{1/4}} \quad (7.63)$$

The authors (Mersmann *et al.*, 1998) found a very good correlation between experimental results and the tip velocity calculated with eq. (7.63).

Stirring by an impeller serves two functions that both contribute to the dispersion of the solids: prevention of settling, and lifting the settled particles off from the bottom. These two functions are expressed in terms of specific power requirement for lifting,  $\mathcal{P}_{ol}$ :

$$\frac{\mathcal{P}_{ol} H \rho^2}{\mu g (\rho_p - \rho)} \left( \frac{D_i}{D_T} \right)^{5/2} \approx 203 Ar^{1/2} [\phi (1 - \phi)^n]^{3/4} \quad (7.64)$$

and specific power requirement for dispersion  $\mathcal{P}_{od}$  as,

$$\mathcal{P}_{od} \left( \frac{\rho^3}{d_p g^3 (\rho_p - \rho)^3} \right)^{1/2} \approx 0.385 A r^{1/8} [\phi(1 - \phi)^n] \quad (7.65)$$

In designing the mixer, the power requirements of these functions are calculated and the design is based on the function requiring the greater power.

#### 7.4.2.2 Dispersion of floating solids

When the density of solid particles or the apparent density of highly porous aggregates is equal or less than the density of the suspending liquid medium, then the particles float on the surface of the liquid. Poorly wetted particles with highly hydrophobic surfaces also tend to float on the surface of the liquid. To draw the particles down into the bulk liquid medium, they should be wetted by the liquid, the stagnancy of the fluid layer should be disrupted by the turbulent eddies reaching the surface, and the velocity of the recirculating liquid currents should be able to carry the particles along. These processes depend on the particle size, the concentration of solids, the surface tension and viscosity of the liquid as well as on the shape factors of the mixer, primarily,  $S_1$  and  $S_3$ , given by eqs. (7.48) and (7.50), respectively. Besides these parameters, the extent of axial mixing induced by the impeller and pumping direction of the impeller are also significant parameters. Özcan-Taşkın (2006) investigated the effect of recirculation currents created by upward pumping and downward pumping axial-flow impellers on drawdown paths of the buoyant particles. The recirculation paths are given in Figure 7.12(a) for downward pumping and in Figure 7.12(b) for upward pumping impellers.

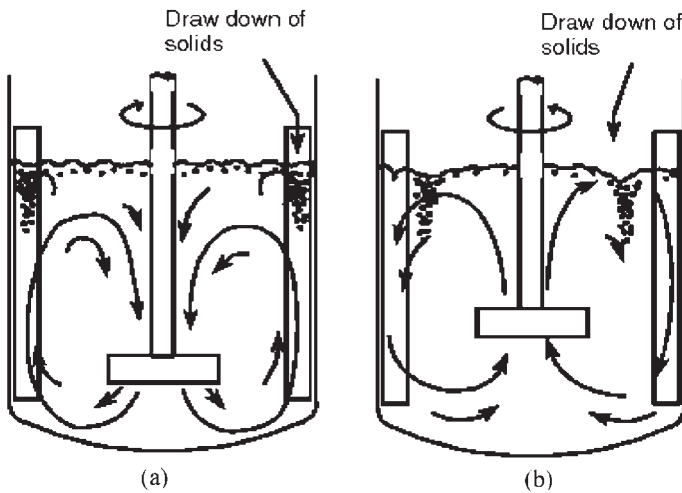


**Figure 7.12** Downward path of particles with the recirculation currents created by axial impellers in fully baffled mixers with  $D_i/D_T = 0.33$ : (a) down-pumping impeller, (b) up-pumping impeller. (Özcan-Taşkın, 2006. Reproduced with permission of Elsevier, Figures 5(a) and 5(c) in the original.)

Since the particles do not experience frictional resistance on contact with the vessel walls, upward pumping impellers draw less power for the same duty. Similar conclusions were arrived at by Kuzmanić and coworkers (Kuzmanić and Žanetić, 1999; Kuzmanić and Ljubičić, 2001). They also found the surface tension of the liquid as an effective parameter in determining the mixing time and minimum draw-down speed  $N_{JD}$  of the impeller. Reduction in the surface tension of the liquid increases spreading, penetration and wetting rates of the particles and reduces the ability of the surface to support the particles floating on it.

### 7.4.3 Power consumption in mixers

Power requirement for the mixing processes such as defined by eqs. (7.64) and (7.65) for lifting and dispersion of the particles in the mixing vessel is supplied by the impeller. The diameter and the stirring rate of the impeller determine the power consumption of the impeller, which should ideally correspond to the power required.

The power consumption of the impeller can be obtained from the definition of power as the product of the volumetric flow rate  $Q$  of the suspension circulated by the impeller ( $Q \propto ND_i^3$ ) and the hydrodynamic pressure converted into kinetic energy of the turbulent eddies ( $\Delta P_h \propto \rho N^2 D_i^2$ ).

$$\mathcal{P}_o \propto \rho N^3 D_i^5 \quad (7.66)$$

The ratio of the power consumption,  $\mathcal{P}_o$  to the equivalent expression for power gives the *Power number*,  $Po$  (also called the *Newton number*,  $Ne$ ).

$$Po = \frac{\mathcal{P}_o}{\rho N^3 D_i^5} \quad (7.67)$$

Power consumption increases with the fifth power of the impeller diameter  $D_i$ , and the cube of the stirring rate  $N$ , so the rotation rate of the impeller has to decrease as the impeller diameter increases for a given power consumption. Power consumption of the impeller is mainly due to drag forces created by the impact on the faces of the blades normal to the direction of motion. Therefore, the variation of the Power number with the Reynolds number follows the same trends as the drag coefficient,  $C_D$ ; i.e., a linear variation in the laminar regime and a constant value in fully developed turbulence as shown in Figure 7.13:

$$Po = K_p Re^{-1} + Po_{\text{turb}} \quad (7.68)$$

where, the Reynolds number is defined as,

$$Re = \frac{ND_i^2 \rho}{\eta_{\text{eff}}} \quad (7.69)$$

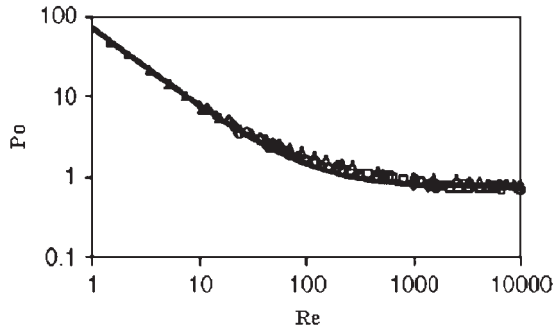


**Figure 7.13** Variation of Power number of shear thinning fluids with Reynolds number (Wassmer and Hungenber 2005. Redrawn with permission of Wiley-VCH, Figure 1 in the original.)

$\eta_{\text{eff}}$  being the apparent viscosity of the solid-liquid suspension, including non-Newtonian suspensions. The linear region in Figure 7.13 depicts the *laminar regime* in mixers, which extends up to  $Re \leq 10$ . The power number  $Po$  levels off starting from  $Re \geq 300$ , with the onset of turbulence, reaching a constant value around  $Re = 1000$ , under fully developed *turbulent regime*. In between these two limits,  $10 \leq Re \leq 300$ , *transition regime* exists in the liquid to be mixed. Eq. (7.68) is expressed as,

$$Re Po = K_p \quad (7.70)$$

for mixing in the laminar regime, such as in the case of blending, use of large diameter impellers or in mixing highly viscous concentrated suspensions.

#### 7.4.3.1 Power consumption of impellers in shear thinning suspensions

Suspensions of solid particles exhibit shear thinning behavior with an increase in the shear rate. In mixers where high rates of shear are employed to keep the particles in suspension, the viscosity of the suspension will vary locally as fluid currents circulate within the mixed volume as well as with the level of the average shear rate generated by the impeller motion. It will then be difficult to assign a value to the Reynolds number given by eq. (7.69), to be used in the correlation of eq. (7.68) to calculate the power requirement by eq. (7.67). The classical procedure proposed by Metzner and Otto (1957) for flat bladed turbine impellers, assumes a linear variation of the shear rate with the impeller tip speed:

$$\dot{\gamma} = K_s N \quad (7.71)$$

The empirical constant  $K_s$  is equated to 13, approximated by  $4\pi$  found by theoretical derivations assuming Couette flow between the impeller tip and the walls of the mixer for close-clearance impellers. The effective or apparent viscosity for power law fluids can be expressed as

$$\eta_{\text{eff}} = K(K_s N)^{n-1} \quad (7.72)$$



with the use of eq. (7.71). Metzner–Otto correlation is shown to give a good prediction of the effective shear rate at low stirring rates corresponding to the laminar regime. At high stirring rates corresponding to the transition regime, power requirement is overestimated with the use of a constant determined under laminar conditions.

Recently, Wassmer and Hungenberg (2005) extended the Metzner–Otto correlation into the transition regime by a generalized derivation based on the power consumption of the impeller. Their model is reported to show minimum deviation from experimental data in comparison with other models under all flow regimes and employs only one empirical constant to be determined. The authors validated their result with eight different stirrer systems. The derivation based on basic principles that relate the torque of the impeller to the variations in shear rate is outlined below.

Power consumption  $\mathcal{P}_o$  of an impeller is equal to the torque  $M$  generated times the revolution rate in radians per second:

$$\mathcal{P}_o = M(2\pi N) \quad (7.73)$$

Collecting the frictional losses into the proportionality constants, torque is related to the effective force,  $F_{\text{eff}}$  and effective shear stress,  $\tau_{\text{eff}}$  through the equation,

$$M \propto F_{\text{eff}} D_i \propto \tau_{\text{eff}} D_i^3 \quad (7.74)$$

Since impeller performance is evaluated as power per unit volume, and since the fluid volume to be mixed with the impeller,  $v$  ( $\equiv Q \propto ND^3$ ), is related to its diameter  $D_i$  through the shape factors,

$$v \propto D_i^3 \quad (7.75)$$

Eqs. (7.73)–(7.75) are combined to give a relation between power per unit volume and the effective shear stress,

$$\tau_{\text{eff}}(2\pi N) = C_p \frac{\mathcal{P}_o}{v} \quad (7.76)$$

where,  $C_p$  is proportionality constant. Using the basic relation between the effective shear stress  $\tau_{\text{eff}}$  and the effective shear rate  $\dot{\gamma}_{\text{eff}}$ ,

$$\tau_{\text{eff}} = \eta_{\text{eff}} \dot{\gamma}_{\text{eff}} \quad (7.77)$$

and the definition of the Power number (eq. (7.67)), the effective shear rate is related to the power number through,

$$\dot{\gamma}_{\text{eff}} = C_s \frac{N^2 D_i^5 \rho P_o}{\eta_{\text{eff}} v} \quad (7.78)$$

The coefficient  $C_s = C_p/2\pi$  is related to the shape factors of the mixer and the variation of the power number with the Reynolds number in the laminar regime.

The volume of the stirred fluid in a mixer with a flat bottom,

$$v = \frac{\pi D_T^2}{4} H \quad (7.79)$$

can be expressed in terms of the impeller diameter  $D_i$  as

$$v = \frac{\pi S_2}{4 S_1^3} D_i^3 = C_{\text{geom}} D_i^3 \quad (7.80)$$

Replacing the first term in eqs. (7.68), for laminar regime, (7.69), and (7.80) into eq. (7.78), the effective shear rate  $\dot{\gamma}_{\text{eff}}$  is related to the revolution rate of the impeller  $N$ , through the constants of the system,

$$\dot{\gamma}_{\text{eff}} = \left( C_s \frac{K_p}{C_{\text{geom}}} \right) N \quad (7.81)$$

The coefficient  $C_s$  is related to the Metzner–Otto coefficient  $K_s$ , the slope of the Power number versus the Reynolds number plot in the laminar regime,  $K_p$ , and the geometric constant of the mixer,  $C_{\text{geom}}$ :

$$C_s = \frac{K_s C_{\text{geom}}}{K_p} \quad (7.82)$$

Wassmer and Hungenberg (2005) suggest the iterative technique in Figure 7.14 to check the correspondence of the Power number (Power consumption), with the effective shear rate and effective viscosity, for a system of given rheological properties under the existing conditions.

The analysis assumes that the coefficient  $C_s$  or equivalently,  $C_p$  is known, or determined with a Newtonian fluid, for a given impeller for which the analysis will be conducted. In addition, the shape factors of the mixer or equivalently the geometrical constant should also be known. Then the iterative procedure in Figure 7.14 is conducted to determine the effective rheological constants of the non-Newtonian fluid under given power input and mixing conditions.

The authors tested their procedure with the experimental data of Zeppenfeld and Mersmann (1998) and found good agreement between their procedure and experimental results given as the data points in Figure 7.13.

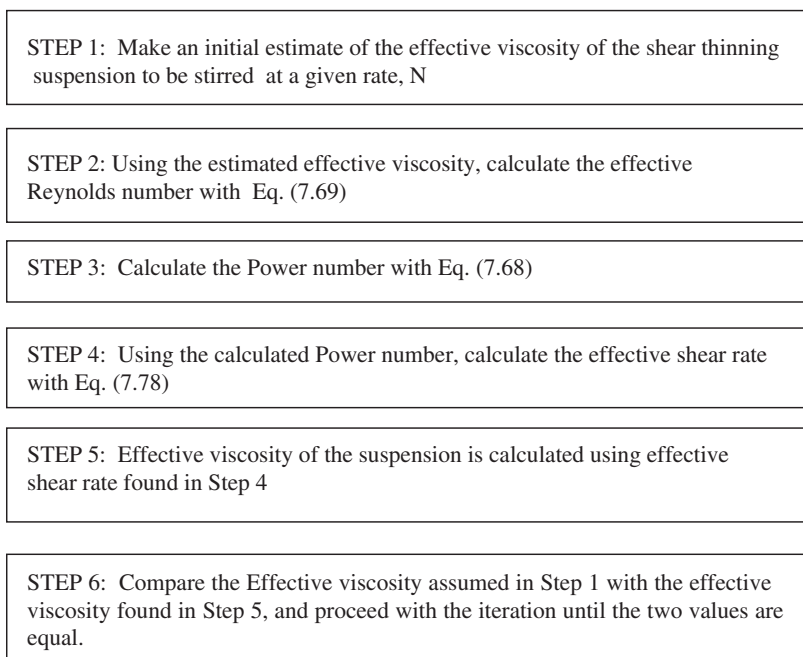


**Figure 7.14** Iteration procedure for correlation of rheological properties with the Power number.

#### 7.4.3.2 Power consumption of close-clearance impellers in Newtonian fluids

Anchor, gate, screw, and ribbon type of impellers constitute the close clearance impellers where the diameter of the impeller approaches the diameter of the mixing vessel (Figure 7.10(b)–(d)). These impellers are used in mixing highly viscous suspensions such as pastes and polymers and suspensions where the solids tend to segregate due to crystallization or solidification and in exothermic or endothermic reactions in jacketed stirred reactors. Secondary convection currents and circulation patterns created within the mixing vessel dictate the performance of these impellers. The flow patterns created by the impeller as a function of the Reynolds number or speed of rotation is used as a criterion in the selection of the type of impeller to be used for a given duty. The circulation pattern created by helical ribbon type of impellers is given in Figure 7.15. As the area vector normal to the surfaces of the impeller also rotate along its length, the fluid striking the surfaces are pushed in varying directions along the length of the impeller. In addition, depending on the clearance  $c$  ( $c = (D_T - D_i)/2$ ) between the blades and the wall of the vessel, strong axial currents are generated within the mixer. These properties make ribbon impellers suitable for use as homogenization agents where heat transfer between the walls and the fluid is important (Nagata, 1975), and when a narrow size distribution of solids is required (Yao *et al.*, 2001). On the other hand, gate type mixers create strong elongational flow as the ribs of the impeller drag the fluid along at moderate to high Reynolds numbers, so the gate type of impellers are used to disperse aggregates within a

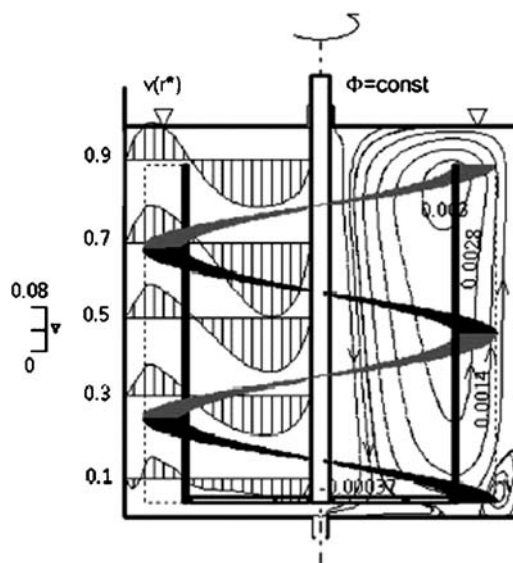


**Figure 7.15** Velocity profiles and stream functions in a mixing vessel with a helical ribbon type of impeller:  $Re = 53.6$ ,  $D_i = 0.28$  m.,  $D_T = 0.312$  m,  $p = 0.13$  m.  $\rho = 1400 \text{ kg m}^{-3}$ ,  $\mu = 0.2\text{--}1.5$  Pas. (Niedzińska and Kuncewicz, 2005. Reproduced with permission of Elsevier, Figure 5 in the original.)

fluid. Because of poor recirculation characteristics, they are not efficient as dispersing agents at low Reynolds numbers. Anchor type of impellers create a single recirculation loop within each arm of the impeller. The drag and elongational flow are limited to the single blade and not efficient throughout the mixer volume. However, when the clearance of the impellers is low, they aid in heat transfer and prevent deposition of solids by creating high shear rates along the walls.

Clearance is one of the most effective shape factors in the use of these impellers. As the clearance decreases, the peripheral and axial velocities increase, enhancing the liquid recirculation in the boundary layer. Pitch is also an important shape factor in helical ribbon type impellers. Instead of a continuous trend in its effect, the pitch exhibits an optimum value, presumably depending on the rotation rate of the impeller and the viscosity of the suspension. If, the fluid is pushed by the impeller surface with a force adequate to increase its kinetic energy so that it can reach the next coil within one revolution period of the impeller, then the axial velocity will increase. If the pitch is large, so that the fluid cannot reach the upper coil within the rotation period, then the axial velocity will decrease (Niedzińska and Kuncewicz, 2005). Increasing the rotation rate will increase the power requirement proportional to the third power of stirring rate. As the diameter of these impellers are considered from edge-to-edge of the impeller and as  $D_i/D_T \approx 1$ , power consumption of these impellers is an important issue, requiring careful consideration.

As the close-clearance impellers are used with concentrated suspensions, or viscous liquids, they generally operate in the laminar regime. The power requirement is calculated

with eq. (7.70), using eq. (7.67) and eq. (7.69). The proportionality constant  $K_p$ , depends on the shape factors of the impeller and the mixing vessel. Some of the correlations for helical ribbon impellers in the literature are given in Table 7.1 adapted from Niedzielska and Kuncewicz (2005). There is general agreement between the models on the effect of clearance, denoted by  $c$ , or  $(D_T - D_i)$  terms, on the power consumption of the impellers: As the clearance decreases power consumption increases with a power of the clearance that ranges between 0.25 and 0.53.

**Table 7.1**

$K_p$  ( $\equiv Po Re$ ) Correlations for helical ribbon type impellers in Newtonian fluids

Correlations	Equation Numbers	References
$K_p = 34.1 N_r^{0.79} \left( \frac{1}{2} \left( \frac{D_T}{D_i} - 1 \right) \right)^{-0.53} \left( \frac{p}{D_i} \right)^{-0.63} \left( \frac{H}{D_i} \right)^{0.45} \left( \frac{h}{D_i} \right)^{1.01}$	(7.83)	Blasiński and Ryzyski (1980)
$K_p = 66 \left( \frac{p}{D_i} \right)^{-0.44} \left[ \frac{1}{2} \left( \frac{D_T}{D_i} - 1 \right) \right]^{-0.29} \left( \frac{h}{D_i} \right) N_r^{0.84}$	(7.84)	Delaplace <i>et al.</i> (2000)
$K_p = 60 N_r^{0.8} \left( \frac{1}{2} \left( \frac{D_T}{D_i} - 1 \right) \right)^{-0.3} \left( \frac{p}{D_i} \right)^{-0.5}$	(7.85)	Käppel (1979)
$K_p = 52.5 \left( \frac{D_T - D_i}{D_i} \right)^{-0.5} \left( \frac{N_r D_i}{p} \right)^{0.5}$	(7.86)	Nagata (1975)
$K_p = 98 \left( \frac{D_T - D_i}{D_i} \right)^{-0.25} \left( \frac{p}{D_i} \right)^{-0.55}$	(7.87)	Niedzielska and Kuncewicz (2005)
$K_p = 100 \left( \frac{w}{D_i} \right) \left( \frac{h}{D_i \sin \theta_B} \right) \left( \frac{\bar{D}_i}{D_i} \right) \left( \frac{c}{D_T} \right)^{-0.5} N_r$	(7.88)	Shekhar and Jayanti (2003, a–b)
$K_p = 91 \left( \frac{p}{D_i} \right)^{-0.37} \left[ \frac{1}{2} \left( \frac{D_T}{D_i} - 1 \right) \right]^{-0.31} \left( \frac{h}{D_i} \right) \left( \frac{w}{D_i} \right)^{0.16} N_r^{0.79}$	(7.89)	Delaplace <i>et al.</i> (2006)

*Nomenclature for the Table:*  $N_r$ : number of helical blades,  $p$ : pitch,  $h$ : height of the helical impeller as the distance in between the attachment points of the blades to the shaft,  $\theta_B$ : blade angle,  $w$ : width of the blades,  $c$ : clearance between the impeller and the wall,  $D_i$ : diameter of the blades at the points of largest departure from the shaft,  $\bar{D}_i$ : average diameter of the impeller,  $D_T$ : diameter of the mixing vessel.

Clearance is also a determining factor in the power consumption of anchor type impellers. Two of the correlations given in the literature for power consumption of anchors in Newtonian fluids are,

$$K_p = PoRe = 82 \left( \frac{ND_i^2 \rho}{\mu} \right)^{0.07} \left( \frac{c}{D_T} \right)^{-0.25} \quad (7.90)$$

by Beckner and Smith (1966), and

$$K_p = PoRe = 8.5\pi^3 N_r \left( \frac{h}{D_i} \right) \left( \frac{w}{D_i} \right) \left( \frac{c}{D_T} \right)^{-0.5} \quad (7.91)$$

by Shamlou Ayazi and Edwards (1989).  $N_r$  in eq. (7.91) denotes the number of blades.

#### 7.4.3.3 Power consumption of close-clearance impellers in shear thinning fluids

Effect of shear thinning on the power consumption of close-clearance impellers is also taken into account by the  $K_s$  factor of Metzner and Otto (1957) in eq. (7.72) together with eqs. (7.69)–(7.71), but the defining function is not necessarily a constant. There are four groups of correlations proposed for  $K_s$  in *anchor shaped impellers* (Shekhar and Jayanti, 2003). Examples to the types of correlations are given in Table 7.2.

**Table 7.2**

Examples to the functions used for  $K_s$  in anchor type of impellers

Types of Function	Examples	Equation Numbers	References
$K_s = \text{const}$	$K_s = 25$	(7.92)	Nagata (1975)
$K_s = f(n)$	$K_s = 35^{n/(1-n)}$	(7.93)	Sestak <i>et al.</i> , (1986)
$K_s = f\left(\frac{c}{D_T}\right)$	$K_s = 33 - 172 \frac{c}{D_T}$	(7.94)	Shamlou Ayazi and Edwards (1989)
$K_s = f\left(\frac{n, c}{D_T}\right)$	$K_s = \left(37 - 120 \frac{c}{D_T}\right)(1 - n)$	(7.95)	Beckner and Smith (1966)

$K_s$  factor for *helical ribbon type of impellers* is similarly defined by a complex function of shape factors, power law index, and  $K_p$  by Delaplace *et al.* (2006) through an analytical model developed based on analogy of flow in an annulus with the inner cylinder rotating and flow in mixing tanks with helical ribbon type impellers. The authors tested their model with reported power consumption data of helical ribbon type of impellers in the literature, covering a very wide range of flow behavior index,  $n$ , and found good agreement with most of the data.

$$K_s = \frac{2}{N_r} \frac{1}{n} \frac{S^{2/n}}{S^2} \frac{S_e^2 - 1}{S_e^{2/n} - 1} \frac{K_p}{\pi^2 (h/D_i)} \left[ \frac{n}{2-n} \frac{S^{(2/n)-1} - 1}{S-1} \right]^{1/(n-1)} \quad (7.96)$$

$S$ , in this equation gives the ratio of tank diameter to helical ribbon diameter ( $D_T/D_i$ ) as shown in Figure 7.10(d).  $S_e$  is the same diameter ratio of the equivalent coaxial cylinders ( $D_T/D_e$ ) used to simulate the flow between the tank wall and the impeller, in the region of maximum shear:

$$S_e = \frac{D_T}{D_e} = \frac{D_T/D_i}{D_T/D_i - \frac{2w/D_i}{\ln\left(\frac{D_T/D_i - (1 - 2w/D_i)}{D_T/D_i - 1}\right)}} \quad (7.97)$$

A plot of  $K_s$  as given by eq. (7.96), as a function of the flow behavior index,  $n$ , gives an increasing curve up to  $n = 0.45$ , which then levels off in the interval,  $0.45 \leq n \leq 0.77$ , to remain constant at higher values of  $n$ . The authors proposed the trend in the variation of  $K_s$  with  $n$  to be a possible cause for the appearance of different defining functions for  $K_s$  according to the range of flow behavior indices used in the experimental work on which the model is built. Reported values of the rheological constants for the systems used in the literature show a wide range of  $n$  though, suggesting that this variation may not be the only cause.

The values of the dimensionless parameters for geometrical similarity of helical ribbon impellers are given by Ho and Kwong (1973) as  $N_r = 2$ ,  $p/D_i = 0.5 - 1$ ,  $w/D_i = 0.1$ ,  $c/D_i = 0.025$ . The range of dimensionless parameters in helical ribbon impeller type of mixers in the comprehensive review of Delaplace *et al.* (2000) based on 148 impellers can be taken as an indication of the range of values generally used, which are:  $0.725 \leq D_i/D_T \leq 0.988$ ,  $0.07 \leq w/D_i \leq 0.22$ ,  $0.32 \leq p/D_i \leq 2.16$ , and  $0.88 \leq h/D_i \leq 1.30$ .

#### 7.4.4 Scale-up in agitated mixers

Scale-up in mixing means creating the same conditions of mixing in an industrial mixer as observed in a laboratory-size mixer. Scaling down is based on the same principles and is required to solve a problem encountered in an industrial scale mixer by experiments conducted in a laboratory size mixer under the same hydrodynamic conditions.

#### 7.4.4.1 General criteria used in scale-up of mixers

In agitated vessels mixing proceeds through turbulence mechanisms. Similar conditions of turbulence can be maintained if recirculation currents and convective eddy size and energy distribution are the same in each case. Geometrical similarity, maintained by identical values of the shape factors in every case, ensures the similarity of flow patterns. It is more difficult to generate eddies with the same size and energy distribution. As a first approximation, similitude in mechanisms generating eddies are searched for. Once geometrical similarity is maintained, then different criteria presumed to be effective in determining the mixing conditions are tested for validity in scale-up. The criteria generally used are: (1) Identical quantity of power delivered to the mixer per unit volume of suspension in both mixers; (2) identical impeller tip speeds in both cases; (3) identical Froude numbers in both cases.

The first criterion is based on equating the Kolmogoroff length scales of isotropic turbulence given by eq. (7.38). For liquid suspending medium of the same density and viscosity, equating power inputs per unit volume is equivalent to equating the size of the minimum eddies. The second criterion in effect, sets the upper limit of the maximum shear rate and therefore both the laminar ( $\tau \propto dV/dr$ ) and the turbulent ( $\tau \propto \rho V'V'$ ) shear stresses. As turbulent conditions exist in the mixers if the viscosity is not too high, the impeller tip speed also sets the maximum fluctuation velocity of the eddies. The third criterion is based on the ratio of the kinetic energy dispersing the particles (or liquid eddies) to the potential energy segregating the particles, or equivalency of the Froude numbers ( $Fr' = D_i N^2/g \propto \rho V'V'/\rho g l_e$ ),  $l_e$  being the length scale of the eddies. The validity of these criteria has to be determined experimentally with the use of geometrically similar mixers of different sizes.

#### 7.4.4.2 Scale-up in mixing of floating solids

Scale-up studies were made by Özcan-Taşkın (2006) in two geometrically similar fully baffled tanks of diameter 0.61 and 2.68 m, stirred with PBT (with four 45° inclined blades) and a narrow 3-blade hydrofoil impeller, both with  $D_i/D_T = 0.33$ . Various liquid (water) heights of  $H/D_T = 1, 5/6, 2/3, 1/2$  were used in the experiments, with off-bottom clearance of impellers  $E, E/D_T = 1/8, 1/6, 1/4, 1/3, 1/2, 2/3$ . Polyethylene particles of density 904 kg m<sup>-3</sup> and dimensions 2 mm × 3 mm × 5 mm were used at a volumetric concentration of 1% in the smaller and 0.5% in the larger vessel at  $H/D_T = 1$ . Under these dilute conditions, the effect of solid concentration was found to be negligible and the amount of solids was not changed when the height of liquid,  $H$  was varied.

The results showed that as the distance of the axial impeller from the surface of the liquid (submergence,  $C_s$ ) increases, the rate of rotation  $N_{JD}$ , and the specific power requirement for suspension per unit volume of liquid ( $\mathcal{P}_{JD}/v$ ) increases, as given in Figure 7.16(a) and (b), for the two different size of mixers denoted as T61 and T268 stirred by the hydrofoil impellers. The variation in the impeller tip speed,  $N_{JD}D$  and Froude number (not divided by the constant  $g$ ) as a function of dimensionless submergence,  $C_s/D_T$  (denoted as  $C_s/T$  in the figures) of the impeller in up-pumping direction are also given in Figure 7.16(c) and (d). The data for the 0.61 and 2.68 m diameter mixers coincide only in the case of power per unit volume  $\mathcal{P}_{JD}/v$  data plotted as a function of dimensionless submergence



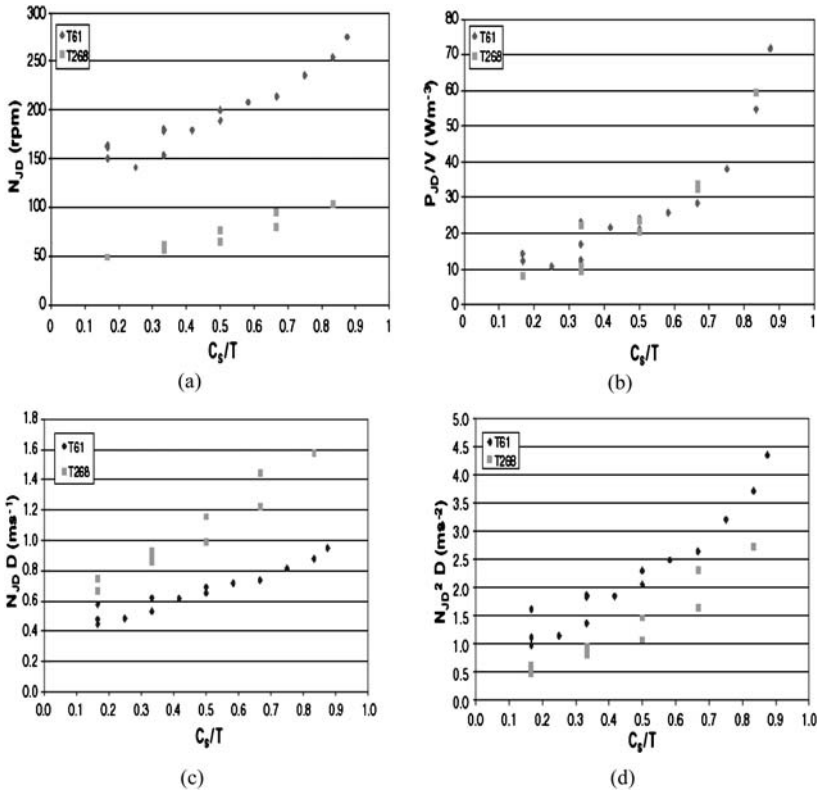


**Figure 7.16** Variation of: (a) just-draw-in speed of the impeller, (b) power required to draw in the solids per unit volume of suspension, (c) tip speed of the impeller, (d) Froude number as a function of submergence ratio ( $C_s/T \equiv C_s/D_T$ ) for hydrofoil impellers oriented in the up-pumping direction. (Özcan-Taşkın, 2006. Reproduced with permission of Elsevier, Figures 4(a), 10, 11, and 4(b) in the original.)

$C_s/D_T$ , showing the suitability of this criterion for scale-up. A scale-up criterion appropriate for the same impellers connected in the down-pumping direction could not be found in the investigation and was attributed to different ways the solids were drawn down depending on the level of submergence of the impellers.

#### 7.4.4.3 Scale-up of mixers with multiple impellers

As the power consumption of an impeller is proportional to the fifth power of its diameter ( $\mathcal{P}_o \propto \rho N^3 D_i^5$ ), increase in the volume of suspension to be mixed in a batch mixer or an increase in the required retention time in a reactor is handled by increasing the height of the mixing vessel. Using the same criteria for geometrical similarity,  $S_2 = 1$  or  $H = D_T$ , an additional impeller connected to the same shaft is used for every incremental increase in height equivalent to one tank diameter. Axial impellers are used in these mixers to maintain the average concentration of solids constant in every level.

In a multiple-impeller mixer, concentration distribution of solids in the axial direction is given by eq. (7.41). If mixing is ideal throughout the vessel, then the concentration of particles would be equal to the average concentration along the height of the suspension. Due to unavoidable settling, the concentration of solid particles increases at the lower stages. Magelli and coworkers (Montante *et al.*, 2003; Pinelli *et al.*, 2004 and the references cited therein) propose the use of eq. (7.41) in determining the mixing efficiency and therefore, as a criterion for comparing the performance of impellers in geometrically similar mixers. The revised Péclet number in eq. (7.42) was expressed empirically by effective dimensionless numbers as,

$$Pe_s = \frac{V_s H}{D_{pM}} = A \left( \frac{ND}{V_t} \right)^\alpha \left( \frac{\mu^3}{\rho^3 \varepsilon d_p^4} \right)^\beta \left( \frac{H}{D_T} \right)^2 \quad (7.98)$$

where  $\varepsilon$  is average power input into a unit mass of the agitated liquid, defined as ( $\varepsilon = (\text{number of impeller}) \times (\text{power of single impeller/mass})$ ). The constants  $A$ ,  $\alpha$ , and  $\beta$  have to be determined experimentally. The first dimensionless number is the ratio of the impeller tip speed to the terminal velocity of the particles; the second dimensionless number is the Kolmogoroff length scale for energy dissipating eddies (eq. (7.38)) scaled to the particle diameter  $d_p$ ; and the third is the shape factor  $S_2$ . The authors found  $\alpha = 1.404$  and  $\beta = 0.161$  for pitched blade turbines and  $\alpha = 1.195$  and  $\beta = 0.101$  for Rushton turbines, respectively. The dispersion coefficient of the solids  $D_{pM}$  was found to be the same as the axial dispersion coefficient of the liquid that depends on the mixer geometry and scale and has to be determined experimentally. The settling velocity of the solids  $V_s$  in the mixer is related to their terminal velocity  $V_t$  under free settling conditions through the empirical relationship (Pinelli and Magelli, 2001),

$$\frac{V_s}{V_t} = 0.4 \tanh \left( \frac{16l_K}{d_p} - 1 \right) + 0.6 \text{ for } \left( \frac{l_K}{d_p} \right) \leq 0.2 \quad (7.99)$$

This equation was found to hold for Rushton turbines as well as pitched blade and hydrofoil turbines and in Newtonian and pseudoplastic (shear-thinning) liquids. Eq. (7.71) is plotted in Figure 7.17, as  $V_s/V_t$  versus the dimensionless Kolmogoroff isotropic length scale  $l_K$ , non-dimensionalised with the particle diameter  $d_p$ , shown as the solid S-shaped curve in the figure. The data points shown correspond to experiments conducted in mixing vessels of 0.13, 0.23, and 0.48 m diameter, with Rushton and pitched blade impellers. The particles were glass or plastic within the size range,  $0.3 \leq d_p \leq 3$  mm, and density greater than that of the suspending medium with viscosity in the range of  $3 \leq \eta \leq 30$  mPas. The stirring rate of the impellers ranged in the interval  $12.4 \leq N \leq 25 \text{ s}^{-1}$ .

The experimental data was found to lie in the range  $\pm 30\%$  of the S-shaped curve based on eq. (7.71). The trend of the variation of the dimensionless velocity of large particles, in the range  $l_K/d_p \leq 0.01$  seem to be independent of the Kolmogoroff length scale, suggesting that the pattern of recirculation currents dominate the convective turbulent eddy interactions in the mechanism of mixing. When the particle size is approximately equal to the isotropic length scale  $l_K$  of the suspending medium, the particle velocity again becomes constant at the terminal velocity of the particles. In between these length scales, particle velocity is strongly affected by the intensity of turbulence.

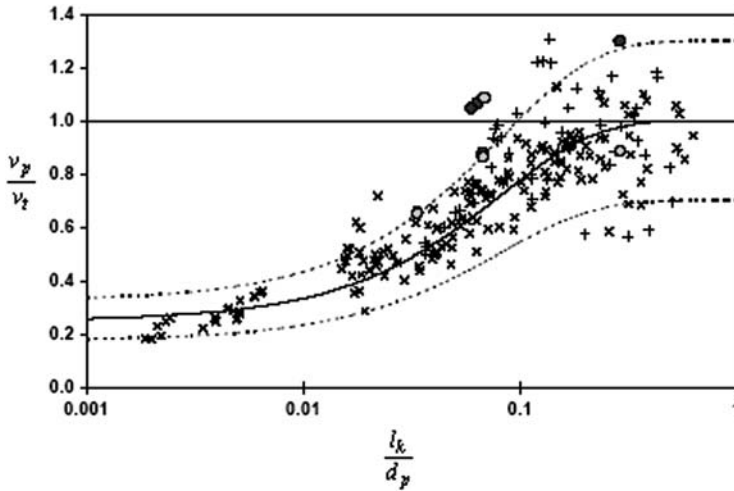


**Figure 7.17** Variation of dimensionless particle velocity in the mixer with the dimensionless Kolmogoroff length scale. (Montante *et al.*, 2003. Reproduced with permission of Elsevier, Figure 6 in the original.)

## 7.5 STATIC MIXERS

If the components readily blend with each other, mere change in direction and elongation during flow will be sufficient for mixing, as in the case of static mixers. Static mixers are used in blending highly viscous fluids such as polymers and colloidal fluid-like pastes. Static mixers are also used where strict hygienic rules should be applied and the suspension be prevented from possible pollution. They are efficient mixers in terms of power requirement, space utilization, therefore requiring lower capital and operating costs. Static mixers operate by laminating and remixing the fluid layers as described in Section 7.3.2. Internal structure of a typical static mixer is sketched in Figure 7.18, in cross-sectional and longitudinal view. Basically, it consists of sets of cross bars making an angle of  $45^\circ$  with the axis of the pipe. The orientation of each consecutive set makes an angle of  $90^\circ$  with the previous one. Thus, the fluid is forced to change direction in passing through the grids. This effect can further be enhanced by changing the shape of the cross bars so the frequency of the change in direction is increased, and elongational flow is introduced along with the shear flow. Sections of screws, oriented with respect to each other can also be used instead of the cross bars (Gramann *et al.*, 2007). Length of standard static mixers equals the diameter of the mixer. Longer static mixers are also employed with lengths approaching twice the diameter of the pipes.

As the fluids mixed in static mixers are extremely viscous, the flow regime is generally laminar. Pressure drop in static mixers can be calculated with two different models of the mixer, as pipe flow and flow through a porous medium. If the packing is not very compact, then it can be taken as pipe flow with enhanced frictional losses. The static mixer can also be viewed as a packed bed, if the cross bars intermesh with each other. Depending on the

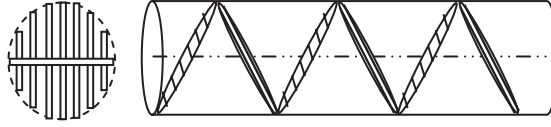


**Figure 7.18** Cross-sectional and longitudinal view of a typical static mixer.

model chosen, the definition of the Reynolds number will also change. Even though the exact value of the transition Reynolds number is an unsettled issue (Hirech *et al.*, 2003), there is general agreement on an early transition to turbulence, in comparison to empty tubes.

When the static mixer is considered as pipe flow with enhanced shear losses (Liu *et al.*, 2006) then the pressure losses  $\Delta P_{SM}$  are scaled with the pressure losses in an empty pipe  $\Delta P_0$  under the same flow conditions:

$$k = \frac{\Delta P_{SM}}{\Delta P_0} = \frac{f_{D_{SM}} Re}{f_{D_0} Re} \quad (7.100)$$

$f_D$  in this equation signifies the Darcy friction factor equivalent to four times the Fanning friction factor,  $4f$ .

The effect of non-Newtonian behavior in static mixers depends on the type of nonlinearity. Viscoelasticity increases the friction factor and decreases the mixing quality (Langer and Werner, 1996). On the other hand, shear thinning decreases the pressure drop and increases the mixing quality in a static mixer. A computational study was made by Liu *et al.* (2006) of the pressure losses of shear thinning power-law fluids as a function of the flow behavior index,  $n$  in the range of viscosities,  $0.001 \leq \eta_{eff} \leq K$  Pas, where the maximum corresponds to  $\dot{\gamma} = 1 \text{ s}^{-1}$ . By a procedure similar to that given in Section 2.3.1.3, the pressure drop in the empty tube,

$$\Delta P_0 = 4K \left( \frac{3n+1}{4n} \right)^n \left( \frac{8V}{D} \right)^n \frac{L}{D} = 4K \left( \frac{3n+1}{4n} \right)^n \left( \frac{32Q}{\pi D^3} \right)^n \frac{L}{D} \quad (7.101)$$

was calculated with the use of Metzner–Reed Reynolds number given by eq. (2.135). Results of the computations showed that shear thinning reduces the pressure drop ratio,  $k$  in eq. (7.100) in comparison with Newtonian fluids, which can be correlated with flow behavior index,  $n$  and  $Re_{MR}$  as,

$$k = 39.5 \times 6^{n-1} \left( \frac{4n}{3n+1} \right)^n \times \exp[(0.01094 - 0.00835n)Re_{MR}] \quad (7.102)$$

A plot of pressure drop ratio  $k$ , as a function of Metzner–Reed Reynolds number shows that  $k$  increases with an increase of  $n$  in the range  $0.2 \leq n \leq 1$ , but for any given value of

$n$  remains constant for  $Re_{MR} \leq 10(4n/(3n + 1))$ . With the use of eqs. (7.100)–(7.102), the friction factor for a static mixer was found as a function of  $n$  and  $Re_{MR}$ , decreasing with a decrease in  $n$  and  $Re_{MR}$ , according to the relation,

$$f_{D_{SM}} = kf_{D_0} = \frac{2528}{Re_{MR}} \times 6^{n-1} \left( \frac{4n}{3n+1} \right)^n \times \exp[(0.01094 - 0.00835n)Re_{MR}] \quad (7.103)$$

Particle tracking studies and lower frictional losses support the observation that the mixing efficiency of shear thinning fluids in a static mixer is higher than that of Newtonian fluids.

## 7.6 MIXING OF CONCENTRATED SUSPENSIONS

In many industrial processes the solid–liquid mixtures are too concentrated to be handled with the mixers presented above. In fact, the term *kneading* is used instead of mixing in these operations. After the kneading operation, the concentrated suspensions, called *pastes*, are either subjected to molding as in the case of casting metals, or *extrusion*, as in the case of ceramics, polymers, and foods such as pasta. In this section, these special equipments used in mixing and shaping pastes will be introduced.

### 7.6.1 Kneading

Kneading equipments are similar to agitated mixers. The difference lies in the composition and rheological properties of the pastes to be mixed. Generally, the ratio of the volume of the suspending medium to the total volume concentration is only a small fraction and the number concentration of particles is very high in these pastes. This makes the distribution and spreading of the liquid over the particle surfaces, the main concern in the kneading operation. Considerable power consumption is required to overcome frequent jamming of the contacting particles and for thorough turn over of the particles. In kneading process, power consumption is the major parameter in the determination of the operating torque range and the degree of mixing. The major issue then becomes the definition of a rheological model including a specific equipment factor.

The relation between the power number,  $Po$  and the Reynolds number,  $Re$  for kneaders in the case of Newtonian fluids can be expressed by eq. (7.70), using the Power and Reynolds number definitions in eqs. (7.67) and (7.69), respectively. However, in the case of non-Newtonian fluids the power consumption cannot be directly calculated due to the difficulty of accurate determination of the rheological parameters  $\eta$  and  $\tau_0$  at high concentrations. Kamiwano and coworkers (2000; Nishi *et al.*, 2006) modified the Reynolds number given by eq. (7.71) with an apparent viscosity definition for non-Newtonian fluids.

$$Re' = \frac{\rho ND_1^2}{\eta_a} \quad (7.104)$$

The authors described the rheological behavior of the system they studied by Casson Model (eq. (2.50)). The apparent viscosity  $\eta_a$  of Casson model is obtained by dividing both sides of eq. (2.50) by shear rate  $\dot{\gamma}$ :

$$\eta_a^{1/2} = \left( \frac{\tau_0}{\dot{\gamma}} \right)^{1/2} + \eta^{1/2} \quad (7.105)$$

The relation between the average shear rate  $\dot{\gamma}_{av}$  and rotational speed  $N$  is given as,

$$\dot{\gamma}_{av} = BN \quad (7.106)$$

The term  $B$  in eq. (7.106) is a specific equipment constant. Substituting eq. (7.106) into eq. (7.105) and apparent viscosity  $\eta_a$  into the eq. (7.104) gives

$$Re' = \frac{\rho ND_i^2}{\eta(1 + \sqrt{\tau_0/\eta BN})^2} \quad (7.107)$$

The relation between the Power number and modified Reynolds number can be given with a relation similar to eq. (7.70):

$$Po Re' = K_p \quad (7.108)$$

Thus, substituting eqs. (7.67), (7.73) and (7.107) into eq. (7.108) gives a relation for determination of the rheological parameters  $\tau_0$  and  $\eta$  without the need for rheological measurements,

$$\sqrt{\frac{2\pi M}{D_i^3 K_p}} = \sqrt{\frac{\tau_0}{B}} + \sqrt{\eta N} \quad (7.109)$$

In this case, the relation between the torque,  $M$  and rotational speed,  $N$  in a kneader can be measured and,  $\eta$  and  $\tau_0/B$  can be calculated by eq. (7.109).

Nagata (1968) proposed an expression for power requirement in kneaders,

$$\mathcal{P}_0 = \psi(1 + \alpha)(2\pi R_i N)^2 \frac{R_i L \eta_a}{75C} \quad (7.110)$$

where  $N$  is the rotational speed of the blade,  $\eta$  the apparent viscosity of the wet particles,  $\alpha$  the ratio of the power consumed in the region excluding clearance between the blade and

the vessel wall of the kneader.  $\psi$ ,  $R$ ,  $L$ ,  $C$  are the geometric factors of the kneader:  $L$ , the length of the vessel;  $R$ , effective radius of the rotating impeller;  $C$ , the clearance between blade and vessel wall; and  $\psi$  is the angle retained clearance. According to eq. (7.110), power consumption is proportional to  $(1 + \alpha)$  and apparent viscosity  $\eta_a$ .  $(1 + \alpha)$  gives the ratio of the total power consumption to the power consumption in the clearance. The clearance region is included into equation as the region where the velocity gradient is highest and the effect of the non-Newtonian behavior is observed the most. Apparent viscosity changes with average shear rate in the kneader mixer, and average shear rate changes with the kind of blade and rotational speed. Therefore it is difficult to determine the appropriate average shear rates in the kneader mixer (Kamiwano *et al.*, 2000) without experimental verification with a system of known and reproducible properties.

### 7.6.2 Extrusion

Extrusion as a manufacturing process is used for creating long materials (continuous extrusion) or a large number of short pieces (semi-continuous extrusion) with a fixed cross-sectional profile. The widely used extruder types for concentrated suspensions and pastes are the screw extruders (single screw or twin screw) and the ram extruders. The typical twin-screw extruder shown in Figure 7.19 consists of two screws with mixing paddles. These screws convey the loaded materials through the barrel toward a die, where final extrusion takes place.

The screws used in twin modes may be corotating or counter rotating with variable intermesh of the screws, clearance and pitch. Screw is the major part of an extruder which conveys the material from feed end to the die end. Rotation in a tightly fitting barrel results in mixing and compression of the components. The screw outer and root diameters as well as pitch and flight width are the key parameters in determining the capacity of the extruder. The barrel in which the screws rotate, must be mechanically strong to withstand the high operating pressures. The physical properties such as density, surface texture, and shape of the product are determined by the die. The ratio of length to cross-sectional area of the die hole determines the final shape of the product. (Senanayake and Clarke, 1999).

In ram extrusion, the material is fed from a hopper and packed into a cylinder in repeated increments by a piston. The compressed material moves through the cylinder with a profile matching the cross section of the barrel and the die in sequence. The output rate

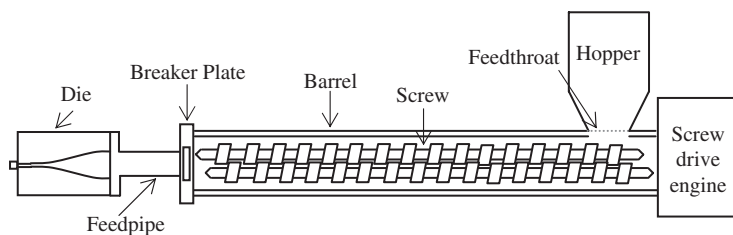


**Figure 7.19** Schematic representation of a twin screw extruder.

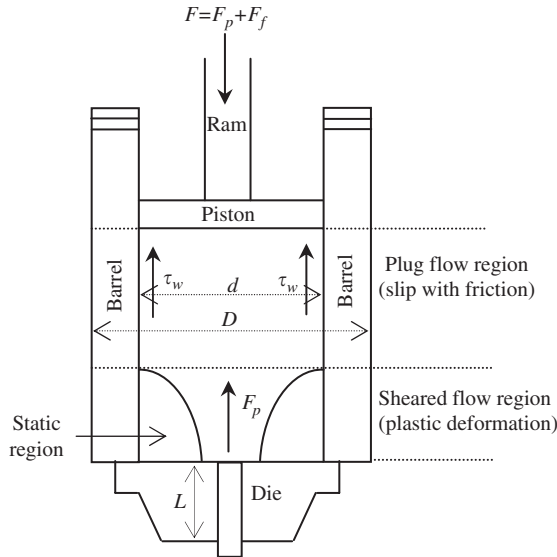


**Figure 7.20** Schematic representation of a ram extruder and the forces acting on the paste.

is proportional to the length and frequency of the ram. The force applied onto the piston must overcome the friction against the die wall and viscous drag forces during compression. In the final stage when ram contacts with the material in the die, an extremely high force is required to overcome the static friction. Incremental motion of the compacted paste leads to slip at the walls and plug flow. The die must be designed to withstand the high internal stresses generated. A typical ram extruder is shown in Figure 7.20.

The extrusion flow can be examined under three sections. (1) Plug flow region in the central part where the paste slips over a highly sheared layer along the extruder wall, (2) the deformation region near the die where the material is shaped, and (3) the static (dead) zone where the material is stationary around the die entry (Perrot *et al.*, 2006).

The force applied on the ram must be equivalent to the sum of the frictional force  $F_f$  and the force related with plastic deformation,  $F_p$  as,

$$F = F_f + F_p \quad (7.111)$$

Friction force can be expressed as,

$$F_f = \int_{\text{pipezone}} \tau_w dA \quad (7.112)$$

where  $\tau_w$  is the wall shear stress over the barrel surface wall and  $A$  is the cross-sectional area. The force related with plastic deformation (shaping force) varies with the flow of material and is proportional to the yield stress  $\tau_0$ , and the consistency  $K$ , of the material.



Extrusion can be considered as a constant pressure process all along the ram displacement. The extrusion pressure is given by Benbow's model which defines the pressure gradient in two parts: pressure due to the plastic deformation of the paste from the barrel to the die and the other one being the paste flow in the die portion of the extruder. Benbow's model can be expressed as (Lombois-Burger *et al.*, 2006),

$$P = (\tau_0 + aV_e) \ln \frac{A_b}{A_d} + (\tau_w + bV_e) \frac{LC}{A_d} \quad (7.113)$$

where  $A_d$  the cross-section area of the die,  $A_b$  the cross-section area of the barrel,  $C$  the perimeter of the die,  $V_e$  the exit velocity of the extrudate which is calculated under plug flow conditions,  $L$  the length of the die and  $a, b$  the constants related with viscosity per unit length giving the velocity dependence of the flow behavior. The  $aV_e$  and  $bV_e$  terms in eq. (7.113) are related with the viscous contributions of the fluid velocity. The  $\tau_w$  term is smaller than the true yield stress value at the wall because of slippage over the wall.

Yilmazer and Kalyon (1989) investigated slip effects induced by plug flow of highly filled suspensions. The authors expressed the total volumetric flow rate of suspension including slip effects as:

$$Q_s = \frac{\pi}{4} D^2 V_{\text{slip}} \quad (7.114)$$

which is also calculated by solving eq. (2.115). The slip velocity  $V_{\text{slip}}$  in eq. (7.114) is defined as;

$$V_{\text{slip}} = \beta \tau_w \quad (7.115)$$

where  $\beta$  is the wall slip coefficient (Lawal and Kalyon, 1997). The ratio of the volumetric flow rate due to slip  $Q_s$  to the total volumetric flow rate,  $Q$  then becomes;

$$\frac{Q_s}{Q} = \frac{V_{\text{slip}}}{V} = \frac{8V_{\text{slip}}}{D\dot{\gamma}_a} \quad (7.116)$$

where  $\dot{\gamma}_a$  denotes the apparent shear rate.

Another issue encountered in extrusion is the physical aging that necessitates an increase in the extrusion pressure of the paste with resting time (Lombois-Burger *et al.*, 2006),

$$P_{\text{ex}} = C_1 \ln(1 + \Delta t) + C_2 \quad (7.117)$$

where  $\Delta t$  is the resting (aging) time,  $C_1$  a constant dependent on the viscosity of the fluid, and  $C_2$  a constant related with the initial extrusion pressure. The authors investigated the kneading and extrusion behavior of dense-polymer cement pastes taking the Benbow's model given in eq. (7.113) as a guide. They proposed a free volume model for the paste

flow (see Section 1.2 in Chapter 3). The viscosity of the system is given with Doolittle equation in this model,

$$\eta = A \exp \left( B \frac{v_o}{v_f} \right) \quad (7.118)$$

where  $v_o$  is the occupied,  $v_f$  is the free volume,  $A$  a reference pressure, and  $B$  an experimental fitting parameter ( $B = 11$  in their study). The viscosity of soft glassy systems depends on the unoccupied free volume  $v_f$ , which the authors related to the closed-packed volumetric fraction ( $\phi = \phi_m$ ) of the paste with,

$$\frac{v_f}{v_o} = \left( \frac{1}{\phi} - \frac{1}{\phi_m} \right) \quad (7.119)$$

In this equation  $\phi$  is the actual volumetric fraction of the solids. By taking the aging time as a constant value such as 20 min they replaced the  $\eta$  term with  $P_{\text{ex}}^{20 \text{ min}}$  and found a relation which satisfies their experimental data in the form of eq. (7.121):

$$P_{\text{ex}}^{20 \text{ min}} = A \exp \left( -B \frac{v_o}{v_f} \right) \quad (7.120)$$

$$P_{\text{ex}}^{20 \text{ min}} = A \exp \left[ -B \left( \frac{1}{\phi} - \frac{1}{\phi_m} \right) \right] \quad (7.121)$$

By evaluating eqs. (7.120) and (7.121) they concluded that the free volume of particles is a distinctive control parameter of the extrusion pressure.

## 7.7 MIXING IN THE MICROSCALE

Microscale mixing involves quantities in the range of pico- to microliter in devices of dimensions in the order of micrometers and lengths not exceeding a few hundred micrometers. Micromixing concept evolved in the last decade as part of micro total analysis systems related with the “lab-on-a-chip” project, involving various miniaturized analytical operations. Various unit processes and operations developed within the context of micro-sized analysis systems include reactors, separation systems such as chromatographs, electrophoresis devices, pumps, valves, mixers, along with the microchannels connecting these devices. When the reaction rates are fast, the rates in the other devices have to be in the same order of magnitude if the designed system is intended to work continuously. Analysis of biomolecules requires high mixing rates at very low throughputs. On the other hand, the materials to be analyzed include bulky molecules with diffusion rates less than the diffusion rates of ordinary molecules by at least an order of magnitude. The small dimensions

of the channels and mixing devices cause the magnitude of the Reynolds number to remain below 100, placing the operation into the range of laminar regime. Turbulent convective motions employed for mixing do not exist in the laminar regime. Alternative mechanisms are developed to bring the components or phases into close contact and extend the interfacial area across which mixing of the components takes place through diffusion. Extension of the interfacial area can be brought about by frequent changing of the flow direction, or by dividing and remixing streams within a designed network. This type of mixing that depends solely on the geometry of the channel, and requires only energy to maintain flow is called *passive mixing*. In the case of *active mixing*, an external control of the flow field is exerted by means of varying pressure gradients, oscillating electro-osmotic flow, or actual moving parts that regulate the flow.

### 7.7.1 Passive mixing

Passive mixers are preferred over the active mixers due to simplicity in their manufacturing processes, ease of operation without excessive frictional heat evolution, and adequacy for use with shear sensitive biomolecules and microorganisms. Passive mixers can be “in-plane” or “out-of-plane” with respect to the flow direction.

In-plane mixers divide and recombine fluid streams within a flow network to assist mixing without significant stretching of the interface. Example for the development of in-plane mixer designs (He *et al.*, 2001) are given in Figures 7.21(a) and (b). The design in Figure 7.21(a) is an idealization of mixing in a packed bed. The fluids A and B mix as they flow down in the longitudinal direction. The dark triangular crosshatched channels in the lower central region show the actual mixing area. As this area constitutes less than half of the total flow area, this type of design is not particularly suitable for compact miniaturized systems. The authors (He *et al.*, 2001) developed the more efficient design

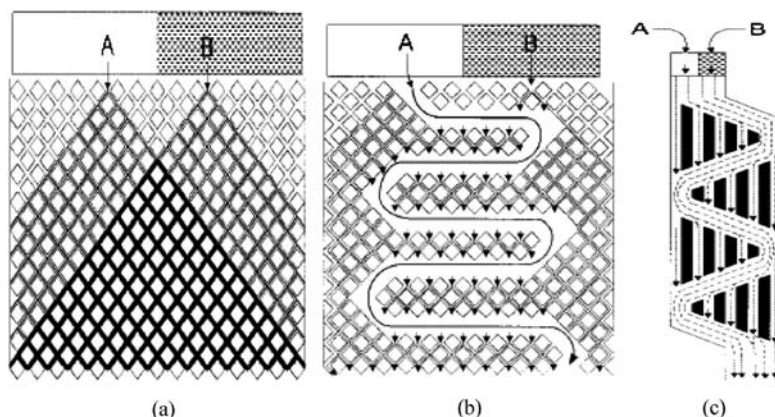


**Figure 7.21** Development of microfabricated mixer designs based on flow and mixing within a packed column: (a) Two dimensional idealization of the packed column; (b) More effective usage of the area through channeling; (c) Microfabricated compact form of the mixer. (He *et al.*, 2001. Redrawn with permission of the American Chemical Society, Figure 5 in the original.)

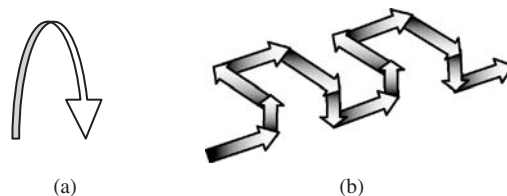
given in Figure 7.21(b), by removing some of the particles from the design given in the (a) part to improve the lateral mixing. The final consolidated channel flow mixer, properly designed for microfabrication is given in the (c) part of the figure. As there is no stretching involved in the flow, the efficiency of mixing would be low, if flow had occurred under a pressure gradient. Therefore, liquids are moved through the mixer exclusively by electro-osmotic flow using a computer-controlled power supply.

Generalization of this design concept leads to a need for identification and augmentation of the mixing mechanisms in the absence of convective diffusion: that of creating additional area in between the two phases or streams to be mixed and diffusion through this interfacial area. *Chaotic advection* developed by Aref (1984, 1990, 2002) is one method of increasing the interfacial area to increase the efficiency in mixing of the component streams. Essentially it is a mechanism by which certain filaments or layers of the fluid are stretched and then fold over resulting in a chaotic convection of the components, as given in Figure 7.22(a). Secondary flows leading to chaotic advection arise when flow fields exist in three dimensions in steady and unsteady flows. If the flow is two dimensional only, time dependence enters in place of the third component of the field, and advection is observed in unsteady flows, only.

One way to create a three dimensional velocity field is to twist the pipes. Twisted pipe flow design is used in the laminar flow of viscous pastes to enhance mixing, or to enhance heat and mass transfer, in macro-scale operations. To introduce advection in microchannels Liu *et al.* (2000) developed a serpentine channel, where flow proceeds in three dimensions through C-shaped connections oriented at an angle of 90 with respect to each other, as shown schematically in Figure 7.22(b). Rectangular channels obtained by KOH etching, were 300  $\mu\text{m}$  wide and 150  $\mu\text{m}$  deep, and so the Reynolds numbers based on the channel dimensions are in the range of  $6 \leq \text{Re} \leq 70$ . The arrows in Figure 7.22 show the flow direction of the fluids, with the lighter shaded regions around the corners denoting the stretched fluids. Stretching is converted into chaotic motions in these regions. Mixing rate was shown to increase with an increase in the Reynolds number, achieving 97% of the maximum intensity (denoting complete, homogeneous mixing) within fractions of a second at a Reynolds number of 25 with this design.

### 7.7.2 Active mixing

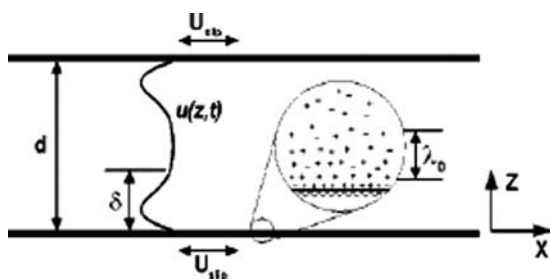
Advection in the fluids to be mixed can also be created by an external applied field. An active mixer working under an oscillating electric field was developed by Oddy *et al.* (2001). In a rectangular channel with dielectric walls, an electrolyte solution will form a diffuse ion cloud along the walls, an electrical double layer, similar to those shown in



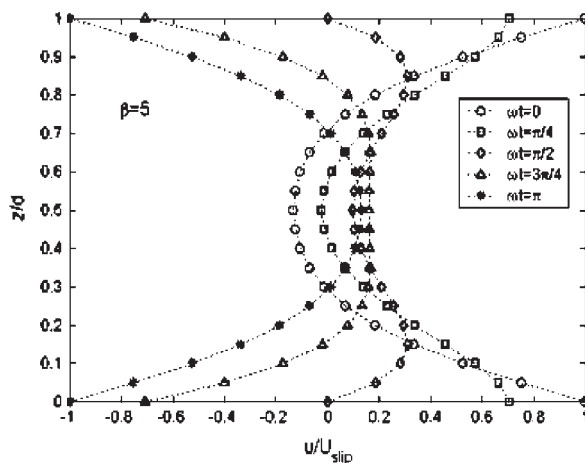
**Figure 7.22** Mixing by advection: (a) Stretching and folding over of a liquid filament, (b) Serpentine mixer operating with the principle of advection.

Figure 1.2. An external electric field will cause a shift in the diffuse layer ions, in the direction of the applied force. This shift, will effectively take place within a distance equivalent to the Debye length  $\kappa^{-1}$  (denoted as  $\lambda_0$  in the inlay of Figure 7.23) that is much smaller than the dimensions of the channel. As such, it will appear as a slip boundary to the electrically neutral liquid suspension in oscillatory motion under the action of the alternating electric field. The velocity profiles during a period of oscillation are shown in Figure 7.24. These profiles were obtained by solving the Navier–Stokes Equation, eq. (A3.5.1), for flow in the  $x$  direction between two plates extending to infinity in the  $y$  direction with the slip boundary condition,

$$V_{\text{slip}}(z = 0, d) = \frac{\varepsilon \zeta |E|}{\mu} \exp(i\omega t) \quad (7.122)$$



**Figure 7.23** The Debye layer and various dimensions effective in electroosmotic flow. (Oddy *et al.*, 2001. Redrawn with permission of The American Chemical Society, Figure 1 in the original.)



**Figure 7.24** Theoretically predicted velocity profiles during an oscillation period in flow between two infinite planes (Oddy *et al.*, 2001. Reproduced with permission of the American Chemical Society, Figure 2 in the original.)

where,  $\varepsilon$  is the permittivity of the liquid medium,  $\zeta$  the zeta potential along the wall with charge  $E$ ,  $\mu$  the viscosity of the liquid suspension medium, and  $\omega$  the period of the oscillations. The solution of eq. (A3.5.1) that is reduced to

$$\rho \frac{\partial V}{\partial t} = \mu \frac{\partial^2 V}{\partial z^2} \quad (7.123)$$

under the given conditions, will have both steady and time dependent components. Scaling  $z$ , with the diameter of the channel  $d$ , time  $t$  with the frequency of the oscillating field  $\omega$ , and velocity with the slip velocity in eq. (7.122) a dimensionless equation was obtained for the time dependent velocity distribution, in the form:

$$\hat{V}(\hat{z}, \hat{t}) = \text{Re} \left\{ \frac{\sinh[\beta(1+i)(1-\hat{z})] + \sinh[\beta(1+i)\hat{z}]}{\sinh[\beta(1+i)]} \exp(i\hat{t}) \right\} \quad (7.124)$$

$\beta$  in the equation is the aspect ratio of the channel,  $d/\delta$ , where the Stokes penetration depth  $\delta$  is the ratio of the kinematic viscosity of the liquid resisting the motion, to the frequency of the oscillation inducing the motion:

$$\delta = \left( \frac{2\nu}{\omega} \right)^{1/2} = \left( \frac{2\mu}{\rho\omega} \right)^{1/2} \quad (7.125)$$

The oscillatory flow provides limited stretching of the liquid layers. The authors observed the occurrence of a flow instability that was much more effective in mixing, at frequencies below 100Hz, electric field strengths greater than  $100 \text{ V mm}^{-1}$ , and channel dimensions greater than  $50 \mu\text{m}$ . The advective motion observed under these conditions were much more effective in mixing in comparison with the stretching due to stable oscillatory flow, but the origins of the instability is yet an unresolved issue.

## REFERENCES

- Aref, H., 1984. Stirring by chaotic advection. *Journal of Fluid Mechanics*, 143, 1–21.  
 Aref, H., 1990. Chaotic advection of fluid particles. *Philosophical Transactions: Physical Sciences and Engineering*, 333, 273–288.  
 Aref, H., 2002. The development of chaotic advection. *Physics of Fluids*, 14, 1315–1325.  
 Beckner, J.L., Smith, J.M., 1966. Anchor agitated systems: Power input with Newtonian and pseudo-plastic fluids. *Transactions of the Institute of Chemical Engineering*, 44, 224.  
 Błasiński, H., Rzyski, E., 1980. Power requirements of helical ribbon mixers. *Chemical Engineering Journal*, 19, 157–160.  
 Bouillard, J.X., Lyczkowski, R.W., Gidaspow, D., 1989. Porosity distributions in a fluidized bed with an immersed obstacle. *American Institute of Chemical Engineering Journal*, 35, 24–31.

- Delaplace, G., Guerin, R., Lueliet, J., Chhabra, R.P., 2006. An analytical model for the prediction of power consumption for shear-thinning fluids with helical ribbon and helical screw ribbon impellers. *Chemical Engineering Science*, 61, 3250–3259.
- Delaplace, G., Lueliet, J., Relandeau, V., 2000. Circulation and mixing times for helical ribbon impellers. Review and experiments. *Experiments in Fluids*, 28, 170–182.
- Faderani, S., Tüzün, U., Thorpe, R.B., 1998a. Discharge and transport of nearly buoyant granular solids in liquids—Part I. *Chemical Engineering Science*, 53(3), 553–574.
- Faderani, S., Tüzün, U., Thorpe, R.B., 1998b. Discharge and transport of nearly buoyant granular solids in liquids—Part II. *Chemical Engineering Science*, 53(3), 575–598.
- Gramann, P., Davis, B., Osswald, T., Rauwendaal, C., 2007. A new dispersive and distributive static mixer for the compounding of highly viscous materials. *Madison Group News*, ([www.madisongroup.com/news/news.html](http://www.madisongroup.com/news/news.html); 26 February 2007).
- Grimsey, I.M., Feeley, J.C., York, P., 2002. Analysis of the surface energy of pharmaceutical powders by inverse gas chromatography. *Journal of Pharmaceutical Sciences*, 91, 571–583.
- He, B., Burke, B.J., Zhang, X., Zhang, R., Regnier, F.E., 2001. A picoliter-volume mixer for microfluidic analytical systems. *Analytical Chemistry*, 73, 1942–1947.
- Heng, Y.Y., Bismarck, A., Williams, D.R., 2006. Anisotropic surface chemistry of crystalline pharmaceutical solids. *AAPS PharmSciTech*, 7(4) Article 84 (<http://www.aapspharmscitech.org>).
- Hirech, K., Arhaliass, A., Legrand, J., 2003. Experimental investigation of flow regimes in an SMX Sulzer Static Mixer. *Industrial and Engineering Chemistry Research*, 42, 1478–1484.
- Ho, F., Kwong, A., 1973. A guide to designing. *Chemical Engineering*, 80, 95–104.
- Kamiwano, M., Kaminoyama, M., Nishi, K., Suzuki, Y., 2000. Power consumption diagram for wet particle kneader mixers—in the case that rheological properties for wet particles cannot be measured. *Journal of Chemical Engineering of Japan*, 39, 1041–1049.
- Käppel, M., 1979. Development and application of a method for measuring the mixture quality of miscible liquids. III. Application of the new method for highly viscous Newtonian liquids *International Chemical Engineering*, 19, 571–590.
- Kuzmanić, N., Ljubičić, B., 2001. Suspension of floating solids with up-pumping pitched blade impellers; mixing time and power characteristics. *Chemical Engineering Journal*, 84, 325–333.
- Kuzmanić, N., Žanetić, R., 1999. Influence of floating suspended solids on the homogenization of the liquid phase in a mixing vessel. *Chemical Engineering and Technology*, 22, 943–950.
- Langer, G., Werner, U., 1996. Viskoelastische effekte beim “laminaren” statischen mischen. *Chemie-Ingenieur-Technik*, 68, 283–287.
- Lawal, A., Kalyon, D.M., 1997. Nonisothermal extrusion flow of viscoplastic fluids with wall slip. *International Journal of Heat and Mass Transfer*, 40, 3883–3897.
- Liu, R.H., Stremmer, M.A., Sharp, K.V., Olsen, M.G., Santiago, J.G., Adrian, R.J., Aref, H., Beebe, D.J., 2000. Passive mixing in a three-dimensional serpentine microchannel. *Journal of Microelectromechanical Systems*, 9, 190–197.
- Liu, S., Hrymak, A.N., Wood, P.E., 2006. Laminar mixing of shear thinning fluids in a SMX static mixer. *Chemical Engineering and Science*, 61, 1753–1759.
- Lombois-Burger, H., Colombet, P., Halary, J.L., VanDamme, H., 2006. Kneading and extrusion of dense polymer-cement pastes. *Cement and Concrete Research*, 36, 2086–2097.
- Mersmann, A., Werner, F., Maurer, S., Bartosch, K., 1998. Theoretical prediction of the minimum speed in mechanically agitated suspensions. *Chemical Engineering and Processing*, 37, 503–510.
- Metzner, A.B., Otto, R.E., 1957. Agitation of non-Newtonian fluids. *American Institute of Chemical Engineering Journal*, 3, 3–10.
- Montante, G., Pinelli, D., Magelli, F., 2003. Scale-up criteria for the solids distribution in slurry reactors stirred with multiple impellers. *Chemical Engineering Science*, 58, 5363–5372.
- Nagata, S., 1968. *Kagakukogaku Binran*, 3rd edn., Kagakukogakukai eds., Tokyo, 1103–1105.



- Nagata, S., 1975. *Mixing Principles and Applications*, Wiley, New York.
- Niedzielska, A., Kuncewicz, Cz., 2005. Heat transfer and power consumption for ribbon impellers. Mixing efficiency. *Chemical Engineering Science*, 60, 2439–2448.
- Nishi, K., Matsuda, K., Suzuki, Y., Misumi, R., Kamiwano, M., Kaminoyama, M., 2006. Power consumption of double-bladed kneaders of various shapes. *Journal of Chemical Engineering of Japan*, 33, 489–498.
- Oddy, M.H., Santiago, J.G., Mikkelsen, J.C., 2001. Electrokinetic instability micromixing. *Analytical Chemistry* 73, 5822–5832.
- Özcan-Taşkın, G., 2006. Effect of scale on the draw down of floating solids. *Chemical Engineering Science*, 61, 2872–2879.
- Patton, T., 1979. *Paint Flow and Pigment Dispersion—A Rheological Approach to Coating and Ink Technology*, 2nd edn., Wiley, New York.
- Perrot, A., Lanos, C., Estellé, Y., Melinge, Y., 2006. Ram extrusion force for a frictional plastic material: Model prediction and application to cement paste. *Rheologica Acta*, 45, 457–467.
- Pinelli, D., Magelli, F., 2001. Solids settling velocity and distribution in slurry reactors with dilute pseudoplastic suspensions. *Industrial and Engineering Chemical Research*, 40, 4456–4462.
- Pinelli, D., Montante, G., Magelli, F., 2004. Dispersion coefficients and settling velocities of solids in slurry vessels stirred with different types of multiple impellers. *Chemical Engineering Science*, 59, 3081–3089.
- Rieger, F., 1999. Calculation of critical agitator speed necessary for complete suspension. In: 8th Polish Seminar on Mixing, Politechnika Warszawska, Warszawa.
- Rieger, F., 2000. Effect of particle content on agitator speed for off-bottom suspension. *Chemical Engineering Journal*, 79, 171–175.
- Rieger, F., 2002. Effect of particle content on agitator speed for off-bottom suspension. *Chemical Engineering Process*, 41, 381–384.
- Schultz, J., Lavielle, L., 1989. Interfacial properties of carbon fibre-epoxy matrix composites. In: *Inverse Gas Chromatography Characterisation of Polymers and Other Materials* (eds. D.R. Lloyd, T.C. Ward, H.P. Schreiber), ACS Symp. Ser. 391. American Chemical Society, Washington, DC, pp. 185–202.
- Senanayake, S.A.M.A.N.S., Clarke, B., 1999. A simplified twin screw co-rotating food extruder: Design, fabrication and testing. *Journal of Food Engineering*, 40, 129–137.
- Sestak, J., Zitny, R., Houska, M., 1986. Anchor agitated systems: Power input correlation for pseudoplastic and thixotropic fluids in equilibrium. *American Institute of Chemical Engineering Journal*, 32, 155–158.
- Shamlou Ayazi, P., Edwards, M.F., 1989. Power consumption of anchor impellers in Newtonian and non-Newtonian liquids. *Chemical Engineering Research and Design*, 67a, 537–543.
- Shekhar, S.M., Jayanti, S., 2003a. Mixing of power-law fluids using anchors: Metzner-Otto concept revisited. *American Institute of Chemical Engineering Journal*, 49, 30–40.
- Shekhar, S.M., Jayanti, S., 2003b. Mixing of pseudoplastic fluids using helical ribbon impellers. *American Institute of Chemical Engineering Journal*, 49, 2768–2772.
- Smith, K.M., Davidson, M.R., Lawson, N.J., 2000. Dispersion of neutrally buoyant solids falling vertically into stationary liquid and horizontal channel flow. *Computers and Fluids*, 29, 369–384.
- Stremmer, M.A., Haselton, F.R., Aref, H., 2004. Designing for chaos: Applications of chaotic advection at the microscale. *Philosophical Transactions of The Royal Society of London Series A*, 362, 1019–1036.
- Teipel, U., Mikonsaari, I., 2004. Determining contact angles of powders by liquid penetration. *Particle & Particle Systems Characterization*, 21, 255–260.
- Wallis, G.B., 1969. *One-dimensional Two-Phase Flow*, McGraw-Hill, London.



- Wassmer, K.H., Hungenberg, K.D., 2005. A unified model for the mixing of non-Newtonian fluids in the laminar, transition, and turbulent region. *Macromolecular Materials and Engineering*, 290, 294–301.
- Yao, W., Mishima, M., Takahashi, K., 2001. Numerical investigation on dispersive mixing characteristics of MAXBLEND and double helical ribbons. *Chemical Engineering Journal*, 84, 565–571.
- Yilmazer, Ü., Kalyon, D.M., 1989. Slip effects in capillary and parallel disk torsional flows of highly filled suspensions. *Journal of Rheology*, 33, 1197–1212.
- Zeppenfeld, R., Mersmann, A.B., 1998. *Chemical Engineering and Technology*, 11, 162.
- Zhang, D., Flory, J.H., Panmai, S., Batra, U., Kaufman, M.J., 2002. Wettability of pharmaceutical solids: Its measurement and influence on wet granulation. *Colloids and Surfaces A: Physicochemical and Engineering Aspects*, 206, 547–554.
- Zografi, G., Tam, S.S., 1976. Wettability of pharmaceutical solids: Estimates of solid surface polarity. *Journal of Pharmaceutical Sciences*, 65, 1145–1149.
- Zumbrunnen, D.A., Subrahmanian, R., Kulshreshtha, B., Mahesha, C., 2006. Smart blending technology enabled by chaotic advection. *Advances in Polymer Technology*, 25, 152–169.

## – 8 –

# Classification and Separation of Solid–Liquid Systems

---

Separation of solids from the liquid medium is generally the last step in processes that employ slurry systems, where the solid particles separate out by settling in the suspension medium. Particles need to be placed in a field or a potential energy gradient to be able to be separated from the liquid phase or to its constituents depending on the differences in physical property relevant to the field. This field can be gravitational or its analogue centrifugal, electrical, or magnetic. The particles will then be separated according to their mass, the charge that they carry, or their magnetic susceptibility, respectively, depending on the field in which they are placed. By far, the most extensively used separation is based on the differences in the mass of the particles in a gravitational, or centrifugal field in macroscale industrial operations, the principles of which are given in Chapter 4. The solid material to be separated is generally of colloidal size range, ranging from submicron sizes to not more than a few millimeters. Other than the cases of large-scale settling in minerals processing in one extreme, and separation of large biomolecules in the other extreme, the terms “macroscale” and “microscale” overlap in terms of the particle size range operated in many separation systems.

## 8.1 CLASSIFICATION AND SEPARATION IN A GRAVITATIONAL FIELD

A separation process can be converted to a classification process by manipulating either the time allowed for separation, or the resistance to the motion of the particles, or both. Manipulation of the retention time in a cascade type of separator is the simplest way to control the cut point, or the particle size limit in a certain fraction. Fine-tuning for the separation can be provided by introducing additional resistance to the motion of the particles through operative parameters that take place in the general force-balance equation, eq. (4.57). Thus,

1. The particles may be forced to move against a counter-current stream of liquid to decrease the net velocity of the particles—eq. (4.138).
2. The density of the suspending medium can be increased by addition of extremely fine particles of a neutral substance to reduce the  $(\rho_p - \rho)$  term in eq. (4.136).

3. The viscosity of the medium can be increased by addition of a polymeric substance or extremely fine particles to increase the resistance of the fluid to the motion of the particles—eq. (4.143).
4. The particles may be forced to move in a direction opposite to the effective external force, i.e., the gravitational force, as in the case of fluidized classifiers.
5. The shape of the flow channel can be so designed that the moment of inertia prevents particles greater than a predetermined size from following the motion of the liquid without colliding with the walls. This is the basis of the operation of centrifugal classifiers.

There are no clear-cut differences in the design of the classifiers, used industrially or investigated experimentally, and the operation of many classifiers is based on more than one of the parameters listed above.

### 8.1.1 Sedimentation as a separation process

In the simplest case, particles separate in a stagnant medium due to differences in density with the liquid medium. The terminal velocity relations of particles under hindered settling conditions (eq. (4.154)), coupled with the mass-balance equations for the total particles (eq. (4.137)) and for particles of a given size range (eq. (4.153)) will determine the rate of separation as given in Section 4.5 of Chapter 4. If the particles are lighter than the suspending medium, ( $\rho_p - \rho$ ) term will be negative and so will be the direction of the terminal velocity. The particles will collect at the surface of the liquid, to be removed by skimming or a similar process. If the density of the particles is greater than that of the suspending medium, then ( $\rho_p - \rho$ ) term will be positive and the particles will settle in the direction of the acting force.

#### 8.1.1.1 Parallel channel classifiers

In batch sedimentation, a polydisperse mixture with  $N$  different sizes of particles with equal densities will create  $N$  zones of settling suspensions above the lowest layer, a mixed zone of early sedimentation. The first layer above the mixed zone will be rich in large-sized particles. The particle composition for the smaller components will be the same as the feed, since the particles are not buoyant and the suspension is assumed to be well mixed before entering the sedimentation tank. Each zone above the first will be devoid of the next larger-sized particle, until the final top zone will contain only the smallest-sized particles.

The efficiency of a separation/classification process based on hindered settling is increased by providing parallel channels in the sedimentor to decrease the settling distance and inclining the settler so that a larger settling area will be provided at each channel. Such an inclined sedimentor is shown in Figure 8.1(a), where two sets of inclined channels are coupled to serve as a reflux classifier in fluidized beds (Nguyentranlam and Galvin, 2004). The sedimentation process was analyzed by Davis and Gecol (1996) for solid suspensions made up of  $N$  different-size classes. The sedimentation profiles on the inclined channel wall of a single layer in parallel-channel classifiers are shown in Figure 8.1(b), under stable, steady-state operating conditions. Stability in these separators is maintained by operating with polydispersed suspensions with particle densities either higher or lower than the

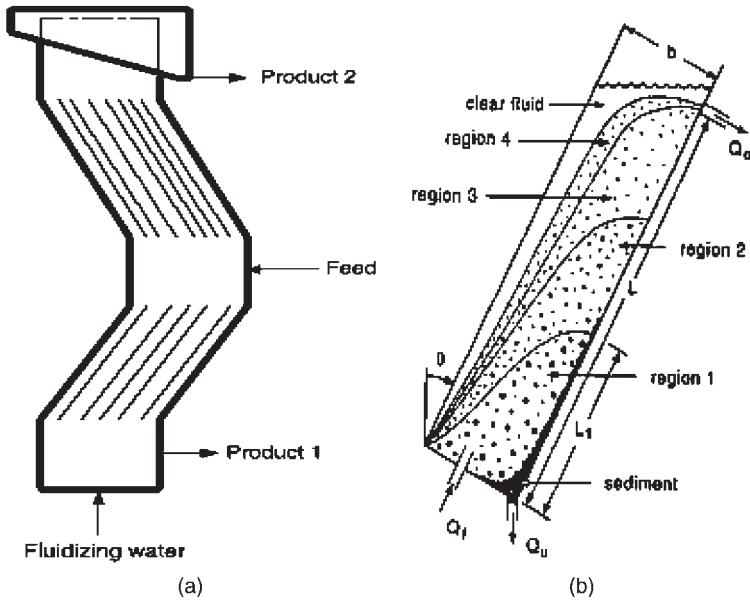


**Figure 8.1** Inclined wall classifiers. (a) Two sets of inclined parallel channel separators used as a reflux classifier in fluidization (Nguyentranlam and Galvin, 2004), (b) Sedimentation of solids on the inclined-wall (Davis and Gecol, 1996). Redrawn with permission of Elsevier.

suspending fluid density, but not when some of the components have a density that is higher and some lower than the density of the suspending fluid.

The thickness, width, and length of each section are denoted by  $b$ ,  $w$  and  $L$ , respectively, and inclination with respect to the vertical direction by  $\theta$ . The feed is given from the bottom section, parallel to the wall at a flow rate  $Q_f$ . Particles settle in the vertical direction and are taken from the corner at the bottom as underflow at a volumetric flow rate,  $Q_u$ , and the liquid together with very small, unsettled particles, as overflow  $Q_o$ , from the top of the inclined plane. The analysis is based on the presence of regions where each size fraction settles, together with the sediment and clarified-fluid regions. The section given in Figure 8.1(b) portrays the differential settling of four different-size fractions of solid particles. The volumetric fraction of particles in the first region shown in the figure will be the same as in the feed. As the largest and densest particles settle, the volumetric fraction of particles in the upward going stream will decrease, as will the average size of the particles. The suspension is fed parallel to the walls, whereas, the particles settle in the vertical direction. A clear liquid layer appears below the upper wall of the channel and the boundaries of the layers become curved. If complete separation of the solids from the liquid is desired, the total flow rates in and out should be adjusted to increase the retention time, so that only clear liquid will come out of the overflow pipe. Otherwise, the particle-size distribution in the overflow will depend on the flow rates in and out of the separator determined by the total mass,

$$Q_f = Q_o + Q_u \quad (8.1)$$

total solids,

$$Q_f \phi_f = Q_o \phi_o + Q_u \phi_u \quad (8.2)$$

and component balance equations for particles of size  $j$ ,

$$Q_f \phi_{j,f} = Q_o \phi_{j,o} + Q_u \phi_{j,u} \quad (8.3)$$

where,  $Q$  is the volumetric flow rate,  $\phi$ , the volumetric fraction of solids, the first letter in the suffix denotes the size fraction of the particle ( $j = 1, 2, \dots, N$ ) and the second suffix, the flow stream, feed, overflow and underflow, respectively. In an inclined sedimentor, clarification rate of any zone shown on Figure 8.1(b) is equal to the vertical settling velocity of the largest species  $V_{j,j}$  in that zone ( $j$ ) multiplied by the projection of the interfacial area on the settling direction.

$$S_j = V_{j,j} w (L_j \sin \theta + b \cos \theta) \quad (8.4)$$

The settling velocities of the particles  $V_{j,j}$  are found by using eqs. (4.154), (4.155), and (4.158) in Chapter 4. As the particle size is reduced toward the overflow region, the settling velocity of the particles and the clarification rate of the region will be reduced proportionately. If the overflow rate  $Q_o$  from the sedimentor is greater than the clarification rate of any zone, then particles within that zone will mix in the overflow stream shown as Regions 3 and 4 in Figure 8.1(b). To be consistent with the notation of the figure, let us assume the overflow rate  $Q_o$  to be made up of clear liquid, the contents of Region 4 and the unclarified section of Region 3. Then a particle balance in the mixing zone can be written as,

$$Q_o \phi_o = (Q_o - S_{4\max}) \phi_{j,4} + (S_{3\max} - S_{4\max}) \phi_{j,3} \quad (8.5)$$

denoting that the overflow will contain all the size range of particles in Region 4 and Region 3 in proportion with the clarification rates of these zones.

As the overflow rate increases, concentration of small, slow-settling particles increases, since the retention time in the sedimentor becomes insufficient for the particles to settle. At low overflow rates, all the particles will find time to settle and the classifier functions as a clarifier. As the volumetric concentration of particles in the feed increases, hindered settling conditions set in and slow down the settling process. As a result, more particles with a wider margin of size distribution will be present in the overflow.

#### 8.1.1.2 Sedimentation with simultaneous precipitation

In the section above, the particle sizes were assumed not to change with time or shear rate in flowing through the layers. The particle size and number concentration varies as a function of time in crystallization and precipitation processes. In crystallization, the materials making up the particles are initially soluble in the suspending medium. Particle formation starts on the molecular level with a decrease in the temperature or the amount of the solvent, the suspending medium. Initially there are extremely large numbers of crystal seeds in the nanometer scale suspended in the medium. With time, the sizes of the crystals

increase, but their characteristic geometrical shape does not. Crystallization is generally carried out with gentle mixing to maintain uniformity in concentration of the solution. As crystals are generally not spherical in shape, their settling should be handled with the principles and equations given in Section 4.4 of Chapter 4.

Precipitation is different from crystallization in that the material making up the particle is not soluble in the solvent, the suspending medium. The precipitates grow by aggregation of the primary particles. The primary particles may have a characteristic shape that is not spherical, as in the case of worm-like particles of  $\text{Mg}_3(\text{OH})_2[\text{SiO}_5]_2$ , approximately 1  $\mu\text{m}$  in length and diameter in the order of nanometers, making up apparently spherical clusters (Kind, 2002) with equivalent diameters of 5  $\mu\text{m}$  or more. The sedimentation of these particles should be handled with the fractal theory with settling rates given in Section 4.4.2 of Chapter 4.

Additional issues arise as a consequence of simultaneous aggregation during settling. The large number of particles of nanometric dimensions changes the rheology of the suspending medium and causes it to behave nonlinearly, even though the solvent is a Newtonian fluid. As the particles aggregate, the rheology of the medium changes due to the decrease in the number concentration of primary particles and increase in the number of clusters formed.

In the scale of the initial particle sizes, Péclet number becomes the controlling parameter and relates the shear rates with the diameter of the particles (eqs. (3.9) and (3.10)). In regions where the shear rate is not sufficient for complete dispersion of the primary particles, the depletion forces created by the primary particles enhance aggregation in regions where the local shear rate is low. Nonuniform shear rates end up with a nonhomogeneous particle size distribution, not desirable in nanotechnologies.

### 8.1.2 Fluidization as a separation process

Fluidized bed classifiers work continuously, and solid particles are introduced into the classifier by a liquid jet stream. As the liquid velocity is greater than the terminal velocities of the particles, and no settled bed is involved, and minimum fluidization velocity is not a parameter in these classifiers. In classification by fluidization, the velocity of the fluid stream is set equal to the settling velocity of a critical particle size with the aim of separating the solids in the feed stream to two classes with particle dimensions less and greater than the *critical dimension*, called the *cut size*. Ideally, all the particles with diameters smaller than the cut size should appear in the overflow and those that are greater, in the discharge stream. In such a case, the total efficiency of separation,  $\eta_T$ , defined as the product of the efficiency of separation of the overflow  $\eta_o$ , and the efficiency of separation in the discharge  $\eta_d$ ,

$$\eta_T = \eta_o \eta_d \quad (8.6)$$

would be equal to one ( $\eta_T = 1$ ), with the stream efficiencies defined as,

$$\eta_o = \frac{Q_o \phi_o F_o(d_{pc})}{Q_f \phi_f F_f(d_{pc})} \quad (8.7)$$

and

$$\eta_d = \frac{Q_d \phi_d [1 - F_d(d_{pc})]}{Q_f \phi_f [1 - F_f(d_{pc})]} \quad (8.8)$$

In these equations,  $F$  denotes the cumulative fraction undersize expressed as a mass fraction, for particles of constant density. Eqs. (8.7) and (8.8) then denote ratio of the mass of the undersize and oversize particles, respectively, in the overflow and discharge streams to that in the feed stream. The classifiers work at conditions far from the ideal, mainly due to circulation currents present in the fluidization column, hindered settling conditions and loss of the momentum of the particles through frequent collisions. The settling velocity of the particles approaches their free-stream terminal velocities only in the case of dilute feed streams.

#### 8.1.2.1 Bottom-feed separation vessels

One of the simplest fluidization classifiers is the bottom-feed separation vessel shown in Figure 8.2. The ordinate and the abscissa show the dimensionless height and radius of the separator, respectively. The scale at the top can be taken as a relative scale for the volumetric concentration of particles, as actual values are not given in the original

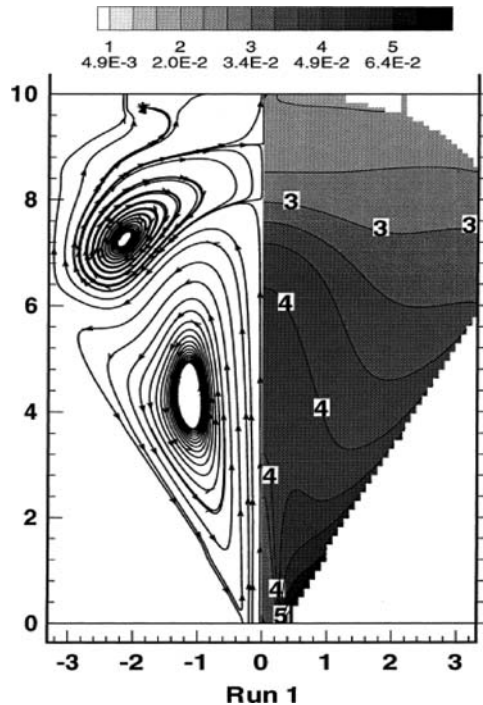


**Figure 8.2** Bottom feed-separation vessel (Li *et al.*, 1998. Reproduced with permission of Elsevier, Figure 4 in the original).

publication (Li *et al.*, 1998). The streamlines on the left portion and the volumetric concentration of solids on the right portion of the figure are obtained by modeling the separator using Navier–Stokes equations for total mass (eq. (5.89)), momentum (eq. (5.90)), component-particle mass balances (eq. (5.94)), and kinetic energy-dissipation ( $k - \varepsilon$ ) model of turbulence (eqs. (5.99) and (5.100)). The time-averaged Navier–Stokes equations were solved by finite volume technique. The feed stream containing the particles is given as jet flow from the bottom of the separator. The particle-laden stream rises vertically upwards, creating toroidal circulation currents in the lower section of the separator. The discharge leaves from the pipe at the bottom, modeled as an annulus around the feed pipe to maintain axial symmetry. The toroidal current in the lower section creates circulation currents near the walls of the upper section. The overflow leaves from the top of the separator. The superficial velocity at the upper section, calculated by dividing the volumetric outflow rate with the largest cross-sectional area of the sedimentor is adjusted to the settling velocity of the cut diameter,  $V_{pc}$ . The feed jet is negatively buoyant, as the particles tend to move opposite to the velocity of the jet stream. The height of the jet stream is a significant parameter in the efficiency of separation of larger particles from the overflow stream. The height of the feed jet stream is controlled by the Froude number,  $Fr$ , defined as,

$$Fr = \left[ \frac{\rho V_{fs}}{(\rho_{fs} - \rho)Rg} \right] \quad (8.9)$$

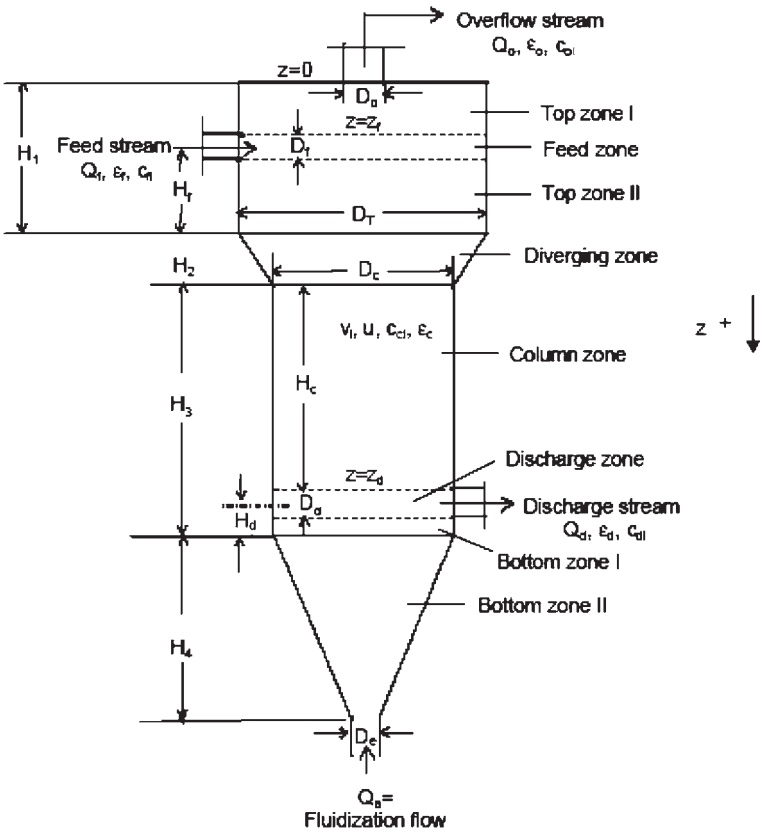
where  $R$  is the radius of the feed inlet pipe and the subscript fs stands for the feed stream. The efficiency of separation in the outlet stream is improved by increasing the feed-pipe radius,  $R$ , to reduce the feed-stream velocity,  $V_{fs}$ . Reduction of the feed-stream velocity decreases the height of the jet, draws down the upper circulation currents, leaving more room for the large particles to settle.

### 8.1.2.2 Fluidized bed classifiers

A fluidized bed classifier with two inlet streams is shown in Figure 8.3 (Chen *et al.*, 2002). The design of the separator is similar to a hydrocyclone, with the exception of the inlet pipe, which does not create circulatory flow, but turbulence for initial dispersion of the particles. The fluidizing liquid stream enters from the bottom of the separator, below the discharge stream. The overflow stream leaves from the top. The, volumetric concentration of solids denoted by  $c$  in the figure is equivalent to  $\phi$ , and voidage  $\varepsilon$  is equivalent to  $(1 - \phi)$  in the nomenclature adopted in this book. The various dimensions (in mm) of the five fluidized bed liquid–solid classifiers investigated are given in the table below the schematic diagram. Spherical glass beads ( $\rho_p = 2470 \text{ kg m}^{-3}$ ) were dispersed in water. Monodispersed ( $d_p = 0.9 \text{ mm}$ ), bidispersed,  $d_p = 0.9 \text{ mm}$  and  $d_p = 0.55 \text{ mm}$ , and polydispersed particles within this range, obeying the Rosin–Rammler cumulative distribution

$$F = 1 - \exp \left[ - \left( \frac{d_p}{d_{50}/(\ln 2)^{1/n_r}} \right)^{n_r} \right] \quad (8.10)$$





Unit	D <sub>f</sub>	D <sub>c</sub>	H <sub>1</sub>	H <sub>2</sub>	H <sub>3</sub>	H <sub>4</sub>	H <sub>c</sub>	H <sub>d</sub>	D <sub>c</sub>	D <sub>f</sub>	D <sub>d</sub>	D <sub>o</sub>
T-2	191	191	292	102	686	794	127	64	51	51	51	76
C-0	292	191	292	102	686	457	127	64	51	51	51	76
C-1	292	191	292	102	102	457	127	64	51	51	51	76
C-2	292	191	292	102	349	457	127	64	51	51	51	76
C-3	292	191	292	102	1035	457	127	64	51	51	51	76

**Figure 8.3** Fluidized bed classifier. (Chen *et al.*, 2002. Redrawn with permission of Elsevier, Figure 1 in the original).

were used to analyze the parameters effective in the efficiency of separation. The width of the particle-size distribution was characterized by the particle-size ratios corresponding to 90 and 10% undersize:

$$\frac{d_{90}}{d_{10}} = \left[ \frac{\ln(0.1)}{\ln(0.9)} \right]^{1/n_r}$$

(8.11)

The range of variables investigated in the research is:

$$0.06 \leq \phi_f \leq 0.46; \quad 1.5 \leq \left( \frac{d_{90}}{d_{10}} \right)_f \leq 4.3; \quad 0.13 \leq \frac{H_c}{D_c} \leq 12; \quad 31 \leq Re_{p50} \leq 165;$$

$$5.4 \times 10^3 \leq Re_c \leq 1.7 \times 10^5; \quad 1.7 \times 10^4 \leq Ar \leq 1.4 \times 10^5$$

The Reynolds number based on the particle diameter  $Re_p$ , and based on the column diameter  $Re_c$  are defined with the equations,

$$Re_{p50} = \frac{\rho d_{50,f} V_a}{\mu} \quad (8.12)$$

$$Re_c = \frac{\rho D_c V_a}{\mu} \quad (8.13)$$

$V_a$  in these equations is the velocity of the fluidizing stream ( $V_a = 4Q_a / \pi D_c^2$ ). Archimedes number  $Ar$  is defined as,

$$Ar = \frac{d_{50,f}^3 \rho_f (\rho_p - \rho) g}{\mu^2} \quad (8.14)$$

The experimental results were in good agreement with the model predictions (Chen *et al.*, 2002). The two major findings of the work regarding the operation of the classification column were:

1. The volumetric concentration of solids in the discharge stream,  $\phi_d$ , decreased as the velocity of the fluidizing stream,  $V_a$ , increased and it was independent of the variations in the velocity,  $V_f$ , or volumetric flow rate of the feed stream,  $Q_f$ , volumetric concentration of solids in the feed stream,  $\phi_f$ , the particle-size range  $d_{90}/d_{10}$ , the volumetric flow rate of the discharge stream and height of the column  $H_c$ .
2. As the volumetric flow rate  $Q_f$  increased or the concentration of solids  $\phi_f$  decreased in the feed stream, the particle concentration was found to decrease throughout the column, but the other parameters were not affected.

The separation efficiencies in the fluidized classifier calculated with eqs. (8.6)–(8.8) are reproduced in Figure 8.4. The experimental results were nearer to the no-separation curves found through the model studies. The total efficiency,  $\eta_T$ , of the classifier *increased* with a *decrease* in the velocity of the fluidizing stream and the volumetric concentration of solids in the feed stream,  $\phi_f$ , and an *increase* in the volumetric flow rate of the feed stream  $Q_f$ , the volumetric flow rate of the discharge stream,  $Q_d$ , the particle-size range  $d_{90}/d_{10}$ , and height of the column,  $H_c$ .

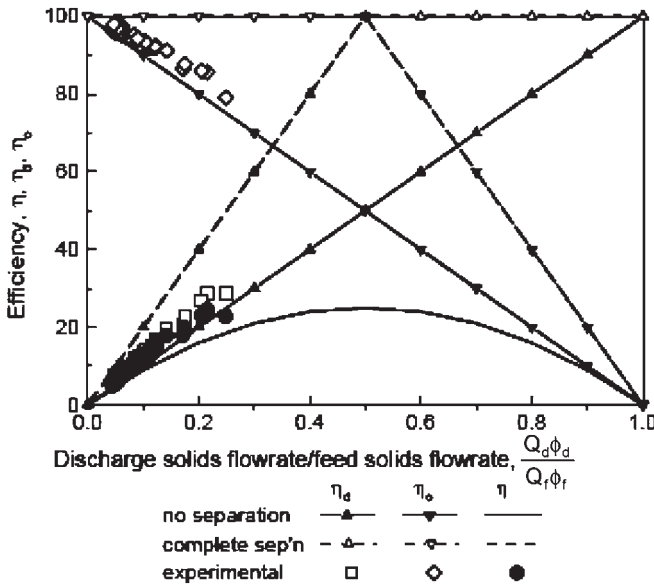


**Figure 8.4** Variation of the efficiency of fluidized bed classifier with the ratio of the solids in the discharge stream to that in the feed stream. (Chen *et al.*, 2002. Redrawn with permission of Elsevier, Figure 13 in the original).

### 8.1.3 Classification in hydrocyclones

As in the case of fluidized classifiers, hydrocyclones are also dynamic systems where the flow patterns of the suspension are controlled by the design and dimensions of the hydrocyclones. Hydrocyclones are used with small-sized or low-density solid particles, where separation under the action of gravity would be too slow to be economically feasible. The gravitational field acting on the particles is increased and changed in direction by centrifugal acceleration. Centrifugal motion is created by injecting the suspension tangentially into a cylindrical section, as shown in Figure 8.5. The cylindrical section of the hydrocyclone serves as the classification unit, where the particles line up in the radial direction within the swirling suspension. As the dominant direction of acceleration is now radially outwards,  $a = r\omega^2$ , the largest particles are pushed farthest from the axis, toward the wall of the cyclone. When the swirling suspension reaches the conical section, starting from the largest, the particles strike the walls, lose their momentum, slide down the walls under the action of gravity, and leave the cyclone from the bottom as underflow. The remaining particles that did not have a chance to strike with the walls of the cyclone are carried along with the fluid stream that leaves the cyclone from the top as overflow. The other functional parts of the cyclone are the *vortex finder* tube at the top and *apex cone* at the bottom that guide the internal vortex flow going upwards. Hydrocyclones are small, compact units with a high capacity, requiring low maintenance and operating cost and therefore, are extensively used.

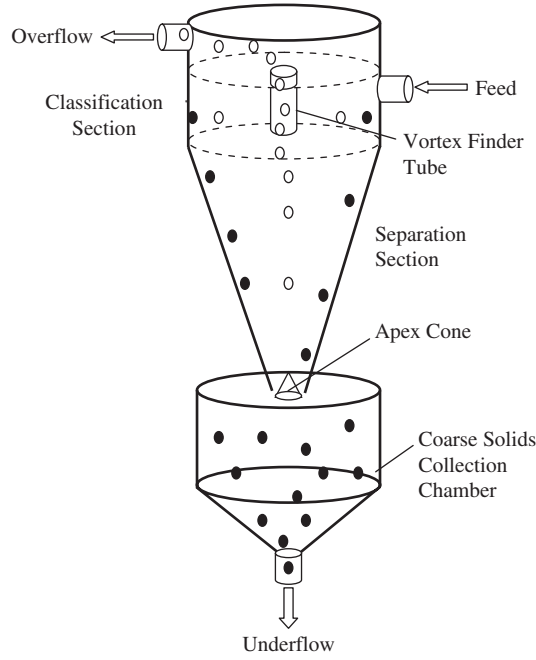


**Figure 8.5** Functional parts of a hydrocyclone.

Yoshida *et al.* (2004) investigated the effect of the inlet to the hydrocyclone on the separation efficiency. The inlets to be evaluated are the tangential inlet given in Figure 8.6(a) with the spiral inlet given in (b) of the same figure. The performance of the cyclone separators could have been evaluated with eqs. (8.7) and (8.8), but evaluation by *partial-separation efficiency*,  $\Delta\eta$ , based on particle-size distribution functions may be more handy when particle sizes are determined by light-scattering techniques:

$$\Delta\eta = \frac{m_c f_c \Delta d_p}{m_c f_c \Delta d_p + m_s f_s \Delta d_p} \quad (8.15)$$

$m_c$  and  $m_s$  in this equation are the masses of the coarse and small particles collected in the underflow and overflow curves, respectively;  $f_c$  and  $f_s$  are their respective particle-size distribution functions and  $\Delta d_p$  denotes particle-size range of the distribution functions ( $F = \int_{d_{p1}}^{d_{p2}} f d(d_p)$ ). Classification performance is evaluated by the ratio of the particle diameters corresponding to  $\Delta\eta = 75\%$  and  $\Delta\eta = 25\%$  partial separation efficiency,

$$\kappa = \frac{d_{p75\%}}{d_{p25\%}} \quad (8.16)$$

The results are given in Figure 8.7.

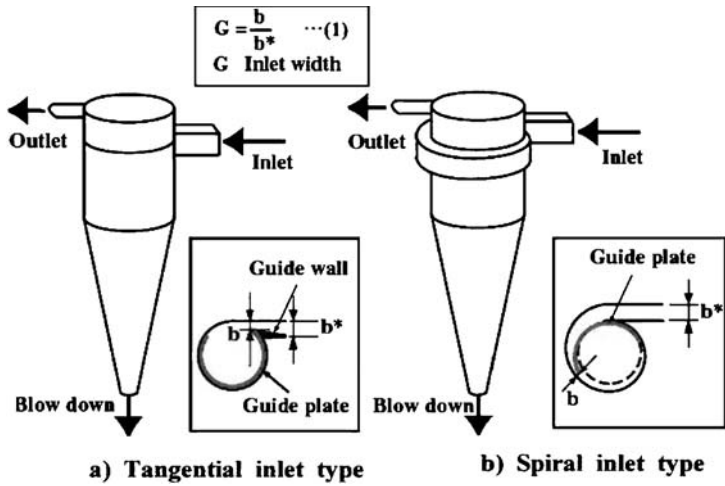


**Figure 8.6** Fluid inlet designs of hydrocyclones. (Yoshida *et al.*, 2004. Reproduced with permission of Elsevier, Figure 4 in the original).

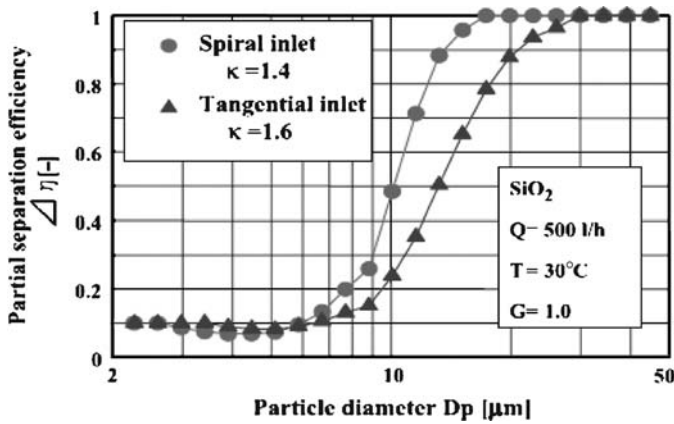


**Figure 8.7** Comparison of the separation efficiency in hydrocyclones with spiral and tangential entry. (Yoshida *et al.*, 2004. Reproduced with permission of Elsevier, Figure 5 in the original).

The steeper the curve around the cut point, the better is the efficiency of separation. The steepness of the curve is greater in the case of spiral inlet. The separation efficiency of the spiral inlet is attributed to the formation of a smooth stream at the inlet, without the formation turbulence as in the case of tangential inlets. Turbulence effect deters the lining-up effect (classification of the particles) in the cylindrical section leading to poorer separation efficiency.

Another cause for the decrease in the separation efficiency of hydrocyclones could be the short circuiting of the feed through the vortex finder without remaining for a sufficient time in the hydrocyclone for particle classification to take place. In such a case, part of the feed stream leaks over the outer walls of the vortex finder, and mixes with the outflow stream. Another source of malfunctioning could be the section just above the apex cone in Figure 8.5, from where the coarse particles climb up and mix with the outflow stream.

**Table 8.1**

Dimensions (mm) of the experimental hydrocyclones

Hydrocyclone number	1	2	3	4	5
Hydrocyclone diameter	75	75	75	75	150
Inlet diameter (mm)	25	25	25	25	64 <sup>a</sup>
Vortex finder diameter (mm)	25	25	22	25	67
Spigot diameter (mm)	12.5	15	12.5	12.5	19
Vortex finder length (mm)	50	50	50	50	135
Cylindrical section length (mm)	75	75	75	75	413
Included cone angle (°)	20	20	20	15	5.5 <sup>b</sup>

<sup>a</sup>Rectangular involute inlet 64 mm high.<sup>b</sup>The included cone angle increases to 13° at a location 127 mm above the spigot opening.Source: Monredon *et al.*, 1992. Redrawn with permission of Elsevier.

To elucidate the parameters effective on the separation efficiency, Monredon *et al.* (1992) measured the tangential and axial velocities in five hydrocyclones given in Table 8.1.

The first hydrocyclone in Table 8.1 is taken as a reference with which the performances of the other cyclones are compared. The second hydrocyclone is identical to the first cyclone, except the spigot (underflow tube) diameter is larger. Similarly, the only difference of the third cyclone is the use of vortex finder with a smaller diameter. The fourth hydrocyclone differs in the cone angle only, and the fifth in all of the overall dimensions.

The total height of the hydrocyclones is 260 mm in each case. Velocity measurements are taken at the critical points leading to poor separation performance: just below the vortex finder (50 mm depth) and near the underflow pipe (200 mm depth). The velocities are measured with the laser-Doppler velocimeter, therefore, only water was present in the hydrocyclone, with an air core at the center, since laser beams cannot penetrate even dilute suspensions. In the separation of suspensions, liquid phase carrying the smaller particles move upwards in place of the air core and leave through the overflow pipe, and a slurry of larger particle leaves from the underflow pipe.

The results in Figure 8.8(a) and (b) show that tangential velocities show a maximum a short distance away from the vortex finder pipe walls and decrease sharply as vortex finder pipe walls are approached. The maximum velocity is affected by the diameter of vortex finder pipe, only. The increase in the tangential velocity causes the pressure losses ( $\Delta P_{hc}$ ) in the hydrocyclone to increase also. The axial velocities measured just below the vortex finder in Figure 8.8(c) are not affected by any of the parameters investigated. But the axial velocities at a depth of 200 mm in Figure 8.8(d) are severely affected. The negative velocities observed in the case of the second hydrocyclone indicate that a larger diameter underflow pipe withdraws a large proportion (21% of the feed stream instead of the 8% observed in other hydrocyclones) of the feed stream. The entrainment of the already classified coarse particles by the upward flow is reduced, but a greater fraction of smaller particles that had to be entrained in the upflow goes through the underflow pipe together with the larger particles.

The flow in hydrocyclones are generally modeled with the use of Navier–Stokes equations and vorticity and stream-function tensors. Although a reasonable agreement is reached with experimental results in each case, there is no general model that can describe the flow patterns in the hydrocyclones.

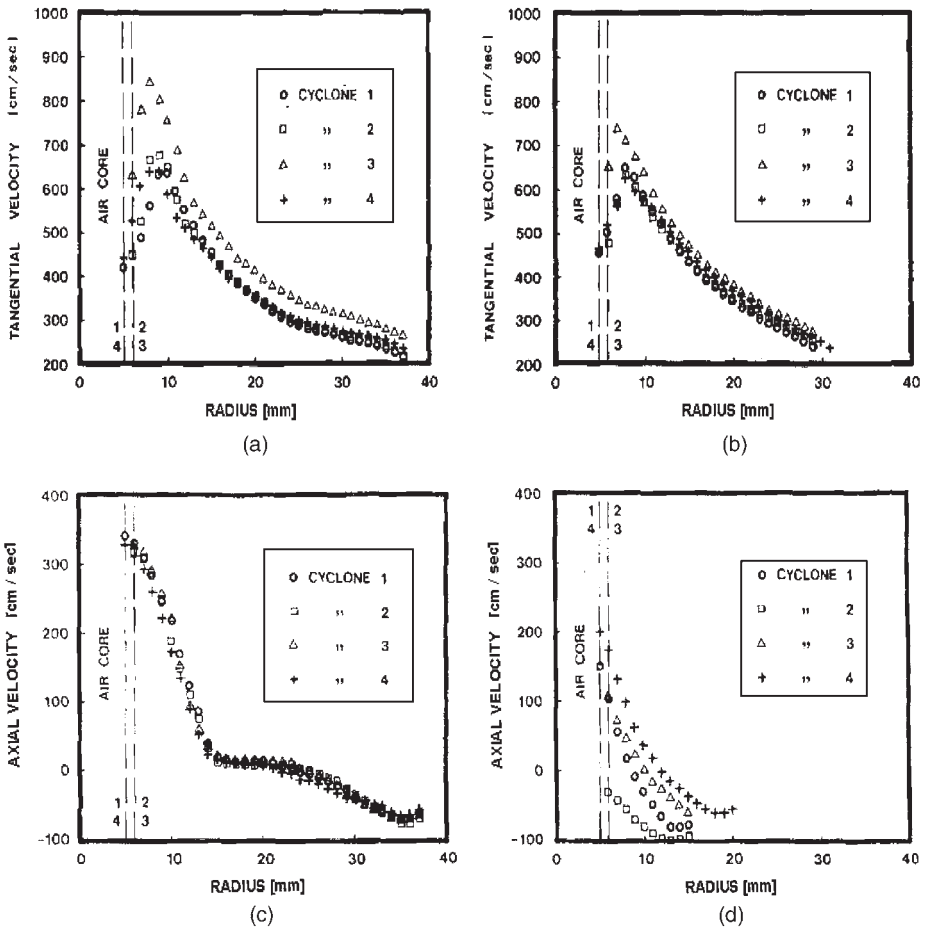


**Figure 8.8** Tangential and axial velocities in a hydrocyclone. (a) Tangential velocity at 50 mm depth, (b) Tangential velocity at 200 mm depth, (c) Axial velocity at 50 mm depth, (d) Axial velocity at 200 mm depth. (Monredon *et al.*, 1992. Redrawn with permission of Elsevier, Figures 2 and 3 in the original).

Similar problems exist with the empirical design equations developed by different authors. The design procedure of hydrocyclones is outlined by Kraipech *et al.* (2006) and the reliability of the design equations are validated with different solid–liquid mixtures to be separated and different types of hydrocyclones. Four fundamental parameters were identified in the design of hydrocyclones, given with empirical design relations:

1. Pressure drop  $\Delta P$  (Table 8.2),
2. Flow recovery to underflow  $R_f$  ( $R_f = Q_d/Q_f$ ) (Table 8.3),
3. Corrected cut size  $d_{50}$  (Table 8.4),

**Table 8.2**

Correlations for pressure drop in hydrocyclones

Equations	Key parameters	Default values	Equation numbers	References
$\ln \Delta P = a \ln F - b$	$a, b$	$a = 2.3, b = 3.6$	(8.17)	Besendorfer (1996)
$F = K_{\text{QO}} [D_c^{1.90}] \left( \frac{D_o}{D_c} \right)^{0.67} \left( \frac{D_i}{D_c} \right)^{0.45} \left( \frac{L_c}{D_c} \right)^{0.2} \theta^{-0.1} \left( \frac{\Delta P}{\rho_f} \right)^{0.5}$	$K_{\text{QO}}$	—	(8.18)	Nageswararao (1995)
$\Delta P = \frac{F_3 1.88 F^{1.78} e^{0.55 \phi_{sf}}}{D_c^{0.37} D_i^{0.94} h_{fv}^{0.28} (D_u^2 + D_o^2)^{0.87}}$	$F_3$	$F_3 = 1$	(8.19)	Flintoff <i>et al.</i> (1987)
$\Delta P = \frac{Eu \rho v_a^2}{2}$ Where $Eu = 371.5 Re^{k2} e^{n \phi_{sf}}$ and	$k2$	$k2 = 0.116, n = -2.12$	(8.20)	Svarovsky (1994)
$Re = \frac{v_a D_c \rho}{\mu}$				

Source: Reprinted from Kraipecth *et al.* (2006) with permission of Elsevier.



Table 8.3

Correlations for flow recovery to underflowing hydrocyclones

Equations	Key parameters	Default values	Equation numbers	References
$S = C_1 \left( \frac{D_u}{D_o} \right)^x F^y$	$C_1, x, y$	$C_1 = 61.3, x = 4.4, y = -0.44$	(8.21)	Moder and Dahlstrom (1952)
$R_f = K_{VO} \left( \frac{\Delta P}{\rho_{fg} D_c} \right)^{-0.31} \left( \frac{D_o}{D_c} \right)^{-0.96} \left( \frac{D_u}{D_c} \right)^{1.83} \left( \frac{D_i}{D_c} \right)^{-0.25} \left( \frac{L_c}{D_c} \right)^{0.22} \theta^{-0.24}$	$K_{VO}$	—	(8.22)	Nageswararao (1995)
$S = \frac{F_4 8.7 (D_u / D_o)^{3.31} h_{fv}^{0.54} (D_u^2 + D_c^2)^{0.36} \rho_f^{0.24} e}{\Delta P^{0.24} D_c^{1.11}}$	$F_4$	$F_4 = 1$	(8.23)	Flintoff <i>et al</i> (1987)
$R_f = 1 - \frac{a}{a + \exp(b(D_u / D_o))}$	$a, b$	$a = 400, b = 6.9$	(8.24)	Abbott (1968)
$R_f = 1 - \frac{1}{1 + a(D_u / D_o)^b}$	$a, b$	$a = 1.1, b = 3$	(8.25)	Tarjan (1961)
$R_f = 1 - \frac{a}{1 + (D_u / D_o)^b}$	$a, b$	$a = 0.95, b = 4$	(8.26)	Yoshioka and Hotta (1955)

Source: Reprinted from Kraipech *et al.* (2006) with permission of Elsevier.

Table 8.4

Correlations for the cut size in hydrocyclones

Equations	Key parameters	Default values	Equation numbers	References
$d'_{50} = R5.27D_c^{0.66} \left( \frac{0.53 - \phi_{sf}}{0.53} \right)^{-1.43} \sqrt{\frac{1.65}{\rho_p - \rho}} 1.91 \Delta P^{-1.28} \mu^{0.5}$	$R$	$R = 1$	(8.27)	Besendorfer (1996)
$\frac{d'_{50}}{D_c} = K_{DO} [D_c^{-0.65}] \left( \frac{\Delta P}{\rho_f g D_c} \right)^{-0.22} \lambda^{0.93} \left\{ \frac{(D_o/D_c)^{0.52} (D_o/D_c)^{-0.47}}{(D_i/D_c)^{-0.40} (L_c/D_c)^{0.20} \theta^{0.20}} \right\}$	$K_{DO}$	—	(8.28)	Nageshwararao (1995)
$d'_{50} = \frac{F_1 39.7 D_c^{0.46} D_i^{0.6} D_o^{1.21} \mu^{0.5} e^{6.3 \phi_{sf}}}{D_u^{0.71} h_{iv}^{0.38} F^{0.45} ((\rho_p - 1)/1.6)^k}$	$F_1, k$	$F_1 = 1, k = 1$	(8.29)	Flintoff <i>et al.</i> (1987)
$d'_{50} = \sqrt{\frac{Stk'_{50} 18 \mu D_c}{(\rho_p - \rho) v_a}}$	$k_1$	$k_1$	(8.30)	Svarovsky (1994)
$k_1 = Eu Stk'_{50} = 0.0474 \left[ \ln \left( \frac{1}{R_f} \right) \right]^{0.742} e^{8.96 \phi_{sf}}$				

Eu given in eq. (8.20)

Source: Reprinted from Kraipech *et al.* (2006) with permission of Elsevier.

Table 8.5

Correlations for the classification function in hydrocyclones

Equations	Key parameters	Default values	Equation numbers	References
$C(d) = \frac{\exp[m(d/d'_{50})] - 1}{\exp[m(d/d'_{50})] + \exp[m] - 2}$	$m$	$m = 4$	(8.31)	Lynch and Rao (1968)
$C(d) = 1 - \exp\left[-0.693\left(\frac{d}{d'_{50}}\right)^m\right]$	$m$	$m = 3$	(8.32)	Plitt (1971)

Source: Reprinted from Kraipech *et al.* (2006) with permission of Elsevier.

4. The sharpness of classification  $m$  (the slope of the separation efficiency curve in Figure 8.7), and the classification function,  $C(d)$ , used to calculate the particle-size distribution of the overflow and underflow streams (Table 8.5).

Empirical equations developed for these parameters are summarized in Tables 8.2–8.5, and the nomenclature identified and units to be used are given in Table 8.6. The default values of the key parameters are the values suggested by the authors that developed the relations.

The input parameters to be used in the design equations of Tables 8.2–8.5 are:

1. Pressure drop  $\Delta P$ , or equivalently volumetric flow rate of the feed stream,  $Q_f$  (denoted as  $F$  in the tables);
2. Hydrocyclone dimensions, i.e., diameter, cone angle, height of the hydrocyclone, and the geometry of the inlet pipe, the sizes of the vortex finder pipe and apex cone;
3. Conditions of the flow streams: concentration of the feed slurry, particle-size distribution of the feed slurry, density, and viscosity of the phases.

The input parameters are used in the design equations to calculate:

1. Volumetric flow rate  $Q_f$  if  $\Delta P$  is given or  $\Delta P$  if  $Q_f$  is given.
2. Overflow and underflow (discharge) volumetric flow rates  $Q_o$  and  $Q_d$ , using eq. (8.1) and

$$R_f = \frac{Q_d}{Q_f} \tag{8.33}$$

The selectivity function  $S(d_p)$  is calculated from the  $C(d_p)$  relations given in Table 8.5 with eq. (8.34),

$$S(d_p) = C(d_p) + R_f(1 - C(d_p)) \tag{8.34}$$

Particle-size distributions in the overflow and underflow (discharge) streams are calculated by component material balances with the use of eq. (8.34),

$$Q_o(d_p) = Q_f(d_p)(1 - S(d_p)) \quad (8.35)$$

$$Q_d(d_p) = Q_f(d_p)S(d_p) \quad (8.36)$$

The volumetric concentration of solids in the overflow and underflow streams is calculated by summing up the fraction of particles at each size interval:

$$\phi_o = \sum_{i=1}^N \left( \frac{Q_o(d_{pi})}{Q_o} \right) \quad (8.37)$$

$$\phi_d = \sum_{i=1}^N \left( \frac{Q_d(d_{pi})}{Q_d} \right) \quad (8.38)$$

The authors could not find a satisfactory agreement with the predictions of the design equations with the use of default values and the experimental results. Fitting the design equations to experimental data and selecting the set of relations that gave the best fit to the experimental values were next examined. Satisfactory predictions were obtained only in the hydrocyclone where the values of the constants were obtained. Even with the refined constants, changing the dimensions of the cyclone, made the design equation unusable. The authors concluded that the design relations given in Tables 8.2–8.5 should only be used when the constants are determined experimentally and then only in the hydrocyclone where these constants were determined. All of the equations were sensitive to variations in *pressure drop* and *feed concentration* but could not be reliably used in predicting the effect of other parameters.

## 8.2 SEPARATION IN A MAGNETIC FIELD

Separation based on magnetic properties is possible in a magnetic field if the particles have different magnetic susceptibilities. Ferromagnetic materials are relatively easy to separate. Para- and diamagnetic materials require ingenious methods for separation that are currently under development. In addition, the strength of a magnetic field is rarely so high that the effects of other fields such as gravitational, centrifugal, or electrical be neglected in comparison. So, a particle will be subjected to various forces according to the strength of the other fields. Separation based on magnetic forces is possible only if the magnetic force predominates the other forces. In modeling magnetic separators, all of the forces effective under the given fields are taken into consideration in momentum-balance equations (Abdelsalam, 1987). The hydrodynamic conditions specific to the design of the separator are also included into the model formulation.

Two different types of separations based on magnetism are possible: Separation of magnetic particles themselves and separation of nonmagnetic particles within a magnetic medium.

Table 8.6

Units to be used in the correlations given in Tables 8.2–8.5

Symbols	Parameters	Design equations presented by				
		Besendorfer (1996)	Svarovsky (1994)	Nageswararao (1995)	Moder and Dahlstrom (1952)	Flintoff <i>et al.</i> (1987)
$d, d_{50},$ and $d'_{50}$	Particle size, cut size, and corrected cut size	$\mu\text{m}$	m	m	—	$\mu\text{m}$
$D_c$	Hydrocyclone diameter	inch	m	m	—	cm
$D_o$	Vortex finder diameter	inch	—	m	Same as $D_u$	cm
$D_i$	Inlet diameter	—	—	m	—	cm
$D_u$	Apex diameter	inch	—	m	Same as $D_o$	cm
$F$	Feed flow rate	$\text{gal min}^{-1}$	$\text{m}^3 \text{s}^{-1}$	$\text{m}^3 \text{s}^{-1}$	$\text{gal/min}$	$\text{l min}^{-1}$
$G$	Gravitational acceleration	—	—	$\text{kg m}^{-2}$	—	—
$h_{fv}$	Free vortex height	—	—	M	—	cm
$L_c$	Total length of hydrocyclone	—	—	m	—	—
$\Delta P$	Pressure drop	psi	Pa	Pa	—	kPa
$v_a = \frac{4F}{\pi D_c^2}$	The characteristic velocity	$\text{m s}^{-1}$	—	—	—	—
$\mu$	Fluid viscosity	cp	Pa s	—	—	Pa sec
$\phi_{sf}$	Solid volume fraction in feed	—	—	—	—	—
$\lambda = \phi_{sf}(1 - \phi_{sf})^3$		—	—	—	—	—
$\theta$	Cone angle	—	—	degree	—	—
$\rho_F, \rho,$ and $\rho_P$	Density of feed slurry, liquid, and solid	$\text{g cm}^{-3}$	$\text{kg m}^{-3}$	$\text{kg m}^{-3}$	—	$\text{g cm}^{-3}$

Source: Reprinted from Kraipech *et al.* (2006) with permission of Elsevier.

### 8.2.1 Separation of magnetic particle

Separation of magnetic particles is brought about by the action of a magnetic force in a nonuniform magnetic field, as given by eq. (4.38). The parameters effective on the magnitude of this force are particle volume, susceptibility of the particle, and the strength of the magnetic field inside the particle and externally applied field strength. For a good discussion of magnetic forces acting on the particles in a separator under a magnetic field, the readers are referred to the article by Smolkin and Smolkin (2006).

As the particle size is effective in determining the magnitude of the magnetic force, one way of increasing the separation efficiency would be to subject the particles to preflocculation under a weak magnetic field ( $\approx 0.03$  T). This method, termed as magnetic flocculation screening, is used in upgrading magnetite concentrates in the presence of silica. The larger magnetite flocculates are then separated from silica by screening for further refinement (Garcia-Martinez *et al.*, 2004).

### 8.2.2 Separation of nonmagnetic particles in a magnetic medium

Nonmagnetic particles are separated in a stationary magnetic fluid situated in the magnetic field of two magnets placed at the two sides of a chamber called, ferrohydrostatic separator. The nonmagnetic particle immersed in the magnetic medium will be subjected to gravitational and buoyancy forces due to gravitational and magnetic fields. In addition, drag forces will arise when the particle moves under the action of these three forces. Body and buoyancy forces under a gravitational field are given by eqs. (4.34) and (4.36). Buoyancy force  $F_{bM}$  in a magnetic field is given by,

$$\mathbf{F}_{bM} = \mu_0 v_p M_f \nabla \mathbf{H}_0 \quad (8.39)$$

where  $\mu_0$  is the magnetic permeability of vacuum [ $\text{T m A}^{-1}$ ],  $v_p$  is the volume of the particle,  $M_f$  is the saturation magnetization, and  $\nabla H_0$  is the external magnetic field gradient. The resulting drag force on the particle is given by the Stokes law, eq. (4.48). The particle trajectories, and separation process in a ferrohydrostatic separator are modelled and solved using discrete element method by Murariu *et al.* (2005), and the recent developments in separation techniques are reviewed by Svoboda and Fujita (2003), which the interested reader can refer.

## 8.3 SEPARATIONS IN THE MICROSCALE

Microseparations involve the separation of colloidal particles in submicron size range and in channels of micrometer dimensions, at least in depth and width. As the Reynolds number is extremely small in this range of particle and channel sizes, an external force acting on the particle is required to overcome the viscous forces resisting the motion of the particles. External forces should also dominate the Brownian motion to reduce random scattering. As in the case of micromixing, microseparation devices are still in the development stage. The external forces acting on the particles are given in Chapter 4. In this section,

some of the microseparation techniques developed to separate and/or fractionate particles in the submicron size range will be presented.

### 8.3.1 Field flow fractionation techniques

Field flow fractionation techniques use gravitational field as an external field in separation and fractionation of particles in a polydisperse population according to their size and shape. The technique is based on the principles of elution through a column with diameter much greater than the diameter of particles to be separated ( $(D/d_p) \geq 100$ ). The particles are separated by sedimenting across the channel diameter, or width, in the case of rectangular channels. Fractionation according to the shape of the particles is also possible based on differences in terminal velocity. The technique was successfully used to separate spherical  $\text{TiO}_2$  particles of  $0.31\ \mu\text{m}$  average diameter from ellipsoidal particles of  $0.45\ \mu\text{m}$  hydrodynamic diameter in the Brownian elution mode (Rasouli *et al.* (2001). In this method, the flow is stopped after introduction to the channel to allow the sample to sediment across the channel thickness. This stop flow, or primary relaxation time, is closely related with the density, size distribution, and shape of the particles as discussed in Chapter 4. Prevention of the aggregation of particles is an essential requisite in the proper operation of the system. Electrolyte concentration of the carrier fluid is critical in suppressing aggregation through repulsive forces between the particles, as discussed in Chapter 1. Surfactants are also used to maintain steric stabilization as well as to reduce the drag on the walls. As the use of surfactants is multifunctional in this technique, better results are obtained with mixtures of surfactants. The final condition for the operation of the system rests on the attainment of hindered settling conditions. As the shape of the particles are less determinative than the size of the particles on the settling rate, hindered settling conditions where interactions between the particles are appreciable should be maintained for differentiation with respect to the shape of the particles. Rasouli *et al.* (2001) could obtain bimodal peaks only at  $\text{TiO}_2$  concentration greater than 1% (w/w).

### 8.3.2 Separations in flow through microfluidic bifurcations

Separations in flow through bifurcations are basically a separation technique, rather than classification, in its present state of development. The operation principle is based on the differences in the moment of inertia of the liquid suspending medium and the particles: The particles cannot turn around corners as easily as the fluids and therefore, prefer straight-through channels. The second factor in the separation technique is the preference of the particles to remain along the inside walls after a bifurcation, instead of changing streamlines and distribute evenly over the entire cross-sectional area, under the prevailing very low Reynolds number conditions.

Roberts and Olbricht (2006) investigated the parameters that affect the separation of particles in bifurcations reproduced in Figure 8.9. The multiple bifurcation in (c) is obtained by the combination of symmetric (a) and oblique (b) bifurcations. The experimental conditions were selected so that Brownian motions would not interfere with the

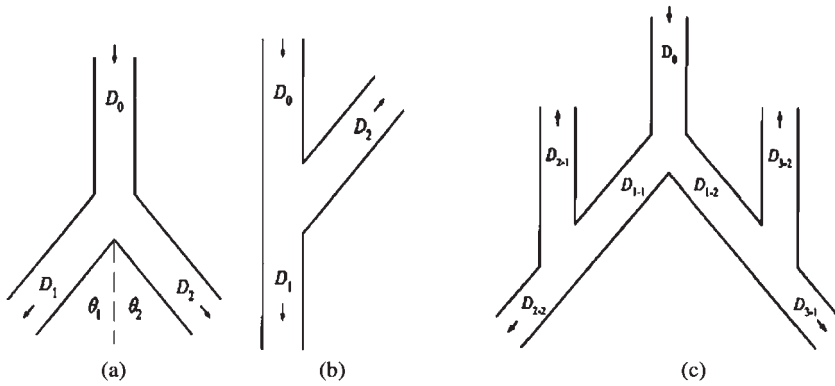


**Figure 8.9** Bifurcation patterns: (a) Y-shaped bifurcation with  $\theta_1 = \theta_2 = 45^\circ$  (b) Oblique bifurcation,  $\theta_1 = 45^\circ, \theta_2 = 135^\circ$ , (c) Multiple bifurcation obtained by combining (Roberts and Olbricht, 2006. Reproduced with permission of John Wiley, Figure 1 in the original).

particle motions, that the attractive and repulsive surface forces would be negligible in comparison with the hydrodynamic forces. Nevertheless, surfactants were used in the suspending medium, to eliminate the bubbles, to stabilize the suspension and to reduce the wall drag, and glycerine was used to adjust the suspension-medium density so that the particles would be selfbuoyant. The aspect ratio  $a/b$  (square or rectangular), flow rate partitioning  $Q_1/Q_T$ , and the ratio of the particle diameter to the microchannel diameter  $d_p/D$  were investigated as parameters.

The results showed that the aspect ratio had a negligible effect on the separation. Diameter ratio  $d_p/D$  was found to be critical: Good separation efficiencies were obtained only when the diameter ratio approached one (0.8 in the experiments). By far, flow-rate partitioning  $Q_1/Q_T$  has the largest effect on the separation. When the ratio of the number of particles going through the collinear  $N_1/N_T$  pipe to the total number of particles is plotted as a function of the flow-rate ratio  $Q_1/Q_T$ , the trend line for the experimental points intersect the no-separation line,  $N_1/N_T = Q_1/Q_T$ , at  $Q_1/Q_T = 0.5$ . At a critical value of the flow-rate partitioning function,  $(Q_1/Q_T)^*$ , all the particles go to the first stream and  $N_1/N_T = 1$ . If the particles are separated with the aim of clarifying the liquid, then the ratio of the clarified liquid flow rate to the total flow rate,  $(1 - (Q_1/Q_T)^*)$  indicates the efficiency of bifurcation flow in separating the particles from the fluid. Roberts and Olbricht (2006) found that the overall efficiency of the multiple bifurcation was greater than that of its counterparts and that a bifurcation pattern could be designed according to the purpose of the separation. It should be mentioned in passing, that the blood cells are partitioned according to the regional needs of the body through bifurcations.

### 8.3.3 Ultrasonic separations

When a standing sound wave is set up in a suspension of particles with radii much smaller than the wavelength of sound, an acoustic force in the axial direction will act on the particles



(Kapishnikov *et al.*, 2006), given by eqs. (4.42) and (4.43) in Chapter 4 for a medium of negligible viscosity. The particles will be forced to move either to the nodes of the standing wave, if the densities of the particles are greater than the density of water, the suspension medium ( $\rho_p \geq \rho_w$ ), or toward the antinodes if the particles are lighter than water ( $\rho_p \leq \rho_w$ ), in an aqueous medium (Bekker *et al.*, 1997) as given in Figure 8.10(a) and (b), respectively. Separation by ultrasound acoustic energy then depends on a balance between the frictional forces and the acoustical forces acting on the particle. This method can only be used if the viscosity of the medium is low enough to permit the diffusion of the particle (eq. (3.2), Chapter 3) in a reasonable time toward the node or the antinode during the passage through the microchannel. In addition, if the particle is extremely small, then the area exposed to the acoustic force will decrease making separation more difficult.

Kapishnikov *et al.* (2006) developed a separation and classification method based on the tendency of the particles to collect at the nodes or antinodes of a standing wave. If Figure 8.10(a) or (b) is rotated by  $90^\circ$  and a microchannel of width adjusted to half or quarter of the wavelength of sound placed in between two transducers, a separation system will be obtained. Channels of width equal to one-half of the wavelength of sound in the medium, with nodes coincident with the walls of the channel, are used as separators, while a channel width of one-quarter of the wavelength are used to classify heavy and light particles tending to collect at the nodes and antinodes, respectively.

The separator developed by Kapishnikov *et al.* (2006) for the separation of particles from an aqueous medium or blood cells from plasma is shown schematically in Figure 8.11(a). The outlet is branched to aid in the separation of particles from the liquid. Contrary to the tendency in the flow of particles in bifurcations, the path of the particles can now be adjusted to divert their flow to the side channels by the application of the acoustic external force: If the aim of separation is the clarification of the liquid, it is diverted to the central channel for ease in connecting the units in series as in Figure 8.11(b). If the unit is used for separating the solids from the liquid only, the channel width is  $160\mu\text{m}$ , or about half the wavelength of sound.

The view of the ultrasonic separator captured with a polarized microscope is shown in Figure 8.12. The path of the particles is that given for flow in a bifurcation—only this time the path is adjusted by the width of the channel and the location of the nodes of sound waves.

By adjusting the width of the channel to quarter of a wavelength, or about  $100\mu\text{m}$ , the unit can also be used as a classifier with slight modifications in the geometry of the channel as

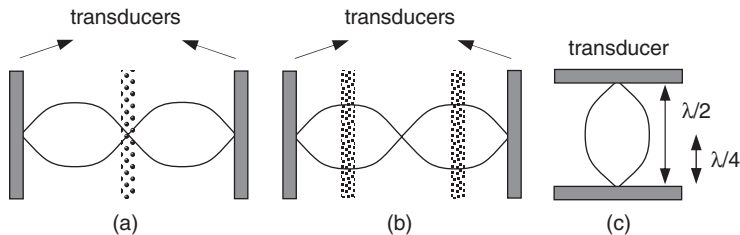


**Figure 8.10** Principle of operation of ultrasonic separators. (a) Collection of dense particles ( $\rho_p \geq \rho_w$ ) at the nodes of a standing wave. (b) Collection of light particles ( $\rho_p \leq \rho_w$ ) at the antinodes of a standing wave. (c) Adjustment of the channel width to bring about separation.

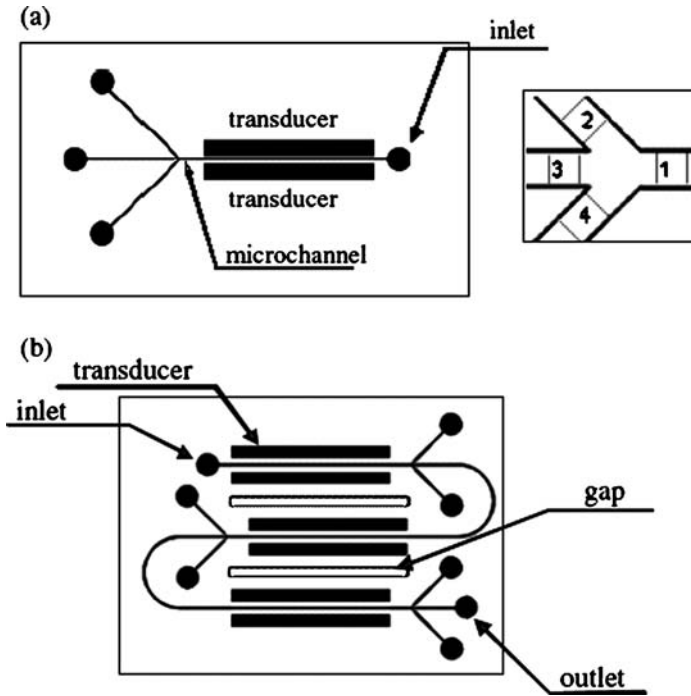


**Figure 8.11** Schematic presentation of the ultrasonic separator. (a) Single stage, (b) Three stages connected in series (Kapishnikov *et al.*, 2006. Reproduced with permission of IOP publishing, Figure 4 in the original).

given in Figure 8.13. Use is made of the fact that the acoustic force will be greater on the larger particles as indicated in eq. (4.42). The node is placed near the lower wall of the channel and the antinode, near the upper wall toward which the lighter particles are diverted.

The performance of the separation efficiency  $\eta$  was evaluated in terms of the clearance constant  $K$ ,

$$K = \frac{N_{\text{out}}}{(N_{\text{in}} - N_{\text{out}})} \quad (8.40)$$

where  $N_{\text{in}}$  and  $N_{\text{out}}$  are the initial and final number concentrations of particles in the inlet and outlet channels, respectively, through the relations,

$$K = \eta \left( \frac{1}{(100 - \eta)} \right) \quad (8.41)$$

$$\eta = \left( \frac{N_{\text{out}}}{N_{\text{in}}} \right) \quad (8.42)$$

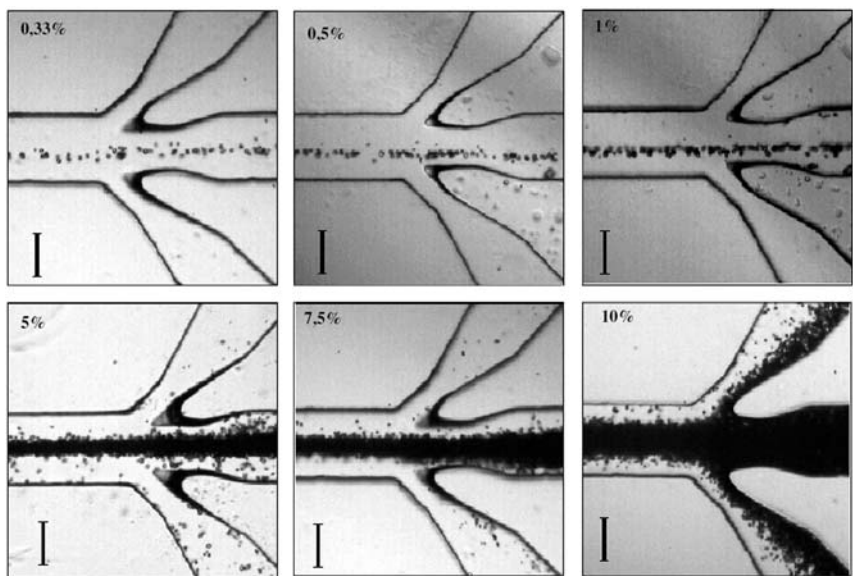


**Figure 8.12** Separation of particles as a function of volumetric concentration of solids (indicated on the figures) in an ultrasonic separator as viewed in a polarized microscope. The scale indicates 100  $\mu\text{m}$ . Particle size  $R = 5 \mu\text{m}$ . (Kapishnikov *et al.*, 2006. Reproduced with permission of IOP publishing, Figure 7 in the original).

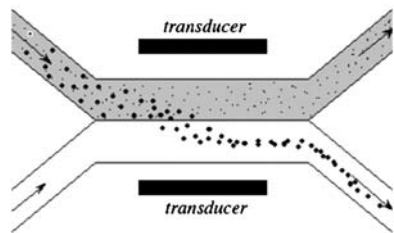


**Figure 8.13** Ultrasonic classification. (Kapishnikov *et al.*, 2006. Reproduced with permission of IOP publishing, Figures 5 and 6 in the original).

The variation of the clearance factor  $K$  is given as a function of the flow rate through the channel and volumetric concentration of solid particles in Figure 8.14. As the flow rate increases, the efficiency of separation decreases. The relation between the efficiency of separation and the volumetric concentration is not linear due to random motion of some of the particles at low volumetric concentrations, scattering of ultrasonic waves on particles, and the interference between the particles at high concentrations.

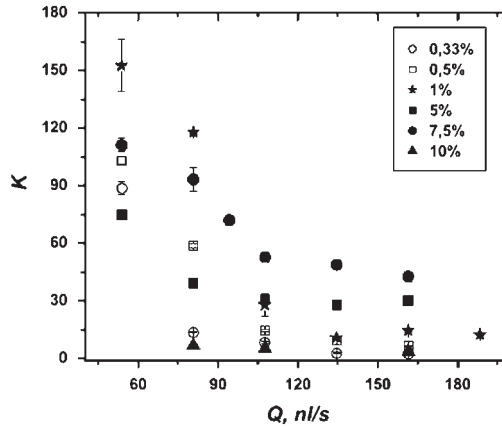


**Figure 8.14** Variation of the clearance coefficient as a function of the flow rate through the microchannel and volumetric concentration of solids. (Kapishnikov *et al.*, 2006. Reproduced with permission of IOP publishing, Figures 5 and 6 in the original).

#### 8.3.4 Separations based on magnetic properties

Magnetic separations in microscale are oriented to microbiological applications at the present, and used in separating pathogenic microorganisms from water, food, or soil medium. Blood cells could also be separated with the aid of magnetic fields (Hirota *et al.*, 2004; Popa *et al.*, 2006).

Since biological microorganisms and blood cells are not magnetic themselves, use is made of other magnetic particles or induced magnetism of the medium. In the immuno-magnetic separation (Rotariu *et al.*, 2002), superparamagnetic carrier microparticles coated with antibodies specific to the pathogenic microorganisms are used in their isolation from a medium. The microorganisms are bound to these carrier particles through random collisions. In the second stage of the process, these particles together with their attached microorganisms are separated under an external magnetic field.

Blood cells could be separated by magneto-Archimedes levitation technique developed by Hirota *et al.* (2004). Levitation technique depends on the difference in densities and magnetic susceptibilities between the particles and the surrounding medium. The magnetic susceptibilities of the components of blood determined by the authors are given in Table 8.7. The differences in the magnetic susceptibilities of the components enable these to be separated from each other under a magnetic field. Since the magnetic properties of the medium are also effective in the separation, the forces acting on the medium is also taken into account in the force balance equations for each component.

$$-\rho_p g + \frac{\chi_p}{\mu_0} B \frac{dB}{dz} + \rho_m g + \frac{\chi_m}{\mu_0} B \frac{dB}{dz} = 0 \quad (8.43)$$

**Table 8.7**

Measured magnetic susceptibilities and densities of biological materials

Name of sample	Density, $\rho$ ( $10^3 \text{ kg m}^{-3}$ )	Magnetic susceptibility, $\chi$ ( $10^{-6}$ )
Hemoglobin	1.33	−3.38
Fibrinogen	1.57	−6.12
Cholesterol	1.02	−7.61
Albumin	1.28	−5.68
DNA	1.28	−4.99

Source: Hirota *et al.*, 2004. Redrawn with permission of Elsevier, Table 1 in the original.

The subscript p denotes the particles and m, the medium in this equation.  $\mu_0$  is the magnetic permeability of vacuum [ $\text{T mA}^{-1}$ ],  $\chi$  is the magnetic susceptibility and  $B$  is the magnetic induction related to the magnetic field strength  $H$  through the relation,

$$B = \mu_0(H + M) = \mu_0(1 + \chi_m)H = \mu H. \quad (8.44)$$

$\mu$  and  $M$  in this equation are the permeability and the magnetization of the material. At equilibrium, the total forces acting on the particles are equal to the total forces acting on the medium. Therefore, each component has a definite, specific levitation position that cannot be changed. When the particles are diamagnetic and the medium is paramagnetic, a buoyancy force is exerted on the particles that pushes them upwards. The required field conditions,  $B(dB/dz)$ , decrease with the pressure of the medium, (i.e., oxygen gas) at a rate depending on the component. The order of separation (levitation) of the components can be controlled by changing the magnetic field conditions and the pressure of the medium.

### 8.3.5 Separations based on electrical properties

Electrically driven flow of electrolytic solutions in microchannels, electro osmotic flow (EOF) is controlled by the surface charge of the adsorbed layers on the walls of the microchannels. Adsorbed ionic species can be simple ions as well as polyelectrolytes and zwitterionic surfactants. The factors affecting flow are the electrical charge density of the walls, the applied electrical field and the zeta potential of the microchannel walls. By changing the charge of the adsorbed layers, the direction of flow can be changed. Flow in different directions can be obtained even within the same channel, by changing the surface charge of the adsorbed layers of polyelectrolytes [Barker *et al.*, 2000; Sui and Schlenoff, 2003]. A double layer forms along the walls by preferential adsorption of oppositely charged ions from the flowing electrolyte solution. The thickness of the double layer, or equivalently the Debye length of the diffuse ionic cloud along the walls depends on the ionic strength  $I$

$$I = \sum_i^N z_i^n C_i \quad (8.45)$$

with the notation of Chapter 1) of the flowing electrolyte solution.

The velocity profile in fully developed microchannel flow is uniform nearly up to the electrical double layer, within the order of nanometers, depending on the Debye length of the diffuse double layer. The average velocity, observed by tracer particles with nanoparticle image velocimeter technique (Sadr *et al.*, 2004) varies linearly with the applied electrical field and the zeta potential of the microchannel walls. In electro-osmotic flow, the volumetric flow rate was found to vary directly with the height (or the equivalent diameter of the channel) instead of with its cube as in the case of pressure driven flow. Of special technological interest is the phenomenon known as electrokinetic pumping, the increase of the flow rate in electro-osmotic flow above that of pressure driven flows in microchannels with dimensions less than about 10 nm.

Separation in EOF is either based on the difference in mobilities of the components or by preferential adsorption on the charged walls. Separation by electro-osmotic mobility is similar to chromatographic separation, with the difference in the driving force, electric field instead of a pressure field. An example for the recent applications is the separation of DNA. The electro-osmotic mobility  $\mu_{eo}$ , is defined as the bulk electro-osmotic speed divided by the driving electric field  $E$ , (Sadr *et al.*, 2004). Electro-osmotic mobility depends on the electrical permittivity  $\epsilon_e$  and viscosity  $\mu$  of the fluid, wall mol fraction of cationic  $g^o$  and anionic  $f^o$  species and the Faraday constant,  $F$ , in the model proposed by Conlisk *et al.* (2002):

$$\mu_{eo} = \frac{\epsilon_e RT}{2\mu F} \ln \left( \frac{g^o}{f^o} \right) \quad (8.46)$$

Separation by preferential adsorption on the surfaces of microchannels by immobilized protein structures is a recently developed process. To separate blood cells, biomimetic surfaces were created with the use of phospholipid polymers [Ito *et al.*, 2005]. Blood cells that adsorbed on these surfaces were found to retain their original morphology.

## REFERENCES

- Abbott, J., 1968. The design and performance of hydrocyclones on viscous suspensions. PhD Thesis, University of Leeds, England.
- Abdelsalam, M.K., 1987. Theory of separation in the helical flow superconducting magnetic ore separator. IEEE Transactions on Magnetics, 23(5), 2758–2760.
- Barker, S.L.R., Ross, D., Tarlov, M.J., Gaitan, M., Locascio, L.E., 2000. Control of flow direction in microfluidic devices with polyelectrolyte multilayers. Analytical Chemistry, 72(24), 5925–5929.
- Bekker, M.C., Meyer, J.P., Pretorius, L., Van Der Merve, D.F., 1997. Separation of solid–liquid suspensions with ultrasonic acoustic energy. Water Research, 31(10), 2543–2549.
- Besendorfer, C., 1996. Exert force of hydrocyclone. Chemical Engineering, 9, 108–114.
- Chen, A., Grace, J.R., Epstein, N., Lim, C.J., 2002. Steady state dispersion of mono-size, binary and multi-size particles in a liquid fluidized bed classifier. Chemical Engineering Science, 57, 991–1002.
- Conlisk, A.T., McFerran, J., Zheng, Z., Hansford, D.J., 2002. Mass transfer and flow in electrically charged micro- and nano- channels. Analytical Chemistry, 74, 2139–2150.

- Davis, R.H., Gecol, H., 1996. Classification of concentrated suspensions using inclined settlers. *International Journal of Multiphase Flow*, 22, 563–574.
- Flintoff, B.C., Plitt, L.R., Turak, A.A., 1987. Cyclone modeling a review of present technologies. *CIM Bulletin*, 80, 39–50.
- Garcia-Martinez, H.A., Llamas-Bueno, M., Song, S., Lopez-Valdivieso, A., 2004. Magnetic flocculation of mineral fines in an external magnetic field. *Mineral Processing & Extractive Metallurgy Review*, 25, 67–90.
- Hirota, N., Kurashige, M., Iwasaka, M., Ikehata, M., Uetake, H., Takayama, T., Nakamura, H., Ikezoe, Y., Ueno, S., Kitazawa, K., 2004. Magneto-Archimedes separation and its application to the separation of biological materials. *Physica B*, 346–347, 267–271.
- Ito, T., Iwasaki, T., Natira, T., Akiyoshi, K., Ishihara, K., 2005. Cell separation in microcanal coated with electrically charged phospholipid polymers. *Colloids and Surfaces B: Biointerfaces*, 41, 175–180.
- Kapishnikov, S., Kantsler, V., Steinberg, V., 2006. Continuous particle size separation and size sorting using ultrasound in a microchannel. *Journal of Statical Mechanics: Theory and Experiment*, P01012, 1–15.
- Kind, M., 2002. Colloidal aspects of precipitation processes. *Chemical Engineering Science*, 57, 4287–4293.
- Kraipech, W., Chen, W., Dyakowski, T., Nowakowski, A., 2006. The performance of the empirical models on industrial hydrocyclone design. *International Journal of Mineral Processing*, 80, 100–115.
- Li, Y., Rudman, M., Brown, G., 1998. Particle transport in a bottom-feed separation vessel. *Applied Mathematical Modelling*, 22, 1023–1036.
- Lynch, A.J., Rao, T.C., 1968. Studies on the operating characteristics of hydrocyclone classifiers. *Indian Journal of Technology*, 6, 106–114.
- Moder, J.J., Dahlstrom, D.A., 1952. Fine-size, close-specific solid separation with the liquid–solid cyclone. *Chemical Engineering Progress*, 48, 75–88.
- Monredon, T.C., Hsieh, K.T., Rajamani, R.K., 1992. Fluid flow model of the hydrocyclone: An investigation of device dimensions. *International Journal of Mineral Processing*, 35, 65–83.
- Murariu, V., Svoboda, P., Sergeant, P., 2005. The modelling of the separation process in a ferrohydrostatic separator. *Minerals Engineering*, 18, 449–457.
- Nageswararao, K., 1995. A Generalized model for hydrocyclone classifiers. *Australasian Institute of Mining and Metallurgy Proceedings*, 300, 21–29.
- Nguyentranlam, G., Galvin, K. P., 2004. Applications of the reflux classifier in solid–liquid operations. *International Journal of Mineral Processing*, 73, 83–89.
- Plitt, L.R., 1971. The analysis of solid–solid separations in classifiers. *CIM Bulletin*, 64, 42–47.
- Popa, C., Su, B., Vadgama, P., Cotter, F., 2006. Magnetic counter-gravity flow separation of electrically prepolarised lymphoid cells. *British Journal of Haematology*, 136, 433–438.
- Rasouli, S., Blanchart, P., Clédat, D., J.P. Cardot, P., 2001. Size- and shape dependent separation of  $\text{TiO}_2$  colloidal sub-populations with gravitational field flow fractionation. *Journal of Chromatography A*, 923, 119–126.
- Roberts, B.W., Olbricht, W.L., 2006. The distribution of freely suspended particles at microfluidic bifurcations. *American Institute of Chemical Engineers AIChE Journal*, 52, 199–206.
- Rotariu, O., Strachan, N.J.C., Badescu, V., 2002. Modelling of microorganism capture on magnetic carrier particles. *Journal of Magnetism and Magnetic Materials* 252, 390–392.
- Sadr, R., Yoda, M., Zheng, Z., Conlisk, A.T., 2004. An experimental study of electro-osmotic flow in rectangular microchannels. *Journal of Fluid Mechanics*, 506, 357–367.
- Smolkin, M.R., Smolkin, R.D., 2006. Calculation and analysis of the magnetic force acting on a particle in the magnetic field of separator. Analysis of the equations used in the magnetic methods of separation. *IEEE Transactions on Magnetics*, 42(11), 3682–3693.

- Sui, Z., Schlenoff, J.B., 2003. Controlling electroosmotic flow in microchannels with pH-responsive polyelectrolyte multilayers. *Langmuir*, 19, 7829–7831.
- Svarovsky, L., 1994. A short course in cyclones. Manual to Course at the Dow Chemical Co., Freeport, Texas, USA, January 10–11.
- Svoboda, J., Fujita, T., 2003. Recent developments in magnetic methods of material separation. *Minerals Engineering*, 16, 785–792.
- Tarjan, G., 1961. Some theoretical questions on classifying and separating in hydrocyclones. *Acta Technica Hungaria*, 32, 357–388.
- Yoshida, H., Takashina, T., Fukui, K., Iwanaga, T., 2004. Effect of inlet shape and slurry temperature on the classification performance of hydro-cyclones. *Powder Technology*, 140, 1–9.
- Yoshioka, N., Hotta, Y., 1955. Liquid cyclone as a hydraulic classifier. *Chemical Engineering Japan*, 19, 632–641.



This page intentionally left blank

# Appendix A

## Mathematical Operations

---

### APPENDIX A1: DERIVATIVES, VECTOR, AND TENSOR OPERATIONS

#### A1.1 Substantial derivative

A change of a property (i.e., density, concentration, solid volume fraction, velocity, etc.) with respect to time  $t$  in the control volume at a fixed location is expressed as the *partial derivative*,  $(\partial/\partial t)_{x,y,z}$ . A balance equation written in terms of changes that occur at a fixed point in space is in the *Eulerian* form (Bird *et.al.*, 2002; Faheini, 1983). Volumetric fraction of solids suspended in a liquid medium can be given as an example of a property that changes with respect to both time and position. The total derivative of the volumetric fraction of solids is then

$$d\phi = \frac{\partial\phi}{\partial t} dt + \frac{\partial\phi}{\partial x} dx + \frac{\partial\phi}{\partial y} dy + \frac{\partial\phi}{\partial z} dz \quad (\text{A1.1})$$

The variation in the position of the control volume with respect to time gives the local fluid velocities in each direction

$$V_x = \frac{dx}{dt}, \quad V_y = \frac{dy}{dt}, \quad V_z = \frac{dz}{dt} \quad (\text{A1.2})$$

Dividing each term by  $dt$  and using the above equation yields

$$\frac{D\phi}{Dt} = \left( \frac{d\phi}{dt} \right)_{\text{moving with fluid}} = \frac{\partial\phi}{\partial t} + \underbrace{V_x \frac{\partial\phi}{\partial x} + V_y \frac{\partial\phi}{\partial y} + V_z \frac{\partial\phi}{\partial z}}_{\text{rate of change of } \phi \text{ with time due to fluid motion}} \quad (\text{A1.3})$$

The derivative  $(D/Dt)$  in this equation indicates the rate of change of the property for an observer moving with the fluid which is the *Lagrangian approach* (Bird *et al.*, 2002). This derivative is known as *convective*, *substantial*, or *material derivative*. The convective derivative (eq. (A1.3)) can also be considered in two parts: the first term on the RHS

indicates the rate of change of the property with time at a fixed point which corresponds to the *Eulerian approach*. The last three terms on RHS emphasize the rate of change of the property with time due to the fluid motion as explained in the equation. Hence, the convective differential derivative of the solid volume fraction in terms of  $\nabla$  operator is

$$\frac{D\phi}{Dt} = \frac{\partial\phi}{\partial t} + \mathbf{V} \cdot \nabla\phi \tag{A1.4}$$

where  $\mathbf{V}$  is the velocity vector. The convective operator for any property is defined as

$$\frac{D}{Dt} = \frac{\partial}{\partial t} + V_x \frac{\partial}{\partial x} + V_y \frac{\partial}{\partial y} + V_z \frac{\partial}{\partial z} = \frac{\partial}{\partial t} + \mathbf{V} \cdot \nabla \tag{A1.5}$$

**A1.2 Tensors**

Tensors are most general form of representation of quantities. Vectors and tensors are sub-groups of tensor with reduced number of dimensions. They are explained in Table A1.1. The multiplication signs related to tensors and their results are summarized in Table A1.2.

**A1.3 First-order tensors (vectors)**

Vector definitions in terms of:

- vectorial components on the coordinate axes 1–3:

$$\mathbf{v} = \mathbf{v}_1 + \mathbf{v}_2 + \mathbf{v}_3 = \sum_{i=1}^{i=3} \mathbf{v}_i \tag{A1.6}$$

**Table A1.1**

Tensors encountered in balance equations

Tensor	Name	Notation	A quantity which	Property	Example
Zero order	Scalar	$s$	Has only magnitude	Magnitude	Time, volume, mass, energy, temperature
First order	Vector	$\mathbf{v}$	Associates a scalar with each coordinate direction	Magnitude <sup>a</sup> and direction	Velocity, force, momentum, acceleration
Second order	Tensor	$\mathbf{T}$	Associates (a) a vector with each coordinate direction or (b) a scalar with each ordered pair of directions	Magnitude and direction	Shear stress, shear rate, vorticity, etc.

<sup>a</sup>Except zero vector. It has zero length and arbitrary direction.

**Table A1.2**

The operations on tensors

Product	Product sign	Calculation of order	Example	Results of example	
				Order	Notation
Dyadic	None	Sum of the orders, $\Sigma$	Scalar and a vector	$0 + 1 = 1 \equiv \text{vector}$	$s\mathbf{v}$
			Two vectors	$1 + 1 = 2 \equiv \text{tensor}$	$\mathbf{vu}$
Scalar	$\cdot$	$\Sigma - 2$	Identical vector	$1 + 1 - 2 = 0 \equiv \text{scalar}$	$\mathbf{v} \cdot \mathbf{v} =  \mathbf{v} ^2 = v^2$
			Two vectors	$1 + 1 - 2 = 0 \equiv \text{scalar}$	$\mathbf{v} \cdot \mathbf{u} =  \mathbf{v}  \mathbf{u}  \cos \theta_{vu}$
			Second-order tensor and a vector	$2 + 1 - 2 = 1 \equiv \text{vector}$	$\mathbf{T} \cdot \mathbf{v}$
			Two second-order tensors	$2 + 2 - 2 = 2 \equiv \text{tensor}$	$\mathbf{T} \cdot \boldsymbol{\gamma}$
			Identical vectors	$1 + 1 - 1 = 1 \equiv \text{vector}$	$\mathbf{v} \times \mathbf{v} = 0$
			Two vectors	$1 + 1 - 1 = 1 \equiv \text{vector}$	$\mathbf{v} \times \mathbf{u} = (vu \sin \theta_{vu}) \mathbf{n}_{vu}$
Vector (cross)	$\times, \otimes$	$\Sigma - 1$			
Double dot (scalar)	$:$	$\Sigma - 4$	Second-order tensors	$2 + 2 - 4 = 0 \equiv \text{scalar}$	$\mathbf{T} : \boldsymbol{\gamma}$

- unit vectors on the coordinate axes 1–3:

$$\mathbf{v} = v_1 \boldsymbol{\delta}_1 + v_2 \boldsymbol{\delta}_2 + v_3 \boldsymbol{\delta}_3 = \sum_{i=1}^{i=3} v_i \boldsymbol{\delta}_i \quad (\text{A1.7})$$

where  $v_1, v_2$ , and  $v_3$  are the magnitudes of the projections of  $\mathbf{v}$  vector on the coordinate axes 1, 2, and 3. Here,  $\boldsymbol{\delta}_1, \boldsymbol{\delta}_2$ , and  $\boldsymbol{\delta}_3$  are *unit vectors* with unit length in the direction of the 1, 2, and 3 axes.

Two vectors  $\mathbf{v}$  and  $\mathbf{u}$  are equal when their magnitudes are equal and they point in the same direction:

$$\mathbf{v} = \mathbf{u}, \quad \text{if } v_1 = u_1, v_2 = u_2, v_3 = u_3 \quad (\text{A1.8})$$

If  $\mathbf{v}$  and  $\mathbf{u}$  have the same magnitude and they are in opposite directions,  $\mathbf{v}$  and  $\mathbf{u}$  are equal but reverse vectors:

$$\mathbf{v} = -\mathbf{u}, \quad \text{if } v_1 = -u_1, v_2 = -u_2, v_3 = -u_3 \quad (\text{A1.9})$$

Magnitude of a vector,  $|\mathbf{v}|$ :

$$|\mathbf{v}| = v = \sqrt{v_1^2 + v_2^2 + v_3^2} = \sqrt{\sum_{i=1}^{i=3} v_i^2} \quad (\text{A1.10})$$

### A1.3.1 First-order tensor (vector) operations

Properties of unit vectors summarized in Table A1.3 are useful in vector operations. Equations given below are examples of operations on vectors. The properties of these vector operations can be seen in Table A1.4.

*Addition and subtraction of vectors:*

$$\mathbf{v} + \mathbf{u} = \sum_{i=1}^{i=3} v_i \delta_i + \sum_{i=1}^{i=3} u_i \delta_i = \sum_{i=1}^{i=3} \delta_i (v_i + u_i) \quad (\text{A1.11})$$

$$\mathbf{v} - \mathbf{u} = \sum_{i=1}^{i=3} v_i \delta_i - \sum_{i=1}^{i=3} u_i \delta_i = \sum_{i=1}^{i=3} \delta_i (v_i - u_i) \quad (\text{A1.12})$$

**Table A1.3**

Properties of unit vectors

Product		Summary
Scalar (dot)	$(\delta_1 \cdot \delta_1) = (\delta_2 \cdot \delta_2) = (\delta_3 \cdot \delta_3) = 1$ $(\delta_1 \cdot \delta_2) = (\delta_2 \cdot \delta_3) = (\delta_3 \cdot \delta_1) = 0$	$(\delta_i \cdot \delta_j) = \delta_{ij}$
Vector (cross)	$(\delta_1 \times \delta_1) = (\delta_2 \times \delta_2) = (\delta_3 \times \delta_3) = 0$ $(\delta_1 \times \delta_2) = \delta_3, (\delta_2 \times \delta_3) = \delta_1, (\delta_3 \times \delta_1) = \delta_2$ $(\delta_2 \times \delta_1) = -\delta_3, (\delta_3 \times \delta_2) = -\delta_1, (\delta_1 \times \delta_3) = -\delta_2$	$(\delta_i \times \delta_j) = \sum_{k=1}^3 \varepsilon_{ijk} \delta_k$

$\delta_{ij}$  : Kronecker delta and  $\varepsilon_{ijk}$  : the alternating unit tensor.

**Table A1.4**

Operations on first-order tensors (vectors)

Operations on vectors	Property	Algebraic rules satisfied
Addition	Commutative Associative Identity Inverse	$\mathbf{v} + \mathbf{u} = \mathbf{u} + \mathbf{v}$ $\mathbf{w} + (\mathbf{v} + \mathbf{u}) = (\mathbf{w} + \mathbf{v}) + \mathbf{u}$ $\mathbf{v} + 0 = \mathbf{v}$ $\mathbf{v} + (-\mathbf{v}) = 0$
Subtraction		$\mathbf{v} - \mathbf{u} = \mathbf{v} + (-\mathbf{u})$
Multiplication by a scalar	Associative Identity Distributive Distributive	$\alpha(\beta\mathbf{v}) = (\alpha\beta)\mathbf{v}$ $1\mathbf{v} = \mathbf{v}$ $\alpha(\mathbf{v} + \mathbf{u}) = \alpha\mathbf{v} + \alpha\mathbf{u}$ $(\alpha + \beta)\mathbf{v} = \alpha\mathbf{v} + \beta\mathbf{v}$
Scalar (dot) product of two vectors	Commutative Not associative Distributive Distributive	$\mathbf{v} \cdot \mathbf{u} = \mathbf{u} \cdot \mathbf{v}$ $\mathbf{w} \cdot (\mathbf{v} \cdot \mathbf{u}) \neq (\mathbf{w} \cdot \mathbf{v}) \cdot \mathbf{u}$ $\mathbf{w} \cdot (\mathbf{v} \cdot \mathbf{u}) = \mathbf{w} \cdot \mathbf{v} + \mathbf{w} \cdot \mathbf{u}$ $(\beta\mathbf{w}) \cdot (\mathbf{v} + \mathbf{u}) = \mathbf{w} \cdot (\beta\mathbf{v}) + \beta(\mathbf{w} \cdot \mathbf{u})$
Vector (cross) product of two vectors	Not commutative Not associative Distributive Associative w.r.t. scalar multiplication	$\mathbf{v} \times \mathbf{u} \neq \mathbf{u} \times \mathbf{v}$ $\mathbf{w} \times (\mathbf{v} \times \mathbf{u}) \neq (\mathbf{w} \times \mathbf{v}) \times \mathbf{u}$ $(\mathbf{w} + \mathbf{v}) \times \mathbf{u} = \mathbf{w} \times \mathbf{u} + \mathbf{v} \times \mathbf{u}$ $\beta(\mathbf{v} \times \mathbf{u}) = \beta\mathbf{v} \times \mathbf{u} = \mathbf{v} \times \beta\mathbf{u}$

*Multiplication of a vector by a scalar results in a vector:*

$$s\mathbf{v} = s \sum_{i=1}^{i=3} v_i \boldsymbol{\delta}_i = \sum_{i=1}^{i=3} \boldsymbol{\delta}_i (sv_i) \quad (\text{A1.13})$$

*Dyadic product of two vectors:*

$$\mathbf{vu} = (v_1 \quad v_2 \quad v_3)(u_1 \quad u_2 \quad u_3) = \begin{pmatrix} v_1 u_1 & v_1 u_2 & v_1 u_3 \\ v_2 u_1 & v_2 u_2 & v_2 u_3 \\ v_3 u_1 & v_3 u_2 & v_3 u_3 \end{pmatrix} \quad (\text{A1.14})$$

*Dot product of two vectors results in a scalar:*

$$\mathbf{v} \cdot \mathbf{u} = \left( \sum_{i=1}^{i=3} v_i \boldsymbol{\delta}_i \right) \cdot \left( \sum_{i=1}^{i=3} u_i \boldsymbol{\delta}_i \right) = \sum_{i=1}^{i=3} v_i u_i \quad (\text{A1.15})$$

*Cross product of two vectors results in a vector:*

$$\begin{aligned} \mathbf{v} \times \mathbf{u} &= \left( \sum_{j=1}^{j=3} v_j \boldsymbol{\delta}_j \right) \times \left( \sum_{k=1}^{k=3} u_k \boldsymbol{\delta}_k \right) = \sum_{j=1}^{j=3} \sum_{k=1}^{k=3} (\boldsymbol{\delta}_j \times \boldsymbol{\delta}_k) v_j u_k \\ &= \sum_{i=1}^{i=3} \sum_{j=1}^{j=3} \sum_{k=1}^{k=3} \epsilon_{ijk} \boldsymbol{\delta}_i v_j u_k = \begin{vmatrix} \boldsymbol{\delta}_1 & \boldsymbol{\delta}_2 & \boldsymbol{\delta}_3 \\ v_1 & v_2 & v_3 \\ u_1 & u_2 & u_3 \end{vmatrix} \end{aligned} \quad (\text{A1.16})$$

Some identities in multiple vector product operations are tabulated in Table A1.5. An example to multiple vector products is

$$\mathbf{w} \cdot (\mathbf{v} \times \mathbf{u}) = \sum_{i=1}^{i=3} w_i (\mathbf{v} \times \mathbf{u})_i = \sum_{i=1}^{i=3} \sum_{j=1}^{j=3} \sum_{k=1}^{k=3} \epsilon_{ijk} w_i v_j u_k = \begin{vmatrix} w_1 & w_2 & w_3 \\ v_1 & v_2 & v_3 \\ u_1 & u_2 & u_3 \end{vmatrix} \quad (\text{A1.17})$$

**Table A1.5**

Identities of multiple vector products

---

Multiplication

---

$$\begin{aligned} \mathbf{w} \cdot (\mathbf{v} \times \mathbf{u}) &= \mathbf{v} \cdot (\mathbf{u} \times \mathbf{w}) \\ \mathbf{w} \times (\mathbf{v} \times \mathbf{u}) &= \mathbf{v} \cdot (\mathbf{w} \times \mathbf{u}) - \mathbf{u} \cdot (\mathbf{w} \times \mathbf{v}) \\ (\mathbf{w} \times \mathbf{v}) \cdot (\mathbf{u} \times \mathbf{z}) &= (\mathbf{w} \cdot \mathbf{u})(\mathbf{v} \cdot \mathbf{z}) - (\mathbf{w} \cdot \mathbf{z})(\mathbf{v} \cdot \mathbf{u}) \\ (\mathbf{w} \times \mathbf{v}) \times (\mathbf{u} \times \mathbf{z}) &= ((\mathbf{w} \times \mathbf{v}) \cdot \mathbf{z})\mathbf{u} - ((\mathbf{w} \times \mathbf{v}) \cdot \mathbf{u})\mathbf{z} \end{aligned}$$


---

### A1.4 Second-order tensors (tensors)

A vector  $\mathbf{v}$  is specified by giving a set of components  $v_1$ ,  $v_2$ , and  $v_3$  in Section A1.2. A second-order tensor  $\mathbf{T}$  is similarly specified by giving the nine components  $T_{11}$ ,  $T_{12}$ ,  $T_{13}$ ,  $T_{21}$ , etc. Transpose of a tensor,  $\mathbf{T}^T$ , is the replacement of its columns by its rows as follows:

Tensor:

$$\mathbf{T} = \begin{pmatrix} T_{11} & T_{12} & T_{13} \\ T_{21} & T_{22} & T_{23} \\ T_{31} & T_{32} & T_{33} \end{pmatrix}$$

and transpose of a tensor:

$$\mathbf{T}^T = \begin{pmatrix} T_{11} & T_{21} & T_{31} \\ T_{12} & T_{22} & T_{32} \\ T_{13} & T_{23} & T_{33} \end{pmatrix}$$

*Unit tensor:* If the components of the tensor are given by the Kronecker delta  $\delta_{ij}$ , the result is unit tensor which is shown as  $\delta$

$$\delta = \sum_i \sum_j \delta_i \delta_j \delta_{ij} \quad (\text{A1.18})$$

A tensor can be written as the sum of three “double vectors (dyads)”

$$\mathbf{T} = \delta_1 \mathbf{t}_1 + \delta_2 \mathbf{t}_2 + \delta_3 \mathbf{t}_3 \quad (\text{A1.19})$$

#### A1.4.1 Tensor operations

*Addition of tensors and dyadic products:*

$$\mathbf{T} + \gamma = \sum_i \sum_j \delta_i \delta_j T_{ij} + \sum_i \sum_j \delta_i \delta_j \gamma_{ij} = \sum_i \sum_j \delta_i \delta_j (T_{ij} + \gamma_{ij}) \quad (\text{A1.20})$$

*Dyadic products:* The dyad has two directions, one of them is the plane on which the stress vector acts and the other one is the direction of the vector itself. Dot product of a normal vector,  $\mathbf{n}$ , and a tensor,  $\mathbf{T}$ , is a standard matrix multiplication, and its result is a vector,  $\mathbf{t}_n$

$$\mathbf{t}_n = \mathbf{n} \cdot \mathbf{T} = \begin{pmatrix} n_1 & n_2 & n_3 \end{pmatrix} \begin{bmatrix} T_{11} & T_{12} & T_{13} \\ T_{21} & T_{22} & T_{23} \\ T_{31} & T_{32} & T_{33} \end{bmatrix} = \begin{bmatrix} n_1 T_{11} + n_2 T_{21} + n_3 T_{31} \\ n_1 T_{12} + n_2 T_{22} + n_3 T_{32} \\ n_1 T_{13} + n_2 T_{23} + n_3 T_{33} \end{bmatrix} = \begin{bmatrix} A_1 \\ A_2 \\ A_3 \end{bmatrix} \quad (\text{A1.21})$$

The magnitude of a vector is given as

$$|\mathbf{t}_n| = (\mathbf{t}_n \mathbf{t}_n)^{1/2} \quad (\text{A1.22})$$

$$|\mathbf{t}_n| = (\mathbf{t}_n \mathbf{t}_n)^{1/2} = \left[ (A_1 \quad A_2 \quad A_3) \begin{bmatrix} A_1 \\ A_2 \\ A_3 \end{bmatrix} \right]^{1/2} = (A_1^2 + A_2^2 + A_3^2)^{1/2} \quad (\text{A1.23})$$

The expansion of eq. (A1.22) yields

$$|\mathbf{t}_n| = ((n_1 T_{11} + n_2 T_{21} + n_3 T_{31})^2 + (n_1 T_{12} + n_2 T_{22} + n_3 T_{32})^2 + (n_1 T_{13} + n_2 T_{23} + n_3 T_{33})^2)^{1/2} \quad (\text{A1.24})$$

*Multiplication of a tensor by a scalar:*

$$s\mathbf{T} = \sum_i \sum_j \delta_i \delta_j T_{ij} = \sum_i \sum_j \delta_i \delta_j (sT_{ij}) \quad (\text{A1.25})$$

*Dot product of two tensors:*

$$\mathbf{T} \cdot \boldsymbol{\gamma} = \left( \sum_i \sum_j \delta_i \delta_j T_{ij} \right) \cdot \left( \sum_k \sum_l \delta_k \delta_l \gamma_{kl} \right) = \sum_i \sum_l \delta_i \delta_l \left( \sum_j T_{ij} \gamma_{jl} \right) \quad (\text{A1.26})$$

*Dot product of a tensor with a vector:*

$$\mathbf{T} \cdot \mathbf{v} = \left( \sum_i \sum_j \delta_i \delta_j T_{ij} \right) \cdot \left( \sum_k \delta_k v_k \right) = \sum_i \delta_i \left( \sum_j T_{ij} v_j \right) \quad (\text{A1.27})$$

*Cross product of a tensor with a vector:*

$$\begin{aligned} \mathbf{T} \times \mathbf{v} &= \left( \sum_i \sum_j \delta_i \delta_j T_{ij} \right) \times \left( \sum_k \delta_k v_k \right) \\ &= \sum_i \sum_j \sum_k (\delta_i \delta_j \times \delta_k) T_{ij} v_k = \sum_i \sum_l \delta_i \delta_l \left( \sum_j \sum_k \varepsilon_{jkl} T_{ij} v_k \right) \end{aligned} \quad (\text{A1.28})$$

*Symmetric tensors:* If a tensor  $\mathbf{T}$  is symmetric,  $\mathbf{T} = \mathbf{T}^T$  and  $\mathbf{T}^T$  is given as

$$\mathbf{T}^T = \sum_i \sum_j \delta_i \delta_j T_{ji} = \sum_i \sum_j \delta_i \delta_j (T_{ij})^T \quad (\text{A1.29})$$



For a symmetric tensor,  $\mathbf{t}_n$  is also defined in terms of  $\mathbf{T}^T$  as

$$\mathbf{t}_n = \mathbf{n} \cdot \mathbf{T} = \mathbf{T}^T \cdot \mathbf{n} \quad (\text{A1.30})$$

$$\mathbf{t}_n = \mathbf{T}^T \mathbf{n} = \begin{bmatrix} T_{11} & T_{21} & T_{31} \\ T_{12} & T_{22} & T_{32} \\ T_{13} & T_{23} & T_{33} \end{bmatrix} \begin{pmatrix} n_1 & n_2 & n_3 \end{pmatrix} = \begin{bmatrix} n_1 T_{11} + n_2 T_{21} + n_3 T_{31} \\ n_1 T_{12} + n_2 T_{22} + n_3 T_{32} \\ n_1 T_{13} + n_2 T_{23} + n_3 T_{33} \end{bmatrix} \quad (\text{A1.31})$$

### A1.5 Vector and tensor differential operations

The vector differential operator  $\nabla$ , known as “nabla” or “del,” is defined in rectangular coordinates as

$$\nabla = \delta_1 \frac{\partial}{\partial x_1} + \delta_2 \frac{\partial}{\partial x_2} + \delta_3 \frac{\partial}{\partial x_3} = \sum_{i=1}^3 \delta_i \frac{\partial}{\partial x_i} \quad (\text{A1.32})$$

where  $x_i$  are the variables associated with 1, 2, and 3 axes.  $x_i$  are the position coordinates normally referred as  $x$ ,  $y$ , and  $z$ .  $\nabla$  cannot stand alone and must operate on scalar, vector, or tensor function. The various uses of  $\nabla$  in its operations on scalars and vectors and their properties are summarized in Tables A1.6–A1.8.

Similarly Laplacian operator is

$$\nabla^2 = \frac{\partial^2}{\partial x_1^2} + \frac{\partial^2}{\partial x_2^2} + \frac{\partial^2}{\partial x_3^2} = \sum_{i=1}^3 \frac{\partial^2}{\partial x_i^2} \quad (\text{A1.33})$$

**Table A1.6**

Operations on the vector differential equations

$\nabla$ operations on	Operation	Property	Algebraic rules satisfied
Scalar	Dyadic product by a scalar	Not commutative	$(\nabla s) \neq s \nabla$
		Not associative	$(\nabla r)s \neq (\nabla rs)$
		Distributive	$\nabla(r + s) = \nabla r + \nabla s$
Vector	Scalar (dot) product by a vector	Not commutative	$(\nabla \cdot \mathbf{v}) \neq (\mathbf{v} \cdot \nabla)$
		Not associative	$(\nabla \cdot s\mathbf{v}) \neq (\nabla s \cdot \mathbf{v})$
		Distributive	$(\nabla \cdot (\mathbf{v} + \mathbf{u})) = (\nabla \cdot \mathbf{v}) + (\nabla \cdot \mathbf{u})$
	Scalar (dot) product of two vectors	Commutative	$(\mathbf{u} \cdot \mathbf{v}) = (\mathbf{v} \cdot \mathbf{u})$
		Associative	$(\nabla \cdot \mathbf{uv}) = (\nabla \mathbf{u} \cdot \mathbf{v})$
		Distributive	$(\nabla \cdot (\mathbf{v} + \mathbf{u})) = (\nabla \cdot \mathbf{v}) + (\nabla \cdot \mathbf{u})$
	Vector (cross) product of two vectors	Not commutative	$(\mathbf{u} \times \mathbf{v}) \neq (\mathbf{v} \times \mathbf{u})$
		Associative	$(\nabla \times \mathbf{uv}) = (\nabla \mathbf{u} \times \mathbf{v})$
		Distributive	$(\nabla \times (\mathbf{v} + \mathbf{u})) = (\nabla \times \mathbf{v}) + (\nabla \times \mathbf{u})$

Delta,  $\nabla$ , and Laplacian operators,  $\nabla^2$ , for cylindrical coordinates are

$$\nabla = \delta_r \frac{\partial}{\partial r} + \delta_\theta \frac{\partial}{r \partial \theta} + \delta_z \frac{\partial}{\partial z} \quad (\text{A1.34})$$

$$\nabla^2 = \frac{\partial}{r \partial r} \left( \frac{\partial}{\partial r} \right) + \frac{\partial^2}{r^2 \partial \theta^2} + \frac{\partial^2}{\partial z^2} \quad (\text{A1.35})$$

and for spherical coordinates are

$$\nabla = \delta_r \frac{\partial}{\partial r} + \delta_\theta \frac{\partial}{r \partial \theta} + \delta_\varphi \frac{\partial}{\sin \theta \partial \varphi} \quad (\text{A1.36})$$

$$\nabla^2 = \frac{\partial}{r^2 \partial r} \left( r^2 \frac{\partial}{\partial r} \right) + \frac{\partial}{r^2 \sin \theta \partial \theta} \left( \sin \theta \frac{\partial}{\partial \theta} \right) + \frac{\partial^2}{r^2 \sin^2 \theta \partial \varphi^2} \quad (\text{A1.37})$$

**Table A1.7**

Differential equations of a scalar field

Operation	Notation	Result	Algebraic rules satisfied
Dyadic product of $\nabla$ by a scalar $s$	$\nabla s$ (grad $s$ )	<i>Gradient</i> of the scalar field $s$	$\nabla s = \delta_1 \frac{\partial s}{\partial x_1} + \delta_2 \frac{\partial s}{\partial x_2} + \delta_3 \frac{\partial s}{\partial x_3}$ $= \sum_{i=1}^{i=3} \delta_i \frac{\partial s}{\partial x_i}$ $(\nabla \cdot \nabla s) = \left( \sum_{i=1}^{i=3} \delta_i \frac{\partial}{\partial x_i} \right) \cdot \left( \sum_{j=1}^{j=3} \delta_j \frac{\partial s}{\partial x_j} \right)$
Scalar (dot) product of $\nabla$ by $\nabla s$	$(\nabla \cdot \nabla s)$	<i>Laplacian</i> of the scalar field $s$ , $\nabla^2(s)$	$= \sum_{i=1}^{i=3} \sum_{j=1}^{j=3} (\delta_i \cdot \delta_j) \frac{\partial}{\partial x_i} \frac{\partial s}{\partial x_j}$ $= \sum_{i=1}^{i=3} \sum_{j=1}^{j=3} \delta_{ij} \frac{\partial}{\partial x_i} \frac{\partial s}{\partial x_j} = \sum_{i=1}^{i=3} \frac{\partial^2}{\partial x_i^2} s$
Substantial <sup>a</sup> derivative	$\frac{Ds}{Dt}$		$\frac{Ds}{Dt} = \frac{\partial s}{\partial t} + (\mathbf{V} \cdot \nabla) = \frac{\partial s}{\partial t} + \sum_{i=1}^{i=3} V_i \frac{\partial s}{\partial x_i}$

<sup>a</sup>Derivative operator: eq. (A1.5). Here,  $\mathbf{V}$  is the local fluid velocity (or “mass average velocity” in fluid mixtures).

**Table A1.8**

Operations on the vector differential equations

Operation	Notation	Result	Algebraic rules satisfied
Scalar (dot) product of $\nabla$ by a vector	$(\nabla \cdot \mathbf{V})$	<i>Divergence</i> of the vector field ( $\text{div } \mathbf{v}$ )	$(\nabla \cdot \mathbf{V}) = \left( \sum_{i=1}^{i=3} \delta_i \frac{\partial}{\partial x_i} \right) \cdot \left( \sum_{j=1}^{j=3} \delta_j V_j \right)$ $= \sum_{i=1}^{i=3} \sum_{j=1}^{j=3} (\delta_i \cdot \delta_j) \frac{\partial}{\partial x_i} V_j$ $= \sum_{i=1}^{i=3} \sum_{j=1}^{j=3} \delta_{ij} \frac{\partial}{\partial x_i} V_j = \sum_{i=1}^{i=3} \frac{\partial V_i}{\partial x_i}$ <span style="float: right;">(A1.41)</span>
Vector (cross) product of $\nabla$ by a vector	$(\nabla \times \mathbf{V})$	<i>Curl</i> of the vector field curl $\mathbf{V}$ (rot $\mathbf{V}$ )	$(\nabla \times \mathbf{V}) = \left( \sum_{j=1}^{j=3} \delta_j \frac{\partial}{\partial x_j} \right) \times \left( \sum_{k=1}^{k=3} \delta_k V_k \right)$ $= \sum_{j=1}^{j=3} \sum_{k=1}^{k=3} (\delta_j \times \delta_k)$ $\frac{\partial}{\partial x_j} V_k = \begin{vmatrix} \delta_1 & \delta_2 & \delta_3 \\ \frac{\partial}{\partial x_1} & \frac{\partial}{\partial x_2} & \frac{\partial}{\partial x_3} \\ \mathbf{v}_1 & \mathbf{v}_2 & \mathbf{v}_3 \end{vmatrix}$ $= \delta_1 \left( \frac{\partial V_3}{\partial x_2} - \frac{\partial V_2}{\partial x_3} \right)$ $+ \delta_2 \left( \frac{\partial V_1}{\partial x_3} - \frac{\partial V_3}{\partial x_1} \right)$ $+ \delta_3 \left( \frac{\partial V_2}{\partial x_1} - \frac{\partial V_1}{\partial x_2} \right)$ <span style="float: right;">(A1.42)</span>
<i>In rectangular coordinates<sup>a</sup></i>			
Dyadic product of $\nabla$ by $(\nabla \cdot \mathbf{V})$	$\nabla(\nabla \cdot \mathbf{V})$	<i>Laplacian</i> of the vector field ( $\nabla^2 \mathbf{V}(\Delta \mathbf{V})$ )	$\nabla^2 V = \nabla^2 \sum_{i=1}^{i=3} \delta_i V_i$ $= \delta_1 \nabla^2 V_1 + \delta_2 \nabla^2 V_2 + \delta_3 \nabla^2 V_3$ <span style="float: right;">(A1.43)</span>
Substantial derivative of a vector	$\frac{D\mathbf{V}}{Dt}$		$\frac{D\mathbf{V}}{Dt} = \frac{\partial \mathbf{V}}{\partial t} + (\mathbf{V} \cdot \nabla) \mathbf{V}$ $= \sum_{i=1}^{i=3} \left( \delta_i \frac{\partial \mathbf{V}_i}{\partial t} + (\mathbf{V} \cdot \nabla) \mathbf{V}_i \right)$ <span style="float: right;">(A1.44)</span>

<sup>a</sup>These are not applicable in curvilinear coordinates. It is preferable to define the operation  $\nabla^2 \mathbf{V}$  as  $\nabla^2 \mathbf{V} = \nabla(\nabla \cdot \mathbf{V}) - (\nabla \times (\nabla \times \mathbf{V}))$

## APPENDIX A2: INVARIANTS

A dot product of two identical velocity vectors gives a scalar quantity ( $\mathbf{V} \cdot \mathbf{V} = \sum_i V_i V_i = V_i^2$ ) independent of the coordinate system. The dot product has also a physical meaning, since it is used to define kinetic energy and known as the *invariant* of the velocity vector. Whenever a dot product of two identical vectors gives a scalar quantity having a physical meaning, the quantity is called the *invariant* of the vector. Although a vector has only one common invariant, a tensor  $\mathbf{T}$  has three meaningful invariants (scalar functions) that form a principal stress tensor (Macosko, 1994), defined by

$$\mathbf{T}_{ij}^p = \begin{bmatrix} \delta_1 & 0 & 0 \\ 0 & \delta_2 & 0 \\ 0 & 0 & \delta_3 \end{bmatrix} \quad (\text{A2.1})$$

However,  $\mathbf{T}$  will directly be used to define  $\mathbf{T}_{ij}^p$  in this section.

If the magnitude of the stress tensor  $\mathbf{T}$  is considered as  $\delta$ , eq. (A2.1) is written as

$$\mathbf{T} = \begin{bmatrix} \delta_1 & 0 & 0 \\ 0 & \delta_2 & 0 \\ 0 & 0 & \delta_3 \end{bmatrix} = \delta \begin{bmatrix} 1 & 0 & 0 \\ 0 & 1 & 0 \\ 0 & 0 & 1 \end{bmatrix} \quad (\text{A2.2})$$

Matrix on the RHS of the above equation denotes unit tensor,  $\mathbf{I}$ . The Gibbs notation for the unit tensor is  $\mathbf{I} = \sum_i \mathbf{I}_i \mathbf{I}_i = \mathbf{I}_1 \mathbf{I}_1 + \mathbf{I}_2 \mathbf{I}_2 + \mathbf{I}_3 \mathbf{I}_3$ . Thus, the stress tensor in terms of unit tensor is

$$\mathbf{T} = \delta \mathbf{I} \quad (\text{A2.3})$$

A dot product of the stress tensor  $\mathbf{T}$  and its normal vector  $\mathbf{n}$  gives a vector  $\mathbf{t}_n$  as explained in Section A1.4 (eq. (A1.21)).  $\mathbf{t}_n$  vector is written as

$$\mathbf{t}_n = \mathbf{n} \mathbf{T} \quad (\text{A2.4})$$

Substitution of eq. (A2.3) into the above equation gives

$$\mathbf{t}_n = \delta \mathbf{I} \mathbf{n} \quad (\text{A2.5})$$

Equating eqs. (A2.4) and (A2.5) yields

$$\mathbf{n}(\mathbf{T} - \delta \mathbf{I}) = 0 \quad (\text{A2.6})$$

or

$$n_i (T_{ij} - \delta \mathbf{I}_{ij}) = 0 \quad (\text{A2.6a})$$

To satisfy these equations,  $(\mathbf{T} - \delta \mathbf{I})$  and  $(T_{ij} - \delta \mathbf{I}_{ij})$  terms must equal to zero, since the normal vector is not zero. So

$$(\mathbf{T} - \delta \mathbf{I}) = 0 \quad (\text{A2.7})$$

Both the stress and unit tensors are in matrix form and  $(\mathbf{T} - \delta \mathbf{I})$  is written as

$$\mathbf{T} - \delta \mathbf{I} = \begin{bmatrix} T_{11} - \delta & T_{12} & T_{13} \\ T_{21} & T_{22} - \delta & T_{23} \\ T_{31} & T_{32} & T_{33} - \delta \end{bmatrix} \quad (\text{A2.8})$$

To find the magnitude of the stress tensor,  $\delta$ , eq. (A2.7) is solved by taking determinant of the matrix given in the above equation as

$$\det(\mathbf{T} - \delta \mathbf{I}) = \det \begin{bmatrix} T_{11} - \delta & T_{12} & T_{13} \\ T_{21} & T_{22} - \delta & T_{23} \\ T_{31} & T_{32} & T_{33} - \delta \end{bmatrix} = 0 \quad (\text{A2.9})$$

Expansion of the determinant gives the characteristic equation of the matrix as

$$\delta^3 - I_1 \delta^2 + I_2 \delta - I_3 = 0 \quad (\text{A2.10})$$

where  $I_1, I_2$ , and  $I_3$  are coefficients, known as first, second, and third invariants of the tensor  $\mathbf{T}$ , respectively. They are

$$I_1 = \text{tr} \mathbf{T} = T_{11} + T_{22} + T_{33} = \delta_1 + \delta_2 + \delta_3 \quad (\text{A2.11})$$

In this equation,  $\text{tr} \mathbf{T}$  denotes the trace of a second-order tensor that is the sum of the diagonal components in the matrix.

$$\begin{aligned} I_2 &= \frac{1}{2} [I_1^2 - \text{tr} \mathbf{T}^2] = T_{11}T_{22} + T_{11}T_{33} + T_{22}T_{33} \\ &\quad - T_{12}T_{21} - T_{13}T_{31} - T_{23}T_{32} = \delta_1\delta_2 + \delta_1\delta_3 + \delta_2\delta_3 \end{aligned} \quad (\text{A2.12})$$

$$\begin{aligned} I_3 &= \det \mathbf{T} = T_{11}T_{22}T_{33} + T_{12}T_{23}T_{31} + T_{13}T_{32}T_{21} \\ &\quad - T_{11}T_{23}T_{32} - T_{21}T_{12}T_{33} - T_{31}T_{22}T_{13} = \delta_1\delta_2\delta_3 \end{aligned} \quad (\text{A2.13})$$

When a fluid is at rest, the principle stresses are equal ( $\delta_1 = \delta_2 = \delta_3 = \delta$ ) and equivalent to the pressure,  $p = -\delta$

$$\mathbf{T} = \begin{bmatrix} -p & 0 & 0 \\ 0 & -p & 0 \\ 0 & 0 & -p \end{bmatrix} = -p \begin{bmatrix} 1 & 0 & 0 \\ 0 & 1 & 0 \\ 0 & 0 & 1 \end{bmatrix} \quad (\text{A2.14})$$

Matrix on the RHS of the above equation denotes unit tensor,  $\mathbf{I}$ . Hence, the stress tensor for a fluid at rest is

$$\mathbf{T} = -p\mathbf{I} \quad (\text{A2.15})$$

When a fluid is in motion, the stress tensor  $\mathbf{T}$  comprises viscous stress terms:

$$\mathbf{T} = f(2\mathbf{D}) \quad (\text{A2.16})$$

The function is expanded as a power series and the general stress equation becomes

$$\mathbf{T} = f_0\mathbf{D}^0 + f_1\mathbf{D}^1 + f_2\mathbf{D}^2 + f_3\mathbf{D}^3 + \dots \quad (\text{A2.17})$$

where  $\mathbf{D}^0 = \mathbf{I}$  and  $f_i$  are the scalar function of the invariants of  $2\mathbf{D}$ . Using the Cayley–Hamilton theorem, eq. (A2.17) can be written for *incompressible* ( $f_0 = -p$ ) *viscous fluids* ( $2\mathbf{D} = \dot{\gamma}$ ) as

$$\mathbf{T} = -p\mathbf{I} + \eta_1(I_{2\dot{\gamma}}, I_{3\dot{\gamma}})\dot{\gamma} + \eta_2(I_{2\dot{\gamma}}, I_{3\dot{\gamma}})\dot{\gamma}^2 \quad (\text{A2.18})$$

known as *Reiner–Rivlin equation*. In this equation,  $\eta_i$  are scalar functions of the invariant of  $\dot{\gamma}$ .  $\dot{\gamma}$  is the summation of rate of deformation tensor  $\mathbf{L}$  and its transpose,  $\mathbf{L}^T$ , defined as

$$2\mathbf{D} = \dot{\gamma} = \mathbf{L} + \mathbf{L}^T \quad (\text{A2.19})$$

or

$$2D_{ij} = \dot{\gamma}_{ij} = L_{ij} + L_{ji} \quad (\text{A2.19a})$$

Shear-rate tensor in terms of velocity gradient is given as

$$2\mathbf{D} = \dot{\gamma} = (\nabla\mathbf{V})^T + \nabla\mathbf{V} \quad (\text{A2.20})$$

### A2.1 Invariants of simple shear fluids

For a simple steady-state shear flow, rate of deformation tensor is

$$L_{ij} = \begin{bmatrix} 0 & \dot{\gamma} & 0 \\ 0 & 0 & 0 \\ 0 & 0 & 0 \end{bmatrix} \quad (\text{A2.21})$$

and substitution of the above equation into eq. (A2.19a) gives

$$2D_{ij} = \dot{\gamma}_{ij} = \begin{bmatrix} 0 & \dot{\gamma} & 0 \\ 0 & 0 & 0 \\ 0 & 0 & 0 \end{bmatrix} + \begin{bmatrix} 0 & 0 & 0 \\ \dot{\gamma} & 0 & 0 \\ 0 & 0 & 0 \end{bmatrix} = \begin{bmatrix} 0 & \dot{\gamma} & 0 \\ \dot{\gamma} & 0 & 0 \\ 0 & 0 & 0 \end{bmatrix} \quad (\text{A2.22})$$

The invariants of the shear-rate tensor are obtained from eqs. (A2.11)–(A2.13):

$$I_{1\dot{\gamma}} = \text{tr}\dot{\gamma} = 0 \quad (\text{A2.11a})$$

$$\dot{\gamma}_{ij}^2 = \begin{bmatrix} 0 & \dot{\gamma} & 0 \\ \dot{\gamma} & 0 & 0 \\ 0 & 0 & 0 \end{bmatrix} \begin{bmatrix} 0 & \dot{\gamma} & 0 \\ \dot{\gamma} & 0 & 0 \\ 0 & 0 & 0 \end{bmatrix} = \begin{bmatrix} 0 + \dot{\gamma}^2 + 0 & 0 + 0 + 0 & 0 \\ 0 & \dot{\gamma}^2 + 0 + 0 & 0 \\ 0 & 0 & 0 \end{bmatrix} = \begin{bmatrix} \dot{\gamma}^2 & 0 & 0 \\ 0 & \dot{\gamma}^2 & 0 \\ 0 & 0 & 0 \end{bmatrix} \quad (\text{A2.23})$$

$$I_{2\dot{\gamma}} = \frac{1}{2}[I_{1\dot{\gamma}}^2 - \text{tr } \dot{\gamma}^2] = \dot{\gamma}_{ij}^2 = \frac{1}{2}(0 - 2\dot{\gamma}^2) = -\dot{\gamma}^2 \quad (\text{A2.12a})$$

$$I_3 = \det \dot{\gamma} = 0 \quad (\text{A2.13a})$$

As a result, only the second invariant of shear-rate tensor is present, so the scalar functions only depend on the second invariant

$$\mathbf{T} = -p\mathbf{I} + \eta_1(I_{2\dot{\gamma}})\dot{\gamma} + \eta_2(I_{2\dot{\gamma}})\dot{\gamma}^2 \quad (\text{A2.18a})$$

The above equation can also be written as

$$T = -p \begin{bmatrix} 1 & 0 & 0 \\ 0 & 1 & 0 \\ 0 & 0 & 1 \end{bmatrix} + \eta_1(I_{2\dot{\gamma}}) \begin{bmatrix} 0 & \dot{\gamma} & 0 \\ \dot{\gamma} & 0 & 0 \\ 0 & 0 & 0 \end{bmatrix} + \eta_2(I_{2\dot{\gamma}}) \begin{bmatrix} \dot{\gamma}^2 & 0 & 0 \\ 0 & \dot{\gamma}^2 & 0 \\ 0 & 0 & 0 \end{bmatrix} \quad (\text{A2.18b})$$

and the elements of tensor  $\mathbf{T}$  are

$$T_{11} = T_{22} = -p + \eta_2(I_{2\dot{\gamma}})\dot{\gamma}^2 \quad (\text{A2.24})$$

$$T_{33} = -p \quad (\text{A2.25})$$

$$T_{12} = T_{21} = \eta_1(I_{2\dot{\gamma}})\dot{\gamma} \quad (\text{A2.26})$$

$$T_{13} = T_{31} = T_{23} = T_{32} = 0 \quad (\text{A2.27})$$

The first  $N_1$  and second  $N_2$  normal stress differences are defined as:

$$N_1 = T_{11} - T_{22} = 0 \quad (\text{A2.28})$$

$$N_2 = T_{22} - T_{33} = \eta_2(I_{2\dot{\gamma}})\dot{\gamma}^2 \quad (\text{A2.29})$$

Thus,  $\eta_2$  term gives rise to normal stresses in steady shear flow (eqs. (A2.23), (A2.27), and (A2.28)). As the normal stresses in steady shear flow cannot be related to any function of the rate of deformation tensor in this group of fluids,  $\eta_2$  term is set equal to zero. So

$$\mathbf{T} = -p\mathbf{I} + \eta_1(I_{2\dot{\gamma}})\dot{\gamma} = -p\mathbf{I} + \boldsymbol{\tau} \quad (\text{A2.18c})$$

where

$$\boldsymbol{\tau} = \eta_1(I_{2,\dot{\gamma}})\dot{\boldsymbol{\gamma}} \quad (\text{A2.30})$$

## A2.2 Common expressions for $\eta_1(I_{2,\dot{\gamma}})$ power-law model

Power-law model is defined as a function of  $\eta_1(I_{2,\dot{\gamma}})$  as

$$\tau_{ij} = K |I_{2,\dot{\gamma}}|^{(n-1)/2} \dot{\gamma}_{ij} = K (\dot{\gamma}_{ij}^2)^{(n-1)/2} \dot{\gamma}_{ij} = m \dot{\gamma}_{ij}^n \quad (\text{A2.31})$$

Substituting eq. (A2.30) into eq. (A2.26) the component of the tensor  $T_{12} = \tau_{12}$  and the viscosity are described by power-law model:

$$\tau_{12} = m \dot{\gamma}^n \quad (\text{A2.32})$$

$$\frac{\tau_{12}}{\dot{\gamma}} = \eta = m \dot{\gamma}^{n-1} \quad (\text{A2.33})$$

Power law and other models are given in Chapter 2.

## APPENDIX A3: NAVIER–STOKES EQUATIONS

See Tables A3.1–A3.3 (Bird *et al.*, 2002).

**Table A3.1**

Equation of continuity<sup>a</sup>

$$\left[ \frac{\partial \rho}{\partial t} + (\nabla \cdot \rho \mathbf{V}) = 0 \right]$$

*Cartesian coordinates* ( $x, y, z$ )

$$\frac{\partial \rho}{\partial t} + \frac{\partial}{\partial x}(\rho V_x) + \frac{\partial}{\partial y}(\rho V_y) + \frac{\partial}{\partial z}(\rho V_z) = 0 \quad (\text{A3.1})$$

*Cylindrical coordinates* ( $r, \theta, z$ )

$$\frac{\partial \rho}{\partial t} + \frac{1}{r} \frac{\partial}{\partial r}(\rho r V_r) + \frac{1}{r} \frac{\partial}{\partial \theta}(\rho V_\theta) + \frac{\partial}{\partial z}(\rho V_z) = 0 \quad (\text{A3.2})$$

*Spherical coordinates* ( $r, \theta, \phi$ )

$$\frac{\partial \rho}{\partial t} + \frac{1}{r^2} \frac{\partial}{\partial r}(\rho r^2 V_r) + \frac{1}{r \sin \theta} \frac{\partial}{\partial \theta}(\rho V_\theta \sin \theta) + \frac{1}{r \sin \theta} \frac{\partial}{\partial \phi}(\rho V_\phi) = 0 \quad (\text{A3.3})$$

<sup>a</sup>When the fluid is assumed to have constant mass density  $\rho$ , the equation simplifies to  $(\nabla \cdot \mathbf{v}) = 0$ .



**Table A3.2**The equation of motion in terms of  $\tau$ 

---


$$\left[ \frac{\rho D\mathbf{V}}{Dt} = -\nabla p - [\nabla \cdot \boldsymbol{\tau}] + \rho \mathbf{g} \right]$$


---

*Cartesian coordinates* ( $x, y, z$ )<sup>a</sup>

$$\rho \left( \frac{\partial V_x}{\partial t} + V_x \frac{\partial V_x}{\partial x} + V_y \frac{\partial V_x}{\partial y} + V_z \frac{\partial V_x}{\partial z} \right) = -\frac{\partial p}{\partial x} - \left[ \frac{\partial}{\partial x} \tau_{xx} + \frac{\partial}{\partial y} \tau_{yx} + \frac{\partial}{\partial z} \tau_{zx} \right] + \rho g_x \quad (\text{A3.4})$$

$$\rho \left( \frac{\partial V_y}{\partial t} + V_x \frac{\partial V_y}{\partial x} + V_y \frac{\partial V_y}{\partial y} + V_z \frac{\partial V_y}{\partial z} \right) = -\frac{\partial p}{\partial y} - \left[ \frac{\partial}{\partial x} \tau_{xy} + \frac{\partial}{\partial y} \tau_{yy} + \frac{\partial}{\partial z} \tau_{zy} \right] + \rho g_y \quad (\text{A3.5})$$

$$\rho \left( \frac{\partial V_z}{\partial t} + V_x \frac{\partial V_z}{\partial x} + V_y \frac{\partial V_z}{\partial y} + V_z \frac{\partial V_z}{\partial z} \right) = -\frac{\partial p}{\partial z} - \left[ \frac{\partial}{\partial x} \tau_{xz} + \frac{\partial}{\partial y} \tau_{yz} + \frac{\partial}{\partial z} \tau_{zz} \right] + \rho g_z \quad (\text{A3.6})$$

*Cylindrical coordinates* ( $r, \theta, z$ )<sup>b</sup>

$$\rho \left( \frac{\partial V_r}{\partial t} + V_r \frac{\partial V_r}{\partial r} + \frac{V_\theta}{r} \frac{\partial V_r}{\partial \theta} + V_z \frac{\partial V_r}{\partial z} - \frac{V_\theta^2}{r} \right) = -\frac{\partial p}{\partial r} - \left[ \frac{1}{r} \frac{\partial}{\partial r} (r \tau_{rr}) + \frac{1}{r} \frac{\partial}{\partial \theta} \tau_{\theta r} + \frac{\partial}{\partial z} \tau_{zr} - \frac{\tau_{\theta\theta}}{r} \right] + \rho g_r \quad (\text{A3.7})$$

$$\rho \left( \frac{\partial V_\theta}{\partial t} + V_r \frac{\partial V_\theta}{\partial r} + \frac{V_\theta}{r} \frac{\partial V_\theta}{\partial \theta} + V_z \frac{\partial V_\theta}{\partial z} + \frac{V_r V_\theta}{r} \right) = -\frac{1}{r} \frac{\partial p}{\partial \theta} - \left[ \frac{1}{r^2} \frac{\partial}{\partial r} (r^2 \tau_{r\theta}) + \frac{1}{r} \frac{\partial}{\partial \theta} \tau_{\theta\theta} + \frac{\partial}{\partial z} \tau_{z\theta} + \frac{\tau_{\theta r} - \tau_{r\theta}}{r} \right] + \rho g_\theta \quad (\text{A3.8})$$

$$\rho \left( \frac{\partial V_z}{\partial t} + V_r \frac{\partial V_z}{\partial r} + \frac{V_\theta}{r} \frac{\partial V_z}{\partial \theta} + V_z \frac{\partial V_z}{\partial z} \right) = -\frac{\partial p}{\partial z} - \left[ \frac{1}{r} \frac{\partial}{\partial r} (r \tau_{rz}) + \frac{1}{r} \frac{\partial}{\partial \theta} \tau_{\theta z} + \frac{\partial}{\partial z} \tau_{zz} \right] + \rho g_z \quad (\text{A3.9})$$

*Spherical coordinates* ( $r, \theta, \phi$ )<sup>b</sup>

$$\rho \left( \frac{\partial V_r}{\partial t} + V_r \frac{\partial V_r}{\partial r} + \frac{V_\theta}{r} \frac{\partial V_r}{\partial \theta} + \frac{V_\phi}{r \sin \theta} \frac{\partial V_r}{\partial \phi} - \frac{V_\theta^2 + V_\phi^2}{r} \right) = -\frac{\partial p}{\partial r} - \left[ \frac{1}{r^2} \frac{\partial}{\partial r} (r^2 \tau_{rr}) + \frac{1}{r \sin \theta} \frac{\partial}{\partial \theta} (\tau_{\theta r} \sin \theta) + \frac{1}{r \sin \theta} \frac{\partial}{\partial \phi} \tau_{\phi r} - \frac{\tau_{\theta\theta} + \tau_{\phi\phi}}{r} \right] + \rho g_r \quad (\text{A3.10})$$

$$\rho \left( \frac{\partial V_\theta}{\partial t} + V_r \frac{\partial V_\theta}{\partial r} + \frac{V_\theta}{r} \frac{\partial V_\theta}{\partial \theta} + \frac{V_\phi}{r \sin \theta} \frac{\partial V_\theta}{\partial \phi} + \frac{V_r V_\theta - V_\phi^2 \cot \theta}{r} \right) = -\frac{1}{r} \frac{\partial p}{\partial \theta} - \left[ \frac{1}{r^3} \frac{\partial}{\partial r} (r^3 \tau_{r\theta}) + \frac{1}{r \sin \theta} \frac{\partial}{\partial \theta} (\tau_{\theta\theta} \sin \theta) + \frac{1}{r \sin \theta} \frac{\partial}{\partial \phi} \tau_{\phi\theta} + \frac{(\tau_{\theta r} - \tau_{r\theta}) - \tau_{\phi\phi} \cot \theta}{r} \right] + \rho g_\theta \quad (\text{A3.11})$$

**Table A3.2** (Continued)

$$\rho \left( \frac{\partial V_\phi}{\partial t} + V_r \frac{\partial V_\phi}{\partial r} + \frac{V_\theta}{r} \frac{\partial V_\phi}{\partial \theta} + \frac{V_\phi}{r \sin \theta} \frac{\partial V_\phi}{\partial \phi} + \frac{V_\phi V_r + V_\theta V_\phi \cot \theta}{r} \right) = -\frac{1}{r \sin \theta} \frac{\partial p}{\partial \phi} - \left[ \frac{1}{r^3} \frac{\partial}{\partial r} (r^3 \tau_{r\phi}) + \frac{1}{r \sin \theta} \frac{\partial}{\partial \theta} (\tau_{\theta\phi} \sin \theta) + \frac{1}{r \sin \theta} \frac{\partial}{\partial \phi} \tau_{\phi\phi} + \frac{(\tau_{\phi r} - \tau_{r\phi}) + \tau_{\phi\theta} \cot \theta}{r} \right] + \rho g_\phi \quad (\text{A3.12})$$

These equations are written without making the assumption that  $\tau$  is symmetric. This means, when the usual assumption is made that the stress tensor is symmetric.

<sup>a</sup> $\tau_{xy}$  and  $\tau_{yx}$  may be interchanged.

<sup>b</sup> $\tau_{r\theta} - \tau_{\theta r} = 0$ .

**Table A3.3**

The equation of continuity for species  $\alpha$  in terms of molar flux

$$\left[ \frac{\rho D \omega_\alpha}{Dt} = -(\nabla \cdot \mathbf{j}_\alpha) + r_\alpha \right]^a$$

*Cartesian coordinates* ( $x, y, z$ )

$$\rho \left( \frac{\partial \omega_\alpha}{\partial t} + V_x \frac{\partial \omega_\alpha}{\partial x} + V_y \frac{\partial \omega_\alpha}{\partial y} + V_z \frac{\partial \omega_\alpha}{\partial z} \right) = - \left[ \frac{\partial j_{\alpha x}}{\partial x} + \frac{\partial j_{\alpha y}}{\partial y} + \frac{\partial j_{\alpha z}}{\partial z} \right] + r_\alpha \quad (\text{A3.13})$$

*Cylindrical coordinates* ( $r, \theta, z$ )

$$\rho \left( \frac{\partial \omega_\alpha}{\partial t} + V_r \frac{\partial \omega_\alpha}{\partial r} + \frac{V_\theta}{r} \frac{\partial \omega_\alpha}{\partial \theta} + V_z \frac{\partial \omega_\alpha}{\partial z} \right) = - \left[ \frac{1}{r} \frac{\partial}{\partial r} (r j_{\alpha r}) + \frac{1}{r} \frac{\partial j_{\alpha \theta}}{\partial \theta} + \frac{\partial j_{\alpha z}}{\partial z} \right] + r_\alpha \quad (\text{A3.14})$$

*Spherical coordinates* ( $r, \theta, \phi$ )

$$\rho \left( \frac{\partial \omega_\alpha}{\partial t} + V_r \frac{\partial \omega_\alpha}{\partial r} + \frac{V_\theta}{r} \frac{\partial \omega_\alpha}{\partial \theta} + \frac{V_\phi}{r \sin \theta} \frac{\partial \omega_\alpha}{\partial \phi} \right) = \left[ \frac{1}{r^2} \frac{\partial}{\partial r} (r^2 j_{\alpha r}) + \frac{1}{r \sin \theta} \frac{\partial}{\partial \theta} (j_{\alpha \theta} \sin \theta) + \frac{1}{r \sin \theta} \frac{\partial j_{\alpha \phi}}{\partial \phi} \right] + r_\alpha \quad (\text{A3.15})$$

<sup>a</sup>To obtain the corresponding equations in terms of mass flux,  $\mathbf{J}_\alpha^*$ , the following replacements can be done:

Replace mass quantities       $\rho$        $\omega_\alpha$        $\mathbf{j}_\alpha = -\rho D_{\alpha\beta} \nabla w_\alpha$        $\mathbf{V} = \sum_{\alpha=1}^N w_\alpha \mathbf{V}_\alpha$        $r_\alpha$

by molar quantities       $c$        $x_\alpha$        $\mathbf{J}_\alpha^* = -c D_{\alpha\beta} \nabla x_\alpha$        $\mathbf{V}^* = \sum_{\alpha=1}^N x_\alpha \mathbf{V}_\alpha$        $R_\alpha = x_\alpha \sum_{\beta=1}^N R_\beta$

$\rho$ : mass density,  $c$ : total molar concentration,  $\omega_\alpha$  and  $x_\alpha$ : mass and mole fractions of species  $\alpha$ , respectively;  $\mathbf{j}_\alpha$  and  $\mathbf{J}_\alpha^*$ : mass and molar fluxes of species  $\alpha$ , respectively;  $D_{\alpha\beta}$ : diffusivity of species  $\alpha$ ;  $\mathbf{V}$ : mass average velocity;  $\mathbf{V}^*$ : molar average velocity;  $r_\alpha$ : mass reaction rate of the species  $\alpha$  per unit volume;  $R_\alpha$ : molar reaction rate of the species  $\alpha$  per unit volume.

### A3.1. Equations for Newtonian fluids

See Tables A3.4 and A3.5 (Bird *et al.*, 2002).

**Table A3.4**

Newton's law of viscosity

$$\left[ \tau = -\mu(\nabla\mathbf{V} + (\nabla\mathbf{V})^T) + \left(\frac{2}{3}\mu - \kappa\right)(\nabla \cdot \mathbf{V})\delta \right]$$

*Cartesian coordinates* ( $x, y, z$ ),

$$\left[ (\nabla \cdot \mathbf{V}) = \frac{\partial V_x}{\partial x} + \frac{\partial V_y}{\partial y} + \frac{\partial V_z}{\partial z} \right]$$

$$\tau_{ii} = -\mu \left[ 2 \frac{\partial V_i}{\partial i} \right] + \left( \frac{2}{3} \mu - \kappa \right) (\nabla \cdot \mathbf{V}), \text{ where } i = x, y, z \quad (\text{A3.16})^a$$

$$\tau_{ij} = \tau_{ji} = -\mu \left[ \frac{\partial V_j}{\partial i} + \frac{\partial V_i}{\partial j} \right], \text{ where } i = x, y, z; j = x, y, z; \text{ and } i \neq j \quad (\text{A3.17})$$

*Cylindrical coordinates* ( $r, \theta, z$ ),

$$(\nabla \cdot \mathbf{V}) = \frac{1}{r} \frac{\partial}{\partial r} (r V_r) + \frac{1}{r} \frac{\partial V_\theta}{\partial \theta} + \frac{\partial V_z}{\partial z}$$

$$\tau_{ii} = -\mu \left[ 2 \frac{\partial V_i}{\partial i} \right] + \left( \frac{2}{3} \mu - \kappa \right) (\nabla \cdot \mathbf{V}), \text{ where } i = r, z \quad (\text{A3.18})^a$$

$$\tau_{\theta\theta} = -\mu \left[ 2 \left( \frac{1}{r} \frac{\partial V_\theta}{\partial \theta} + \frac{V_r}{r} \right) \right] + \left( \frac{2}{3} \mu - \kappa \right) (\nabla \cdot \mathbf{V}) \quad (\text{A3.19})^a$$

$$\tau_{ij} = \tau_{ji} = -\mu \left[ \frac{\partial V_j}{\partial i} + \frac{\partial V_i}{\partial j} \right], \text{ where } i = r, z; j = r, z; \text{ and } i \neq j \quad (\text{A3.20})$$

$$\tau_{r\theta} = \tau_{\theta r} = -\mu \left[ r \frac{\partial}{\partial r} \left( \frac{V_\theta}{r} \right) + \frac{1}{r} \frac{\partial V_r}{\partial \theta} \right] \quad (\text{A3.21})$$

$$\tau_{\theta z} = \tau_{z\theta} = -\mu \left[ \frac{1}{r} \frac{\partial V_z}{\partial \theta} + \frac{\partial V_\theta}{\partial z} \right] \quad (\text{A3.22})$$

**Table A3.4** (Continued)*Spherical coordinates* ( $r, \theta, \phi$ ),

$$\left[ (\nabla \cdot \mathbf{V}) = \frac{1}{r^2} \frac{\partial}{\partial r} (r^2 V_r) + \frac{1}{r \sin \theta} \frac{\partial}{\partial \theta} (V_\theta \sin \theta) + \frac{1}{r \sin \theta} \frac{\partial V_\phi}{\partial \phi} \right]$$

$$\tau_{rr} = -\mu \left[ 2 \frac{\partial V_r}{\partial r} \right] + \left( \frac{2}{3} \mu - \kappa \right) (\nabla \cdot \mathbf{V}) \quad (\text{A3.23})^a$$

$$\tau_{\theta\theta} = -\mu \left[ 2 \left( \frac{1}{r} \frac{\partial V_\theta}{\partial \theta} + \frac{V_r}{r} \right) \right] + \left( \frac{2}{3} \mu - \kappa \right) (\nabla \cdot \mathbf{V}) \quad (\text{A3.24})^a$$

$$\tau_{\phi\phi} = -\mu \left[ 2 \left( \frac{1}{r \sin \theta} \frac{\partial V_\phi}{\partial \phi} + \frac{V_r + V_\theta \cot \theta}{r} \right) \right] + \left( \frac{2}{3} \mu - \kappa \right) (\nabla \cdot \mathbf{V}) \quad (\text{A3.25})^a$$

$$\tau_{r\theta} = \tau_{\theta r} = -\mu \left[ r \frac{\partial}{\partial r} \left( \frac{V_\theta}{r} \right) + \frac{1}{r} \frac{\partial V_r}{\partial \theta} \right] \quad (\text{A3.26})$$

$$\tau_{\theta\phi} = \tau_{\phi\theta} = -\mu \left[ \frac{\sin \theta}{r} \frac{\partial}{\partial \theta} \left( \frac{V_\phi}{\sin \theta} \right) + \frac{1}{r \sin \theta} \frac{\partial V_\theta}{\partial \phi} \right] \quad (\text{A3.27})$$

$$\tau_{\phi r} = \tau_{r\phi} = -\mu \left[ \frac{1}{r \sin \theta} \frac{\partial V_r}{\partial \phi} + r \frac{\partial}{\partial r} \left( \frac{V_\phi}{r} \right) \right] \quad (\text{A3.28})$$

<sup>a</sup>When  $\rho$  is assumed to be constant, the term containing  $(\nabla \cdot \mathbf{V})$  may be omitted. For monatomic gases at low density, the dilatational viscosity  $\kappa$  is zero.

**Table A3.5**Equation of motion of a Newtonian fluid with constant  $\rho$  and  $\mu$ 

$$\left[ \frac{\rho D\mathbf{V}}{Dt} = -\nabla p + \mu \nabla^2 \mathbf{V} + \rho \mathbf{g} \right]$$

*Cartesian coordinates* ( $x, y, z$ )

$$\rho \left( \frac{\partial V_x}{\partial t} + V_x \frac{\partial V_x}{\partial x} + V_y \frac{\partial V_x}{\partial y} + V_z \frac{\partial V_x}{\partial z} \right) = -\frac{\partial p}{\partial x} + \mu \left[ \frac{\partial^2 V_x}{\partial x^2} + \frac{\partial^2 V_x}{\partial y^2} + \frac{\partial^2 V_x}{\partial z^2} \right] + \rho g_x \quad (\text{A3.29})$$

$$\rho \left( \frac{\partial V_y}{\partial t} + V_x \frac{\partial V_y}{\partial x} + V_y \frac{\partial V_y}{\partial y} + V_z \frac{\partial V_y}{\partial z} \right) = -\frac{\partial p}{\partial y} + \mu \left[ \frac{\partial^2 V_y}{\partial x^2} + \frac{\partial^2 V_y}{\partial y^2} + \frac{\partial^2 V_y}{\partial z^2} \right] + \rho g_y \quad (\text{A3.30})$$

(Continued)

**Table A3.5** (Continued)

---


$$\rho \left( \frac{\partial V_z}{\partial t} + V_x \frac{\partial V_z}{\partial x} + V_y \frac{\partial V_z}{\partial y} + V_z \frac{\partial V_z}{\partial z} \right) = -\frac{\partial p}{\partial z} + \mu \left[ \frac{\partial^2 V_z}{\partial x^2} + \frac{\partial^2 V_z}{\partial y^2} + \frac{\partial^2 V_z}{\partial z^2} \right] + \rho g_z \quad (\text{A3.31})$$

*Cylindrical coordinates* ( $r, \theta, z$ )

$$\begin{aligned} \rho \left( \frac{\partial V_r}{\partial t} + V_r \frac{\partial V_r}{\partial r} + \frac{V_\theta}{r} \frac{\partial V_r}{\partial \theta} + V_z \frac{\partial V_r}{\partial z} - \frac{V_\theta^2}{r} \right) &= -\frac{\partial p}{\partial r} \\ &+ \mu \left[ \frac{\partial}{\partial r} \left( \frac{1}{r} \frac{\partial}{\partial r} (r V_r) \right) + \frac{1}{r^2} \frac{\partial^2 V_r}{\partial \theta^2} + \frac{\partial^2 V_r}{\partial z^2} - \frac{2}{r^2} \frac{\partial V_\theta}{\partial \theta} \right] + \rho g_r \end{aligned} \quad (\text{A3.32})$$

$$\begin{aligned} \rho \left( \frac{\partial V_\theta}{\partial t} + V_r \frac{\partial V_\theta}{\partial r} + \frac{V_\theta}{r} \frac{\partial V_\theta}{\partial \theta} + V_z \frac{\partial V_\theta}{\partial z} + \frac{V_r V_\theta}{r} \right) &= -\frac{1}{r} \frac{\partial p}{\partial \theta} \\ &+ \mu \left[ \frac{\partial}{\partial r} \left( \frac{1}{r} \frac{\partial}{\partial r} (r V_\theta) \right) + \frac{1}{r^2} \frac{\partial^2 V_\theta}{\partial \theta^2} + \frac{\partial^2 V_\theta}{\partial z^2} + \frac{2}{r^2} \frac{\partial V_r}{\partial \theta} \right] + \rho g_\theta \end{aligned} \quad (\text{A3.33})$$

$$\rho \left( \frac{\partial V_z}{\partial t} + V_r \frac{\partial V_z}{\partial r} + \frac{V_\theta}{r} \frac{\partial V_z}{\partial \theta} + V_z \frac{\partial V_z}{\partial z} \right) = -\frac{\partial p}{\partial z} + \mu \left[ \frac{1}{r} \frac{\partial}{\partial r} \left( r \frac{\partial V_z}{\partial r} \right) + \frac{1}{r^2} \frac{\partial^2 V_z}{\partial \theta^2} + \frac{\partial^2 V_z}{\partial z^2} \right] + \rho g_z \quad (\text{A3.34})$$

*Spherical coordinates* ( $r, \theta, \phi$ )

$$\begin{aligned} \rho \left( \frac{\partial V_r}{\partial t} + V_r \frac{\partial V_r}{\partial r} + \frac{V_\theta}{r} \frac{\partial V_r}{\partial \theta} + \frac{V_\phi}{r \sin \theta} \frac{\partial V_r}{\partial \phi} - \frac{V_\theta^2 + V_\phi^2}{r} \right) &= -\frac{\partial p}{\partial r} \\ &+ \mu \left[ \frac{1}{r^2} \frac{\partial^2}{\partial r^2} (r^2 V_r) + \frac{1}{r^2 \sin \theta} \frac{\partial}{\partial \theta} \left( \sin \theta \frac{\partial V_r}{\partial \theta} \right) + \frac{1}{r^2 \sin^2 \theta} \frac{\partial^2 V_r}{\partial \phi^2} \right] + \rho g_r \end{aligned} \quad (\text{A3.35})$$

$$\begin{aligned} \rho \left( \frac{\partial V_\theta}{\partial t} + V_r \frac{\partial V_\theta}{\partial r} + \frac{V_\theta}{r} \frac{\partial V_\theta}{\partial \theta} + \frac{V_\phi}{r \sin \theta} \frac{\partial V_\theta}{\partial \phi} + \frac{V_r V_\theta - V_\phi^2 \cot \theta}{r} \right) &= -\frac{1}{r} \frac{\partial p}{\partial \theta} \\ &+ \mu \left[ \frac{1}{r^2} \frac{\partial}{\partial r} \left( r^2 \frac{\partial V_\theta}{\partial r} \right) + \frac{1}{r^2} \frac{\partial}{\partial \theta} \left( \frac{1}{\sin \theta} \frac{\partial}{\partial \theta} (V_\theta \sin \theta) \right) + \frac{1}{r^2 \sin^2 \theta} \frac{\partial^2 V_\theta}{\partial \phi^2} + \frac{2}{r^2} \frac{\partial V_r}{\partial \theta} - \frac{2 \cot \theta}{r^2 \sin \theta} \frac{\partial V_\phi}{\partial \phi} \right] + \rho g_\theta \end{aligned} \quad (\text{A3.36})$$

$$\begin{aligned} \rho \left( \frac{\partial V_\phi}{\partial t} + V_r \frac{\partial V_\phi}{\partial r} + \frac{V_\theta}{r} \frac{\partial V_\phi}{\partial \theta} + \frac{V_\phi}{r \sin \theta} \frac{\partial V_\phi}{\partial \phi} + \frac{V_\phi V_r + V_\theta V_\phi \cot \theta}{r} \right) &= -\frac{1}{r \sin \theta} \frac{\partial p}{\partial \phi} \\ &+ \mu \left[ \frac{1}{r^2} \frac{\partial}{\partial r} \left( r^2 \frac{\partial V_\phi}{\partial r} \right) + \frac{1}{r^2} \frac{\partial}{\partial \theta} \left( \frac{1}{\sin \theta} \frac{\partial}{\partial \theta} (V_\phi \sin \theta) \right) + \right. \\ &\quad \left. + \frac{1}{r^2 \sin^2 \theta} \frac{\partial^2 V_\phi}{\partial \phi^2} + \frac{2}{r^2 \sin \theta} \frac{\partial V_r}{\partial \phi} + \frac{2 \cot \theta}{r^2 \sin \theta} \frac{\partial V_\theta}{\partial \phi} \right] + \rho g_\phi \end{aligned} \quad (\text{A3.37})$$


---

## REFERENCES

- Bird, R.B., Steward, W.E., Lightfoot, E.N., 2002. Transport Phenomena, second ed. John Wiley and Sons, New York (Chapter 3, Appendices).
- Fahein, R.W., 1983. Fundamentals of Transport Phenomena, McGraw-Hill, Inc., New York (Chapter 9).
- Macosko, C.W., 1994. Rheology Principles, Measurements and Applications, VCH Publishers, New York.

This page intentionally left blank

# Appendix B

## Population Balances

---

This appendix supplements the brief description of the population balance equation given in Chapter 1. In this appendix the physical background of the population balance equation, formulation of the models, and solution of the population balance equation are explained in more detail.

### APPENDIX B1: POPULATION BALANCE EQUATION: PHYSICAL BACKGROUND

Many of the processes with particulate solids involve not only a single particle, but many particles that can be considered as a population. To describe the aggregation mechanism of this population, Smoluchowski (1917) developed a population balance equation, which can be used to predict the evolution of the particle-size distribution in time  $t$ . The following assumptions are made in the development of the model:

1. All particle collisions lead to attachment.
2. Cluster formation takes place under a laminar flow regime.
3. The particles are all of the same size.
4. No breakage of flocs occurs after they are formed.
5. All particles are spherical in shape and remain so after collision.
6. Collisions involve only two particles.

The last assumption of Smoluchowski's model takes every particle in a suspension as the reference particle, in turn. The other particles diffuse toward the reference particle and collision occurs. The model assumes the concentration of the particle decreases toward the site of collision, not to take into account the concentration effects (many-body interactions) in the collision process. The solution of the diffusion equation in spherical coordinates results in a population balance equation for the aggregation of particles:

$$\left( \frac{dn_k}{dt} \right)_{\text{agg}} = \frac{1}{2} \sum_{i+j=k} \alpha \beta(i, j) n_i n_j - n_k \sum_{i=1}^{\infty} \alpha \beta(i, k) n_i \quad (\text{B1.1})$$



where  $\alpha$  is the collision efficiency factor and  $\beta$  the collision frequency function [ $\text{m}^3\text{s}^{-1}$ ].  $n_i$ ,  $n_j$ , and  $n_k$  are the number concentrations [ $\text{m}^{-3}$ ] of particles of size  $i$ ,  $j$ , and  $k$ , respectively. The first term on the right hand side of eq. (B1.1) is the rate of formation of particles of size  $k$  by collision of particles of size  $i$  and  $j$ . The second term is the rate of loss of particles of size  $k$  by collision with all other particles. The factor  $1/2$  is introduced to prevent replication of the number of collisions.

Aggregation process described mathematically by Smoluchowski's population balance equation includes two mechanisms: transport to the collision site and attachment of the particles after the collision. The transport mechanisms causing particle collisions depend on the physical properties of the suspending medium, particle size, and number concentration of the particles. The effect of the transport mechanism is introduced into eq. (B1.1) by the collision frequency function,  $\beta$ . On the other hand, the attachment of the particles is related with the interaction potential between the particles and is represented by collision efficiency factor  $\alpha$  in eq. (B1.1). The effects of both the collision frequency function and the collision efficiency on the particle-size distribution of a population should be taken into account in the development of the models.

### B1.1 Colliding entities

Smoluchowski's coagulation model is based on the assumption that aggregation proceeds only between two equal sized spherical particles and the resulting aggregate is also spherical in shape. In real systems, however, particles are different both in size and in shape, so aggregation may occur as a result of particle–particle, particle–cluster, or cluster–cluster collisions as given in Figure B1.1.

In an aggregation process, the success of the attachment and final aggregate structure depends on the regimes in which aggregation takes place. The aggregation regimes are called *diffusion-limited* (DLA) or *reaction-limited* (RLA) depending on the level of the repulsive energy barrier between the approaching particles. In the DLA regime, the repulsive energy barrier between the colliding entities is minimum, so diffusion to the collision site is the only rate limiting step. Aggregation that takes place in DLA regime is fast and all collision events end-up by an attachment. In this regime, fast aggregation results in open structured clusters. However, in the RLA regime the success of the attachment is a function of interaction

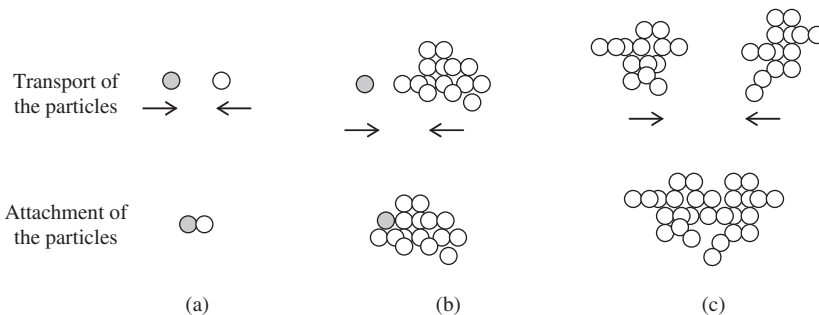


**Figure B1.1** Schematic diagram of aggregation process occurring between (a) particle–particle, (b) particle–cluster, and (c) cluster–cluster.

energy barrier that the particles have to overcome. Only the particles that have sufficient energy can attach and form more compact clusters. If the attractive energy between the particles is not strong enough, fragmentation of the particles may occur under the effect of applied external forces. The depth of the primary and/or secondary energy minimum in Figure 1.3 is an indication of the attractive energy.

## B1.2 Suspending medium

In population balance equations the suspending medium is generally taken as a Newtonian fluid, so all the correlations for Newtonian fluids are used. The hydrodynamic properties of the fluid affect the collisions of the particles through the transport mechanisms. The effect of the fluid properties on the particle aggregation is introduced into the population balance equation by the collision frequency function.

# APPENDIX B2: FORMULATION OF THE MODELS

Populations under different system conditions have different particle-size distributions. To predict the behavior of the population under the given conditions all the mechanisms effective on the particle-size distribution should be determined. Population balance equation given in eq. (B1.1) represents the aggregation mechanism of the particles. Two important parameters in population balance equation are the collision frequency function  $\beta$  and the collision efficiency  $\alpha$ . The expression or equation with which  $\beta$  is described is called the *collision frequency kernel*. According to the system under consideration, appropriate kernel for the  $\beta$  functions defining the system conditions should be selected.

## B2.1 Collision frequency function, $\beta$

The simplest kernel is the *size independent kernel* where all collisions have the same chance of occurrence independent of the particle/aggregate size.

$$\beta = \beta_0 = \text{constant} \quad (\text{B2.1})$$

This forms the reference state for the frequency function  $\beta$  (Hounslow *et al.*, 2001).

### B2.1.1 Aggregation under stagnant conditions

Aggregation of the particles in Brownian motion is known as *perikinetic coagulation*. The collision frequency function for perikinetic coagulation is defined by Smoluchowski (1917) and given as

$$\beta_{\text{perikinetic}} = \frac{2k_{\text{B}}T}{3\mu} \left( \frac{1}{d_i} + \frac{1}{d_j} \right) (d_i + d_j) \quad (\text{B2.2})$$

where  $k_{\text{B}}$  is the Boltzmann's constant [ $1.38 \times 10^{-23} \text{JK}^{-1}$ ],  $T$  the absolute temperature [K], and  $\mu$  the fluid viscosity [Pas].  $d_i$  and  $d_j$  are the diameters of particles  $i$  and  $j$ , respectively.

### B2.1.2 Aggregation under gravitational forces

The collision frequency function for particles with different settling velocities (differential sedimentation) is defined by Camp and Stein (1943) based on the Smoluchowski's approach

$$\beta_{\text{dif.sed.}} = \frac{g\pi}{72\mu}(\rho_p - \rho)(d_i + d_j)^3 |d_i - d_j| \quad (\text{B2.3})$$

where  $g$  is the acceleration of gravity [ $\text{ms}^{-2}$ ], and  $\rho_p$  and  $\rho$  the particle and fluid densities [ $\text{kgm}^{-3}$ ], respectively.

### B2.1.3 Aggregation under external shear

*Laminar regime* Orthokinetic coagulation takes place under the effect of laminar shear applied by the fluid. The collision frequency for orthokinetic coagulation is defined by Smoluchowski (1917) as

$$\beta_{\text{orthokinetic}} = \left(\frac{1}{6}\right)\left(\frac{dv}{dy}\right)(d_i + d_j)^3 \quad (\text{B2.4})$$

where  $dv/dy$  is the velocity gradient of the fluid.

*Isotropic turbulence* The collision frequency function for the collision of the particles smaller than the length of the smallest eddies is derived by Saffman and Turner (1956) as

$$\beta_{\text{isoturb}} = \frac{1.294}{8}\left(\frac{\varepsilon}{\nu}\right)^{1/2}(d_i + d_j)^3 \quad (\text{B2.5})$$

where  $\varepsilon$  is the energy dissipation rate [ $\text{Jkg}^{-1}\text{s}^{-1}$ ] and  $\nu$  the kinematic viscosity [ $\text{m}^2\text{s}^{-1}$ ] of the fluid.

### B2.1.4 Aggregation under magnetic forces

Magnetic forces increase the interactions between the particles during the transport and facilitate collisions. The effect of the magnetic forces on the particle collisions are greater than on the collisions due to the Brownian motion. The collision frequency function in the presence of an external magnetic force  $\beta_{\text{mag}}$ . Is defined by the ratio of collision frequency function due to the magnetic force to the collision frequency function due to Brownian motion,  $\beta_{\text{perikinetiic}}$ , given by (Kumar and Biswas, 2005)

$$\frac{\beta_{\text{mag}}}{\beta_{\text{perikinetiic}}} = \frac{1}{\left(\frac{d_i + d_j}{2}\right) \int_{(d_i + d_j)/2}^{\infty} \frac{1}{r^2} \exp\left(\frac{M}{k_B T}\right) dr} \quad (\text{B2.6})$$

Here  $M$  is the averaged magnetic interaction potential which is averaged over all the possible orientation of the particles. The magnetic potential has different forms in the case of randomly distributed

$$M'_{\text{md.}}(r) = -\frac{\mu_0}{4\pi r^3} m_i m_j [2\cos\theta_i \cos\theta_j - \cos(\phi_i - \phi_j) \sin\theta_i \sin\theta_j] \quad (\text{B2.7})$$

and aligned particles in the direction of a strong magnetic field

$$M'_{\text{aln.}}(r) = -\frac{\mu_0}{4\pi r^3} m_i m_j (3\cos^2\theta - 1) \quad (\text{B2.8})$$

The magnetic potentials given by eqs. (B2.7) and (B2.8) are averaged over all possible orientations of the particles to give  $M$  in eq. (B2.6). The solution of eq. (B2.6) with the proper magnetic potential definition gives the collision frequency function under the effect of magnetic force

$$\beta_{\text{mag.}} = C \left[ \frac{\pi \chi_i \chi_j B^2}{\mu_0} \right]^{1/3} (k_B T)^{2/3} \frac{1}{\mu} (d_i + d_j) \quad (\text{B2.9})$$

where  $\chi_i$  and  $\chi_j$  are the magnetic susceptibility of the particles  $i$  and  $j$  [dimensionless],  $B$  the magnetic flux density [ $\text{T} \equiv \text{kgA}^{-1}\text{s}^{-2}$ ] and  $\mu_0$  the permeability of free space [ $4\pi \times 10^{-7} \text{TmA}^{-1}$ ] and  $\mu$  the viscosity [Pas]. The constant  $C$  takes the value  $(2^{2/3}/3^{11/6})$  for randomly oriented and  $(2/3^{8/3})$  for aligned magnetic particles.

## B2.2 Aggregation of clusters

All particles are assumed to remain spherical in shape after the collisions in Smoluchowski's coagulation model. Since particles do not remain spherical in shape after the collisions and grow as fractals, their characteristic length is corrected with a nondigit number called fractal dimension,  $d_f$  (Section 1.4.2.1). In the case of spherical particles, the characteristic length is the particle diameter and the fractal dimension is equal to 3 proportional with the particle volume. However, in fractal structures that have different geometrical shapes, the fractal dimensions are less than 3 inversely proportional with the extent of void space existing between the particles. For diffusion-limited aggregation the aggregates formed are highly porous with an open structure, so the fractal dimension is  $\sim 1.8$ . The particles have to collide many times before a reaction-limited aggregation takes place, so the aggregate is more compact, described with a fractal dimension of 2.1 (Lattuada *et al.*, 2004). The relation between the diameters of the primary particle and the aggregate consisting of  $k$  primary particles is expressed as

$$d_{\text{agg,k}} = d_p (k)^{1/d_f} \quad (\text{B2.10})$$

where  $d_{\text{agg,k}}$  is the diameter of aggregates composed of  $k$  primary particles,  $d_p$  the primary particle diameter, and  $d_f$  the fractal dimension. Fractal dimension is introduced into the collision

frequency function to take into account the effect of fractal nature on the net rate of formation of particles. The generally accepted expression for the collision frequency function in terms of the fractal dimension is given by Odriozola *et al.* (1999) and Sandkühler *et al.* (2003) as

$$\beta_{\text{perikinet}} = \frac{2k_B T}{3\mu} \left( \frac{1}{d_{\text{agg},i}} + \frac{1}{d_{\text{agg},j}} \right) (d_{\text{agg},i} + d_{\text{agg},j}) \quad (\text{B2.11})$$

where  $d_{\text{agg},i}$  and  $d_{\text{agg},j}$  denote the characteristic dimensions of the aggregates.

### B2.3 Collision efficiency, $\alpha$

Smoluchowski's coagulation model depends on the assumption that interaction energy between the particles has no effect on the particle coagulation. The collision efficiency factor is taken as unity in this approach; that is, every collision ends up with an attachment. However, in real systems, the success of the attachment depends primarily on the interaction between the particles and the collision efficiency changes in the range of  $0 < \alpha < 1$  the limits denoting no aggregation and immediate aggregation. To describe a disperse system in a more realistic manner, Fuchs (1934) introduced a new definition, the stability ratio  $W$ , as the inverse of the collision efficiency factor that is a function of interaction energies between the aggregates given in eqs. (1.54) and (1.55). Runkana *et al.* (2004) computed the stability ratio thereby the collision efficiency by considering the DLVO theory where the total aggregate interaction is equal to the sum of the van der Waals energy of attraction and electrical double layer repulsion. Lattuada *et al.* (2004) determined the stability ratio through independent experiments in which different surface properties affecting the interactions are examined as parameters. The stability ratio found, is introduced into the Smoluchowski population balance equation in the collision frequency function as  $W$ .

$$\beta_{\text{perikinet}} = \frac{2k_B T}{3\mu W} \left( \frac{1}{d_{\text{agg},i}} + \frac{1}{d_{\text{agg},j}} \right) (d_{\text{agg},i} + d_{\text{agg},j}) \quad (\text{B2.12})$$

### B2.4 Incorporation of the break-up mechanism into the model equations

In systems where shear is applied on the particles, aggregate break-up should be considered simultaneously with the coagulation resulting from the applied shear

$$\left( \frac{dn_k}{dt} \right) = \left( \frac{dn_k}{dt} \right)_{\text{agg}} + \left( \frac{dn_k}{dt} \right)_{\text{break-up}} \quad (\text{B2.13})$$

where the rate of aggregation is given in eq. (B1.1). The rate of breakage differs from the rate of aggregation in that breakage depends on the extent of the shear applied on the particles,

whereas aggregation on the efficiency of the collision. Thus, an increase in fluid strain causes an increase in the rate of break-up (Kim and Kramer, 2006), expressed as

$$r_{\text{break-up}} = K_B(\gamma)^b (r_k)^s (n_k)^a \quad (\text{B2.14})$$

where  $K_B$  is the break-up rate constant,  $\gamma$  the elongational strain of the fluid,  $r_k$  the radius, and  $n_k$  the concentration of the aggregates denoted by  $k$ .  $b$  and  $s$  are the exponents defining the geometrical properties of a particle.  $a$  is the break-up concentration exponent and depends on the break-up distribution function. To describe the aggregate breakage the population balance equation is written in terms of the break-up mechanism. The break-up equation is expressed similar to that of aggregation given in eq. (B1.1)

$$\left( \frac{dn_k}{dt} \right)_{\text{break-up}} = \sum_{i=k+1}^{\infty} b_{k,i} K_B(\gamma)^b (r_i)^s (n_i)^a - K_B(\gamma)^b (r_k)^s (n_k)^a \quad (\text{B2.15})$$

where  $b_{k,i}$  is the distribution function of the aggregates  $k$  formed from the breakage of aggregates  $i$ . The first term on the right hand side of eq. (B2.15) is the increase in the number of the size  $k$  aggregates by the fracture of larger size aggregates and the second term is the decrease in the number of size  $k$  aggregates due to fracture. The break-up distribution functions defining the aggregate breakage can be given with a linear, logarithmic or exponential expression some of which are recently summarized by Han *et al.* (2003) and Kim and Kramer (2007). Appropriate break-up distribution functions defining the system under consideration should be selected. The generally used and simplest distribution function is the binary breakage in which equal sized aggregates are produced (Spicer and Pratsinis, 1996).

$$b_{k,i} = c \frac{v_i}{v_k} \quad (\text{B2.16})$$

where  $v_i$  and  $v_k$  are the volume of particles  $i$  and  $k$ . For a binary breakage  $c = 1$  and for a ternary breakage  $c = 2$ . Another frequently used distribution function is the log-normal breakage distribution which is the asymptotic limit of a repeated breakage. Pandya and Spielman (1982) showed that particles can be described by a lognormal distribution after the breakage process, defined as,

$$b_{k,i} = \frac{v_i}{v_k} \int_{c_i=1}^{c_i} \frac{1}{\sqrt{2\pi \log \sigma}} \exp \left[ - \left( \frac{\log(v/v_m)^2}{\log \sigma} \right) \right] dv \quad (\text{B2.17})$$

where  $\sigma$  is the standard deviation and  $v_m$  the mean value of the aggregate size distribution. Similar to the log-normal distribution function Spicer and Pratsinis (1996) assumed a normal

distribution function for the fragmentation of the particles that break up randomly and given by

$$b_{k,i} = \frac{v_i}{v_k} \int_{c_i=1}^{c_i} \frac{1}{\sqrt{2\pi}\sigma} \exp \left[ - \left( \frac{(v - v_m)^2}{2\sigma^2} \right) \right] dv \quad (\text{B2.18})$$

The overall population balance equation describing both coagulation and break-up mechanisms is obtained by the summation of eqs. (B1.1) and (B2.15), and is expressed as

$$\begin{aligned} \frac{dn_k}{dt} = & \frac{1}{2} \sum_{k=i+j} \alpha\beta(i,j)n_i n_j - n_k \sum_{i=1}^{\infty} \alpha\beta(i,j)n_i \\ & + \sum_{m=k+1}^{\infty} b_{k,m} K_B(\gamma)^b (r_m)^s (n_m)^a - K_B(\gamma)^b (r_k)^s (n_k)^a \end{aligned} \quad (\text{B2.19})$$

If other mechanisms exist such as restructuring, diffusion or chemical reaction that affect the particle-size distributions, the related expressions should be included into the population balance, eq. (B2.19).

### APPENDIX B3: SOLUTION OF THE POPULATION BALANCE EQUATION

Population balance equation given in eq. (B2.17) is a nonlinear differential equation, difficult to solve by analytical or numerical methods. Analytical solution necessitates the assumption of monodispersity as the initial condition and drastic simplifications in the collision kernels  $\beta$ . Numerical solutions give more realistic results than the analytical solutions for the prediction of the behavior of a population.

Population balance model covers a wide range of particle sizes. Thus, to represent all of the population, infinite numbers of differential equations as eq. (B2.17) should be written for each particle size. To make the solutions of these equations manageable, they should be discretized into the size classes. For a real solution the  $\infty$  limit in eq. (B2.17) is replaced by  $i_{\max}$  and eq. (B2.17) becomes

$$\begin{aligned} \frac{dn_k}{dt} = & \frac{1}{2} \sum_{k=i+j} \alpha\beta(i,j)n_i n_j - n_k \sum_{i=1}^{i_{\max}} \alpha\beta(i,j)n_i \\ & + \sum_{i=k+1}^{i_{\max}} b_{k,i} K_B(\gamma)^b (r_i)^s (n_i)^a - K_B(\gamma)^b (r_k)^s (n_k)^a \end{aligned} \quad (\text{B3.1})$$

where  $i_{\max}$  represents the maximum size class in the population. Discretization of the population size classes can be made by applying uniform or nonuniform discretization models.

### B3.1 Uniform discretization method

In uniform discretization method the smallest particle size is selected as the primary size and all other particles are taken as integer multiples of this class. Thus, the ratio of upper and lower bounds of an interval is constant and given by

$$\frac{V_{k+1}}{V_k} = q \quad (\text{B3.2})$$

A large number of size classes are needed to predict the size distribution of a population in this type of discretization method. Since each size class is defined by a nonlinear differential equation, a large number of equations should be used. Although uniform discrete model gives a good prediction for the size distribution of a population, simultaneous solution of the equations requires long computational times, which make the method computationally nonefficient.

### B3.2 Nonuniform discretization method

To reduce the number of equations used in the uniform discretization methods, nonuniform discretization methods are developed that require a smaller number of equations. In nonuniform discretization methods, the size classes are grouped by using geometrical size intervals where the ratio of upper and lower bounds is fixed. Since the number of size classes is limited in this model, it is less accurate than the uniform discretization method. However, the decrease in the number of equations results in a computationally efficient solution.

Different approaches are developed in nonuniform discretization methods where the ratio  $q$  in eq. (B3.2) is defined by various assumptions. The generally used approach is developed by Batterham *et al.* (1981), which takes the geometrical size interval  $q$  in eq. (B3.2) as 2. Hounslow *et al.* (1988) also used a model with a geometrical size interval of 2 that differs from the Batterham model in the consideration of continuous intervals rather than discrete intervals. However, the models developed by Batterham *et al.* (1981) and Hounslow *et al.* (1988) do not work well for large size classes since a fixed class size interval causes a broad distribution of size ranges. To overcome this inaccuracy adjustable size interval methods are developed (Kim and Kramer, 2007). By using adjustable size intervals both the large number of size classes, thereby the nonefficient computational solution of the uniform discrete model, and the inaccurate approaches of geometrical size interval of 2 are corrected.

Population balance equation covers a wide range of particle concentrations leading to a big difference between the minimum (1 particle initially) and maximum number concentrations of the particles. This may cause a stiffness problem during the simultaneous solution of the discretized population balance equations. In the solution of stiff ordinary differential equations (ODE), there is a transient region whose behavior is on a different scale from the solution region. To overcome this stiffness problem several numerical integration methods for the solution of ODEs are developed. By selecting the appropriate method the nonlinear ordinary differential population balance equations can be solved and the size distribution of the population can be predicted.



## REFERENCES

- Batterham, R.J., Hall, J.S., Barton, G., 1981. Pelletizing kinetics and simulation of full scale balling circuits. In: International Symposium on Agglomeration (3rd), Nurnberg, A136–A150.
- Camp, T.R., Stein, P.C., 1943. Velocity gradients and internal work in fluid motion. *Journal of the Boston Society of Civil Engineers*, 30, 219–237.
- Fuchs, N., 1934. Über die Stabilität und Aufladung der Aerosole. *Zeitschrift für Physik*, 89, 736–743.
- Han, B., Akeprathumchai, S., Wickramasinghe, S.R., Oian, X., 2003. Flocculation of biological cells: experiment vs. theory. *AIChE Journal*, 49, 1687–1701.
- Hounslow, M.J., Pearson, J.M.K., Instone, T., 2001. Tracer studies of high shear granulation: II. Population balance modeling. *AIChE Journal*, 47, 1984–1999.
- Hounslow, M.J., Ryall, R.L., Marshall, V.R., 1988. A discretized population balance for nucleation, growth, and aggregation. *AIChE Journal*, 34, 1821–1832.
- Kim, J., Kramer, T.A., 2006. Improved orthokinetic coagulation model for fractal colloids: aggregation and breakup. *Chemical Engineering Science*, 61, 45–53.
- Kim, J.W., Kramer, T.A., 2007. Adjustable discretized population balance equations: numerical simulation and parameter estimation for fractal aggregation and break-up. *Colloids and Surfaces A: Physicochemical Engineering Aspects*, 292, 173–188.
- Kumar, P., Biswas, P., 2005. Analytical expressions of the collision frequency function for aggregation of magnetic particles. *Journal of Aerosol Science*, 36, 455–469.
- Lattuada, M., Wu, H., Sandkühler, P., Sefcik, J., Morbidelli, M., 2004. Modelling of aggregation kinetics of colloidal systems and its validation by light scattering measurements. *Chemical Engineering Science*, 59, 1783–1798.
- Odriozola, G., Schmitt, A., Callejas-Fernandez, J., Martinez-Garcia, R., Hidalgo-Alvarez, R., 1999. Dynamic scaling concepts applied to numerical solutions of Smoluchowski's rate equation. *Journal of Chemical Physics*, 111, 7657–7667.
- Pandya, J.D., Spielman, L.A., 1982. Floc breakage in agitated suspensions: theory and data processing strategy. *Journal of Colloid and Interface Science*, 90, 517.
- Runkana, V., Somasundaran, P., Kapur, P.C., 2004. Mathematical modeling of polymer-induced flocculation by charge neutralization. *Journal of Colloid and Interface Science*, 270, 347–358.
- Saffman, P.G., Turner, J.S., 1956. On the collision of drops in turbulent clouds. *Journal of Fluid Mechanics*, 1, 16.
- Sandkühler, P., Sefcik, J., Lattuada, M., Wu, H., Morbidelli, M., 2003. Modelling structure effects on aggregation kinetics in colloidal dispersions. *AIChE Journal*, 49, 1542–1555.
- Smoluchowski, M., 1917. Versuch Einer Mathematischen Theorie der Koagulations-Kinetik Kolloider Lösungen. *Zeitschrift für Physikalische Chemie*, 92, 129.
- Spicer, P.T., Pratsinis, S.E., 1996. Coagulation and fragmentation: universal steady-state particle size distribution. *AIChE Journal*, 42, 1612.

# Appendix C

## Tables for Use in Plug Flow in an Annulus

See Tables C.1 and C.2.

Table C.1

Calculated values of  $\lambda_0(k, n, T_0)$  where  $\lambda_0 = \lambda$  for  $T_0 = 0$

$T_0$	$n$									
	0.1	0.2	0.3	0.4	0.5	0.6	0.7	0.8	0.9	1
$k = 0.1$										
0.00	0.3442	0.3682	0.3884	0.4052	0.4193	0.4312	0.4412	0.4498	0.4572	0.4637
0.05	0.3701	0.3940	0.4142	0.4309	0.4448	0.4562	0.4656	0.4733	0.4797	0.4851
0.10	0.3978	0.4216	0.4415	0.4579	0.4711	0.4818	0.4903	0.4972	0.5028	0.5075
0.15	0.4273	0.4507	0.4703	0.4860	0.4984	0.5081	0.5158	0.5219	0.5268	0.5308
0.20	0.4584	0.4815	0.5004	0.5152	0.5266	0.5353	0.5421	0.5474	0.5517	0.5552
0.25	0.4912	0.5137	0.5317	0.5454	0.5556	0.5633	0.5692	0.5739	0.5776	0.5806
0.30	0.5254	0.5472	0.5641	0.5765	0.5855	0.5922	0.5973	0.6013	0.6045	0.6070
0.35	0.5611	0.5820	0.5975	0.6085	0.6163	0.6220	0.6263	0.6296	0.6323	0.6345
0.40	0.5980	0.6178	0.6317	0.6412	0.6478	0.6526	0.6562	0.6589	0.6612	0.6629
0.45	0.6361	0.6544	0.6666	0.6746	0.6801	0.6840	0.6869	0.6892	0.6910	0.6924
0.50	0.6752	0.6918	0.7021	0.7087	0.7131	0.7162	0.7186	0.7204	0.7218	0.7229
0.55	0.7152	0.7298	0.7382	0.7434	0.7469	0.7493	0.7511	0.7524	0.7535	0.7544
0.60	0.7559	0.7681	0.7748	0.7787	0.7813	0.7831	0.7844	0.7854	0.7862	0.7868
0.65	0.7970	0.8068	0.8117	0.8145	0.8163	0.8176	0.8185	0.8192	0.8197	0.8202
0.70	0.8384	0.8456	0.8490	0.8508	0.8520	0.8528	0.8534	0.8538	0.8542	0.8544
0.75	0.8798	0.8845	0.8865	0.8875	0.8882	0.8887	0.8890	0.8892	0.8894	0.8896
0.80	0.9209	0.9233	0.9242	0.9247	0.9250	0.9252	0.9253	0.9254	0.9255	0.9256
0.85	0.9611	0.9618	0.9620	0.9622	0.9622	0.9623	0.9623	0.9624	0.9624	0.9624
$k = 0.2$										
0.00	0.4687	0.4856	0.4991	0.5100	0.5189	0.5262	0.5324	0.5377	0.5422	0.5461
0.05	0.4943	0.5113	0.5247	0.5355	0.5442	0.5512	0.5569	0.5615	0.5653	0.5684
0.10	0.5213	0.5382	0.5515	0.5620	0.5702	0.5766	0.5816	0.5856	0.5889	0.5916
0.15	0.5496	0.5664	0.5794	0.5894	0.5969	0.6026	0.6070	0.6104	0.6132	0.6155
0.20	0.5792	0.5957	0.6083	0.6175	0.6243	0.6292	0.6330	0.6360	0.6383	0.6402
0.25	0.6100	0.6262	0.6381	0.6464	0.6523	0.6565	0.6597	0.6622	0.6642	0.6658
0.30	0.6421	0.6578	0.6686	0.6759	0.6809	0.6845	0.6872	0.6892	0.6909	0.6922
0.35	0.6752	0.6902	0.6998	0.7060	0.7102	0.7132	0.7153	0.7170	0.7183	0.7194

(Continued)

Table C.1 (Continued)

$T_0$	$n$									
	0.1	0.2	0.3	0.4	0.5	0.6	0.7	0.8	0.9	1
0.40	0.7095	0.7233	0.7316	0.7368	0.7401	0.7425	0.7442	0.7455	0.7466	0.7474
0.45	0.7447	0.7571	0.7640	0.7680	0.7707	0.7725	0.7738	0.7748	0.7756	0.7762
0.50	0.7807	0.7914	0.7967	0.7998	0.8018	0.8031	0.8041	0.8048	0.8054	0.8059
0.55	0.8174	0.8259	0.8299	0.8321	0.8335	0.8344	0.8351	0.8356	0.8360	0.8363
0.60	0.8545	0.8607	0.8634	0.8648	0.8657	0.8663	0.8668	0.8671	0.8674	0.8676
0.65	0.8917	0.8956	0.8972	0.8980	0.8985	0.8989	0.8991	0.8993	0.8995	0.8996
0.70	0.9286	0.9305	0.9313	0.9316	0.9319	0.9320	0.9321	0.9322	0.9323	0.9323
0.75	0.9648	0.9654	0.9655	0.9656	0.9657	0.9657	0.9658	0.9658	0.9658	0.9658
$k = 0.3$										
0.00	0.5632	0.5749	0.5840	0.5912	0.5970	0.6018	0.6059	0.6093	0.6122	0.6147
0.05	0.5887	0.6004	0.6095	0.6165	0.6223	0.6268	0.6304	0.6333	0.6357	0.6377
0.10	0.6154	0.6271	0.6360	0.6429	0.6481	0.6522	0.6553	0.6578	0.6597	0.6614
0.15	0.6431	0.6547	0.6635	0.6699	0.6745	0.6780	0.6807	0.6827	0.6844	0.6857
0.20	0.6720	0.6834	0.6917	0.6974	0.7015	0.7044	0.7066	0.7084	0.7097	0.7108
0.25	0.7019	0.7130	0.7206	0.7256	0.7290	0.7314	0.7332	0.7346	0.7357	0.7366
0.30	0.7328	0.7434	0.7501	0.7543	0.7570	0.7590	0.7604	0.7615	0.7624	0.7630
0.35	0.7647	0.7745	0.7801	0.7835	0.7856	0.7871	0.7882	0.7891	0.7897	0.7902
0.40	0.7975	0.8061	0.8106	0.8131	0.8147	0.8159	0.8167	0.8173	0.8178	0.8181
0.45	0.8310	0.8381	0.8414	0.8432	0.8444	0.8452	0.8457	0.8461	0.8465	0.8467
0.50	0.8651	0.8703	0.8726	0.8738	0.8745	0.8750	0.8754	0.8757	0.8759	0.8760
0.55	0.8994	0.9028	0.9041	0.9048	0.9052	0.9055	0.9057	0.9058	0.9059	0.9060
0.60	0.9335	0.9352	0.9358	0.9361	0.9363	0.9364	0.9365	0.9366	0.9366	0.9367
0.65	0.9672	0.9676	0.9678	0.9679	0.9679	0.9680	0.9680	0.9680	0.9680	0.9680
$k = 0.4$										
0.00	0.6431	0.6509	0.6570	0.6617	0.6655	0.6686	0.6713	0.6735	0.6754	0.6770
0.05	0.6686	0.6764	0.6824	0.6871	0.6908	0.6936	0.6959	0.6978	0.6993	0.7005
0.10	0.6950	0.7029	0.7088	0.7132	0.7165	0.7190	0.7209	0.7224	0.7236	0.7246
0.15	0.7224	0.7302	0.7359	0.7399	0.7427	0.7448	0.7463	0.7476	0.7485	0.7493
0.20	0.7508	0.7584	0.7636	0.7671	0.7694	0.7711	0.7723	0.7733	0.7740	0.7746
0.25	0.7801	0.7874	0.7919	0.7947	0.7966	0.7979	0.7989	0.7996	0.8002	0.8006
0.30	0.8103	0.8170	0.8207	0.8229	0.8243	0.8252	0.8259	0.8265	0.8269	0.8272
0.35	0.8413	0.8470	0.8498	0.8514	0.8524	0.8531	0.8536	0.8539	0.8542	0.8545
0.40	0.8730	0.8774	0.8793	0.8804	0.8810	0.8815	0.8818	0.8820	0.8822	0.8823
0.45	0.9051	0.9080	0.9091	0.9097	0.9101	0.9103	0.9105	0.9106	0.9107	0.9108
0.50	0.9372	0.9387	0.9392	0.9395	0.9396	0.9397	0.9398	0.9399	0.9399	0.9399
0.55	0.9689	0.9693	0.9695	0.9695	0.9696	0.9696	0.9696	0.9696	0.9697	0.9697
$k = 0.5$										
0.00	0.7140	0.7191	0.7229	0.7259	0.7283	0.7303	0.7319	0.7333	0.7345	0.7355
0.05	0.7395	0.7445	0.7483	0.7512	0.7535	0.7553	0.7567	0.7578	0.7587	0.7594
0.10	0.7658	0.7708	0.7745	0.7772	0.7792	0.7806	0.7817	0.7826	0.7833	0.7838
0.15	0.7929	0.7979	0.8013	0.8037	0.8053	0.8064	0.8073	0.8079	0.8084	0.8089
0.20	0.8210	0.8257	0.8287	0.8306	0.8318	0.8327	0.8333	0.8338	0.8341	0.8344
0.25	0.8499	0.8542	0.8565	0.8579	0.8588	0.8594	0.8598	0.8601	0.8604	0.8606
0.30	0.8795	0.8830	0.8847	0.8856	0.8862	0.8866	0.8868	0.8870	0.8872	0.8873
0.35	0.9097	0.9121	0.9131	0.9137	0.9140	0.9142	0.9144	0.9145	0.9146	0.9147

(Continued)

Table C.1 (Continued)

$T_0$	$n$									
	0.1	0.2	0.3	0.4	0.5	0.6	0.7	0.8	0.9	1
0.40	0.9401	0.9414	0.9419	0.9421	0.9422	0.9423	0.9424	0.9425	0.9425	0.9425
0.45	0.9703	0.9707	0.9708	0.9709	0.9709	0.9709	0.9710	0.9710	0.9710	0.9710
$k = 0.6$										
0.00	0.7788	0.7818	0.7840	0.7858	0.7872	0.7884	0.7893	0.7902	0.7909	0.7915
0.05	0.8042	0.8072	0.8094	0.8111	0.8124	0.8134	0.8142	0.8148	0.8153	0.8157
0.10	0.8304	0.8333	0.8355	0.8370	0.8380	0.8388	0.8394	0.8398	0.8401	0.8404
0.15	0.8574	0.8602	0.8621	0.8632	0.8640	0.8646	0.8650	0.8653	0.8655	0.8657
0.20	0.8851	0.8877	0.8891	0.8899	0.8904	0.8908	0.8910	0.8912	0.8914	0.8915
0.25	0.9136	0.9156	0.9165	0.9169	0.9172	0.9174	0.9176	0.9177	0.9178	0.9178
0.30	0.9425	0.9436	0.9441	0.9443	0.9444	0.9445	0.9446	0.9446	0.9447	0.9447
0.35	0.9715	0.9718	0.9719	0.9720	0.9720	0.9720	0.9721	0.9721	0.9721	0.9721
$k = 0.7$										
0.00	0.8389	0.8404	0.8416	0.8426	0.8433	0.8439	0.8444	0.8449	0.8452	0.8455
0.05	0.8642	0.8658	0.8670	0.8679	0.8685	0.8690	0.8693	0.8696	0.8699	0.8700
0.10	0.8904	0.8919	0.8929	0.8936	0.8941	0.8944	0.8946	0.8948	0.8949	0.8950
0.15	0.9172	0.9186	0.9193	0.9197	0.9200	0.9202	0.9203	0.9204	0.9205	0.9205
0.20	0.9447	0.9456	0.9460	0.9462	0.9463	0.9464	0.9464	0.9465	0.9465	0.9465
0.25	0.9725	0.9728	0.9729	0.9729	0.9730	0.9730	0.9730	0.9730	0.9730	0.9730
$k = 0.8$										
0.00	0.8954	0.8960	0.8965	0.8969	0.8972	0.8975	0.8977	0.8979	0.8980	0.8981
0.05	0.9207	0.9214	0.9218	0.9222	0.9224	0.9226	0.9227	0.9228	0.9228	0.9229
0.10	0.9467	0.9473	0.9476	0.9478	0.9479	0.9480	0.9480	0.9481	0.9481	0.9481
0.15	0.9734	0.9736	0.9737	0.9738	0.9738	0.9738	0.9738	0.9738	0.9738	0.9738
$k = 0.9$										
0.00	0.9489	0.9491	0.9492	0.9493	0.9493	0.9494	0.9495	0.9495	0.9495	0.9496
0.05	0.9742	0.9744	0.9744	0.9745	0.9745	0.9745	0.9745	0.9745	0.9746	0.9746

Source: Gücüyener, H.I., Mehmetoğlu, T., 1992. Flow of yield-pseudo-plastic fluids through a concentric annulus. AIChE Journal, 38, 1139–1143 (with permission of American Institute of Chemical Engineers).

Table C.2

Values of  $\lambda$  for various values of  $k$ ,  $T_0$ , and  $n$

$T_0$	$n$									
	0.1	0.2	0.3	0.4	0.5	0.6	0.7	0.8	0.9	1
$k = 0.1$										
0.00	0.3442	0.3682	0.3884	0.4052	0.4193	0.4312	0.4412	0.4498	0.4572	0.4637
0.05	0.3427	0.3656	0.3851	0.4014	0.4153	0.4269	0.4369	0.4455	0.4529	0.4594
0.10	0.3412	0.3630	0.3817	0.3975	0.4110	0.4225	0.4323	0.4408	0.4482	0.4547
0.15	0.3397	0.3604	0.3782	0.3935	0.4065	0.4178	0.4274	0.4358	0.4432	0.4496
0.20	0.3382	0.3577	0.3747	0.3893	0.4019	0.4128	0.4222	0.4305	0.4377	0.4441

(Continued)

Table C.2 (Continued)

$T_0$	$n$									
	0.1	0.2	0.3	0.4	0.5	0.6	0.7	0.8	0.9	1
0.25	0.3367	0.3550	0.3710	0.3850	0.3971	0.4076	0.4167	0.4248	0.4319	0.4381
0.30	0.3352	0.3523	0.3673	0.3805	0.3920	0.4021	0.4109	0.4187	0.4256	0.4317
0.35	0.3337	0.3495	0.3635	0.3759	0.3868	0.3964	0.4048	0.4123	0.4189	0.4248
0.40	0.3321	0.3466	0.3596	0.3711	0.3813	0.3904	0.3988	0.4055	0.4118	0.4175
0.45	0.3306	0.3438	0.3556	0.3663	0.3757	0.3841	0.3916	0.3983	0.4043	0.4097
0.50	0.3290	0.3409	0.3516	0.3612	0.3699	0.3776	0.3846	0.3908	0.3964	0.4014
0.55	0.3275	0.3379	0.3474	0.3561	0.3639	0.3709	0.3772	0.3829	0.3880	0.3926
0.60	0.3259	0.3349	0.3432	0.3508	0.3577	0.3639	0.3695	0.3746	0.3792	0.3834
0.65	0.3243	0.3319	0.3389	0.3454	0.3512	0.3566	0.3615	0.3659	0.3699	0.3736
0.70	0.3227	0.3288	0.3345	0.3398	0.3446	0.3491	0.3531	0.3568	0.3602	0.3633
0.75	0.3215	0.3257	0.3301	0.3341	0.3378	0.3413	0.3444	0.3473	0.3499	0.3524
0.80	0.3259	0.3226	0.3255	0.3283	0.3308	0.3332	0.3354	0.3375	0.3392	0.3409
0.85	0.3349	0.3194	0.3209	0.3223	0.3236	0.3248	0.3260	0.3270	0.3280	0.3289
$k = 0.2$										
0.00	0.4687	0.4856	0.4991	0.5100	0.5189	0.5262	0.5324	0.5377	0.5422	0.5461
0.05	0.4674	0.4835	0.4965	0.5070	0.5157	0.5230	0.5291	0.5344	0.5389	0.5429
0.10	0.4661	0.4814	0.4938	0.5040	0.5124	0.5195	0.5256	0.5308	0.5353	0.5392
0.15	0.4649	0.4792	0.4910	0.5008	0.5089	0.5158	0.5218	0.5269	0.5313	0.5353
0.20	0.4636	0.4770	0.4882	0.4974	0.5053	0.5119	0.5177	0.5227	0.5270	0.5309
0.25	0.4623	0.4748	0.4852	0.4940	0.5014	0.5078	0.5133	0.5181	0.5224	0.5261
0.30	0.4610	0.4725	0.4822	0.4904	0.4974	0.5034	0.5087	0.5133	0.5174	0.5210
0.35	0.4596	0.4701	0.4790	0.4866	0.4932	0.4988	0.5038	0.5082	0.5120	0.5155
0.40	0.4583	0.4678	0.4758	0.4828	0.4888	0.4940	0.4986	0.5027	0.5063	0.5096
0.45	0.4570	0.4653	0.4725	0.4788	0.4842	0.4890	0.4932	0.4969	0.5002	0.5032
0.50	0.4556	0.4629	0.4692	0.4747	0.4795	0.4837	0.4875	0.4908	0.4938	0.4965
0.55	0.4542	0.4604	0.4657	0.4704	0.4745	0.4782	0.4815	0.4844	0.4870	0.4894
0.60	0.4528	0.4578	0.4622	0.4660	0.4694	0.4725	0.4752	0.4776	0.4798	0.4818
0.65	0.4525	0.4552	0.4586	0.4615	0.4641	0.4665	0.4732	0.4705	0.4723	0.4738
0.70	0.4589	0.4526	0.4549	0.4569	0.4587	0.4603	0.4618	0.4631	0.4643	0.4654
0.75	0.4700	0.4499	0.4511	0.4521	0.4530	0.4539	0.4546	0.4553	0.4560	0.4565
$k = 0.3$										
0.00	0.5632	0.5749	0.5840	0.5912	0.5970	0.6018	0.6059	0.6093	0.6122	0.6147
0.05	0.5621	0.5732	0.5819	0.5889	0.5946	0.5993	0.6033	0.6067	0.6096	0.6122
0.10	0.5611	0.5715	0.5798	0.5864	0.5919	0.5966	0.6005	0.6038	0.6068	0.6093
0.15	0.5601	0.5698	0.5775	0.5839	0.5892	0.5936	0.5974	0.6007	0.6036	0.6061
0.20	0.5590	0.5680	0.5752	0.5812	0.5862	0.5905	0.5941	0.5973	0.6001	0.6025
0.25	0.5579	0.5661	0.5728	0.5784	0.5831	0.5871	0.5906	0.5936	0.5963	0.5987
0.30	0.5568	0.5642	0.5704	0.5755	0.5798	0.5836	0.5868	0.5897	0.5922	0.5944
0.35	0.5557	0.5623	0.5678	0.5724	0.5764	0.5798	0.5828	0.5854	0.5878	0.5898
0.40	0.5546	0.5604	0.5652	0.5693	0.5728	0.5759	0.5785	0.5809	0.5830	0.5849
0.45	0.5535	0.5584	0.5625	0.5660	0.5690	0.5717	0.5740	0.5761	0.5779	0.5796
0.50	0.5524	0.5563	0.5597	0.5626	0.5651	0.5673	0.5693	0.5710	0.5726	0.5740
0.55	0.5520	0.5542	0.5568	0.5590	0.5610	0.5627	0.5643	0.5656	0.5668	0.5680
0.60	0.5616	0.5521	0.5539	0.5554	0.5567	0.5579	0.5590	0.5599	0.5608	0.5616
0.65	0.5765	0.5499	0.5508	0.5516	0.5523	0.5529	0.5535	0.5540	0.5544	0.5548

(Continued)

**Table C.2** (Continued)

(Continued)

Table C.2 (Continued)

$T_0$	$n$									
	0.1	0.2	0.3	0.4	0.5	0.6	0.7	0.8	0.9	1
0.10	0.8954	0.8953	0.8956	0.8958	0.8961	0.8962	0.8964	0.8965	0.8966	0.8967
0.15	0.8960	0.8949	0.8950	0.8952	0.8953	0.8954	0.8955	0.8956	0.8956	0.8957
$k = 0.9$										
0.00	0.9489	0.9491	0.9492	0.9493	0.9493	0.9494	0.9495	0.9495	0.9495	0.9496
0.05	0.9488	0.9489	0.9490	0.9490	0.9491	0.9491	0.9491	0.9492	0.9492	0.9492

Source: Hanks, R.W., 1979. The axial laminar flow of yield-pseudoplastic fluids in a concentric annulus. Industrial and Engineering Chemistry Process Design and Development, 18, 488–493 (with permission of American Chemical Society).

# Index

- Adhesion, 389–390
- Aggregation
  - diffusion limited, 27, 41, 497
  - ferromagnetic particles, 36–39
  - in biological systems, 59–71
  - kinetics, 26
  - light-induced, 39
  - number, 58
  - orthokinetic, 26
  - perikinetic, 26, 495, 496, 498
  - reaction limited, 26, 29, 41, 494, 497
  - reversibility, 38
- Amplitude sweep
  - strain, 80, 217
  - stress, 80, 81
- Angle of internal friction, 341
- Angle-averaged potential, 3
- Anisotropic, 30, 208, 209, 211–212
- Annulus
  - concentric, 142–149
  - eccentric, 149–151
- Archimedes number, 259, 408, 409, 447
- Aspect ratio, 30, 153, 208, 209, 211, 264, 265, 461
- Averaged
  - drag force, 311
  - interfacial force, 311–312
  - pressure difference, 310–311
- Averaging techniques
  - area, 298–299
  - ensemble, 299–300
  - time, 297–298
  - volume, 298–299
- Bagnold dispersive stress, 352, 354–355, 364
- Bartosik and Shook model, 364
- Bending modulus, 48, 49, 230
- Bifurcation, 460–461
- Bjerrum length, 200
- Blood, 59–64, 225–229
  - flow, 225–227
  - rheology, 228–245
- Boltzmann distribution, 3, 10
- Bridging, 18, 22, 24, 25, 32, 33, 41, 56, 62, 63, 203, 229, 389
- Brownian
  - force, 167–169, 174, 179, 185, 188
  - motion, 1, 26, 168, 185, 188, 217, 284, 349, 495
  - particle, 209, 211
- Cage structure, 171, 173, 191, 192
- Capillary
  - force, 388–389
  - number, 392
- Chaotic advection, 402, 433
- Charge reversing ion, 13, 14
- Circulatory system, 225–239
- Clarification rate, 442
- Classifiers
  - bottom feed (vessels), 444–445
  - fluidized bed, 445–448
  - parallel channel, 440–442
- Clearance, 407, 416–420
- Cluster
  - fractal, 29, 174, 188, 194–196, 274
  - hydrocluster, 174, 188, 189, 191, 192–193
  - percolation, 29, 194–195
  - thermodynamic, 188, 191
- Cohesive, 175, 255
- Collision
  - efficiency, 26, 27, 494, 495, 498
  - frequency, 26, 494, 495, 496, 497, 498
- Contact angle, 387–388
  - dynamic, 392
  - static, 392
- Contact value theorem, 19
- Contours
  - viscosity, 136, 137, 138
  - velocity, 154, 155



- Coordination number, 201, 204, 385–386
- Core repulsion energy, 15
- Correlation
  - deposition velocity, 371–376, 377
  - pressure drop, 372–374
  - Turian, 374, 375, 378
- Creep and recovery, 75, 78, 85, 196, 197, 235, 236
- Creeping flow, 246–252, 270–276
- Critical micelle concentration (CMC), 46, 216
- Critical packing parameter, 48
- Critical stress, 90, 176, 177, 189, 214, 238
- Cut size, 443, 455
  
- Darcy-Weisbach equation, 118, 131, 338, 353
- Deborah number, 74, 219–220, 230
- Debye interaction, 4
  - length, 11–13, 17
- Deformation history, 217
- Depletion, 18, 22, 23, 32, 34, 41, 42, 63, 169, 179, 189, 190, 191, 203, 207, 225, 443
- Diameter
  - equivalent projected area, 263
  - equivalent surface area, 264
  - equivalent-volume sphere, 263, 264
- Diffusivity
  - momentum, 351
  - particle, 167, 206, 351
- Dilatant, 88, 188
- Dipolar coupling constant, 37
- Dipole
  - induced, 4, 5, 7, 391
  - moment, 2, 3, 4, 37, 38, 39, 170
  - permanent, 5
- Discharge of suspensions, 394–400
- Discrete charges, 33
- Dispersion
  - Brownian diffusion, 172
  - flow induced, 348–349
  - in mixers, 407–412
    - of floating solids, 411–412
    - of settling solids, 408–411
  - into stagnant liquids, 397–399
  - of solid, 397–400, 407–412
  - shear induced, 347–348
- DLVO force, 17, 30, 31–32
- Dodge-Metzner correlation, 131
- Double layer
  - repulsion, 34, 50, 203
  
- Drag
  - coefficient, 256, 258–259, 260, 264–265, 266, 272, 412
  - form, 252, 256, 354
  - friction, 252, 256
  - reduction, 215–217
- Durand parameter, 372, 373
- Dynamic
  - response, 79, 198
  - yield stress, 206, 207, 214, 234, 238
  
- Efficiency
  - separation, 449–459, 463
  - partial separation, 449
- Einstein equation, 280
- Elastic contact modulus, 222, 223
- Elasticity, 48, 71–86
- Electroviscous effect, 212
- Elongated particle, 209–210
- Ensemble averaging of
  - basic transport equations, 303–305
  - mathematical requirements, 300–303
- Equivalent liquid model, 340, 354
- Erythrocytes, 59, 60, 62, 228
- Eulerian, *see* Simulation models
- Excluded volume, 23, 63, 168–169, 211
- Extensional flow, 216
- Extrusion, 428–431
  
- Fahraeus-Lindquist, 228
- Ferrofluid, 36–39
- Ferromagnetic particle, 36–38
- Fibrinogen, 60, 63, 64, 225, 229
- Field
  - electrical, 258, 466, 467
  - gravitational, 253, 257, 439–457
  - magnetic, 38, 254, 457–459
- Field flow fractionation, 460
- Flocculates, 27
- Flocculation, 279, 459
- Flow number, 400
- Force
  - acoustic, 255, 461–462
  - Basset history, 295
  - buoyancy, 253–254, 459
  - centrifugal, 253, 254
  - drag, 245, 255–257, 268, 271, 311
  - electrostatic, 254–255
  - fluid acceleration, 295

- gravity-gravitational, 65–66, 253, 277, 359, 496
- interfacial, 311–312
- lift, 312, 356–357
- magnetic, 254, 496–497
- Saffmann lift, 295
- shear, 168, 174, 255, 368
- turbulent dispersion, 309, 311
- virtual (added) mass, 311
- Fractal dimension, 28, 29–32, 34, 42, 66, 497
- Fracture, 31, 213, 499
- Fragmentation, 26, 29, 31
- Friction
  - dry-state, 340, 344, 355, 356, 371
  - model, 340, 363
  - velocity, *see* Shear velocity
- Friction factor,
  - as a criterion for transition, 125–127
  - charts, 132, 133
  - in flow through annulus, 150
  - in flow through microchannels, 158–159
  - in flow through rectangular channels, 156–157
  - in fully suspended flow, 335
  - laminar regime, 116–118
  - turbulent regime, 131–134
- Frictional velocity, 128
- Fully suspended flow, 330–331, 335–336, 351–352
- Gel
  - clay, 196–199
  - colloidal, 173
  - formation, 41, 173, 188, 191, 193, 206, 212
  - micro, 214, 221, 224
  - microstructure, 194
  - network, 84, 193, 230
  - particle, 193, 194, 223, 224
  - starch, 77
  - state, 171, 173, 193
  - structure, 41–42, 174, 194, 195, 217
- Glass
  - state, 40, 41, 173, 211
  - transition, 40, 173, 196
- Gouy-Chapman equation, 10, 13, 15
- Hagen-Poiseuille equation, 111, 118, 391
- Hamaker constant, 7, 8, 9, 17, 39, 168
- Hanks relation, 120, 125
- Hard sphere, 168, 171, 173–179, 183–184, 188–194, 208–209
- Hard sphere suspensions
  - colloidal glasses, 174–177
  - shear behavior, 188–193
  - viscoelastic behavior, 193–200
  - viscosity, 177–178
- Hedström number, 120, 125, 131, 134
- Helical flow, 151–153
- Hematocrit, 59, 93, 212, 225, 228, 231
- Hertz theory, 54
- Hopper, 394–397
- Huggins coefficient, 178, 210–211
- Hydration, 17, 20, 21, 25, 203
- Hydraulic performance, 312
- Hydrocyclone, 448–457
- Hydrodynamic
  - diameter, 13, 56–57
  - force, 168, 169, 179, 188
  - radius, 169
  - resistance, 65
- Hydrophobic, 17, 20, 21–22, 25
- Impeller
  - helical, 418
  - multiple, 422–424
  - ribbon, 416
- Inclined sedimentor, 440–442
- Indifferent ion, 13
- Interaction
  - particle-liquid, 310, 355–357
  - particle-pipe wall, 354–358
- Interactive
  - energy, 48, 58, 172
  - force, 27, 167, 169, 179, 386, 387
- Interfacial area, 401, 402, 432, 433
- Interfacial energy, 386–387
- Internal energy, 1, 18, 24, 168
- Interparticle contact, 332, 352
- Inverse gas chromatography, 391–392
- Isoelectric point, 14, 32, 36, 202, 203, 206
- Isotropic
  - length scale, 421, 423, 424
  - turbulence, 401, 421, 496
- Jamming, 174–177
- Just-draw-down speed, 406

- Keesom interaction, 3, 5
- Kneading, 426–428
- Knudsen number, 158
- Kolmogoroff length scale, 401, 421, 423–424
- Lagrangian, *see* Simulation models
- Laminar sub-layer, 353, 354
- Langevin
  - equation, 167, 179, 184
  - function, 37
- Lennard-Jones potential, 5, 14
- Leucocytes, 59, 228
- Lindemann criterion, 171
- Linear viscoelasticity, 76, 231
- Localization, 174, 186, 192, 193, 206, 208
- London potential, 4
- Lubrication effect, 159, 215
- Magnetic
  - permeability, 37, 254, 459, 466
  - susceptibility, 170, 439, 457, 465, 466
- Maximum packing, 220–221
- Mean free path, 1, 158
- Memory function, 173
- Micelle, 42, 44–49, 51
- Microchannels, 157–160
- Microemulsion, 13, 41, 42
- Microorganism, 65–66
- Microstructure, 24, 167, 175, 178, 179–183, 193–194, 208, 221–225
- Migration, 212–213, 347–348
- Mixers
  - design concepts, 403–407
  - dispersion of floating solids, 411–412
  - dispersion of settling solids, 408–411
  - power consumption, 412–420
  - scale-up, 420–424
  - static mixers, 424–426
- Mixing
  - active, 433–439
  - concentrated suspension, 426–431
  - efficiency, 402
  - passive, 432
- Mixing mechanisms
  - chaotic advection, 402
  - lamination, 401
  - turbulent convection, 401
- Modulus
  - elastic, 81, 174, 175, 196, 224
  - loss, 76, 80, 198
  - of elasticity, 48, 49, 75, 76, 80, 81, 193, 196, 207, 217, 224
  - storage, 76, 80, 198, 217, 235
  - viscous, 81, 95, 175, 235, 237
- Molecular recognition, 63
- Monodisperse, 170, 206–207, 279–282
- Motion of particles
  - spherical, 257–263
  - non-spherical, 263–268
  - porous aggregates, 268–276
  - with non-uniform density
    - distribution, 276–278
- Nernst equation, 13, 14
- Neutrally buoyant solid, 394, 397
- Newton
  - number, 412
  - regime, 256, 258, 259, 262
- Non-ergodic, 174, 193
- Non-Newtonian fluids, *see* rheological models
- Non-Newtonian fluid flow
  - in cylindrical pipes, 95–141
  - in microchannels, 157–160
  - in open channels, 160–167
  - through annulus, 141–153
  - through fittings, 135–141
  - through rectangular channels, 153–157
  - through sudden expansion, 135–141
  - laminar, 97–121, 153
  - transition, 125–127
  - turbulent, 121–135, 154
- Normal stress
  - coefficients, 73, 80
  - difference
    - first, 73, 80, 81, 83, 84, 85, 218, 231, 234–236
    - second, 73, 80
- Off-bottom-lifting, 406
- Oldroyd number, 110, 153
- Onsager equation, 210
- Oscillatory, 17, 20–21, 25, 33
- Osmotic pressure, 15, 18, 19, 23, 190, 207, 214, 223, 224
- Overlap concentration, 191, 210

- Particle diffusivity
  - rotational, 350–351
  - translational, 350–351
- Particle mobility, *see* Shield number
- Particle string, 218, 231, 235
- Paste, 72, 207–208, 221
- Péclet
  - number, 172, 185, 186, 188, 208, 210, 281, 443
  - time, 172, 181
- Penetration, 216, 385, 389–390, 391
- Percolation, 29, 174, 193, 194–195
  - threshold, 225
- Permittivity
  - electrical, 2, 467
  - relative, 2
- Phase shift angle, 76, 77, 79, 80
- Physical aging, 430
- Plasma, 59, 62, 228, 231
- Platelet, 60, 63–64, 208, 216
- Poisson
  - equation, 9
  - ratio, 83
  - Boltzmann, 10, 11, 15
- Polarization coefficient, 4
- Polydispersity, 173, 174, 207–208, 225
- Polyelectrolytes
  - coagulation by, 32–36
  - in separations, 466–471
  - stabilization by, 55–58
- Population balance, 493–500
- Potential determining ion, 13
- Power
  - consumption, 412–420
  - number, 405, 412, 413, 414, 415, 416
- Primary energy minimum, 12, 15
- Pseudo-plastic, 88
- Pulmonary circulation, 226
- Rabinowitsch-Mooney, 112, 113, 156
- Radial distribution function, 173, 188, 201, 223
- Radius
  - hydrodynamic, 169
  - of gyration, 23–24, 42, 58, 169, 189, 191, 192, 193
- Red blood cell, 13, 59, 61, 225, 230
- Reiner-Rivlin equation, 87
- Relaxation time, 198, 217, 460
- Restructuring, 15, 29, 31, 41
- Reynolds number
  - critical, 97, 125, 126, 127, 134
  - modified, 139, 140, 141
  - Metzner and Reed, 119, 123
  - transitional, 127
- Rheological models
  - Bingham, 91, 94, 101, 115, 122
  - Carreau, 89, 95
  - Casson, 91–92, 94, 101, 115, 153, 237, 427
  - Cross, 89
  - Herschel-Bulkley, 91, 92, 94, 100, 143
  - Ostwald-de Waele (Power law), 88, 94
  - Quemada, 92, 93–94, 211
  - Robertson-Stiff, 92–93, 148, 149
  - Sisko, 88–89, 95
- Rod, 208
- Roughness
  - Nikarudse, 354
  - relative, 353
- Rouleaux, 61, 62, 63, 225, 228, 229, 234, 235, 239
- Rouse-Schmidt model, 351, 366, 367
- Screening-reduced adsorption, 32
- Secondary energy minimum, 34, 35, 36, 495
- Secondary flow, 140, 192, 193, 433
- Segregation, 207, 291
- Separation
  - based on electrical properties, 466–471
  - based on magnetic properties, 465
  - field flow fractionation, *see* field flow separation
  - microfluidic bifurcations, 460
  - of magnetic particles, 459
  - of non-magnetic particles, 459
  - ultrasonic, 461–465
- Serum, 36, 225, 231, 232, 233, 234, 238
- Settling of
  - concentrated suspensions, 281
  - dilute suspensions, 280–281
  - polydisperse suspensions, 282–285
- Settling slurries
  - flow in horizontal pipes, 360–364
  - flow in inclined pipes, 365–366
  - flow in vertical pipes, 364–365
  - fine particle effect on flow pattern, 369–371
  - flow patterns, 330–332, 366–371, 376–385

- flow with stationary bed, 372–376
  - frictional losses, 353–358,
  - fully suspended flow, 330–331, 335–336, 351–352
  - particle size effect on flow pattern, 366–369
  - particle support mechanisms, 332
  - three-layer flow, 331, 332, 342–345, 349–351
  - two-layer flow, 331, 336–341, 363, 378
  - velocity effect on flow pattern, 369
- Settling velocity
  - hindered, 280, 281, 283, 346, 347, 352, 395, 408
  - terminal, 270, 350
- Shape factor (particles), 30, 263, 406–407
  - circulatory, 264
  - Corey, 264
  - skin factor, 264
  - sphericity, 264
- Shear
  - history dependence, 201
  - layer thickness, 23, 34, 53, 212, 215, 368–369
  - thickening, 88, 132, 134, 188–192
  - thinning, 88, 91, 125, 188–192, 413–415
- Shear behavior
  - of hard-sphere gels, 192–193
  - of hard-sphere suspensions, 188–192
  - of soft particle suspensions, 206–207
  - effect of aspect ratio, 208
  - effect of particle concentration, 212
  - effect of polydispersity, 207–208
  - of viscoelastic suspensions, 217–225
- Shield number, 357
- Shull correction factor, 54
- Simulation models
  - drift flux, 324–329
  - Eulerian-Eulerian, 294, 296–297
  - Eulerian-Fast Eulerian, 294
  - Eulerian-Lagrangian, 294–296
  - mixture, 312–325
  - single fluid, 312–315
  - super-particle Lagrangian, 294
  - two-fluid, 294, 305–312
- Single fluid model
  - in laminar flow, 312–314
  - in turbulent flow, 314
  - on macro-scale, 315–324
- Slip
  - apparent, 213
  - true, 213
  - velocity, 213
    - dimensionless, 318, 319, 324
    - mean, 318
- Soft particle suspensions
  - aspect ratio, 208
  - flow behavior, 206–212
  - polydispersity, 207–208
- Solvation force, *see* Hydration
- Specific
  - energy consumption, 408
  - power input, 408
- Spreading, 387, 389–390
- Square channel, 155, 157
- Stability ratio, 27, 31, 498
- Stabilization of suspensions by
  - nano-particles, 58
  - polymers and polyelectrolytes, 55–58
  - surfactants, 50–55
- Static mixer, 424–426
- Steric
  - force, 18, 22, 23–24, 36, 55, 62, 204
  - stabilization, 55, 460
- Stern layer, 11, 13
- Stokes
  - flow, 127, 246
  - law, 252, 270, 274, 276
  - regime, 256, 257, 259, 277, 279, 280, 295
  - velocity, 259, 282
- Stream function, 246, 248, 250
- Streamline, 246, 445
- Structure factor, 173
- Surface
  - charge density, 9, 51, 60–61, 62
  - forces, 25, 51–53, 201–206, 211–212
  - potential, 13, 14
  - tension, 385–393
- Surfactants, 42–55, 215–217
  - drag reduction by-, 215–217
  - self-assemblies
    - in solution, 46–49
    - on solid surfaces, 49
    - thermodynamics, 45
  - stabilization by-, 50–55
  - use in separations, 460

- Taylor number, 151
- Thermal
  - energy, 1, 37, 168, 171, 179, 185, 188
  - fluctuation, 168, 209
  - force, 184, 186
  - gel, 42, 193
- Theta temperature, 24, 34
- Thixotropic, 197
- Thixotropy, 199, 201
- Three-layer flow, 331, 332, 342–345, 349–351
- Thrombocytes, 59, 228
- Time scale
  - characteristic, 292, 293
  - particle, 296
- Torque, 265, 268, 276, 277, 345
- Transition velocity
  - limit deposit, 332, 333
  - suspending, 332, 333
- Trouton's rule, 74
- Turbulent diffusion, *see* Dispersion mechanisms
- Turbulent flow of non-Newtonian fluids
  - definition of Reynolds number, 122–125
  - in cylindrical channels, 121–134
  - in rectangular channels, 153
  - velocity distribution, 127–130
- Turbulent viscosity, 314
- Two-layer flow, 331, 336–341, 363, 378
- Two fluid model equations
  - continuity, 307
  - generalized, 305–307
  - momentum, 308–312
- Ultrasonic separation, 461–465
- van der Waals, 5, 6, 8, 62
- Velocity
  - characteristic, 358, 373
  - dimensionless, 127, 423
  - relative, 279, 284, 395
  - shear, 358
- Viscoelastic behavior, 77–86, 121, 183–184, 193–199, 217, 235, 236, 237
- Viscoelastic suspensions
  - particle viscoelasticity, 218–221
  - suspending medium viscoelasticity, 217
  - viscoelasticity due to microstructure, 221
- Viscoelasticity models
  - Burger, 198
  - Kelvin-Voigt, 198, 219
  - Maxwell, 198
- Viscosity
  - apparent, 88, 89, 91, 228, 413, 427, 428
  - based on Stokesian Dynamics simulations, 184–188
  - based on suspension microstructure, 179–183
  - complex, 77, 81, 82, 83, 184
  - dynamic, 83, 84
  - elongational, 216
  - extensional, 74
  - infinite shear, 191, 206
  - intrinsic, 177, 178, 209, 210
  - non-Newtonian fluids, 87–90, 95
  - of colloidal suspensions, 177
  - reduced, 212
  - reduced specific, 177
  - relative, 177–178, 186, 192, 210, 221, 231, 234
  - zero shear, 189, 191
- Volume exclusion, 179
- Wall
  - effect, 261–263
  - factor, 261, 262
  - slip, 201, 430
- Weissenberg
  - effect, 73, 218
  - number, 73, 231
- Wetting, 385–393
- White blood cell, 59
- Work of cohesion, 386
- Yield stress, 90–92, 214
- Young's modulus, 53
- Young-Laplace equation, 388–389
- Zeta potential, 13, 202, 203, 204

This page intentionally left blank